PARTICLES, STRINGS AND THE EARLY UNIVERSE

The Structure of Matter and Space-Time

Particles, Strings and the Early Universe

The Structure of Matter and Space-Time

Research Results of the Collaborative Research Centre SFB 676 in Hamburg

July 2006–June 2018

Universität Hamburg and DESY

Editors: Johannes Haller, Michael Grefe

Verlag Deutsches Elektronen-Synchrotron

Impressum

Particles, Strings and the Early Universe: The Structure of Matter and Space-Time

Research Results of the Collaborative Research Centre SFB 676 in Hamburg

July 2006–June 2018, Universität Hamburg and DESY

Webpage
`http://www.iexp.uni-hamburg.de/sfb676/`

Unless otherwise stated the copyright is governed by the Creative Commons agreement under CC BY 4.0, which allows to copy, distribute, display and perform the work and make derivative works and remixes based on it only if they give the author or licensor the credits (attribution) in the manner specified by these.



Editors:
Johannes Haller, Michael Grefe
September 2018
DOI: 10.3204/PUBDB-2018-00782
ISBN 978-3-945931-21-9

Published by
Verlag Deutsches Elektronen-Synchrotron
Notkestraße 85
22607 Hamburg
Germany

Printed by
Kopierzentrale Deutsches Elektronen-Synchrotron

Preface

Within the Collaborative Research Centre SFB 676 “Particles, Strings and the Early Universe: The Structure of Matter and Space-Time” funded by the German Research Foundation (DFG), scientists of Universität Hamburg and DESY have performed research at the interface of mathematical physics, particle physics and cosmology. Started in June 2006, the SFB 676 has approached its completion in June 2018, after a maximum funding period of 12 years. During these years, the research areas of the SFB have seen tremendous progress on many fronts, highlighted by the scientific breakthroughs of the discovery of the Higgs boson in 2012 and the first observation of gravitational waves in 2015.

In this book, we take the opportunity to review the scientific achievements and research highlights obtained in the context of the SFB 676, the current state and the perspectives of the respective fields. The content of the book reflects the organisational structure of the SFB 676 with its three research areas: A) String Theory, B) Particle Physics and C) Cosmology. The individual chapters have been contributed by the principal investigators and other key researchers of the various sub-projects whom we would like to thank for their contributions, for their commitment, and for their brilliant research work during the course of the SFB. In addition to the involved local scientists, many guest researchers whom we welcomed in Hamburg provided essential contributions to the research of the SFB.

The success of the SFB 676 would not have been possible without the help of many people in the administration and management. We would like to thank in particular Marco Baumgartl, Elizabeth Duarte, Holger Enderle, Manfred Fleischer, Irmgard Flick, Daniel Gildenhorn, Frank Laubert, Juan Mercado, Natalia Potylitsina-Kube, Harald Schlüter and Department 4 of Universität Hamburg, Lilija Seskute, and Peter Siebeneichner. Very special thanks go to our closest companions Michael Grefe, Petra Hinzer, and Wiebke Kircheisen, who have strongly shaped this SFB over the years with their savvy and clever ideas and initiatives, their unbreakable enthusiasm, and their indispensable help. In addition, we are of course grateful to the DFG for their help and support during the last 12 years, in particular we would like to thank Brit Redöhl. Last but not least, we acknowledge the continuous enormous support of our two hosting institutions in Hamburg: Universität Hamburg and DESY.

Thank you very much!

Hamburg, September 2018

Johannes Haller
Jan Louis

Contents

A String Theory **1**

Particle Physics from String Compactifications **3**
Wilfried Buchmüller, Jan Louis

Strings and High Energy Scattering **19**
Jochen Bartels, Sven-Olaf Moch, Volker Schomerus

Non-Abelian Gerbes and some Applications in String Theory **39**
Christoph Schweigert, Konrad Waldorf

Mathematical Aspects of String Compactifications **57**
Vicente Cortés, Jan Louis

Loops and Legs **69**
Rutger H. Boels, Bernd A. Kniehl

Topological Field Theories from and for 4d SUSY Gauge Theories **89**
Christoph Schweigert, Jörg Teschner

Integrable Deformations of the AdS Superstring and their Dual Gauge Theories **103**
Gleb Arutyunov, Inko Runkel, Jörg Teschner

B Particle Physics **123**

Optimising the ILC Setup **125**
Jenny List, Gudrid Moortgat-Pick, Jürgen Reuter

Studies of Boosted Topologies and Jet Substructure at the LHC **155**
Johannes Haller, Roman Kogler, Frank J. Tackmann

Studies of the MSSM Parameter Space at the LHC **169**
Sam Bein, Christian Sander, Peter Schleper

Neutrinos in the Standard Model **179**
Alessandro Mirizzi

Unstable Quantum Fields and Higgs Vacuum **189**
Bernd A. Kniehl

Global SM and BSM Fits using Results from LHC and other Experiments **203**
Emanuele Bagnaschi, Philip Bechtle, Johannes Haller, Roman Kogler, Thomas Peiffer, Tim Stefaniak, Georg Weiglein

Probing the Nature of Higgs Physics and Electroweak Symmetry Breaking **231**
Peter Schleper, Kerstin Tackmann, Georg Weiglein

Top-Quark Physics at the LHC **255**
Sven-Olaf Moch, Jürgen Reuter

SUSY Phenomenology—From the Early Universe to the LHC Era **271**
Jörn Kersten

C Cosmology **283**

Axions and other WISPs **285**
Dieter Horns, Andreas Ringwald, Le Hoang Nguyen, Andrei Lobanov

Dark Matter Searches **301**
Marcus Brüggen, Dieter Horns, Christian Spiering, Jannis Kummer, Chao Zhang

Leptogenesis and Dark Matter **317**
Wilfried Buchmüller

Supernovae Type Ia & Dark Energy **333**
Peter Hauschildt

Scalar Fields in Cosmology: Inflation, Dark Matter, Dark Energy **341**
Jan Louis, Alexander Westphal

Thermodynamics of Quantum Fields in Nonstationary Spacetimes **363**
Klaus Fredenhagen, Thomas-Paul Hack, Nicola Pinamonti

Propagation of Very High Energy Radiation in the Universe **379**
Günter Sigl

Cosmic Magnetic Fields and their Role in High Energy Astrophysics **387**
Robi Banerjee, Günter Sigl

Cosmological Implications of First-Order Phase Transitions **407**
Thomas Konstandin, Günter Sigl

Section A

String Theory

Particle Physics from String Compactifications

Wilfried Buchmüller[1], *Jan Louis*[2]

[1]DESY, Hamburg, Germany
[2]II. Institut für Theoretische Physik, Universität Hamburg, Germany

DOI: http://dx.doi.org/10.3204/PUBDB-2018-00782/A1

We briefly review the work carried out in project A1 of the SFB 676. This includes in particular string compactifications to vacua containing the Standard Model. We compare heterotic compactifications with F-theory, and we mention a number of technical developments. Motivated by string compactifications, several aspects of six-dimensional field theories are described, which shed some light on supersymmetry breaking, moduli stabilization and the little hierarchy problem. We highlight some virtues of flux compactifications and conclude with a brief discussion of LHC phenomenology.

1 Introduction

String theory remains the most promising framework for a unification of the Standard Model with gravity. The key features of the Standard Model, chiral gauge interactions and the Brout–Englert–Higgs mechanism of mass generation for chiral fermions, naturally emerge in string compactifications. On the other hand, the vacuum structure of string theories is complicated, which makes it difficult to understand details of the Standard Model as consequences of a string compactification. It has been the goal of project A1 to contribute to the work needed to bridge the gap between particle physics and string theory.

A major effort has been made to study in detail phenomenologically promising string compactifications, starting from the heterotic string with symmetry group $E_8 \times E_8$, and also from F-theory. As an intermediate step, compactifications to six dimensions have been investigated. Six-dimensional supergravity theories with gauge unification turned out to be a good starting point for deriving four-dimensional supersymmetric extensions of the Standard Model with some specific predictions for experiments at the Large Hadron Collider (LHC), which we have also studied.

In 2012, right in the middle between beginning and end of the Collaborative Research Center 676, the Higgs boson was discovered with a mass of 125 GeV. This mass value allows a consistent extrapolation of the Standard Model as a weakly coupled theory from the electroweak scale up to the scale of grand unification. This is in accord with expectations based on supersymmetric theories. On the other hand, so far extensive searches at the LHC have shown no signs of supersymmetry. Hence, the scale of supersymmetry breaking may lie much above the electroweak scale, so that the mass of the Higgs boson cannot be entirely protected by supersymmetry. The matching of the Standard Model to a supersymmetric theory at scales far above the electroweak scale has therefore been an important topic during the second phase of the project A1.

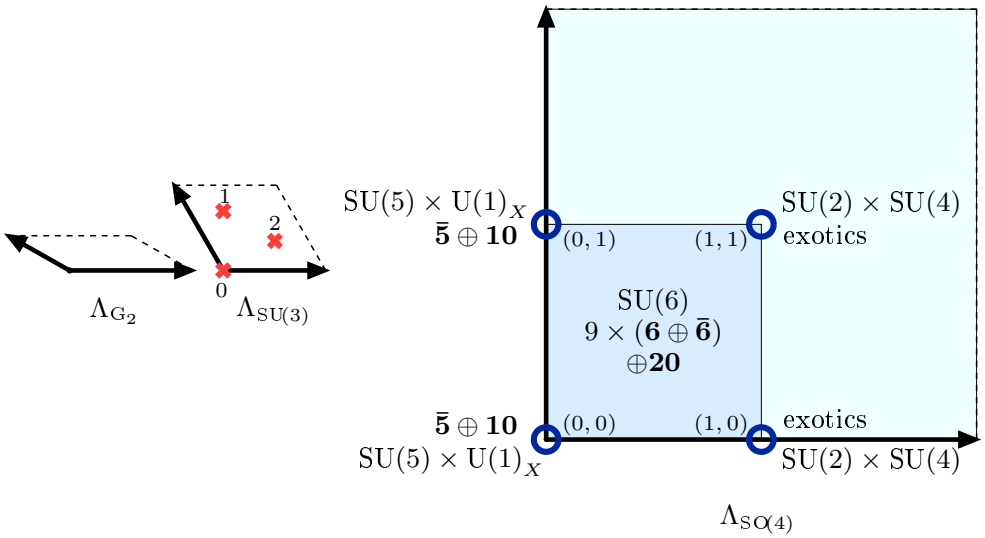


Figure 1: The six-dimensional orbifold GUT model with the unbroken non-Abelian subgroups of the visible E_8 and the corresponding non-singlet hyper and chiral multiplets in the bulk and at the $SU(5)$ fixed points, respectively. Fixed points under the $\mathbb{Z}_2$ subtwist in the $SO(4)$ plane are labelled by tupels (n, m), those under the $\mathbb{Z}_3$ subtwist in the $SU(3)$ plane are indicated by the red crosses. The $\mathbb{Z}_6$ fixed point in the G_2 plane is located at the origin. Reprinted from Ref. [3], with permission from Elsevier.

In the report we shall first discuss results on string compactifications. Subsequently, we will deal with *string inspired* supersymmetric models in six and four dimensions as well as some specific predictions for collider physics. We shall conclude with an outlook on *Particle physics from string compactifications*. It is impossible to give adequate references to all the work that motivated and stimulated the research carried out within the project A1. Excellent reviews of basics and recent developments of supergravity and string theory are [1, 2]. These reviews also contain extensive references. Beyond that we refer the reader to the references given in the papers described below.

2 String compactifications

During the first phase of the project the focus has been on compactifications of the $E_8 \times E_8$ heterotic string. This was partly motivated by the success of orbifold GUTs, higher-dimensional field theories with grand unified gauge groups compactified on orbifolds. In these theories the GUT gauge groups can be broken in an elegant way by means of boundary conditions, and one can easily understand why the Higgs doublet has no colour-triplet partner, which is the so-called doublet-triplet splitting problem. In [4, 5] it was shown that a six-dimensional (6d) orbifold GUT can indeed be obtained as intermediate step in an anisotropic compactification of the heterotic string on a $\mathbb{Z}_6$ orbifold. First, the ten-dimensional string is compactified on the orbifold $T^4/\mathbb{Z}_3$ to six dimensions where one obtains a theory with $\mathcal{N} = 2$ supersymmetry and

unbroken gauge group

$$G_6 = SU(6) \times U(1)^3 \times [SU(3) \times SO(8) \times U(1)^2] \,,$$

where the brackets denote the unbroken subgroup of the second E_8. In a second step, the 6d theory with one Wilson line is compactified to four dimensions, with unbroken $\mathcal{N} = 1$ supersymmetry. The intersection of unbroken subgroups at the two pairs of inequivalent fixed points yields the Standard Model gauge group,

$$G_{SM} = SU(3) \times SU(2) \times U(1) \subset SU(5) \times U(1) \cap SU(2) \times SU(4) \,.$$

Two quark-lepton families are located at the $SU(5)$ fixed points of the $SO(4)$ plane, and a third family consists of split multiplets of the 6d bulk hypermultiplets, see Figure 1. As a consequence, there is only one large Yukawa coupling, the top quark coupling, which is related to the 6d gauge coupling. All other Yukawa couplings are generated by higher-dimensional operators.

In a parallel development M-theory compactifications on seven-dimensional manifolds with SU(3) structure were studied [6], which lead to $\mathcal{N} = 2$ supersymmetric theories in four dimensions. These compactifications were shown to be dual to compactifications of the heterotic string on $K3 \times T^2$, with background gauge field fluxes on T^2. The low energy effective action was derived, and the Kähler potential, the superpotential and the D-terms were computed in terms of geometrical quantities. For comparison with anisotropic orbifold compactifications with an intermediate 6d orbifold GUT, heterotic compactifications on generalized $K3$ manifolds with $SU(2)$ structure are particularly interesting. Such compactifications were investigated in [7] where the kinetic terms and the scalar potential were derived. Directly relevant for the orbifold compactification of [4] is the computation of the $\mathcal{N} = 1$ low-energy effective action for the compactification of the heterotic string on a smooth $K3$-surface to six dimensions [8,9]. The gauge symmetry breaking was studied at the level of the effective Lagrangian and special attention was payed to the couplings of the charged matter multiplets to the geometrical moduli fields. It turned out that these couplings are heavily contrained by gauge invariance together with supersymmetry. Possible embeddings of line bundles into the ten-dimensional gauge groups of heterotic strings were systematically investigated in [10] and the associated gauge symmetry breakings and spectra were analyzed. The naive expectation that one may be able to construct an infinite number of MSSM-like models by varying the line bundles appears to be incorrect [11]. It is possible, however, to construct supersymmetric as well as non-supersymmetric Standard Model-like compactifications to four dimensions for the three ten-dimensional gauge groups $E_8 \times E_8$, $SO(32)$ and $SO(16) \times SO(16)$, respectively [12–14]. Generically, in heterotic orbifold compactifications magnetic gauge flux in the compact dimensions is not incorporated. In higher-dimensional field theories magnetic flux can be taken into account, which leads to interesting effects. According to the index theorem, a multiplicity of quark-lepton families can arise as zero modes, and the supersymmetry breaking scale is determined by the size of the compact dimensions, yielding a picture of *split symmetries* with respect to GUT gauge symmetries on the one hand, and supersymmetry on the other hand [15–17].

A challenging topic is the relation between heterotic orbifold models and their smooth counterparts. In [18] a specific Borsea-Voison manifold of the form $(K3 \times T^2)/\mathbb{Z}_2$ was identified which corresponds to a specific blow-up of the $T^6/\mathbb{Z}_6$ orbifold considered in [4]. The blow-up process is illustrated in Figure 2. At the top $T^4/\mathbb{Z}_3$ is shown, a singular $K3$ that is elliptically fibered over the base $T^2/\mathbb{Z}_3$. Over the singular points of the base, the torus degenerates to

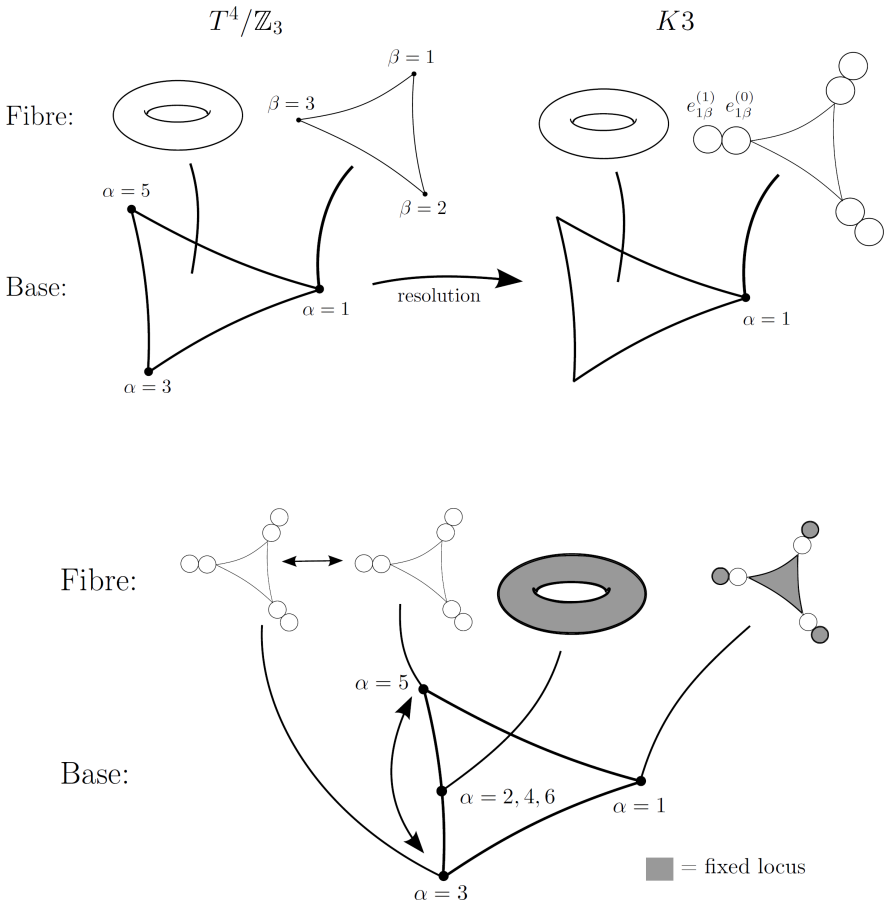


Figure 2: Top: The singular space $T^4/\mathbb{Z}_3$ (left) is blown up to a smooth $K3$ manifold (right). In this process each singularity is replaced by two spheres. Bottom: $\mathbb{Z}_2$ fixed locus on the smooth $K3$. Figures taken from Ref. [18].

$T^2/\mathbb{Z}_3$. $T^4/\mathbb{Z}_3$ has nine singularities, see Figure 1. The transformation of the shrinking cycles under the $\mathbb{Z}_2$ involution is illustrated at the bottom of Figure 2. Surprizingly little was known about the moduli space of the Borsea-Voison manifolds. We found that the vacuum expectation values (VEV) needed to blow up the orbifold completely, break the orbifold gauge group to a small subgroup. Moreover, by going to a smooth point in moduli space, all massless twisted states, which correspond to geometric moduli, aquire non-zero VEVs, breaking the orbifold gauge group. It turns out that the resulting light spectrum is non-chiral with respect to the unbroken gauge group, which matches with the results obtained for smooth compactifications. Phenomenologically, one wants a massless chiral spectrum with respect to the Standard Model gauge group. To fully understand the connection between successful singular orbifold constructions and compactifications of the ten-dimensional $E_8 \times E_8$ supergravity theory on smooth manifolds, further investigations are necessary.

An important technical aspect in the construction of 4d effective actions for orbifold com-

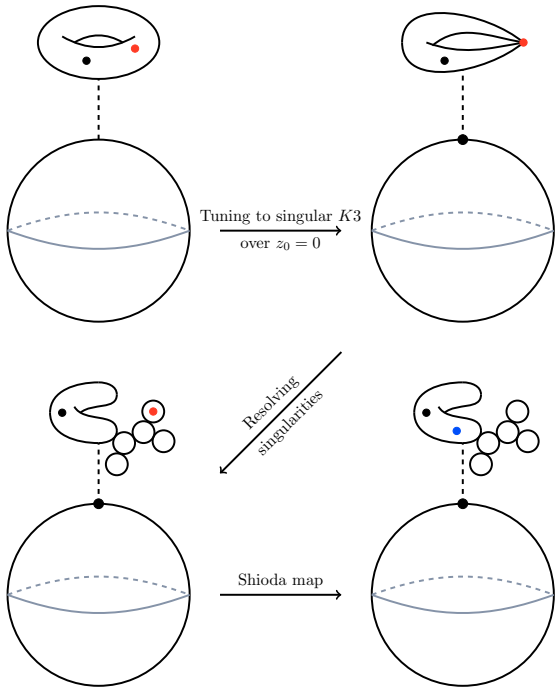


Figure 3: Construction of $SO(10) \times U(1)$ models. The fibration of the torus over $\mathbb{P}^1$ (top left) turns via tuning into a singular $K3$ manifold (top right). Resolution of the singularity generates five $\mathbb{P}^1$s with intersections corresponding to the extended $SO(10)$ Dynkin diagram (bottom left); after the Shioda map has been carried out, the $U(1)$ divisor intersects the affine node $\mathbb{P}^1_0$ (bottom right). Figure taken from Ref. [29].

pactifications of 5d and 6d supergravity theories are the brane-bulk couplings, since at the orbifold fixed points supersymmetry is broken. Several subtle points could be clarified in [19–23]. The boundary conditions also affect the fluctuations of the various bosonic fields around the gravitational background [24] and the stability of gauge flux compactifications [25]. In the effective 4d supergravity actions a crucial role is played by Fayet–Iliopoulos (FI) D-terms. The relation between computations of such D-terms in field theory and string theory was studied in [26].

An important and lasting result is the complete classification of six-dimensional symmetric toroidal orbifolds which yield $\mathcal{N} \geq 1$ supersymmetry in four dimensions for the heterotic string [27]. The starting point was a classification of the crystallographic space groups in six dimensions. In total 520 inequivalent toroidal orbifolds were found, 162 of them with Abelian point groups such as $\mathbb{Z}_3$, $\mathbb{Z}_4$, $\mathbb{Z}_{6-I}$ etc. and 358 with non-Abelian point groups such as S_3, D_4 etc. For some of these orbifolds the Hodge numbers were calculated and possible mechanisms of gauge symmetry breaking were explored. Particle spectra for heterotic compactifications on non-Abelian orbifolds were studied in [28].

During the course of the project the emphasis shifted from heterotic compactifications to F-theory where four-dimensional theories are obtained by compactifications on elliptic Calabi–

Yau fourfolds. In order to obtain chiral models it is necessary to turn on four-form flux G_4 on the fourfold. In [30, 31] a new construction of globally well defined G_4 flux was given which relies on identifying certain algebraic cycles in the Weierstrass equation of the fourfold. Subsequently, in [32] explicit chiral models were constructed with moduli stabilized in terms of magnetized D7-branes on smooth Calabi–Yau spaces. The previously encountered problems, such as the tension between chiral matter and moduli stabilization, the tension between Freed-Witten anomaly cancellation, nonperturbative effects and shrinking induced by D-terms, were overcome. This was extended in [33] where quasi-realistic models on branes at singularities were constructed with a fully consistent global embedding (including tadpole, K-theory charges and Freed-Witten anomaly cancellation) combined with moduli stabilization. The connection between heterotic and F-theory to six dimensions was analyzed in [34]. Using the Weierstrass description the complex structure of the Calabi–Yau threefold could be restricted such that the gauge group and the matter spectrum of the heterotic compactification on singular $T^4/\mathbb{Z}_N$ orbifolds were reproduced.

As we shall see in the following section, 6d supergravity models with gauge symmetry $SO(10) \times U(1)$ provide phenomenologically interesting GUT extensions of the Standard Model. This raises the question whether such models can be embedded in string theory. This question was systematically investigated in the context of F-theory. In [29], using toric geometry, 6d F-theory vacua with gauge group $SO(10)$ were completely classified, taking into account Mordell–Weil $U(1)$ and discrete gauge factors. The full matter spectrum of these models was determined, including charged and neutral $SO(10)$ singlets. Based solely on the geometry, all matter multiplicities were computed and the cancellation of gauge and gravitational anomalies was confirmed independent of the base space. The principle of the construction of the models is illustrated in Figure 3.

3 Model building

The compactifications of the heterotic string described above yield the Standard Model (SM) gauge group and a supersymmetric extension of the chiral SM matter spectrum with two Higgs doublets (MSSM). However, in addition a large number of massless SM singlet fields occur. Their vacuum expection values are largely undetermined since the superpotential of the theory is only partially known. This leads to a large vacuum degeneracy of the theory. Different vacua, corresponding to different sets of singlet vacuum expectation values, can differ significantly in their physical properties. For instance, they can realize gauge-Higgs unification or partial gauge-Higgs unification (for only one Higgs doublet) [3], and they also have different unbroken discrete R-symmetries [3, 35, 36]. These R-symmetries can be used to suppress perturbative contributions to the μ-term and the expectation value of the superpotential, i.e. the gravitino mass. Nonperturbative contributions can then generate large hierarchies. The many SM singlets in heterotic compactifications can partly also play the role of sterile neutrinos, which significantly modifies the seesaw mechanism [37]. In general, the discrete symmetries of heterotic vacua have important phenomenological implications for axion-like particles [38], family symmetries [39], the proton lifetime [40] and neutrino masses [41]. Interesting discrete symmetries also arise in MSSM type quiver models [42]. Flavour symmetries are more hidden in flux compactifications where the multiplicity of quark-lepton generations is generated by magnetic flux in the compact dimensions [43]. Nevertheless, there exist a number of relations between Yukawa couplings, remnants of the underlying GUT symmetry and the wave function

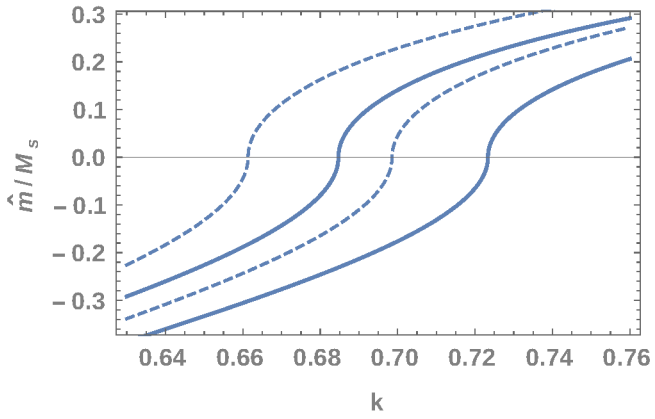


Figure 4: The scale ratio $\hat{m}^2/M_s^2$ as function of the mass ratio $k = M_{1/2}/m_0$ for $\lambda_0 = 0.4, 0.001$ (left to right) and $\tan\beta = 6, 15$ (dashed, full). $M_s = 3$ TeV. Figure taken from Ref. [47].

profiles of the zero modes. This can lead to a successful flavour phenomenology, including thermal leptogenesis [44].

One of the SM singlets in heterotic compactifications can play the role of a singlet Higgs field, extending the minimal supersymmetric standard model (MSSM) to the next-to-minimal supersymmetric standard model (NMSSM) [45,46]. Here the μ-parameter becomes a field, which alleviates the *μ-problem* of the MSSM. However, since no superparticles were discovered at the LHC so far, both the MSSM and the NMSSM have a *little hierarchy problem*: The ratio between the Fermi scale of electroweak symmetry breaking and the scale of supersymmetry breaking is much smaller than one, contrary to early expectations, which calls for an explanation.

Characteristic parameters for the scale of electroweak symmetry breaking and supersymmetry breaking are $\hat{m}$, a function of the two soft Higgs mass parameters, together with $\tan\beta$, the ratio of the Higgs VEVs, and the geometric mean M_s of the scalar top masses, respectively,

$$\hat{m}^2 = \frac{m_{h_d}^2 - \tan^2\beta\; m_{h_u}^2}{\tan^2\beta - 1}\,, \quad M_s = \sqrt{m_{\tilde{t}_1} m_{\tilde{t}_2}}\,.$$

The little hierarchy problem then corresponds to the unexpected observational fact

$$\hat{m}^2/M_s^2 \ll 1\,.$$

In typical gravity mediation schemes, such as dilaton domination [48], this inequality can only be satified by a rather fine-tuned choice of the soft supersymmetry breaking parameters. One may hope that such fine-tuned parameters are an automatic consequence of relations between supersymmetry breaking terms at the GUT scale, predicted by supersymmetry. This can indeed happen, for instance, in hybrid gauge-gravity mediation [49] due to a particular choice of messenger fields [50]. Alternatively, one can hide the fine-tuning in a particular mass relation between the universal gaugino and scalar masses at the GUT scale, $M_{1/2} = km_0$ [51]. An example of this type is shown in Figure 4 for the NMSSM, where the ratio of mass scales $\hat{m}^2/M_s^2$ is plotted as function of k for different choices of the Yukawa coupling λ_0 between SM singlet and doublet Higgs fields and $\tan\beta$ [47,52]. For values of k around 0.7, which can be derived in

Parameters	P1	P2	P3	P4
λ_0	0.33	10^{-4}	0.1	10^{-3}
M_0 [GeV]	2000	2500	3000	3500
m_0^2 [GeV^2]	$7 \cdot 10^6$	$9.5 \cdot 10^6$	$1.35 \cdot 10^7$	$1.75 \cdot 10^7$
m_{h_s} [GeV]	1850	114.5	907.4	178.3
m_h [GeV]	123.6	126	125.7	127.9
$m_H, m_{H^\pm}, m_A$ [GeV]	2824	3434	4067	4660
m_{a_s} [GeV]	1040	66.65	561	108.8
$m_{\tilde{\chi}_s}$ [GeV]	1659	93.65	814.4	147.8
$m_{\tilde{\chi}_{\mu_1}}$ [GeV]	491	695	693	766.2
$m_{\tilde{\chi}_{\mu_2}}$ [GeV]	497	700	696	770
$m_{\tilde{\chi}_{\rm bino}}$ [GeV]	880	1106	1335	1569
$m_{\tilde{\chi}_{\rm wino}}$ [GeV]	1642	2056	2473	2893
$m_{\tilde{g}}$ [GeV]	4070	5145	6104	7047
$m_{\rm squark}$ [GeV]	2680-3760	3330-4630	3930-5480	4540-6310
$m_{\rm slepton}$ [GeV]	667-1300	840-1620	1000-1940	1180-2250

Table 1: Higgs and superparticle masses for typical parameter sets P1, P2, P3, P4, with $\tan\beta = 15$ and $M_s = 3.0, 3.8, 4.5, 5.0$ TeV (from left ro right). Table taken from Ref. [47].

a higher-dimensional model with gaugino mediation, a small ratio $\hat{m}^2/M_s^2$ can be obtained. It is instructive to work out the mass spectrum of Higgs bosons, higgsinos, gauginos, squarks and sleptons. As Table 1 demonstrates, except for the Higgs boson h, and possibly the higgsinos h_s and the singlino $\tilde{\chi}_s$, all superparticles have masses outside the discovery range of the LHC. The lightest superparticle is typically the gravitino with a mass in the range between 10 GeV and 100 GeV. Such a Higgs and superparticle mass spectrum, containing as light particles only singlinos in addition to the Higgs boson, is typical for models that address the little hierarchy problem. In the MSSM the supersymmetry breaking scale M_{SS} cannot exceed a value of about 10^{10} GeV. Otherwise, the running quartic Higgs coupling $\lambda(M_{SS})$ of the SM cannot be matched to the corresponding combination of gauge couplings in the MSSM. Note that this situation changes in the NMSSM where the effective quartic Higgs coupling is modified. As a consequence, in the NMSSM the supersymmetry breaking scale can be as large as the GUT scale [53].

A notoriously difficult problem in string compactifications is the stabilization of all moduli fields at a vacuum with vanishing or very small cosmological constant. Contributions from various perturbative and non-perturbative effects to the stabilization of bulk moduli were studied for explicit heterotic orbifold compactifications. Several de Sitter solutions could be found which, however, all turned out to be unstable [54]. As already mentioned in the previous section, considerable progress was made in stabilizing Kähler moduli for chiral D7-brane models within the framework of type IIB flux compactifications. World-volume fluxes can be chosen to obtain GUT- or MSSM-like theories. Moreover, TeV-scale supersymmetry breaking can be realized [32, 33].

It is instructive to study moduli stabilization also in higher-dimensional field theories. Here one only has a few moduli and the system is simple enough that quantum corrections can be

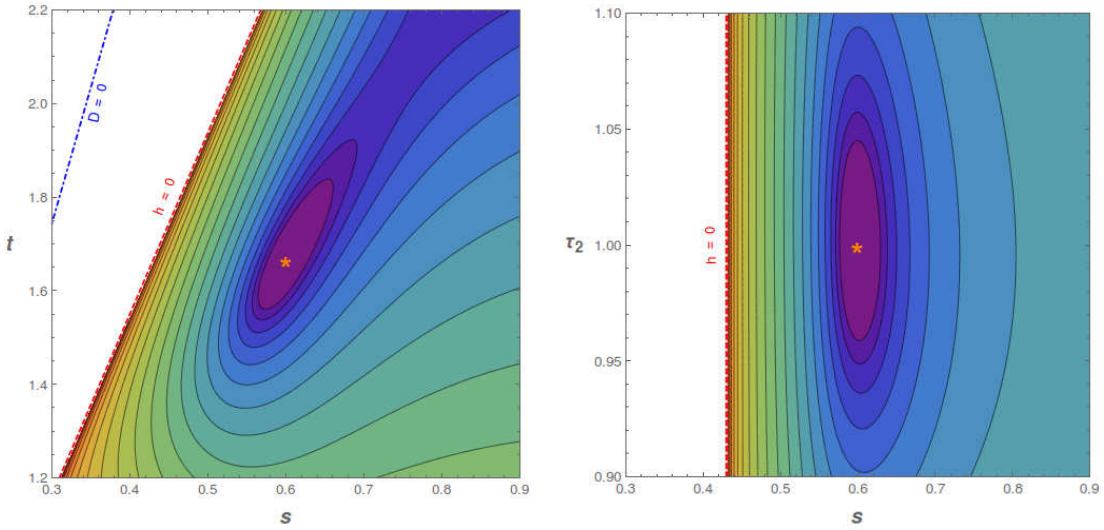


Figure 5: Contour plot of the moduli potential as function of the 3 fields s, t and τ_2 in the $s-t$ plane, $\tau_2 = 1$ (left) and in the $s-\tau_2$ plane, $t = 5/6$ (right). The remaining 3 moduli are stabilized at the origin. The size of the volume is $V = L^2/2$, with $L = 200$ in Planck units. Reprinted figure with permission from Ref. [60]. Copyright (2016) by the American Physical Society.

taken into account. In [55–57] it was shown that the Casimir energy together with localized FI terms can lead to a stabilization of shape and volume moduli. Moreover, the interplay of quantum corrections of the Kähler potential, localized FI terms and the Casimir energy can yield *almost no-scale* models with light moduli [58]. Particularly interesting are 6d orbifold models with magnetic flux. The D-term potential contains two FI terms which are induced by the flux and by the Green–Schwarz term canceling the gauge anomalies, respectively. The Green–Schwarz term also leads to a correction of the gauge kinetic function which turns out to be crucial for the existence of Minkowski and de Sitter vacua. The stabilization of all 6 moduli is achieved by the interplay of the D-terms and a nonperturbative superpotential [59–61], see Figure 5.

Moduli fields have important cosmological implications. For instance, a light axion-dilaton system can lead to recurrent acceleration [62, 63]. An interesting aspect of heterotic orbifold compactifications with several axions is the possible alignment of more than one axion, which can lead to inflation with trans-Plankian field values [64]. In the superpotential of these models gaugino condensates play an important role. Here one has to take into account that hidden Yang–Mills sectors are cosmologically strongly constrained by possible dark glueball overproduction during the cosmological evolution [65].

Since no hints for supersymmetry have been observed at the LHC, one is left with some kind of hierarchy problem in supersymmetric theories, maybe a *little hierarchy problem* or a *GUT hierarchy problem*. It is clear that supersymmetry alone is not sufficient to protect the Higgs mass and the question arises whether higher-dimensional theories can provide other mechanisms to screen the Higgs mass from quadratic divergencies. In recent work it was observed that in flux

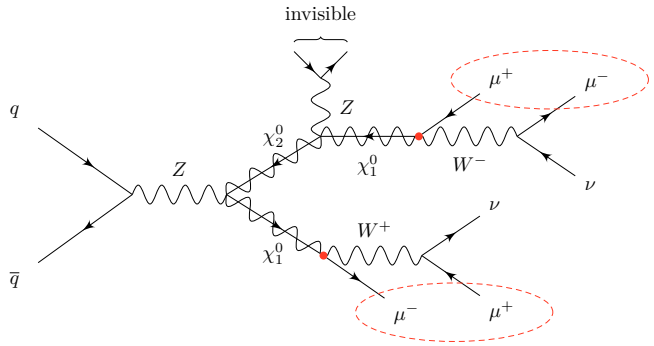


Figure 6: Typical R-parity violating decay chain involving higgsinos at the LHC. The secondary vertices as well as the two possibilities of interesting muon combinations are highlighted. The Z-boson decay is invisible, due to the small mass difference between the heavier higgsino and the lightest higgsino. Figure taken from Ref. [68].

compactifications, contrary to the case without flux, a cancellation of quadratic divergencies occurs, which can be traced back to a spontaneously broken symmetry of the higher-dimensional field theory [66]. In fact, in the 4d effective theory this manifests itself as a shift symmetry of a complex scalar, which forbids the generation of a mass term to all orders in perturbation theory [67]. So far the described cancellation of quadratic divergencies has only been studied in a toy model, an Abelian gauge theory in six dimensions. It remains to be seen whether the mechanism also works for more realistic non-Abelian gauge theories.

4 Connection to collider phenomenology

Collider phenomenology did not play a significant role in project A1. Nevertheless, trying to derive particle physics from string theory, some phenomenological signatures at the LHC, aside the main stream, were studied for a few aspects of the theoretical models described above.

An intriguing aspect of the models described in [47,49–51], which address the little hierarchy problem, and also of the model [15,43] with high-scale supersymmetry breaking, is the occurence of light higgsinos, with masses between hundred and a few hundred GeV. This is not too surprizing, since their mass is protected by a Peccei–Quinn type symmetry, contrary to gauginos. At the LHC one can search for light higgsinos by means of monojet events, but this is very challenging. A further possibility exists in the case of a light gravitino and small R-parity breaking, which is of particular interest also in connection with leptogenesis. Gravitinos can then be the dark matter of the universe, and their decay to neutrino-photon pairs produces monochromatic γ-rays, which in particular the Fermi-LAT collaboration has searched for. This has led to a current upper bound on the R-parity breaking parameter ζ of about 10^{-8}. Such a small breaking of R-parity can be understood, for instance, by dynamical symmetry breaking in a strongly interacting hidden sector of the theory [69]. Gravitino decays and R-parity violating decays of the lightest higgsino χ_1^0 are controlled by the same parameter ζ,

$$\Gamma_{3/2} \propto \zeta^2 \frac{m_{3/2}^3}{M_P^2}\,, \qquad \Gamma_{\chi_1^0} \propto \zeta^2 m_{\chi_1^0}\,,$$

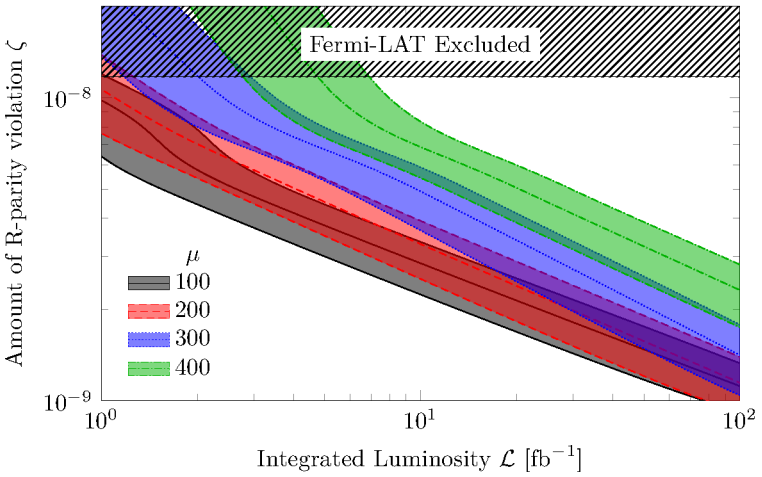


Figure 7: Estimation of the discovery reach for R-parity breaking higgsino decays at the LHC with 14 TeV center-of-mass energy. Each coloured band represents a value of the higgsino mass parameter μ. Figure taken from Ref. [68].

which implies interesting direct relations between astrophysics and collider physics. Moreover, R-parity violating higgsino decays, e.g. $\chi_1^0 \to W^\pm \mu^\mp$, can significantly help in the search for light higgsinos at the LHC [68,70]. A typical R-parity violating decay chain involving higgsinos with two $\mu^+\mu^-$-pairs is shown in Figure 6. Based on these and similar R-parity violating decay chains, the discovery reach at the LHC for R-parity breaking supersymmetry has been derived in a detailed investigation, see Figure 7. It is remarkable that the current run at 13 TeV center-of-mass energy is about one order of magnitude more sensitive to R-parity breaking than the astrophysical searches for monochromatic gamma-ray lines [68].

A characteristic feature of the models with flux compactification [15, 43] is the difference of supersymmetry breaking in the matter sector and the Higgs sector, respectively. Quarks and leptons, which come in three copies of complete GUT representations, have very heavy superpartners, with masses at the GUT scale. On the contrary, the Higgs sector consists of split multiplets, one pair of Higgs doublets and higgsinos, and has $\mathcal{N} = 1$ supersymmetry at tree-level. Note that gauge coupling unification is realized with acceptable accuracy. To verify the consistency of such a scheme, one has to show that the running couplings of the Higgs potential can be matched to a supersymmetric theory at the GUT scale, where they are known functions of the gauge couplings, satisfying also constraints from vacuum (meta)stability. It was shown that, contrary to the SM with one Higgs doublet, this is indeed possible [71]. The results severely constrain the ratio of Higgs VEVs, and the Higgs masses,

$$\tan\beta \lesssim 2\,, \quad m_A, m_H, m_{H^\pm} \gtrsim 1 \text{ TeV}\,.$$

The precise bounds depend on the values of Higgs mass and top mass. They are shown in Figure 8. Clearly, the search of such heavy Higgs bosons at the LHC is very challenging.

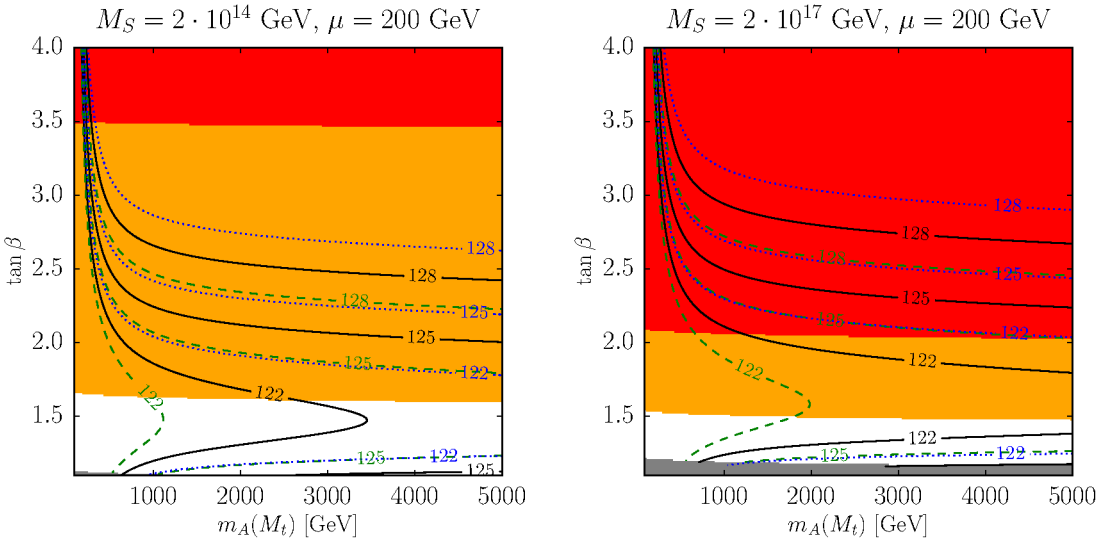


Figure 8: Contours of the lightest Higgs mass M_h in the $m_A(M_t) - \tan\beta$ plane for a two-Higgs-doublet model with higgsinos, with mass $\mu = 200$ GeV. Supersymmetry matching scale: $M_S = 2{\cdot}10^{14}$ GeV (left) and $M_S = 2{\cdot}10^{17}$ GeV (right). The Higgs mass prediction is computed for $M_t = 173.34 \pm 0.76$ GeV (solid black, dashed green, dotted blue). Unshaded regions are allowed by vacuum stability. In the orange regions, the electroweak vacuum is metastable, i.e. its lifetime is larger than the age of the universe. Red regions are excluded by vacuum (meta)stability. Figures taken from Ref. [71].

5 Outlook

We have briefly reviewed the work carried out within the project A1, which has been focussed on string compactifications and string-inspired model building, with a few phenomenological applications to LHC physics. The central goal has been to contribute to bridging the gap between string theory and particle physics.

During the course of the project our studies of string compactifications have shifted from the heterotic string to F-theory. Both versions of string theory can accomodate the Standard Model gauge group and its matter spectrum, with an embedding in the exceptional group E_8. The heterotic string as well as F-theory also provide an appealing geometrical picture of the localization of matter in the compact dimensions and the generation of Yukawa couplings. F-theory is more flexible to construct GUT gauge groups at intermediate steps and to vary matter representations. Also the separation between matter fields and moduli fields is more transparent and, consequently, the problem of moduli stabilization can be more satisfactorily treated. On the other hand, in F-theory the compact space is a del Pezzo surface. In this way one looses the attractive mechanism of Wilson-line breaking of symmetries, which is one of the advantages of heterotic compactifications. An interesting direction for future research would be to generalize the approach of F-theory to compact surfaces with non-trivial topology, and therefore beyond del Pezzo surfaces.

We have concentrated on anisotropic compactifications, with two compact dimensions larger

than the other four, and we have also studied compactifications to six dimensions, which are technically considerably simpler. A physical motivation has been that the size of the two larger dimensions may be related to the scale of grand unification. The six-dimensional theory can then be treated as an effective field theory. For this simplified system some problems could be studied in greater depth compared to a full string theory compactification. Particularly interesting are compactifications from six to four dimensions with magnetic flux. In this case Minkowski and de Sitter vacua can be obtained with complete stabilization of all moduli. Flux compactifications also lead to phenomenologically interesting models which realize high-scale supersymmetry.

Since no hints of supersymmetry have been observed at the LHC, particle physics has to deal with a hierarchy problem, maybe a little hierarchy problem or even a GUT hierarchy problem. Supersymmetry alone is clearly not sufficient to protect the Higgs mass. In supersymmetric models that address this hierarchy problem one typically finds a superparticle mass spectrum, which is almost completely outside the discovery reach of the LHC. A possible exception are light higgsinos, as well as additional Higgs bosons. It is therefore mandatory to search for these particles at the LHC, despite the fact that these searches are very demanding.

It is an attractive, and at the same time challenging aspect of string theory, that in studies of particle physics problems also gravity is always present. For example, the requirement to have vanishing or very small cosmological constant, relates D-term and F-term breaking of supersymmetry. As illustrated by the examples discussed above, in this way the cosmological constant directly influences gaugino masses. Furthermore, the complicated vacuum structure manifests itself in the presence of many moduli with important cosmological consequences. In principle, this is very interesting, but in practice this often limits the possible progress in string compactifications.

A related problem is the huge range of mass scales, which have to be explained as ratios of vacuum expectation values: the cosmological constant (10^{-12} GeV), the scale of electroweak symmetry breaking (100 GeV), the Planck mass (10^{18} GeV), the unknown scale of supersymmetry breaking etc. It appears that further progress will depend most crucially on experimental hints for the scale of supersymmetry breaking.

References

[1] D. Z. Freedman and A. Van Proeyen, *Supergravity*. Cambridge Univ. Press, Cambridge, UK, 2012.

[2] L. E. Ibañez and A. M. Uranga, *String theory and particle physics: An introduction to string phenomenology*. Cambridge University Press, 2012.

[3] W. Buchmüller and J. Schmidt, *Higgs versus Matter in the Heterotic Landscape*, *Nucl.Phys.* **B807** (2009) 265–289, [0807.1046].

[4] W. Buchmüller, C. Ludeling and J. Schmidt, *Local SU(5) Unification from the Heterotic String*, *JHEP* **0709** (2007) 113, [0707.1651].

[5] J. Schmidt, *Local Grand Unification in the Heterotic Landscape*, *Fortsch. Phys.* **58** (2010) 3–111, [0906.5501].

[6] I. Benmachiche, J. Louis and D. Martinez-Pedrera, *The Effective action of the heterotic string compactified on manifolds with SU(3) structure*, *Class.Quant.Grav.* **25** (2008) 135006, [0802.0410].

[7] J. Louis, D. Martinez-Pedrera and A. Micu, *Heterotic compactifications on SU(2)-structure backgrounds*, *JHEP* **09** (2009) 012, [0907.3799].

[8] J. Louis, M. Schasny and R. Valandro, *6D Effective Action of Heterotic Compactification on K3 with Nontrivial Gauge Bundles*, *JHEP* **1204** (2012) 028, [1112.5106].

[9] M. Schasny, *Effective action of heterotic compactification on K3 with non-trivial gauge bundles*, Ph.D. thesis, Universität Hamburg, 2012. DESY-THESIS-2012-043 http://www-library.desy.de/cgi-bin/showprep.pl?thesis12-043.

[10] S. Groot Nibbelin and F. Ruehle, *Line bundle embeddings for heterotic theories*, *JHEP* **04** (2016) 186, [1601.00676].

[11] S. Groot Nibbelink, O. Loukas, F. Ruehle and P. K. S. Vaudrevange, *Infinite number of MSSMs from heterotic line bundles?*, *Phys. Rev.* **D92** (2015) 046002, [1506.00879].

[12] S. Groot Nibbelink, O. Loukas and F. Ruehle, *(MS)SM-like models on smooth Calabi-Yau manifolds from all three heterotic string theories*, *Fortsch. Phys.* **63** (2015) 609–632, [1507.07559].

[13] M. Blaszczyk, S. Groot Nibbelink, O. Loukas and F. Ruehle, *Calabi-Yau compactifications of non-supersymmetric heterotic string theory*, *JHEP* **10** (2015) 166, [1507.06147].

[14] S. Groot Nibbelink and P. K. S. Vaudrevange, *Schoen manifold with line bundles as resolved magnetized orbifolds*, *JHEP* **03** (2013) 142, [1212.4033].

[15] W. Buchmüller, M. Dierigl, F. Ruehle and J. Schweizer, *Split symmetries*, *Phys. Lett.* **B750** (2015) 615–619, [1507.06819].

[16] W. Buchmüller, M. Dierigl, F. Ruehle and J. Schweizer, *Chiral fermions and anomaly cancellation on orbifolds with Wilson lines and flux*, *Phys. Rev.* **D92** (2015) 105031, [1506.05771].

[17] M. Dierigl, *Aspects of Six-Dimensional Flux Compactifications*, Ph.D. thesis, U. Hamburg, Dept. Phys., Hamburg, 2017. DESY-THESIS-2017-036, 10.3204/PUBDB-2017-09253 http://inspirehep.net/record/1618124/files/PhD_Thesis_Markus_Dierigl_Pub.pdf.

[18] W. Buchmüller, J. Louis, J. Schmidt and R. Valandro, *Voisin-Borcea Manifolds and Heterotic Orbifold Models*, *JHEP* **1210** (2012) 114, [1208.0704].

[19] D. V. Belyaev and P. van Nieuwenhuizen, *Tensor calculus for supergravity on a manifold with boundary*, *JHEP* **02** (2008) 047, [0711.2272].

[20] D. V. Belyaev, *Bulk-brane supergravity*, in *SUSY 2007 Proceedings, 15th International Conference on Supersymmetry and Unification of Fundamental Interactions, July 26 - August 1, 2007, Karlsruhe, Germany*, pp. 562–565, 2007, 0710.4540, http://www.susy07.uni-karlsruhe.de/Proceedings/proceedings/susy07.pdf.

[21] D. V. Belyaev and P. van Nieuwenhuizen, *Rigid supersymmetry with boundaries*, *JHEP* **04** (2008) 008, [0801.2377].

[22] D. V. Belyaev and P. van Nieuwenhuizen, *Simple d=4 supergravity with a boundary*, *JHEP* **09** (2008) 069, [0806.4723].

[23] S. L. Parameswaran and J. Schmidt, *Coupling Brane Fields to Bulk Supergravity*, *Phys.Lett.* **B696** (2011) 131–137, [1008.3832].

[24] S. L. Parameswaran, S. Randjbar-Daemi and A. Salvio, *General Perturbations for Braneworld Compactifications and the Six Dimensional Case*, *JHEP* **03** (2009) 136, [0902.0375].

[25] C. P. Burgess, S. L. Parameswaran and I. Zavala, *The Fate of Unstable Gauge Flux Compactifications*, *JHEP* **05** (2009) 008, [0812.3902].

[26] R. Kappl, *The Fayet-Iliopoulos D-term in field and string theory*, Master's thesis, Universität Ulm, 2008.

[27] M. Fischer, M. Ratz, J. Torrado and P. K. S. Vaudrevange, *Classification of symmetric toroidal orbifolds*, *JHEP* **01** (2013) 084, [1209.3906].

[28] M. Fischer, S. Ramos-Sanchez and P. K. S. Vaudrevange, *Heterotic non-Abelian orbifolds*, *JHEP* **07** (2013) 080, [1304.7742].

[29] W. Buchmüller, M. Dierigl, P. K. Oehlmann and F. Rühle, *The Toric SO(10) F-Theory Landscape*, *JHEP* **12** (2017) 035, [1709.06609].

[30] A. P. Braun, A. Collinucci and R. Valandro, *G-flux in F-theory and algebraic cycles*, *Nucl.Phys.* **B856** (2012) 129–179, [1107.5337].

[31] A. P. Braun, A. Collinucci and R. Valandro, *Algebraic description of G-flux in F-theory: new techniques for F-theory phenomenology*, *Fortsch.Phys.* **60** (2012) 934–940, [1202.5029].

[32] M. Cicoli, C. Mayrhofer and R. Valandro, *Moduli Stabilisation for Chiral Global Models*, *JHEP* **1202** (2012) 062, [1110.3333].

[33] M. Cicoli, S. Krippendorf, C. Mayrhofer, F. Quevedo and R. Valandro, *D-Branes at del Pezzo Singularities: Global Embedding and Moduli Stabilisation*, *JHEP* **1209** (2012) 019, [1206.5237].

[34] C. Lüdeling and F. Ruehle, *F-theory duals of singular heterotic K3 models*, *Phys. Rev.* **D91** (2015) 026010, [1405.2928].

[35] R. Kappl, H. P. Nilles, S. Ramos-Sanchez, M. Ratz, K. Schmidt-Hoberg and P. K. S. Vaudrevange, *Large hierarchies from approximate R symmetries*, *Phys. Rev. Lett.* **102** (2009) 121602, [0812.2120].

[36] H. P. Nilles, S. Ramos-Sánchez, M. Ratz and P. K. S. Vaudrevange, *A note on discrete R symmetries in $\mathbb{Z}_6$-II orbifolds with Wilson lines*, *Phys. Lett.* **B726** (2013) 876–881, [1308.3435].

[37] W. Buchmüller, K. Hamaguchi, O. Lebedev, S. Ramos-Sanchez and M. Ratz, *Seesaw neutrinos from the heterotic string*, *Phys.Rev.Lett.* **99** (2007) 021601, [hep-ph/0703078].

[38] K.-S. Choi, H. P. Nilles, S. Ramos-Sanchez and P. K. S. Vaudrevange, *Accions*, *Phys. Lett.* **B675** (2009) 381–386, [0902.3070].

[39] H. P. Nilles, M. Ratz and P. K. S. Vaudrevange, *Origin of Family Symmetries*, *Fortsch. Phys.* **61** (2013) 493–506, [1204.2206].

[40] S. Forste, H. P. Nilles, S. Ramos-Sanchez and P. K. Vaudrevange, *Proton Hexality in Local Grand Unification*, *Phys.Lett.* **B693** (2010) 386–392, [1007.3915].

[41] M.-C. Chen, M. Ratz, C. Staudt and P. K. S. Vaudrevange, *The mu Term and Neutrino Masses*, *Nucl. Phys.* **B866** (2013) 157–176, [1206.5375].

[42] P. Anastasopoulos, M. Cvetic, R. Richter and P. K. S. Vaudrevange, *String Constraints on Discrete Symmetries in MSSM Type II Quivers*, *JHEP* **03** (2013) 011, [1211.1017].

[43] W. Buchmüller and J. Schweizer, *Flavor mixings in flux compactifications*, *Phys. Rev.* **D95** (2017) 075024, [1701.06935].

[44] W. Buchmüller and K. M. Patel, *Flavour physics without flavour symmetries*, *Phys. Rev.* **D97** (2018) 075019, [1712.06862].

[45] O. Lebedev and S. Ramos-Sanchez, *The NMSSM and String Theory*, *Phys.Lett.* **B684** (2010) 48–51, [0912.0477].

[46] S. Ramos-Sanchez, *The mu-problem, the NMSSM and string theory*, *Fortsch.Phys.* **58** (2010) 748–752, [1003.1307].

[47] J. Louis and L. Zárate, *Hiding the little hierarchy problem in the NMSSM*, *JHEP* **08** (2015) 062, [1506.01616].

[48] J. Louis, K. Schmidt-Hoberg and L. Zárate, *Dilaton domination in the MSSM and its singlet extensions*, *Phys. Lett.* **B735** (2014) 1–6, [1402.2977].

[49] F. Brümmer and W. Buchmüller, *Light Higgsinos as Heralds of Higher-Dimensional Unification*, *JHEP* **1107** (2011) 010, [1105.0802].

[50] F. Brümmer and W. Buchmüller, *The Fermi scale as a focus point of high-scale gauge mediation*, *JHEP* **1205** (2012) 006, [1201.4338].

[51] F. Brümmer and W. Buchmüller, *A low Fermi scale from a simple gaugino-scalar mass relation*, *JHEP* **03** (2014) 075, [1311.1114].

[52] L. Zárate, *String inspired soft terms and the Higgs mass in the NMSSM*, Ph.D. thesis, Universität Hamburg, 2016. http://ediss.sub.uni-hamburg.de/volltexte/2016/8029.

[53] L. Zárate, *The Higgs mass and the scale of SUSY breaking in the NMSSM*, *JHEP* **07** (2016) 102, [1601.05946].

[54] S. L. Parameswaran, S. Ramos-Sanchez and I. Zavala, *On Moduli Stabilisation and de Sitter Vacua in MSSM Heterotic Orbifolds*, *JHEP* **1101** (2011) 071, [1009.3931].

[55] W. Buchmüller, R. Catena and K. Schmidt-Hoberg, *Small Extra Dimensions from the Interplay of Gauge and Supersymmetry Breaking*, *Nucl.Phys.* **B804** (2008) 70–89, [0803.4501].

[56] W. Buchmüller, R. Catena and K. Schmidt-Hoberg, *Enhanced Symmetries of Orbifolds from Moduli Stabilization*, *Nucl.Phys.* **B821** (2009) 1–20, [0902.4512].

[57] J. Möller, *GUT scale extra dimensions and light moduli in supergravity and cosmology*, Ph.D. thesis, Universität Hamburg, 2010. 10.3204/DESY-THESIS-2010-017 http://inspirehep.net/record/855913/files/desy-thesis-10-017.pdf.

[58] W. Buchmüller, J. Möller and J. Schmidt, *Light Moduli in Almost No-Scale Models*, *Nucl.Phys.* **B826** (2010) 365–378, [0909.0482].

[59] W. Buchmüller, M. Dierigl, F. Ruehle and J. Schweizer, *de Sitter vacua from an anomalous gauge symmetry*, *Phys. Rev. Lett.* **116** (2016) 221303, [1603.00654].

[60] W. Buchmüller, M. Dierigl, F. Ruehle and J. Schweizer, *de Sitter vacua and supersymmetry breaking in six-dimensional flux compactifications*, *Phys. Rev.* **D94** (2016) 025025, [1606.05653].

[61] J. Schweizer, *Fermion families and soft supersymmetry breaking from flux in six dimensions*, Ph.D. thesis, DESY, 2016. 10.3204/PUBDB-2017-00893 http://inspirehep.net/record/1513406/files/thesis.pdf.

[62] R. Catena and J. Möller, *Axion-dilaton cosmology and dark energy*, *JCAP* **0803** (2008) 012, [0709.1931].

[63] J. Möller, *Dark energy in scalar-tensor theories*, Master's thesis, Universität Hamburg, 2007. http://www-library.desy.de/cgi-bin/showprep.pl?thesis07-043.

[64] F. Ruehle and C. Wieck, *Natural inflation and moduli stabilization in heterotic orbifolds*, *JHEP* **05** (2015) 112, [1503.07183].

[65] J. Halverson, B. D. Nelson and F. Ruehle, *String Theory and the Dark Glueball Problem*, *Phys. Rev.* **D95** (2017) 043527, [1609.02151].

[66] W. Buchmüller, M. Dierigl, E. Dudas and J. Schweizer, *Effective field theory for magnetic compactifications*, *JHEP* **04** (2017) 052, [1611.03798].

[67] W. Buchmüller, M. Dierigl and E. Dudas, *Flux compactifications and naturalness*, *JHEP* **08** (2018) 151, [1804.07497].

[68] S. Bobrovskyi, J. Hajer and S. Rydbeck, *Long-lived higgsinos as probes of gravitino dark matter at the LHC*, *JHEP* **1302** (2013) 133, [1211.5584].

[69] J. Schmidt, C. Weniger and T. T. Yanagida, *Dynamical Matter-Parity Breaking and Gravitino Dark Matter*, *Phys.Rev.* **D82** (2010) 103517, [1008.0398].

[70] S. Bobrovskyi, F. Brümmer, W. Buchmüller and J. Hajer, *Searching for light higgsinos with b-jets and missing leptons*, *JHEP* **1201** (2012) 122, [1111.6005].

[71] E. Bagnaschi, F. Brümmer, W. Buchmüller, A. Voigt and G. Weiglein, *Vacuum stability and supersymmetry at high scales with two Higgs doublets*, *JHEP* **03** (2016) 158, [1512.07761].

Strings and High Energy Scattering

Jochen Bartels[1], *Sven-Olaf Moch*[1], *Volker Schomerus*[2]

[1]II. Institut für Theoretische Physik, Universität Hamburg, Germany
[2]DESY, Hamburg, Germany

DOI: http://dx.doi.org/10.3204/PUBDB-2018-00782/A3

While early string theory provided an intriguing explanation for the observed Regge trajectories of meson resonances, it failed to reproduce the correct high energy behavior of scattering amplitudes. This has changed with the AdS/CFT correspondence. In fact, string theory can now produce precision results even in the multi-Regge regime. In this note we review the status of high energy scattering in planar $\mathcal{N} = 4$ super-Yang–Mills theory, at weak, strong and intermediate coupling, with a focus on its integrability and the relation to string theory.

1 Introduction

Back at the end of the 1960ies, string theory seemed to offer an intriguing explanation for the Regge trajectories of meson resonances that experimentalists had seen in pion scattering amplitudes. In fact, the observed linear trajectories of particles with mass along $M_J^2 = \alpha' J + \alpha_0, J = 0, 1, \ldots$ were interpreted as vibrational modes of a 1-dimensional object of tension $T_s = 1/\alpha'$. On the other hand it was also noticed early on that the scattering amplitudes of strings, such as the famous Veneziano amplitude, do not possess the correct high energy limit in the physical regime since they fall off exponentially with the center of mass energy and hence much faster than in nature. This fall-off behavior may be understood from the extended nature of strings which makes the interaction region in coordinate space a bit fuzzy and hence localizes the amplitudes sharply in momentum space. So, in spite of its beautiful interpretation of meson resonances, it appeared that string theory could not describe hadronic physics and the field was left to Quantum Chromo Dynamics (QCD). The latter was very efficient in particular in the high energy asymptotically free regime. On the other hand, even after decades of experience it remains difficult to use QCD for low energy physics, the regime in which string theory had seemed so promising.

Ideas in particular of 't Hooft [1] and Polyakov [2] nurtured hopes that one may eventually be able to reconcile the two approaches to hadronic physics, i.e. combine the advantages of QCD with those of string theory. But it was only through Maldacena's celebrated AdS/CFT correspondence [3] that a concrete route opened up which would eventually allow for precision computations of the type described below. The correspondence also showed very clearly that early attempts to model hadronic physics with strings had suffered from one problematic assumption: It had always been taken for granted that strings and particles propagate in the same space-time. For the modern string theory descriptions of 4-dimensional gauge theory to work, however, it is absolutely crucial that the strings propagate an a 5-dimensional curved

geometry. In the AdS/CFT correspondence the geometry is curved by the presence of stack of D3 branes with a 4-dimensional world-volume. The curvature introduces a red-shift factor that depends on the 5^{th} coordinate, i.e. on the distance r from the stack of branes. Through this r-dependent red-shift factor, string theory can reproduce both hard high energy scattering and low energy meson resonances [4].

The gauge theory that lives on the stack of D3 branes is of course not QCD but a maximally supersymmetric cousin thereof, the $\mathcal{N} = 4$ supersymmetric Yang–Mills (SYM) theory. According to the AdS/CFT correspondence, this theory is equivalent to type IIB superstring theory on $\mathrm{AdS}_5 \times S^5$. It was realized early on [5] that the classical world-sheet models which describe strings in this background are integrable, at least on a world-sheet of genus $g = 0$. This tied in nicely with an earlier observation by Minahan and Zarembo [6] according to which the one-loop dilation operator in a subsector of planar $\mathcal{N} = 4$ SYM theory is given by the Hamiltonian of the integrable Heisenberg spin chain. For a review of integrability in the AdS/CFT correspondence and many more references see [7]. Integrability of strings in $\mathrm{AdS}_5 \times S^5$ suggested that – within the framework of the AdS/CFT correspondence – the string theoretic description could even be used for precision computations in $\mathcal{N} = 4$ SYM theory at finite coupling.

The potential of string theoretic calculations was first seen in the context of anomalous dimensions. This is a topic with a long history in gauge theory. In particular, matrix elements of singlet local twist-two Wilson operators of spin L and their evolution equations were studied extensively. For the fields in the $\mathcal{N} = 4$ SYM multiplet, i.e., one gluon g, four Majorana fermions ψ and three complex scalars ϕ, it was realized [8], that the anomalous dimension matrix governing those evolution equations is fixed completely by the super-conformal invariance and one universal anomalous dimension $\gamma^{\mathrm{uni}}(L)$, whose argument is shifted by an integer number, depending on the field, g, ψ or ϕ. Moreover, it turns out [8, 9] that the most complicated contributions in the anomalous dimensions for the corresponding matrix elements of quark and gluon operators in QCD [10,11], that is an $\mathrm{SU}(n_c)$ gauge theory with fermions and bosons in the fundamental and adjoint representation, respectively, directly deliver the universal anomalous dimension $\gamma^{\mathrm{uni}}(L)$ in the $\mathcal{N} = 4$ SYM theory, provided the color $SU(n_c)$ invariants are adjusted accordingly. The leading coefficient of the universal anomalous dimension in the large L limit is known as the cusp anomalous dimension and it was the first interesting gauge theory quantity that has been computed with string theoretic techniques [12].

Putting all this together it seemed very natural to finally address the computation of high energy scattering amplitudes in $\mathcal{N} = 4$ SYM theory through the dual string theoretic description. Our goal was to show that string theory in an AdS geometry was not only compatible with gauge theoretic high energy scattering, as argued in [4], but that it could even produce precision results in the regime that had challenged early string theory. The aim of this review is to explain how this goal has been achieved, at least for (MHV) scattering amplitudes of up to six external gluons in planar $\mathcal{N} = 4$ SYM theory.

In order to do so, we will provide some basics on scattering amplitudes in perturbative $\mathcal{N} = 4$ SYM theory in the next section. Our discussion is centered around the well-known Bern–Dixon–Smirnov (BDS) formula and it includes a brief survey of the Beisert–Eden–Staudacher equation, as a first non-trivial example of a string theoretic precision result in gauge theory, see section 3. In the forth subsection we then zoom into the high energy regime and explain a remarkable formula from [13] that addresses high energy scattering amplitudes for $n = 6$ gluons at any loop order in the so-called leading logarithmic approximation (LLA), along with some extensions most notably from [14]. Then we turn to strong coupling. Here, our discussion begins with

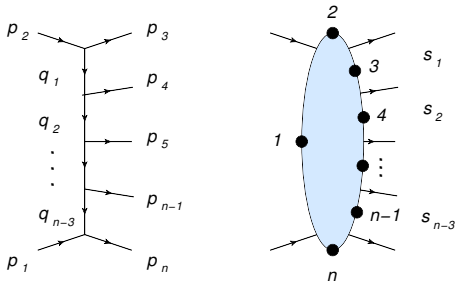


Figure 1: Kinematics of the scattering process $2 \to n-2$. On the right-hand side we show a graphical representation of the dual variables x_i. Figure taken from Ref. [19].

the geometric description of scattering amplitudes in terms of minimal area surfaces that was suggested in [15]. The latter has been reformulated in [16,17] through an auxiliary 1D integrable system which was specifically designed to solve the minimal area problem in AdS. In section 6 we will explain two beautiful insights from [18,19]. Namely, it turns out that the gauge theoretic high energy limit actually corresponds to the low energy limit of the auxiliary 1D integrable system. Moreover, the Regge cuts in gauge theory are mapped to quasi-particle excitations in 1D. When taken together, the two statements give rise to a set of Bethe ansatz equations for high energy scattering amplitudes in strongly coupled $\mathcal{N} = 4$ SYM theory [20]. One special solution of these equations determines the strong coupling limit of the six-gluon amplitude in the multi-Regge limit. In the concluding section we finally present a formula from [21] that smoothly interpolates between the weak and strong coupling results in [13] and [22], respectively.

2 The weak coupling theory

We consider the scattering of n gluons. With later kinematical limits in mind we shall think of two incoming particles whose momenta we denote by p_1, p_2 and $n-2$ outgoing particles of momentum $p_3, ..., p_n$ as shown in Fig. 1. It will be convenient to label momenta p_i by arbitrary integers i such that $p_{i+n} = p_i$. In the context of $\mathcal{N} = 4$ SYM theory it is advantageous to pass to a set of dual variables x_i such that

$$p_i = x_{i-1} - x_i. \tag{1}$$

The variables x_i inherit their periodicity $x_{i+n} = x_i$ from the periodicity of the p_i and momentum conservation. Let us also introduce the notation $x_{ij} = x_i - x_j$. The x_{ij}^2 provide a large set of Lorentz invariants $x_{ij}^2 = x_{ji}^2$. Throughout this note we use a Lorentzian metric with signature $(-,+,+,+)$. When expressed in terms of the momenta, the invariants read

$$x_{ij}^2 = (p_{i+1} + \cdots + p_j)^2 . \tag{2}$$

Lorentz symmetry along with the mass-shell conditions $p_i^2 = 0$ imply that only $3n-10$ of these variables are independent. We will not make any specific choice here. In the physical regime, all the energies p_i^0 are assumed to be positive. We will refer to the Mandelstam invariants x_{ij}^2 that are positive in the physical regime as s-like. Those that obey $x_{ij}^2 \leq 0$ in the physical regime are called t-like.

Let us recall that in planar $\mathcal{N} = 4$ super-Yang–Mills theory the full color ordered maximally helicity violating amplitude takes the following form

$$A_n \sim A_n^{(0)} e^{F_n^{\rm BDS}(s,t,\epsilon;a)+R_n(u;a)} \ . \tag{3}$$

Each of the terms on the right hand side has a rich story to tell. Here, we only mention that the tree level factor $A_n^{(0)}$ is given by a surprisingly simple formula that was found by Parke and Taylor [23]. The function $F_n^{\rm BDS}$ was introduced by Bern, Dixon and Smirnov in [24]. It depends on $3n-10$ Mandelstam variables which we denote collectively as s, t, according to our split into s- and t-like invariants. In addition, F_n are functions of the cut-off ϵ and of the 't Hooft coupling a. BDS designed the F_n to incorporate all terms that are singular in the cut-off ϵ along with a relatively simple finite term. The latter was included to reproduce the correct one-loop amplitude. Explicit formulas for F_n can be found in [24] and we will also discuss some more features below. By definition, the so-called finite remainder functions R_n contain the part of the amplitude that is not captured by the tree level factor $A_n^{(0)}$ and the BDS formula. The remainder functions are not known in general. So, most of our discussion below will concern the functions R_n.

Before we get there, we want to go into a bit more detail about the BDS amplitudes F_n. Bern, Dixon and Smirnov had actually suggested that its dependence on the Mandelstam variables s, t was determined entirely by one-loop computations. The dependence on the coupling a, on the other hand, enters their expression for F_n only through a few numbers, most prominently the so-called cusp anomalous dimension $\gamma_c(a)$, i.e. somewhat symbolically, their proposal for F_n reads

$$F_n^{\rm BDS}(s,t,\epsilon;a) \sim \gamma_c(a) M_n^{(1)}(s,t,\epsilon) + \dots \ , \tag{4}$$

see [24] for the explicit formula. The factorization of the dependence on the kinematical variables and the coupling constant is the central feature of the BDS formula. Obviously, the functions M_n were easy to work out since they just contain one-loop contributions. We will not give explicit expressions here. What is much less obvious is that also the dependence of $\gamma_c(a)$ on the coupling a has been determined. In fact it is known to any loop order as a solution to the remarkable Beisert–Eden–Staudacher (BES) non-linear integral equation [12]. We will discuss this is the next section. Here, we only state the first few orders of its weak coupling expansion.

$$\gamma_c(a) = 4a - 4\zeta_2 a^2 + \frac{44}{5}\zeta_2^2 a^3 - \left(\frac{876}{35}\zeta_2^2 + 4\zeta_3^2\right) a^4 + \mathcal{O}(a^5) \, . \tag{5}$$

Let us now turn to the main actors of our review, the finite remainder functions R_n. By construction, the BDS ansatz is one-loop exact and hence R_n can only start from two loops. Moreover, since F_n contains all singular terms, R_n is finite at all loops. It was argued in [25] to be invariant under dual conformal transformations, i.e. conformal transformations in momentum space. Hence, R_n depends on the Mandelstam invariants only through conformal invariant cross ratios. Since the four-dimensional conformal group has 15 generators, there are $3n-15$ such cross ratios which we denote as u. For the discussion of the multi-Regge limit we adopt the following choice [18, 19]

$$u_{1\sigma} = \frac{x^2_{\sigma+1,\sigma+5} x^2_{\sigma+2,\sigma+4}}{x^2_{\sigma+2,\sigma+5} x^2_{\sigma+1,\sigma+4}} \quad , \quad u_{2\sigma} = \frac{x^2_{\sigma+3,n} x^2_{1,\sigma+2}}{x^2_{\sigma+2,n} x^2_{1,\sigma+3}} \quad , \quad u_{3\sigma} = \frac{x^2_{2,\sigma+3} x^2_{1,\sigma+4}}{x^2_{2,\sigma+4} x^2_{1,\sigma+3}} \, , \tag{6}$$

where $\sigma = 1, ..., n-5$. Note that for $n < 6$ one cannot form any cross ratios and hence the remainder functions R_n must be trivial for $n = 4, 5$. In the case of $n = 6$ external gluons, however, there exits 3 independent cross ratios which we shall simply denote by u_1, u_2, u_3. And indeed it has been argued in [26] that R_6 must be a non-vanishing function of the cross ratios u_a in order to correct for the unphysical analytical structure of the BDS ansatz.

The remainder functions R_n are not known in general, but quite a few results have been obtained within the last decade. One line of calculations aims at exact multi-loop results at fixed order perturbation theory. Another approach computes, in the Regge limit, amplitudes at all loop orders in perturbation theory, restricted to the leading logarithmic approximation, making use of analytic properties, unitarity and conventional perturbation theory. The first approach started with a computation of R_6 at two loops in [27] which was turned into a very compact formula for R_6 in [28]. We refrain from stating an explicit expression here, but stress that this R_6 possesses non-trivial branch cuts. We will discuss these results in more detail in section 4. Computations of $2 \to 4$ scattering amplitudes in the multi-Regge limit started in [13, 26], see also section 4. In the meantime, the determination of remainder functions for arbitrary kinematics has been pushed to higher orders and a larger number of external gluons, see e.g. [29, 30] and [31, 32].

3 Interlude: Anomalous dimensions

In our discussion of the BDS Ansatz for planar amplitudes above the entire dependence on the coupling constant a entered through some functions that were independent of the kinematic data. The most important of these functions is the cusp anomalous dimensions γ_c. We want to pause our main story for a moment and discuss in a bit more detail what is actually known about the cusp anomalous dimension and how these results were obtained. While a large part of this section is devoted to the weak coupling expansion we will also review the BES equation along with some strong coupling results, thereby providing a first view on the remarkable interplay between gauge and string theory we promoted in the introduction.

The earliest results on the cusp anomalous dimension were obtained from the study of anomalous dimensions of twist-two spin-L Wilson operators for large spins, i.e. in the limit $L \to \infty$. To begin with, we will describe the setup in QCD before going back to $\mathcal{N} = 4$ SYM theory. In QCD the relevant set of (flavor-singlet) operators for quark and gluon fields, ψ and g, is given by

$$O^{\psi}_{\{\mu_1,\dots,\mu_L\}} = \overline{\psi}\,\gamma_{\{\mu_1} D_{\mu_2} \dots D_{\mu_L\}}\,\psi\,, \tag{7}$$

$$O^{g}_{\{\mu_1,\dots,\mu_L\}} = F_{\nu\{\mu_1} D_{\mu_2} \cdots D_{\mu_{L-1}} F_{\mu_L\}}{}^{\nu}\,, \tag{8}$$

where $F_{\mu\nu}$ denotes the field strength, D_μ the covariant derivative and $\{\dots\}$ symmetrization of the indices μ_i. The local operators are subject to renormalization (in a minimal subtraction scheme) as $[O^i] = Z^{ij}\,O^j$ where the square brackets $[\dots]$ denote renormalized operators and the corresponding anomalous dimensions $\gamma_{ij}(L)$ which are obtained from $\gamma_{ij} = \mu d/(d\mu) \ln Z^{ij}$ can be expressed in terms of harmonic sums. These are subject to the recursive definition

$$S_{m_1,m_2,\dots,m_n}(L) = \sum_{k=1}^{L} \mathrm{sgn}(m_1)^k\, k^{-m_1}\, S_{m_2,\dots,m_n}(k)\,, \tag{9}$$

and their weight w is given by $w = \sum_{i=1}^{n} \mathrm{abs}(m_i)$. In the weak coupling expansion of $\gamma_{ij}(L)$ at l-loop order harmonic sums up to weight $w \leq 2l-1$ contribute and the terms with maximal weight, $w = 2l-1$, are referred to as terms of leading transcendentality. Upon adjusting the color $\mathrm{SU}(n_c)$ invariants of the QCD results and, at the same time, keeping only terms of leading transcendentality, one extracts the universal anomalous dimension $\gamma^{\mathrm{uni}}(L)$ of $\mathcal{N} = 4$ SYM theory, as has been verified up to three loops [8–11]. Interestingly, $\gamma^{\mathrm{uni}}(L)$ has an additional property, see, e.g., [33], that is it consists of certain combinations of harmonic sums which are reciprocity-respecting, i.e., invariant under the replacement $L \to 1-L$. Explicit expressions for $\gamma^{\mathrm{uni}}(L)$ in the $\mathcal{N} = 4$ SYM theory have now been constructed up to seven loops [34–37], while the complete computation of the four-loop anomalous dimensions $\gamma_{ij}(L)$ in QCD is still a formidable task, see [38] for first results on the flavor non-singlet part in the planar limit.

Of particular interest for further studies of the relations between the $\mathcal{N} = 4$ SYM theory and QCD are the so-called wrapping corrections, which complement the so-called asymptotic Bethe ansatz and control the high energy behavior for $L \to 0$. These occur for the first time at four loops [34] as $\gamma^{\mathrm{uni}}(L)|_{\mathrm{wrap}} \simeq a^4\, S_1(L)^2\, f^{\mathrm{wrap}}(L)$ with a function

$$\begin{aligned} f^{\mathrm{wrap}}(L) &= 5\zeta_5 - 2S_{-5}(L) + 4S_{-2}(L)\zeta_3 - 4S_{-2,-3}(L) + 8S_{-2,-2,1}(L) \\ &\quad + 4S_{3,-2}(L) - 4S_{4,1}(L) + 2S_5(L)\ . \end{aligned} \tag{10}$$

cf. [39], where $f^{\mathrm{wrap}}(L)$ falls off as $1/L^2$ for $L \to \infty$, so that $\gamma^{\mathrm{uni}}(L)|_{\mathrm{wrap}}$ is compatible with Eq. (5) for the cusp anomalous dimension. Likewise, in QCD quartic Casimir invariants occur at four loops for the first time. They are proportional to $d^{(4)}_{xy} \equiv d^{abcd}_x d^{abcd}_y$ for representation labels x, y with generators T^a_r

$$d^{abcd}_r = \frac{1}{6}\,\mathrm{Tr}\,(\,T^a_r\,T^b_r\,T^c_r\,T^d_r + \text{ five } bcd \text{ permutations}\,)\,, \tag{11}$$

so that one has, e.g., $d^{(4)}_{AA}/n_A = n_c^2(n_c^2+36)/24$ with normalization $n_A = (n_c^2-1)$ for the adjoint representation 'A' in an $SU(n_c)$ gauge theory. Such terms are effectively 'leading-order' and therefore scheme-independent and subject to particular relations, such as those of an $\mathcal{N} = 1$ SYM theory upon properly adjusting all $SU(n_c)$ color factors. Moreover, they consist entirely of reciprocity-respecting combinations of harmonic sums and rational polynomials in L. Using these insights and a recent computation [40] of fixed moments up to $L \leq 16$ of those quartic color factors of the QCD anomalous dimensions it has been possible to reconstruct analytic expressions in L from the solution of Diophantine equations. For example, the four-loop contribution to the gluon-gluon anomalous dimension proportional to $d^{(4)}_{AA}/n_A$ and ζ_5 is given by

$$\begin{aligned} \gamma^{(3)}_{gg}(L)\Big|_{a^4\,\zeta_5\,d^{(4)}_{AA}/n_A} &= 640\,\big(12\,\eta^2 - 4\,\nu^2 - S_1(L)(4\,S_1(L) + 8\,\eta - 8\,\nu - 11) - 7\nu\big) \\ &\quad + \frac{12032}{3}\,\eta - \frac{48064}{9} - \frac{32}{9}\,L\,(L+1)\Big) \end{aligned} \tag{12}$$

with abbreviations for the reciprocity respecting combinations $\eta = 1/L - 1/(L+1)$ and $\nu = 1/(L-1) - 1/(L+2)$.

Interestingly, the leading terms in the limit $L \to \infty$ of Eq. (12) behave as $L\,(L+1)\zeta_5$ and $\ln(L)^2\zeta_5$. This contradicts the single logarithmic rise of the anomalous dimensions as $\ln(L)$ for

large L, which is a universal property of massless gauge theories. E.g., the cusp anomalous dimension in Eq. (5) for a $\mathcal{N}=4$ SYM theory derives from the factorization $\gamma^{\text{uni}}(L) \simeq \ln(L)\gamma_c(a)$. Therefore, it has been conjectured [40] that the terms proportional to $L\,(L+1)\zeta_5$ and $\ln(L)^2\zeta_5$ are, in fact, the first glimpse of the wrapping corrections at four loops in Eq. (10). While the particular combination $a^4\,S_1(L)^2\,f^{\text{wrap}}(L)$ is known from $\gamma^{\text{uni}}(L)$ [34], the other instance is also known from the computation of the three-loop QCD Wilson coefficients in deep-inelastic scattering [39], which contain the term $C_{\text{ns}}(L) \simeq a^3(n_c^2-1)/n_c^3\,\{L(L+1)\,f^{\text{wrap}}(L)\}$. Thus, completion of the ζ_5 in Eq. (12) as indicated would allow to recover the expected behavior for large spins, $L\to\infty$.

Similar relations between quantities in QCD and $\mathcal{N}=4$ SYM theory are also expected for other cases. One such case are the energy-energy correlations (EEC), proposed back in 1978 in [41], which measure the correlations of the energies E_a and E_b of partons a and b as a function of an angular variable ξ in electron-positron collisions

$$\Sigma(\xi) = \sum_{a,b} \int \text{dPS}\,\frac{E_a E_b}{Q^2}\,\sigma\big(e^+ + e^- \to a + b + X\big)\,\delta\left(\xi - \cos\theta_{ab}\right)\,. \tag{13}$$

Due to the involved phase space integration of the cross section σ with the measure dPS in Eq. (13), the analytical expressions for the NLO QCD corrections have been unavailable for long in contrast to $\mathcal{N}=4$ SYM theory, where the corresponding results have been derived [42]. Quite recently significant progress towards the EEC at NLO in QCD has been reported [43] and full analytical results have been published [44], which in particular display again the correspondence between QCD and $\mathcal{N}=4$ SYM theory regarding contributions of leading transcendentality, i.e. the polylogarithms of highest weight in the angular variable ξ.

In the case of planar $N=4$ SYM theory all-loop results on anomalous dimensions can be obtained systematically with the help of methods from integrable systems. The first example of such results concerned the dependence of $\gamma_c(a)$ on the coupling a, which is known to any loop order as a solution to the BES non-linear integral equation [12]. The latter is easiest to appreciate from the string theory perspective. String theory in an AdS_5 is classically integrable, i.e. the classical equations of motion possess an infinite number of conservation laws. Many solutions have been constructed explicitly, the most famous of which is known as the Gubser–Klebanov–Polyakov (GKP) string [45]. It describes a folded string that rotates in a three-dimensional subspace of AdS_5. The conservation laws can be thought of as moments of some charge density function $Q_a(\tau)$ of the GKP string. From the solutions one can certainly compute all these charge densities at infinite coupling $a=\infty$. But it is possible to do a lot better: One can actually compute the charge density function $Q_a(\tau)$ for any value of the coupling a by solving the following infinite set of coupled integral equations [12],

$$\int_0^\infty \frac{d\tau}{\tau}\,J_\nu(\tau)\,Q_a((-1)^{\nu+1}\tau) = \frac{1}{2}\delta_{\nu,1}\,. \tag{14}$$

Here $\nu=1,2,\ldots$ runs through all positive integers, and $J_\nu(\tau)$ are Bessel functions of first kind. In order to reconstruct the infinite set of charge densities q_a^ν from the charge density function $Q_a(\tau)$ one expands the latter as

$$Q_a(\tau) = \sum_{\nu=1}^\infty q_a^\nu B_\nu(a,\tau)\,, \qquad \text{where} \qquad B_\nu(a,\tau) = (-1)^\nu\,\frac{2\nu J_\nu(2g\tau)}{1-e^{(-1)^\nu\tau}}\,. \tag{15}$$

The cusp anomalous dimension $\gamma_c(a)$ is claimed to coincide with the first coefficient in this expansion, i.e. $\gamma_c(a) = q_a^1$. It is actually surprisingly simple to construct the weak and strong coupling expansions of the cusp anomalous dimension from this description, at least when compared to perturbative gauge theory computations at weak coupling, see [12, 46] and [47]. The first few orders at weak coupling were displayed in Eq. (5) already. At strong coupling the leading terms reads

$$\gamma_c(a) = 2\sqrt{a} - \frac{3\ln 2}{2\pi} + \mathcal{O}(1/a)\,, \tag{16}$$

The determination of the cusp anomalous dimension was the first instance where the string theoretic description of gauge theories paid off. In fact, when the BES proposal appeared, $\gamma_c(a)$ was only known to three loops from [9, 10].

4 High energy scattering at weak coupling

In gauge theory, scattering amplitudes in the high energy regime are of particular relevance. They describe the behavior of typical collider kinematics with two highly energetic incoming particles and a final state in which two highly energetic outgoing particles are accompanied by a certain number of lower energy particles. Remarkably, this regime is not only most relevant but also computationally more accessible than generic kinematics. From S-matrix theory, general Regge theory [48] and from a vast number of studies of the high energy behavior in QED and in nonabelian gauge theories it is known that, in the multi-Regge limit, signatured scattering amplitudes show remarkable structural simplicity. For example, for the $2 \to n-2$ process with Regge pole exchanges the amplitudes factorize into impact factors and production vertices. This factorization is expected to hold also beyond the leading order approximations. The Regge limit, therefore, provides possibilities of testing higher loop calculations in perturbation theory. Furthermore, it has been known for a long time that integrable Heisenberg spin chains enter the expressions for scattering amplitudes in the so-called multi-Regge (high energy) limit [49, 50]. To leading logarithmic order, this is even true for usual QCD.

In the multi-Regge limit, the s-like variables are much larger than the t-like ones which are kept finite. The precise characterization of the limit in terms of Mandelstam invariants can be found in [19]. Here we shall mostly focus on the multi-Regge limit of the remainder functions R_n which depends on the Mandelstam invariants only through the cross ratios u, see Eq. (6) for a complete set of such cross ratios. In the multi-Regge limit, the cross ratios $u_{1\sigma}$ tend to $u_{1\sigma} \sim 1$ while the remaining ones tend to zero, i.e. $u_{2\sigma}, u_{3\sigma} \sim 0$. Cross ratios with the same index σ approach their limit values such that the following ratios remain finite

$$\left[\frac{u_{2\sigma}}{1-u_{1\sigma}}\right]^{\text{MRL}} =: \frac{1}{|1+w_\sigma|^2} \quad , \quad \left[\frac{u_{3\sigma}}{1-u_{1\sigma}}\right]^{\text{MRL}} =: \frac{|w_\sigma|^2}{|1+w_\sigma|^2}\,. \tag{17}$$

Through these equations we have introduced the $n-5$ complex parameters w_σ. Here and in the following the superscript MRL instructs us to evaluate the expression in square brackets in multi-Regge kinematics.

We are going to evaluate the multi-Regge limit for functions which possess branch cuts and so in order to make it well-defined, we need to specify the sheet on which the limit is actually performed. There exist 2^{n-4} different sheets or regions, depending on the sign of the energies p_i^0 for $i = 4, \ldots, n-1$. Different regions can be reached from the one in which all p_i^0 are positive by analytic continuations. We will put the sign of these p_i^0 into an array $\varrho = (\text{sgn}(p_i^0))$ with $n-4$

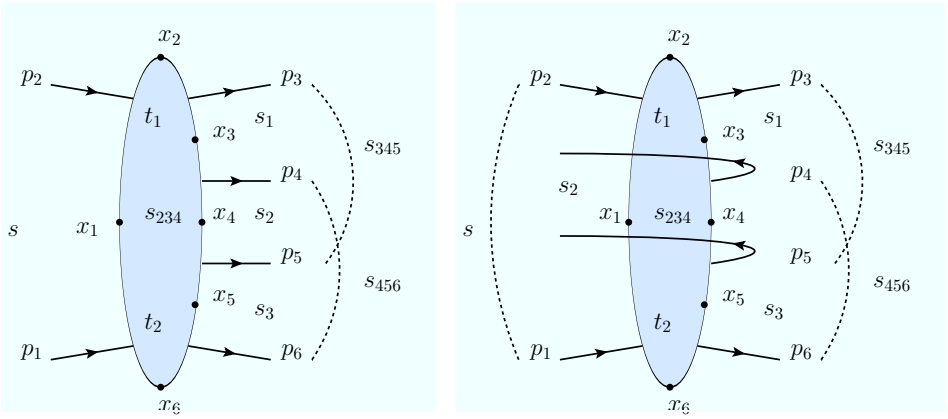


Figure 2: Kinematic configuration for the multi-Regge limit before (on the left) and after (on the right) the analytical continuation with the kinematic invariants. Momenta are denoted by p_i while dual coordinates x_i label cusps of a polygon. Figures taken from Ref. [18].

entries. The region with $\varrho_0 = (+,+,\ldots,+)$ is the one in which all outgoing particles possess non-negative energy $p_i^0 \geq 0$. If we perform the multi-Regge limit of the remainder functions R_n in this region, the result turns out to vanish

$$[R_n(u,a)]^{\mathrm{MRL}}_{++\cdots+} = 0\,. \tag{18}$$

In other words, on the sheet ϱ_0 the BDS formula is actually multi-Regge exact. So if it was only for this region, the multi-Regge limit would not be able to see the difference between a vanishing and non-vanishing remainder function.

As we have anticipated in the introduction, however, there exists other regions in which the Regge limit of the remainder functions does not vanish. Of course, the non-vanishing terms must be associated with the cut contributions that are picked up when we analytically continue from the region ϱ_0 into a new region ϱ. Hence, the multi-Regge limit is able to detect that the remainder functions are non-zero, in spite of Eq. (18). Let us discuss this in a bit more detail at the example of the 2-loop 6-gluon remainder function $R_6^{(2)}$. In this case it turns out that only one of the 2^2 regions gives a non-trivial result, namely the one with $\varrho = (--)$. The continuation into this region is depicted in Fig. 2. As one can read off from the figure, upon continuation four of the s-like invariants become negative, namely

$$x_{24}^2\,,\; x_{46}^2\,,\; x_{25}^2 \;\text{ and }\; x_{36}^2 \tag{19}$$

while all other invariants x_{ij}^2 have the same sign as in the physical regime. Each of the three cross ratios $u_a = u_{a1}$ that we introduced in Eq. (6) contains two of the sign changing invariants from the list (19). Hence the cross ratios possess the same sign after continuation. But while u_2 and u_3 contain a ratio of the cross ratios from Eq. (19), u_1 involves a product. Hence, upon continuation into the $\varrho = (--)$ region, we can keep the cross ratios u_2 and u_3 fixed while u_1 must perform a full rotation around $u_1 = 0$. We shall do this by continuing the variable $u = u_1$ along a full circle

$$u(\varphi) \;=\; e^{-2i\varphi} u \tag{20}$$

where $\varphi \in [0, \pi]$. Because of the branch cuts, the behavior of the remainder functions R_n can depend very drastically on the sheet on which it is considered. Before we state the result for the R_6 at two loops, let us briefly look at the functions $Li_2(1-1/u)$ as an illustrative example. Upon analytic continuation of u along the circle (20), this function behaves as

$$Li_2\left(1-\frac{1}{e^{-2\pi i}u}\right) = Li_2\left(1-\frac{1}{u}\right) + 2\pi i \log\left(1-\frac{1}{u}\right) \ . \tag{21}$$

The second term on the right hand side is the cut contribution that arises when we pass through the branch cut of the di-logarithm Li_2. When we send u to $u = 1$, the first term actually vanishes, in complete analogy to the behavior (18) of the remainder functions on the physical sheet. The second term on the right hand side of equation (21), however, is non-zero in the limit. In fact, it is actually singular.

A similar computation can be performed for the two loop remainder function $R_6^{(2)}$. As we stated in section 2, there exits a nice and relatively simple analytical formula for this function due to Goncharov et al. [28]. Lipatov and Prygarin continued this expression along the path (20) into the only non-trivial multi-Regge region for $n = 6$ [51]. It turns out that the cut contributions that are picked up during the analytic continuation do not vanish in the Regge limit. After taking the Regge limit, their result takes the following form

$$\frac{1}{2\pi i}\left[R_6^{(2)}\right]_{--}^{\mathrm{MRL}} \sim a^2 \ln(1-u) \ln|1+w|^2 \ln\left|1+\frac{1}{w}\right|^2 + g_0^{(2)}(w) \ . \tag{22}$$

Here $u = u_1$ is the cross ratio that goes to $u \sim 1$ in the Regge limit and $w = w_1$. The function $g_0^{(2)}(w)$ is also known explicitly. Since we continued a two-loop result, all terms come with a factor a^2. Let us note that the first term actually diverges as we send $u \to 1$ while the remaining terms are finite. One refers to the first term as the leading logarithmic (LL) contribution. The other term is next to leading (NLL). More generally one may show that the Regge limit of the l-loop remainder function $R_6^{(l)}$ in the region $\varrho = (--)$ contains terms which diverge as $\ln^k(1-u)$ with $k = 0, \ldots, l-1$. These are referred to as $N^{l-1-k}LL$ contributions.

As long as the remainder function is only known to a few loop orders, one cannot repeat the computation that lead to Eq. (22) for higher orders. But there exists a remarkable formula due to [13] that encodes at least the leading logarithmic terms to all loop orders. The result of Bartels et al. takes the following form

$$\left[e^{R_6+i\delta_6}\right]_{--}^{\mathrm{MRL}} \sim \sum_{k=-\infty}^{\infty} (-1)^k \left(\frac{w}{w^*}\right)^{\frac{k}{2}} \int \frac{d\nu}{\nu^2+\frac{k^2}{4}} |w|^{2i\nu} \Phi_4 \cdot \left((u-1)\frac{|w|}{|1+w|^2}\right)^{-\omega_a(\nu,k)} \cdot \Phi_5 \tag{23}$$

where δ_6 contains the known cut contributions of he BDS Ansatz and we omitted the so-called Regge pole contributions, see [13] for the full result. The right hand side involves two functions of the coupling, the impact factors $\Phi_4 = \Phi_4(\nu, k)$ and $\Phi_5 = \Phi_5(\nu, k)$ related to the production of particles 4 and 5, resp., and the so-called BFKL eigenvalue $\omega = \omega(\nu, k)$. They all possess a power series expansion in a. In order to construct the LL contributions of the remainder function at any loop order it is sufficient to know Φ and ω in leading order. Bartels et al. showed that the impact factors Φ are trivial at leading order in a while the BFKL eigenvalue is given by the expression

$$\omega_a(\nu,k) = 2a\psi(1) - a\psi\left(1+i\nu+\frac{|k|}{2}\right) - a\psi\left(1-i\nu+\frac{|k|}{2}\right) + \frac{a}{2}\frac{|k|}{\nu^2+\frac{k^2}{4}} + \mathcal{O}(a^2) \, . \tag{24}$$

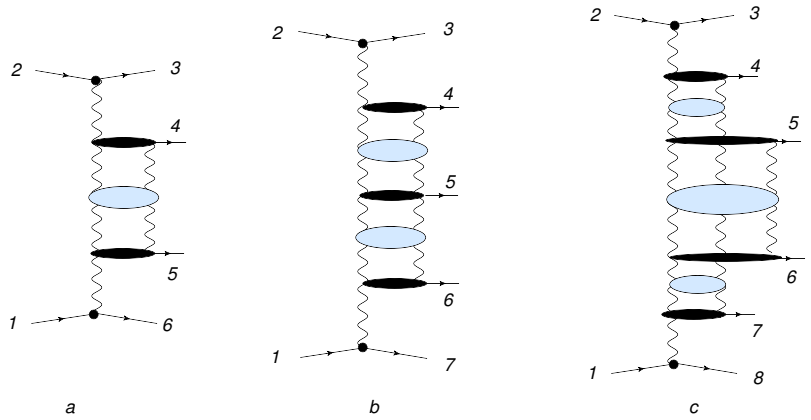


Figure 3: Illustration of the remainder functions R_6 (a), and pieces of R_7 (b) of R_8 (c): the wavy lines denote reggeized gluons. R_6 and R_7 consist of the bound state of two gluons (BFKL), R_8 contains, as a new piece, a three-gluon state. The grey circles denote Green's function; their bound state poles are given by the eigenvalues of the spin chain Hamiltonian (see text).

It is not too difficult to reconstruct the LL term in Eq. (22) from formula (23) and in fact to carry these computations to higher loop orders and even beyond the leading logarithmic order, see [14] for an extensive discussion.

The so-called BFKL eigenvalues $\omega(\nu, k)$ are the lowest eigenvalues of a non-compact SL(2,$\mathbb{C}$) Heisenberg Hamiltonian on an spin chain of length two, see [49,50,52]. The parameters ν, k label irreducible representations of SL(2,$\mathbb{C}$). Explicit expression for $\omega(\nu, k)$ in NLL were first given in [53]. Later, these were extended to NNLL using input from the amplitude bootstrap [54] and finally to all loops in [21], see below.

In the meantime, the LL calculations have been extended to $2 \to 5$ [55, 56] and even $2 \to 8$ [57] scattering processes, see Fig.3. Results for the $2 \to 5$ scattering amplitude include (a) a list of kinematic regions where the multi-Regge limit of the remainder function R_7 is nonzero and (b) an all order expression for the relevant pieces of R_7, analogous to the Eq. (23) we displayed for R_6. When compared to R_6, the multi-Regge limit of the remainder function R_7 contains a new production vertex for the centrally produced gluon, the central emission vertex. The other building blocks, i.e. the BFKL eigenvalues and the impact factors Φ are the same as for R_6. All these elements possess an expansion in the coupling a, and they are universal, i.e. they also appear in processes with higher numbers of legs, see also [58] and [59].

The remainder function R_8 for $n = 8$ external gluons contains, for the first time, a new eigenvalue of the Heisenberg Hamiltonian which extends the spin chain to length three. While in leading order this new Hamiltonian is just the sum of two length two Hamiltonians, the NLL approximation gives rise to a term which represents a new three body interaction between reggeized gluons [60]. Again, the detailed composition of R_8 depends upon the kinematic region. The next extensions of the spin chain is expected to be seen in the $n = 10$ point scattering process, $2 \to 8$, the $n = 12$ point process, $2 \to 10$ etc. One of the challenges will be to find, beyond the LL approximation, the eigenvalues of this spin chain: The three body interaction found in [60] raises some doubts whether they are simply obtained from the sum of two body interactions. This issue certainly deserves further investigation.

5 The strong coupling theory

At strong coupling, scattering amplitudes in the planar limit of $\mathcal{N} = 4$ SYM possess a geometric interpretation, namely as the area of a minimal two-dimensional surface that approaches the boundary of AdS_5 along a light-like polygon [15]. The latter is made up from the light-like four-momenta of the external gluons. In other words, the corners the polygon are given by the variables x_i we introduced in Eq. (1). Hence, the polygon encodes all the kinematic data of the process. The two-dimensional surface is drawn into AdS_5 by the gravitational field that is created by the D3-branes. As it stands, this beautiful geometric description of scattering processes does not seem to be very helpful in computing high energy limits of the kind we considered in the weakly coupled theory.

However, the minimal area problem was shown to possess an intriguing reformulation in which the area is reproduced by the free energy of a 1-dimensional integrable quantum system [16, 17]. The particle content and interactions of the latter are designed so as to solve the original geometric minimal area problem. The 1-dimensional quantum system contains a number of mass parameters and chemical potentials which match precisely the number of kinematic invariants in the scattering process, i.e. there are $3n - 15$ such parameters. The basic excitations turn out to interact through integrable $2 \mapsto 2$ scattering phases $S_{AB}(\theta)$ which depend on the rapidity θ of the 1-dimensional scattering process. As in any other quantum field theory, the vacuum of this 1-dimensional interacting quantum system is a complicated state that is determined by the quantum dynamics of the fundamental excitations, the external parameters and the interaction. More precisely, the rapidity densities of the various particles must be determined self-consistently as a function of the masses and chemical potentials. This is done by solving a system of coupled non-linear integral equations which involve both the external parameters and the scattering phases. Roughly, such equations take the form

$$\log Y_A(\theta) = -m_A \cosh\theta + \mu_A + \sum_B \int_\infty^\infty d\theta' \, K_{AB}(\theta - \theta' + i\phi_{AB}) \, \log\left(1 + Y_B(\theta')\right) \ . \tag{25}$$

Here the indices A, B run over the various particles and $\phi_{AB} = \phi_A - \phi_B$. The parameters $\mathfrak{m}_A = m_A \exp(i\phi_A)$ and μ_A play the role of the (complex) mass parameters and chemical potentials. The integration kernels

$$K_{AB}(\theta) = \partial_\theta \log S_{AB}(\theta) \tag{26}$$

are directly related to the scattering phases $S_{AB}(\theta)$. Once the density of excitations has been found, it can be used to determine the total energy of the system as

$$\mathcal{E}(\mathfrak{m}, \mu) \sim \sum_A \int d\theta \, m_A \, \cosh\theta \, \log(1 + Y_A(\theta)) \ . \tag{27}$$

The right hand side depends on m and μ through the explicit factor in the integrand as well as through the dependence of the rapidity densities Y_A on the external parameters. As we stressed before, the number of mass parameters and chemical potentials in the auxiliary 1-dimensional system was designed to match the number of cross-ratios u that describe the gauge theory scattering process. It is actually possible to provide a precise relation between the two sets of parameters,

$$u_{\alpha\sigma} = \frac{Y_{A(\alpha,\sigma)}}{1 + Y_{A(\alpha,\sigma)}} \left(\theta = i\frac{\pi}{4} r(\alpha,\sigma) - i\phi_{A(\alpha,\sigma)}\right) \ . \tag{28}$$

The dependence of the particle label $A = A(\alpha, \sigma)$ and the integer $r = r(\alpha, \sigma)$ on the indices $\alpha\sigma$ of the cross ratio can be found in Eq. (3.16) of [19]. The expressions on the right hand side of Eqs. (28) are functions of the masses $\mathfrak{m}_A$ and chemical potentials μ_A. These may be inverted at least numerically to determine the external parameters $\mathfrak{m}_A$ and μ_A of the 1-dimensional quantum system in terms of the kinematic data of the gauge theoretic scattering process.

According to [16, 17], the free energy we have just described provides the most non-trivial contribution to the remainder functions R_n at strong coupling. Explicit formulas for all the other terms can be found in the original literature. As we have stressed in the second section, the remainder function has a rather intricate analytic structure as a function of the kinematical variables u, at least at weak coupling. It turns our that the same is true at strong coupling [18], i.e. that the energy possesses interesting branch cuts as a function or the mass parameters and chemical potentials. From the point of view of the auxiliary 1-dimensional quantum system the basic mechanism goes back to an observation of Dorey and Tateo [61, 62]. As we move $\mathfrak{m}_A$ and μ_A through the complex plane to some new values m'_A and μ'_A the solutions $Y_B(\theta)$ are going to change. In particular, the solutions of the equation $Y_B(\theta_*) = -1$ will move through the space of complex rapidities θ. By inserting the relation (26) into Eq. (25) we can see that solutions of $Y_B(\theta_*) = -1$ are associated with poles in the integrand of the nonlinear integral equation. When these poles cross the integration contour, the equation picks up some residue contribution and hence assumes the new form

$$\begin{aligned} \log Y_A(\theta) \quad = \quad & -m'_A \cosh\theta + \mu'_A + \sum_{B,i} \sigma_i \log S_{AB}(\theta - \theta_{B,i} + i\phi_{AB}) \\ & + \sum_B \int_\infty^\infty d\theta' K_{AB}(\theta - \theta' + i\phi_{AB}) \, \log(1 + Y_B) \end{aligned} \tag{29}$$

with sign factors σ_i depending on whether the solution $\theta_{B,i}$ of $Y_B(\theta_i) = -1$ crosses from the lower half of the complex plane into the upper or vice versa. Here, the index $i = 1, \ldots, q_B$ was introduced in order to enumerate the crossing solutions and we denote by q_B the total number of them. Whenever such crossing happens, there is appears a new contribution to the total energy of the system,

$$\mathcal{E}(\mathfrak{m}', \mu') \sim \sum_{B,i} m'_B \sinh\theta_{B,i} + \sum_A \int d\theta \, m'_A \, \cosh\theta \, \log(1 + Y_A(\theta)) \, . \tag{30}$$

One may interpret these changes to the system as excitations that have been produced while we continued the system parameter $\mathfrak{m}_A, \mu_A$. Given the relation (28) between the mass parameters and chemical potentials of the 1-dimensional quantum system and the kinematical variables of the gauge theory, it is tempting to conjecture that the cut contributions of gauge theory amplitudes are related to the energy of excitations above the ground state in the 1-dimensional quantum system [18]. We will provide very strong evidence in the next section.

6 High energy scattering at strong coupling

Given the special features of the multi-Regge limit in gauge theory one may wonder about the nature of the corresponding limit for string theory on AdS_5. An important hint actually comes from the fact (18) that the remainder functions vanishes when the multi-Regge limit

is performed on the main sheet. Recall that at strong coupling the remainder functions is computed from the free energy $\mathcal{E}$ of the auxiliary 1-dimensional quantum system. As we argued before, due to quantum fluctuations the latter is a highly non-trivial function of the system parameters. But there is a way to turn off fluctuations and force the free energy to zero, namely by making the fundamental excitations of the 1-dimensional system infinitely massive so that it costs too much energy to produce them. This intuition is indeed correct as was shown in [18] for $n = 6$ gluons and then generalized to any number of external gluons in [19]. In other words, the high energy limit of gauge theory is directly related to the low energy limit of the auxiliary 1-dimensional quantum system.

As we have seen in section 4, on the gauge theory side the multi-Regge limit can become non-trivial if it is performed after continuation to a different multi-Regge region. According to our discussion in the previous section, such an analytic continuation can produce quasi-particle excitations of the ground state in the 1-dimensional auxiliary quantum system. The energy of these excitations contributes to the remainder function, see Eq. (30). In general the equations (29) for the rapidities are difficult to solve since the new quasi-particle excitations are dressed by clouds of quantum fluctuations. But as we take the multi-Regge limit, i.e. send all the mass parameters m_A to infinity, we freeze quantum fluctuations and the energy of the system is simply a sum of the bare quasi-particle energies. This physical picture suggests some drastic simplifications in the multi-Regge limit, even at strong coupling.

Our very qualitative discussion in the previous two paragraphs can actually be turned into an exact mathematical statement by analyzing the relation (28) between the cross ratios and the mass parameters. Indeed, it is possible to prove that the cross ratios possess the correct limiting behavior, i.e.

$$(u_{1\sigma}, u_{2\sigma}, u_{3\sigma}) \to (1, 0, 0) \quad \text{if} \quad \mathfrak{m}_A e^{i\frac{\pi}{4}s_A} \to \infty \,. \tag{31}$$

This result of [19] instructs us to send the masses to infinity along certain directions in the space of complex mass parameters. The value of the integer s_A can be found in the original paper. To be more precise let us stress that the parameters m_A are actually dimensionless and should rather be thought of as products $m_A = M_A L$ of a physical mass M_A and the system size L. Sending m_A to infinity is then achieved be making the physical mass M_A large or by going to the limit of large system size. In such a limit, the first term on the right hand side (25) goes to minus infinity and hence the function $Y(\theta)$ that appears in the logarithm on the left hand side must approach zero. This in turn implies that $\log(1 + Y_B(\theta')) \sim 0$ so that we can neglect the integral on the right hand side of the non-linear integral equations. This leaves us with the first two terms on the right hand side hand side of Eq. (29). The fact that we can drop the integral term from the Eqs. (25) and (29) in the low energy limit is the mathematical realization of what we referred to as freezing of fluctuations above. It clearly turns the complicated non-linear integral equations into a much simpler system.

With a little bit of additional massaging we can actually bring the resulting system into a more standard form. To this end we evaluate the first line of Eq. (29) at the points $\theta = \theta_{B,j}$, use that $Y(\theta_{B,j}) = -1$ and exponentiate both sides. As a result we obtain a set of $Q = \sum_A q_A$ algebraic Bethe ansatz equations,

$$e^{m'_A \cosh\theta_{A,j} - \mu'_A} = \prod_{(B,i)} S_{AB}^{\sigma_i}(\theta_{A,j} - \theta_{B,i} + i\phi'_{AB}) \,, \tag{32}$$

for Q unknown rapidities $\theta_{A,j}$. We called these equations the *Regge Bethe ansatz* in [20]. Let us stress once again that these equations are fully explicit once we insert the known expressions for

the phase shifts S_{AB} from [16]. Hence the system (32) can be solved for the rapidities $\theta_{A,j}$ of the excitations. Once the rapidities have been determined one can compute the energy as a sum of Q quasi-particle energies, one summand for each solution of $Y(\theta_{B,i}) = -1$ that has crossed the contour. From there it is an easy step to obtain the multi-Regge limit of the remainder function $[R_n^{(\infty)}]^{\mathrm{MRL}}$ at infinite coupling. The only tricky issue that remains is to know which solution of the Regge Bethe ansatz equations actually corresponds to a given multi-Regge region ϱ. At the moment there exists no general prescription that would relate discrete set of regions to the discrete set of solutions to Eqs. (32). But a few examples have been worked out.

This includes the case of $n = 6$ external gluons, see [18, 22]. In this case the index A runs through $A = 1, 2, 3$ and the corresponding mass parameters $\mathfrak{m}_A$ and chemical potentials μ_A are determined by a single real mass parameter m, an angle ϕ and a chemical potential μ, see the original literature for concrete formulas. In order to understand which solution of the Regge Bethe ansatz equation is relevant for the $\varrho = (--)$ region the system parameters m, ϕ and μ were continued along curves that kept u_2 and u_3 fixed while moving u_1 around the origin of the complex u_1 plane as prescribed in Eq. (20). Along the entire curve one can solve the non-linear integral equations and follow the solutions of $Y_A(\theta_*) = -1$. It turns out that only a single pair of such solutions for the function $Y_A = Y_3$ actually crosses the real line, see Fig. 4. This implies that the continuation produces $\mathcal{Q} = 2$ excitations or, more precisely, that $q_3 = 2$ while $q_1 = 0 = q_2$. The rapidities $\theta_{A,1} = \theta_{3,1}$ and $\theta_{A,2} = \theta_{3,2}$ of these excitations at the end of the path may be read off from Fig. 4, but they can also be found analytically. In fact, in the limit $m_3 = m \to \infty$, the two roots $\theta_{3,1}$ and $\theta_{3,2}$ must take the values [22]

$$\theta_{3,1} = i\frac{\pi}{4} + i\phi' \,, \qquad \theta_{3,2} = -i\frac{\pi}{4} + i\phi' \quad , \tag{33}$$

which is consistent with the position of endpoints in Fig. 4 since the plot was produced for $\phi = \phi' = 0$. Once the roots are known their values can be inserted to compute the remainder function in multi-Regge kinematics,

$$\left[e^{R_6^{(\infty)} + i\delta_6}\right]_{(--)}^{\mathrm{MRL}} \sim \left((u-1)\frac{|w|}{|1+w|^2}\right)^{-\omega_\infty} \quad , \tag{34}$$

where

$$\omega_\infty = \sqrt{\frac{a}{2}}\left(\sqrt{2} - \log(1+\sqrt{2})\right) \,. \tag{35}$$

Let us point out that expression in brackets is the same function of the kinematic variables that appears in the weak coupling result (23). As we will discuss shortly, the exponent ω_∞ can be considered as the universal leading term in the strong coupling expansion of the all order ($\mathrm{N}^\infty\mathrm{LL}$) BFKL eigenvalues $\omega_a(\nu, k)$ which turn out not to depend on the quantum numbers ν and k.

For the case of $n = 7$ external gluons, a similar analysis has been carried out for three of the four multi-Regge regions in which one expects a non-trivial result, namely for the regions $\varrho = (--+), (+--)$ and $(---)$. The results for the first two regions can essentially be copied from the study of $n = 6$ gluons that we sketched in the previous paragraph. For the region $\varrho = (---)$ things are a little more interesting. When $n = 7$ there are six functions Y_A which are labeled by Y_{as} with $a = 1, 2, 3$ and $s = 1, 2$. When we continue the system parameters to get to the region $\varrho = (---)$ four solutions of $Y_A(\theta_*) = -1$ cross the real line, namely two

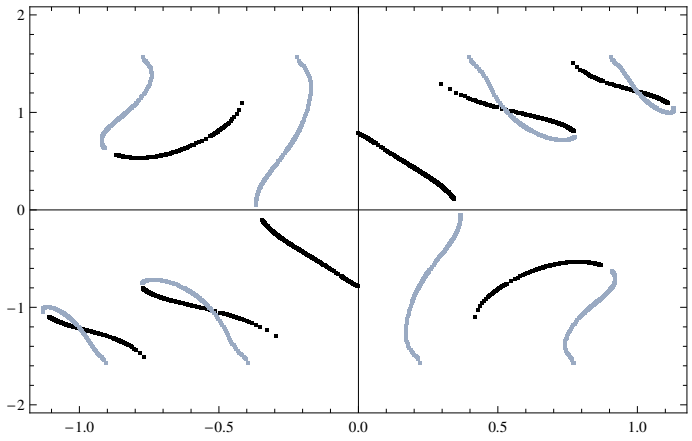


Figure 4: Solutions of the equation $Y_3(\theta_*) = -1$ in the complex θ plane for a family of parameters that implements the path (20) with $u_2 = u_3$ kept constant. The condition $u_2 = u_3$ corresponds to setting $\phi = 0$. The curves start in the light grey portions and proceed to the dark grey part. The change of color signals the point at which the pair of solutions crosses the real line. Figure taken from Ref. [18].

solutions of $Y_{31}(\theta_*) = -1$ and two solutions of $Y_{12}(\theta_*) = -1$. Hence there are four Bethe ansatz equations for four Bethe roots. These can be solved to obtain the following result for the strong coupling limit in the $\varrho = (- - -)$ region

$$\left[e^{R_7^{(\infty)}+i\delta_7}\right]^{\rm MRL}_{(---)} \sim \left((u_{11}-1)\frac{|w_1|}{|1+w_1|^2}(u_{12}-1)\frac{|w_2|}{|1+w_2|^2}\right)^{-\omega^\infty}, \tag{36}$$

where ω^∞ is once again given by Eq. (35). This is in fact nicely consistent with the weak coupling analysis. There is one more region $\varrho = (- + -)$ for which the remainder function is expected to possess a non-trivial multi-Regge limit. But in this case no solution of the Bethe ansatz has been identified that could give a reliable strong coupling prediction. We will comment a bit more on this issue below.

7 Interpolation and Outlook

In this work we have reviewed results on the multi-Regge limit of the remainder function in planar $\mathcal{N} = 4$ SYM theory. In particular we discussed this limit both at weak and strong coupling. The techniques and resulting formulas were completely different. As an example we provided expressions for the BFKL eigenvalues $\omega_a(\nu, k)$ in LLA, see Eq. (24), and for the quantity ω_∞ at strong coupling. Given the completely different calculational schemes for the two quantities it is stunning fact that Basso, Caron-Huot and Sever were able to smoothly interpolate between both expressions [21]. Based on the understanding of the flux tube in $\mathcal{N} = 4$ SYM theory that was achieved in [63–69] Basso and al. proposed the following formula

for the BFKL eigenvalue $\omega_a(\nu, k)$ at any value of the coupling a,

$$\omega_a(u,k) = -\int_0^\infty \frac{d\tau}{\tau}\left(\frac{1}{2}(Q_a(-\tau)+Q_a(\tau))\cos(ut)e^{-|k|\tau/2} - Q_a(\tau)\right), \tag{37}$$

$$\nu_a(u,k) = u + \int_0^\infty \frac{d\tau}{4\tau}(Q_a(-\tau)-Q_a(\tau))\sin(u\tau)e^{-|k|\tau/2}. \tag{38}$$

Here, $Q_a(\tau)$ is the generating function for the infinite set of charge densities of the GKP string that is determined by the BES equation (14), including its entire dependence on the coupling a. E.g. we displayed an explicit result for the first charge q_a^1 up to forth order in Eq. (5) and a some terms of the strong coupling expansion in Eq. (16). With such expressions one can then go ahead and calculate the integrals $\omega(u,k)$ and $\nu_a(u,k)$, invert the second expression to compute $u = u(\nu,k)$ and eliminate u from $\omega_a(u,k)$ to obtain $\omega_a(\nu,k)$. It is quite straightforward to re-derive expressions such as Eq. (24) in leading order as well as higher order corrections at weak coupling. At strong coupling, it turns out that the solution becomes independent of ν and k and it indeed coincides with our formula (35).

Similar interpolation equations for those BFKL eigenvalues that correspond to Heisenberg spin chains of more than two sites at weak coupling have not been published. The first region in which these are expected to occur is $\varrho = (-++-)$ for $n = 8$. Regions in which $-$ signs are separated by $+$ signs are generally less studied than those in which all $-$ signs appear on consecutive legs. The first example of such a region appears for $n = 7$, namely the region $\varrho = (-+-)$. As we have commented above, there exists no satisfactory strong coupling prediction for this region. It would certainly be interesting to determine the relevant solution of our Regge Bethe ansatz. Let us point out that Basso et al. also determined the impact factor Φ to all loops [21]. On the other hand, the amplitudes for higher number of external gluons contain additional building blocks, such as the central emission vertex we discussed briefly in section 4. It would certainly be interesting to construct all these elements for arbitrary coupling. While the relevant equations have not appeared in the literature yet, there is a concrete path towards a complete understanding of scattering amplitudes for planar $\mathcal{N} = 4$ SYM theory, at least in the multi-Regge limit. And even the complete all loop results for $n = 6$ demonstrate that finally string theory can cope with high energy scattering, not just qualitatively but even in precision calculations and it does so with astonishing efficiency.

Acknowledgements

It is a great pleasure to thank all our collaborators for their contributions to the joint research we reviewed here, especially Jan Kotanski and Martin Sprenger. We are particularly grateful to Lev Lipatov for sharing his deep insights over so many years. Finally, we acknowledge the support from the SFB 676 on "Particles, Strings and the Early Universe".

References

[1] G. 't Hooft, *A Planar Diagram Theory for Strong Interactions*, *Nucl. Phys.* **B72** (1974) 461. [,337(1973)].

[2] A. M. Polyakov, *Thermal Properties of Gauge Fields and Quark Liberation*, *Phys. Lett.* **72B** (1978) 477–480.

[3] J. M. Maldacena, *The Large N limit of superconformal field theories and supergravity*, *Int. J. Theor. Phys.* **38** (1999) 1113–1133, [hep-th/9711200]. [Adv. Theor. Math. Phys.2,231(1998)].

[4] J. Polchinski and M. J. Strassler, *Hard scattering and gauge / string duality*, *Phys. Rev. Lett.* **88** (2002) 031601, [hep-th/0109174].

[5] I. Bena, J. Polchinski and R. Roiban, *Hidden symmetries of the AdS(5) × S^5 superstring*, *Phys. Rev.* **D69** (2004) 046002, [hep-th/0305116].

[6] J. A. Minahan and K. Zarembo, *The Bethe ansatz for N=4 superYang-Mills*, *JHEP* **03** (2003) 013, [hep-th/0212208].

[7] N. Beisert et al., *Review of AdS/CFT Integrability: An Overview*, *Lett. Math. Phys.* **99** (2012) 3–32, [1012.3982].

[8] A. V. Kotikov and L. N. Lipatov, *DGLAP and BFKL equations in the $N = 4$ supersymmetric gauge theory*, *Nucl. Phys.* **B661** (2003) 19–61, [hep-ph/0208220]. [Erratum: Nucl. Phys.B685,405(2004)].

[9] A. V. Kotikov, L. N. Lipatov, A. I. Onishchenko and V. N. Velizhanin, *Three loop universal anomalous dimension of the Wilson operators in $N = 4$ SUSY Yang-Mills model*, *Phys. Lett.* **B595** (2004) 521–529, [hep-th/0404092]. [Erratum: Phys. Lett.B632,754(2006)].

[10] S. Moch, J. A. M. Vermaseren and A. Vogt, *The Three loop splitting functions in QCD: The Nonsinglet case*, *Nucl. Phys.* **B688** (2004) 101–134, [hep-ph/0403192].

[11] A. Vogt, S. Moch and J. A. M. Vermaseren, *The Three-loop splitting functions in QCD: The Singlet case*, *Nucl. Phys.* **B691** (2004) 129–181, [hep-ph/0404111].

[12] N. Beisert, B. Eden and M. Staudacher, *Transcendentality and Crossing*, *J. Stat. Mech.* **0701** (2007) P01021, [hep-th/0610251].

[13] J. Bartels, L. N. Lipatov and A. Sabio Vera, *N=4 supersymmetric Yang Mills scattering amplitudes at high energies: The Regge cut contribution*, *Eur. Phys. J.* **C65** (2010) 587–605, [0807.0894].

[14] L. J. Dixon, C. Duhr and J. Pennington, *Single-valued harmonic polylogarithms and the multi-Regge limit*, *JHEP* **10** (2012) 074, [1207.0186].

[15] L. F. Alday and J. M. Maldacena, *Gluon scattering amplitudes at strong coupling*, *JHEP* **06** (2007) 064, [0705.0303].

[16] L. F. Alday, D. Gaiotto and J. Maldacena, *Thermodynamic Bubble Ansatz*, *JHEP* **09** (2011) 032, [0911.4708].

[17] L. F. Alday, J. Maldacena, A. Sever and P. Vieira, *Y-system for Scattering Amplitudes*, *J. Phys.* **A43** (2010) 485401, [1002.2459].

[18] J. Bartels, J. Kotanski and V. Schomerus, *Excited Hexagon Wilson Loops for Strongly Coupled N=4 SYM*, *JHEP* **01** (2011) 096, [1009.3938].

[19] J. Bartels, V. Schomerus and M. Sprenger, *Multi-Regge Limit of the n-Gluon Bubble Ansatz*, *JHEP* **11** (2012) 145, [1207.4204].

[20] J. Bartels, V. Schomerus and M. Sprenger, *The Bethe roots of Regge cuts in strongly coupled $\mathcal{N} = 4$ SYM theory*, *JHEP* **07** (2015) 098, [1411.2594].

[21] B. Basso, S. Caron-Huot and A. Sever, *Adjoint BFKL at finite coupling: a short-cut from the collinear limit*, *JHEP* **01** (2015) 027, [1407.3766].

[22] J. Bartels, J. Kotanski, V. Schomerus and M. Sprenger, *The Excited Hexagon Reloaded*, 1311.1512.

[23] S. J. Parke and T. R. Taylor, *An Amplitude for n Gluon Scattering*, *Phys. Rev. Lett.* **56** (1986) 2459.

[24] Z. Bern, L. J. Dixon and V. A. Smirnov, *Iteration of planar amplitudes in maximally supersymmetric Yang-Mills theory at three loops and beyond*, *Phys. Rev.* **D72** (2005) 085001, [hep-th/0505205].

[25] J. M. Drummond, J. Henn, G. P. Korchemsky and E. Sokatchev, *Dual superconformal symmetry of scattering amplitudes in N=4 super-Yang-Mills theory*, *Nucl. Phys.* **B828** (2010) 317–374, [0807.1095].

[26] J. Bartels, L. N. Lipatov and A. Sabio Vera, *BFKL Pomeron, Reggeized gluons and Bern-Dixon-Smirnov amplitudes*, *Phys. Rev.* **D80** (2009) 045002, [0802.2065].

[27] V. Del Duca, C. Duhr and V. A. Smirnov, *The Two-Loop Hexagon Wilson Loop in $N = 4$ SYM*, *JHEP* **05** (2010) 084, [1003.1702].

[28] A. B. Goncharov, M. Spradlin, C. Vergu and A. Volovich, *Classical Polylogarithms for Amplitudes and Wilson Loops*, *Phys. Rev. Lett.* **105** (2010) 151605, [1006.5703].

[29] L. J. Dixon, J. M. Drummond, C. Duhr, M. von Hippel and J. Pennington, *Bootstrapping six-gluon scattering in planar N=4 super-Yang-Mills theory*, *PoS* **LL2014** (2014) 077, [1407.4724].

[30] B. Basso, A. Sever and P. Vieira, *Hexagonal Wilson loops in planar $\mathcal{N} = 4$ SYM theory at finite coupling*, *J. Phys.* **A49** (2016) 41LT01, [1508.03045].

[31] J. Golden and M. Spradlin, *An analytic result for the two-loop seven-point MHV amplitude in $\mathcal{N} = 4$ SYM*, *JHEP* **08** (2014) 154, [1406.2055].

[32] L. J. Dixon, J. Drummond, T. Harrington, A. J. McLeod, G. Papathanasiou and M. Spradlin, *Heptagons from the Steinmann Cluster Bootstrap*, *JHEP* **02** (2017) 137, [1612.08976].

[33] B. Basso and G. P. Korchemsky, *Anomalous dimensions of high-spin operators beyond the leading order*, *Nucl. Phys.* **B775** (2007) 1–30, [hep-th/0612247].

[34] Z. Bajnok, R. A. Janik and T. Lukowski, *Four loop twist two, BFKL, wrapping and strings*, *Nucl. Phys.* **B816** (2009) 376–398, [0811.4448].

[35] T. Lukowski, A. Rej and V. N. Velizhanin, *Five-Loop Anomalous Dimension of Twist-Two Operators*, *Nucl. Phys.* **B831** (2010) 105–132, [0912.1624].

[36] C. Marboe, V. Velizhanin and D. Volin, *Six-loop anomalous dimension of twist-two operators in planar $\mathcal{N} = 4$ SYM theory*, *JHEP* **07** (2015) 084, [1412.4762].

[37] C. Marboe and V. Velizhanin, *Twist-2 at seven loops in planar $\mathcal{N} = 4$ SYM theory: full result and analytic properties*, *JHEP* **11** (2016) 013, [1607.06047].

[38] S. Moch, B. Ruijl, T. Ueda, J. A. M. Vermaseren and A. Vogt, *Four-Loop Non-Singlet Splitting Functions in the Planar Limit and Beyond*, *JHEP* **10** (2017) 041, [1707.08315].

[39] J. A. M. Vermaseren, A. Vogt and S. Moch, *The Third-order QCD corrections to deep-inelastic scattering by photon exchange*, *Nucl. Phys.* **B724** (2005) 3–182, [hep-ph/0504242].

[40] S. Moch, B. Ruijl, T. Ueda, J. A. M. Vermaseren and A. Vogt, *On quartic colour factors in splitting functions and the gluon cusp anomalous dimension*, *Phys. Lett.* **B782** (2018) 627–632, [1805.09638].

[41] C. L. Basham, L. S. Brown, S. D. Ellis and S. T. Love, *Energy Correlations in electron-Positron Annihilation in Quantum Chromodynamics: Asymptotically Free Perturbation Theory*, *Phys. Rev.* **D19** (1979) 2018.

[42] A. V. Belitsky, S. Hohenegger, G. P. Korchemsky, E. Sokatchev and A. Zhiboedov, *Energy-Energy Correlations in N=4 Supersymmetric Yang-Mills Theory*, *Phys. Rev. Lett.* **112** (2014) 071601, [1311.6800].

[43] O. Gituliar and S. Moch, *Fuchsia and Master Integrals for Energy-Energy Correlations at NLO in QCD*, *Acta Phys. Polon.* **B48** (2017) 2355, [1711.05549].

[44] L. J. Dixon, M.-X. Luo, V. Shtabovenko, T.-Z. Yang and H. X. Zhu, *Analytical Computation of Energy-Energy Correlation at Next-to-Leading Order in QCD*, *Phys. Rev. Lett.* **120** (2018) 102001, [1801.03219].

[45] S. S. Gubser, I. R. Klebanov and A. M. Polyakov, *A Semiclassical limit of the gauge / string correspondence*, *Nucl. Phys.* **B636** (2002) 99–114, [hep-th/0204051].

[46] Z. Bern, M. Czakon, L. J. Dixon, D. A. Kosower and V. A. Smirnov, *The Four-Loop Planar Amplitude and Cusp Anomalous Dimension in Maximally Supersymmetric Yang-Mills Theory*, *Phys. Rev.* **D75** (2007) 085010, [hep-th/0610248].

[47] B. Basso, G. P. Korchemsky and J. Kotanski, *Cusp anomalous dimension in maximally supersymmetric Yang-Mills theory at strong coupling*, *Phys. Rev. Lett.* **100** (2008) 091601, [0708.3933].

[48] R. C. Brower, C. E. DeTar and J. H. Weis, *Regge Theory for Multiparticle Amplitudes*, *Phys. Rept.* **14** (1974) 257.

[49] L. N. Lipatov, *Asymptotic behavior of multicolor QCD at high energies in connection with exactly solvable spin models*, *JETP Lett.* **59** (1994) 596–599, [hep-th/9311037]. [Pisma Zh. Eksp. Teor. Fiz.59,571(1994)].

[50] L. D. Faddeev and G. P. Korchemsky, *High-energy QCD as a completely integrable model*, *Phys. Lett.* **B342** (1995) 311–322, [hep-th/9404173].

[51] L. N. Lipatov and A. Prygarin, *Mandelstam cuts and light-like Wilson loops in N=4 SUSY*, *Phys. Rev.* **D83** (2011) 045020, [1008.1016].

[52] L. N. Lipatov, *Integrability of scattering amplitudes in N=4 SUSY*, *J. Phys.* **A42** (2009) 304020, [0902.1444].

[53] V. S. Fadin and L. N. Lipatov, *BFKL equation for the adjoint representation of the gauge group in the next-to-leading approximation at N=4 SUSY*, *Phys. Lett.* **B706** (2012) 470–476, [1111.0782].

[54] L. J. Dixon, J. M. Drummond, C. Duhr and J. Pennington, *The four-loop remainder function and multi-Regge behavior at NNLLA in planar N = 4 super-Yang-Mills theory*, *JHEP* **06** (2014) 116, [1402.3300].

[55] J. Bartels, A. Kormilitzin and L. Lipatov, *Analytic structure of the $n = 7$ scattering amplitude in $\mathcal{N} = 4$ SYM theory in the multi-Regge kinematics: Conformal Regge pole contribution*, *Phys. Rev.* **D89** (2014) 065002, [1311.2061].

[56] J. Bartels, A. Kormilitzin and L. N. Lipatov, *Analytic structure of the $n = 7$ scattering amplitude in $\mathcal{N} = 4$ theory in multi-Regge kinematics: Conformal Regge cut contribution*, *Phys. Rev.* **D91** (2015) 045005, [1411.2294].

[57] J. Bartels, *in preparation*, .

[58] T. Bargheer, G. Papathanasiou and V. Schomerus, *The Two-Loop Symbol of all Multi-Regge Regions*, *JHEP* **05** (2016) 012, [1512.07620].

[59] V. Del Duca, S. Druc, J. Drummond, C. Duhr, F. Dulat, R. Marzucca et al., *The seven-gluon amplitude in multi-Regge kinematics beyond leading logarithmic accuracy*, *JHEP* **06** (2018) 116, [1801.10605].

[60] J. Bartels, V. S. Fadin, L. N. Lipatov and G. P. Vacca, *NLO Corrections to the kernel of the BKP-equations*, *Nucl. Phys.* **B867** (2013) 827–854, [1210.0797].

[61] P. Dorey and R. Tateo, *Excited states by analytic continuation of TBA equations*, *Nucl. Phys.* **B482** (1996) 639–659, [hep-th/9607167].

[62] P. Dorey and R. Tateo, *Excited states in some simple perturbed conformal field theories*, *Nucl. Phys.* **B515** (1998) 575–623, [hep-th/9706140].

[63] L. F. Alday, D. Gaiotto, J. Maldacena, A. Sever and P. Vieira, *An Operator Product Expansion for Polygonal null Wilson Loops*, *JHEP* **04** (2011) 088, [1006.2788].

[64] B. Basso, *Exciting the GKP string at any coupling*, *Nucl. Phys.* **B857** (2012) 254–334, [1010.5237].

[65] B. Basso and A. Rej, *Bethe ansätze for GKP strings*, *Nucl. Phys.* **B879** (2014) 162–215, [1306.1741].

[66] B. Basso, A. Sever and P. Vieira, *Spacetime and Flux Tube S-Matrices at Finite Coupling for N=4 Supersymmetric Yang-Mills Theory*, *Phys. Rev. Lett.* **111** (2013) 091602, [1303.1396].

[67] B. Basso, A. Sever and P. Vieira, *Space-time S-matrix and Flux tube S-matrix II. Extracting and Matching Data*, *JHEP* **01** (2014) 008, [1306.2058].

[68] B. Basso, A. Sever and P. Vieira, *Space-time S-matrix and Flux-tube S-matrix III. The two-particle contributions*, *JHEP* **08** (2014) 085, [1402.3307].

[69] B. Basso, A. Sever and P. Vieira, *Space-time S-matrix and Flux-tube S-matrix IV. Gluons and Fusion*, *JHEP* **09** (2014) 149, [1407.1736].

Non-Abelian Gerbes and some Applications in String Theory

Christoph Schweigert[1], *Konrad Waldorf*[2]

[1]Fachbereich Mathematik, Universität Hamburg, Germany
[2]Institut für Mathematik und Informatik, Universität Greifswald, Germany

DOI: http://dx.doi.org/10.3204/PUBDB-2018-00782/A4

We review a systematic construction of the 2-stack of bundle gerbes via descent, and extend it to non-abelian gerbes. We review the role of non-abelian gerbes in orientifold sigma models, for the anomaly cancellation in supersymmetric sigma models, and in a geometric description of so-called non-geometric T-duals.

1 Introduction

Higher structures are an important recent trend in mathematics. They arise in many fields, most notably in representation theory and in geometry. In geometric applications, one considers not only classical geometric objects, e.g. manifolds and fibre bundles on them, but also objects of a higher categorical nature. In this contribution, we explain why higher structures naturally appear in string theory and, more generally, in sigma models.

Various categories of manifolds (with additional structure) appear in string theory: bosonic sigma models can be defined on smooth manifolds with a metric; for fermions, a spin structure (and even a string structure) has to be chosen. Symplectic manifolds appear in the discussion of A-models, and complex manifolds for B-models of topologically twisted string backgrounds. Already in the very early days of string theory, it was clear that one should go beyond manifolds to get more interesting classes of models: in the orbifold construction, one considers manifolds with a group action that is not necessarily free. In modern language, an orbifold is a proper étale Lie groupoid and thus an object of a bicategory. Thus, in a certain sense, orbifolds can be seen as a first instance of a higher structure in string theory.

Another source of higher structures in string theory are p-form gauge fields. Bosonic string theory has a 2-form gauge field, the Kalb–Ramond field. It comes with gauge transformations parameterized by 1-form gauge fields, and there are gauge transformations of gauge transformations parameterized by $U(1)$-valued functions. Later, Ramond–Ramond fields in superstring theory have been a rich source of gauge fields associated to forms of higher degree. The modern framework to describe such gauge fields are gerbes and their higher categorical generalizations. They have played an important role in this project of the SFB 676.

The appropriate mathematical framework for the description of ordinary 1-form gauge fields are principal $U(1)$-bundles with connection. Given such a connection, one obtains parallel transport, and a holonomy map that assigns to a closed curve an endomorphism of the fibre, which can be identified with a group element. This holonomy enters in the action functional

of charged particles, and plays an important role e.g. in the discussion of the Aharonov–Bohm effect.

The framework for 2-form gauge fields are $U(1)$-gerbes with connection. Various concrete realizations are available: Dixmier–Douady sheaves of groupoids, Čech–Deligne cocycles, bundle gerbes, principal 2-bundles etc. In this contribution we will focus on bundle gerbes. A connection on a $U(1)$-bundle gerbe leads to surface holonomy, i.e. it associates to a closed oriented surface an element in $U(1)$. This provides a rigorous geometric description of Wess–Zumino terms in general target space topology. Similarly, connections on higher bundle gerbes lead to a notion of holonomy for higher-dimensional manifolds. The Chern–Simons term in three-dimensional field theories, for example, can be interpreted as the holonomy of a 2-gerbe. A review concentrating on surface holonomy of gerbes and their applications in string theory has been written by the authors, together with Jürgen Fuchs and Thomas Nikolaus, based on earlier results obtained in this project in the SFB 676 [1].

In this contribution, we focus on another, equally important aspect of higher geometry, namely its treatment in the framework of higher stacks. In a certain sense, this exhibits geometric objects as local objects. Some aspects of the theory of higher stacks (mostly: 2-stacks), as well as a number of applications to string theory have been developed within this project of the SFB 676.

We start in Section 2 by a gentle introduction to stacks and 2-stacks, and provide a new and conceptually clear definition of the bicategory of abelian bundle gerbes. In Section 3, we generalize this definition to non-abelian bundle gerbes, clarifying many open issues in an elegant way. In Section 4 we show that our treatment in the framework of 2-stacks has the additional advantage that it automatically extends the whole theory from manifolds to Lie groupoids. In particular, equivariant (non-abelian) gerbes are a canonical output of this approach. In Section 5 we study Jandl gerbes, the gauge fields in orientifold sigma models, as non-abelian gerbes over certain action groupoids. This allows a systematic approach to Jandl gerbes. In Section 6 we report some recent results about string structures on manifolds, and their applications to supersymmetric sigma models, with an emphasis on a description of string structures by non-abelian gerbes for the string group. Finally, in Section 7, we describe another application of non-abelian gerbes in the context of T-duality. The 2-stack-theoretical properties of non-abelian gerbes are essential in this application: we glue locally defined T-duality correspondences to obtain a globally defined new object, a version of a so-called T-fold.

2 A new perspective to bundle gerbes

A hallmark of any geometric theory is the possibility to obtain global objects from locally defined objects by a gluing procedure. In this way, globally defined geometric objects keep aspects of locality. The essential information for gluing is the categorical structure of the local model. For instance, principal G-bundles (with G a finite-dimensional Lie group) can be glued from trivial bundles along G-valued transition functions. In this example, the local model is a category with a single object (the trivial G-bundle), whose morphisms are smooth G-valued maps (the automorphisms of the trivial bundle). All information is contained in this local model; in this case, even, only in its morphisms. The local model should be contravariant in the base manifold, so that one can restrict to smaller subsets. In more technical terms, it should form a *presheaf of categories* over the category of smooth manifolds: a (weak) functor

$$\mathfrak{X} : \mathcal{M}an^{op} \to \mathcal{C}at.$$

It includes the assignment of a category $\mathfrak{X}(M)$ to each smooth manifold M, and of a functor $f^* : \mathfrak{X}(N) \to \mathfrak{X}(M)$ to each smooth map $f : M \to N$, compatible with the composition of smooth maps in a certain way. In the example of principal G-bundles, we have $\mathfrak{X}(M) = BC^\infty(M, G)$, using the notation BG for the category with a single object whose automorphism group is G. The functor $f^* : BC^\infty(N, G) \to BC^\infty(M, G)$ is trivial on the level of objects, and $g \mapsto f \circ g$ on the level of morphisms.

Usually (and so in our example) local models do not contain the global objects. In other words, the gluing of local objects will not produce another local object. In more technical terms, the presheaves $\mathfrak{X}$ are usually not *sheaves of categories*, or *stacks*. The notion of a stack depends, in the first place, on a notion of locality for the underlying category. Essentially, one has to specify a class of morphisms that correspond to open covers in an abstract sense. In case of $\mathcal{M}an$, one may consider all maps of the form

$$\coprod_{i \in I} U_i \to M : (i, x) \mapsto x, \tag{1}$$

where $(U_i)_{i \in I}$ is an open cover of M. We shall be more specific about what we want to glue. Given an open cover $U = (U_i)_{i \in I}$ of M, we consider a collection $(X_i)_{i \in I}$ of local objects $X_i \in \mathfrak{X}(U_i)$, together with a collection of isomorphisms $g_{ij} : X_i|_{U_i \cap U_j} \to X_j|_{U_i \cap U_j}$ in $\mathfrak{X}(U_i \cap U_j)$, for all two-fold overlaps, which are compatible in the sense that a cocycle condition

$$g_{jk} \circ g_{ij} = g_{ik} \tag{2}$$

is satisfied in $\mathfrak{X}(U_i \cap U_j \cap U_k)$, for all three-fold overlaps. A pair $((X_i), (g_{ij}))$ is called a *descent object* for the presheaf $\mathfrak{X}$ with respect to the cover U. There is a natural notion of morphisms between descent objects, so that a category $\mathcal{D}esc_{\mathfrak{X}}(U)$ is formed.

If the gluing of a descent object $((X_i), (g_{ij}))$ within $\mathfrak{X}$ could be performed, then it is expected to result in a global object $X \in \mathfrak{X}(M)$ that locally restricts to the given local objects X_i in a way compatible with the gluing isomorphisms g_{ij}. More precisely, we associate to X the descent object $X_U := (X|_{U_i}, \mathrm{id})$ and require that $(X|_{U_i}, \mathrm{id}) \cong ((X_i), (g_{ij}))$ in $\mathcal{D}esc_{\mathfrak{X}}(U)$. In other words, we consider the functor

$$\mathfrak{X}(M) \to \mathcal{D}esc_{\mathfrak{X}}(U) : X \mapsto X_U \tag{3}$$

and demand it to be essentially surjective. For the definition of a stack we require even a bit more, in order to be able to glue not only objects but also morphisms: a presheaf $\mathfrak{X}$ of categories is called a *stack*, if the functor (3) is an equivalence of categories for every open cover U.

As mentioned before, typical local models do not form stacks but only so-called *prestacks*, meaning that the functors (3) are not essentially surjective, but still fully faithful. However, there is a procedure, called *plus construction*, to turn a prestack $\mathfrak{X}$ into a stack $\mathfrak{X}^+$. The idea is very simple: an object in $\mathfrak{X}^+(M)$ is a pair of an open cover U and an object in $\mathcal{D}esc_{\mathfrak{X}}(U)$. The morphisms are defined over common refinements of open covers, and we shall omit the details here. One can show that the plus construction is idempotent for prestacks, i.e. $\mathfrak{X}^{++} \cong \mathfrak{X}^+$ [2]. In our example of the local model $\mathfrak{X} = BC^\infty(-, G)$ for principal G-bundles, one can then check that $\mathfrak{X}^+(M)$ is canonically equivalent to the usual category $\mathcal{B}un_G(M)$ of principal G-bundles over M, via the clutching construction.

One can admit more general morphisms in our notion of locality, for example one can consider all surjective submersions $\pi : Y \to M$ instead of just the one of the form (1). This

has for example advantages in the construction of bundle gerbes on compact Lie groups. The k-fold intersections are then replaced by the k-fold fibre product $Y^{[k]} = Y \times_M ... \times_M Y$, and the definition of the descent category $\mathcal{D}esc_{\mathfrak{X}}(\pi)$ is fully analogous. In fact, it turns out that the resulting stackification $\mathfrak{X}^+$ will be the same as before [2].

The main advantage of this approach to geometrical objects over manifolds is that it is very general: its only input is the local model $\mathfrak{X}$. For example, we let $\mathfrak{X}$ be the following prestack: the objects of $\mathfrak{X}(M)$ are all $\mathfrak{g}$-valued 1-forms on M, and the morphisms are all gauge transformations. Then, $\mathfrak{X}^+$ is the stack $\mathcal{B}un_G^\nabla$ of principal G-bundles with connections. On the other hand, this approach does often not bring much new insight into the geometric objects themselves, since nice geometric models are well-known, as in the cases of principal G-bundles with and without connections.

Analogous considerations persist in higher-categorical settings with more interesting results [2]. For instance, in one categorical degree higher we consider presheaves $\mathfrak{X}$ of bicategories as our local models. Now, the definition of the descent category has to be changed in order to incorporate 2-morphisms. A descent object in $\mathcal{D}esc_{\mathfrak{X}}(U)$ is a collection of objects X_i in $\mathfrak{X}(U_i)$ and of morphisms g_{ij} in $\mathfrak{X}(U_i \cap U_j)$ as before, but instead of the cocycle condition (2) it includes additionally a collection of 2-isomorphisms

$$\mu_{ijk} : g_{jk} \circ g_{ij} \Rightarrow g_{ik}$$

in $\mathfrak{X}(U_i \cap U_j \cap U_k)$ satisfying a new cocycle condition in $\mathfrak{X}(U_i \cap U_j \cap U_k \cap U_l)$. Again, there is a 2-functor

$$\mathfrak{X}(M) \to \mathcal{D}esc_{\mathfrak{X}}(U)$$

and we call $\mathfrak{X}$ a *pre-2-stack* if – for all open covers U – it induces an equivalence on Hom-categories, and a *2-stack* if it is an equivalence of bicategories. A generalization of the plus construction produces a 2-stack $\mathfrak{X}^+$ out of any pre-2-stack $\mathfrak{X}$ [2]. A concrete example, and the main motivation for this section, is a local model where the morphisms are principal $U(1)$-bundles. We consider the pre-2-stack $\mathfrak{X} = B\mathcal{B}un_{U(1)}$: the bicategory $\mathfrak{X}(M)$ has a single object, its automorphisms are principal $U(1)$-bundles over M, and the 2-morphisms are all bundle morphisms. The composition is the tensor product of principal $U(1)$-bundles. Again, all information is in the morphisms, this time in the morphism categories. The reader is encouraged to perform a brief check, that the plus construction (with respect to surjective submersions) produces exactly the bicategory of $U(1)$-bundle gerbes,

$$\mathcal{BG}rb_{U(1)}(M) = (B\mathcal{B}un_{U(1)})^+(M)$$

as described by Murray and Stevenson [3–5]. Let us summarize three advantages of this result:

1. It derives the definition of a bundle gerbe from first principles.
2. It automatically produces the quite complicated bicategorical structure of bundle gerbes, whose development by hand took many years.
3. By construction, $\mathcal{BG}rb_{U(1)}$ is a 2-stack, i.e. bundle gerbes can be glued. Variants of this result have been proved by hand by Stevenson [5] and Meinrenken [6].

It is straightforward to find interesting variations. For example, one can take any abelian Lie group A instead of $U(1)$, since then $\mathcal{B}un_A$ is still a monoidal category. One can take hermitian line bundles instead of principal $U(1)$-bundles, resulting in a line bundle version of

bundle gerbes. One can even consider hermitian vector bundles of *higher* (but finite) rank. The reader is again encouraged to check that this does not change the definition of a single bundle gerbe, but it produces a bicategory with more 1-morphisms, in particular, non-invertible ones. Finally, one can add connections to the picture, and thus consider a pre-2-stack $\mathfrak{X}$ whose bicategory $\mathfrak{X}(M)$ is the following:

- Its objects are 2-forms $B \in \Omega^2(M)$.
- The Hom-category between objects B_1 and B_2 is the full subcategory of hermitian vector bundles E over M with unitary connections ∇ of curvature

$$\frac{1}{\mathrm{rk}(E)}\,\mathrm{tr}(\mathrm{curv}(\nabla)) = B_2 - B_1. \tag{4}$$

The plus construction results precisely in the bicategory of bundle gerbes with connection described in [7]. The proof of the fact that bundle gerbes with connection form a 2-stack should be seen as one important mathematical result of this project of the SFB676.

We remark that bundle gerbes with connection give rise to a notion of surface holonomy. Surface holonomy is the basis of many applications of bundle gerbes in string theory: connections on bundle gerbes are the Kalb–Ramond gauge fields for strings, and surface holonomy provides the coupling term in the string action. The extension from line bundles to vector bundles allows to discuss twisted Chan–Paton gauge fields on D-branes within this framework [7]. For a more detailed discussion of surface holonomy we refer to our review [1].

3 Non-abelian gerbes

In this section we demonstrate the full power of the plus construction in the case of so-called non-abelian gerbes. The terminology is not totally accurate, as the abelian group $U(1)$ of the previous section is generalized to a *Lie 2-group* (instead of a non-abelian group). Non-abelian gerbes have found several possible applications in string theory:

- Connections on non-abelian gerbes are the gauge fields in higher gauge theory; see [8] for an overview. In M-theory, they arise in the Lagrangian description of M5-branes, see [9–11].
- Non-abelian gerbes have been used to describe 4-dimensional topological quantum field theories that control the long-distance behaviour of surface operators in gapped phases of 4-dimensional gauge theories [12].
- Graded $U(1)$-gerbes can be seen as non-abelian gerbes; they appear in orientifold sigma models (see Section 5 and the references therein), and as geometrical models for twistings of K-theory [13].
- Non-abelian gerbes for the string 2-group are relevant for the anomaly cancellation in supersymmetric sigma models, see Section 6 and the references therein.
- There is a reformulation of topological T-duality in terms of non-abelian gerbes provides a geometric description of so-called non-geometric T-duals, see Section 7 and [14].

The definition of a non-abelian bundle gerbe has been extrapolated manually from the abelian case [15, 16], but can be derived systematically via the plus construction [17]. Before starting to describe the second approach, we shall explain the notion of a *Lie 2-group*, which plays the role of the „structure group" of a non-abelian gerbe.

A Lie 2-group is a Lie groupoid with a certain kind of monoidal structure. A Lie 2-group is called *strict*, if the monoidal structure is strictly associative, i.e. its associator is trivial. We will concentrate on the strict case. Strict Lie 2-groups can equivalently be described by *crossed modules* of Lie groups. A crossed module is a Lie group homomorphism $t : H \to G$ together with an action α of G on H by group homomorphisms, such that

$$\alpha(t(h), x) = hxh^{-1} \quad \text{and} \quad t(\alpha(g, h)) = gt(h)g^{-1}.$$

The Lie groupoid that corresponds to such a crossed module has objects $\Gamma_0 := G$ and morphisms $\Gamma_1 := H \times G$, with source map $(h, g) \mapsto g$ and target map $(h, g) \mapsto t(h)g$. The composition is given by the group structure of H, and the monoidal structure is given by the group structures of G and of the semi-direct product $H \ltimes G$ formed using the action α of G on H. The standard examples of Lie 2-groups are the following; more examples will be mentioned in Sections 6 and 7.

- For an abelian Lie group A, there is a Lie 2-group BA with a single object and the group A as its automorphisms; this construction (and notation) is analogous to Section 2. Composition and monoidal structure are both given by the group structure of A; since the monoidal structure is a functor, the classical Eckmann–Hilton argument requires A to be abelian. The corresponding crossed module is $A \to \{e\}$.

- For a general Lie group G, there is a Lie 2-group G_{dis} with objects given by the elements of G and only identity morphisms. The corresponding crossed module is $\mathrm{id} : G \to G$, together with the conjugation of G on itself.

- If the automorphism group $\mathrm{Aut}(H)$ of a Lie group H is again a Lie group (for example, it is discrete when H is compact and simple), then there is a Lie 2-group $\mathrm{AUT}(H)$ called the automorphism 2-group of H. Its crossed module is the assignment $i : H \to \mathrm{Aut}(H)$ of inner automorphisms, together with the natural action of $\mathrm{Aut}(H)$ on H.

We explain two more facts about Lie 2-groups that will be relevant later. Lie 2-groups have two interesting invariants, $\pi_0\Gamma$ (the group of isomorphism classes of objects) and $\pi_1\Gamma$ (the abelian group of automorphisms of the monoidal unit). There is an action of $\pi_0\Gamma$ on $\pi_1\Gamma$ obtained by conjugation with identity morphisms, and the Lie 2-group is called *central* if this action is trivial. In terms of crossed modules, $\pi_0\Gamma = G/t(H)$ and $\pi_1\Gamma = \ker(t) \subset H$, and the action is induced from α. For example, $\pi_0\mathrm{AUT}(H) = \mathrm{Out}(H)$ and $\pi_1\mathrm{AUT}(H) = Z(H)$, and $\mathrm{AUT}(H)$ is central if and only if every outer automorphism fixes the center.

A Lie 2-group is called *smoothly separable*, if $\pi_0\Gamma$ is a Lie group such that $\Gamma_0 \to \pi_0\Gamma$ is a submersion. Every smoothly separable Lie 2-group gives rise to an extension

$$B\pi_1\Gamma \to \Gamma \to (\pi_0\Gamma)_{dis} \tag{5}$$

of Lie 2-groups in the sense of Schommer-Pries [18]. If Γ is central then this extension is central.

In order to specify the input data for the plus construction, we have to specify a local model for non-abelian gerbes. The idea is analogous to the abelian case: we want to define a monoidal

category of bundles related to the given Lie 2-group Γ. For any Lie groupoid Γ one can consider principal Γ-bundles, and we refer to [17] for a review. Principal Γ-bundles are ordinary fibre bundles $\pi : P \to M$, whose total spaces are equipped with an „anchor map“ $\phi : P \to G$ and an action of Γ – this means that a morphism $\gamma : a \to b$ acts on points $p \in P$ with anchor $\phi(p) = a$, resulting in a new point $p \circ \gamma$ with anchor b, in the same fibre over M. The action is supposed to satisfy the usual conditions for principal bundles. The monoidal structure on Γ is used for the definition of the tensor product of principal Γ-bundles.

In terms of a crossed module $t : H \to G$, a principal Γ-bundle is an ordinary principal H-bundle P equipped with a smooth, anti-equivariant map $\phi : P \to G$, i.e. $\phi(p \cdot h) = t(h)^{-1} \cdot \phi(p)$. The tensor product $P \otimes Q$ is the fibre product of the underlying bundles, $P \times_M Q$, modulo an equivalence relation $(ph, q) \sim (p, q\alpha(\phi_P(p)^{-1}, h))$, with the H-action defined by $[p, q]h = [ph, q]$ and the anti-equivariant map defined by $[p, q] \mapsto \phi_P(p)\phi_Q(q)$.

The reader may easily verify that principal Γ-bundles for the three Lie 2-groups of the previous list are the following:

- Principal BA-bundles are the same as ordinary principal A-bundles, with the ordinary tensor product.
- Principal G_{dis}-bundles are the same as smooth maps $M \to G$, with the pointwise group structure.
- Principal $\Gamma = \mathrm{AUT}(H)$-bundles are ordinary principal H-bundles P together with an H-anti-equivariant map $\phi : P \to \mathrm{Aut}(H)$. Due to the anti-equivariance, one can define an additional *left* H-action $hp := p\alpha(\phi(p)^{-1}, h)$, turning P into a H-bibundle. The tensor product is the tensor product of H-bibundles. The theory of non-abelian gerbes started with considering bibundles and corresponding $\mathrm{AUT}(H)$-bundle gerbes [15, 16].

So far we have explained the monoidal category $\mathcal{B}un_\Gamma(M)$ of principal Γ-bundles over M. The local model for Γ-bundle gerbes is now the pre-2-stack $B\mathcal{B}un_\Gamma$. The plus construction yields then the 2-stack of Γ-bundle gerbes,

$$\mathcal{BG}rb_\Gamma := (B\mathcal{B}un_\Gamma)^+.$$

Unpacking the details of the plus construction, a Γ-bundle gerbe consists of a surjective submersion $\pi : Y \to M$, a principal Γ-bundle P over $Y^{[2]}$, and a bundle isomorphism

$$\mu : pr_{23}^* P \otimes pr_{12}^* P \to pr_{13}^* P$$

over $Y^{[3]}$ that satisfies a cocycle condition over $Y^{[4]}$.

We would like to emphasize that although non-abelian bundle gerbes have been defined earlier, e.g. in [15], neither the full bicategorical structure has been specified, nor any gluing properties have been discussed. Both important aspects are established automatically by the plus construction. A further important aspect that comes for free from the plus construction is the functoriality in the Lie 2-group Γ. That is, if $F : \Gamma \to \Omega$ is a Lie 2-group homomorphism, then there is an associated „change of structure 2-group“ 2-functor

$$F_* : \mathcal{BG}rb_\Gamma(M) \to \mathcal{BG}rb_\Omega(M).$$

In particular, as a consequence of the extension (5), if Γ is smoothly separable with $A := \pi_1\Gamma$ and $G := \pi_1\Gamma$, then there is a sequence

$$\mathcal{BG}rb_A(M) \to \mathcal{BG}rb_\Gamma(M) \to (\mathcal{B}un_G(M))_{dis} \tag{6}$$

of 2-functors. Here we have employed an identification between (non-abelian) BA-bundle gerbes and (abelian) A-bundle gerbes, and another identification $\mathcal{BG}rb_{G_{dis}} = (\mathcal{B}un_G)_{dis}$ between G_{dis}-bundle gerbes and ordinary principal G-bundles (regarded as a bicategory with only identity 2-morphisms). Loosely speaking, the sequence (6) exhibits non-abelian gerbes as an extension of ordinary principal bundles by abelian gerbes. In particular, every non-abelian Γ-bundle gerbe $\mathcal{G}$ comes with an underlying ordinary principal $\pi_0\Gamma$-bundle, which we denote by $\pi_0(\mathcal{G})$. This bundle plays an important role in the applications, as we will see in Sections 5, 6 and 7. In work with Thomas Nikolaus we have studied several lifting and reduction statements for non-abelian gerbes that are related to the sequences (5) and (6), see [19].

We remark that connections on non-abelian bundle gerbes can be defined in the very same way via the plus construction. The generalization of surface holonomy to the non-abelian case is more difficult. In joint work with Urs Schreiber we have given a general and axiomatic framework for parallel transport and holonomy of non-abelian gerbes [20–23].

We also point out that there is a formalism of *principal 2-bundles*, initiated by Bartels [24] and Wockel [25]. This formalism is equivalent to non-abelian bundle gerbes [17] but more suitable for connections and parallel transport, see [25, 26].

4 Gerbes over Lie groupoids

Applications (in particular applications to sigma-models and string theory) frequently require not only bundle gerbes, but *equivariant* bundle gerbes. It is fruitful to approach equivariant geometry from a more general point of view: geometry over *Lie groupoids*. The guiding examples of Lie groupoids are the following two:

- If a Lie group G acts on a smooth manifold M in terms of a smooth map $\rho : G \times M \to M$, one can form the *action groupoid* $M/\!\!/G$ with objects $(M/\!\!/G)_0 := M$ and morphisms $(M/\!\!/G)_1 := G \times M$. Source and target maps are given by $s(g,m) := m$ and $t(g,m) := \rho(g,m)$, and the composition is $(g_2, g_1 m) \circ (g_1, m) := (g_2 g_1, m)$. Geometry over an action groupoid $M/\!\!/G$ will be the same as G-equivariant geometry over M.

- Any open cover $U = (U_i)_{i\in I}$ defines the so-called *Čech groupoid* $\check{C}(U)$. Its objects and morphisms are given by, respectively,

$$\check{C}(U)_0 := \coprod_{i\in I} U_i \quad \text{and} \quad \check{C}(U)_1 := \coprod_{i,j\in I} U_i \cap U_i.$$

  Source and target maps are given by $s(i,j,x) := (i,x)$ and $t(i,j,x) := (j,x)$, and the composition is $(j,k,x)\circ(i,j,x) := (i,k,x)$. A similar Lie groupoid $\check{C}(\pi)$ can be constructed using fibre products for any surjective submersion $\pi : Y \to M$.

We remark that a further class of interesting and rich examples of Lie groupoids are orbifolds, see [27–29]. We start again by describing presheaves of categories; now over Lie groupoids. A *presheaf of categories over Lie groupoids* is a weak functor

$$\mathfrak{X} : \mathcal{LG}rpd^{op} \to \mathcal{C}at,$$

i.e., it associates to each Lie groupoid Ω a category $\mathfrak{X}(\Omega)$, and each smooth functor $F : \Omega \to \Omega'$ of Lie groupoids a functor $F^* : \mathfrak{X}(\Omega') \to \mathfrak{X}(\Omega)$ in a way compatible with the composition of

functors. There is a canonical way to extend any presheaf $\mathfrak{X}$ over smooth manifolds to a presheaf $\mathfrak{X}'$ over Lie groupoids [2]. Indeed, if Ω is a Lie groupoid with a manifold Ω_0 of objects and a manifold Ω_1 of morphisms, then an object of $\mathfrak{X}'(\Omega)$ is a pair (X, f) consisting of an object X in $\mathfrak{X}(\Omega_0)$ and an isomorphism $f : s^*X \to t^*X$ in $\mathfrak{X}(\Omega_1)$, such that $pr_2^* f \circ pr_1^* f = c^* f$ as morphisms in $\mathfrak{X}(\Omega_1 \,{}_s\!\times_t \Omega_1)$, where c denotes the composition. A morphism of $\mathfrak{X}'(\Omega)$ between (X, f) and (X', f') is a morphism $g : X \to X'$ in $\mathfrak{X}(\Omega_0)$ such that $f' \circ s^*g = t^*g \circ f$ in $\mathfrak{X}(\Omega_1)$.

It is instructive to evaluate this procedure for the two examples of Lie groupoids described above. An object in $\mathfrak{X}'(M/\!\!/G)$ is an object X over M together with an isomorphism $f : pr_M^* X \to \rho^* X$ over $G \times M$ that satisfies above condition over $G \times G \times M$. In other words, this is a family $\{f_g\}_{g\in G}$ of isomorphisms $f_g : X \to g^*X$ that satisfy $g_1^* f_{g_2} \circ f_{g_1} = f_{g_2 g_1}$ and depend smoothly on G (in the sense that a morphism f over $G \times M$ is formed). If, for example, $\mathfrak{X}$ is the stack of vector bundles, then an object in $\mathfrak{X}'(M/\!\!/G)$ is precisely a G-equivariant vector bundle over M.

In the other example of Čech groupoids, the reader may easily verify that $\mathfrak{X}'(\check{C}(\pi)) = \mathcal{D}esc_{\mathfrak{X}}(\pi)$, for any surjective submersion $\pi : Y \to M$. This observation is useful in the following situation. Suppose the quotient of a G-action on M exists, in the sense that M/G is a smooth manifold and $p : M \to M/G$ is a principal G-bundle. Then, there is a canonical isomorphism of Lie groupoids $\check{C}(p) \cong M/\!\!/G$. Thus, if $\mathfrak{X}$ is any stack over smooth manifolds, we have an equivalence

$$\mathfrak{X}(M/G) \cong \mathcal{D}esc_{\mathfrak{X}}(p) = \mathfrak{X}'(\check{C}(p)) \cong \mathfrak{X}'(M/\!\!/G). \tag{7}$$

In other words, if the quotient exists, geometry over M/G is the same as the induced geometry over the action groupoid. The latter, however, makes sense even if the quotient does not exist.

The passage $\mathfrak{X} \mapsto \mathfrak{X}'$ from presheaves over smooth manifolds to presheaves over Lie groupoids has the feature that it is functorial and preserves stacks [2]. It is a very convenient tool: once we work with presheaves of categories, there is no need to introduce definitions over Lie groupoids. These will follow automatically via $\mathfrak{X} \mapsto \mathfrak{X}'$ from definitions over just smooth manifolds.

The above discussion generalizes in a straightforward way from presheaves of *categories* to presheaves of *bicategories* [2], and hence applies to abelian and non-abelian bundle gerbes. Hence, we automatically obtain a definition of equivariant non-abelian bundle gerbes, together with the equivalence (7) saying that equivariant bundle gerbes descent to quotients (if these exist).

Equivariant bundle gerbes are frequently used in two-dimensional Wess–Zumino–Witten models, whose Wess–Zumino term is the holonomy of a $U(1)$-bundle gerbe on a Lie group. In order to get the right invariances for the theory, this gerbe has to be equivariant with respect to the adjoint action of the Lie group on itself. Concrete constructions of equivariant $U(1)$-bundle gerbes over compact simple Lie groups use descent in the 2-stack $\mathcal{BG}rb'_{U(1)}$ twice: In the first step, a G-equivariant bundle gerbe („basic gerbe“) over a simply-connected Lie group G is obtained by gluing G-equivariant bundle gerbes $\mathcal{G}_i$, which are locally defined over thickened conjugacy classes $U_i \subset G$. In other words, these are bundle gerbes over action groupoids $U_i/\!\!/G$. More precisely, the locally defined bundle gerbes $\mathcal{G}_i$ are so-called lifting gerbes for certain central extensions of stabilizer subgroups. The gluing uses descent along the functor

$$\coprod_i U_i/\!\!/G \to G/\!\!/G.$$

This construction is implicit in Meinrenken's construction [6] and appears explicitly in [30]. In the second step, descent to a non-simply-connected quotient $\tilde{G} := G/Z$, where $Z \subset Z(G)$,

is performed along $G/\!\!/G \to \tilde{G}/\!\!/\tilde{G}$. The required Z-equivariant structures have been provided Lie-theoretically by Gawędzki–Reis [31] (without the G-equivariance) and recently – including the G-equivariance – by Krepski [32].

5 Jandl gerbes are non-abelian

The surface holonomy of a connection on an abelian bundle gerbe depends on an orientation of the surface Σ. If the surface is not oriented, or not orientable, then it is a priori not well-defined. Thus, in the application of bundle gerbes as Kalb–Ramond gauge fields in string theory, unoriented worldsheets (which naturally appear in string theories of type I) require additional attention.

The idea is that a change of orientation should be accompanied on the target space side with an involution $k : M \to M$, under which the gauge field should „change its sign“. For a 2-form gauge field B, we would require $k^*B = -B$ so that the sign obtained from a change of orientation is compensated. Jandl gerbes generalize this transformation behaviour from 2-form gauge fields to bundle gerbes: they are $U(1)$-bundle gerbes equipped with additional structure relating their pullback along k with the dual (for the opposite sign). It is instructive to understand Jandl gerbes as non-abelian gerbes over Lie groupoids.

We are concerned with a smooth manifold M and an involution $k : M \to M$, which we regard as a $\mathbb{Z}_2$-action on M. We consider the associated action groupoid, and denote it by $M/\!\!/k$. The trivial $\mathbb{Z}_2$-bundle $M \times \mathbb{Z}_2$ over M can be equipped with a $\mathbb{Z}_2$-equivariant structure that changes the sign under the involution. Hence, it becomes a $\mathbb{Z}_2$-bundle over $M/\!\!/k$, and we denote it by $\mathrm{Or}(M/\!\!/k)$, the *orientation bundle* of the Lie groupoid $M/\!\!/k$.

The automorphism 2-group $\mathrm{AUT}(U(1))$ gives rise to a (non-central) extension

$$BU(1) \to \mathrm{AUT}(U(1)) \to \mathbb{Z}_2,$$

where the action of $\pi_0(\mathrm{AUT}(U(1))) = \mathrm{Out}(\mathbb{Z}_2) = \mathbb{Z}_2$ on $\pi_1(\mathrm{AUT}(U(1))) = Z(U(1)) = U(1)$ is by inversion. The idea is to couple the $\mathbb{Z}_2$-part of this extension to a change of orientation. With this motivation, a *Jandl gerbe* over $M/\!\!/k$ is an $\mathrm{AUT}(U(1))$-bundle gerbe $\mathcal{G}$ with connection over $M/\!\!/k$ together with a bundle isomorphism $\pi_0(\mathcal{G}) \cong \mathrm{Or}(M/\!\!/k)$.

The above definition of a Jandl gerbe is more conceptual than the original definition given in [33], but equivalent, as we will demonstrate now by unwrapping all involved definitions. We work first over M and ignore the $\mathbb{Z}_2$-equivariance. From the plus construction we recall that the $\mathrm{AUT}(U(1))$-bundle gerbe $\mathcal{G}$ consists of a surjective submersion $\pi : Y \to M$, a principal $\mathrm{AUT}(U(1))$-bundle P over $Y^{[2]}$, and a bundle isomorphism μ over $Y^{[3]}$. We consider $\mathrm{AUT}(U(1))$ as the crossed module $0 : U(1) \to \mathbb{Z}_2$, so that the $\mathrm{AUT}(U(1))$-bundle P is an ordinary $U(1)$-bundle equipped with an anchor map $\phi : P \to \mathbb{Z}_2$. The anchor descends in fact to a map $\phi : Y^{[2]} \to \mathbb{Z}_2$, due to its anti-equivariance. The bundle isomorphism μ is an ordinary $U(1)$-bundle isomorphism with the property that it respects the anchor maps; this implies the cocycle condition for the map ϕ on $Y^{[3]}$. Hence, the pair (π, ϕ) is descent data for a principal $\mathbb{Z}_2$-bundle over M, namely the bundle $\pi_0(\mathcal{G})$.

The isomorphism between $\pi_0(\mathcal{G})$ and $\mathrm{Or}(M/\!\!/k)$ that is part of the definition of a Jandl gerbe determines a trivialization of $\pi_0(\mathcal{G})$, since $\mathrm{Or}(M/\!\!/k)$ is the trivial bundle over M. In terms of descent data, the trivialization is a map $\psi : Y \to \mathbb{Z}_2$ such that $\phi(y_1, y_2)\psi(y_2) = \psi(y_1)$. Let P_ψ be the trivial $U(1)$-bundle over Y, which becomes an $\mathrm{AUT}(U(1))$-bundle equipping it with the

anchor map ψ. Now we pass to the new $\mathrm{AUT}(U(1))$-bundle

$$P_{\mathrm{red}} := pr_2^* P_\psi \otimes P \otimes pr_1^* P_\psi^*$$

over $Y^{[2]}$. By construction P_{red} has the trivial anchor and so is an ordinary $U(1)$-bundle. Similarly, one can equip P_{red} with an isomorphism μ_{red} over $Y^{[3]}$, in such a way that $\mathcal{G}_{\mathrm{red}} := (\pi, P_{\mathrm{red}}, \mu_{\mathrm{red}})$ is an ordinary $U(1)$-bundle gerbe. This reduction procedure works in the same way in the setting with connections. We have studied it in a more general setting in [19].

Next we take care about the $\mathbb{Z}_2$-equivariant structure, which is – in the first place – an isomorphism $\mathcal{A} : s^*\mathcal{G} \to t^*\mathcal{G}$ of $\mathrm{AUT}(U(1))$-bundle gerbes over the morphism space $\mathbb{Z}_2 \times M$ of the action groupoid $M/\!\!/k$. It induces an isomorphism $\mathcal{A} : s^*\mathcal{G}_{\mathrm{red}} \to t^*\mathcal{G}_{\mathrm{red}}$ over $\mathbb{Z}_2 \times M$, which is an isomorphism in the bicategory of $\mathrm{AUT}(U(1))$-bundle gerbes. That space is the disjoint union of two components, and so $\mathcal{A}$ has two components $\mathcal{A}_{\mathrm{id}} : \mathcal{G}_{\mathrm{red}} \to \mathcal{G}_{\mathrm{red}}$ and $\mathcal{A}_k : \mathcal{G}_{\mathrm{red}} \to k^*\mathcal{G}_{\mathrm{red}}$. Employing the equivariance of the isomorphism $\pi_0(\mathcal{G}) \cong \mathrm{Or}(M/\!\!/k)$ one can show that $\mathcal{A}_{\mathrm{id}}$ is actually an isomorphism in the bicategory of $U(1)$-bundle gerbes. For the component $\mathcal{A}_k$ one can show that a sign is involved in such a way that $\mathcal{A}_k$ becomes an isomorphism of $U(1)$-bundle gerbes after its domain bundle gerbe is dualized:

$$\mathcal{A}_k : \mathcal{G}_{\mathrm{red}}^* \to k^*\mathcal{G}_{\mathrm{red}}.$$

Finally, we incorporate the last part of the $\mathbb{Z}_2$-equivariant structure, which is a 2-isomorphism $\varphi : pr_2^*\mathcal{A} \circ pr_1^*\mathcal{A} \Rightarrow c^*\mathcal{A}$ over the space of pairs of composable morphisms of $M/\!\!/k$. It reduces to 2-isomorphisms

$$\mathcal{A}_{\mathrm{id}} \circ \mathcal{A}_{\mathrm{id}} \Rightarrow \mathcal{A}_{\mathrm{id}} \quad \text{and} \quad k^*\mathcal{A}_k \circ \mathcal{A}_k^* \Rightarrow \mathrm{id}_{\mathcal{G}_{\mathrm{red}}}.$$

The first part shows that $\mathcal{A}_{\mathrm{id}} \cong \mathrm{id}$, so that $\mathcal{A}_{\mathrm{id}}$ contains no information. For the second part, the cocycle condition for φ implies $k^*\varphi_k^{-1} = \varphi_k^*$.

Summarizing, we have seen that a Jandl gerbe $\mathcal{G}$ over $M/\!\!/k$ is the same as:

1. A $U(1)$-bundle gerbe with connection over M.
2. A 1-isomorphism $\mathcal{A} : \mathcal{G}^* \to k^*\mathcal{G}$.
3. A 2-isomorphism $\varphi : k^*\mathcal{A} \circ \mathcal{A}^* \Rightarrow \mathrm{id}_{\mathcal{G}}$ such that $k^*\varphi^{-1} = \varphi^*$.

This is precisely the definition given in [7,33]. We remark that Jandl gerbes can also be discussed in terms of cocycle data, or (differential) cohomology with coefficients in equivariant sheaves, see [33–37].

As intended, Jandl gerbes furnish a notion of surface holonomy for unoriented surfaces [33]. More precisely, if Σ is a possibly unoriented surface, it assigns a well-defined element in $U(1)$ to each differentiable stack map $\phi : \Sigma \to M/\!\!/k$. This surface holonomy constitutes the contribution of the orientifold Kalb–Ramond field to the sigma model action, see [1, 33].

In [34] we have classified all Jandl gerbes over compact simple Lie groups, and thereby all Wess–Zumino–Witten orientifolds for these groups. The classification problem was solved using equivariant descent along the universal covering group $\tilde{G} \to G$, employing the fact that $\mathrm{AUT}(U(1))$-bundle gerbes form a 2-stack. Since $G = \tilde{G}/Z$ for a discrete group $Z \subset Z(\tilde{G})$, the essential calculation is the classification of all Z-equivariant structures on $\mathrm{AUT}(U(1))$-bundle gerbes over simply-connected Lie groups. In [34], this was reduced to the computation of the group cohomology of the discrete group $Z \ltimes \mathbb{Z}_2$ (where $\mathbb{Z}_2$ acts on Z by inversion) with

coefficients in $U(1)$, considered as a $(Z \ltimes \mathbb{Z}_2)$-module in which $\mathbb{Z}_2$ acts by inversion. This calculation has been carried out in [34] for all occurring cases of groups Z.

In further work [35] we have treated D-branes in orientifolds, using Jandl gerbes. In this picture, D-branes are submanifolds $Q \subset M$ of the target space, equipped with bundle gerbe modules, i.e. 1-morphisms $\mathcal{G}|_Q \to \mathcal{I}$, where $\mathcal{I}$ is the trivial bundle gerbe. If these bundle gerbe modules are equipped with appropriate equivariance with respect to the involution, the coupling term in the open string action functional can again be defined unambiguously. A different treatment of D-branes in orientifolds has been studied by Distler, Freed, and Moore in [38], in the formalism of twisted K-theory. The relation between the two pictures is that bundle gerbes (with connections) realize those (differential) twistings of K-theory that correspond to $H^3(M, \mathbb{Z})$. Non-abelian $\mathrm{AUT}(U(1))$-bundle gerbes, which underly Jandl gerbes, realize more general twistings that correspond to $H^1(M, \mathbb{Z}_2) \times H^3(M, \mathbb{Z})$. These correspondences persist if M is replaced by an action groupoid; this way the two approaches can be related.

6 String structures

Supersymmetric sigma models include spinors on the worldsheet with values in the tangent bundle of the target space. If M is a spin manifold, then the path integral over the spinors can be interpreted as a Berezinian integral, and then rigorously be performed. The result, however, is not a complex number but an element in a complex line. These form a complex line bundle over the space $C^\infty(\Sigma, M)$ of all worldsheet embeddings, the *Pfaffian line bundle* of a certain family of Dirac operators. The supersymmetric sigma model is hence potentially anomalous, and the anomaly is represented by the Pfaffian line bundle. A general treatment of such anomalies was given by Freed and Moore in [39].

The cancellation of this anomaly requires to trivialize the Pfaffian line bundle. Freed showed [40] that its first Chern class vanishes if the first fractional Pontryagin class of M vanishes,

$$\tfrac{1}{2}p_1(M) = 0 \in H^4(M, \mathbb{Z}).$$

Such manifolds are called *string manifolds*. The problem is that the vanishing of the Chern class of the Pfaffian line bundle is not enough to make the fermionic path integral a well-defined section: additionally, a specific trivialization must be provided. For this purpose, it is desirable to interpret the obstruction class $\frac{1}{2}p_1(M)$ in a geometric way. There are (at least) four different proposals:

1. It is the obstruction against lifting the structure group of the free loop space of M from the loop group $LSpin(n)$ to its universal central extension [41, 42],

$$1 \to U(1) \to \widetilde{LSpin(n)} \to LSpin(n) \to 1$$

2. It is the obstruction against lifting the structure group of the spin-oriented frame bundle $P_{Spin}M$ of M from $Spin(n)$ to the string group

$$String(n) \to Spin(n),$$

   defined as the unique (up to homotopy equivalence) 3-connected covering group [43].

3. It is the „level“ of a Chern–Simons field theory with target space M [43].

4. It is the characteristic class of the Chern–Simons 2-gerbe associated to the spin-oriented frame bundle [44, 45].

Most interesting for us is (a variant of) version 2. Although the (a priori topological) group $String(n)$ can be realized as a Fréchet Lie group [46], it turns out to be more natural to consider it as a Lie 2-group. Concrete models for the String 2-group have been constructed as a Fréchet Lie 2-group [47] and as a diffeological 2-group [48]. Both are central and smoothly separable in the sense explained in Section 3, and give rise to a central extension

$$BU(1) \to String(n) \to Spin(n)_{dis}$$

of (Fréchet/diffeological) Lie 2-groups. A *string structure* is a lift of the structure group of M along this central extension. In other words, a string structure is a $String(n)$-bundle gerbe $\mathcal{G}$ over M such that $\pi_0(\mathcal{G}) \cong P_{Spin}M$.

By a result of Schommer-Pries [18], central extensions of G_{dis} by $BU(1)$ are classified by $\mathrm{H}^4(BG, \mathbb{Z})$, and the string 2-group corresponds to $\frac{1}{2}p_1 \in \mathrm{H}^4(BSpin(n), \mathbb{Z})$. This shows that string structures exist if and only if $\frac{1}{2}p_1(M) = 0$, as desired.

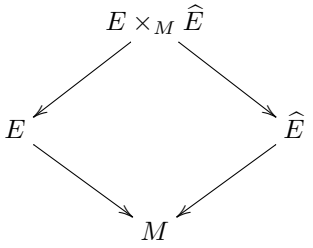
Above notion of a string structure is equivalent [19] to another definition using version 4. In that version a string structure is a trivialization of the Chern–Simons 2-gerbe [45]. This has the additional advantage that it is totally finite-dimensional, and that one can define string connections, together forming a *geometric string structure*. The geometric string structures of [45] are motivated by version 3 of Stolz and Teichner, and closely related to spin structures on the free loop space, which implement version 1 [49].

The relation between string structures and the Pfaffian line bundle over $C^\infty(\Sigma, M)$, namely that a choice of a string structure determines a trivialization of the Pfaffian line bundle, has been conjectured by Stolz and Teichner, and proved by Bunke [50] using the notion of geometric string structures of [45].

7 Topological T-duality

Particularly interesting target spaces for string theory are the total spaces of principal torus bundles. String theories on these target spaces can be equivalent to string theories on different principal torus bundles, in a way that metrics, B-fields, and dilaton fields are mixed up [51]. Such an equivalence is called *T-duality*. The fully-fledged exact mathematical formulation of T-duality, including all topological and differential-geometric information, is not yet known.

Topological T-duality has been invented to study the underlying topological aspects alone. In this context, T-duality can be defined as follows [52]. Let E and $\widehat{E}$ be principal $\mathbb{T}^n$-bundles over M, where $\mathbb{T}^n = U(1) \times \ldots \times U(1)$, and let $\mathcal{G}$ and $\widehat{\mathcal{G}}$ be $U(1)$-bundle gerbes over E and $\widehat{E}$, respectively. The pairs $(E, \mathcal{G})$ and $(\widehat{E}, \widehat{\mathcal{G}})$ are called *topological T-backgrounds*, and the fibre product



is called the *correspondence space*. The two topological T-backgrounds are called *T-dual*, if the pullbacks of the two bundle gerbes to the correspondence space are isomorphic, and an isomorphism $\mathcal{D} : p^*\mathcal{G} \to \widehat{p}^*\widehat{\mathcal{G}}$ exists that has the so-called Poincaré property [52]. The original motivation for this definition was the existence of a so-called Fourier–Mukai transformation, which yields an isomorphism between the twisted K-theories of both pairs.

One of the basic questions in this setting is to decide, if a given T-background has T-duals, and how the possibly many T-duals can be parameterized. To this end, we consider the Serre spectral sequence associated to the torus bundle, which comes with a filtration $\pi^*\mathrm{H}^3(M,\mathbb{Z}) = F_3 \subset F_2 \subset F_1 \subset F_0 = \mathrm{H}^3(E,\mathbb{Z})$. We classify T-backgrounds by the greatest n such that the Dixmier–Douady class $[\mathcal{G}] \in \mathrm{H}^3(E,\mathbb{Z})$ is in F_n. A result of Bunke–Rumpf–Schick [52] is that a T-background $(E,\mathcal{G})$ admits T-duals if and only if it is F_2. Further, up to isomorphism, possible choices are related by a certain action of the additive group $\mathfrak{so}(n,\mathbb{Z})$ of skew-symmetric matrices $B \in \mathbb{Z}^{n\times n}$, where n is the dimension of the torus.

The situation can be reformulated and then improved using non-abelian gerbes [14]. In this joint work with Thomas Nikolaus we have manufactured a Fréchet Lie 2-group $\mathbb{TB}^2$ in such a way that the $\mathbb{TB}^2$-bundle gerbes are precisely the F_2 T-backgrounds. As a crossed module, it is $\mathbb{Z}^n \times C^\infty(\mathbb{T}^n, U(1)) \to \mathbb{R}^n$, defined as $(m,\tau) \mapsto m$, and $a \in \mathbb{R}^n$ acts on $C^\infty(\mathbb{T}^n,U(1))$ by translations modulo $\mathbb{Z}$. It forms a (non-central) extension

$$C^\infty(\mathbb{T}^n,U(1)) \to \mathbb{TB}^2 \to \mathbb{T}^n_{dis}.$$

If $\mathcal{G}$ is a $\mathbb{TB}^2$-bundle gerbe corresponding to a T-background $(E,\mathcal{G})$, then $\pi_0(\mathcal{G})$ is the underlying torus bundle E.

Another, finite-dimensional Lie 2-group $\mathbb{TD}$ can be constructed as the central extension

$$BU(1) \to \mathbb{TD} \to \mathbb{T}^{2n}_{dis}$$

that is classified by the class

$$\rho := \sum_{i=1}^n pr_i^* c \cup pr_{n+i}^* c \in \mathrm{H}^4(\mathbb{T}^{2n},\mathbb{Z}),$$

where $c \in \mathrm{H}^2(BU(1),\mathbb{Z})$ is the universal first Chern class. The associated $\mathbb{TD}$-bundle gerbes are precisely all T-duality correspondences [14]. Lie 2-group homomorphisms $L, R : \mathbb{TD} \to \mathbb{TB}^2$ represent the projection to the left and the right „leg“ of the correspondence. The main advantage of this reformulation is that the $\mathfrak{so}(n,\mathbb{Z})$-action can be implemented as a strict and fully coherent action on $\mathbb{TD}$. This way, our understanding of topological T-duality is formulated completely and coherently in the language of non-abelian bundle gerbes.

If a T-background is only F_1, then it does not have any T-duals; these are then called „mysteriously missing“ [53] or „non-geometric“ T-duals [54]. An approach via non-commutative geometry allows to define them as bundles of non-commutative tori [53, 55, 56]. The fact that non-abelian bundle gerbes form a 2-stack provides an alternative [14]. Indeed, every F_1 background is locally F_2, and so has locally defined T-duals, related to the given F_1 T-background by locally defined T-duality correspondences. Over overlaps, these correspondences are related by the $\mathfrak{so}(n,\mathbb{Z})$-action of Bunke–Rumpf–Schick. Since this action is fully coherent under our reformulation by non-abelian bundle gerbes, one can define a semi-direct product Lie 2-group

$$\mathbb{TD}^{\frac{1}{2}\text{-}geo} := \mathbb{TD} \ltimes \mathfrak{so}(n,\mathbb{Z}).$$

Within the 2-stack of $\mathbb{TD}^{\frac{1}{2}\text{-}geo}$-bundle gerbes one can now *glue* the locally defined T-duality correspondences along their $\mathfrak{so}(n,\mathbb{Z})$-transformations on overlaps. This way, a globally defined $\mathbb{TD}^{\frac{1}{2}\text{-}geo}$-bundle gerbe is obtained, representing a totally new object called a *half-geometric T-duality correspondence*. These new objects should be seen and studied as generalized target spaces for string theory, and may be seen as a realization of Hull's T-folds [57].

Another action of $\mathfrak{so}(n,\mathbb{Z})$ on the Lie 2-group $\mathbb{TB}^2$ can be defined, leading to another Lie 2-group

$$\mathbb{TB}^1 := \mathbb{TB}^2 \ltimes \mathfrak{so}(n,\mathbb{Z}).$$

The non-abelian $\mathbb{TB}^1$-bundle gerbes correspond precisely to the F_1 T-backgrounds [14]. The left leg projection L is $\mathfrak{so}(n,\mathbb{Z})$-equivariant and hence induces a well-defined 2-group homomorphism $L : \mathbb{TD}^{\frac{1}{2}\text{-}geo} \to \mathbb{TB}^1$. In other words, half-geometric T-duality correspondences still have a well-defined „geometric" left leg, but opposed to the theory of [52] this left leg is now in the bigger class of F_1 T-backgrounds. It is shown in [14] that $L : \mathbb{TD}^{\frac{1}{2}\text{-}geo} \to \mathbb{TB}^1$ induces a bijection on isomorphism classes of non-abelian gerbes. Thus, every F_1 T-background is the left leg of a uniquely defined half-geometric T-duality correspondence. They can hence be seen as the non-geometric T-duals of F_1 T-backgrounds. Thus, the higher geometry of non-abelian gerbes provides an alternative to non-commutative geometry.

References

[1] J. Fuchs, T. Nikolaus, C. Schweigert and K. Waldorf, *Bundle gerbes and surface holonomy*, in *Proceedings of the 5th European Congress of Mathematics* (A. Ran, H. te Riele and J. Wiegerinck, eds.), pp. 167–197. EMS, 2008. 0901.2085.

[2] T. Nikolaus and C. Schweigert, *Equivariance In Higher Geometry*, *Adv. Math.* **226** (2011) 3367–3408, [1004.4558].

[3] M. K. Murray, *Bundle gerbes*, *J. Lond. Math. Soc.* **54** (1996) 403–416, [dg-ga/9407015].

[4] M. K. Murray and D. Stevenson, *Bundle gerbes: stable isomorphism and local theory*, *J. Lond. Math. Soc.* **62** (2000) 925–937, [math/9908135].

[5] D. Stevenson, *The geometry of bundle gerbes*, Ph.D. thesis, University of Adelaide, 2000. math.DG/0004117.

[6] E. Meinrenken, *The basic gerbe over a compact simple Lie group*, *Enseign. Math., II. Sér.* **49** (2002) 307–333, [math/0209194].

[7] K. Waldorf, *More morphisms between bundle gerbes*, *Th. Appl. Cat.* **18** (2007) 240–273, [0702652].

[8] J. C. Baez and J. Huerta, *An invitation to higher gauge theory*, *General Relativity and Gravitation* **43** (2011) 2335–2392, [1003.4485].

[9] C. Saemann and M. Wolf, *Non-abelian tensor multiplet equations from twistor space*, *Commun. Math. Phys.* **328** (2014) 527–544, [1205.3108].

[10] D. Fiorenza, H. Sati and U. Schreiber, *Multiple M5-branes, string 2-connections, and 7d non-abelian Chern-Simons theory*, *Adv. Theor. Math. Phys.* **18** (2014) 229–321, [1201.5277].

[11] B. Jurco, C. Saemann and M. Wolf, *Semistrict higher gauge theory*, *J. High Energy Phys.* **04** (2015) 087, [1403.7185].

[12] S. Gukov and A. Kapustin, *Topological quantum field theory, nonlocal operators, and gapped phases of gauge theories*, 1307.4793. Preprint.

[13] D. S. Freed, M. J. Hopkins and C. Teleman, *Loop groups and twisted K-theory I*, *J. Topology* **4** (2016) 737–798, [0711.1906].

[14] T. Nikolaus and K. Waldorf, *Higher geometry for non-geometric T-duals*, 1804.00677. Preprint.

[15] P. Aschieri, L. Cantini and B. Jurco, *Nonabelian bundle gerbes, their differential geometry and gauge theory*, *Commun. Math. Phys.* **254** (2005) 367–400, [hep-th/0312154].

[16] L. Breen and W. Messing, *Differential geometry of gerbes*, *Adv. Math.* **198** (2005) 732–846, [math.AG/0106083].

[17] T. Nikolaus and K. Waldorf, *Four equivalent versions of non-abelian gerbes*, *Pacific J. Math.* **264** (2013) 355–420, [1103.4815].

[18] C. Schommer-Pries, *Central extensions of smooth 2-groups and a finite-dimensional string 2-group*, *Geom. Topol.* **15** (2011) 609–676, [0911.2483].

[19] T. Nikolaus and K. Waldorf, *Lifting problems and transgression for non-abelian gerbes*, *Adv. Math.* **242** (2013) 50–79, [1112.4702].

[20] U. Schreiber and K. Waldorf, *Parallel transport and functors*, *J. Homotopy Relat. Struct.* **4** (2009) 187–244, [0705.0452v2].

[21] U. Schreiber and K. Waldorf, *Smooth functors vs. differential forms*, *Homology, Homotopy Appl.* **13** (2011) 143–203, [0802.0663].

[22] U. Schreiber and K. Waldorf, *Local theory for 2-functors on path 2-groupoids*, *J. Homotopy Relat. Struct.* (2016) 1–42, [1303.4663].

[23] U. Schreiber and K. Waldorf, *Connections on non-abelian gerbes and their holonomy*, *Theory Appl. Categ.* **28** (2013) 476–540, [0808.1923].

[24] T. Bartels, *2-bundles and higher gauge theory*, Ph.D. thesis, University of California, Riverside, 2004. math/0410328.

[25] K. Waldorf, *A global perspective to connections on principal 2-bundles*, *Forum Math.* **30** (2017) 809–843, [1608.00401].

[26] K. Waldorf, *Parallel transport in principal 2-bundles*, 1704.08542. Preprint.

[27] E. Lerman, *Orbifolds as stacks?*, *Enseign. Math* **56** (2010) 315–363, [0806.4160].

[28] I. Moerdijk and D. A. Pronk, *Orbifolds, sheaves and groupoids*, *K-Theory* **12** (1997) 3–21.

[29] I. Moerdijk and J. Mrčun, *Introduction to foliations and Lie groupoids*. Cambridge University Press, 2003.

[30] T. Nikolaus, *Äquivariante Gerben und Abstieg*, diploma thesis, Universität Hamburg, 2009. http://people.mpim-bonn.mpg.de/thoni/Papers/DA_nikolaus.pdf.

[31] K. Gawędzki and N. Reis, *Basic gerbe over nonsimply connected compact groups*, *J. Geom. Phys.* **50** (2004) 28, [math/0307010].

[32] D. Krepski, *Basic equivariant gerbes on non-simply connected compact simple lie groups*, *J. Geom. Phys.* **133** (2018) 30–41, [1712.08294].

[33] U. Schreiber, C. Schweigert and K. Waldorf, *Unoriented WZW models and holonomy of bundle gerbes*, *Commun. Math. Phys.* **274** (2007) 31–64, [hep-th/0512283].

[34] K. Gawędzki, R. R. Suszek and K. Waldorf, *WZW orientifolds and finite group cohomology*, *Commun. Math. Phys.* **284** (2007) 1–49, [hep-th/0701071].

[35] K. Gawędzki, R. R. Suszek and K. Waldorf, *Bundle gerbes for orientifold sigma models*, *Adv. Theor. Math. Phys.* **15** (2011) 621–687, [0809.5125].

[36] K. Waldorf, *Algebraic structures for bundle gerbes and the Wess-Zumino term in conformal field theory*, Ph.D. thesis, Universität Hamburg, 2007. http://www.sub.uni-hamburg.de/opus/volltexte/2008/3519.

[37] P. Hekmati, M. K. Murray, R. J. Szabo and R. F. Vozzo, *Real bundle gerbes, orientifolds and twisted KR-homology*, 1608.06466. Preprint.

[38] J. Distler, D. S. Freed and G. W. Moore, *Orientifold precis*, in *Mathematical foundations of quantum field theory and perturbative string theory*, vol. 83, pp. 159–172. AMS, 2011. 0906.0795.

[39] D. S. Freed and G. W. Moore, *Setting the quantum integrand of M-theory*, *Commun. Math. Phys.* **263** (2006) 89–132, [hep-th/0409135].

[40] D. S. Freed, *Determinants, torsion, and strings*, *Commun. Math. Phys.* **107** (1986) 483–513.

[41] T. Killingback, *World sheet anomalies and loop geometry*, *Nuclear Phys. B* **288** (1987) 578.

[42] D. A. McLaughlin, *Orientation and string structures on loop space*, *Pacific J. Math.* **155** (1992) 143–156.

[43] S. Stolz and P. Teichner, *What is an elliptic object?*, in *Topology, geometry and quantum field theory*, vol. 308 of *London Math. Soc. Lecture Note Ser.*, pp. 247–343. Cambridge Univ. Press, 2004.

[44] A. L. Carey, S. Johnson, M. K. Murray, D. Stevenson and B.-L. Wang, *Bundle gerbes for Chern-Simons and Wess-Zumino-Witten theories*, *Commun. Math. Phys.* **259** (2005) 577–613, [math/0410013].

[45] K. Waldorf, *String connections and Chern-Simons theory*, *Trans. Amer. Math. Soc.* **365** (2013) 4393–4432, [0906.0117].

[46] T. Nikolaus, C. Sachse and C. Wockel, *A smooth model for the string group*, *Int. Math. Res. Not. IMRN* **16** (2013) 3678–3721, [1104.4288].

[47] J. C. Baez, A. S. Crans, D. Stevenson and U. Schreiber, *From loop groups to 2-groups*, *Homology, Homotopy Appl.* **9** (2007) 101–135, [math.QA/0504123].

[48] K. Waldorf, *A construction of string 2-group models using a transgression-regression technique*, in *Analysis, Geometry and Quantum Field Theory* (C. L. Aldana, M. Braverman, B. Iochum and C. Neira-Jiménez, eds.), vol. 584 of *Contemp. Math.*, pp. 99–115. AMS, 2012. 1201.5052. DOI.

[49] K. Waldorf, *String geometry vs. spin geometry on loop spaces*, *J. Geom. Phys.* **97** (2015) 190–226, [1403.5656].

[50] U. Bunke, *String structures and trivialisations of a Pfaffian line bundle*, *Commun. Math. Phys.* **307** (2011) 675–712, [0909.0846].

[51] T. Buscher, *A symmetry of the string background field equations*, *Phys. Lett. B* **194** (1987) 59–62.

[52] U. Bunke, P. Rumpf and T. Schick, *The topology of T-duality for t^n-bundles*, *Rev. Math. Phys.* **18** (2006) 1103–1154, [math/0501487].

[53] V. Mathai and J. Rosenberg, *On mysteriously missing T-duals, H-flux and the T-duality group*, in *Differential geometry and physics*, vol. 10 of *Nankai Tracts Math.*, pp. 350–358. World Sci. Publ., 2006. hep-th/0409073.

[54] C. Hull, *Global aspects of T-duality, gauged sigma models and T-folds*, *J. High Energy Phys.* (2007) 057, [hep-th/0604178].

[55] V. Mathai and J. Rosenberg, *T-duality for torus bundles with H-fluxes via noncommutative topology*, *Commun. Math. Phys.* **253** (2005) 705–721, [hep-th/0401168].

[56] V. Mathai and J. Rosenberg, *T-duality for torus bundles with H-fluxes via noncommutative topology. II. the high-dimensional case and the T-duality group*, *Adv. Theor. Math. Phys.* **10** (2006) 123–158, [hep-th/0508084].

[57] C. Hull, *A geometry for non-geometric string backgrounds*, *J. High Energy Phys.* **10** (2005) 65, [0406102].

Mathematical Aspects of String Compactifications

Vicente Cortés[1], *Jan Louis*[2]

[1]Fachbereich Mathematik, Universität Hamburg, Germany
[2]II. Institut für Theoretische Physik, Universität Hamburg, Germany

DOI: http://dx.doi.org/10.3204/PUBDB-2018-00782/A6

In this report we summarize the research in mathematics and theoretical physics done in project A6 of the SFB 676. The main research directions include the study of internal spaces of string compactifications, geometry of scalar manifolds and moduli spaces, heterotic/type II string duality, partial breaking of supersymmetry and supersymmetric AdS backgrounds. Typical results are the construction of a wealth of new inhomogeneous complete quaternionic Kähler manifolds based on a combination of ideas from supergravity and perturbative string theory with new mathematical tools and the derivation of low energy effective actions in physically relevant situations, among other examples.

1 Geometry of compactification spaces

One of the strands of this project has been the study of G-structures of the type occurring on internal spaces of string compactifications. From a mathematical point of view we were specially interested in Einstein metrics and, in particular, in metrics of special holonomy. From a physics point of view the study of manifolds with G-structures are of interest for two reasons. Firstly they correspond to backgrounds which can exhibit spontaneous supersymmetry breaking. This is a necessary ingredient in order to make contact with experimental observations in particle physics and cosmology where no sign of supersymmetry is so far manifest. Secondly, they appear as the mirror duals of string backgrounds with fluxes. Indeed in [1] the specific class of manifolds with $SU(3) \times SU(3)$ structure where identified as mirror duals of type II compactifications on Calabi–Yau manifolds with magnetic fluxes.

An example of the G-structures we have investigated are half-flat $SU(3)$-structures on six-dimensional manifolds, which are related to Ricci-flat metrics of holonomy a subgroup of G_2 on seven-dimensional manifolds. In fact, a half-flat $SU(3)$-structure is precisely the structure induced on a hypersurface in a manifold with a parallel G_2-structure. By considering a family of equidistant hypersurfaces one arrives at a system of evolution equations for the $SU(3)$-structure known as Hitchin's flow equations. Similar flow equations are obtained by considering foliations by equidistant hypersurfaces in ambient manifolds with a parallel $SU(3)$- or $Spin(7)$-structure. It was shown by Hitchin [2] that for a given initial half-flat $SU(3)$-structure the system has a unique maximal solution on every compact 6-manifold M by exhibiting it as a Hamiltonian system. The solution is a Riemannian metric of holonomy contained in G_2. It is defined on the product $M \times I$, where I is an interval. The Hamiltonian is defined by integration of a certain invariant over the compact manifold. Based on a different approach, in [3] we extend this theory allowing for non-compact manifolds and non-compact structure groups. When $\dim M = 6$, this includes half-flat G-structures on possibly non-compact manifolds M as initial data for metrics

of holonomy contained in the compact or in the non-compact form of G_2, depending on whether the structure group $G \in \{SU(3), SU(1,2), SL(3,\mathbb{R})\}$ is compact or non-compact.

Lie groups admitting a left-invariant half-flat $SU(3)$-structure have been classified in [4–6]. For some of these groups we have determined all left-invariant half-flat $SU(3)$-structures and have solved the Hitchin flow equations with these structures as initial data [3, 7] obtaining metrics with holonomy group G_2 or its noncompact form G_2^*. A particularly interesting case analysed in [7] is the classification of all left-invariant half-flat $SU(3)$-structures on $S^3 \times S^3$. This includes nontrivial deformations of the nearly Kähler structure and Einstein half-flat $SU(3)$-structures. Classification results for certain types left-invariant G_2-structures have been obtained in [8, 9]. Solving the Hitchin flow with some of these structures as initial data, metrics with holonomy group $SU(4) \subset Spin(7)$ have been constructed in [10].

The Ricci-flat Riemannian manifolds of special holonomy obtained by solving the flow equations are in general incomplete, even if the initial manifold M is compact or homogeneous. In [11] we study under which conditions a maximal incomplete solution of the flow equations with homogeneous initial data can be completed to a complete Riemannian manifold of special holonomy. We restrict to the case when M admits a simply transitive action of a solvable Lie group preserving the initial G-structure, where $G \in \{SU(2), SU(3), G_2\}$ and $\dim M = 5, 6, 7$ respectively. We prove under certain natural assumptions in this setting that a completion as above does not exist. As a consequence, the classes of solvable Lie groups considered in our work cannot act with co-homogeneity one on a complete and non-flat Riemannian manifold with a parallel $SU(3)$-, G_2-, or $Spin(7)$-structure. These results do not apply to semi-simple Lie groups, such as $SL(2,\mathbb{C})$. For the latter group we classify all left-invariant half-flat $SU(3)$-structures which are also right-invariant under the maximal compact subgroup $SU(2) \subset SL(2,\mathbb{C})$ and solve the Hitchin flow with these structures as initial data. The solutions are G_2-holonomy metrics defined on $SL(2,\mathbb{C}) \times (a,b)$, where $-\infty < a < b < \infty$. Some of them can be completed at one boundary point of the interval (a,b) but never at both.

We have mentioned above the class of half-flat $SU(3)$-structures. The manifolds carrying these structures can be considered as generalizations of the well known Calabi–Yau three-folds, which are Ricci-flat and Kähler. The differential system satisfied by a half-flat $SU(3)$-structure does not imply the Einstein equations for the metric on the underlying 6-dimensional (real) manifold. Examples of half-flat $SU(3)$-structures which are Einstein include the so-called nearly Kähler structures. Until recently, the only known complete nearly Kähler manifolds were the homogeneous ones, classified by Butruille [12]. In [13] we show that inhomogeneous, locally homogeneous examples exist in abundance. These are obtained as quotients by a finite group of automorphisms acting freely on the simply connected 3-symmetric space

$$(SU(2) \times SU(2) \times SU(2))/SU(2) \cong S^3 \times S^3,$$

where the isotropy group $SU(2)$ is diagonally embedded. These quotients include co-homogeneity one examples. Simply connected examples of co-homogeneity one (diffeomorphic to $S^3 \times S^3$) were later constructed by Foscolo and Haskins [14].

The nearly Kähler metric on $S^3 \times S^3$ has the special property of being a left-invariant Einstein metric, a property shared by the product metric. The simply connected homogeneous Einstein manifolds in dimension 6 have been completely classified with exception of the case of left-invariant Einstein metrics on $S^3 \times S^3$, see [15] for the state of the art. In [16] we classify left-invariant Einstein metrics on $S^3 \times S^3$ under the additional assumption that the stabilizer in the group of proper isometries is neither trivial nor $\mathbb{Z}_2$. Under this assumption we find that

the metric is either the left-invariant nearly Kähler metric or the product metric, which have the stabilizer $SU(2)$ and $SU(2) \times SU(2)$ respectively.

The relation of string theory with particle physics and cosmology is facilitated via the low-energy effective action which consists only of the light modes of string theory while all heavy excitations have been integrated out. String backgrounds with spontaneously broken supersymmetry correspond to a supersymmetric effective action with a scalar potential whose minimum breaks (part of the) supersymmetry. Apart from the scalar potential the metric of the scalar fields in the low-energy effective action is of prime importance. Via supersymmetry it fixes many other physical interesting terms in the action. This metric is the metric on the moduli space of the string compactifications at hand. Thus not only the compactification manifolds but almost more importantly its moduli space contains vital physical information.

Manifolds with $SU(2) \times SU(2)$ structure of dimension four, five and six have been investigated in [17,18]. Such compactifications correspond to backgrounds with spontaneously broken $\mathcal{N} = 4$ supersymmetry. In these cases we determined the moduli space and established the consistency with $\mathcal{N} = 4$ supergravity. Depending on the structure of the intrinsic torsion, antisymmetric tensor fields can become massive in some of these cases. $\mathcal{N} = 2$ orientifolds of these background were studied in detail in [19]. Massive tensor fields and their coupling to three-forms were studied in [20]. (These research projects were also part of the three PhD-theses [21–23] and the Master-thesis [24].)

Furthermore, we studied type II backgrounds with spontaneously broken $\mathcal{N} = 2$ supergravity in [1,25,26]. In [25] we showed that the low-energy effective action of such backgrounds displays the U-duality group $E_{7(7)}$. In particular we derived $E_{7(7)}$-invariant expressions for the Kähler and hyper-Kähler potentials describing the moduli space of vector and hypermultiplets together with the Killing prepotentials defining the scalar potential. In [26] we incorporated perturbative quantum correction in this formalism.

In collaboration with project A1 we also studied heterotic backgrounds with G-structure. This is summarized in the PhD-thesis [27]. M-theory backgrounds with G-structure were studied in [28].

2 Special geometry

Another strand of this project has been the study of the scalar geometry of the low energy limit of string theory. The relevant geometries for type II string theory are governed by $\mathcal{N} = 2$ supergravity and its quantum corrections. They occur in three basic variants: projective special real geometry, projective special Kähler geometry, and quaternionic Kähler geometry. Quaternionic Kähler manifolds are examples of Einstein manifolds and have therefore been intensively studied in mathematics. Despite this fact, there are many open questions in this area and examples are scarce. The three special geometries mentioned above are intimately related by geometric constructions known as the r- and the c-map originating from the dimensional reduction of supergravity theories, respectively from 5 to 4 and from 4 to 3 space-time dimensions [29, 30]. We show in [31] that the supergravity r-map and the supergravity c-map do both preserve the completeness of the underlying metrics. As a consequence, every complete projective special real manifold of dimension n gives rise (by the r-map) to a complete projective special Kähler manifold of (real) dimension $2n + 2$ and every complete projective special Kähler manifold of dimension $2n$ gives rise (by the c-map) to a complete quaternionic Kähler manifold of dimension $4n + 4$. The scalar curvature of the resulting quaternionic Kähler manifolds is always negative.

A *projective special real manifold* of dimension n is by definition a hypersurface $\mathcal{H} \subset \mathbb{R}^{n+1}$ such that there exists a homogeneous cubic polynomial h on $\mathbb{R}^{n+1}$ with the following properties:

(i) $\mathcal{H} \subset \{h = 1\}$ and

(ii) the Hessian $\partial^2 h$ is negative definite on $T\mathcal{H}$.

The manifold $\mathcal{H}$ is endowed with the canonical Riemannian metric $g_{\mathcal{H}}$ induced by the tensor field $-\frac{1}{3}\partial^2 h$. Projective special real manifolds can be intrinsically characterized by a partial differential equation satisfied by their underlying centro-affine structure [32, Theorem 2.3]. We show in [32, Theorem 2.5] that the projective special real manifolds $\mathcal{H}$ for which the metric $g_{\mathcal{H}}$ is complete are precisely those for which the subset $\mathcal{H} \subset \mathbb{R}^{n+1}$ is closed. As a corollary, we proof that every locally strictly convex component of the level set $\{h = 1\} \subset \mathbb{R}^{n+1}$ of a homogeneous cubic polynomial defines an explicit complete quaternionic Kähler metric on $\mathbb{R}^{4n+8}$. Complete projective special real manifolds and the corresponding complete quaternionic Kähler manifolds are classified in low dimensions in [31,33] and in the case of reducible polynomials h in [34]. The examples which we obtain by this method include complete quaternionic Kähler manifolds of cohomogeneity one in all dimensions ≥ 12. Further inhomogeneous complete examples (including the dimensions 4 and 8) were obtained in [35] by combining the above methods with a one-parameter deformation of the metric known as the one-loop quantum correction [36]. In fact, it is shown in [35, Theorem 27] that every quaternionic Kähler manifold associated with a complete projective special real manifold admits a canonical deformation by complete quaternionic Kähler manifolds depending on a parameter $c \geq 0$. The same is true for quaternionic Kähler manifolds associated with projective special Kähler manifolds, provided that the special Kähler manifold has regular boundary behaviour [35, Theorem 13]. These two results imply, in particular, the existence of this type of explicit deformation for all the known homogeneous quaternionic Kähler manifolds of negative Ricci curvature with exception of the simplest such homogeneous spaces, the quaternionic hyperbolic spaces. The fact that the metrics obtained by the one-loop deformation of the supergravity c-map are quaternionic Kähler was proven in [37, 38] based on a geometric construction which allows to reduce the supergravity c-map to the much simpler rigid c-map. (This work was also part of the PhD project [39].) A similar construction allows to reduce the supergravity r-map to its rigid version [40]. (This work was also part of the PhD project [41].) A geometric description of the rigid r-map is given in [42].

The moduli space of complete projective special real manifolds has been systematically studied in the PhD thesis [43]. One of the main results is that the set of normal forms describing these manifolds can be parametrized by a compact convex neighborhood of zero in a finite-dimensional vector space. In particular, any two complete projective special real manifolds can be connected by connecting their normal forms in the convex set. Another important consequence are uniform curvature bounds depending only on the dimension.

In the above geometric constructions pseudo-Riemannian cones play an important role. This is due to the fact that a projective special Kähler manifold is the base of a $\mathbb{C}^*$-bundle the total space of which is a conical affine special Kähler manifold with indefinite metric of index 2. Similarly, quaternionic Kähler manifolds of negative scalar curvature are the base of a bundle the total space of which has a conical hyper-Kähler structure of index 4 (the Swann bundle). In [44] we study pseudo-Riemannian cones and their holonomy. In the Riemannian setting, a metric cone over a complete manifold is either flat or irreducible, by Gallot's theorem [45]. This is no longer true in the in the pseudo-Riemannian setting and we describe the properties of the holonomy representation of the cone and how it relates to the geometry of the base manifold.

In the spirit of Gallot's theorem, we prove that a metric cone over a compact and complete pseudo-Riemannian manifold is either flat or indecomposable. Matveev and Mounoud have later given another proof, which does also apply to incomplete compact manifolds [46].

Homogeneous pseudo-Riemannian manifolds of index 4 with a compatible almost hypercomplex or almost quaternionic structure are classified in [47, 48] in the case of $\mathbb{H}$-irreducible isotropy representation. (This work was also part of the PhD project [49].) We prove that the resulting spaces are always locally symmetric if the dimension is at least 16 and give counterexamples in dimension 12. In [50] we classify homogeneous locally conformally Kähler manifolds under the assumption that the normalizer of the isotropy group is compact.

The special geometry of Euclidean supersymmetry with eight real supercharges has been systematically developed in a collaboration with Mohaupt and his group initiated in [51, 52]. A common feature is the appearance of para-complex and para-quaternionic structures replacing the complex and quaternionic structures present in the standard Minkowskian theories. Time-like and space-like reductions relating the scalar geometries of various Euclidean and Minkowskian theories of supergravity in space-time dimensions $d \in \{3, 4, 5\}$ have been worked out in [53–55]. The twistor spaces of para-quaternionic Kähler manifolds are studied in [56]. Also the geometric construction of the c-map obtained in [37,38] admits a generalization to the Euclidean setting, as shown in [57].

The rigid limit of $\mathcal{N} = 2$ supergravity coupled to vector and hypermultiplets is somewhat subtle. In [58] we showed how the respective scalar field spaces reduce to their global counterparts. In the hypermultiplet sector we focused on the relation between the local and rigid c-map.

For some further geometric aspects related to the themes discussed so far see [59–64].

3 Second quantized mirror symmetry

Apart from the standard perturbative mirror symmetry, which relates two Calabi–Yau manifolds with reversed Hodge numbers, there also is a non-perturbative duality which relates type II Calabi–Yau compactifications to heterotic K3 compactifications. This duality is fairly well understood in the vector multiplet sector of $\mathcal{N} = 2$ supergravity but poorly understood in the hypermultiplet sector.

In [65] we revisited this duality and considered the heterotic string theory compactified on K3 $\times T^2$ and type IIA compactified on a Calabi–Yau threefold X in the hypermultiplet sector. We derived an explicit map between the field variables of the respective moduli spaces at the level of the classical effective actions. We determined the parametrization of the K3 moduli space consistent with the Ferrara–Sabharwal form. From the expression of the holomorphic prepotential we were led to conjecture that both X and its mirror must be K3 fibrations in order for the type IIA theory to have an heterotic dual. We then focused on the region of the moduli space where the metric is expressed in terms of a prepotential on both sides of the duality. Applying the duality we derived the heterotic hypermultiplet metric for a gauge bundle which is reduced to 24 point-like instantons. This result is confirmed by using the duality between the heterotic theory on T^3 and M-theory on K3. We finally studied the hyper-Kähler metric on the moduli space of an $SU(2)$ bundle on K3.

In [66] we continued this investigation and predicted the form of the quaternion-Kähler metric on hypermultiplet moduli space when K3 is elliptically fibered, in the limit of a large fiber and even larger base. The result is in general agreement with expectations from Kaluza–

Klein reduction, in particular the metric has a two-stage fibration structure, where the B-field moduli are fibered over bundle and metric moduli, while bundle moduli are themselves fibered over metric moduli.

A different insight coming out of mirror symmetry has been suggested in [67]. Given a maximally degenerating family of Calabi–Yau varieties of the general kind studied in [68, 69], there is a canonical basis of sections ("generalized theta functions") of the polarizing line bundle of the family. Under homological mirror symmetry this basis of sections is dual to intersection points of a pair of canonical isotopy classes of Lagrangian sections of the mirror SYZ fibration. Generalized theta functions are built by counting tropical versions of holomorphic cylinders connecting two SYZ fibres and in such a way capture tree-level information of the mirror SYZ geometry. The general properties of generalized theta functions have been comprehensively studied in [70]. By generalizing the monomial basis of toric local Calabi–Yaus in the crystal melting picture, we expect that generalized theta functions actually also encode the higher genus and non-perturbative information necessary for second-quantized mirror symmetry for compact Calabi–Yaus. Work is currently under way to prove the mirror enumerative meaning of theta functions [71, 72].

4 Partial supersymmetry breaking

Spontaneous breaking of $\mathcal{N} = 2$ supersymmetry is known to be possible only under very special circumstances. In [73] we used the embedding tensor formalism to give the general conditions for the existence of $\mathcal{N} = 1$ vacua in spontaneously broken $\mathcal{N} = 2$ supergravities. We indeed confirmed the necessity of having both electrically and magnetically charged multiplets in the spectrum, but also showed that no further constraints on the special Kähler geometry of the vector multiplets arise. The quaternionic field space of the hypermultiplets instead must have two commuting isometries. As an example we discussed the special quaternionic-Kähler geometries which appear in the low-energy limit of type II string theories. For these cases we found the general solution for stable Minkowski and AdS $\mathcal{N} = 1$ vacua, and determine the charges in terms of the holomorphic prepotentials. We further found that the string theory realisation of the $\mathcal{N} = 1$ Minkowski vacua requires the presence of non-geometric fluxes, whereas they are not needed for the AdS vacua.

In [74] we derived the low-energy effective action below the scale of partial supersymmetry breaking and computed the $\mathcal{N} = 1$ couplings in terms of the $\mathcal{N} = 2$ input data. We then showed that this effective action satisfies the constraints of $\mathcal{N} = 1$ supergravity in that its sigma-model metric is Kähler, while the superpotential and the gauge kinetic functions are holomorphic. As an example we discussed the $\mathcal{N} = 1$ effective supergravity of type II compactifications.

In [75] we made the construction of the effective $\mathcal{N} = 1$ theory mathematically rigorous. Specifically we proved that, given a certain isometric action of a two-dimensional Abelian group A on a quaternionic Kähler manifold M which preserves a submanifold $N \subset M$, the quotient $M' = N/A$ has a natural Kähler structure. We verified that the assumptions on the group action and on the submanifold $N \subset M$ are satisfied for a large class of examples obtained from the supergravity c-map. In particular, we found that all quaternionic Kähler manifolds M in the image of the c-map admit an integrable complex structure compatible with the quaternionic structure, such that $N \subset M$ is a complex submanifold. Finally, we discussed how the existence of the Kähler structure on M' is required by the consistency of spontaneous $\mathcal{N} = 2$ to $\mathcal{N} = 1$ supersymmetry breaking.

In [76] we gave explicit examples of gauged $\mathcal{N} = 2$ supergravities which arise in the low-energy limit of type II string theories and which exhibit spontaneous partial supersymmetry breaking. Specifically, for the so called quantum STU model we derived the scalar field space and the scalar potential of the $\mathcal{N} = 1$ supersymmetric low-energy effective action. We also studied the properties of the Minkowskian $\mathcal{N} = 1$ supersymmetric ground states for a broader class of supergravities including the quantum STU model. (This project was also part of the Master-thesis [77].)

In [78] we generalized the scope and studied $\mathcal{N} = 2$ vacua in spontaneously broken $\mathcal{N} = 4$ electrically gauged supergravities in four space-time dimensions. We argued that the classification of all such solutions amounts to solving a system of purely algebraic equations. We then explicitly constructed a special class of consistent $\mathcal{N} = 2$ solutions and studied their properties. In particular we found that the spectrum assembles in $\mathcal{N} = 2$ massless or BPS supermultiplets. We showed that (modulo U(1) factors) arbitrary unbroken gauge groups can be realized provided that the number of $\mathcal{N} = 4$ vector multiplets is large enough. Below the scale of partial supersymmetry breaking we calculated the relevant terms of the low-energy effective action and argue that the special Kähler manifold for vector multiplets is completely determined, up to its dimension, and lies in the unique series of special Kähler product manifolds. (This project was also part of the PhD-thesis [79].)

5 Supersymmetric AdS backgrounds

Anti-de Sitter (AdS) backgrounds of string theory and supergravity are of interest for two reasons. On the one hand that serve as an intermediate step in phenomenological investigations before "uplifting" to a de Sitter background. On the other hand, AdS backgrounds feature prominently in the AdS/CFT correspondence and determine properties of strongly coupled gauge theory living on the boundary of the AdS space. In [80] we initiated the study of the structure of the supersymmetric moduli spaces of AdS backgrounds in supergravity theories. This was continued in all space-time dimensions with all possible supercharges in [81–86].

In [80] we studied the structure of the supersymmetric moduli spaces of $\mathcal{N} = 1$ and $\mathcal{N} = 2$ supergravity theories in AdS_4 backgrounds. In the $\mathcal{N} = 1$ case, the moduli space cannot be a complex submanifold of the Kähler field space, but is instead real with respect to the inherited complex structure. In $\mathcal{N} = 2$ supergravity the same result holds for the vector multiplet moduli space, while the hypermultiplet moduli space is a Kähler submanifold of the quaternionic-Kähler field space. These findings are in agreement with AdS/CFT considerations.

In [81] we determined the supersymmetric AdS_7 backgrounds of seven-dimensional half-maximal gauged supergravities and showed that they do not admit any deformations that preserve all 16 supercharges. We compared this result to the conformal manifold of the holographically dual $(1, 0)$ superconformal field theories and showed that accordingly its representation theory implies that no supersymmetric marginal operators exist.

In [82] we classified the $\mathcal{N} = 4$ supersymmetric AdS_5 backgrounds that arise as solutions of five-dimensional $\mathcal{N} = 4$ gauged supergravity. We expressed our results in terms of the allowed embedding tensor components and identify the structure of the associated gauge groups. We showed that the moduli space of these AdS vacua is of the form $SU(1, m)/(U(1) \times SU(m))$ and discussed our results regarding holographically dual $\mathcal{N} = 2$ SCFTs and their conformal manifolds.

In [83] we determined the conditions for maximally supersymmetric AdS_5 vacua of five-

dimensional gauged $\mathcal{N} = 2$ supergravity coupled to vector-, tensor- and hypermultiplets charged under an arbitrary gauge group. In particular, we showed that the unbroken gauge group of the AdS_5 vacua has to contain an $U(1)_R$-factor. Moreover we proved that the scalar deformations which preserve all supercharges form a Kähler submanifold of the ambient quaternionic Kähler manifold spanned by the scalars in the hypermultiplets.

In [84] we studied maximally supersymmetric AdS backgrounds in consistent $\mathcal{N} = 2$ truncations of type IIB supergravity compactified on the Sasaki–Einstein manifold $T^{1,1}$. In particular, we focused on truncations that contain fields coming from the nontrivial second and third cohomology forms on $T^{1,1}$. These give rise to $\mathcal{N} = 2$ supergravity coupled to two vector- and two hypermultiplets or one vector- and three hypermultiplets, respectively. We found that both truncations admit AdS_5 backgrounds with the gauge group always being broken but containing at least an $U(1)_R$ factor. Moreover, in both cases we showed that the moduli space of AdS vacua is nontrivial and of maximal dimension. Finally, we explicitly computed the metrics on these moduli spaces.

In [85] we studied fully supersymmetric AdS_6 vacua of half-maximal $\mathcal{N} = (1, 1)$ gauged supergravity in six space-time dimensions coupled to n vector multiplets. We showed that the existence of AdS_6 backgrounds requires that the gauge group is of the form $G' \times G'' \subset SO(4, n)$ where $G' \subset SO(3, m)$ and $G'' \subset SO(1, n - m)$. In the AdS_6 vacua this gauge group is broken to its maximal compact subgroup $SO(3) \times H' \times H''$ where $H' \subset SO(m)$ and $H'' \subset SO(n-m)$. Furthermore, the $SO(3)$ factor is the R-symmetry gauged by three of the four graviphotons. We further showed that the AdS_6 vacua have no moduli that preserve all supercharges. This is precisely in agreement with the absence of supersymmetric marginal deformations in holographically dual five-dimensional superconformal field theories.

Finally, in [86] we studied maximally supersymmetric AdS_D solutions of gauged supergravities in dimensions $D \geq 4$. We showed that such solutions can only exist if the gauge group after spontaneous symmetry breaking is a product of two reductive groups $H_R \times H_{\mathrm{mat}}$, where H_R is uniquely determined by the dimension D and the number of supersymmetries N while H_{mat} is unconstrained. This resembles the structure of the global symmetry groups of the holographically dual SCFTs, where H_R is interpreted as the R-symmetry and H_{mat} as the flavor symmetry. Moreover, we discussed possible supersymmetry preserving continuous deformations, which correspond to the conformal manifolds of the dual SCFTs. Under the assumption that the scalar manifold of the supergravity is a symmetric space we derived general group theoretical conditions on these moduli. Using these results we determined the AdS solutions of all gauged supergravities with more than 16 real supercharges. We found that almost all of them do not have supersymmetry preserving deformations with the only exception being the maximal supergravity in five dimensions with a moduli space given by $SU(1, 1)/U(1)$. Furthermore, we determined the AdS solutions of four-dimensional $\mathcal{N} = 3$ supergravities and showed that they similarly do not admit supersymmetric moduli.

References

[1] M. Grana, J. Louis and D. Waldram, *SU(3) x SU(3) compactification and mirror duals of magnetic fluxes*, *JHEP* **04** (2007) 101, [hep-th/0612237].

[2] N. Hitchin, *Stable forms and special metrics*, in "Global differential geometry: the mathematical legacy of Alfred Gray" (Bilbao, 2000), *Contemp. Math.* **288** (2001) 70–89, [math/0107101].

[3] V. Cortés, T. Leistner, L. Schäfer and F. Schulte-Hengesbach, *Half-flat Structures and Special Holonomy*, *Proc. London Math. Soc.* **102** (2011) 113–158, [0907.1222].

[4] F. Schulte-Hengesbach, *Half-flat structures on products of three-dimensional Lie groups*, *Journal of Geometry and Physics* **60** (2010) 1726–1740, [0912.3486].

[5] M. Freibert and F. Schulte-Hengesbach, *Half-flat structures on decomposable Lie groups*, *Transform. Groups* **17** (2012) 123–141.

[6] M. Freibert and F. Schulte-Hengesbach, *Half-flat structures on indecomposable Lie groups*, *Transform. Groups* **17** (2012) 657–689.

[7] F. Schulte-Hengesbach, *Half-flat structures on Lie groups*, Ph.D. thesis, Universität Hamburg, 2010. http://ediss.sub.uni-hamburg.de/volltexte/2010/4626.

[8] M. Freibert, *Cocalibrated G_2-structures on products of four- and three-dimensional Lie groups*, *Differential Geom. Appl.* **31** (2013) 349–373.

[9] M. Freibert, *Calibrated and parallel structures on almost Abelian Lie algebras*, *ArXiv e-prints* (July, 2013) , [1307.2542].

[10] M. Freibert, *Geometric structures on Lie algebras and the Hitchin flow*, Ph.D. thesis, Universität Hamburg, 2013. http://ediss.sub.uni-hamburg.de/volltexte/2013/6216/pdf/Dissertation.pdf.

[11] F. Belgun, V. Cortés, M. Freibert and O. Goertsches, *On the boundary behaviour of left-invariant Hitchin and hypo flows*, *J. London Math. Soc.* **92** (2015) 41–62, [1405.1866].

[12] Butruille, J. B., *Classification des variétés approximativement kähleriennes homogènes*, *Ann. Global Anal. Geom.* **27** (2005) 201–225, [math/0401152].

[13] V. Cortés and J. J. Vásquez, *Locally homogeneous nearly Kähler manifolds*, *Annals Glob. Anal. Geom.* **48** (2015) 269–294, [1410.6912].

[14] Foscolo, L. and Haskins, M., *New G_2-holonomy cones and exotic nearly Kähler structures on S^6 and $S^3 \times S^3$*, *Ann. of Math.* **185** (2017) 59–130, [1501.07838].

[15] Nikonorov, Y.G. and Rodionov, E. D., *Compact homogeneous Einstein 6-manifolds*, *Differential Geom. Appl.* **19** (2003) 369–378.

[16] F. Belgun, V. Cortés, A. S. Haupt and D. Lindemann, *Left-invariant Einstein metrics on $S^3 \times S^3$*, *J. Geom. Phys.* **128** (2018) 128–139, [1703.10512].

[17] H. Triendl and J. Louis, *Type II compactifications on manifolds with SU(2) x SU(2) structure*, *JHEP* **07** (2009) 080, [0904.2993].

[18] T. Danckaert, J. Louis, D. Martinez-Pedrera, B. Spanjaard and H. Triendl, *The N=4 effective action of type IIA supergravity compactified on SU(2)-structure manifolds*, *JHEP* **1108** (2011) 024, [1104.5174].

[19] T. Danckaert and J. Louis, *Type IIA orientifold compactification on SU(2)-structure manifolds*, *JHEP* **1001** (2010) 105, [0911.5697].

[20] K. Groh, J. Louis and J. Sommerfeld, *Duality and Couplings of 3-Form-Multiplets in N=1 Supersymmetry*, *JHEP* **1305** (2013) 001, [1212.4639].

[21] H. Triendl, *Generalized Geometry and Partial Supersymmetry Breaking*, Ph.D. thesis, Universität Hamburg, 2010. 1010.1159.

[22] B. Spanjaard, *Compactifications of IIA Supergravity on SU(2)-Structure Manifolds*, Ph.D. thesis, Universität Hamburg, 2008. http://www-library.desy.de/cgi-bin/showprep.pl?desy-thesis-08-016.

[23] T. Danckaert, *Type IIA orientifolds on SU(2)-structure manifolds*, Ph.D. thesis, Universität Hamburg, 2010. 10.3204/DESY-THESIS-2010-046 http://www.desy.de/uni-th/stringth/Works/.

[24] K. Groh, *Dualität und kopplungen von 3-form-multipletts in n=1 supersymmetrie*, Master's thesis, Universität Hamburg, 2009. http://www.desy.de/uni-th/stringth/Works/.

[25] M. Grana, J. Louis, A. Sim and D. Waldram, *E7(7) formulation of N=2 backgrounds*, *JHEP* **07** (2009) 104, [0904.2333].

[26] M. Grana, J. Louis, U. Theis and D. Waldram, *Quantum Corrections in String Compactifications on SU(3) Structure Geometries*, *JHEP* **01** (2015) 057, [1406.0958].

[27] D. M. Martinez Pedrera, *Low-energy supergravities from heterotic compactification on reduced structure backgrounds*, Ph.D. thesis, Universität Hamburg, 2009. 10.3204/DESY-THESIS-2009-037 http://www.desy.de/uni-th/stringth/Works/.

[28] O. Aharony, M. Berkooz, J. Louis and A. Micu, *Non-Abelian structures in compactifications of M-theory on seven-manifolds with SU(3) structure*, *JHEP* **09** (2008) 108, [0806.1051].

[29] B. de Wit and A. Van Proeyen, *Special geometry, cubic polynomials and homogeneous quaternionic spaces*, *Commun. Math. Phys.* **149** (1992) 307–333, [hep-th/9112027].

[30] S. Ferrara and S. Sabharwal, *Quaternionic manifolds for type ii superstring vacua of calabi-yau spaces*, *Nucl. Phys.* **B332** (1990) 317–332.

[31] V. Cortés, X. Han and T. Mohaupt, *Completeness in supergravity constructions*, *Comm. Math. Phys.* **311** (2012) 191–213, [1101.5103].

[32] V. Cortés, M. Nardmann and S. Suhr, *Completeness of hyperbolic centroaffine hypersurfaces*, *Comm. Anal. Geom.* **24** (2016) 59–92, [1407.3251].

[33] V. Cortés, M. Dyckmanns and D. Lindemann, *Classification of complete projective special real surfaces*, *Proceedings of the London Mathematical Society* **109** (2014) 423–445, [1302.4570].

[34] V. Cortés, M. Dyckmanns, M. Jüngling and D. Lindemann, *A class of cubic hypersurfaces and quaternionic Kähler manifolds of co-homogeneity one*, 1701.07882.

[35] V. Cortés, M. Dyckmanns and S. Suhr, *Completeness of projective special Kähler and quaternionic Kähler manifolds*, in "Special metrics and group actions in geometry", *Springer INdAM Series* **23** (2017) 81–106, [1607.07232].

[36] D. Robles-Llana, F. Saueressig and S. Vandoren, *String loop corrected hypermultiplet moduli spaces*, *J. High Energy Phys.* (2006) 081, 35 pp.

[37] D. V. Alekseevsky, V. Cortés and T. Mohaupt, *Conification of Kähler and hyper-Kähler manifolds*, *Comm. Math. Phys.* **324** (May, 2012) 637–655, [1205.2964].

[38] D. V. Alekseevsky, V. Cortés, M. Dyckmanns and T. Mohaupt, *Quaternionic Kähler metrics associated with special Kähler manifolds*, *J. Geom. Phys.* **92** (2015) 271–287, [1305.3549].

[39] M. Dyckmanns, *The hyper-Kähler/quaternionic Kähler correspondence and the geometry of the c-map*, Ph.D. thesis, Universität Hamburg, 2018. http://ediss.sub.uni-hamburg.de/volltexte/2015/7542.

[40] V. Cortés, P.-S. Dieterich and T. Mohaupt, *ASK/PSK-correspondence and the r-map*, *Letters in Mathematical Physics* **108** (2018) 1279–1306.

[41] P.-S. Dieterich, *The affine special Kähler/projective special Kähler correspondence and related constructions*, Ph.D. thesis, Universität Hamburg, 2017. http://ediss.sub.uni-hamburg.de/volltexte/2017/8638/.

[42] D. V. Alekseevsky and V. Cortés, *Geometric construction of the r-map: from affine special real to special kähler manifolds*, *Comm. Math. Phys.* **291** (2009) 579–590, [0811.1658].

[43] D. Lindemann, *Structure of the class of projective special real manifolds and their generalisations*, Ph.D. thesis, Universität Hamburg, 2018. http://ediss.sub.uni-hamburg.de/volltexte/2018/.

[44] D. V. Alekseevsky, V. Cortés, A. Galaev and T. Leistner, *Cones over pseudo-Riemannian manifolds and their holonomy*, *Journal für die reine und angewandte Mathematik (Crelles Journal)* **2009** (Oct., 2009) 23–69, [0707.3063].

[45] S. Gallot, *équations différentielles caractéristiques de la sphère.*, *Ann. Sci. École Norm. Sup. (4)* **12** (1979) 235–267.

[46] V. Matveev and P. Mounoud, *Gallot-tanno theorem for closed incomplete pseudo-riemannian manifolds and applications*, *Ann. Glob. Anal. Geom.* **38** (2010) 259–271, [0909.5344].

[47] V. Cortés and B. Meinke, *Pseudo-Riemannian almost quaternionic homogeneous spaces with irreducible isotropy*, *Geometriae Dedicata* (Dec, 2017) , [1701.04336].

[48] V. Cortés and B. Meinke, *Pseudo-Riemannian almost hypercomplex homogeneous spaces with irreducible isotropy*, *J. of Lie Theory* **27** (2017) 982–993, [1606.06486].

[49] B. Meinke, *Homogeneous almost hypercomplex and almost quaternionic pseudo-Hermitian manifolds with irreducible isotropy groups*, Ph.D. thesis, Universität Hamburg, 2015. http://ediss.sub.uni-hamburg.de/volltexte/2016/7698/.

[50] V. Cortés, D. V. Alekseevsky, K. Hasegawa and Y. Kamishima, *Homogeneous locally conformally Kähler and Sasaki manifolds*, *International Journal of Mathematics* **26** (2015) 1–29, [1403.3268].

[51] V. Cortés, C. Mayer, T. Mohaupt and F. Saueressig, *Special geometry of euclidean supersymmetry i: vector multiplets*, *J. High Energy Phys.* **3** (2004) 028, [hep-th/0312001].

[52] V. Cortés, C. Mayer, T. Mohaupt and F. Saueressig, *Special geometry of euclidean supersymmetry ii: hypermultiplets and the c-map*, *J. High Energy Phys.* **6** (2005) 025, [hep-th/0503094].

[53] V. Cortés and T. Mohaupt, *Special Geometry of Euclidean Supersymmetry III: the local r-map, instantons and black holes*, *J. High Energy Phys.* **7** (2009) 066, [0905.2844].

[54] V. Cortés, P. Dempster, T. Mohaupt and O. Vaughan, *Special Geometry of Euclidean Supersymmetry IV: the local c-map*, *JHEP* **10** (2015) 066, [1507.04620].

[55] V. Cortés, P. Dempster and T. Mohaupt, *Time-like reductions of five-dimensional supergravity*, *JHEP* **1404** (2014) 190, [1401.5672].

[56] D. V. Alekseevsky and V. Cortés, *The twistor spaces of a para-quaternionic Kähler manifold*, *Osaka J. Math.* **45** (2008) 215–251.

[57] M. Dyckmanns and O. Vaughan, *The para-HK/QK correspondence*, *J. Geom. Phys.* **116** (2017) 244–257, [1601.05001].

[58] B. E. Gunara, J. Louis, P. Smyth, L. Tripodi and R. Valandro, *The rigid limit of $N = 2$ supergravity*, *Class. Quant. Grav.* **30** (2013) 195014, [1305.1903].

[59] V. Cortés, ed., *Handbook of pseudo-Riemannian geometry and supersymmetry,* IRMA Lectures in Mathematics and Theoretical Physics, vol. 16. European Mathematical Society (EMS), Zürich, 2010.

[60] V. Cortés and L. Schäfer, *Differential geometric aspects of the tt*-equations*, in "From Hodge Theory to Integrability and TQFT: tt*-geometry", Eds. R. Donagi and K. Wendland, Proceedings of Symposia in Pure Mathematics **78** (2008) 75–86.

[61] V. Cortés and L. Schäfer, *Flat nearly Kähler manifolds*, *Annals of Global Analysis and Geometry* **32** (2007) 379–389, [arXiv:math/0610176].

[62] V. Cortés and L. Schäfer, *Geometric structures on Lie groups with flat bi-invariant metric*, *Journal of Lie Theory* **19** (July, 2009) 423–437, [0907.5492].

[63] V. Cortés and A. Saha, *Quarter-pinched Einstein metrics interpolating between real and complex hyperbolic metrics*, *Math. Z.* (2017) , [1705.04186].

[64] V. Cortés and L. David, *Twist, elementary deformation, and KK correspondence in generalized complex geometry*, 1706.05516.

[65] J. Louis and R. Valandro, *Heterotic-Type II Duality in the Hypermultiplet Sector*, *JHEP* **1205** (2012) 016, [1112.3566].

[66] S. Alexandrov, J. Louis, B. Pioline and R. Valandro, *$N = 2$ Heterotic-Type II duality and bundle moduli*, *JHEP* **08** (2014) 092, [1405.4792].

[67] M. Gross and B. Siebert, *Theta functions and mirror symmetry*, 1204.1991.

[68] M. Gross and B. Siebert, *Mirror symmetry via logarithmic degeneration data, I*, *J. Differential Geom.* **72** (2006) 169–338, [math/0309070].

[69] M. Gross and B. Siebert, *From real affine to complex geometry*, *Ann. of Math.* **174** (2011) 1301–1428.

[70] M. Gross, P. Hacking and B. Siebert, *Theta functions on varieties with effective anti-canonical class*, 1601.07081.

[71] M. Gross and B. Siebert, *Intrinsic mirror symmetry and punctured Gromov-Witten invariants*, 1609.00624.

[72] D. Abramovich, Q. Chen, M. Gross and B. Siebert, *Punctured logarithmic maps*, https://www.dpmms.cam.ac.uk/∼mg475/punctured.pdf.

[73] J. Louis, P. Smyth and H. Triendl, *Spontaneous N=2 to N=1 Supersymmetry Breaking in Supergravity and Type II String Theory*, *JHEP* **1002** (2010) 103, [0911.5077].

[74] J. Louis, P. Smyth and H. Triendl, *The N=1 Low-Energy Effective Action of Spontaneously Broken N=2 Supergravities*, *JHEP* **1010** (2010) 017, [1008.1214].

[75] V. Cortés, J. Louis, P. Smyth and H. Triendl, *On certain Kähler quotients of quaternionic Kähler manifolds*, *Commun. Math. Phys.* **317** (2013) 787–816, [1111.0679].

[76] T. Hansen and J. Louis, *Examples of N = 2 to N = 1 supersymmetry breaking*, *JHEP* **11** (2013) 075, [1306.5994].

[77] T. Hansen, *Examples of N=2 to N=1 supersymmetry breaking*, Master's thesis, Universität Hamburg, 2012. http://www.desy.de/uni-th/stringth/Works/.

[78] C. Horst, J. Louis and P. Smyth, *Electrically gauged N=4 supergravities in D=4 with N=2 vacua*, *JHEP* **1303** (2013) 144, [1212.4707].

[79] C. Horst, $N = 2$ *vacua in electrically gauged* $N = 4$ *supergravities*, Ph.D. thesis, Universität Hamburg, 2013. http://www.desy.de/uni-th/stringth/Works/.

[80] S. de Alwis, J. Louis, L. McAllister, H. Triendl and A. Westphal, *Moduli spaces in* AdS_4 *supergravity*, *JHEP* **05** (2014) 102, [1312.5659].

[81] J. Louis and S. Lüst, *Supersymmetric* AdS_7 *backgrounds in half-maximal supergravity and marginal operators of (1, 0) SCFTs*, *JHEP* **10** (2015) 120, [1506.08040].

[82] J. Louis, H. Triendl and M. Zagermann, $N = 4$ *supersymmetric* AdS_5 *vacua and their moduli spaces*, *JHEP* **10** (2015) 083, [1507.01623].

[83] J. Louis and C. Muranaka, *Moduli spaces of* AdS_5 *vacua in* $N = 2$ *supergravity*, *JHEP* **04** (2016) 178, [1601.00482].

[84] J. Louis and C. Muranaka, AdS_5 *vacua from type IIB supergravity on* $T^{1,1}$, *JHEP* **06** (2017) 035, [1611.02982].

[85] P. Karndumri and J. Louis, *Supersymmetric* AdS_6 *vacua in six-dimensional* $N = (1, 1)$ *gauged supergravity*, *JHEP* **01** (2017) 069, [1612.00301].

[86] S. Lüst, P. Rüter and J. Louis, *Maximally Supersymmetric AdS Solutions and their Moduli Spaces*, *JHEP* **03** (2018) 019, [1711.06180].

Loops and Legs

Rutger H. Boels, Bernd A. Kniehl

II. Institut für Theoretische Physik, Universität Hamburg, Germany

DOI: http://dx.doi.org/10.3204/PUBDB-2018-00782/A9

We summarize the progress of the research performed in project A9 of the SFB 676 and highlight the most important results obtained.

1 Overview

Project A9 of the SFB 676 has produced 34 journal publications [1–34], three of which made it into *Physical Review Letters* [12, 28, 31]. Three papers are still under review [35–37]. Furthermore, nine proceedings contributions [38–44, 44, 45], two master theses [46, 47], and one PhD thesis [48] have emerged from SFB project A9. In the following, we review the scientific results achieved.

2 Loops and legs

The textbook approach (see e.g. Ref. [49]) to computing scattering amplitudes is through perturbation theory in appropriate coupling constants (which correlates with an expansion in Planck's constant) as applied to a path integral, schematically given as

$$\int d[\phi]\,(\ldots)\,e^{i\int d^D x \mathcal{L}(\phi)}\,. \tag{1}$$

The needed integrations are elegantly captured in the famous Feynman graph formalism. The fundamental difficulties faced by this method is illustrated in Table 1. At some point, the generated expressions will overwhelm even modern computing resources. As a rule of thumb, problems with fixed number of loops *plus* number of legs are in a universality class. Cutting edge phenomenological problems are currently roughly found at

$$\#\text{ loops} + \#\text{ legs} = 7\,. \tag{2}$$

Concrete results in this contribution include several which satisfy this rule of thumb.

The algebraic complexity of the final answer is determined to an extent by dimensional analysis. Scattering amplitudes have a fixed mass dimension, and the number of dimensionless ratios made out of all occurring scales (masses, momentum invariants) up to momentum conservation is the number of variables. Computational complexity, therefore, increases considerably and non-linearly with the number of legs. A roughly comparable increase in computational costs is associated to processes with increasing numbers of loops. These processes where particles split and join are inherently quantum effects and are, therefore, physically essential. For unobserved

# legs \ # loops	0	1	2	3	4	5	6
3	1	1	4	23	173	1587	17099
4	3	9	51	381	3477	37242	
5	15	87	675	6315	68745		
6	105	975	9930	113580			
7	945	12645	163170				
8	10395	187425					
9	135135						

Table 1: Feynman graph number statistics for a theory with only trivalent vertices (e.g. ϕ^3 theory), obtained using Ref. [50].

particles all quantum numbers must be summed over. By special relativity one particular, continuous quantum number is the Lorentz momentum, which must, therefore, be *integrated* over. Computing these so-called loop integrals are a major further obstacle to perform explicit computations.

The upshot of the mentioned complications is that, despite its age, the current frontier of calculations within the standard model (SM) of particle physics is given by Eq. (2). This holds even for the simpler case of massless particles only, which has less scales than the full SM. Truly general one-loop computations (the first quantum corrections!) have only become widely available over the last decade. The problem of computation has become even more pressing with the lack of smoking-gun evidence of beyond-the-SM (BSM) physics from LHC experiments. At the LHC, the main colliding particles are hadrons, which interact through all known nuclear forces. Since the strong force is much stronger than the electroweak force, this makes especially those effects captured by Quantum Chromodynamics (QCD) particularly important. Highly interesting physics including that of the Higgs boson, however, is contained in the electroweak sector of the theory. Hence the computation of QCD backgrounds alone is vital to the interpretation of almost any interesting BSM signal. Due to long lead times in next-generation collider building, precision is the most likely vector for discovery in the near- to medium-term future. This leads to a large motivation to develop tools and techniques to break the existing barriers already from a purely phenomenological point of view.

There are also more formal motivations to pursue such a development. The path integral of Eq. (1), for instance, requires a choice of field coordinates to define the integral. Any canonical transformation of these coordinates should leave physics invariant modulo potential anomalies. There is no known way, however, to utilize such symmetry much beyond linear transformations systematically. A general field transformation will, in fact, lead to a radically different looking Feynman graph series. This is one of the drivers of the huge complexity of Feynman-graph-based computations. Whenever a symmetry exists but is explicitly broken in the computation, an enormous intermediate expression swell occurs. An analogue of this in classical physics would be to compute the orbit of the earth around the sun in Cartesian coordinates centered around Pluto: the choice of coordinates leads to significantly larger intermediate expressions leaving the essential physics of the problem unchanged. Intriguingly, there are cases where the complicated Feynman graph computations yields simple answers for scattering amplitudes. This indeed suggests that physical symmetries have been missed, for instance in the example of the Parke–Taylor [51] amplitude in pure Yang–Mills theory (YM). Such examples motivate

the search for computational techniques which bypass the intermediate complexity and intend to arrive straight at the answer.

The range of different motivations to study and develop the computation of observables has led to a healthy research effort throughout the history of quantum field theory, see e.g. `https://en.wikipedia.org/wiki/Timeline_of_quantum_mechanics` for historic aspects and Refs. [52, 53] for a general overview of recent developments.

The maximally supersymmetric $\mathcal{N} = 4$ Yang–Mills theory (SYM) has played a central role in pioneering new computational techniques. The addition of supersymmetry considerably simplifies many perturbative computations, while leaving in place some of the essential difficulties of especially high-loop computations. This makes $\mathcal{N} = 4$ SYM first of all an ideal toy model. Second, there are intriguing and not generically well-understood direct connections between QCD and $\mathcal{N} = 4$ SYM in perturbation theory at higher loop orders through certain number theory properties of the full results known as the maximal transcendentality principle (see below). Third, there is direct interest in studying the theory itself as it connects through AdS/CFT [54] directly to the strongly coupled version of this field theory in 't Hooft's planar limit [55]. In rare cases, this extra insight into the theory even enables the derivation of exact results. A prime example here is the Beisert–Eden–Staudacher (BES) [56] equation for the so-called cusp anomalous dimension in the planar limit. The first non-planar correction to the cusp anomalous dimension at four loops in $\mathcal{N} = 4$ SYM is in fact a central result of SFB project A9. This involves a single-scale problem at four loops with two on-shell and one off-shell legs. This problem satisfies Eq. (2).

On the other hand, the real world is certainly not manifestly supersymmetric and hence neither is the SM of particle physics. While using $\mathcal{N} = 4$ SYM as a toy model has undoubtedly fueled many developments, it has at times led to results which are hard to transpose to or toward the SM of particle physics. Within $\mathcal{N} = 4$ SYM, for instance, one naturally uses a chiral superspace formulated in terms of spinor helicity variables. These variables are hard-wired to four-dimensional physics, which does not mesh well with dimensional regularization in general. For supersymmetric theories, this is usually not a problem. For non-supersymmetric theories, work-arounds have been found at one loop or, on a case by case basis, at higher loops. The latter does not seem to generalize easily. A central product of Sec. 5 is a framework to compute scattering amplitudes without essential use of spinor helicity variables or supersymmetry, demonstrating its applicability, for instance, by computing for the first time analytic results for five gluons at two loops and four gluons at three loops. This involves a two-scale problem at three loops and a five-scale problem at two loops, both of which satisfy Eq. (2).

A particularly important motivational role in SFB project A9 was played by relations between the scattering of gravitons in general relativity (GR) and gluons in pure YM. Both parts can be traced back to this central idea which arose first in string theory. Early on in the development of this theory, Kawai, Lewellen and Tye (KLT) [57] noticed that the scattering of open-string states and that of closed-string states is intimately related at the string tree level. String scattering amplitudes of gravitons can be written as sums over products of string scattering amplitudes of gluons. In the point particle limit, this reduces to a relation between scattering gravitons in GR and gluons in YM. From the path integral point of view of field theory, this relation is rather mysterious but very welcome considering the complexity of Feynman graph perturbation theory in GR noted above. For quite some time, this relation was interpreted as a string theory artifact that was only valid at tree level. Even in this form, it is already useful to determine scattering amplitudes of gravitons through higher loop orders, as was pursued for instance in Ref. [58] for four-graviton scattering in maximal supergravity

theory ($\mathcal{N} = 8$) to the three-loop level. The motivation here is the study of ultraviolet (UV) divergences: at the time, the consensus point of view was that these would set in first at three loops. Instead, using the flood of new insights into gluon scattering amplitudes at higher loop orders, it was initially found that the amplitude did not diverge as expected at this loop order. Instead, it behaved very much like four-gluon scattering amplitudes in $\mathcal{N} = 4$ SYM in the UV: they shared the same so-called critical dimension at the first four-loop orders. The natural conjecture that this persists to higher loop orders has since been pursued vigorously (e.g. in Refs. [59, 60]), and has very recently been disproved [61] at five loops. See Ref. [17] for a heuristic analysis.

3 Color-kinematic duality and amplitude relations at loop level

In systematizing high-loop graviton computations, a remarkable, double discovery was made by Bern, Carrasco and Johanson (BCJ) [62, 63]. First of all, these authors conjectured that gluon scattering amplitudes can always be written in a form where the kinematics-dependent parts obey a Jacobi identity, similar to that obeyed by the Lie algebra structure constants inherent in the formulation of YM. Secondly, these authors conjectured that replacing the color Lie algebra structures with a second copy of the kinematics-dependent parts will yield graviton scattering amplitudes. At tree level, both of these statements are known to hold through a variety of techniques, see e.g. Ref. [64] for an overview. At loop level, they have been verified mostly on a case-by-case basis for the integrands of scattering amplitudes. Together, the two conjectures are known as "color-kinematic duality." What is interesting in the context of this contribution is that, even in its current unproven form, color-kinematic duality functions as an ansatz generator. In short, one writes down an educated ansatz for the integrand of a certain scattering amplitude. Into this ansatz, flow beyond color-kinematic duality a number of expectations of the answer, such as expected manifest UV divergence and any graph symmetries. This ansatz will have a finite number of free parameters. Then Cutkosky-style unitarity cuts are used to match to the behavior of the physical amplitude, fixing terms in the ansatz. If the restricted ansatz matches on all D-dimensional unitarity cuts, one can be certain that it matches the full result as long as all propagators are strictly massless. Enforcing the Lie algebra structure conjectured by color-kinematic duality greatly simplifies a possible ansatz. Hence the conjecture offers a direct and concrete vector for explicit computation. A drawback is that a particular ansatz may not be general enough to capture the physical quantity, see e.g. Ref. [65] for a case where the ansatz needed to be unexpectedly complicated.

4 The full Sudakov form factor at four loops in $\mathcal{N} = 4$ super Yang–Mills theory

A full physical understanding or a derivation of color-kinematic duality has been lacking so far, especially on the gauge theory side. One idea would be to write a Lagrangian for YM whose vertices automatically generate a color-kinematic dual representation. This would immediately prove this part of the conjecture to all loop orders. Several attempts at a Lagrangian understanding of the duality exist [18, 66–68], with earlier, related work directed at the KLT relation [69]. Such a Lagrangian, if it existed, would have a further direct consequence: all

observables in YM would have a color-kinematic-dual representation. The class of all observables is much larger than the set of all scattering amplitudes, containing for instance correlation functions of gauge-invariant operators. An even more general class of observables is formed by mixtures of gauge-invariant operators and on-shell states known as form factors.

The Sudakov form factor is an interesting observable that plays a central role in the analysis of infrared divergences, see e.g. Refs. [70–73]. Powerful theorems guarantee that the divergences of the Sudakov form factor in $\mathcal{N} = 4$ SYM are governed by universal functions up to finite terms in the ϵ expansion of dimensional regularization, see Ref. [74]. These functions are the cusp and collinear anomalous dimensions. While the latter is regularization scheme dependent, the former is not. Both are truly universal functions for a given quantum field theory, appearing in a range of different situations. As noted above, the planar limit of the cusp anomalous dimension in the very special quantum field theory at hand is known to be given as the solution to a differential equation and has been computed up to many loops. The non-planar correction to this quantity first appears at four loops, which provides a major motivation to push to this order in perturbation theory. The motivation was further strengthened by a conjecture [75] that this particular correction vanishes in any quantum field theory. This conjecture was formulated by naive extrapolation of results through three loops to the four-loop order. Up to the three-loop order, the cusp anomalous dimension only depends on the quadratic Casimir invariant of the gauge group under study. The conjecture of Ref. [75], which became widely known as "Casimir scaling" (see e.g. Refs. [75–81]), was that this simply extrapolated to four-loop order for any quantum field theory, thereby implying the vanishing of the non-planar correction. Already prior to our work, there had been several indications that, beyond perturbation theory or in the Regge limit, the conjecture would not hold [82–84]. Eventually, the conjecture was settled conclusively in the negative for the first time in Ref. [31]. Here, the first non-planar correction to the cusp anomalous dimension was computed numerically in $\mathcal{N} = 4$ SYM and shown not to vanish. The conclusion that Casimir scaling is violated at the four-loop order has since been supported by additional results in Ref. [85, 86], see also Ref. [34].

4.1 The general structure of cutting edge computations

Four-loop computations are, with few exceptions, a big challenge, even for current state-of-the-art computational tools. Hence, the results eventually presented in Ref. [31] were obtained in a number of smaller steps contained in several publications. These steps are, in fact, common to many modern computations of observables:

1. Generate an integrand for the quantity under study.
2. Project to scalar integrals.
3. Simplify the integrand by solving so-called integration-by-parts (IBP) identities. The result is then given in terms of a chosen basis of remaining so-called master integrals.
4. Compute the master integrals analytically or numerically, typically by expanding in terms of the dimensional-regularization parameter ϵ, and assemble the aimed-for physics result.

These steps will appear throughout this contribution.

Loop integrals arise necessarily in perturbative computations as explained above. Beyond the complexity highlighted above, there is a specific drawback of Feynman graphs in the context of maximally supersymmetric gauge theory: there is no known way of having this much

supersymmetry manifest off-shell. Hence, cancellations induced by supersymmetry, such as the vanishing of UV divergences, are not directly manifest in Feynman graphs. This leads to considerably more complicated integrals being generated. In the context of the Sudakov form factor at four loops, this would be prohibitive. Another method to obtain the integrand is, as alluded to above, to write an ansatz large enough to contain the physical answer and to fix the coefficients in this ansatz by computing Cutkosky-style unitarity cuts. Crucially, these unitarity cuts contain only lower loop information. For many cuts, only tree-level information is needed. This type of unitarity-based approach is, in fact, the driving factor of the most recent round of advances at one loop in quite general quantum field theories, see, for instance, Refs. [87,88] and references thereto. In maximally supersymmetric theories, it is known that one can take the unitarity cuts not in $D = 4 - 2\epsilon$ dimensions, but instead in four dimensions. Here, the spinor helicity method allows manifest, linearized $\mathcal{N} = 4$ supersymmetry through Nair's [89] on-shell superspace formalism, which drastically simplifies many computations in this theory.

If the observable involves spinning particles, the integrand will typically involve polarization tensors, which keep track of the appropriate spin information. For gluons, for instance, polarization vectors would contract in general with all types of vectors in the problem at hand, including loop momenta. As a first step of simplifying the problem, one would like to reduce to integrals which only involve inner products of loop momenta and external momenta. This class of scalar integrals is referred to as "Feynman integrals." For maximally supersymmetric theories, such as the one under study here, the projection to scalar integrals is automatically performed using spinor helicity methods. This chiral-superspace formalism has also been extended to cover massive particles [2] and form factors [90]. In Sec. 5, an alternative reduction method to scalar integrals will be used and developed, which does not rely on supersymmetry.

Fixing the integrand and projecting to scalar integrals is certainly not enough for most physics goals. The integrals needed to achieve a given physics goal are in general very complicated. The integrand, however, is not nearly a unique object—the physical observables are, for instance, invariant under linear shifts of the loop integration variables. Infinitesimally, this invariance leads to IBP identities: full space-time derivatives with respect to the loop momenta of any integrand vanish after integration. It was realized early on [91, 92] that working out the derivatives gives a system of linear equations on the vector space spanned by a class of loop integrals. In Ref. [93], it was first realized that, if one introduces an ordering of the integrals in this class in terms of expected complexity, one can systematically solve complicated integrals in terms of simpler integrals by essentially a version of Gaussian elimination. This systematic method of solving IBP identities is known as Laporta's algorithm and has been implemented in several public codes such as `AIR` [94], `FIRE` [95–97], KIRA [98], and `Reduze` [99,100]. `LiteRed` [101,102] implements an approach somewhat distinct from IBP reduction. The output is a reduction in terms of a typically much smaller number of so-called master integrals, with the coefficient functions of the external-momentum invariants (generalizations of the traditional Mandelstam invariants) as well as the dimensional-regularization parameter. The master integrals are essentially a choice of basis. The number of master integrals tends to be fairly small and to be universal for classes of physical theories. Calculating master integrals becomes, therefore, a high-value target with benefits for several theories with different matter content at once.

Having expressed a physical result in terms of a basis of master integrals then leads to the postponed question of integrating these basis elements. Even though master integrals tend to be much simpler than the original integrals, the remaining challenge is, in many physically interesting cases, still a prohibitive obstacle. A variety of techniques have been developed over the

years for this task aiming at typically either numerical or analytic integration. For the purposes of this contribution, two mostly numerical general techniques are especially relevant: integration using Mellin–Barnes (MB) integrals [103–105] or sector decomposition [106, 107]. Both of these are supported by a number of public codes, e.g. FIESTA [108–111] and SecDec [112–114] for sector decomposition and [105, 115–118] for MB representations. Both methods are under active development. Typically, the MB approach is numerically much faster and more reliable if efficient and valid MB representations can be found for the integrals at hand. This is known to be a generic problem for Feynman integrals with a non-planar topology [119], with partially automated resolution to the three-loop level [120]. Impressive analytic results have been obtained in those cases where a special form of a system of first-order differential equations with respect to kinematic invariants can be found [121]. Although work-around exists for lower loop orders [122, 123], these techniques do not directly apply to single-scale integrals, such as those that arise in the four-loop Sudakov form factor.

As an illustration of the general strategy for cutting-edge computation outlined here, consider the Sudakov form factor at three loops in massless QCD. Integrand generation and projection to scalar integrals are sub-leading problems here. Reduction to master integrals was reported in Ref. [124], with numeric integration reported first in Ref. [125], followed by several works culminating in the analytic expressions [126–128], see also Ref. [129]. The corresponding computation in $\mathcal{N} = 4$ SYM was performed after the QCD results in Ref. [130]. Below, a roughly similar series of steps will be shown to lead to the four-loop result, with the difference that $\mathcal{N} = 4$ SYM is the starting point.

4.2 The explicit computation

The first concrete step in the computation of the full Sudakov form factor at four loops in $\mathcal{N} = 4$ SYM was taken in Ref. [16]. This particular paper contains the first explicit exploration of color-kinematic duality for observables beyond scattering amplitudes (see also Ref. [131]). After outlining the general motivation and results, explicit examples are constructed for a range of examples in $\mathcal{N} = 4$ SYM, the most complicated one being the four-loop form factor for two on-shell multiplets and a member of the stress tensor multiplet: this is the Sudakov form factor. The approach for each is exactly as outlined above: an ansatz is created for which coefficients are fixed from unitarity cuts. The computation benefited greatly from previous developments for tree-level form factors in Ref. [90]. The result for the four-loop form factor obtained in Ref. [16] still contains a single free parameter, which could not be fixed from the cuts considered. The representation obtained through color-kinematic duality typically has good manifest UV properties in maximally supersymmetric theories, which translates into low numerator powers. This in turn corresponds to structurally simpler integrals. An interesting by-product of the methods developed in this paper is an analysis of the color structure of the Sudakov form factor through eight loops, using the computer algebra developed in Ref. [132]. In later work, a similar strategy yielded the integrand of the five-loop Sudakov form factor [133].

The next step according to the general scheme above for cutting-edge computation is the application of IBP identities to obtain an expression in terms of master integrals. The class of integrals involved, however, is highly complicated and presents a formidable challenge even to cutting-edge IBP reduction codes. The first reduction of integrals in this class was presented in Ref. [25]. The IBP reduction reported here was obtained by using the Reduze [99] code, modified to bypass a disk access problem. With this problem fixed, the code ran parallel on large computing resources for several months. To verify the obtained basis of integrals,

a separate technique due to Ref. [134] for finding master integrals directly was explored. In essence, all steps performed by the MINT package were applied separately, and results were cross-compared. The free parameter left after comparing unitarity cuts turned out to drop out of the physical observable after applying IBP identities. To gauge the remaining difficulty of the master integrals, attempts were made to integrate the maximal propagator master integrals, which are the hardest cases numerically, with the FIESTA code. This was largely unsuccessful for the choice of master integrals used in Ref. [25], with an exception for one particular integral.

One particular problem of using IBP relations is that the result, in general, has complicated coefficients in a Laurent expansion around $\epsilon = 0$. This considerably complicates tracking the error budget at best and leads to large cancellation errors in the final result at worst. As an idea to combat this complexity, the use of 'rational' IBP relations was explored in Ref. [44]. Here, it was shown that a rational IBP reduction, i.e. one that does not depend on the dimensional regularization parameter ϵ, can be obtained as a sub-reduction of the IBP reduction obtained in Ref. [25]. This method does yield an expansion in terms of a choice of master integrals. It was also shown that different choices lead to vastly different expressions. By aiming at small rational expansion coefficients, a reasonably-looking expression was found for the non-planar part of the Sudakov form factor in $\mathcal{N} = 4$ SYM by hand. This again left the problem of integration.

What Ref. [44] clearly showed was the importance of picking a good basis of master integrals to expand the form factor in. Primarily, one would pick integrals for which the integrals are known as a basis. In the absence of advance knowledge of such integrals, such as in the case at hand, one can pick a basis that makes an expected property of the answer manifest. This is the starting point of Ref. [31], which uses a special property of $\mathcal{N} = 4$ SYM known as the "maximal transcendentality principle" [135, 136]. Many of the details of the computation reported here were presented in a longer paper [34].

Feynman integrals, in general, are known to have special number theory properties, especially for the transcendental constants generated by expanding Feynman integrals in the dimensional-regularization parameter. These constants can be assigned a so-called transcendental weight, which is typically a positive integer. Rational numbers are assigned weight zero. This weight is a number theory version of mass dimension and is, for instance, additive under multiplication. The maximal transcendental weight of the constants increases step-wise with the expansion in terms of ϵ, with the leading term being only rational. Most often, these constants fall into the class of multiple zeta values (MZVs), see e.g. Ref. [137] and references therein. For given transcendental weight, there is only a finite number of independent MZVs. It has been observed in many cases that, for $\mathcal{N} = 4$ SYM, a much stronger result holds: *only* MZV-valued terms of maximal weight appear, with potential sub-leading weight terms simply vanishing. Moreover, it has been conjectured [135, 136] that, for every result in QCD, one can match the leading transcendentality terms directly to the corresponding result in $\mathcal{N} = 4$ SYM. This is the aforementioned maximal transcendentality principle.

Given this principle, it is reasonable to expect that the Sudakov form factor at four loops in $\mathcal{N} = 4$ SYM will have a maximally transcendental expansion. Another way of expressing this follows by assigning the dimensional-regularization parameter ϵ transcendental weight -1 and stating that the form factor should have uniform transcendentality $2l$, where l is the loop order. The driver of Ref. [31] is the question if integrals can be found such that this expected property is manifest. This is guaranteed if a basis of master integrals exists which are uniformly transcendental (UT), and, for the Sudakov form factor at three loops, such a basis was found explicitly in Ref. [138]. For the single-scale integrals of the problem at hand, there is a conjecture

that the integrands of UT integrals have constant leading singularities (only simple poles) [123, 139]. In the reported work, this property was used to systematically search for UT integrals within a large enough set of integrals. With additional work to find a reasonably looking representation of these integrals and taking into account the targeted four-loop form factor, this eventually led to a list of master integrals highly likely to be UT. For several integrals, a so-called "dLog" form was found proving the uniform transcendentality property. For others, very extensive checks were made. Using the rational IBP relations found in Ref. [44], it was possible to express the integrand found in Ref. [16] in terms of this basis. Extensive effort was made to find a representation in terms of a small number of UT integrals of a form that can be used easily in available integration programs.

Expressing the four-loop Sudakov form factor in $\mathcal{N} = 4$ SYM in terms of a basis of UT master integrals shows that the expansion of this quantity is indeed highly likely to be UT. This is already an interesting result, especially in the non-planar sector. It immediately implies that the cusp and collinear anomalous dimensions are, in this sector, also maximally transcendental. A second result first reported in Ref. [31] is that UT integrals turn out to be much easier to integrate numerically than generic integrals in the same class. Although this effect can be understood heuristically, both MB integrals as well as sector decomposition do not seem to be related directly to the number theory properties of the integrals. This effect is highly useful as is shown in Ref. [31], where it has resulted in a numerical result for the four-loop non-planar cusp anomalous dimension. This step involves extensive computing resources and careful management of results. Cross-checks between MB and sector decomposition results were obtained for cases where an efficient MB representation could be obtained.

The final result for the non-planar cusp anomalous dimension is statistically significantly non-zero, disproving the Casimir scaling conjecture. At the time it appeared, this result was the first for any four-loop non-planar cusp anomalous dimension in any quantum field theory. Several groups have confirmed the breakdown of Casimir scaling since [85, 86, 140]. Many of the details of the computation, including a full analysis of the errors in the computation and a first result for the non-planar collinear anomalous dimension, can be found in Ref. [34]. The errors can be analyzed by using the UT property to change the first five expansion coefficients into simple rational numbers times single, known MZVs using the PSLQ algorithm. Taking these to be the exact results then allows an estimate of the numerical error of the computation. Hence this procedure uses number theory properties to verify numerical integration results.

5 Scattering amplitudes and integrands from first principles

Where Sec. 4 has dealt with a specific observable at four loops and three legs, in this section tools and techniques for observables with more legs but mostly less loops are developed, including cases satisfying Eq. (2). This includes several observations for tree-level amplitudes. A prime motivation for many of the developments reported in this section is exactly the drive to bypass path integrals and Feynman graphs as crutches used for explicit computations highlighted above. One of the outputs of this section is a complete calculational engine directly based on physical first principles for scattering amplitudes. Another is a thorough physical understanding of perturbative gauge-gravity double-copy-type relations. A third output is a number of techniques and observations that hint at remarkable additional structure in cutting-edge computations, as will be demonstrated by exploring, for instance, the planar three-loop, four-point and two-loop,

five-point gluon amplitudes, solving the remaining bottlenecks to complete analytic computation of the scattering amplitudes.

The input for Sec. 5 was, as was already highlighted above, the quest for the physical origin of color-kinematic duality. Even in its current state, this is already a powerful calculational tool, as was illustrated in Sec. 4 for a specific observable. The duality idea offers, however, no intrinsic, physical understanding where the extra structure comes from, neither in gauge theory itself nor in the relation to perturbative gravity. At tree level, much more is known about scattering amplitudes in general, as they are functionally rational functions of polarizations and momenta. Here, color-kinematic duality has two direct physical consequences: the KLT relations between YM and GR amplitudes and the BCJ relations for YM amplitudes. A first question, therefore, would be to find a physical understanding of these relations. For the BCJ relations, a first paper in this direction was Ref. [141], where the physical origin of the BCJ relations was traced to on-shell gauge invariance, coupled with what amounts to a power counting criterion. On-shell gauge invariance is a fundamental constraint on scattering amplitudes of massless matter [142]. This then begs the question if this can be extended to the KLT relations. This question was answered to the affirmative in Ref. [28]. This work first streamlined and generalized the work of Ref. [141], re-phrasing first-principle constraints on scattering amplitudes into systems of linear equations. Scattering amplitudes become generically vectors in a vector space. Using computer algebra, the dimensions of these vector spaces were mapped for classes of gluon and graviton scattering amplitudes. For gluon scattering through eight points, this shows directly the existence of BCJ relations for scattering amplitudes in pure YM. Up to five gravitons, it was then shown also to lead directly to the KLT relations, taking into account a power counting criterion. In addition, explicit scattering amplitudes were computed by requiring only physical poles to appear, a point emphasized in even greater detail from a different point of view in the later works of Refs. [143,144]. A point of fundamental interest is the observation that scattering amplitudes of gravitons exist which cannot be traced to sum over products of gluon amplitudes. The relation to color-kinematic duality should follow at tree level for all multiplicities by an extension of the techniques of Ref. [17]. Basically, this maps the solutions of two different linear problems to one another.

Having obtained first results mostly at tree level, a natural question is whether these techniques apply at the loop level, where knowledge for scattering amplitudes in general and for color-kinematic duality in particular is rather limited. Both of these are especially true for theories without supersymmetry. To use the first-principle approach effectively at the loop level requires a further idea, the origin of which is described in Ref. [49]. A classic computation described in this textbook is that of the gyromagnetic ratio (colloquially known as "$g-2$") in quantum electrodynamics. This quantity can be isolated from the computation of a form factor with two on-shell legs, basically expanding this quantity in solutions to the first principles used in the work described previously. A particular expansion coefficient then defines the gyromagnetic ratio. This gyromagnetic-ratio computation has recently reached the four-loop level analytically [145]. For scattering amplitudes, one can explore a similar strategy by expanding them into solutions to the on-shell constraints, see for instance Ref. [146] for an example. Central are a number of algebraic manipulations in linear algebra for a choice of basis for all scattering amplitudes for fixed external-particle content. This is a core part of Ref. [33]. This paper showcases a complete strategy for scattering amplitudes beyond path integrals with many example computations. Three-point amplitudes are covered thoroughly as illustrations of the general approach. For four-particle scattering, a complete basis for four-gluon and four-graviton scattering amplitudes is constructed (see also Ref. [147]). Both are

shown to admit a factorization which is closely related to Bose symmetry. This factorization simplifies the analysis. Reference [33] contains additional formal results beyond perturbative gauge-gravity relations. A particularly appealing one is the result that self-interacting theories of massless spin-one bosons with a single dimensionless coupling constant in four dimensions necessarily involve Lie-algebra-valued coupling constants. Special results for scattering in three space-time dimensions are derived, including Hodge duality for gluons and the triviality of graviton scattering. A further formal and interesting result is the four-graviton amplitude at the one-loop order. This result is not new in itself, but is obtained here in such a straightforward computation that it holds the promise of pushing one loop order further, where only the four-helicity-equal amplitude has been obtained recently [148].

Phenomenologically, the results on the integrand of planar four-gluon scattering through two loops are especially promising in Ref. [33]. The one-loop computation could even be performed for basically any theory of gluons, including full effective field theories. This also forms the basis of a technique to iterate the computation of certain cuts to all loop orders, through a version of the so-called rung rule of maximally supersymmetric Yang–Mills theories. This technique tends to introduce highly non-local apparent poles into the computations rendering it less directly useful for explicit computation. The two-loop computation shows clearly how to merge computations of unitarity cuts with the solution of IBP relations obtained using computer algebra. The relation to the spinor helicity method was worked out explicitly. Different renormalization schemes were highlighted, differing in their treatment of the dimensionality of the particles in the loops and on the outside. Instrumental here was the approach to derive rational IBP relations as pioneered in Ref. [44]. It was also shown how color quantum numbers can be studied effectively using projectors. The same computer algebra techniques to compute color factors for form factors deployed in Ref. [16] were used here. Comparisons were made to results in the literature where available, finding full agreement.

The true litmus test for any new calculational technology in high-energy physics is the question if it can tackle cutting-edge computations. While the planar four-gluon, two-loop amplitude has been known for some time, the five-point version of this has been the subject of major recent efforts. Interestingly, the integration of a set of planar master integrals was obtained here first in two contemporaneous publications [149,150], with recent advances for the non-planar integrals [151,152]. The first steps in the general calculational scheme outlined above are, therefore, a bottleneck. Obtaining the integrand with Feynman graphs is, in the case at hand, impractical, requiring some application of unitarity methods. The traditional method to reduce the integrand to scalar integrals is the use of spinor helicity variables for the gluons. IBP reduction is furthermore a major problem previously considered undoable by public codes. Two papers presenting semi-numerical methods to obtain this particular scattering amplitude were presented very recently in Refs. [153, 154], presenting the amplitudes evaluated in a particular phase space point and finding agreement. There have been several works for the special helicity-equal amplitude at two loops through seven external gluons in Refs. [155–157]. The two-loop scattering amplitude for five planar gluons was a prime motivation for Ref. [37]. There are two main obstacles for scaling the techniques of Ref. [33] to say the two-loop planar five-gluon amplitude and beyond: algebraic complexity of the basis manipulations and solving the IBP reduction. In Ref. [37], the first obstacle is removed for most phenomenological applications featuring external bosons. The driver is a clever choice of basis. The basis choice can be motivated by extending the double-copy idea of perturbative gauge-gravity relations. After all, if graviton amplitudes are a double copy of gluons, can the gluons be written as copies of simpler building blocks as well? The conjecture in Ref. [37], verified up to six external gluons and four

external gravitons, is that very simple one- and two-gluon building blocks suffice to span the space of all scattering amplitudes of a given class as tensor products. The tensor product structure greatly facilitates explicit analytic computations of needed matrix inverses, allowing even computation of leading-singularity cuts beyond the demarcation line set by Eq. (2).

The second obstacle to explicit analytic computation of the planar two-loop, five-gluon amplitude is the solution of the systems of IBP relations. In this context, it was observed that a good choice of coordinates for planar integrals can be formed out of coordinates of one-loop progenitors. For the case at hand, these are two one-loop pentagon topologies, glued along a common line. This choice of coordinates is good, as it clearly shows that one particular topology for the chosen parameterization is slightly simpler as an expression than the others—this is critical for being able to solve the required IBP relations using the FIRE code on fairly large computing resources. Intuitively, the good choice of coordinates likely translates into algebraically simpler IBP relations that are, therefore, computationally easier to solve. This then yields a form of the planar five-gluon, two-loop integrand in terms of a chosen basis of master integrals. A similar approach was also explored for the planar four-gluon, three-loop integrand.

The approach through a basis for scattering amplitudes makes clear that the integrand of a scattering amplitude in a basis of master integrals will generically contain manifest nonphysical poles in addition to the expected poles from infrared physics. For planar amplitudes, these are tree-level poles in physically forbidden channels. This is the multi-loop and multi-leg extension of a phenomenon observed in Ref. [33] as well (see also Ref. [158]). The real question is if these poles have non-vanishing residues. In Ref. [33], the explicit integration of the box function was needed to show that these residues vanish. In Ref. [37], it is pointed out that the expansion around these poles can be systematically constructed from differential equations with respect to kinematic invariants. Differential equations have been studied in depth recently following Ref. [121], where a special basis was proposed. Beyond consistency, it is highly interesting that expansions around nonphysical poles involve relations between a-priori independent master integral coefficients. To demonstrate the potential, the contribution of massive particles to four-gluon scattering at one loop is studied. It is well known in the field, see e.g. Ref. [159] for a discussion, that massive particles in loops lead to master integrals that evade all unitarity cuts. At one loop, these are the massive tadpole integrals. Hence, for massive particles flowing in loops, one typically has to resort to various laborious techniques to fix the coefficients of these integrals. Absence of nonphysical singularities, analyzed through differential equations as advocated in Ref. [37], turns out to suffice to fix this coefficient up to an additive renormalization factor. Massive particles are, of course, experimentally highly relevant.

6 Special functions

A powerful illustration of the wide applications the development of basic technology can have may be found within SFB project A9. Special attention was focused on hypergeometric functions, which play a central role in applications of quantum field theory to high-energy physics. In fact, Feynman diagrams may be reduced via MB representations to hypergeometric functions. The differential-reduction algorithm then allows one to systematically relate hypergeometric functions whose parameters differ by integers [13]. In this way, Feynman diagrams may be efficiently reduced to minimal bases of hypergeometric functions [13]. This provides a powerful alternative to the well-established IBP technique and is even superior than the latter because it

can actually lead to a lesser number of master integrals, i.e. the counting of master integrals and their classification are achieved more efficiently and economically. This is bound to lead to dramatic simplifications in calculations of Feynman diagrams and scattering amplitudes because solving the master integrals is frequently the bottleneck to analytic expressions. In fact, in the case of the two-loop sunset diagram with different masses and space-like on-shell kinematics, it could be shown that one of the three master integrals produced by the standard IBP technique is redundant [4], a result which can be recovered by the IBP procedure only after applying the trick of eliminating a one-loop subdiagram in favor of an effective mass to be integrated over, as shown in Ref. [11]. A number of irreducible master integrals for L-loop sunrise-type and bubble Feynman diagrams with generic values of masses and external momenta were explicitly evaluated via the MB representation [30]. The differential-reduction algorithm also allows one to efficiently extract in analytic form the coefficients of the Laurent expansions of Feynman integrals in the parameter $\epsilon = 2 - D/2$ of dimensional regularization [160]. We released a Mathematica-based program package for the differential reduction of hypergeometric functions, called `HYPERDIRE`, which is available from the program library of *Computer Physics Communication*, where a detailed description and a useful manual may be found. Its current version can handle the generalized hypergeometric function ${}_{p+1}F_p$ with one argument, the Appell functions F_p $(p = 1, \ldots, 4)$ with two arguments [3], the residual Horn-type hypergeometric functions of two variables [21], the F_D and F_S Horn-type hypergeometric functions of three variables [22], as well as the Lauricella function F_C of three variables [27], which frequently appear in multi-loop calculations relevant for high-energy physics. This may be applied to Feynman diagrams with arbitrary powers of propagators and arbitrary masses. Another highly efficient method of finding relationships between hypergeometric functions is by comparing the results for Feynman integrals evaluated using different techniques [5].

In Ref. [20], the expansion method for ${}_3F_2$ hypergeometric functions developed by members of SFB project A9 [160] was applied to the field theory expansion of five-point superstring amplitudes on a flat background. Here, the role of the dimensional-regularization parameter ϵ is basically played by the string scale α'. The developed code turns out to be quite a bit faster than two methods proposed almost simultaneously [161, 162].

We also considered the derivatives of Horn hypergeometric functions of any number variables with respect to their parameters [36]. We demonstrated that the derivative of the function in n variables is expressed as a Horn hypergeometric series of $n + 1$ infinite summations depending on the same variables and with the same region of convergence as for original Horn function. The derivatives of Appell functions, generalized hypergeometric functions, confluent and non-confluent Lauricella series and generalized Lauricella series were explicitly presented. Applications to the calculation of Feynman diagrams were discussed, especially the series expansion in ϵ within dimensional regularization. Connections with other classes of special functions were discussed as well.

In Ref. [32], we evaluated the three-loop massive vacuum bubble diagrams in terms of polylogarithms up to weight six. We also constructed the basis of irrational constants being harmonic polylgarithms of arguments $\exp(ki\pi/3)$.

In Ref. [14], we showed that multi-fold MB transforms of Usyukina–Davydychev (UD) functions, which appear in connection with triangle ladder-like scalar diagrams in $D = 4$ dimensions, may be reduced to two-fold MB transforms, which come as as polynomials of logarithms of ratios of Mandelstam variables with certain coefficients. We also showed that these coefficients have a combinatoric origin. In Ref. [19], we presented an explicit formula for these coefficients. The procedure of recovering the coefficients is based on

taking the double-uniform limit in certain series of smooth functions of two variables, which is constructed according to a pre-determined iterative way. This finite double-uniform limit was represented in terms of a differential operator with respect to an auxiliary parameter which acts on the integrand of a certain two-fold MB integral. We demonstrated that our result is compatible with original representations of UD functions. In Ref. [14], a chain of recurrence relations for analytically regularized UD functions was obtained implicitly by comparing the left- and right-hand sides of relations between diagrams of different loop orders. In Ref. [29], we reproduced these recurrence relations by calculating explicitly, via Barnes lemmas, the contour integrals produced by the left-hand sides of the diagrammatic relations. In this way, we explicitly calculated a family of multi-fold contour integrals of certain ratios of Euler gamma functions. We conjectured that similar results for the contour integrals are valid for a wider family of smooth functions which includes the MB transforms of UD functions.

References

[1] R. H. Boels, *On BCFW shifts of integrands and integrals*, *JHEP* **1011** (2010) 113, [1008.3101].

[2] R. H. Boels and C. Schwinn, *On-shell supersymmetry for massive multiplets*, *Phys.Rev.* **D84** (2011) 065006, [1104.2280].

[3] V. V. Bytev, M. Y. Kalmykov and B. A. Kniehl, *HYPERDIRE, HYPERgeometric functions DIfferential REduction: MATHEMATICA-based packages for differential reduction of generalized hypergeometric functions ${}_pF_{p-1}$, F_1, F_2, F_3, F_4, Comput.Phys.Commun.* **184** (2011) 2332–2342, [1105.3565].

[4] M. Y. Kalmykov and B. A. Kniehl, *Counting master integrals: Integration by parts versus differential reduction*, *Phys.Lett.* **B702** (2011) 268–271, [1105.5319].

[5] B. A. Kniehl and O. V. Tarasov, *Finding new relationships between hypergeometric functions by evaluating Feynman integrals*, *Nucl.Phys.* **B854** (2012) 841–852, [1108.6019].

[6] R. H. Boels and R. S. Isermann, *New relations for scattering amplitudes in Yang-Mills theory at loop level*, *Phys.Rev.* **D85** (2012) 021701, [1109.5888].

[7] R. H. Boels and R. S. Isermann, *Yang-Mills amplitude relations at loop level from non-adjacent BCFW shifts*, *JHEP* **1203** (2012) 051, [1110.4462].

[8] R. H. Boels and D. O'Connell, *Simple superamplitudes in higher dimensions*, *JHEP* **1206** (2012) 163, [1201.2653].

[9] R. H. Boels, *Three particle superstring amplitudes with massive legs*, *JHEP* **1206** (2012) 026, [1201.2655].

[10] A. Brandhuber, G. Travaglini and G. Yang, *Analytic two-loop form factors in $\mathcal{N} = 4$ SYM*, *JHEP* **1205** (2012) 082, [1201.4170].

[11] B. A. Kniehl and A. V. Kotikov, *Counting master integrals: integration-by-parts procedure with effective mass*, *Phys.Lett.* **B712** (2012) 233–234, [1202.2242].

[12] R. H. Boels, *Maximal R-symmetry violating amplitudes in type IIB superstring theory*, *Phys.Rev.Lett.* **109** (2012) 081602, [1204.4208].

[13] M. Y. Kalmykov and B. A. Kniehl, *Mellin-Barnes representations of Feynman diagrams, linear systems of differential equations, and polynomial solutions*, *Phys.Lett.* **B714** (2012) 103–109, [1205.1697].

[14] P. Allendes, B. Kniehl, I. Kondrashuk, E. A. N. Cuello and M. R. Medar, *Solution to Bethe-Salpeter equation via Mellin-Barnes transform*, *Nucl.Phys.* **B870** (2013) 243–277, [1205.6257].

[15] I. Bierenbaum, S. Buchta, P. Draggiotis, I. Malamos and G. Rodrigo, *Tree-loop duality relation beyond simple poles*, *JHEP* **1303** (2013) 025, [1211.5048].

[16] R. H. Boels, B. A. Kniehl, O. V. Tarasov and G. Yang, *Color-kinematic Duality for Form Factors*, *JHEP* **1302** (2013) 063, [1211.7028].

[17] R. H. Boels and R. S. Isermann, *On powercounting in perturbative quantum gravity theories through color-kinematic duality*, *JHEP* **1306** (2013) 017, [1212.3473].

[18] R. H. Boels, R. S. Isermann, R. Monteiro and D. O'Connell, *Colour-Kinematics Duality for One-Loop Rational Amplitudes*, *JHEP* **1304** (2013) 107, [1301.4165].

[19] B. A. Kniehl, I. Kondrashuk, E. A. Notte-Cuello, I. Parra-Ferrada and M. Rojas-Medar, *Two-fold Mellin-Barnes transforms of Usyukina-Davydychev functions*, *Nucl. Phys.* **B876** (2013) 322–333, [1304.3004].

[20] R. H. Boels, *On the field theory expansion of superstring five point amplitudes*, *Nucl.Phys.* **B876** (2013) 215–233, [1304.7918].

[21] V. V. Bytev and B. A. Kniehl, *HYPERDIRE HYPERgeometric functions DIfferential REduction: Mathematica-based packages for the differential reduction of generalized hypergeometric functions: Horn-type hypergeometric functions of two variables*, *Comput. Phys. Commun.* **189** (2015) 128–154, [1309.2806].

[22] V. V. Bytev, M. Yu. Kalmykov and S.-O. Moch, *HYPERgeometric functions DIfferential REduction (HYPERDIRE): MATHEMATICA based packages for differential reduction of generalized hypergeometric functions: F_D and F_S Horn-type hypergeometric functions of three variables*, *Comput. Phys. Commun.* **185** (2014) 3041–3058, [1312.5777].

[23] R. H. Boels and T. Hansen, *String theory in target space*, *JHEP* **1406** (2014) 054, [1402.6356].

[24] M. S. Costa and T. Hansen, *Conformal correlators of mixed-symmetry tensors*, *JHEP* **1502** (2015) 151, [1411.7351].

[25] R. Boels, B. A. Kniehl and G. Yang, *Master integrals for the four-loop Sudakov form factor*, *Nucl. Phys.* **B902** (2016) 387–414, [1508.03717].

[26] R. H. Boels and C. Horst, *Perturbative quantum gravity in double field theory*, *JHEP* **04** (2016) 120, [1512.03192].

[27] V. V. Bytev and B. A. Kniehl, *HYPERDIRE—HYPERgeometric functions DIfferential REduction: Mathematica-based packages for the differential reduction of generalized hypergeometric functions: Lauricella function Fc of three variables*, *Comput. Phys. Commun.* **206** (2016) 78–83, [1602.00917].

[28] R. H. Boels and R. Medina, *Graviton and gluon scattering from first principles*, *Phys. Rev. Lett.* **118** (2017) 061602, [1607.08246].

[29] I. Gonzalez, B. A. Kniehl, I. Kondrashuk, E. A. Notte-Cuello, I. Parra-Ferrada and M. A. Rojas-Medar, *Explicit calculation of multi-fold contour integrals of certain ratios of Euler gamma functions. Part 1*, *Nucl. Phys.* **B925** (2017) 607–614, [1608.04148].

[30] M. Yu. Kalmykov and B. A. Kniehl, *Counting the number of master integrals for sunrise diagrams via the Mellin-Barnes representation*, *JHEP* **07** (2017) 031, [1612.06637].

[31] R. H. Boels, T. Huber and G. Yang, *Four-Loop Nonplanar Cusp Anomalous Dimension in N=4 Supersymmetric Yang-Mills Theory*, *Phys. Rev. Lett.* **119** (2017) 201601, [1705.03444].

[32] B. A. Kniehl, A. F. Pikelner and O. L. Veretin, *Three-loop massive tadpoles and polylogarithms through weight six*, *JHEP* **08** (2017) 024, [1705.05136].

[33] R. H. Boels and H. Luo, *A minimal approach to the scattering of physical massless bosons*, *JHEP* **05** (2018) 063, [1710.10208].

[34] R. H. Boels, T. Huber and G. Yang, *The Sudakov form factor at four loops in maximal super Yang-Mills theory*, *JHEP* **01** (2018) 153, [1711.08449].

[35] R. H. Boels and H. Luo, *On-shell recursion relations for generic integrands*, 1610.05283.

[36] V. Bytev, B. Kniehl and S. Moch, *Derivatives of Horn-type hypergeometric functions with respect to their parameters*, 1712.07579.

[37] R. H. Boels, Q. Jin and H. Luo, *Efficient integrand reduction for particles with spin*, 1802.06761.

[38] M. Y. Kalmykov and B. A. Kniehl, *'Sixth root of unity' and Feynman diagrams: Hypergeometric function approach point of view*, *Nucl.Phys.Proc.Suppl.* **205-206** (2010) 129–134, [1007.2373].

[39] S. Yost, V. Bytev, M. Y. Kalmykov, B. Kniehl and B. Ward, *Differential Reduction Techniques for the Evaluation of Feynman Diagrams*, *PoS* **ICHEP2010** (2010) 135, [1101.2348].

[40] S. Yost, V. Bytev, M. Y. Kalmykov, B. Kniehl and B. Ward, *The Epsilon Expansion of Feynman Diagrams via Hypergeometric Functions and Differential Reduction*, 1110.0210.

[41] V. V. Bytev, M. Y. Kalmykov and B. A. Kniehl, *When ϵ expansion of hypergeometric functions is expressible in terms of multiple polylogarithms: the two-variable examples*, *PoS* **LL2012** (2012) 029, [1212.4719].

[42] R. H. Boels and W. Wormsbecher, *Spontaneously broken conformal invariance in observables*, 1507.08162.

[43] R. Boels, B. A. Kniehl and G. Yang, *Towards a four-loop form factor*, in *Proceedings, 12th International Symposium on Radiative Corrections (Radcor 2015) and LoopFest XIV (Radiative Corrections for the LHC and Future Colliders): Los Angeles, CA, USA, June 15-19, 2015*, 2016, 1601.04432.

[44] R. H. Boels, B. A. Kniehl and G. Yang, *On a four-loop form factor in N=4*, *PoS* **LL2016** (2016) 039, [1607.00172].

[45] R. H. Boels, T. Huber and G. Yang, *The nonplanar cusp and collinear anomalous dimension at four loops in $\mathcal{N} = 4$ SYM theory*, *PoS* **RADCOR2017** (2017) 042, [1712.07563].

[46] T. Reichenbächer, *Relations among color-ordered gauge theory scattering amplitudes at higher loop-order*, Master's thesis, Universität Hamburg, 2013.

[47] G. Kalamakis, *Three point scattering amplitudes in string theory*, Master's thesis, Universität Hamburg, 2013.

[48] R. S. Isermann, *Of Gluons and Gravitons: Exploring Color-Kinematics Duality*, Ph.D. thesis, Universität Hamburg, 2013. http://www-library.desy.de/cgi-bin/showprep.pl?thesis13-020.

[49] M. E. Peskin and D. V. Schroeder, *An Introduction to quantum field theory*. Addison-Wesley, Reading, USA, 1995.

[50] S. Yu. Shmakov, V. V. Uzhinsky and A. M. Zadorozhnyi, *DIAGEN: GENERATOR OF INELASTIC NUCLEUS-NUCLEUS INTERACTION DIAGRAMS*, *Comput. Phys. Commun.* **54** (1989) 125–135.

[51] S. J. Parke and T. R. Taylor, *An Amplitude for n Gluon Scattering*, *Phys. Rev. Lett.* **56** (1986) 2459.

[52] J. M. Henn and J. C. Plefka, *Scattering Amplitudes in Gauge Theories*, *Lect. Notes Phys.* **883** (2014) pp.1–195.

[53] H. Elvang and Y.-t. Huang, *Scattering Amplitudes*, 1308.1697.

[54] J. M. Maldacena, *The Large N limit of superconformal field theories and supergravity*, *Int. J. Theor. Phys.* **38** (1999) 1113–1133, [hep-th/9711200]. [Adv. Theor. Math. Phys.2,231(1998)].

[55] G. 't Hooft, *A Planar Diagram Theory for Strong Interactions*, *Nucl. Phys.* **B72** (1974) 461.

[56] N. Beisert, B. Eden and M. Staudacher, *Transcendentality and Crossing*, *J. Stat. Mech.* **0701** (2007) P01021, [hep-th/0610251].

[57] H. Kawai, D. C. Lewellen and S. H. H. Tye, *A Relation Between Tree Amplitudes of Closed and Open Strings*, *Nucl. Phys.* **B269** (1986) 1–23.

[58] Z. Bern, J. J. Carrasco, L. J. Dixon, H. Johansson, D. A. Kosower and R. Roiban, *Three-Loop Superfiniteness of N=8 Supergravity*, *Phys. Rev. Lett.* **98** (2007) 161303, [hep-th/0702112].

[59] Z. Bern, J. J. Carrasco, L. J. Dixon, H. Johansson and R. Roiban, *The Ultraviolet Behavior of N=8 Supergravity at Four Loops*, *Phys. Rev. Lett.* **103** (2009) 081301, [0905.2326].

[60] Z. Bern, J. J. Carrasco, W.-M. Chen, H. Johansson and R. Roiban, *Gravity Amplitudes as Generalized Double Copies of Gauge-Theory Amplitudes*, *Phys. Rev. Lett.* **118** (2017) 181602, [1701.02519].

[61] Z. Bern, J. J. Carrasco, W.-M. Chen, A. Edison, H. Johansson, J. Parra-Martinez et al., *Ultraviolet Properties of $\mathcal{N} = 8$ Supergravity at Five Loops*, 1804.09311.

[62] Z. Bern, J. J. M. Carrasco and H. Johansson, *New Relations for Gauge-Theory Amplitudes*, *Phys. Rev.* **D78** (2008) 085011, [0805.3993].

[63] Z. Bern, J. J. M. Carrasco and H. Johansson, *Perturbative Quantum Gravity as a Double Copy of Gauge Theory*, *Phys. Rev. Lett.* **105** (2010) 061602, [1004.0476].

[64] J. J. M. Carrasco, *Gauge and Gravity Amplitude Relations*, in *Proceedings, Theoretical Advanced Study Institute in Elementary Particle Physics: Journeys Through the Precision Frontier: Amplitudes for Colliders (TASI 2014): Boulder, Colorado, June 2-27, 2014*, pp. 477–557, WSP, WSP, 2015, 1506.00974, DOI.

[65] G. Mogull and D. O'Connell, *Overcoming Obstacles to Colour-Kinematics Duality at Two Loops*, *JHEP* **12** (2015) 135, [1511.06652].

[66] Z. Bern, T. Dennen, Y.-t. Huang and M. Kiermaier, *Gravity as the Square of Gauge Theory*, *Phys. Rev.* **D82** (2010) 065003, [1004.0693].

[67] R. Monteiro and D. O'Connell, *The Kinematic Algebra From the Self-Dual Sector*, *JHEP* **07** (2011) 007, [1105.2565].

[68] M. Tolotti and S. Weinzierl, *Construction of an effective Yang-Mills Lagrangian with manifest BCJ duality*, *JHEP* **07** (2013) 111, [1306.2975].

[69] Z. Bern and A. G. Morgan, *Massive loop amplitudes from unitarity*, *Nucl. Phys.* **B467** (1996) 479–509, [hep-ph/9511336].

[70] A. H. Mueller, *On the Asymptotic Behavior of the Sudakov Form-factor*, *Phys. Rev.* **D20** (1979) 2037.

[71] J. C. Collins, *Algorithm to Compute Corrections to the Sudakov Form-factor*, *Phys. Rev.* **D22** (1980) 1478.

[72] A. Sen, *Asymptotic Behavior of the Sudakov Form-Factor in QCD*, *Phys. Rev.* **D24** (1981) 3281.

[73] L. Magnea and G. F. Sterman, *Analytic continuation of the Sudakov form-factor in QCD*, *Phys. Rev.* **D42** (1990) 4222–4227.

[74] Z. Bern, L. J. Dixon and V. A. Smirnov, *Iteration of planar amplitudes in maximally supersymmetric Yang-Mills theory at three loops and beyond*, *Phys. Rev.* **D72** (2005) 085001, [hep-th/0505205].

[75] T. Becher and M. Neubert, *On the Structure of Infrared Singularities of Gauge-Theory Amplitudes*, *JHEP* **06** (2009) 081, [0903.1126]. [Erratum: *JHEP* **11** (2013) 024].

[76] G. P. Korchemsky, *Asymptotics of the Altarelli-Parisi-Lipatov Evolution Kernels of Parton Distributions*, *Mod. Phys. Lett.* **A4** (1989) 1257–1276.

[77] E. Gardi and L. Magnea, *Factorization constraints for soft anomalous dimensions in QCD scattering amplitudes*, *JHEP* **03** (2009) 079, [0901.1091].

[78] L. J. Dixon, *Matter Dependence of the Three-Loop Soft Anomalous Dimension Matrix*, *Phys. Rev.* **D79** (2009) 091501, [0901.3414].

[79] T. Becher and M. Neubert, *Infrared singularities of QCD amplitudes with massive partons*, *Phys. Rev.* **D79** (2009) 125004, [0904.1021]. [Erratum: *Phys. Rev.* bf D80 (2009) 109901].

[80] L. J. Dixon, E. Gardi and L. Magnea, *On soft singularities at three loops and beyond*, *JHEP* **02** (2010) 081, [0910.3653].

[81] V. Ahrens, M. Neubert and L. Vernazza, *Structure of Infrared Singularities of Gauge-Theory Amplitudes at Three and Four Loops*, *JHEP* **09** (2012) 138, [1208.4847].

[82] L. F. Alday and J. M. Maldacena, *Comments on operators with large spin*, *JHEP* **11** (2007) 019, [0708.0672].

[83] A. Armoni, *Anomalous Dimensions from a Spinning D5-Brane*, *JHEP* **11** (2006) 009, [hep-th/0608026].

[84] G. P. Korchemsky, *Instanton effects in correlation functions on the light-cone*, *JHEP* **12** (2017) 093, [1704.00448].

[85] A. Grozin, J. Henn and M. Stahlhofen, *On the Casimir scaling violation in the cusp anomalous dimension at small angle*, *JHEP* **10** (2017) 052, [1708.01221].

[86] S. Moch, B. Ruijl, T. Ueda, J. A. M. Vermaseren and A. Vogt, *Four-Loop Non-Singlet Splitting Functions in the Planar Limit and Beyond*, *JHEP* **10** (2017) 041, [1707.08315].

[87] G. Ossola, C. G. Papadopoulos and R. Pittau, *Reducing full one-loop amplitudes to scalar integrals at the integrand level*, *Nucl. Phys.* **B763** (2007) 147–169, [hep-ph/0609007].

[88] C. F. Berger, Z. Bern, L. J. Dixon, F. Febres Cordero, D. Forde, H. Ita et al., *An Automated Implementation of On-Shell Methods for One-Loop Amplitudes*, *Phys. Rev.* **D78** (2008) 036003, [0803.4180].

[89] V. P. Nair, *A Current Algebra for Some Gauge Theory Amplitudes*, *Phys. Lett.* **B214** (1988) 215–218.

[90] A. Brandhuber, B. Spence, G. Travaglini and G. Yang, *Form Factors in N=4 Super Yang-Mills and Periodic Wilson Loops*, *JHEP* **01** (2011) 134, [1011.1899].

[91] K. G. Chetyrkin and F. V. Tkachov, *Integration by Parts: The Algorithm to Calculate beta Functions in 4 Loops*, *Nucl. Phys.* **B192** (1981) 159–204.

[92] F. V. Tkachov, *A Theorem on Analytical Calculability of Four Loop Renormalization Group Functions*, *Phys. Lett.* **100B** (1981) 65–68.

[93] S. Laporta, *High precision calculation of multiloop Feynman integrals by difference equations*, *Int. J. Mod. Phys.* **A15** (2000) 5087–5159, [hep-ph/0102033].

[94] C. Anastasiou and A. Lazopoulos, *Automatic integral reduction for higher order perturbative calculations*, *JHEP* **07** (2004) 046, [hep-ph/0404258].

[95] A. V. Smirnov, *Algorithm FIRE – Feynman Integral REduction*, *JHEP* **10** (2008) 107, [0807.3243].

[96] A. V. Smirnov and V. A. Smirnov, *FIRE4, LiteRed and accompanying tools to solve integration by parts relations*, *Comput. Phys. Commun.* **184** (2013) 2820–2827, [1302.5885].

[97] A. V. Smirnov, *FIRE5: a C++ implementation of Feynman Integral REduction*, *Comput. Phys. Commun.* **189** (2015) 182–191, [1408.2372].

[98] P. Maierhöfer, J. Usovitsch and P. Uwer, *Kira—A Feynman integral reduction program*, *Comput. Phys. Commun.* **230** (2018) 99–112, [1705.05610].

[99] A. von Manteuffel and C. Studerus, *Reduze 2 - Distributed Feynman Integral Reduction*, 1201.4330.

[100] C. Studerus, *Reduze-Feynman Integral Reduction in C++*, *Comput. Phys. Commun.* **181** (2010) 1293–1300, [0912.2546].

[101] R. N. Lee, *Presenting LiteRed: a tool for the Loop InTEgrals REDuction*, 1212.2685.

[102] R. N. Lee, *LiteRed 1.4: a powerful tool for reduction of multiloop integrals*, *J. Phys. Conf. Ser.* **523** (2014) 012059, [1310.1145].

[103] V. A. Smirnov, *Analytical result for dimensionally regularized massless on shell double box*, *Phys. Lett.* **B460** (1999) 397–404, [hep-ph/9905323].

[104] J. B. Tausk, *Nonplanar massless two loop Feynman diagrams with four on-shell legs*, *Phys. Lett.* **B469** (1999) 225–234, [hep-ph/9909506].

[105] C. Anastasiou and A. Daleo, *Numerical evaluation of loop integrals*, *JHEP* **10** (2006) 031, [hep-ph/0511176].

[106] T. Binoth and G. Heinrich, *An automatized algorithm to compute infrared divergent multiloop integrals*, *Nucl. Phys.* **B585** (2000) 741–759, [hep-ph/0004013].

[107] G. Heinrich, *Sector Decomposition*, *Int. J. Mod. Phys.* **A23** (2008) 1457–1486, [0803.4177].

[108] A. V. Smirnov and M. N. Tentyukov, *Feynman Integral Evaluation by a Sector decomposiTion Approach (FIESTA)*, *Comput. Phys. Commun.* **180** (2009) 735–746, [0807.4129].

[109] A. V. Smirnov, V. A. Smirnov and M. Tentyukov, *FIESTA 2: Parallelizeable multiloop numerical calculations*, *Comput. Phys. Commun.* **182** (2011) 790–803, [0912.0158].

[110] A. V. Smirnov, *FIESTA 3: cluster-parallelizable multiloop numerical calculations in physical regions*, *Comput. Phys. Commun.* **185** (2014) 2090–2100, [1312.3186].

[111] A. V. Smirnov, *FIESTA4: Optimized Feynman integral calculations with GPU support*, *Comput. Phys. Commun.* **204** (2016) 189–199, [1511.03614].

[112] J. Carter and G. Heinrich, *SecDec: A general program for sector decomposition*, *Comput. Phys. Commun.* **182** (2011) 1566–1581, [1011.5493].

[113] S. Borowka, J. Carter and G. Heinrich, *Numerical Evaluation of Multi-Loop Integrals for Arbitrary Kinematics with SecDec 2.0*, *Comput. Phys. Commun.* **184** (2013) 396–408, [1204.4152].

[114] S. Borowka, G. Heinrich, S. P. Jones, M. Kerner, J. Schlenk and T. Zirke, *SecDec-3.0: numerical evaluation of multi-scale integrals beyond one loop*, *Comput. Phys. Commun.* **196** (2015) 470–491, [1502.06595].

[115] V. A. Smirnov, *Evaluating Feynman integrals*, *Springer Tracts Mod. Phys.* **211** (2004) 1–244.

[116] V. A. Smirnov, *Feynman integral calculus*. Springer, Berlin, Germany, 2006, 10.1007/3-540-30611-0.

[117] M. Czakon, *Automatized analytic continuation of Mellin-Barnes integrals*, *Comput. Phys. Commun.* **175** (2006) 559–571, [hep-ph/0511200].

[118] A. V. Smirnov and V. A. Smirnov, *On the Resolution of Singularities of Multiple Mellin-Barnes Integrals*, *Eur. Phys. J.* **C62** (2009) 445–449, [0901.0386].

[119] V. A. Smirnov, *Analytic tools for Feynman integrals*, *Springer Tracts Mod. Phys.* **250** (2012) 1–296.

[120] I. Dubovyk, J. Gluza and T. Riemann, *Non-planar Feynman diagrams and Mellin-Barnes representations with AMBRE 3.0*, *J. Phys. Conf. Ser.* **608** (2015) 012070.

[121] J. M. Henn, *Multiloop integrals in dimensional regularization made simple*, *Phys. Rev. Lett.* **110** (2013) 251601, [1304.1806].

[122] J. M. Henn, A. V. Smirnov and V. A. Smirnov, *Evaluating single-scale and/or non-planar diagrams by differential equations*, *JHEP* **03** (2014) 088, [1312.2588].

[123] J. M. Henn, A. V. Smirnov, V. A. Smirnov and M. Steinhauser, *A planar four-loop form factor and cusp anomalous dimension in QCD*, *JHEP* **05** (2016) 066, [1604.03126].

[124] T. Gehrmann, G. Heinrich, T. Huber and C. Studerus, *Master integrals for massless three-loop form-factors: One-loop and two-loop insertions*, *Phys. Lett.* **B640** (2006) 252–259, [hep-ph/0607185].

[125] P. A. Baikov, K. G. Chetyrkin, A. V. Smirnov, V. A. Smirnov and M. Steinhauser, *Quark and gluon form factors to three loops*, *Phys. Rev. Lett.* **102** (2009) 212002, [0902.3519].

[126] R. N. Lee, A. V. Smirnov and V. A. Smirnov, *Analytic Results for Massless Three-Loop Form Factors*, *JHEP* **04** (2010) 020, [1001.2887].

[127] T. Gehrmann, E. W. N. Glover, T. Huber, N. Ikizlerli and C. Studerus, *Calculation of the quark and gluon form factors to three loops in QCD*, *JHEP* **06** (2010) 094, [1004.3653].

[128] T. Gehrmann, E. W. N. Glover, T. Huber, N. Ikizlerli and C. Studerus, *The quark and gluon form factors to three loops in QCD through to $O(\epsilon^2)$*, *JHEP* **11** (2010) 102, [1010.4478].

[129] A. von Manteuffel, E. Panzer and R. M. Schabinger, *On the Computation of Form Factors in Massless QCD with Finite Master Integrals*, *Phys. Rev.* **D93** (2016) 125014, [1510.06758].

[130] J. M. Henn and T. Huber, *The four-loop cusp anomalous dimension in $\mathcal{N} = 4$ super Yang-Mills and analytic integration techniques for Wilson line integrals*, *JHEP* **09** (2013) 147, [1304.6418].

[131] O. T. Engelund and R. Roiban, *Correlation functions of local composite operators from generalized unitarity*, *JHEP* **03** (2013) 172, [1209.0227].

[132] T. van Ritbergen, J. A. M. Vermaseren and S. A. Larin, *The Four loop beta function in quantum chromodynamics*, *Phys. Lett.* **B400** (1997) 379–384, [hep-ph/9701390].

[133] G. Yang, *Color-kinematics duality and Sudakov form factor at five loops for N=4 supersymmetric Yang-Mills theory*, *Phys. Rev. Lett.* **117** (2016) 271602, [1610.02394].

[134] R. N. Lee and A. A. Pomeransky, *Critical points and number of master integrals*, *JHEP* **11** (2013) 165, [1308.6676].

[135] A. V. Kotikov and L. N. Lipatov, *DGLAP and BFKL equations in the $N = 4$ supersymmetric gauge theory*, *Nucl. Phys.* **B661** (2003) 19–61, [hep-ph/0208220]. [Erratum: *Nucl. Phys.* **B685** (2004) 405].

[136] A. V. Kotikov, L. N. Lipatov, A. I. Onishchenko and V. N. Velizhanin, *Three loop universal anomalous dimension of the Wilson operators in $N = 4$ SUSY Yang-Mills model*, *Phys. Lett.* **B595** (2004) 521–529, [hep-th/0404092]. [Erratum: *Phys. Lett.* **B632** (2006) 754].

[137] J. Blumlein, D. J. Broadhurst and J. A. M. Vermaseren, *The Multiple Zeta Value Data Mine*, *Comput. Phys. Commun.* **181** (2010) 582–625, [0907.2557].

[138] T. Gehrmann, J. M. Henn and T. Huber, *The three-loop form factor in N=4 super Yang-Mills*, *JHEP* **03** (2012) 101, [1112.4524].

[139] Z. Bern, E. Herrmann, S. Litsey, J. Stankowicz and J. Trnka, *Evidence for a Nonplanar Amplituhedron*, *JHEP* **06** (2016) 098, [1512.08591].

[140] S. Moch, B. Ruijl, T. Ueda, J. A. M. Vermaseren and A. Vogt, *On quartic colour factors in splitting functions and the gluon cusp anomalous dimension*, *Phys. Lett.* **B782** (2018) 627–632, [1805.09638].

[141] L. A. Barreiro and R. Medina, *RNS derivation of N-point disk amplitudes from the revisited S-matrix approach*, *Nucl. Phys.* **B886** (2014) 870–951, [1310.5942].

[142] E. Noether, *Invariant Variation Problems*, *Gott. Nachr.* **1918** (1918) 235–257, [physics/0503066]. [Transp. Theory Statist. Phys.1,186(1971)].

[143] N. Arkani-Hamed, L. Rodina and J. Trnka, *Locality and Unitarity of Scattering Amplitudes from Singularities and Gauge Invariance*, *Phys. Rev. Lett.* **120** (2018) 231602, [1612.02797].

[144] L. Rodina, *Uniqueness from locality and BCFW shifts*, 1612.03885.

[145] S. Laporta, *High-precision calculation of the 4-loop contribution to the electron g-2 in QED*, *Phys. Lett.* **B772** (2017) 232–238, [1704.06996].

[146] E. W. N. Glover and M. E. Tejeda-Yeomans, *Two loop QCD helicity amplitudes for massless quark massless gauge boson scattering*, *JHEP* **06** (2003) 033, [hep-ph/0304169].

[147] Z. Bern, A. Edison, D. Kosower and J. Parra-Martinez, *Curvature-squared multiplets, evanescent effects, and the U(1) anomaly in $N = 4$ supergravity*, *Phys. Rev.* **D96** (2017) 066004, [1706.01486].

[148] Z. Bern, S. Davies, T. Dennen, Y.-t. Huang and J. Nohle, *Color-Kinematics Duality for Pure Yang-Mills and Gravity at One and Two Loops*, *Phys. Rev.* **D92** (2015) 045041, [1303.6605].

[149] T. Gehrmann, J. M. Henn and N. A. Lo Presti, *Analytic form of the two-loop planar five-gluon all-plus-helicity amplitude in QCD*, *Phys. Rev. Lett.* **116** (2016) 062001, [1511.05409]. [Erratum: *Phys. Rev. Lett.* **116** (2016) 189903].

[150] C. G. Papadopoulos, D. Tommasini and C. Wever, *The Pentabox Master Integrals with the Simplified Differential Equations approach*, *JHEP* **04** (2016) 078, [1511.09404].

[151] J. Böhm, A. Georgoudis, K. J. Larsen, H. Schönemann and Y. Zhang, *Complete integration-by-parts reductions of the non-planar hexagon-box via module intersections*, 1805.01873.

[152] H. A. Chawdhry, M. A. Lim and A. Mitov, *Two-loop five-point massless QCD amplitudes within the IBP approach*, 1805.09182.

[153] S. Badger, C. Brønnum-Hansen, H. B. Hartanto and T. Peraro, *First look at two-loop five-gluon scattering in QCD*, *Phys. Rev. Lett.* **120** (2018) 092001, [1712.02229].

[154] S. Abreu, F. Febres Cordero, H. Ita, B. Page and M. Zeng, *Planar Two-Loop Five-Gluon Amplitudes from Numerical Unitarity*, *Phys. Rev.* **D97** (2018) 116014, [1712.03946].

[155] S. Badger, H. Frellesvig and Y. Zhang, *A Two-Loop Five-Gluon Helicity Amplitude in QCD*, *JHEP* **12** (2013) 045, [1310.1051].

[156] S. Badger, G. Mogull and T. Peraro, *Local integrands for two-loop all-plus Yang-Mills amplitudes*, *JHEP* **08** (2016) 063, [1606.02244].

[157] D. C. Dunbar, J. H. Godwin, G. R. Jehu and W. B. Perkins, *Analytic all-plus-helicity gluon amplitudes in QCD*, *Phys. Rev.* **D96** (2017) 116013, [1710.10071].

[158] N. E. J. Bjerrum-Bohr, D. C. Dunbar and W. B. Perkins, *Analytic structure of three-mass triangle coefficients*, *JHEP* **04** (2008) 038, [0709.2086].

[159] S. Badger, C. Brønnum-Hansen, F. Buciuni and D. O'Connell, *A unitarity compatible approach to one-loop amplitudes with massive fermions*, *JHEP* **06** (2017) 141, [1703.05734].

[160] M. Yu. Kalmykov and B. A. Kniehl, *Towards all-order Laurent expansion of generalized hypergeometric functions around rational values of parameters*, *Nucl. Phys.* **B809** (2009) 365–405, [0807.0567].

[161] J. Broedel, O. Schlotterer and S. Stieberger, *Polylogarithms, Multiple Zeta Values and Superstring Amplitudes*, *Fortsch. Phys.* **61** (2013) 812–870, [1304.7267].

[162] J. Broedel, O. Schlotterer, S. Stieberger and T. Terasoma, *All order α'-expansion of superstring trees from the Drinfeld associator*, *Phys. Rev.* **D89** (2014) 066014, [1304.7304].

Topological Field Theories from and for 4d SUSY Gauge Theories

Christoph Schweigert[1], *Jörg Teschner*[1,2]

[1]Fachbereich Mathematik, Universität Hamburg, Germany
[2]DESY, Hamburg, Germany

DOI: http://dx.doi.org/10.3204/PUBDB-2018-00782/A10

AGT-correspondences give profound relations between certain families of $\mathcal{N} = 2$ supersymmetric gauge theories in four dimensions and conformal field theories in two dimensions. Subsequent investigations of the AGT-correspondences revealed a new type of topological field theory associated to these theories that captures completely the dependence of important physical quantities on the gauge coupling constants, including perturbative and non-perturbative corrections.

The topological field theories and chiral data associated to $\mathcal{N} = 2$ supersymmetric field theories are the central objects of study in this project. We present first steps towards a precise mathematical framework for them in which loop and surface operators play a particularly important role.

1 Introduction

Progress made in the recent years has seen several instances where topological quantum field theories (TQFT) served as powerful tools for the study of the non-perturbative dynamics of usual quantum field theories (QFT). At the same time it has developed into an active area of mathematical research, characterised by a profound interplay between various structures of algebraic nature, category theory, and topology.

A striking example for the relevance of TQFT for the study of non-perturbative phenomena in QFT is the work of Kapustin and Witten [1] relating the S-duality conjecture in $\mathcal{N} = 4$ supersymmetric Yang–Mills (SYM) theory to the geometric Langlands program. Mathematical work on the geometric Langlands program thereby provides checks of the S-duality conjecture, and helps to elaborate its quantum field theoretical consequences. Ideas and methods of TQFT play an important role in the approach of Kapustin and Witten.

Even more recent work by Nekrasov and Witten [2] has proposed a reinterpretation of the famous AGT-correspondence (after Alday, Gaiotto and Tachikawa) in terms of TQFT (or some generalisation thereof). The AGT-correspondence relates partition functions of certain four-dimensional $\mathcal{N} = 2$ supersymmetric quantum field theories to correlation functions in two-dimensional conformal field theories. This gives exact results for partition functions and expectation values of certain observables encoding detailed information on the non-perturbative dynamics of these four-dimensional quantum field theories. The work of Nekrasov and Witten reinterprets the partition functions appearing in the AGT-correspondence in terms of objects in a modified version of the four-dimensional $\mathcal{N} = 2$-supersymmetric quantum field theories

which are expected to possess topological invariance while capturing crucial information on the original QFT.

It should be noted that the term TQFT has been used above in a rather loose sense. Important mathematical work has led to precise definitions of certain classes of TQFT, see [3] for a review. The modified versions of QFT mentioned above, often called topologically twisted QFT, are in many cases expected to represent generalisations of TQFT in a sense which remains to be clarified.

The progress achieved within our project has on the one hand shed some light on the relations between the approach to the geometric Langlands correspondence of Beilinson and Drinfeld, Kapustin and Witten, and the AGT-correspondence [4]. On the other hand, within a PhD project, we have developed algebraic tools towards an explicit description of the chiral data associated to $\mathcal{N} = 2$ gauge theories.

2 TQFT in two and four dimensions

In this section we will briefly describe the relations between four- and two-dimensional TQFT which play a basic role in both [1] and [2].

2.1 Two-dimensional topological sigma models

Nonlinear two-dimensional sigma models with $\mathcal{N} = (2, 2)$ supersymmetry can be modified in basically two natural ways to get two-dimensional field theories which are topologically invariant in the sense that they depend only on the topology of the two-dimensional surfaces on which these theories are defined. The modification is called a topological twist. It modifies the Lagrangian of the theory in such a way that the twisted theory coincides with an important subsector of the untwisted theory on surfaces with trivial canonical bundle. From a given two-dimensional sigma model with $\mathcal{N} = (2, 2)$ supersymmetry one can obtain two TQFT in this way, called A- and B-model respectively.

Considering two-dimensional surfaces with boundaries one gets the so-called open topological sigma models. In many cases these sigma models are expected to be examples of two-dimensional TQFT as axiomatised in the mathematical literature, or generalisations thereof. Two-dimensional TQFT are characterised by the collection of boundary conditions $\mathsf{A}, \mathsf{B}, \ldots$ which can be associated to the boundary components of two-dimensional surfaces, and by the vector spaces V_{AB} associated to intervals $I \simeq [0, \pi]$ decorated with particular boundary conditions A and B at the two ends 0 and π, respectively. A TQFT furthermore associates to two-dimensional surfaces having boundaries with fixed choices of boundary conditions a number called the partition function.

It turns out to be useful to regard the collection of defining data as a category having the boundary conditions as its objects, and the spaces V_{AB} as the spaces of morphisms $\mathrm{Hom}(\mathsf{A}, \mathsf{B})$. The strip $I \times \mathbb{R}$ can be mapped to the punctured half-plane, defining a variant of the state-operator correspondence relating elements of V_{AB} to boundary-changing operators $\mathcal{O}_{\mathsf{AB}}$, as depicted in Fig. 1 below. The composition of morphism thereby gets related to the product of boundary-changing operators, see Fig. 2.

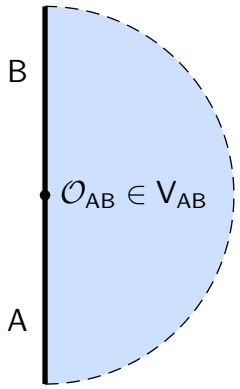


Figure 1: Morphisms in the category of boundary conditions correspond to boundary-changing operators in two-dimensional TQFT. Figure taken from Ref. [5].

2.2 Two-dimensional reductions of four-dimensional TQFT

TQFT in higher dimensions have a much richer structure. Precise mathematical definitions have been given only fairly recently, based on the mathematical framework of higher categories, see [3] for a review. A very readably discussion of the physical motivation for considering higher categories can be found in [5].

There exist higher-dimensional analogs of the topological twisting procedure expected to turn supersymmetric quantum field theories into TQFT, or generalisations thereof. Topological twists of the four-dimensional, $\mathcal{N} = 4$ supersymmetric Yang–Mills theory (SYM) have been investigated in [1]. There is a one-parameter family of such theories labelled by a parameter t.

A key idea in the work of Kapustin and Witten is to use effective representations of the topologically twisted four-dimensional SYM on space-times of the form $\Sigma \times C$, with C being a Riemann surface, provided by two-dimensional topologically twisted sigma models on $\Sigma = \mathbb{R} \times I$. These sigma models are related to the original four-dimensional theory by a variant of the Kaluza–Klein reduction described in [1], leading to sigma models which have the Hitchin moduli spaces $\mathcal{M}_{\mathrm{H}}(C, G)$ as target spaces. The space $\mathcal{M}_{\mathrm{H}}(C, G)$ can be described as the moduli space of pairs $(\mathcal{E}, \varphi)$, where $\mathcal{E} = (E, \bar{\partial}_{\mathcal{E}})$ is a holomorphic structure on a smooth G-bundle E on C, and $\varphi \in H^0(C, \mathrm{End}(\mathcal{E}) \otimes K)$ can be locally represented as a matrix-valued one-form. In the following we will freely use several standard definitions and results concerning Hitchin's moduli spaces. A very brief summary is collected in Appendix A in the form of a glossary. If a glossary entry exists for a term, its first occurrence will appear with a superscript as in term$^{g)}$.

The two-dimensional description is not expected to capture all of the structures of the four-dimensional theory, but it is believed to represent correctly an important part of its structure.

Similar ideas are used in the work of Nekrasov and Witten, where the starting points are theories from a class of four-dimensional $\mathcal{N} = 2$-supersymmetric theories often referred to as class $\mathcal{S}$ in the literature [6, 7]. The members of this class are labelled by the pair of data $(C, \mathfrak{g})$, where C is a Riemann surface and $\mathfrak{g}$ is a semi-simple Lie algebra of ADE-type. On four-dimensional spacetimes which can locally be described in the form $\mathbb{R} \times I \times S^1 \times S^1$ one preserves enough of the supersymmetries of the theory to define topologically twisted versions of the class $\mathcal{S}$ theories depending on two parameters ϵ_1 and ϵ_2. One may furthermore argue

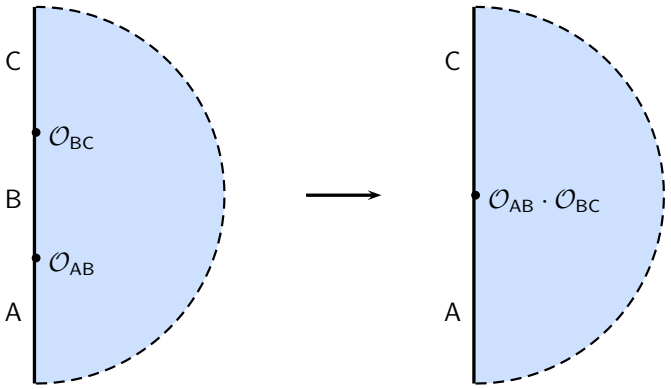


Figure 2: The composition of morphisms corresponds to the product of boundary-changing operators. Figure taken from Ref. [5].

that the resulting four-dimensional theories with topological invariance can be described by an effective two-dimensional topological sigma model on $\mathbb{R} \times I$.

This means that in the both cases one ends up with sigma models having the same target spaces $\mathcal{M}_{\mathrm{H}}(C, G)$. It should be noted, however, that such sigma models have $\mathcal{N} = (4, 4)$ supersymmetry related to the fact that the spaces $\mathcal{M}_{\mathrm{H}}(C, G)$ admit hyperkähler structures. Instead of getting just one A-model and one B-model one may now define a one-parameter family of A- and B-models depending on which part of the supersymmetries are preserved by the topological twist. The relevant parameter can be identified with the hyperkähler parameter determining a particular complex stucture on $\mathcal{M}_{\mathrm{H}}(C, G)$.

It therefore depends sensitively on the precise reduction procedure which particular topological sigma model is ultimately found as an effective description of the original four-dimensional QFT. And indeed, it turns out that the sigma models appearing in the works [1] and [2] are not identical, despite the fact that they have the same target space. Yet, there are reasons to expect that these sigma models should be more closely related than it may appear.

3 What is the geometric Langlands correspondence?

The geometric Langlands correspondence can be schematically formulated as a correspondence between two types of geometric objects naturally assigned to a Riemann surface C and a simple complex Lie group G,

$$\boxed{\mathcal{D}\text{-modules on } \mathrm{Bun}_G} \quad \leftrightarrow \quad \boxed{{}^{L}G\text{-local systems}} \tag{3.1}$$

The following objects appear in this correspondence:

Bun_G is the moduli space of holomorphic G-bundles on C. The $\mathcal{D}$-modules on Bun_G appearing in this context can be described more concretely as systems of partial differential equations taking the form of eigenvalue equations $D_i f = E_i f$ for a family of commuting global differential operators D_i on Bun_G. The differential operators D_i can be regarded as quantum counterparts of the Hamiltonians of Hitchin's integrable system. The representation of the $\mathcal{D}$-modules as

eigenvalue equations $D_i f = E_i f$ is not canonical, it depends on additional choices. Part of the content of the geometric Langlands correspondence describes the eigenvalues E_i geometrically as coordinates on a suitable parameter space, parameterising the objects on the right side of (3.1), which will be explained next.

The group ${}^L G$ is the Langlands dual of G which has as Dynkin diagram the transpose of the Dynkin diagram of G. The ${}^L G$ *local systems*[g)] appearing in this correspondence can be represented by pairs $(\mathcal{E}, \nabla')$ composed of a holomorphic ${}^L G$-bundle $\mathcal{E}$ with a holomorphic connection ∇', or equivalently by the representations ρ of the fundamental group $\pi_1(C)$ defined from the holonomies of $(\mathcal{E}, \nabla')$.

We will mostly be interested in the case of *irreducible* ${}^L G$ local systems. A more ambitious version of the geometric Langlands correspondence has been formulated in [8] extending it to certain classes of reducible local systems.

Some of the original approaches to the geometric Langlands correspondence start from the cases where the ${}^L G$-local systems are *opers*[g)], pairs $(\mathcal{E}, \nabla')$ in which ∇' is gauge-equivalent to a certain standard form. The space of opers forms a Lagrangian subspace in the moduli space of all local systems.

The CFT-based approach of Beilinson and Drinfeld constructs for each oper an object in the category of $\mathcal{D}$-modules on Bun_G as conformal blocks of the affine Lie algebra $\hat{\mathfrak{g}}_k$ at the critical level $k = -h^\vee$. The Ward-identities characterising the conformal blocks equip the sheaves of conformal blocks with a $\mathcal{D}$-module structure. The universal enveloping algebra $\mathcal{U}(\hat{\mathfrak{g}}_k)$ has a large center at $k = -h^\vee$, isomorphic to the space of ${}^L\mathfrak{g}$-opers on the formal disc [9]. This can be used to show that the $\mathcal{D}$-module structure coming from the Ward identities can be described by the system of eigenvalue equations $D_i f = E_i f$ for the quantised Hitchin Hamiltonians, with eigenvalues E_i parameterising the choices of opers [10].

There exists an extension of the Beilinson–Drinfeld construction of the geometric Langlands correspondence described in [10, Section 9.6] from the case of opers to general irreducible local systems. It is based on the fact that such local systems are always gauge-equivalent to opers with certain extra singularities [11]. The construction of Beilinson and Drinfeld associates to such opers conformal blocks of $\hat{\mathfrak{g}}_{-h^\vee}$ with certain degenerate representations induced from the finite-dimensional representations of $\mathfrak{g}$ inserted at the extra singularities.

We may in this sense regard the geometric Langlands correspondence for general irreducible local systems as an extension of the correspondence that exists for ordinary, non-singular opers. Let us remark that the construction of Beilinson–Drinfeld plays an important role in the outline given in [12] for a proof of the strengthened geometric Langlands conjecture formulated in [8].

4 TQFT interpretation of the Langlands correspondence

The variant of the geometric Langlands correspondence proposed by Kapustin and Witten [1] is based on the consideration of $\mathcal{N} = 4$ SYM theory with gauge group G_c, a compact real form of G, on four-manifolds of the form $\Sigma \times C$, where C is a Riemann surface. Compactification on C allows one to represent the topologically twisted version of $\mathcal{N} = 4$ SYM effectively by a topologically twisted $2d$ sigma-model with target being the Hitchin moduli space $M_H(G)$ on Σ. The complete integrability[g)] of the Hitchin moduli space, as is manifest in the description of $M_H(G)$ as a torus fibration, allows one to describe the consequences of the S-duality of $\mathcal{N} = 4$ SYM theory as the SYZ mirror symmetry relating the $2d$ sigma-models with target $M_H(G)$ and $M_H({}^L G)$, respectively.

In order to relate this to the geometric Langlands correspondence, Kapustin and Witten consider the cases when $\Sigma = R \times I$, $I = [0, \pi]$. Supersymmetric boundary condition of $\mathcal{N} = 4$ SYM theory will upon compactification on C define boundary conditions of the N=(4,4) sigma model with target $\mathcal{M}_H(G)$ on Σ. Let $\mathfrak{B}$ be the category having as objects boundary conditions B called branes preserving the maximal number of supersymmetries, with morphisms being the spaces $\mathrm{Hom}_{\mathcal{M}_H(G)}(\mathsf{B}_1, \mathsf{B}_2)$ of the sigma model on the strip $\mathbb{R} \times I$, having associated boundary conditions B_1 and B_2 to the boundaries $\mathbb{R} \times \{0\}$ and $\mathbb{R} \times \{\pi\}$, respectively.

A distinguished role is played by the so-called canonical coisotropic brane B_{cc} [1,2]. The vector space $\mathcal{A}_{\mathrm{cc}} = \mathrm{Hom}_{\mathcal{M}_H(G)}(\mathsf{B}_{\mathrm{cc}}, \mathsf{B}_{\mathrm{cc}})$ has a natural algebra structure with product corresponding to the composition of morphisms depicted in Fig. 2. The spaces $\mathcal{H}(\mathsf{B}) = \mathrm{Hom}_{\mathcal{M}_H(G)}(\mathsf{B}_{\mathrm{cc}}, \mathsf{B})$ are left modules over the algebra $\mathcal{A}_{\mathrm{cc}}$ with action corresponding to the composition of morphisms $\mathrm{Hom}_{\mathcal{M}_H(G)}(\mathsf{B}_{\mathrm{cc}}, \mathsf{B}_{\mathrm{cc}}) \times \mathrm{Hom}_{\mathcal{M}_H(G)}(\mathsf{B}_{\mathrm{cc}}, \mathsf{B}) \to \mathrm{Hom}_{\mathcal{M}_H(G)}(\mathsf{B}_{\mathrm{cc}}, \mathsf{B})$. Kapustin and Witten argue that the algebra $\mathcal{A}_{\mathrm{cc}}$ contains the algebra of global differential operators on Bun_G. It follows that the spaces $\mathcal{H}(\mathsf{B})$ represent $\mathcal{D}$-modules on Bun_G.

In order to describe the dimensional reduction of topologically twisted $\mathcal{N} = 4$ SYM on $\mathbb{R} \times I \times C$ one may find it natural to consider boundary conditions that are purely topological, not depending on the complex structure on C. This point of view motivated Ben-Zvi and Nadler [13] to propose the Betti geometric Langlands conjecture as a purely topological variant of the geometric Langlands correspondence formulated in [8] that captures some aspects of the approach of Kapustin and Witten while having good chances to be realised within a mathematically precise framework for TQFT.

5 TQFT interpretation of the AGT-correspondence

Alday, Gaiotto and Tachikawa discovered a relation between the instanton partition functions of certain $\mathcal{N} = 2$ supersymmetric gauge theories and conformal blocks of the Virasoro algebra [14]. This discovery has stimulated a lot of work leading in particular to various generalisations of such relations. We will now briefly outline the role of topological sigma models in the approach of Nekrasov and Witten to the AGT-correspondence.

5.1 The approach of Nekrasov and Witten

In an attempt to explain the relations discovered in [14] using TQFT-methods Nekrasov and Witten [2] considered four-dimensional $\mathcal{N} = 2$ supersymmetric gauge theories of class $\mathcal{S}$ obtained from the maximally supersymmetric six-dimensional QFT on manifolds of the form $\mathcal{M}^4 \times C$ by compactification on the Riemann surface C. For the case associated to the Lie algebra $\mathfrak{g} = \mathfrak{sl}_2$ one has weakly coupled Lagrangian descriptions of the resulting theory associated to the choice of a pants decomposition σ of C [6]. For four-manifolds $\mathcal{M}^4$ which can be represented as a fibered product locally of the form $\mathbb{R} \times I \times S^1 \times S^1$ it is argued in [2] that (i) an Ω-deformation with parameters ϵ_1, ϵ_2 can be defined, and (ii) an effective representation is obtained by compactification on $S^1 \times S^1$ in terms of a sigma-model with target $\mathcal{M}_H(G)$ on $R \times I$. The coupling parameter of this sigma model is ϵ_1/ϵ_2.

The end points of the interval I in the representation $\mathcal{M}^4 \simeq \mathbb{R} \times I \times S^1 \times S^1$ correspond to points where $\mathcal{M}^4$ is perfectly regular. One must therefore have distinguished boundary condition in the sigma-model with target $\mathcal{M}_H(G)$ on $R \times I$ describing the compactification of a class $\mathcal{S}$ theory on $\mathcal{M}^4$. When the compactification yields a sigma model with target $\mathcal{M}_H(G)$,

it is argued in [2] that the corresponding boundary conditions are described by a variant $\mathsf{B}_{\rm cc}$ of the canonical coisotropic brane at $\mathbb{R}\times\{0\}$, and a new type of brane called the "brane of opers", here denoted by $\mathsf{B}_{\rm op}$, respectively.[1] The brane $\mathsf{B}_{\rm op}$ is the mirror dual of $\mathsf{B}_{\rm cc}$, and it is proposed in [2] that the brane $\mathsf{B}_{\rm op}$ is a Lagrangian brane supported on the variety of opers within $M_H(G)$.

In [2] it is furthermore proposed that the space $\mathcal{H}=\mathrm{Hom}_{\mathcal{M}_H(G)}(\mathsf{B}_{\rm cc},\mathsf{B}_{\rm op})$ can be identified with the space of Virasoro conformal blocks. In order to motivate this identification, Nekrasov and Witten note that the algebra $\mathcal{A}^{\hbar}_{\rm cc}(G)=\mathrm{Hom}_{\mathcal{M}_H(G)}(\mathsf{B}_{\rm cc},\mathsf{B}_{\rm cc})$ with $\hbar=\epsilon_1/\epsilon_2$ is isomorphic to the algebra of Verlinde line operators acting on the space of Virasoro conformal blocks. Mirror symmetry produces a dual description of $\mathcal{H}(G)\simeq\mathcal{H}({}^{\rm L}G)$ as the space $\mathrm{Hom}_{\mathcal{M}_H({}^{L}G)}(\mathsf{B}'_{\rm op},\mathsf{B}'_{\rm cc})$, with $\mathsf{B}'_{\rm op}$ and $\mathsf{B}'_{\rm cc}$ being close relatives of $\mathsf{B}_{\rm op}$ and $\mathsf{B}_{\rm cc}$, respectively, with modified SUSY invariance properties. In the dual representation one has an obvious right action of the algebra $\check{\mathcal{A}}^{1/\hbar}_{\rm cc}({}^{L}G)=\mathrm{Hom}_{\mathcal{M}_H({}^{L}G)}(\mathsf{B}'_{\rm cc},\mathsf{B}'_{\rm cc})$ with action related to the composition of morphisms

$$\mathrm{Hom}_{\mathcal{M}_H({}^{L}G)}(\mathsf{B}'_{\rm op},\mathsf{B}'_{\rm cc})\times\mathrm{Hom}_{\mathcal{M}_H({}^{L}G)}(\mathsf{B}'_{\rm cc},\mathsf{B}'_{\rm cc})\to\mathrm{Hom}_{\mathcal{M}_H({}^{L}G)}(\mathsf{B}'_{\rm op},\mathsf{B}'_{\rm cc}).$$

The existence of (almost) commuting actions of $\mathcal{A}^{\hbar}_{\rm cc}(G)$ and $\check{\mathcal{A}}^{1/\hbar}_{\rm cc}({}^{L}G)$ is a characteristic feature of the space of Virasoro conformal blocks.

5.2 The other way around

It is no accident that the work of Nekrasov and Witten [2] has many elements in common with the approach Kapustin and Witten [1]. A common root can be found in the fact that both the class $\mathcal{S}$-theories and $\mathcal{N}=4$ SYM [15] can be obtained as compactifications of the six-dimensional $(2,0)$-theory on six-manifolds $\mathcal{M}^6=\mathcal{M}^4\times C$, where C is a Riemann surface, and $\mathcal{M}^4$ is a four-manifold locally represented as a circle fibration locally of the form $\mathbb{R}\times I\times S^1\times S^1$. Compactification on C yields class $\mathcal{S}$-theories [7], while compactification on $S^1\times S^1$ yields $\mathcal{N}=4$ SYM on $\mathbb{R}\times I\times C$, the set-up considered in [1] as was further discussed in [15].

One should note, however, that different topological twists are used in the two compactifications, making the comparison of the results somewhat subtle. This fact can nevertheless be used to relate supersymmetric boundary conditions in the 2d sigma model with target $\mathcal{M}_H$ arising from compactification of class $\mathcal{S}$-theories to boundary conditions in $\mathcal{N}=4$ SYM on C. These boundary conditions have been classified in the work of Gaiotto and Witten [16]. The canonical coisotropic brane is related to the pure Neumann boundary conditions in $\mathcal{N}=4$ SYM by the compactification described above [1,17]. Exchanging the two circles in $S^1\times S^1$ gets related to the S-duality of $\mathcal{N}=4$ SYM which implies relations between its boundary conditions studied in [18]. This led [17] to relate the brane $\mathsf{B}_{\rm op}$, the mirror dual of the canonical coisotropic brane in [2], to the boundary condition descending from the so-called Nahm pole boundary conditions in $\mathcal{N}=4$ SYM.

6 Towards a unified picture

One of the goals in our project has been to clarify the relations between the gauge-theoretic approach to the geometric Langlands correspondence, the CFT-based approach of Beilinson

[1] The branes denoted $\mathsf{B}_{\rm cc}$ in this context are similar but not identical with the brane considered in [1]. The paper [2] used the notation $B_{N'}$ for the brane denoted $\mathsf{B}_{\rm op}$ here.

and Drinfeld, and the AGT-correspondence. The results have been announced in [4], with more detailed descriptions being in preparation. In a parallel development [19,20], similar ingredients have been used to outline a large web of relations between $\mathcal{N} = 4$ SYM, vertex algebras, and braided tensor categories.

6.1 Dirichlet boundary condition and affine Lie algebra symmetry

As mentioned above, a key ingredient in the approach of Beilinson and Drinfeld to the geometric Langlands correspondence is the current algebra of WZW conformal field theory at the critical level. The approach of Kapustin and Witten does not by itself reveal the origin of this crucial aspect of the geometric Langlands correspondence. The work of Nekrasov and Witten, on the other hand, relates conformal blocks of the Virasoro algebra to states of an open topological sigma model. A key ingredient has to be added also in this approach to understand the affine Lie algebra symmetry in this context.

Gaiotto and Witten have classified 1/2 BPS boundary conditions of $\mathcal{N} = 4$ SYM in [16] using the data (ρ, H, T), where $\rho : \mathfrak{sl}_2 \to \mathfrak{g}$ is an embedding of $\mathfrak{sl}_2$ into the Lie algebra $\mathfrak{g}$ of the gauge group G_c, H is a subgroup of the commutant in G_c of the image of ρ, and T is a three-dimensional SCFT with $\mathcal{N} = 4$ supersymmetry and at least H global symmetry. We will only need two of the simplest of these boundary conditions. In the following we will first briefly review the so-called Nahm pole boundary condition studied in [17] which is associated to a triple $(\rho, \mathrm{Id}, T_\emptyset)$, where ρ is a *principal* $\mathfrak{sl}_2$-embedding, and $T_\emptyset$ stands for the trivial three-dimensional SCFT. We will then discuss the even simpler case where ρ is replaced by the trivial embedding mapping $\mathfrak{sl}_2$ to $0 \in \mathfrak{g}$, which will be of particular interest for us.

It is for our purposes sufficient to describe the Nahm pole boundary conditions for the solutions of the BPS-equations [1] characterising field configuration in $\mathcal{N} = 4$ SYM preserving certain supersymmetries. Restricting attention to solutions to the BPS-equations on $\mathbb{R}\times\mathbb{R}_+\times C$ which are invariant under translations along $\mathbb{R}$, one gets a system of differential equations of the form

$$[\,\mathcal{D}_z\,,\,\mathcal{D}_{\bar z}\,] = 0\,, \quad [\,\mathcal{D}_y\,,\,\mathcal{D}_z\,] = 0\,, \quad [\,\mathcal{D}_y\,,\,\mathcal{D}_{\bar z}\,] = 0\,, \tag{6.2a}$$

$$\sum_{i=1}^{3} [\,\mathcal{D}_i\,,\,\mathcal{D}_i^\dagger\,] = 0\,., \tag{6.2b}$$

where the notations $z = x_2 + ix_3$ and $y = x_1$ have been used, and the differential operators $\mathcal{D}_i$ are of the form[2]

$$\begin{aligned} \mathcal{D}_z &= \zeta\partial_z + \mathcal{A}_z\,, & \mathcal{A}_z &= \zeta A_z + \phi_z\,, \\ \mathcal{D}_{\bar z} &= \partial_{\bar z} + \mathcal{A}_{\bar z}\,, & \mathcal{A}_{\bar z} &= A_{\bar z} + \zeta\phi_{\bar z}\,, \end{aligned} \qquad \mathcal{D}_y = \partial_y + A_y - i\phi_y\,. \tag{6.3}$$

The parameter ζ determines the supersymmetries that are preserved. It is proposed in [17] that the space of solutions to (6.2) modulo compact gauge transformations is isomorphic to the moduli space of the solutions to the "F-term" equations (6.2a) modulo complex gauge transformations. Equations $[\mathcal{D}_z, \mathcal{D}_{\bar z}] = 0$ determine a flat complex connection on C at each fixed y. The remaining equations in (6.2a) imply that the y-dependence of this flat connection is represented by complex gauge transformations.

[2] Our conventions differ slightly from [17].

Boundary conditions of Nahm pole type are defined in [17] by demanding that the solutions to (6.2) have a singular behaviour of the form

$$\mathcal{A}_z \underset{y\to 0}{\sim} \mathfrak{t}_- \, y^{-1} + \mathcal{O}(y^0)\,, \qquad \mathcal{A}_{\bar{z}} \underset{y\to 0}{\sim} \mathcal{O}(y^0)\,, \qquad \mathcal{A}_1 \underset{y\to 0}{\sim} \mathfrak{t}_3\, y^{-1} + \mathcal{O}(y^0)\,, \tag{6.4}$$

with $\mathfrak{t}_+ = \mathfrak{t}_1 + i\mathfrak{t}_2$, and $\mathfrak{t}_i$, $i = 1,2,3$, being the generators of a principal $\mathfrak{sl}_2$ subalgebra of $\mathfrak{g}$. By a gauge transformation we may always set $\mathcal{A}_{\bar{z}}$ to zero, allowing us to represent the flat connection on C we get at each y as a local system $(\mathcal{E}_y, \nabla'_y)$ consisting of a holomorphic bundle and a holomorphic connection $\nabla'_y = dz(\partial_z + \mathcal{A}_z(z;y))$. In the case $\mathfrak{g} = \mathfrak{sl}_2$, we may reformulate the first condition in (6.4) as the condition that there exists a basis of sections $s = \{s_1, s_2\}$ with respect to which $\mathcal{A}$ has the form $\mathcal{A} = g\tilde{\mathcal{A}}g^{-1} + gdg^{-1}$, with

$$\tilde{\mathcal{A}}_z \underset{y\to 0}{\sim} \begin{pmatrix} 0 & t \\ 1 & 0 \end{pmatrix} + \mathcal{O}(y^1)\,, \qquad g \underset{y\to 0}{\sim} \begin{pmatrix} y^{1/2} & 0 \\ 0 & y^{-1/2} \end{pmatrix} + \mathcal{O}(y^0). \tag{6.5}$$

Horizontal sections $(d + \mathcal{A})s = 0$ will then have a first component s_1 vanishing as $y^{1/2}$. As explained in [17], this implies that the local system $\lim_{y\to 0}(\tilde{\mathcal{E}}_y, \tilde{\nabla}'_y)$ on C is an oper.

The Nahm pole boundary condition has the feature that it breaks G_c maximally since the commutant of the principal $\mathfrak{sl}_2$-embedding is trivial. At the opposite extreme, associated to the trivial $\mathfrak{sl}_2$-embedding, one gets a similar boundary condition associated to a triple $(0, \mathrm{Id}, T_\emptyset)$ by fixing the boundary value of the gauge field $\mathcal{A}_{\bar{z}}$.

In the reduction to two dimensions having fixed $\mathcal{A}_{\bar{z}}$ at the boundary of I implies having fixed a holomorphic bundle on C, leaving the $(1,0)$ part of the complex gauge field unconstrained. The moduli space $\mathcal{M}_{dR}(G)$ of pairs $(\mathcal{E}, \nabla'_\zeta)$ is isomorphic to the Hitchin moduli space $\mathcal{M}_H(G)$ via the non-abelian Hodge (NAH) correspondence[g]. Fixing $\mathcal{E}$ therefore defines a submanifold in $\mathcal{M}_H(G)$ which is Lagrangian with respect to the holomorphic symplectic form Ω_ζ, and holomorphic w.r.t. to the complex structure I_ζ. For $\zeta = i$ one has $\Omega_\zeta = \Omega_J$, $I_\zeta = J$, leading to the identification of the brane coming from the reduction of the zero Nahm pole boundary condition as an (A,B,A)-brane in the A-model with the symplectic structure ω_I used in [2].

One may then argue that the $\mathcal{H}^{(2)}_x = \mathrm{Hom}_{\mathcal{M}_H(G)}(\mathsf{B}_{\mathrm{cc}}, \mathsf{L}^{(2)}_x)$ can be identified with the space of conformal blocks of the affine Lie algebra $\hat{\mathfrak{g}}_k$ at level $k = -h^\vee - \frac{\epsilon_2}{\epsilon_1}$ on C. Different arguments leading to this identification have been presented in [4] and in [20], respectively.

From the point of view of class $\mathcal{S}$-theories it has been pointed out in [4] that the zero Nahm pole boundary condition corresponds to the presence of a surface operator of co-dimension two. Indeed, as was argued in [21], the presence of a co-dimension two surface operator naturally introduces additional background data which can be geometrically represented as the choice of a holomorphic bundle on C.

6.2 Conformal blocks as triangle partition functions

We now describe yet another key extension of the TQFT formalism proposed in [4]. Using the reduction of class $\mathcal{S}$-theories to the two-dimensions we will in the following motivate a description of the four-dimensional partition functions of class $\mathcal{S}$-theories within the two-dimensional sigma model with target $\mathcal{M}_H(G)$. This description will use yet another type of boundary condition denoted $\mathsf{L}^{(1)}_a$.

Following [2] we will consider topologically twisted class $\mathcal{S}$-theories on hemispheres $B^4_{\epsilon_1\epsilon_2}$ with Omega-deformation. The topologically twisted class $\mathcal{S}$-theory associates a vector space

$\mathcal{H}_{\rm top} = Z(M^3_{\epsilon_1\epsilon_2})$ to $M^3_{\epsilon_1\epsilon_2} = \partial B^4_{\epsilon_1\epsilon_2}$, here identified with the cohomology of Q, the supercharge that can be preserved on $B^4_{\epsilon_1\epsilon_2}$. One may use the path integral over the 4d hemisphere $B^4_{\epsilon_1\epsilon_2}$ to define a vector $\Psi \in \mathcal{H}_{\rm top}$. Wave-functions $\Psi(a)$ of the vector Ψ may be identified with the partition functions $Z(B^4_{\epsilon_1,\epsilon_2}; \mathsf{B}_a)$ defined by imposing suitable Q-invariant boundary conditions B_a labelled by parameters a at $M^3_{\epsilon_1\epsilon_2}$. Such boundary conditions are determined by the boundary conditions at the infinity of $\mathbb{R}^4_{\epsilon_1\epsilon_2}$ used to define the Nekrasov partition functions, fixing in particular the zero modes of the scalars in the vector multiplets to have values collected in the vector $a = (a_1, \ldots, a_{3g-3+n})$. The boundary conditions B_a define a family of boundary states β_a, allowing us to represent $Z(B^4_{\epsilon_1,\epsilon_2}; \mathsf{B}_a)$ as an overlap $\langle \beta_a, \Psi \rangle$.

In the reduction of the class $\mathcal{S}$-theory to a $2d$ topological sigma model one should get the following representation of the 4d TQFT data introduced above:

- The vector space $\mathcal{H}_{\rm top} \simeq Z(S^3_{\epsilon_1,\epsilon_2}) \to Z(I)$.
- The vector $\Psi = Z(B^4_{\epsilon_1,\epsilon_2}) \to Z(T_{\epsilon_1,\epsilon_2}) \in \mathcal{H}_{\rm top}$, where $T_{\epsilon_1,\epsilon_2}$ is the open triangle with "upper" side removed, topologically equivalent to $\mathbb{R}_- \times I$, partially compactified by adding a point at the infinity of $\mathbb{R}_-$. The boundary of $T_{\epsilon_1,\epsilon_2}$ is $\{0\} \times I$.
- The partition function $Z(B^4_{\epsilon_1,\epsilon_2}; \mathsf{B}_a) \to Z(T_{\epsilon_1,\epsilon_2}; \mathsf{B}_a)$ gets associated to a triangle $T_{\epsilon_1,\epsilon_2}$ with a boundary condition $\mathsf{L}^{(1)}_a$ assigned to the upper side $\{0\} \times I$. $\mathsf{L}^{(1)}_a$ is defined from the boundary condition B_a assigned to $M^3_{\epsilon_1\epsilon_2}$ by the reduction to one dimension.

This means that the instanton partition functions $\mathcal{Z}(a; x; \tau; \epsilon_1, \epsilon_2)$ get represented by partition functions of the sigma model on a triangle which has sides coloured by $(\mathsf{B}_{\rm cc}, \mathsf{L}^{(1)}_a, \mathsf{L}^{(2)}_x)$.

The two-dimensional description of the boundary conditions $\mathsf{L}^{(1)}_a$ has been indentified in [4] as the family of Lagrangian submanifolds defined by identifying the parameters a with complex Fenchel–Nielsen coordinates for Hitchin's moduli spaces[g].

6.3 Geometric Langlands: CFT versus gauge theory

Having established the interpretation of conformal blocks in terms of TQFT prepares the groundwork for understanding the relations between the Beilinson–Drinfeld approach to the geometric Langlands correspondence and the work of Kapustin and Witten [4]. To understand the full picture it is important, however, to note that the geometric Langlands correspondence can be regarded as a limiting case of a one-parameter family of relations between $\mathcal{D}$-modules on Bun_G and $\mathcal{D}$-modules on $\mathrm{Bun}_{^L G}$ related to a generalisation of WZW conformal field theory having affine Lie algebra symmetry $\hat{\mathfrak{g}}_k$ with generic level k [22, 23]. This one-parameter generalisation of the geometric Langlands correspondence has a counterpart on the gauge theory side discussed in [1, 24].

Part of our work in [4] is a careful discussion of how this continuation with respect to the level can be understood from the point of view of the topological sigma model. The discussion is based on the hyperkähler structure of the Hitchin moduli space. We refer to [4] for further details.

7 Boundary line operators

Part of the rich structure of an four-dimensional TQFT is the category of boundary line operators, one-dimensional extended objects supported on three-dimensional boundary components

of the four-dimensional space-time. The category $\mathcal{L}_\hbar(\mathsf{B})$ of boundary line operators depends on the choice of a boundary condition B and the parameter $\hbar = \epsilon_1/\epsilon_2$. The structure of a four-dimensional TQFT includes the structure of a braided tensor category on $\mathcal{L}_\hbar(\mathsf{B})$. For TQFT like topologically twisted $\mathcal{N} = 4$ SYM one may expect to find a rich family of categories $\mathcal{L}_\hbar(\mathsf{B})$ when the boundary conditions are varied. The resulting picture remains largely unexplored. Very subtle are in particular the cases where $\hbar = \epsilon_1/\epsilon_2$ is a rational number. In this case one can see indications both from topologically twisted $\mathcal{N} = 4$ SYM [20] and from the representation theory of vertex algebras that the precise relation between the category $\mathcal{L}_\hbar(\mathsf{B})$ and representation categories of suitable vertex algebras must be very interesting.

In the following we will briefly describe results obtained within the project A10 that can be regarded as first steps in this direction. These will be followed by a short description of a result from [4] giving a dual interpretation of the boundary line operators representing the Hecke functors in the geometric Langlands correspondence according to [1] in the context of the AGT-correspondence.

7.1 Non semi-simple braided tensor categories

For special non-generic values of the quotient ϵ_1/ϵ_2, the analytic continuation of the usual 3-point-functions becomes singular, as the representation theory becomes non-semisimple. It is expected that the situation is related to certain logarithmic vertex algebra models, starting with the triplet algebra $\mathcal{W}_{p,p'}$ for $\mathfrak{g} = \mathfrak{sl}_2$.

These vertex algebras are recently an intense subject of study, and their nonsemisimple representation category is conjectured to be equivalent to the representation category of a small quantum group [25–27], i.e. a finite-dimensional quasi-triangular Hopf algebra.

However, this equivalence cannot be an equivalence of *monoidal* categories, as the respective quantum groups may not even admit a braiding, if the deformation parameter is an even root of unity. It was pointed out [28] for the example $\mathfrak{g} = \mathfrak{sl}_2, q = i$ that one should consider instead a quasi-Hopf algebra related to $u_q(\mathfrak{sl}_2)$ to get an equivalence of monoidal categories. The 3-cocycle involved in this quasi-Hopf algebra also appears in the corresponding conformal field theory.

Within this project, a PhD student has analyzed systematically [29] the existence and nondegeneracy of braidings for quantum groups $u_q(\mathfrak{g})$ at even order root of unity, which is the case relevant for conformal field theory. This produces many braided tensor categories, including examples that are definitely new. However, only few of them are modular tensor categories, i.e. they obey a non-degeneracy condition on the braiding, and are thus candidates for the chiral data of a conformal field theory. However, given the very explicit form of the results in [29], it was possible [30] to construct explicitly a large family of quasi-Hopf algebra relatives of $u_q(\mathfrak{g})$, which have representation categories that are indeed modular categories. (In fact, these categories appear as a non-semisimple variant of a modularization of the former categories.)

At present, it is still out of reach to prove for a general reductive Lie algebra $\mathfrak{g}$ that the representation categories of these quasi-Hopf algebras are braided equivalent to representation categories of vertex algebras and are thus realized in conformal field theory. Still, it has been shown that the previously mentioned quasi-Hopf algebra is reproduced for $\mathfrak{g} = \mathfrak{sl}_2$. Moreover, for all $\mathfrak{g}$ the 3-cocycle precisely coincides with the one on the CFT side. Put differently, both the Hopf algebra and the vertex algebra admit a functor to the same quadratic space defined by the root lattice of $\mathfrak{g}$. It is an even more challenging question at the time of writing to what extent

these algebraic data appear in descriptions of four-dimensional supersymmetric field theories.

7.2 The Hecke eigenvalue property

A beautiful feature of the approach of Kapustin and Witten is an alternative derivation of the so-called Hecke-eigenvalue property of the $\mathcal{D}$-modules appearing the geometric Langlands correspondence. Part of the work [4] was yet another interpretation of the Hecke-eigenvalue property in relation to the AGT-correspondence, as we will now briefly review.

The reduction of Wilson- and 't Hooft line operators in $\mathcal{N} = 4$ SYM with support on $\mathbb{R} \times \{x\} \times P$, $x \in I$, $P \in C$, to the two dimensional TQFT defines natural functors on the category of branes, inducing modifications of the spaces $\mathcal{H}(\mathsf{B})$. The functors defined in this way are identified in [1] with the Hecke functors in the geometric Langlands correspondence. For some branes B one may represent for each fixed $P \in C$ the resulting modification as the tensor product of $\mathcal{H}(\mathsf{B})$ with a finite-dimensional representation V of ${}^LG$. One says that the brane B satisfies the Hecke eigenvalue property if the family of modifications obtained by varying the point $P \in C$ glues into a local system.

A family of branes F_μ is identified in [1] having this property. The branes F_μ are supported on fibers of Hitchin's torus fibration[g)]. S-duality of $\mathcal{N} = 4$ SYM gets represented within the sigma model with target $\mathcal{M}_H(G)$ as a variant of SYZ mirror symmetry, relating the branes F_μ to branes in the dual sigma model with target $\mathcal{M}_H({}^LG)$ represented by skyscraper sheaves $\check{\mathsf{F}}_\mu$ having pointlike support at $\mu \in \mathcal{M}_H({}^LG)$.

Part of the results presented in [4] is a dual interpretation of the Hecke eigenvalue property in the context of class $\mathcal{S}$ theories. The Wilson- and 't Hooft line operators have a dual representation in this context as surface operators of a specific type defined by coupling certain two-dimensional quantum field theories on a two-dimensional subspace to the four-dimensional class $\mathcal{S}$-theories. The relevant two-dimensional quantum field theories have $(2,2)$ supersymmetry and can be described as gauged linear sigma models (GLSM). It was observed in [4] that the tt^* connection [31] of the GLSM turns in the limit $\epsilon_2 \to 0$ into the oper connection appearing on one side of the geometric Langlands correspondence. The limit $\epsilon_2 \to 0$ furthermore implies a factorisation of the partition functions into a four-dimensional part and a two-dimensional part. This factorisation directly expresses the Hecke eigenvalue property of the geometric Langlands correspondence in the dual picture in terms of class $\mathcal{S}$ theories [4].

A Hitchin's moduli spaces

We assume that $G = SL(2)$, and that C is a Riemann surface with genus g and n punctures.

Hitchin moduli space $\mathcal{M}_H(G)$ [32]. Moduli space of pairs $(\mathcal{E}, \varphi)$, where $\mathcal{E} = (E, \bar\partial_{\mathcal{E}})$ is a holomorphic structure on a smooth vector bundle E, and $\varphi \in H^0(C, \mathrm{End}(\mathcal{E}) \otimes K)$. The moduli space of such pairs modulo natural gauge transformations is denoted by $\mathcal{M}_H(G)$.

Hitchin's integrable system [32]. Given $(\mathcal{E}, \varphi)$ one constructs the spectral curve $\Sigma = \{(u,v); v^2 = \frac{1}{2}\mathrm{tr}(\varphi^2)\} \subset T^*C$, and the line bundle $\mathcal{L}$ representing the cokernel of $\varphi - v$. One may reconstruct $(\mathcal{E}, \varphi)$ from $(\Sigma, \mathcal{L})$ as $\mathcal{E} = \pi_*(\mathcal{L})$ and $\varphi = \pi_*(v)$. This describes $\mathcal{M}_H(G, C)$ as a torus fibration over the base $\mathcal{B} \simeq H^0(C, K^2)$, with fibres representing the choices of $\mathcal{L}$ identified with the Jacobian of Σ if $G = GL(2)$, and with the Prym variety if $G = SL(2)$. Natural coordinates for the base $\mathcal{B}$ are provided by Hitchin's Hamiltonians, defined by expanding $\frac{1}{2}\mathrm{tr}(\varphi^2) = \sum_{r=1}^{3g-3+n} \vartheta_r H_r$, with $\{\vartheta_r, r = 1, \ldots, 3g-3+n\}$ being a basis for $H^0(C, K^2)$.

Local systems. Pairs $(\mathcal{E}, \nabla'_\epsilon)$, where $\mathcal{E}$ is a holomorphic vector bundle as above, and ∇'_ϵ is a holomorphic ϵ-connection, satisfying $\nabla'_\epsilon(fs) = \epsilon(\partial f)s + f\nabla'_\epsilon s$ for functions f and smooth sections s of E. The moduli space of such pairs is denoted $\mathcal{M}_{dR}(G)$. Local systems are here often identified with the corresponding *flat bundles*, systems of local trivialisations with constant transitions functions, or the representations of the fundamental group (modulo conjugation) obtained as holonomy of $(\mathcal{F}, \nabla'_\epsilon)$, leading to the isomorphism between $\mathcal{M}_{dR}(G)$ and the

Character variety $\mathcal{M}_B(G)$: The space of representations of $\pi_1(C)$ into G, modulo overall conjugation, as algebraic variety described as a GIT quotient $\mathbb{C}[\mathrm{Hom}(\pi_1(C), G]^G$.

Opers. Special local systems, where $\mathcal{E} = \mathcal{E}_{\mathrm{op}}$, the unique extension $0 \to K^{1/2} \to \mathcal{E}_{\mathrm{op}} \to K^{-1/2} \to 0$ allowing a holomorphic connection ∇'_ϵ of the form $\nabla'_\epsilon = dz\big(\epsilon\partial_z + \left(\begin{smallmatrix} 0 & u \\ 1 & 0 \end{smallmatrix}\right)\big)$.

Non-Abelian Hodge (NAH) correspondence [32,33]. Given a Higgs pair $(\mathcal{E}, \varphi)$, there exists a unique harmonic metric h on E satisfying $F_{\mathcal{E},h} + R^2[\varphi, \varphi^{\dagger_h}] = 0$ where $F_{\mathcal{E},h}$ is the curvature of the unique h-unitary connection $D_{\mathcal{E},h}$ having $(0,1)$-part $\bar\partial_{\mathcal{E}}$. One may then form the corresponding two-parameter family of flat connections $\nabla_{\zeta,R} = \zeta^{-1}R\,\varphi + D_{\mathcal{E},h} + R\zeta\,\varphi^{\dagger_h}$. Decomposing $\nabla_{\zeta,R}$ into the $(1,0)$ and $(0,1)$-parts defines a pair $(\mathcal{F}, \nabla'_\epsilon)$ consisting of $\mathcal{F} = (E, \bar\partial_{\mathcal{F}})$ and the ϵ-connection $\nabla'_\epsilon = \epsilon\nabla' = \epsilon\partial_{\mathcal{E},h} + \varphi$, with $\epsilon = \zeta/R$, holomorphic in the complex structure defined by $\bar\partial_{\mathcal{F}}$.

Hyperkähler structure [32]. There exists a $\mathbb{P}^1$ worth of complex structures I_ζ and holomorphic symplectic structures Ω_ζ. The latter are defined as $\Omega_\zeta = \frac{1}{2}\int_C \mathrm{tr}(\delta\mathcal{A}_\zeta \wedge \delta\mathcal{A}_\zeta)$. A triplet of symplectic forms $(\omega_I, \omega_J, \omega_K)$ can be defined by expanding Ω_ζ as $\Omega_\zeta = \frac{1}{2\zeta}(\omega_J + i\omega_K) + i\omega_I + \frac{1}{2}\zeta(\omega_J - i\omega_K)$. The corresponding complex structures are $I_\zeta = \frac{1}{1+|\zeta|^2}((1-|\zeta|^2)I - i(\zeta - \bar\zeta)J - (\zeta + \bar\zeta)K)$.

Complex Fenchel–Nielsen coordinates [34]. Darboux coordinates for $\mathcal{M}_B(G)$ associated to pants decompositions σ of C obtained by cutting along closed curves γ_i, $i = 1, \ldots, 3g-3+n$. The complex length coordinates parameterise the trace functions $L_i = \mathrm{tr}(\rho(\gamma_i))$ as $L_r = 2\cosh(a_r/2)$. One may define canonically conjugate coordinates κ_r such that the natural Poisson structure gets represented as $\{a_r, \kappa_s\} = \delta_{r,s}$, $\{a_r, a_s\} = 0 = \{\kappa_r, \kappa_s\}$.

References

[1] A. Kapustin and E. Witten, *Electric-Magnetic Duality And The Geometric Langlands Program*, *Commun. Num. Theor. Phys.* **1** (2007) 1–236, [hep-th/0604151].

[2] N. Nekrasov and E. Witten, *The Omega Deformation, Branes, Integrability, and Liouville Theory*, *JHEP* **1009** (2010) 092, [1002.0888].

[3] D. S. Freed, *The cobordism hypothesis*, *Bull. Amer. Math. Soc.* **50** (2013) 57–92, [1210.5100].

[4] A. Balasubramanian and J. Teschner, *Supersymmetric field theories and geometric Langlands: The other side of the coin*, in *Proceedings of Symposia in Pure Mathematics*, vol. 98, pp. 79–105, 2018, 1702.06499.

[5] A. Kapustin, *Topological Field Theory, Higher Categories, and Their Applications*, in *Proceedings of the International Congress of Mathematicians (ICM 2010) Hyderabad, India, August 19-27, 2010*, pp. 2021–2043, World Scientific, 2010, 1004.2307, DOI.

[6] D. Gaiotto, *Surface Operators in N = 2 4d Gauge Theories*, *JHEP* **11** (2012) 090, [0911.1316].

[7] D. Gaiotto, G. W. Moore and A. Neitzke, *Wall-crossing, Hitchin systems, and the WKB approximation*, *Adv. Math.* **234** (2013) 239–403.

[8] D. Arinkin and D. Gaitsgory, *Singular support of coherent sheaves and the geometric langlands conjecture*, *Selecta Mathematica* **21** (2015) 1–199.

[9] B. Feigin and E. Frenkel, *Affine Kac-Moody algebras at the critical level and Gelfand-Dikii algebras*, *Int. J. Mod. Phys.* **A7,** Suppl. 1A (1992) 197–215.

[10] E. Frenkel, *Lectures on the langlands program and conformal field theory*, in *Frontiers in Number Theory, Physics, and Geometry II* (P. Cartier, P. Moussa, B. Julia and P. Vanhove, eds.), pp. 387–533. Springer Berlin Heidelberg, Berlin, Heidelberg, 2007. hep-th/0512172. DOI.

[11] D. Arinkin, *Irreducible connections admit generic oper structures*, *ArXiv e-prints* (Feb., 2016) , [1602.08989].

[12] D. Gaitsgory, *Outline of the proof of the geometric Langlands conjecture for GL_2*, *Astérisque* (2015) 1–112.

[13] D. Ben-Zvi and D. Nadler, *Betti Geometric Langlands*, *ArXiv e-prints* (June, 2016) , [1606.08523].

[14] L. F. Alday, D. Gaiotto and Y. Tachikawa, *Liouville Correlation Functions from Four-dimensional Gauge Theories*, *Lett.Math.Phys.* **91** (2010) 167–197, [0906.3219].

[15] E. Witten, *Geometric Langlands From Six Dimensions*, 0905.2720.

[16] D. Gaiotto and E. Witten, *Supersymmetric Boundary Conditions in N=4 Super Yang-Mills Theory*, *J. Statist. Phys.* **135** (2009) 789–855, [0804.2902].

[17] D. Gaiotto and E. Witten, *Knot Invariants from Four-Dimensional Gauge Theory*, *Adv. Theor. Math. Phys.* **16** (2012) 935–1086, [1106.4789].

[18] D. Gaiotto and E. Witten, *S-Duality of Boundary Conditions In N=4 Super Yang-Mills Theory*, *Adv. Theor. Math. Phys.* **13** (2009) 721–896, [0807.3720].

[19] D. Gaiotto and M. Rapčák, *Vertex Algebras at the Corner*, 1703.00982.

[20] E. Frenkel and D. Gaiotto, *Quantum Langlands dualities of boundary conditions, D-modules, and conformal blocks*, 1805.00203.

[21] E. Frenkel, S. Gukov and J. Teschner, *Surface Operators and Separation of Variables*, *JHEP* **01** (2016) 179, [1506.07508].

[22] D. Gaitsgory, *Twisted whittaker model and factorizable sheaves*, *Selecta Math. (N.S.)* **13** (2008) 617–59.

[23] J. Teschner, *Quantization of the Hitchin moduli spaces, Liouville theory, and the geometric Langlands correspondence I*, *Adv. Theor. Math. Phys.* **15** (2011) 471–564, [1005.2846].

[24] A. Kapustin, *A Note on Quantum Geometric Langlands Duality, Gauge Theory, and Quantization of the Moduli Space of Flat Connections*, 0811.3264.

[25] B. L. Feigin, A. M. Gainutdinov, A. M. Semikhatov and I. Yu. Tipunin, *Kazhdan-Lusztig correspondence for the representation category of the triplet W-algebra in logarithmic CFT*, *Theor. Math. Phys.* **148** (2006) 1210–1235, [math/0512621]. [Teor. Mat. Fiz.148,398(2006)].

[26] K. Nagatomo and A. Tsuchiya, *The triplet vertex operator algebra $\sqsupseteq(p)$ and the restricted quantum group $u_q(\mathfrak{sl}_2)$ at $q = e^{i\pi}$*, *Adv. Stud. Pure Math* **61** (2011) 1–49.

[27] S. D. Lentner, *Quantum groups and Nichols algebras acting on conformal field theories*, 1702.06431.

[28] A. M. Gainutdinov and I. Runkel, *Symplectic fermions and a quasi-Hopf algebra structure on $\bar{U}_i sl(2)$*, *J. Algebra* **476** (2017) 415–458, [1503.07695].

[29] S. Lentner and T. Ohrmann, *Factorizable R-Matrices for Small Quantum Groups*, *SIGMA* **13** (2017) 076, [1612.07960].

[30] A. M. Gainutdinov, S. Lentner and T. Ohrmann, *Modularization of small quantum groups*, 1809.02116.

[31] S. Cecotti and C. Vafa, *Topological antitopological fusion*, *Nucl. Phys.* **B367** (1991) 359–461.

[32] N. J. Hitchin, *The self-duality equations on a Riemann surface*, *Proc. London Math. Soc. (3)* **55** (1987) 59–126.

[33] C. Simpson, *Higgs bundles and local systems*, *Publ. Math. IHES* **75** (1992) 5–95.

[34] N. Nekrasov, A. Rosly and S. Shatashvili, *Darboux coordinates, Yang-Yang functional, and gauge theory*, *Nucl. Phys. Proc. Suppl.* **216** (2011) 69–93, [1103.3919].

Integrable Deformations of the AdS Superstring and their Dual Gauge Theories

Gleb Arutyunov[1], *Ingo Runkel*[2] *and Jörg Teschner*[2,3]

[1]II. Institut für Theoretische Physik, Universität Hamburg, Germany
[2]Fachbereich Mathematik, Universität Hamburg, Germany
[3]DESY, Hamburg, Germany

DOI: http://dx.doi.org/10.3204/PUBDB-2018-00782/A11

We study a new class of two-dimensional field theories which are integrable deformations of the string sigma model on $\mathrm{AdS}_5 \times S^5$. We show that some of these theories are scale but not Weyl invariant. For the real deformation parameter we find the quantum spectral curve equations which encode the energy spectrum. More generally, we investigate a relation between integrable deformations of CFTs and functional equations as well as lattice integrable discretisations based on the universal R-matrix.

1 Introduction

In recent years significant progress has been made towards understanding the excitation spectrum of strings moving in five-dimensional anti-de Sitter space-time and, accordingly, the spectrum of scaling dimensions of composite operators in planar $\mathcal{N} = 4$ supersymmetric gauge theory. This progress became possible due to the fundamental insight that strings propagating in AdS space can be described by an integrable model. In certain aspects, however, the deep origin of this exact solvability has not yet been unraveled, mainly because of tremendous complexity of the corresponding model. A related question concerns robustness of integrability in the context of the gauge-string correspondence [1], as well as the relationship between integrability and the amount of global (super)symmetries preserved by the target space-time in which strings propagate. To shed further light on these important issues, one may attempt to search for new examples of integrable string backgrounds that can be solved by similar techniques. One such instance, where this program is largely promising to succeed, is to study various deformations of the string target space that preserve the integrability of the two-dimensional quantum field theory on the world sheet. Simultaneously, this should provide interesting new information about integrable string models and their dual gauge theories.

There are two known classes of integrable deformations of the $\mathrm{AdS}_5 \times S^5$ superstring. The first of these is a class of backgrounds obtained either by orbifolding $\mathrm{AdS}_5 \times S^5$ by a discrete subgroup of the corresponding isometry group or by applying a sequence of T-duality – shift – T-duality transformations (also known as γ-deformations) to this space, giving a string theory on a TsT-transformed background. Eventually all deformations of this class can be conveniently described in terms of the original string theory, where the deformations result into quasi-periodic but still integrable boundary conditions for the world-sheet fields.

The second class of deformations affects the $\mathrm{AdS}_5 \times S^5$ model on a much more fundamental level and is related to deformations of the underlying symmetry algebra. In the light-cone gauge this symmetry algebra constitutes two copies of the centrally extended Lie superalgebra $\mathfrak{psu}(2|2)$ with the same central extension for each copy. It appears that this centrally extended $\mathfrak{psu}(2|2)$, or more precisely its universal enveloping algebra, admits a natural deformation $\mathfrak{psu}_q(2|2)$ in the sense of quantum groups. This algebraic structure is the starting point for the construction of a $\mathfrak{psu}_q(2|2) \oplus \mathfrak{psu}_q(2|2)$-invariant S-matrix, giving a quantum deformation of the $\mathrm{AdS}_5 \times S^5$ world-sheet S-matrix [2]. The deformation parameter q can be an arbitrary complex number, but in physical applications is typically taken to be either real or a root of unity.

Some time ago there was an interesting proposal on how to deform the sigma-model for strings on $\mathrm{AdS}_5 \times S^5$ with a real deformation parameter η, preserving classical integrability [3, 4]. In the following we call these models η-deformed and we will talk about η-deformations. Deformations of this type constitute a general class of deformations governed by solutions of the classical Yang–Baxter equation [5]. This class is not solely restricted to the string model in question but includes a large variety of two-dimensional integrable models based on (super)groups or their cosets.

The paper is organised as follows. In the next three sections we summarise the main results of our investigation of the η-deformed string sigma models and discuss a number of important related issues. We concentrate on three directions – the η-deformed background, the access to the spectrum of the model via the quantum spectral curve and finite-dimensional integrable systems obtained through various reductions of the sigma model. In section 5 we address a more general problem on finding perturbations of CFTs which preserve integrability and also investigate a vital question on uniqueness of solutions of functional equations that suppose to encode the spectrum of a deformed CFT. Finally, in section 6, aiming at developing direct quantisation tools for world-sheet theories, including string sigma model on $\mathrm{AdS}_5 \times S^5$ and its deformations, we consider lattice discretisations of integrable systems in the formalism of the universal R-matrix. Importantly, we outline a general program of constructing such integrable discretisations and solving the corresponding spectral problem. The results presented in sections 5 and 6 constitute a continuation of the research line of the former SFB project A8.

2 The nature of the deformed background

Recall that the Lagrangian density of the η-deformed model is given by [3]

$$\mathscr{L} = -\frac{g}{4}(1+\eta^2)\big(\gamma^{\alpha\beta} - \epsilon^{\alpha\beta}\big)\,\mathrm{str}\Big[\tilde{d}(A_\alpha)\frac{1}{1-\eta R_{\mathfrak{g}} \circ d}(A_\beta)\Big]\,.$$

We use the notations and conventions from [6], in particular g is the effective string tension. The current $A_\alpha = -\mathfrak{g}^{-1}\partial_\alpha \mathfrak{g}$, where $\mathfrak{g} \equiv \mathfrak{g}(\tau,\sigma)$ is a coset representative from $\mathrm{PSU}(2,2|4)/\mathrm{SO}(4,1) \times \mathrm{SO}(5)$. The operators d and $\tilde{d}$ acting on the currents A_α are defined as

$$d \;=\; P_1 + \frac{2}{1-\eta^2}P_2 - P_3, \qquad\qquad \tilde{d} = -P_1 + \frac{2}{1-\eta^2}P_2 + P_3\,,$$

where P_i, $i = 0,1,2,3$, are projections on the corresponding components of the $\mathbb{Z}_4$-graded decomposition of the superalgebra $\mathscr{G} = \mathfrak{psu}(2,2|4)$. The operator $R_{\mathfrak{g}}$ acts on $M \in \mathscr{G}$ as follows

$$R_{\mathfrak{g}}(M) = \mathfrak{g}^{-1} R(\mathfrak{g} M \mathfrak{g}^{-1})\mathfrak{g}\,,$$

where R is a linear operator on $\mathscr{G}$ which in this paper we define as

$$R(M)_{ij} = -i\,\tau_{ij}M_{ij}\,, \quad \tau_{ij} = \begin{cases} 1 & \text{if} \quad i<j \\ 0 & \text{if} \quad i=j \\ -1 & \text{if} \quad i>j \end{cases}\,,$$

where M is an arbitrary 8×8 matrix. This choice of R corresponds to the standard Dynkin diagram of $\mathfrak{psu}(2,2|4)$.

The η-deformed model appears to be rather involved, primarily because of fermionic degrees of freedom. The strategy is therefore to first switch off fermions and proceed by studying the corresponding bosonic action. This action can be further used to determine $2\to 2$ scattering matrix for the η-deformed model in the limit of large string tension g and to compare the corresponding result with the known q-deformed S-matrix found from quantum group symmetries, unitarity and crossing [2]. Of course, the perturbative S-matrix computed from this action will not coincide with the full world-sheet S-matrix but nevertheless will give a sufficient part of the scattering data to provide a non-trivial test for both integrability (the Yang–Baxter equation) and a comparison with the q-deformed S-matrix.

This preliminary work has been carried out in [6], where it was shown that for a particular choice of the bosonic coset element the η-deformed metric G and the B-field (NSNS background) can be written in the form

$$\begin{aligned}
\frac{1}{\tilde g}ds^2_{\mathfrak{a}} =& -\frac{dt^2\left(1+\rho^2\right)}{1-\varkappa^2\rho^2}+\frac{d\rho^2}{\left(1+\rho^2\right)\left(1-\varkappa^2\rho^2\right)}\\
&+\frac{d\zeta^2\rho^2}{1+\varkappa^2\rho^4\sin^2\zeta}+\frac{d\psi_1^2\rho^2\cos^2\zeta}{1+\varkappa^2\rho^4\sin^2\zeta}+d\psi_2^2\rho^2\sin^2\zeta\,,\\
\frac{1}{\tilde g}ds^2_{\mathfrak{s}} =& \frac{d\phi^2\left(1-r^2\right)}{1+\varkappa^2r^2}+\frac{dr^2}{\left(1-r^2\right)\left(1+\varkappa^2r^2\right)}\\
&+\frac{d\xi^2r^2}{1+\varkappa^2r^4\sin^2\xi}+\frac{d\phi_1^2r^2\cos^2\xi}{1+\varkappa^2r^4\sin^2\xi}+d\phi_2^2r^2\sin^2\xi\,,\\
\frac{1}{\tilde g}B =& \varkappa\left(\frac{\rho^4\sin 2\zeta}{1+\varkappa^2\rho^4\sin^2\zeta}d\psi_1\wedge d\zeta-\frac{r^4\sin 2\xi}{1+\varkappa^2r^4\sin^2\xi}d\phi_1\wedge d\xi\right)\,,
\end{aligned}$$

where $\varkappa=\frac{2\eta}{1-\eta^2}$ and $\tilde g = g\sqrt{1+\varkappa^2}$. This metric corresponds to a product of two five-dimensional spaces with coordinates $\{t,\rho,\zeta,\psi_1,\psi_2\}$ and $\{\phi,r,\xi,\phi_1,\phi_2\}$ respectively. The range of ρ is restricted to $[0,1/\varkappa)$ to preserve the time-like nature of t, with a curvature singularity at $\rho=1/\varkappa$. At $\varkappa=0$ there is no singularity but rather the conformal boundary of anti-de Sitter space at $\rho=\infty$. The bosonic two-body S-matrix computed from this action perfectly coincides with the large tension limit of the exact S-matrix based on the $\mathfrak{psu}_q(2|2)$ symmetry [6].

The next step is to clarify an important question of whether or not the η-deformed model is a type IIB string sigma model. As we will show, the answer turns out to be negative.

One way to approach this question would be to try to find an embedding of the given NSNS background into a full solution of type IIB supergravity. Given the complexity of the NSNS background, this appears however a rather difficult task. First of all the equation for the dilaton has many solutions and also many components of the RR forms seem to be switched on. Even if successful, this approach does not however guarantee that the string sigma model in the corresponding supergravity background will actually coincide with a deformed model.

Another way to proceed is to note that the Green–Schwarz (GS) action restricted to quadratic order in fermions contains all the information about the background fields. The corresponding Lagrangian has the form, see *e.g.* [7],

$$\mathscr{L}_{\Theta^2} = -\frac{g}{2}\, i\, \bar{\Theta}_I\, (\gamma^{\alpha\beta}\delta^{IJ} + \epsilon^{\alpha\beta}\sigma_3^{IJ}) e_\alpha^m \Gamma_m\, D_\beta^{JK} \Theta_K,$$

where Θ_I are two Majorana–Weyl fermions of the same chirality. The operator D_α^{IJ} acting on fermions has the following expression

$$\begin{aligned} D_\alpha^{IJ} =& \delta^{IJ}\left(\partial_\alpha - \frac{1}{4}\omega_\alpha^{mn}\Gamma_{mn}\right) + \frac{1}{8}\sigma_3^{IJ} e_\alpha^m H_{mnp}\Gamma^{np} \\ & - \frac{1}{8} e^\phi \left(\epsilon^{IJ}\Gamma^p F_p^{(1)} + \frac{1}{3!}\sigma_1^{IJ}\Gamma^{pqr}F_{pqr}^{(3)} + \frac{1}{2\cdot 5!}\epsilon^{IJ}\Gamma^{pqrst}F_{pqrst}^{(5)}\right) e_\alpha^m \Gamma_m\,, \end{aligned}$$

where (e, ω, H) constitute a vielbein, the spin connection and the field strength of a B-field, while F's are RR forms and ϕ is a dilaton. Note that the dilaton and RR forms appear only through the combination $\mathcal{F}_n = e^\phi F_n$. Our approach is therefore to work out the quadratic fermionic action starting from the η-deformed action of [3] and find a field redefinition which brings this action into the GS canonical form above. This would allow us to identify the background fields and further check if they satisfy the equations of motion of type IIB supergravity and, in particular, to find a solution for the dilaton.

Performing the corresponding calculations, we arrive at the following result for non-vanishing RR forms written with *flat* indices of the tangent space [8]

$$\begin{aligned}
&\mathcal{F}_1 = -4\varkappa^2\ c_F^{-1}\ \rho^3 \sin\zeta, && \mathcal{F}_6 \ = +4\varkappa^2\ c_F^{-1}\ r^3 \sin\xi, \\
&\mathcal{F}_{014} = +4\varkappa\ c_F^{-1}\ \rho^2 \sin\zeta, && \mathcal{F}_{123} = -4\varkappa\ c_F^{-1}\ \rho, \\
&\mathcal{F}_{569} = +4\varkappa\ c_F^{-1}\ r^2 \sin\xi, && \mathcal{F}_{678} = -4\varkappa\ c_F^{-1}\ r, \\
&\mathcal{F}_{046} = +4\varkappa^3\ c_F^{-1}\ \rho r^3 \sin\xi, && \mathcal{F}_{236} = -4\varkappa^3\ c_F^{-1}\ \rho^2 r^3 \sin\zeta \sin\xi, \\
&\mathcal{F}_{159} = -4\varkappa^3\ c_F^{-1}\ \rho^3 r \sin\zeta, && \mathcal{F}_{178} = -4\varkappa^3\ c_F^{-1}\ \rho^3 r^2 \sin\zeta \sin\xi, \\
&\mathcal{F}_{01234} = +4\ c_F^{-1}, && \mathcal{F}_{02346} = -4\varkappa^4\ c_F^{-1} \rho^3 r^3 \sin\zeta \sin\xi, \\
&\mathcal{F}_{01459} = +4\varkappa^2\ c_F^{-1} \rho^2 r \sin\zeta, && \mathcal{F}_{01478} = +4\varkappa^2\ c_F^{-1} \rho^2 r^2 \sin\zeta \sin\xi, \\
&\mathcal{F}_{04569} = +4\varkappa^2\ c_F^{-1} \rho r^2 \sin\xi, && \mathcal{F}_{04678} = -4\varkappa^2\ c_F^{-1} \rho r.
\end{aligned}$$

Here we defined the common coefficient

$$c_F = \frac{1}{\sqrt{1+\varkappa^2}}\sqrt{1-\varkappa^2\rho^2}\sqrt{1+\varkappa^2\rho^4\sin^2\zeta}\sqrt{1+\varkappa^2 r^2}\sqrt{1+\varkappa^2 r^4 \sin^2\xi}.$$

For the five-form we presented here only half of all its non-vanishing components, namely those which involve the index 0. The other half is obtained from the self-duality equation for the five-form. The answer appears to be rather simple and in the limit $\varkappa \to 0$ all the components vanish except $\mathcal{F}_{01234}$ which reduces to the constant five-form flux of the $\mathrm{AdS}_5 \times S^5$ background. In the following we will use for the background found above the name "ABF background".

Inspection of the found RR couplings reveals that contrary to the natural expectations they do not obey equations of motion of type IIB supergravity. First of all for the Bianchi identities

this is already obvious from the expression for the 1-form F_1. To fit the supergravity content this form must be exact $F^{(1)} = \mathrm{d}\chi$, where χ is axion. One can verify that there is no way to split off an integrating factor e^{ϕ}, such that the corresponding $F^{(1)}$ becomes exact. Concerning other equations of motion, consider, for instance, the Einstein equations which involve an unknown dilaton. One can show that to achieve vanishing of the off-diagonal components of the Einstein equations the dilaton ϕ *must* be of the form $\phi = \Phi_{\mathfrak{a}}(\rho,\zeta) + \Phi_{\mathfrak{s}}(r,\xi)$, where $\Phi_{\mathfrak{a}}$ and $\Phi_{\mathfrak{s}}$ are some functions. However, analysis of the diagonal components of the Einstein equations shows that a solution for $\Phi_{\mathfrak{a}}$ and $\Phi_{\mathfrak{s}}$ does not exist. The next surprising observation is that the RR couplings do not meet the necessary conditions of the mirror duality [9], and, as a consequence, the mirror background [10] is not reproduced in the expected limit $\eta \to 1$. Although this duality is a symmetry of the exact S-matrix, it involves rescaling of the string tension and therefore its absence in the classical Lagrangian might be explained by the order of limits problem.

While not solving the standard type IIB equations directly this ABF background still turns out to be very special: it is related by T-duality to an exact type IIB supergravity solution [11]. The latter HT background involves a non-diagonal metric $\hat{G}$, an imaginary 5-form $\hat{F}_5$ and the dilaton $\hat{\phi}$, and the T-duality applied in all 6 isometric directions acts only on the fields $\hat{G}$ and $\hat{\mathcal{F}}_5 = e^{\hat{\phi}}\hat{F}_5$ entering the corresponding GS action on a flat 2d background. The GS action for any type II solution (and thus for the HT background) should be Weyl invariant and, in particular, scale invariant. As the T-duality applied to the GS action is a simple path integral transformation, the T-duality relation between the ABF and HT backgrounds implies that the action should define a scale invariant 2d theory at least to 1-loop order.

However, there may be a problem with Weyl invariance for the η-deformed sigma-model on a curved 2d background. The HT dilaton $\hat{\phi}$ has a term linearly depending on the isometric directions of $\hat{G}$ and $\hat{\mathcal{F}}_5$ and thus one cannot directly apply the standard T-duality transformation rules to the full HT background to get a full T-dual supergravity solution, and thus the Weyl invariance of the T-dual sigma model requires further investigation. This is of course consistent with the observation [8] that the ABF background does not satisfy the IIB supergravity equations.

In the work [12] we have found that the ABF background, while not a supergravity solution, satisfies the following two generalisations or "modifications" of the type II supergravity equations:

(i) the scale invariance conditions for the type II superstring sigma model (with equations on the R-R fields $\mathcal{F}$ being of 2nd order in derivatives);

(ii) a set of equations that are structurally similar to those of type II supergravity (with 1st-order equations for the RR fields $\mathcal{F}$) but involving, instead of derivatives of the dilaton, a certain co-vector Z_m playing now the role of the dilaton one-form and a Killing vector I^m responsible for the "modification" of the equations from their standard form.

The conditions of scale invariance for the bosonic NSNS fields have the familiar form involving the β-function for the metric and the B-field

$$\beta^G_{mn} \equiv R_{mn} - \tfrac{1}{4}H_{mkl}H_n{}^{kl} - \mathcal{T}_{mn} = -D_mX_n - D_nX_m \ ,$$
$$\beta^B_{mn} \equiv \tfrac{1}{2}D^kH_{kmn} + \mathcal{K}_{mn} = X^kH_{kmn} + \partial_mY_n - \partial_nY_m \ ,$$

where

$$\mathcal{T}_{mn} \equiv \tfrac{1}{2}\mathcal{F}_m\mathcal{F}_n + \tfrac{1}{4}\mathcal{F}_{mpq}\mathcal{F}_n{}^{pq} + \tfrac{1}{4\times 4!}\mathcal{F}_{mpqrs}\mathcal{F}_n{}^{pqrs} - \tfrac{1}{2}G_{mn}(\tfrac{1}{2}\mathcal{F}_k\mathcal{F}^k + \tfrac{1}{12}\mathcal{F}_{kpq}\mathcal{F}^{kpq}) \ ,$$
$$\mathcal{K}_{mn} \equiv \tfrac{1}{2}\mathcal{F}^k\mathcal{F}_{kmn} + \tfrac{1}{12}\mathcal{F}_{mnklp}\mathcal{F}^{klp} \ .$$

Here $\mathcal{T}_{mn}$ is the stress tensor that follows from the type IIB action upon variation over G_{mn}. For $X_m = \partial_m \phi,\ Y_m = 0$ these equations follow from the standard type IIB supergravity action.

The key observation is that indeed there exist vectors X_m and Y_m such that the equations above are satisfied for the ABF background. The vector X_m turns out to be

$$\begin{aligned} X \equiv X_m dx^m = {} & c_0\,\frac{1+\rho^2}{1-\varkappa^2\rho^2}dt + c_1\,\rho^2\sin^2\zeta\,d\psi_2 + c_2\,\frac{\rho^2\cos^2\zeta}{1+\varkappa^2\rho^4\sin^2\zeta}d\psi_1 \\ & + c_3\,\frac{1-r^2}{1+\varkappa^2 r^2}d\varphi + c_4\,r^2\sin^2\xi\,d\phi_2 + c_5\,\frac{r^2\cos^2\xi}{1+\varkappa^2 r^4\sin^2\xi}d\phi_1 \\ & + \frac{\varkappa^2\rho^4\sin 2\zeta}{2(1+\varkappa^2\rho^4\sin^2\zeta)}d\zeta + \frac{1}{\rho}\big(1 - \frac{3}{1-\varkappa^2\rho^2} + \frac{2}{1+\varkappa^2\rho^4\sin^2\zeta}\big)d\rho \\ & + \frac{\varkappa^2 r^4\sin 2\xi}{2(1+\varkappa^2 r^4\sin^2\xi)}d\xi + \frac{1}{r}\big(1 - \frac{3}{1+\varkappa^2 r^2} + \frac{2}{1+\varkappa^2 r^4\sin^2\xi}\big)dr\ , \end{aligned}$$

and it can be split in the following way

$$X_m = I_m + Z_m\ , \qquad D_m I_n + D_n I_m = 0\ , \qquad D^m I_m = 0\ ,$$

where $I^m = \sum_{i=1}^6 c_i (I^{(i)})^m$. The index i labels the 6 isometric directions $y^i = (t, \psi_2, \psi_1, \varphi, \phi_2, \phi_1)$ of the 10d ABF metric and c_i are arbitrary constant coefficients. The quantities $(I^{(i)})^m$ are the 6 independent commuting Killing vectors of the ABF background: the Lie derivatives of the G, B and $\mathcal{F}$-fields along I^m all vanish. If we split the coordinates as $x^m = (y^i, x^\mu)$ where $\mu = 1, 2, 3, 4$ labels the non-isometric directions $x^\mu = (\zeta, \rho, \xi, r)$, then

$$I_m = \sum_{i=1}^6 \delta^i_m c_i G_{ii}(x^\mu)\ , \qquad I^m = \delta^i_m c_i = \text{const}\ , \qquad Z_m = \delta^\mu_m Z_\mu(x^\nu)\ .$$

For the ABF background the vector Y_m turns out to coincide with X provided we fix c_i to the following specific values

$$c_0 = c_3 = 4\varkappa\ , \qquad c_1 = c_4 = 0\ , \qquad c_2 = -c_5 = 2\varkappa\,.$$

The next surprising observation is that for these specially chosen values of c_i the vector X_m satisfies also a direct generalisation of the dilaton equation

$$\beta^X \equiv R - \tfrac{1}{12}H^2_{mnk} + 4D_k X^k - 4X_k X^k = 0\ .$$

The scale invariance equations for the $\mathcal{F}$-fields (to be discussed later) will not, however, have the familiar supergravity form of 1st-order equations for $\mathcal{F}$ (these should follow from the Weyl invariance conditions). Instead they will be of 2nd order, $D^2\mathcal{F} + ... = X$-dependent terms, and for $X_m = \partial_m\phi$ will be a consequence of the 1st-order supergravity equations.

Now we come to the discussion of the modified type IIB equations for the RR couplings satisfied by the ABF background [12]. Introduce $Z = Z_m dx^m$ and $I = I_m dx^m$. The equations for the one-form are

$$\begin{aligned} & D^m\mathcal{F}_m - Z^m\mathcal{F}_m - \tfrac{1}{6}H^{mnp}\mathcal{F}_{mnp} = 0\ , \qquad I^m\mathcal{F}_m = 0\ , \\ & (d\mathcal{F}_1 - Z\wedge\mathcal{F}_1)_{mn} - I^p\mathcal{F}_{mnp} = 0\ . \end{aligned}$$

We have added the condition $I^m \mathcal{F}_m = 0$ as an independent equation on $\mathcal{F}_1$. Similarly, the equations satisfied for the three-form $\mathcal{F}_3$ are found to be

$$D^p \mathcal{F}_{pmn} - Z^p \mathcal{F}_{pmn} - \tfrac{1}{6} H^{pqr} \mathcal{F}_{mnpqr} - (I \wedge \mathcal{F}_1)_{mn} = 0 \ ,$$
$$(d\mathcal{F}_3 - Z \wedge \mathcal{F}_3 + H_3 \wedge \mathcal{F}_1)_{mnpq} - I^r \mathcal{F}_{mnpqr} = 0 \ .$$

Finally, the equations satisfied by $\mathcal{F}_5$ of the ABF background are

$$D^r \mathcal{F}_{rmnpq} - Z^r \mathcal{F}_{rmnpq} + \tfrac{1}{36} \varepsilon_{mnpqrstuvw} H^{rst} \mathcal{F}^{uvw} - (I \wedge \mathcal{F}_3)_{mnpq} = 0 \ ,$$
$$(d\mathcal{F}_5 - Z \wedge \mathcal{F}_5 + H_3 \wedge \mathcal{F}_3)_{mnpqrs} + \tfrac{1}{6} \varepsilon_{mnpqrstuvw} I^t \mathcal{F}^{uvw} = 0 \ .$$

These two are equivalent in view of the self-duality of $\mathcal{F}_5$.

These modified equations reduce back to the standard type II equations if we drop all terms with I_m and assume that $dZ = 0$, *i.e.* if we set

$$Z_m \to \partial_m \phi \ , \qquad\qquad I_m \to 0 \ .$$

The structure of modified equations supports the interpretation of Z as a generalised "dilaton one-form", while the isometry vector I effectively drives the deformation of the standard type IIB equations.

An interesting observation is that there exist certain combinations of the modified supergravity equations that depend on Z and I only through the combination $X = Z + I$, which entered the NS-NS equations of the previous section. These are found by adding together equations of equal form degree, for example, the equation of motion for the R-R three-form and the Bianchi identity for the R-R one-form. The resulting X-dependent equations are given by

$$D^m \mathcal{F}_m - X^m \mathcal{F}_m - \tfrac{1}{6} H^{mnp} \mathcal{F}_{mnp} = 0 \ ,$$
$$D^p \mathcal{F}_{pmn} - X^p \mathcal{F}_{pmn} - \tfrac{1}{6} H^{pqr} \mathcal{F}_{mnpqr} + (d\mathcal{F}_1 - X \wedge \mathcal{F}_1)_{mn} = 0 \ ,$$
$$D^r \mathcal{F}_{rmnpq} - X^r \mathcal{F}_{rmnpq} + \tfrac{1}{36} \varepsilon_{mnpqrstuvw} H^{rst} \mathcal{F}^{uvw} + (d\mathcal{F}_3 - X \wedge \mathcal{F}_3 + H_3 \wedge \mathcal{F}_1)_{mnpq} = 0 \ .$$

Using the self-duality of $\mathcal{F}_5$ the last equation can be also written as

$$(d\mathcal{F}_5 - X \wedge \mathcal{F}_5 + H_3 \wedge \mathcal{F}_3)_{pqrlmn} - \tfrac{1}{6} \varepsilon_{pqrlmnvstu} (D^v \mathcal{F}^{stu} - X^v \mathcal{F}^{stu} - \mathcal{F}^v H^{stu}) = 0 \ .$$

As will be discussed below, these three equations are already sufficient for deriving candidates for the scale invariance equations for the $\mathcal{F}$-fields, which are 2nd order in derivatives.

Let us return to the discussion of the scale invariance conditions for the couplings of the GS sigma model and consider the equations for the RR couplings $\mathcal{F}$ that should follow from the requirement of (1-loop) UV finiteness of the 2d model. One can argue that the conditions for the G and B-field couplings should have the form

$$\beta^{\mathcal{F}}_{k_1 \dots k_s} \equiv \frac{1}{2} D^2 \mathcal{F}_{k_1 \dots k_s} + \dots = X^m \partial_m \mathcal{F}_{k_1 \dots k_s} + \sum_i \mathcal{F}_{k_1 \dots m \dots k_s} \partial_{k_i} X^m \ ,$$

where we have omitted possible non-linear terms such as $R\mathcal{F} + DH\mathcal{F} + \dots$ on the l.h.s. The X-dependent Lie derivative term on the r.h.s. reflects the reparametrisation (or off-shell x^m-renormalisation) freedom.

For $X_m = \partial_m \phi$ the equation for $\beta^{\mathcal{F}}_{k_1 \dots k_s}$ should be a consequence of stronger Weyl invariance conditions, which should be equivalent to the type II supergravity equations with $Z = X = d\phi$.

Indeed, combining ("squaring") the familiar $dF + ... = 0,\ d \star F + ... = 0$ equations leads to $d \star d \star F + \star d \star dF + ... = 0$ or $D^2 F + ... = 0$, where the leading term is the Hodge–de Rham operator.

Moreover, the same equations should follow also from the modified type II equations (as, e.g., the ABF background that solves the modified equations should also be a solution of the scale invariance conditions). This should provide a non-trivial consistency check: after properly "squaring" the equations of modified supergravity, the dependence on the Z and I vectors in any candidate scale invariance equations should appear only through their sum $X = Z + I$. Note that to be a candidate for the scale invariance conditions these equations should have the following properties:

(i) vanish on the modified supergravity equations with $X = d\phi,\ Y = 0$

(ii) depend on Z and I through $X = Z + I$

(iii) depend on X through Lie derivatives.

Starting with the modified equations and properly acting with $\star d \star$ and $d \star$, we arrive at the equations, which satisfies the above properties. For $\mathcal{F}_1$ we find

$$\begin{aligned} &D^2\mathcal{F}_m - R_{mn}\mathcal{F}^n + \tfrac{1}{4}(R - \tfrac{3}{4}H^2)\mathcal{F}_m \\ &\qquad + \tfrac{1}{2}H^{pnk}H_{mpn}\mathcal{F}_k - \tfrac{1}{6}D_m H^{pnk}\mathcal{F}_{pnk} - \tfrac{1}{2}H^{pnk}D_p\mathcal{F}_{nkm} \\ &= 2(X^p D_p\mathcal{F}_m + D_m X^p \mathcal{F}_p) + \beta^G_{mn}\mathcal{F}^n - \tfrac{1}{2}\beta^B_{nk}\mathcal{F}^{nk}{}_m \ . \end{aligned}$$

The equation for $\mathcal{F}_3$ reads as

$$\begin{aligned} &D^2\mathcal{F}_{nkm} - R_{a[n}\mathcal{F}^a{}_{km]} + R_{ab[nk}\mathcal{F}^{ab}{}_{m]} + \tfrac{1}{4}(R - \tfrac{3}{4}H^2)\mathcal{F}_{nkm} \\ &\quad + \tfrac{1}{2}H^{abc}H_{ab[n}\mathcal{F}_{km]c} - \tfrac{1}{2}H^{abc}H_{a[nk}\mathcal{F}_{m]bc} \\ &\quad + D^a H_{a[nk}\mathcal{F}_{m]} + H_{a[nk}D^a\mathcal{F}_{m]} - \mathcal{F}_a D^a H_{nkm} \\ &\quad - \tfrac{1}{6}D_{[n}H^{abc}\mathcal{F}_{km]abc} - \tfrac{1}{2}H^{abc}D_a\mathcal{F}_{bcnkm} \\ &\qquad = 2(X^a D_a\mathcal{F}_{nkm} + D_{[n}X^a\mathcal{F}_{km]a}) + \beta^G_{a[n}\mathcal{F}^a{}_{km]} + \beta^B_{[nk}\mathcal{F}_{m]} - \tfrac{1}{2}\beta^B_{ab}\mathcal{F}^{ab}{}_{nkm} \ , \end{aligned}$$

while the equation for $\mathcal{F}_5$ is

$$\begin{aligned} &D^2\mathcal{F}_{ijklm} - R_{a[i}\mathcal{F}^a{}_{jklm]} + R_{ab[ij}\mathcal{F}^{ab}{}_{klm]} + \tfrac{1}{4}(R - \tfrac{3}{4}H^2)\mathcal{F}_{ijklm} \\ &\quad + \tfrac{1}{2}H^{abc}H_{ab[i}\mathcal{F}_{jklm]c} - \tfrac{1}{2}H^{abc}H_{a[ij}\mathcal{F}_{klm]bc} \\ &\quad + D^a H_{a[ij}\mathcal{F}_{klm]} + H_{a[ij}D^a\mathcal{F}_{klm]} - \mathcal{F}_{a[ij}D^a H_{klm]} \\ &\quad + \tfrac{1}{12}\varepsilon_{ijklmbdef}(D_a H^{abc}\mathcal{F}^{def} + H^{abc}D_a\mathcal{F}^{def} - \mathcal{F}^{abc}D_a H^{def}) = \\ &\quad = 2(X^a D_a\mathcal{F}_{ijklm} + D_{[i}X^a\mathcal{F}_{jklm]a}) + \beta^G_{a[i}\mathcal{F}^a{}_{jklm]} + \beta^B_{[ij}\mathcal{F}_{klm]} + \tfrac{1}{12}\varepsilon_{ijklmabcde}(\beta^B)^{ab}\mathcal{F}^{cde} \ . \end{aligned}$$

This expression is consistent with the self-duality of $\mathcal{F}_5$ (in particular, the third and fourth lines are manifestly dual to each other).

These 2nd-order equations for $\mathcal{F}_1$, $\mathcal{F}_3$ and $\mathcal{F}_5$ exhibit obvious structural similarities. In particular, they contain the expected Hodge–de Rham operator terms and the vector X only enters through the reparametrisation terms.

In summary, we have suggested the modified supergravity equations that replace the condition of Weyl invariance and proved that they are satisfied by the background fields of the η-deformed theory. We have also derived the equations expressing the conditions of scale invariance and showed that they are satisfied by the corresponding background fields. Thus, the

η-deformed model is a new interesting example of a sigma model which is scale but not Weyl invariant.

3 Quantum spectral curve

As alluded to in the introduction, finding the excitation spectrum of the $\mathrm{AdS}_5 \times S^5$ superstring theory – also dubbed the $\mathrm{AdS}_5 \times S^5$ *spectral problem* – has been an important goal on the way to understanding the AdS/CFT correspondence. For the $\mathrm{AdS}_5 \times S^5$ superstring theory string excitations can be related to scaling dimensions of local operators of planar $\mathcal{N} = 4$ SYM theory, such that finding a description of the former directly also yields a description of the latter. Apart from its consequences for the AdS/CFT correspondence, having a clear description of these sets of observables is desirable in itself: it is very rare to have so much control over the observables in an interacting quantum field theory.

Using the integrability present in both the planar gauge and string theory discussed above it is possible to give a very simple but exact description of the spectral problem. This description has gotten simpler over the years, going through various intermediate stages, and at present the simplest form known is the *quantum spectral curve* (QSC) [13]. The QSC has led to many interesting results: not only did it allow for the analysis of arbitrary states such as twist operators, it turned out to be a starting point for the study of different observables in $\mathcal{N} = 4$ SYM, such as the BFKL pomeron, the cusped Wilson line and the quark-anti-quark potential. This is remarkable, as these observables are outside of the scope of the original spectral problem. Its wide applicability suggests a deeper level to the QSC that is yet to be understood. One might also wonder whether the occurrence of such a drastic simplification to the spectral problem is unique to the $\mathrm{AdS}_5 \times S^5$ case.

In an effort to gain more understanding of the QSC and more generally the role played by integrability in the simplification of the spectral problem a project was undertaken to construct the quantum spectral curve for the η-deformed superstring theory. More precisely, starting from the exact quantum scattering theory described by the S-matrix constructed in [2] one can follow the same path as was taken for the original $\mathrm{AdS}_5 \times S^5$ case: the first step was already undertaken in [14] in the construction of the η-deformed Thermodynamic Bethe Ansatz equations, an infinite set of non-linear integral equations.

To understand these equations and their constructions better the Thermodynamic Bethe Ansatz (TBA) method was applied to a simpler model first: Inozemtsev's elliptic spin chain. This spin chain with elliptic long-range interactions was never analyzed in the thermal regime, despite interesting claims being made about its thermodynamic behaviour [15], namely being insensitive to the presence of supersymmetry. The TBA-equations were derived in [16], allowing for the numerical analysis necessary to confirm the insensitivity to supersymmetry. Moreover, the succesful application of this approach provides further evidence towards the integrability of the model, which has still not been established.

After these introductory remarks we come to the derivation of the η-deformed quantum spectral curve. The first step is to rewrite the TBA-equations in the form of a Y-system: a set of finite-difference equations for the unknown 2π-periodic functions $Y_{a,s}$ that can be compactly written as

$$Y^+_{a,s} Y^-_{a,s} = \frac{(1 + Y_{a-1,s})(1 + Y_{a+1,s})}{(1 + Y_{a,s-1})(1 + Y_{a,s+1})},$$

where $f^+(u) = f(u + ic)$ with c the parameter carrying the η-deformation and where the

indices (a, s) take values on what is known as the Y-hook. To specify which solutions of the Y-system should be considered to describe the spectral problem one has to impose additional conditions known as discontinuity equations. These discontinuities relate the jump of the various Y functions at their infinitely many branch cuts on the complex plane. These discontinuities were derived in [17], moreover showing equivalence of the Y-system with the original TBA-equations in line with the original work in [18].

The second step consists in further simplifying the Y-system equations by the introduction of a new parametrisation known as the T-system: the Y-system equations simplify further and can now be written as

$$T^+_{a,s}T^-_{a,s} = T_{a,s+1}T_{a,s-1} + T_{a+1,s}T_{a-1,s},$$

where the (a, s) live on the T-hook. This equation is known as the Hirota equation, a ubiquitous equation in integrability. The price to pay for the further simplicity of the equations is that the additional conditions become more convoluted. The T-functions and the Hirota equations admit a huge gauge freedom that makes it hard to select a convenient gauge to work in, and moreover it seems that no single convenient gauge exists. Nevertheless, in [17] four sets of T-gauges were proposed inspired by T-system for $\mathrm{AdS}_5 \times S^5$ in [19]. Their construction is based on spectral theory for periodic functions on the complex plane, more details of which can be found in [20]. Combined with gluing conditions that relate the different gauges this gives a full description of the spectral problem. In principal this T-system can be used to analyse the spectrum of η-deformed $\mathrm{AdS}_5 \times S^5$ superstring theory, but like in the $\mathrm{AdS}_5 \times S^5$ case a further simplification exists.

Using the solution theory of the Hirota equation [21] one can reparametrise one of the T-gauges into so-called $\mathbf{P}$ functions, which can be regarded as the first step in the construction of the quantum spectral curve. Working out all the constraints ultimately yields five independent functions $\mathbf{P}_1, \mathbf{P}_2, \mathbf{P}^3, \mathbf{P}^4, \mu_{12}$ which describe all the T-gauges. All these functions are 2π (anti)-periodic (at least just above the real axis) and have branch cuts: the $\mathbf{P}$ have only one on the real axis whereas μ_{12} has an infinite ladder that goes all the way to imaginary infinity. This analytic structure is illustrated in Fig. 1. All of these branch cuts are of square-root type though, allowing for a relatively large amount of control. Introducing auxiliary functions $\mathbf{P}_a, \mathbf{P}^a$ and μ_{ab} the equations that these objects need to satisfy – known as the $\mathbf{P}\mu$ system – become particularly pleasing. Written for $a, b = 1, \ldots, 4$ it reads

$$\tilde{\mu}_{ab} - \mu_{ab} = \mathbf{P}_a\tilde{\mathbf{P}}_b - \mathbf{P}_b\tilde{\mathbf{P}}_a, \quad \tilde{\mathbf{P}}_a = \mu_{ab}\mathbf{P}^b, \quad \mathbf{P}_a\mathbf{P}^a = 0, \quad \mathrm{Pf}(\mu) = 1,$$

where the tilde indicates the second sheet evaluation of the function involved, the summation convention is followed and $\mathrm{Pf}(\mu)$ is the Pfaffian of the antisymmetric matrix μ. The form of these equations exactly coincide with the $\mathbf{P}\mu$ system derived for the undeformed $\mathrm{AdS}_5 \times S^5$ superstring, consistent with the similarities between the representation theory of the $\mathrm{AdS}_5 \times S^5$ superstring and its η-deformed counterpart. These equations form one of the many equivalent ways to write the QSC-equations. Another important set of equations one can derive is the dual $\mathbf{Q}\omega$ system, which also has the same form as in the undeformed case.

As before, these equations do not give a full description of the spectral problem, which need to be supplemented by boundary conditions that encode which solution of the $\mathbf{P}\mu$ system corresponds to which state in the η-deformed string theory. Clearly, this is also where the difference between the undeformed and deformed becomes most pronounced. In the undeformed case, the extra boundary conditions come in the form of asymptotics, that is prescribed limiting behaviour for all the functions in the $\mathbf{P}\mu$ system as one sends $u \to \infty$. Clearly, such a condition

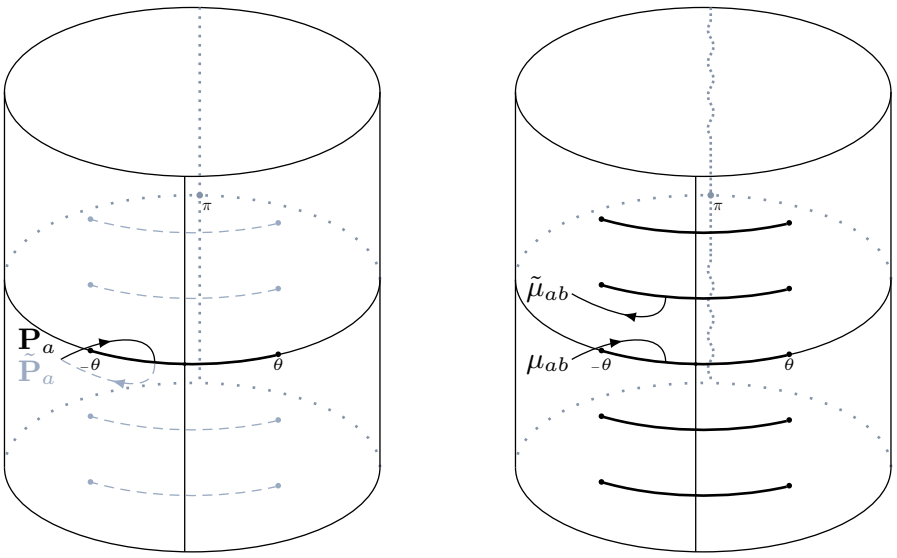


Figure 1: The analytic structure of the $\mathbf{P}_a$ (a) and the μ_{ab} (b) on the cylinder. The thick lines indicate branch cuts between $\pm\theta$ on the first sheet. The continuation of short-cutted μ_{ab} can be expressed on the first sheet using its $2ic$ periodicity. The squiggly line in (b) indicates that for generic θ outside the physical strip the μ_{ab} cannot be put on (a finite cover of) the cylinder. Figure taken from Ref. [17].

is impossible for 2π-periodic functions and one should consider other options. Using the TBA-equations it proved possible to prove that at least some of the functions carry information about the quantum labels of an excited state in their asymptotics as one considers the limit $u \to i\infty$, i.e. moves infinitely far up the cylinder. Postulating that this limit should yield the charges also for the other functions in the QSC one can deduce a fairly simple set of asymptotics [17]: for $z = e^{-iu/2}$ one finds that

$$\mathbf{P}_a \simeq A_a z^{-\tilde{M}_a}, \quad \mathbf{Q}_i \simeq B_i z^{\hat{M}_i} \quad \mathbf{P}^a \simeq A^a z^{\tilde{M}_a}, \quad \mathbf{Q}^i \simeq B^i z^{-\hat{M}_i},$$

where

$$\tilde{M} = \frac{1}{2}\left\{J_1 + J_2 - J_3 + 2, J_1 - J_2 + J_3, -J_1 + J_2 + J_3, -J_1 - J_2 - J_3 - 2\right\},$$
$$\hat{M} = \frac{1}{2}\left\{\Delta - S_1 - S_2 + 2, \Delta + S_1 + S_2, -\Delta - S_1 + S_2, -\Delta + S_1 - S_2 - 2\right\}.$$

The six labels $(\Delta, J_1, J_2, J_3, S_1, S_2)$ are the quantum labels for states in the η-deformed string theory. The prefactors A_a, A^a, B_i and B^i are explicitly known trigonometric functions of the quantum labels.

This defines the η-deformed QSC, which can be used for further analysis of the η-deformed string theory. Particularly interesting questions are (1) what is the field of numbers involved in the actual computation of string energies, (2) can the deformed BFKL eigenvalue be computed and possibly shed light on the thermal BFKL theory through the mirror duality of the η-deformed string theory and (3) which operator is related to the Hagedorn temperature computation through the same mirror duality.

4 New and old integrable models

The string sigma model on $\mathrm{AdS}_5 \times S^5$ and its deformations provide a source for a number of known as well as new finite-dimensional integrable models that can be obtained by applying various reduction schemes. At first glance this concerns a particle limit, *i.e.* the limit of vanishing string length. Studying this limit, as well as other finite-dimensional reductions, is principally important since in spite of the progress relying on the surmised quantum integrability, quantization of the $\mathrm{AdS}_5 \times S^5$ superstring from first principles is still an open problem. Especially for light string states, for which the $\mathfrak{psu}(2,2|4)$ charges take finite values, it has been a renowned challenge to determine the spectrum beyond the leading order [22], $E \sim \lambda^{1/4}$, where λ is the 't Hooft coupling. A way to proceed was offered in [23], where, arguing about supersymmetric effects heuristically, an investigation of the isometry group orbits of a pulsating string allowed to reproduce the first quantum corrections of order $\lambda^{-1/4}$. For this the crucial step has been to reformulate the system as a massive $\mathrm{AdS}_5 \times S^5$ particle with the mass term determined by the stringy non-zero-modes. But since quantization of massive as well as massless AdS superparticles is not yet understood, to attack this question we utilised the gauge invariant Kirillov–Kostant–Souriau method of coadjoint orbits .

In particular, in [24] we applied the orbit method quantization to the AdS_2 superparticle on $\mathrm{OSP}(1|2)/\mathrm{SO}(1,1)$, yielding a Holstein–Primakoff-like realization of the superisometries $\mathfrak{osp}(1|2)$. However, for the massless case the κ-symmetry transformation leaves only one physical real fermion, rendering the model quantum inconsistent. This problem was overcome in [25] by studying the AdS_3 superparticle on $\mathrm{OSP}(1|2) \times \mathrm{OSP}(1|2)/\mathrm{SL}(2,\mathbb{R})$. Here, calculation of the symplectic form as well as of the Noether charges naturally split up into left and right chiral sectors, yielding a quantum realization of $\mathfrak{osp}_l(1|2) \oplus \mathfrak{osp}_r(1|2)$. For the massless particle it was then found that the superisometry algebra extends to the corresponding superconformal algebra $\mathfrak{osp}(2|4)$, with its 19 charges realized by all possible real quadratic combinations of the phase space variables.

With the goal to prepare the formalism for general semi-symmetric spaces, in [26] we devised orbit method quantization of the massive bosonic AdS_N particle in a scheme manifestly exposing the coset nature of AdS_N. Apart from reproducing previous results, this led to a new quantization scheme in terms of dual oscillator variables. Furthermore, we also generalized the results of [24] and [25] and proposed an ansatz for the AdS_4 superparticle.

In [27] and [28] we continued probing the integrability of sigma models on η-deformed backgrounds. Building on previous work for the η-deformed Neumann model [29], in [27] we studied generalized bosonic string solutions on $\mathrm{AdS}_5 \times S^5$, yielding a novel η-deformed Neumann–Rosochatius model. By constructing a 4×4 Lax representation we obtained a set of abelian integrals of motion, ensuring Liouville integrability of the system. We furthermore established how these generalize the integrals of motion of the known limiting cases, *i.e.*, of the η-deformed Neumann and geodesic systems as well as of the undeformed Neumann–Rosochatius model.

As sigma models on η-deformed backgrounds enjoy a quantum deformed symmetry algebra, $\mathrm{U}_q(\mathfrak{psu}(2,2|4))$ in the case of $(\mathrm{AdS}_5 \times S^5)_\eta$, it is interesting to track how the non-abelian symmetry charges behave under the η-deformation. In [28] this question was posed in the simplest possible setup, the geodesic motion on the squashed sphere $(\mathrm{S}^2)_\eta$, the manifold of the Fateev sausage model [30]. New local integrals of motion were found, which by construction form an $\mathfrak{sl}(2)$ Poisson algebra and therefore amount to maximal superintegrability of the system. With this observation we devised a canonical map to an auxiliary sphere, by which we completely

solve the geodesics problem.

5 Integrable deformations of CFTs and functional equations

While the discussion in sections 1–4 focusses on the analysis of concrete world-sheet theories directly related to the AdS/CFT correspondence, here we take a step back and look at some general questions that arise in the above procedure:

1. Give a quantum world-sheet theory, how can one describe its integrable structure? And how can one detect deformations which preserve all or part of the integrability?

2. How much ambiguity is there in solutions to functional equations, such as T- and Y-systems? What additional conditions make their solution unique?

We will not answer any of these questions for the models discussed in sections 1–4, but we will outline a framework which is convenient to discuss the questions in point 1, and we will answer question 2 at least for a much simpler type of Y-system than those arising in AdS/CFT.

The fundamental example of our approach is the integrable structure of the free boson, perturbed and unperturbed, captured in terms of non-local conserved charges, as developed by Bazhanov, Lukyanov and Zamolodchikov [31, 32]. There, the authors construct mutually commuting families of conserved charges by path-ordered integrals of free boson vertex operators which depend on a spectral parameter λ. They argue that the large-λ expansion encodes the values of all local conserved charges, i.e. conserved charges obtained by integrating conserved currents of the model.

The setting in which we discuss question 1 is that of two-dimensional conformal quantum field theory in euclidean signature. We allow the world sheet to be decorated with one-dimensional line defects, across which the bulk fields of the theory may have discontinuities. The line defects themselves are topological in the sense that they can be deformed without affecting the value of a correlator, as long as they are not taken across field insertions. The most basic example here is the critical Ising model, where across the line defect the sign of the spin-spin coupling is inverted (this is called a disorder line). When taken across such a disorder line, the Ising spin field changes sign, while the energy field (the field dual to the temperature perturbation) is continuous, see e.g. [33].

One now observes that in addition to bulk fields, there are new fields in a CFT with line defects, namely fields which are localised on the line defect itself. These fields behave differently from bulk fields in that they are not local (they have monodromies) when moved around other field insertions. Geometrically this is very intuitive, as in moving a defect field around another field tangles up the defect lines and there is no reason for the resulting value of the correlator to be equal to the initial one.

Consider now a world sheet which is a cylinder, with a topological defect line with defect condition X wrapped around it. This defines an operator D_X on the state space $\mathcal{H}$ of the CFT. Since X is a topological defect condition, this operator commutes with the Hamiltonian of the CFT:

$$[D_X, H_{\mathrm{CFT}}] = 0 \quad , \quad H_{\mathrm{CFT}} = \tfrac{1}{2\pi}(L_0 + \bar{L}_0 - \tfrac{c}{12}) \ .$$

The operator D_X is thus a *conserved charge* for the conformal field theory, albeit one which typically does not arise by integrating a conserved current. We can now ask the following natural question:

> Is it possible to deform the CFT and at the same time deform some of the conserved charges D_X such that they remain conserved for the perturbed theory?

Let us start with the perturbation of the CFT. Fix a bulk field Φ, which we assume to spinless, that is, of chiral/anti-chiral conformal weight (h, h) (so its total scaling dimension is $2h$). We assume Φ to be relevant or marginal ($h \leq 1$), so that the perturbation does not affect the UV fixed point, which is our starting CFT. The perturbed Hamiltonian is

$$H_{\mathrm{pert}}(\mu) = H_{\mathrm{CFT}} + \mu \int_0^{2\pi} \Phi(\theta) d\theta \ ,$$

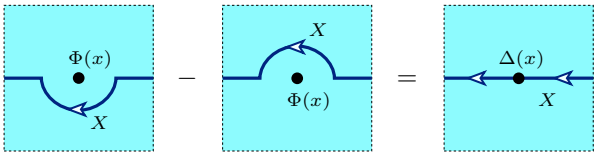
where the integral is around the cylinder, and where $\mu \in \mathbb{C}$ is the strength of the perturbation. On the defect X we consider a perturbation by a chiral defect field ψ_X and an anti-chiral defect field $\bar{\psi}_X$. We demand that their conformal weights are $(h, 0)$ and $(0, h)$, respectively, with h the same value as for the bulk perturbation. We perturb the defect X by the defect field

$$\lambda \psi_X(\theta) + \tilde{\lambda} \bar{\psi}_X(\theta) \ ,$$

where $\lambda, \tilde{\lambda} \in \mathbb{C}$ give the strengths of the perturbations. Write $D_X(\lambda, \tilde{\lambda})$ for the perturbed defect operator (defined by expanding an exponentiated integral of the above defect field, see [34,35]). We would like to understand when

$$[D_X(\lambda, \tilde{\lambda}), H_{\mathrm{pert}}(\mu)] = 0 \ ,$$

that is, when $D_X(\lambda, \tilde{\lambda})$ is a conserved charge for the perturbed Hamiltonian. In this setup, there is a surprisingly simple sufficient condition, the *commutation condition* which has to hold locally in correlators of the unperturbed CFT, and which guarantees the vanishing of the above commutator to all orders in the perturbing parameters [34, 35]:



The left hand side is the difference between passing the topological defect line X above and below the perturbing field Φ. The defect field $\Delta(x)$ on the right hand side is the difference of placing the two defect fields ψ_X and $\bar{\psi}_X$ in either order on the defect line,

$$\Delta(x) = \lim_{\epsilon \to 0} \left(\psi_X(x+\epsilon) \bar{\psi}_X(x) - \bar{\psi}_X(x+\epsilon) \psi_X(x) \right) \ .$$

Finally, the perturbing parameters have to satisfy the relation (the constant depends on normalisation choices and is conventional, see [35] for details):

$$\mu = -2i \, \lambda \tilde{\lambda} \ .$$

This simple observation is the starting point of a host of interesting structural insights:

- For a fixed value of μ, so for a fixed perturbation of the CFT, a solution to the commutation condition gives rise to a *one-parameter-family* of conserved charges, parametrised by $\zeta \in \mathbb{C} \setminus \{0\}$ via $\lambda = \zeta$, $\tilde{\lambda} = \mu/\zeta$.
- One important class of solutions to the commutation condition is the case $\mu = 0$, where the CFT is not perturbed at all. Then the condition is $\Delta = 0$, which in turn can be guaranteed by simply choosing $\bar{\psi}_X = 0$ (or $\psi_X = 0$). In this way, one can investigate the integrable structure of a CFT.
- The commutation condition can be expressed in terms of representation theoretic data obtained from the conformal field theory [35], and in examples can be related to representations of certain quantum groups. This recovers results of [31, 32].
- For example by using the relation to quantum groups, or by direct computation, one can establish that for certain choices of perturbing defect fields and defect labels X, the various conserved charges $D_X(\lambda, \tilde{\lambda})$ commute with each other, for different values of X and λ, $\tilde{\lambda}$, provided one keeps fixed the value of μ. Furthermore, one finds in examples that the $D_X(\lambda, \tilde{\lambda})$ satisfy functional relations of T-system type.

Since the $D_X(\lambda, \tilde{\lambda})$ mutually commute, they can be simultaneously diagonalised[1] on the state space $\mathcal{H}$, the same T-system functional relations are also satisfied by the eigenvalues. One arrives at a question in complex analysis: given a system of functional relations between functions which are analytic in a certain domain, what can we say about the solutions?

To address this question, it has turned out to be useful to rewrite T-system functional equations as Y-system functional equations. In a simple variant, these look as follows:

$$Y_n(x+is)Y_n(x-is) = \prod_{m=1}^{N} (1+Y_m(x))^{G_{nm}} \quad . \tag{Y}$$

Here, $s > 0$ is a parameter, G is the adjacency matrix of a Dynkin diagram with N nodes, and the equation has to hold for $n = 1, \ldots, N$ and all $x \in \mathbb{R}$. The functions Y_n are required to be analytic in the strip $\mathbb{R} \times (-is, is)$ and to have a continuous extension to the closure $\mathbb{R} \times [-is, is]$. Note that this is the smallest connected domain on which one can make sense of the above functional relation.

We have the following remarkable uniqueness and existence result, proven in [36], where also numerous references to the physical literature can be found on which the method used in the proof is based:

Theorem: Let $a_1, \ldots, a_n : \mathbb{R} \times [-is, is] \to \mathbb{C}$ be valid asymptotics (see below). Then there exists a unique solution $Y_1, \ldots, Y_N$ to (Y) which satisfies the above analyticity conditions, as well as, for $n = 1, \ldots, N$,

1. $Y_n(\mathbb{R}) \subseteq \mathbb{R}_{>0}$, *(real & positive)*
2. $Y_n(z) \neq 0$ for all $z \in \mathbb{R} \times [-is, is]$. *(no roots)*
3. $\log Y_n(z) - a_n(z)$ is bounded on $\mathbb{R} \times [-is, is]$. *(asymptotics)*

[1] In this exposition we ignore all question of convergence and existence of integrals in perturbative expansions, as well as analytic questions such as discreetness of spectra – these points need a careful treatment in each example.

The notion of "valid asymptotics" is somewhat technical (see [36] for details), but the most important examples are, for $n = 1, \ldots, N$,

$$a)\ a_n(z) = 0 \quad , \quad b)\ a_n(z) = e^{\gamma z/s} w_n \quad , \quad c)\ a_n(z) = \cosh(\gamma z/s) w_n \ ,$$

where w is the Perron–Frobenius eigenvector of G and $\gamma > 0$ is related to the corresponding eigenvalue by $Gw = 2\cos(\gamma)w$.

The physical interpretation of this mathematical result is that the Y_n describe the ground state eigenvalues of the corresponding conserved charges in (a) the unperturbed case (one proves that the $Y_n(x)$ are independent of x in this case); (b) the massless case $\mu = 0$; (c) for a massive perturbation. Moreover, it is shown in [36] that the unique solution can be obtain by solving a non-linear integral equation of TBA-type.

In summary, the above constructions and results indicate that a promising approach to obtain non-perturbative information about a perturbed CFT is to first try to establish functional relations satisfied by families of mutually commuting perturbed defect operators, and to then try to prove existence and uniqueness statements for the functional equations satisfied by their eigenvalues, similar to the theorem above.

6 Integrable lattice discretisation from the universal R-matrix

Establishing that the integrability of the world-sheet sigma model for strings on AdS persists at the quantum level is a hard probem that has remained elusive up to now. Most importantly, one has to make sure that renormalisation of ultraviolet divergencies does not spoil integrability. A promising strategy to reach this goal is based on the use of lattice regularisations for integrable two-dimensional quantum field theories. There are some well-known examples including the Sine–Gordon model where lattice regularisations have been constructed which manifestly preserve integrability. However, up to now there does not exist a sufficiently general framework to construct integrable lattice regularisations for all integrable models of our interest, and in particular for the sigma models relevant for string theory on $\mathrm{AdS}_5 \times S^5$.

In a part of our project, carried out jointly with the postdoc Carlo Meneghelli, we have described a systematic approach for the construction of large families of integrable lattice regularisations [37]. This approach has been fully realised in the examples of affine Toda field theories, prototypical examples of integrable quantum field theories sharing some qualitative features with the sigma models relevant for the study of string theory on AdS spaces. The results of the recent paper [38] offer very encouraging hints that the generalisation of the approach developed in [37] to integrable sigma models is getting within our reach.

The approach taken in [37] is based on two main ingredients.

(A) In all known examples one can view integrability as the consequence of powerful algebraic structures organising the algebras of observables of the field theories in question. The relevant algebraic structures are often referred to as quantum groups. It is in many cases possible to identify the quantum group relevant for integrability of a given quantum field theory from its Lagrangian description, or alternatively from its description as perturbed conformal field theory [35, 39].

This step is performed in [39] by considering the light-cone representation of the dynamics. The interaction terms generate a non-commutative algebra which can often be identified with a subalgebra of the relevant quantum group from which the full quantum group can be reconstructed by a standard construction (quantum double).

(B) The main proposal made in [37] is that the corresponding integrable lattice regularisation can then be constructed by following a systematic procedure reducing the main steps to problems in quantum group representation theory. The main ingredients are the so-called Lax-Matrix, R-matrices and the Baxter Q-operators. The proposal of [37] offers a recipe for the construction of these key ingredients by breaking it up into two steps: First finding representations of the relevant quantum group organising the algebra of observables on the lattice, and then evaluating the known universal R-matrix on these representations. The power of this approach has been illustrated in [37] by working it out in full detail in the example of the affine Toda field theories.

In the following we will describe this approach in a bit more detail. The algebraic structures called quantum groups are characterised to a large extend by an algebra structure (non-commutative product operation) and a co-product, essentially a rule for how to act with the algebra on tensor products of its representations. The co-product will generically not be symmetric with respect to exchange of the tensor factors in a tensor product $R_1 \otimes R_2$. A useful description of this asymmetry is provided by the R-matrices, operators $\mathsf{R}_{R_1 R_2} : R_1 \otimes R_2 \to R_1 \otimes R_2$ relating the quantum group action on $R_1 \otimes R_2$ to the one defined from the action on $R_2 \otimes R_1$ by subsequent permutation of tensor factors. Basic results in quantum group theory assert the existence of a universal object of the form $R = \sum_{\imath \in \mathcal{I}} x_\imath \otimes y_\imath$, with $\{x_\imath; \imath \in \mathcal{I}\}$ and $\{y_\imath; \imath \in \mathcal{I}\}$ being suitable sets of generators for the quantum group, such that

$$\mathsf{R}_{R_1 R_2} = (\pi_{R_1} \otimes \pi_{R_2})(R) = \sum_{\imath \in \mathcal{I}} \pi_{R_1}(x_\imath) \otimes \pi_{R_2}(y_\imath),$$

with $\pi_R(x)$ being the operator representing the quantum group element x within the representation R.

Two types of quantum representations are relevant in the context of integrable lattice models. Most basic is a representation π_q of the quantum group on the physical Hilbert space of the lattice model, often referred to as quantum space. It then turns out to be useful to consider one-parameter families of auxiliary representations $\pi_{a,\lambda}$ allowing us to define useful generating functions as

$$M(\lambda) = (\pi_{a,\lambda} \otimes \pi_q)(R). \tag{1}$$

If, for example, the auxiliary representations $\pi_{a,\lambda}$ are finite-dimensional one may view $M(\lambda)$ as a matrix having matrix elements which are operators acting on quantum space. The matrix $M(\lambda)$ turns out to be related to the monodromy matrix of the Lax connection in the corresponding classically integrable model.

It is known that infinite-dimensional representations $\pi_{a,\lambda}$ can also be of interest in this context. This requires in particular that it is possible to define a partial trace over the space $\mathcal{H}_a$ on which the representation $\pi_{a,\lambda}$ is realised

$$Q(\lambda) = \mathrm{Tr}_{H_a}(M(\lambda)). \tag{2}$$

Some choices for $\pi_{a,\lambda}$ will produce particularly useful families of operators $Q(\lambda)$, distinguished by two main properties:

- By specialising the parameter λ one can obtain from $Q(\lambda)$ evolution operators generating a lattice version of the physical time-evolution.
- The operators $Q(\lambda)$ and $Q(\mu)$ associated to any two values of the parameter always commute with each other, $[Q(\lambda), Q(\mu)] = 0$.

This implies that $Q(\lambda)$ represents a generating function for the conserved quantities of the integrable lattice model constructed in this framework.

Having identified the relevant quantum group in step (A) of this program, it remains to

1) find suitable representations π_q and $\pi_{a,\lambda}$, and
2) calculate $Q(\lambda)$ from (1) and (2).

It was shown in [37] in the example of the affine Toda theories that taking the first step 1) is often very simple. It turns out that the relevant representations can be found among the simplest possible representations the relevant quantum groups have. Given that the operators $\pi_q(x)$ represent physical observables, one gets important constraints on the representation π_q from the requirement that the behavior of $\pi_q(x)$ under hermitian conjugation should reflect the reality properties of the corresponding physical observable. It was found in [37] that such requirements single out a unique choice for the representation π_q to be used for the models of interest.

In order to complete this program it remains to perform step 2) above, the calculation of $Q(\lambda)$. A possible starting point is provided by the known explicit formulae for the universal R-matrices R, taking the form of infinite products. These formulae are very complicated. Somewhat unexpectedly, it has turned out that the representations the $\pi_{a,\lambda}$ and π_q we found to be relevant in this context have very useful special features simplifying the evaluation of $M(\lambda)$ via (1) enormously. As a result we have obtained fairly simple formulae representing the operators $Q(\lambda)$ as integral operators with explicitly known kernels.

In this way one not only obtains all the key ingredients for the construction of integrable lattice regularisation. The algebraic structures of the quantum group imply that $Q(\lambda)$ satisfies a system of functional equations. The known representation of $Q(\lambda)$ as an integral operator enables us to determine the analytic properties of the eigenvalues of $Q(\lambda)$. Taken together, functional equations and analytic properties lead to a complete mathematical characterisation of the set of functions $q(\lambda)$ representing the possible eigenvalues of $Q(\lambda)$. This constitutes the necessary groundwork for the solution of the spectral problem in these integrable quantum field theories.

The models studied in [37] are not yet the models of our ultimate interest from the point of view of applications to AdS/CFT. It was for a long time believed that the step to be taken to treat integrable sigma models in a similar way is big, requiring to overcome the problem of non-ultralocality of the Poisson brackets for the Lax matrices describing the integrable structures of nonlinear sigma models on the classical level. More recently at least two possible ways out have become visible. For some integrable nonlinear sigma models a modified zero curvature representation of the classical equations of motion has been found leading to fully ultralocal Poisson brackets [40]. It may be hoped that this approach can be generalised considerably. There furthermore exist proposals for dual descriptions of various nonlinear sigma models (see [38, 41] for recent progress containing further references) which should be accessible with only a modest generalisation of the approach in [37, 39]. These observations give us hope that a full derivation of the integrability of string theory on $\mathrm{AdS}_5 \times S^5$ and its deformations is getting within reach.

References

[1] J. M. Maldacena, *The Large N limit of superconformal field theories and supergravity*, *Int. J. Theor. Phys.* **38** (1999) 1113–1133, [hep-th/9711200]. [Adv. Theor. Math. Phys.2,231(1998)].

[2] N. Beisert and P. Koroteev, *Quantum Deformations of the One-Dimensional Hubbard Model*, *J. Phys.* **A41** (2008) 255204, [0802.0777].

[3] F. Delduc, M. Magro and B. Vicedo, *An integrable deformation of the* $\mathrm{AdS}_5 \times S^5$ *superstring action*, *Phys. Rev. Lett.* **112** (2014) 051601, [1309.5850].

[4] F. Delduc, M. Magro and B. Vicedo, *Derivation of the action and symmetries of the q-deformed* $\mathrm{AdS}_5 \times S^5$ *superstring*, *JHEP* **10** (2014) 132, [1406.6286].

[5] C. Klimcik, *On integrability of the Yang-Baxter sigma-model*, *J. Math. Phys.* **50** (2009) 043508, [0802.3518].

[6] G. Arutyunov, R. Borsato and S. Frolov, *S-matrix for strings on* η*-deformed* $\mathrm{AdS}_5 \times S^5$, *JHEP* **04** (2014) 002, [1312.3542].

[7] A. A. Tseytlin, *On dilaton dependence of type II superstring action*, *Class. Quant. Grav.* **13** (1996) L81–L85, [hep-th/9601109].

[8] G. Arutyunov, R. Borsato and S. Frolov, *Puzzles of* η*-deformed* $\mathrm{AdS}_5 \times S^5$, *JHEP* **12** (2015) 049, [1507.04239].

[9] G. Arutyunov and S. J. van Tongeren, *Double Wick rotating Green-Schwarz strings*, *JHEP* **05** (2015) 027, [1412.5137].

[10] G. Arutyunov and S. J. van Tongeren, $\mathrm{AdS}_5 \times S^5$ *mirror model as a string sigma model*, *Phys. Rev. Lett.* **113** (2014) 261605, [1406.2304].

[11] B. Hoare and A. A. Tseytlin, *Type IIB supergravity solution for the T-dual of the* η*-deformed* $\mathrm{AdS}_5 \times S^5$ *superstring*, *JHEP* **10** (2015) 060, [1508.01150].

[12] G. Arutyunov, S. Frolov, B. Hoare, R. Roiban and A. A. Tseytlin, *Scale invariance of the* η*-deformed* $\mathrm{AdS}_5 \times S^5$ *superstring, T-duality and modified type II equations*, *Nucl. Phys.* **B903** (2016) 262–303, [1511.05795].

[13] N. Gromov, V. Kazakov, S. Leurent and D. Volin, *Quantum spectral curve for arbitrary state/operator in* AdS_5/CFT_4, *JHEP* **09** (2015) 187, [1405.4857].

[14] G. Arutyunov, M. de Leeuw and S. J. van Tongeren, *The exact spectrum and mirror duality of the* $(AdS_5 \times S^5)_\eta$ *superstring*, *Theor. Math. Phys.* **182** (2015) 23–51, [1403.6104]. [Teor. Mat. Fiz.182,no.1,28(2014)].

[15] J. A. Carrasco, F. Finkel, A. González-López, M. A. Rodríguez and P. Tempesta, *Critical behavior of su(1|1) supersymmetric spin chains with long-range interactions*, *Phys. Rev.* **E93** (2016) 062103, [1603.03668].

[16] R. Klabbers, *Thermodynamics of Inozemtsev's Elliptic Spin Chain*, *Nucl. Phys.* **B907** (2016) 77–106, [1602.05133].

[17] R. Klabbers and S. J. van Tongeren, *Quantum Spectral Curve for the eta-deformed* $\mathrm{AdS}_5 \times S^5$ *superstring*, *Nucl. Phys.* **B925** (2017) 252–318, [1708.02894].

[18] A. Cavaglia, D. Fioravanti and R. Tateo, *Extended Y-system for the* AdS_5/CFT_4 *correspondence*, *Nucl. Phys.* **B843** (2011) 302–343, [1005.3016].

[19] N. Gromov, V. Kazakov, S. Leurent and D. Volin, *Solving the AdS/CFT Y-system*, *JHEP* **07** (2012) 023, [1110.0562].

[20] R. Klabbers, *Quantum Spectral Curve for the* η*-deformed* $\mathrm{AdS}_5 \times S^5$ *superstring*, Ph.D. thesis, Universität Hamburg, 2017. http://ediss.sub.uni-hamburg.de/volltexte/2018/9073.

[21] N. Gromov, V. Kazakov, S. Leurent and Z. Tsuboi, *Wronskian Solution for AdS/CFT Y-system*, *JHEP* **01** (2011) 155, [1010.2720].

[22] S. Gubser, I. Klebanov and A. M. Polyakov, *A Semiclassical limit of the gauge / string correspondence*, *Nucl.Phys.* **B636** (2002) 99–114, [hep-th/0204051].

[23] S. Frolov, M. Heinze, G. Jorjadze and J. Plefka, *Static gauge and energy spectrum of single-mode strings in* $\mathrm{AdS}_5 \times S^5$, *J.Phys.* **A47** (2014) 085401, [1310.5052].

[24] M. Heinze, B. Hoare, G. Jorjadze and L. Megrelidze, *Orbit method quantization of the AdS_2 superparticle*, *J. Phys.* **A48** (2015) 315403, [1504.04175].

[25] M. Heinze and G. Jorjadze, *Quantization of the* AdS_3 *superparticle on* $\mathrm{OSP}(1|2)^2/\mathrm{SL}(2,\mathbb{R})$, *Nucl. Phys.* **B915** (2017) 44–68, [1610.03519].

[26] M. Heinze, G. Jorjadze and L. Megrelidze, *Coset construction of AdS particle dynamics*, *J. Math. Phys.* **58** (2017) 012301, [1610.08212].

[27] G. Arutyunov, M. Heinze and D. Medina-Rincon, *Integrability of the η-deformed Neumann-Rosochatius model*, *J. Phys.* **A50** (2017) 035401, [1607.05190].

[28] G. Arutyunov, M. Heinze and D. Medina-Rincon, *Superintegrability of Geodesic Motion on the Sausage Model*, *J. Phys.* **A50** (2017) 244002, [1608.06481].

[29] G. Arutyunov and D. Medina-Rincon, *Deformed Neumann model from spinning strings on* $(\mathrm{AdS}_5 \times S^5)_\eta$, *JHEP* **10** (2014) 50, [1406.2536].

[30] V. A. Fateev, E. Onofri and A. B. Zamolodchikov, *The Sausage model (integrable deformations of O(3) sigma model)*, *Nucl. Phys.* **B406** (1993) 521–565.

[31] V. V. Bazhanov, S. L. Lukyanov and A. B. Zamolodchikov, *Integrable structure of conformal field theory, quantum KdV theory and thermodynamic Bethe ansatz*, *Commun. Math. Phys.* **177** (1996) 381–398, [hep-th/9412229].

[32] V. V. Bazhanov, S. L. Lukyanov and A. B. Zamolodchikov, *Integrable quantum field theories in finite volume: Excited state energies*, *Nucl. Phys.* **B489** (1997) 487–531, [hep-th/9607099].

[33] J. Fröhlich, J. Fuchs, I. Runkel and C. Schweigert, *Kramers-Wannier duality from conformal defects*, *Phys. Rev. Lett.* **93** (2004) 070601, [cond-mat/0404051].

[34] I. Runkel, *Non-local conserved charges from defects in perturbed conformal field theory*, *J. Phys.* **A43** (2010) 365206, [1004.1909].

[35] D. Bücher and I. Runkel, *Integrable perturbations of conformal field theories and Yetter-Drinfeld modules*, *J. Math. Phys.* **55** (2014) 111705, [1211.4726].

[36] L. Hilfiker and I. Runkel, *Existence and uniqueness of solutions to Y-systems and TBA equations*, 1708.00001.

[37] C. Meneghelli and J. Teschner, *Integrable light-cone lattice discretizations from the universal R-matrix*, *Adv. Theor. Math. Phys.* **21** (2017) 1189–1371, [1504.04572].

[38] V. V. Bazhanov, G. A. Kotousov and S. L. Lukyanov, *Quantum transfer-matrices for the sausage model*, *JHEP* **01** (2018) 021, [1706.09941].

[39] D. Ridout and J. Teschner, *Integrability of a family of quantum field theories related to sigma models*, *Nucl. Phys.* **B853** (2011) 327–378, [1102.5716].

[40] S. L. Lukyanov, *The integrable harmonic map problem versus Ricci flow*, *Nucl. Phys.* **B865** (2012) 308–329, [1205.3201].

[41] A. V. Litvinov and L. A. Spodyneiko, *On dual description of the deformed $O(N)$ sigma model*, 1804.07084.

Section B

Particle Physics

Optimising the ILC Setup: Physics Programme, Running Scenarios and Design Choices

Jenny List[1], *Gudrid Moortgat-Pick*[1,2], *Jürgen Reuter*[1]

[1]DESY, Hamburg, Germany
[2]II. Institut für Theoretische Physik, Universität Hamburg, Germany

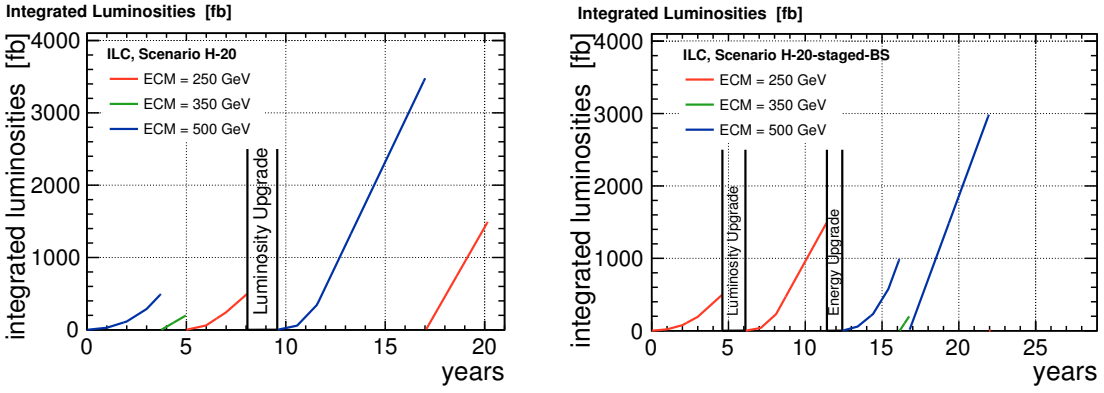
DOI: http://dx.doi.org/10.3204/PUBDB-2018-00782/B1

A high-energy e^+e^- Linear Collider has been considered since a long time as an important complement to the LHC. Unprecedented precision measurements as well as the exploration of so far untouched phase space for direct production of new particles will provide unique information to advance the limits of our understanding of our universe. Within this project, the physics prospects of such a collider as well as their interplay with design of the accelerator and the detectors have been investigated in a quantitative way. This kind of study required a close collaboration between theory and experiment, always taking into account results of the LHC and other relevant experiments. In this article we will summarize some of the most important developments and results, covering all core areas of the physics progamme of future e^+e^- colliders.

1 Introduction

A high energy electron positron collider enables unprecedented precision studies of the Higgs boson, the top quark, the heavy gauge bosons and possibly yet unknown particles, and would thus be an ideal complement to the LHC. From its beginning, the SFB676-B1 project has been dedicated to the quantitative assessment of the physics case of such a future e^+e^- collider [1], considering existing LHC results as well as still to be expected measurements from the HL-LHC. As a concrete example the most advanced of such projects, namely the International Linear Collider (ILC) [2], has been used in order to study the impact of accelerator parameters and detector performance on the physics prospects [3]. In many cases, the assessment was based on realistic technology assumptions verified e.g. with prototypes in testbeam.

The actual discovery of the Higgs boson at the LHC in 2012, near the mid-term of this project, gave a tremendous boost to the planning of such a collider. With the knowledge of the Higgs mass being close to 125 GeV, the energy thresholds of important processes like single or double Higgsstrahlung could be pin-pointed with certainty for the first time. As a result, the Linear Collider Collaboration (LCC) defined concrete operating scenarios for the ILC [4], with strong involvement of this SFB project. The total amount of integrated luminosity collected at each energy stage were defined such as to optimize the expected precision on the couplings of the Higgs boson for a total operation period of about 20 years. The official default running scenario is shown in Fig. 1a, which serves as a reference for all ILC physics studies since. An optimal early physics performance is achieved when starting operation at a center-of-mass energy of 500 GeV, runs at 250 GeV are very important for ultimate precision on the coupling



(a) (b)

Figure 1: Integrated luminosity vs time in two construction scenarios for the ILC (a) immediate construction of a 500 GeV machine (b) staged construction starting with a 250 GeV collider. Figures taken from Refs. [4] and [5], respectively.

of the Higgs to the Z boson. The initial construction costs, however, are much lower when starting at the lowest possible energy, because only a part of the accelerating modules is needed at the beginning. Therefore, also a staged version of the default running scenario has been developed [5], again with leading contributions from this project. The staged scenario, which after the full program delivers the same integrated luminosities as Fig. 1a, is shown in Fig. 1b.

Besides the center-of-mass energy and the luminosity, the polarisation of the electron and positrons beams is an important top-level parameter of electron-positron colliders. The impact of beam polarisation on the physics program of future e^+e^- colliders has been an important topic throughout the lifetime of this project, and has been summarized in [6,7]. Also the precise monitoring of the luminosity-weighted average beam polarisation from collision data received several imporant contributions from this project [8–10]. In particular a global fit framework has been developed which can for the first time combine total and differential cross-section measurements from many different physics processes as well as the polarimeter measurements [10]. This framework has been used to study the ultimately achievable precisions for each dataset in the H20 running scenario, as well as to study the impact of systematic uncertainties and their correlations. Most recently, the role of positron polarisation has been reviewed in view of the staging proposal for the ILC [11], again with leading contributions from this project.

All the studies of the physics potential of a future e^+e^- collider which will be summarized in the following sections rest on advanced software tools from MC generators over detector simulations to reconstruction and data analysis. Nearly all studies for future linear colliders world-wide rely on the MC Generator WHIZARD [12]. In close collaboration with the project B11 of this SFB, strong contributions have been made the automation of NLO QCD corrections in WHIZARD, but also to the implementation of Linear Collider specific features and requirements [13]. The latter profited strongly from the direct collaboration between WHIZARD developers and users within the SFB.

Algorithmic developments to event reconstruction at Linear Colliders comprise e.g. a novel technique to account for initial state radiation and Beamstrahlung in kinematic fits [14, 15]. Prior to this development the benefit of kinematic fits was considered to be much smaller

at Linear Colliders than e.g. at LEP due to the much higher radiation losses. With the new technique, $e^+e^- \to W^+W^-/ZZ \to 4$ jet-events with significant photon radiation could be fitted equally well as events without radiation, achieving comparable resolutions e.g. on di-jet masses. This technique was applied successfully since in several ILC and CLIC analyses, e.g. in a PhD thesis written in context of this project on the prospects for measuring the triple-Higgs coupling at the ILC [16].

In the following sections, we will highlight results obtained in this project in the some of main areas of the physics program of future e^+e^- colliders: Precision studies of the Higgs boson and searches for its potential siblings, precision studies of the W and Z bosons, as well as seaches for the direct production of new particles.

2 Higgs physics in the SM and beyond

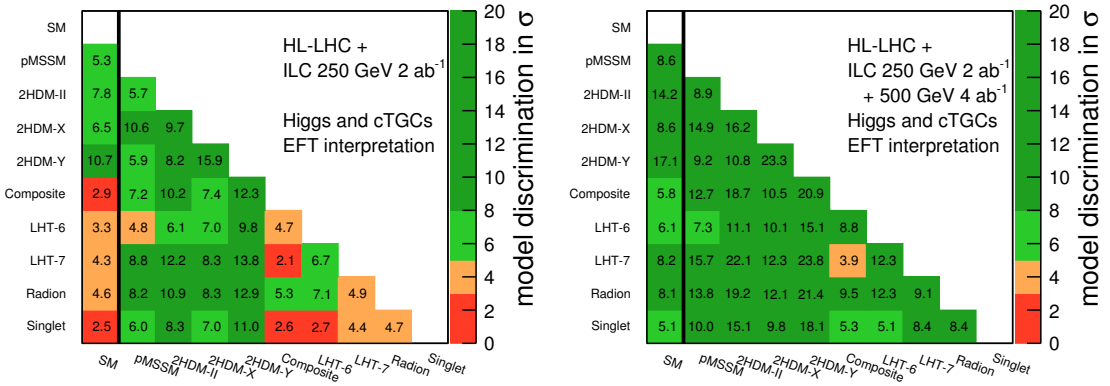
With the discovery of the Higgs boson the questions of the inner workings of electroweak symmetry breaking and of the stabilisation of the Higgs mass became unavoidable. Precision measurements of the Higgs boson's properties provide unique key information for solving these puzzles. The SFB-B1 project contributed in many aspects to the quantitative understanding of the possible measurements and to their interpretation. These will be summarized in this section together with the experimentally closely related search for siblings of the Higgs boson with reduced couplings to the Z boson.

2.1 Higgs couplings to fermions and bosons

One of the unique opportunities at e^+e^- colliders is the determination of the total decay width of the Higgs boson. This can be achieved either by measuring the total Higgsstrahlungs cross section and the subsequent decay of the Higgs into a pair of Z bosons – or by studying Higgs production in WW fusion with subsequent decay of the Higgs into a pair of W bosons. Since the former is limited by the small branching ratio of $H \to ZZ$, the latter has been studied in [17], considering especially dependency of the achievable precision on the center-of-mass energy. It was shown that without making any assumptions on the relations between the couplings of the Higgs to W and Z bosons, e.g. by custodial symmetry, data-taking at center-of-mass energies of at least 350 GeV, better 500 GeV is mandatory.

The prospects and challenges of measuring the Higgs branching ratios into pairs of b- or c-quarks or of gluons has been studied at a center-of-mass energy of 350 GeV [18]. At this energy, the Higgsstrahlung production mode with subsequent decay of the Z into two neutrinos and WW fusion production mode contribute about equally. Within this project it was shown for the first time that all three hadronic decay modes as well as the two production channels can be disentangled simultaneously by using not only the flavour tag information but also the invariant mass of the missing four-momentum as discriminating variables.

These results as well as many more which have been obtained within the world-wide ILC community have been used as input to the definition of default running scenarios for the ILC mentioned in the Introduction. While these were still based on a κ-framework type of interpretation, a new approach was implemented in 2017 within an effective operator framework considering all dim-6 operators consistent with $SU(2) \times U(1)$ symmetry [19]. In such a framework, the symmetry assumptions as well as the inclusion of triple gauge coupling constraints allow to constrain the total decay width of the Higgs boson much better than in the κ-framework



(a) (b)

Figure 2: Discrimination power between the SM and various examplatory BSM benchmarks from ILC Higgs and electroweak precision measurements. All benchmarks have been chosen to be unobservable at the (HL-)LHC. (a) For the 250 GeV stage of the ILC (b) Adding the full 500 GeV program. Figures taken from Ref. [19].

already at $\sqrt{s} = 250\,\text{GeV}$. A special contribution from the SFB-B1 project is shown in Fig. 2, which illustrates the power of Higgs (and electroweak) precision measurements for discriminating various new physics benchmark scenarios from the SM and from each other, based on the EFT-interpretation of projected ILC measurements. All benchmark points have been chosen such that they will not be observable at the HL-LHC, their definition can be found in [19]. Fig. 2a displays the discrimination power in terms of the number of standard deviations for the 250 GeV ILC, while Fig. 2b corresponds to the full H20 program, including the 500 GeV data.

Another important measurement is the direct determination of the Higgs self-coupling λ from double-Higgs production. High-energy Linear Colliders offer two very complementary opportunities for this measurement: At energies of about 1 TeV and higher, pairs of Higgs bosons can be produced in vector boson fusion, where the cross section decreases with larger values of λ, like in the analogous process at hadron colliders. At energies around 500 GeV, double Higgs-strahlung is accessible, whose cross section grows with increasing λ. A PhD thesis written in the context of the SFB-B1 project showed for the first time the feasibility of this measurement at the ILC with $\sqrt{s} = 500\,\text{GeV}$ in full detector simulation and including pile-up from soft photon-photon collisions [16].

2.2 Additional light Higgs bosons

Beyond the precision study of the 125 GeV Higgs boson, the e^+e^- colliders also offer unique possibilities to search for additional light scalars S^0 with reduced couplings to the Z boson, be it additional Higgs bosons or PNGBs which occur frequently in various extensions of the SM. The special handle here is to use the same recoil method which also ensures the model-independent determination of the total Higgsstrahlungs cross section. Thereby, the four-momentum of the S^0 is reconstructed solely from the decay products of the Z boson, e.g. in $Z \to \mu^+\mu^-$ and $Z \to e^+e^-$, and the known initial state. Within the SFB-B1 project, the sensitivity of the 250 GeV ILC to such additional scalars has been studied in an interdisciplinary endeavour in

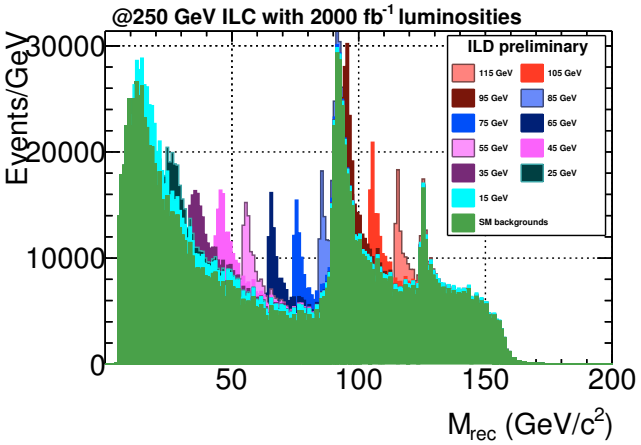


Figure 3: Search for additional light scalars: SM backgrounds superimposed with S^0 signals for various masses in full simulation of the ILD concept [21].

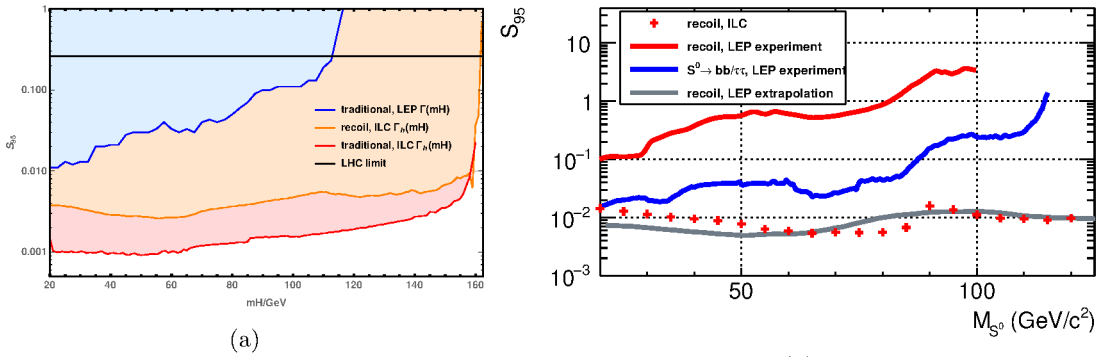
two approaches: a) by extrapolating the analogous LEP searches [20], as well as b) in full simulation of the ILD detector concept [21].

At LEP such light Higgses have been studied in two ways: i) via analyzing both decaying particles explicitly, $Z \to \mu^+\mu^-$ and $H \to b\bar{b}$ (called 'LEP traditional'), and ii) via applying a Higgs-decay independent method, the recoil method, and analyzing only the decays $Z \to \mu^+\mu^-, e^+e^-$. After a reproducing the LEP sensitivities as a verification of the method, both LEP searches were extrapolated to ILC energy, luminosity and polarization, i.e. for $\sqrt{s} = 250$ GeV, $\mathcal{L} = 500$ fb^{-1} and the polarization configuration $(P_{e^-}, P_{e^+}) = (-80\%, +30\%)$ [20]. The resulting expected limit on S at the 95% C.L. can be seen in Fig. 4a. Following the LEP convention, the sensitivity is expressed as a ratio of the cross section for ZS^0 production over the (by now hypothetical) SM ZH cross section for the same mass, called S. This ratio is proportional to the squares of the involved couplings $S \sim \left|g^2_{S^0ZZ}/g^2_{HZZ}\right|$.

The channel $e^+e^- \to S^0Z$, $Z \to \mu^+\mu^-$ was studied in in full simulation of the ILD detector concept for $\mathcal{L} = 2000$ fb^{-1} splitted up into the four polarization configurations $(P_{e^-}, P_{e^+}) = (\mp 80\%, \pm 30\%)$ $[(\mp 80\%, \mp 30\%)]$ with 40% [10%] of the total luminosity, respectively [21]. Figure 3 shows the resulting recoil mass spectrum from all SM backgrounds (note that this includes the 125 GeV Higgs) and S^0 signals of different masses with an arbitrary normalisation. These spectra were then be used to project sensitivities on S at 95% C.L. as a function of the S^0 mass, shown in Fig. 4b.

While the two analyses are broadly consistent, there are some differences in the results: for very light Higgs masses they originate from different approaches in treating the width of the S^0, while at higher masses the different considered final states of the Z-boson play a role.

These studies show that the ILC covers significant additional parameter space down to about a 1% of the SM ZH cross section in a decay-mode independent way over a broad range of light Higgs masses, even at a center-of-mass energy of only 250 GeV.



(a) (b)

Figure 4: Expected sensitivity at 95% C.L. as a function of the mass of the S^0 in terms of the signal cross section normalized to the SM Higgsstrahlung cross section for the same mass at the ILC with $\sqrt{s} = 250\,\text{GeV}$: (a) Decay-mode independent recoil analysis in the process $e^+e^- \to HZ$, $Z \to \mu^+\mu^-$, e^+e^- as well as the decay-mode dependent analysis in the process $e^+e^- \to HZ \to b\bar{b}\mu^+\mu^-$ with $\mathcal{L} = 500$ fb^{-1} and $(P_{e^-}, P_{e^+}) = (-80\%, +30)$; method checked against LEP data analysis and extrapolated to ILC. (b) Decay-mode independent recoil analysis in the process $e^+e^- \to HZ$, $Z \to \mu^+\mu^-$. The red crosses show the reach of the ILC in full detector simulation for an integrated luminosity of 2000 fb^{-1} and $(P_{e^-}, P_{e^+}) = (\mp 80\%, \pm 30\%)$ $[(\mp 80\%, \mp 30\%)]$ in the luminosity ratio 40% [10%], respectively. The red line shows the directly comparable exclusion limit from LEP, the blue line a decay mode-dependent search from LEP. The grey line corresponds to the yellow line from panel (a). Figures taken from Ref. [20] and [21], respectively.

2.3 Off-shell effects and the Higgs width

The exploitation of off-shell contributions in Higgs processes can play an important role to determine properties of the Higgs particles. In [22] the off-shell contributions in $H \to VV^*$ with $V = Z, W$ have been studied. Both dominant production processes $e^+e^- \to ZH \to ZVV^{(*)}$ and $e^+e^- \to \nu\bar{\nu}H \to \nu\bar{\nu}VV^{(*)}$ are taken into account. The relative size of the off-shell contributions is strongly dependent on the centre-of-mass energy. These contributions can have an important impact on the determination of cross sections and branching ratios. Furthermore, the combination of on- and off-shell contributions can be exploited to test higher-dimensional operators, unitarity and light and heavy Higgs interferences in extended Higgs. sectors.

The fact that the mass of the observed Higgs boson of about 125 GeV is far below the threshold for on-shell W^+W^- and ZZ production has the consequence that the decay $H \to VV^*$ of an on-shell Higgs boson suffers from a significant phase-space suppression. This implies on the one hand that the partial width $H \to VV^*$, where H is on-shell, depends very sensitively on the precise numerical value of the Higgs-boson mass. On the other hand, contributions of an off-shell Higgs with decays into two on-shell VV are relatively large. The relative importance of contributions of an off-shell Higgs boson increases with increasing cms energy, cf. Table1. For $\sqrt{s} > 500\,\text{GeV}$ those off-shell contributions to the total Higgs induced cross section are of $\mathcal{O}(10\%)$.

The extraction of Higgs couplings to gauge bosons from branching ratios of $H \to VV^*$ re-

quire a very precise measurement of the Higgs-boson mass (preferably better than 100 MeV). At low cms energies $\sqrt{s}$, i.e. close to the production threshold, the effects of off-shell contributions are insignificant for the extraction of Higgs couplings. For an accurate determination of Higgs couplings at higher $\sqrt{s}$, however, the off-shell contributions have to be incorporated.

A particular focus of our analysis has been on the determination of the total width of the Higgs boson at a linear collider. We have investigated two aspects in this context. On the one hand, we have analysed to what extent the standard method at a linear collider, which is based on the Z recoil method providing an absolute measurements of Higgs branching ratios in combination with an appropriate determination of a partial width, is affected by off-shell contributions. We have found that at low cms energies the effect of the off-shell contributions in $H \to VV^{(*)}$ is at the sub-permil level. At higher energies, however, the off-shell effects are larger and need to be properly taken into account and/or reduced by appropriate cuts. However, the method based on the comparison of on-shell and off-shell contributions has several draw-backs. Besides relying heavily on theoretical assumptions, this method requires very high statistics and is limited by the negative interference term. We therefore conclude that the standard method at a linear collider based on the Z recoil method is far superior for determining the Higgs width, both because of its model-independence and the much higher achievable precision. We have also discussed the corresponding method at the LHC and we have pointed out that the destructive interference contribution between the Higgs-induced contributions and the background will make it difficult to reach the sensitivity to the SM value of the width even for high statistics.

As an example of the relevance of off-shell effects in the context of an extended Higgs sector, we discussed the case of a 2-Higgs-Doublet model with a SM-like Higgs at 125 GeV and an additional heavier neutral CP-even Higgs boson with suppressed couplings to gauge bosons. We demonstrated the importance of the interference between off-shell contributions of the light Higgs and the on-shell contribution of the heavy Higgs. If the suppression of the couplings of the heavy Higgs boson to gauge bosons is not too strong, the $H \to VV^{(*)}$ channel can in this way lead to the detection of a heavy Higgs boson at a linear collider, even beyond the kinematical limit for producing a pair of heavy Higgs bosons, H and A.

3 Top quark and electroweak physics in the SM and beyond

Precision measurements of the properties of the top quark and the electroweak gauge bosons present an important part of the physics program of future e^+e^- colliders as they offer additional opportunities to reveal signs of physics beyond the SM and provide important input to the global interpretation of Higgs properties. A crucial role plays the measurement of the top quark mass in continuums measurements as well as via threshold scans, these studies are covered in the project B11 of this SFB [23, 24]. The impact of measurements at the ILC and in particular of its Z-pole option on the global electroweak fit have been studied for instance in the project B8 of this SFB [25].

3.1 Off-shell processes in top quark pair production

Within this project, the prospocts to access the top-quark width by exploiting off-shell regions in the process $e^+e^- \to W^+W^-b\bar{b}$ have been studied [26]. Next-to-leading order QCD corrections have been taken into account and we showed that carefully selected ratios of off-shell regions to on-shell regions in the reconstructed top and anti-top invariant mass spectra are, *independently*

$\sqrt{s}$	$\sigma_{\rm off}^{Z_1Z_2Z_3}$ ($\sigma_{\rm off}^{ZZZ}$)	$\Delta_{\rm off}^{Z_1Z_2Z_3}$ ($\Delta_{\rm off}^{ZZZ}$)	$\sigma_{\rm off}^{\nu\bar{\nu}ZZ}$	$\Delta_{\rm off}^{\nu\bar{\nu}ZZ}$
250 GeV	3.12(3.12) fb	0.03(0.03) %	0.490 fb	0.12 %
300 GeV	2.36(2.40) fb	0.46(1.83) %	1.12 fb	0.40 %
350 GeV	1.71(1.82) fb	1.82(7.77) %	1.91 fb	0.88 %
500 GeV	0.802(0.981) fb	7.20(24.1) %	4.78 fb	2.96 %
1 TeV	0.242(0.341) fb	30.9(50.9) %	15.0 fb	13.0 %
$\sqrt{s}$	$\sigma_{\rm off}^{ZWW}$	$\Delta_{\rm off}^{ZWW}$	$\sigma_{\rm off}^{\nu\bar{\nu}WW}$	$\Delta_{\rm off}^{\nu\bar{\nu}WW}$
250 GeV	76.3 fb	0.03 %	3.98(3.99) fb	0.13(0.12) %
300 GeV	57.7 fb	0.42 %	9.07(9.08) fb	0.29(0.26) %
350 GeV	41.4 fb	0.92 %	15.5(15.5) fb	0.49(0.43) %
500 GeV	18.6 fb	2.61 %	38.2(38.1) fb	1.21(0.96) %
1 TeV	4.58 fb	11.0 %	110.8(108.9) fb	4.45(2.78) %

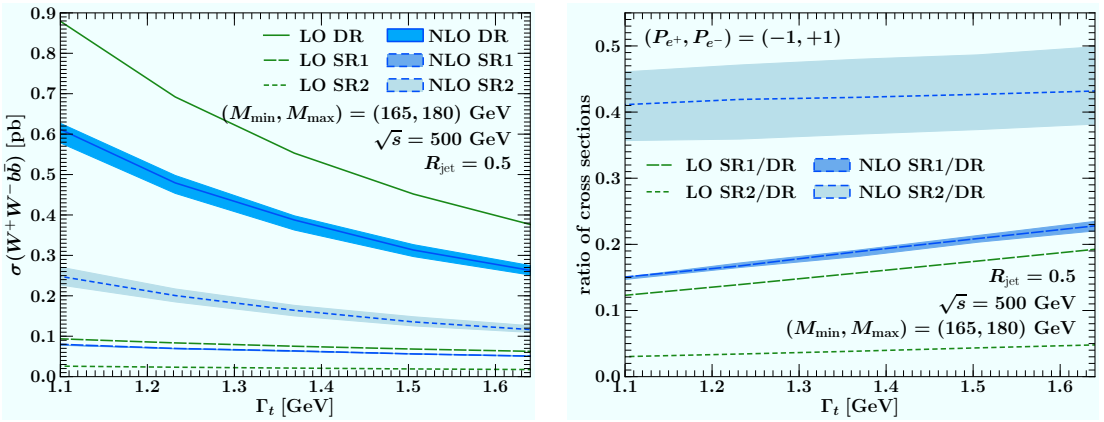
Table 1: Inclusive cross sections $\sigma_{\rm off}(0, \sqrt{s} - m_Z)$ for $e^+e^- \to ZH \to ZVV$ and $\sigma_{\rm off}(0, \sqrt{s})$ for $e^+e^- \to \nu\bar{\nu}H \to \nu\bar{\nu}VV$ for $P(e^+, e^-) = (0.3, -0.8)$ and relative size of the off-shell contributions $\Delta_{\rm off}$ in %. In brackets we add the results averaging over the ZZ pairs for $e^+e^- \to ZZZ$ and taking into account the t-channel Higgs contribution for $e^+e^- \to \nu\bar{\nu}WW$. $\Delta_{\rm off}$ is independent of the polarisation. Table taken from Ref. [22].

of the coupling g_{tbW}, but sensitive to the top-quark width. We have examined the structure of reconstructed top-quark masses allowing for a detailed understanding of the double-, single- and non-resonant contributions of the total cross section. The ratio of single-resonant to double-resonant cross section contributions, cf. Fig. 5, is sensitive to the top-quark width whilst simultaneously being independent of the g_{tbW} coupling. The central results of [26] are the in-depth investigation of this ratio. We have shown that with a careful choice of the single-resonant region of the cross section, such a ratio can successfully be exploited to extract the width at an e^+e^- collider. We have explored the effects that variations in both the jet radius as well as the resonance window (in which reconstructed top quarks are defined to be resonant) have on the ratios. We find that attainable accuracies of < 200 MeV for determining Γ_t are already possible with unpolarised beams at $\sqrt{s} = 500$ GeV. Using polarised beams or higher centre of mass energies would lead to an enhanced sensitivity to Γ_t. We note that this is comparable to the accuracies quoted in the literature obtained from invariant-mass lineshape fitting, but that the results can significantly be improved by further exploiting this methods including polarised initial states.

3.2 Electroweak precision measurements

As an early synergy within the SFB, the fermionic electroweak two-loop corrections to $sin^2\theta_{eff}^{b\bar{b}}$ where calculated in close collaboration with the project B4 [27]. An accurate theoretical prediction is indispensable for the interpretation of b quark asymmetry measurements — at the Z pole, or at the 250 GeV stage of the ILC. It was found that these corrections were sizable, especially for the by now known value of the Higgs mass of about 125 GeV. The experimental capabilities of the ILC at 250 GeV for measuring the couplings of the b quark to the Z boson have been studied recently by our Paris colleagues [28], showing that considerable improvements w.r.t. LEP can be reached even at 250 GeV.

Another important measurement at future e^+e^- colliders will be triple gauge couplings,



(a) (b)

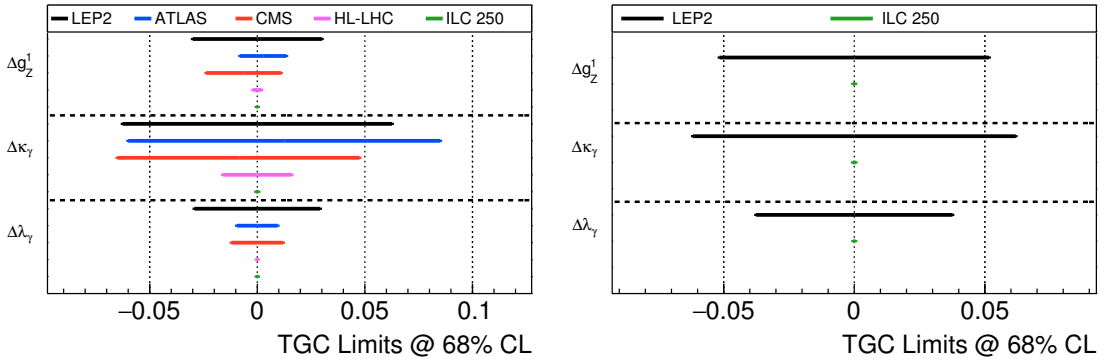
Figure 5: (a) Dependence of cross section $\sigma(e^+e^- \to W^+W^-b\bar{b})/[\text{pb}]$ at $\sqrt{s} = 500$ GeV at LO and NLO on the top-quark width. 'DR' denotes the double resonance region (= two intermediate top-quarks), $SR1$ and $SR2$ (= one intermediate top-quark) or the choice $R_{\text{jet}} = 0,5$ and mass region $M_{\min} = 165$ GeV and $M_{\min} = 180$ GeV. (b) Dependence of the ratios of the single resonant cross sections (SR1 = long dashed, SR2 = short dashed) to the double resonant cross section (DR) on Γ_t and for polarized beams $(P_{e^+}, P_{e^-}) = (-1, +1)$ at $\sqrt{s} = 500$ GeV (LO = green lines, NLO = blue regions). Figures taken from Ref. [26].

especially those involving W bosons. The relevant processes like W pair production or single-W production are highly sensitive to the beam polarisations. Therefore it is important to understand a) the role of beam polarisation in disentangling the effects of the various possible anomalous couplings and b) whether the triple gauge couplings and the actual value of the luminosity-weighted average polarisation cn be extracted simultaneously from the data. The ILC prospects have been studied in the SFB-B1 project w.r.t. both aspects at all relevant center-of-mass energies [9, 29, 30].

Figure 6 compares the most recent study of the ILC prospects at a first 250 GeV stage in comparison to the final LEP2 results, the current ATLAS and CMS measurements based on their 8 TeV data as well as HL-LHC projections [30]. Thereby Fig. 6a shows the achieved or expected uncertainties when only a single parameter at the time is allowed to differ from its SM value, while Fig. 6b is based on a simulataneous extraction of all three considered couplings, which to date is not considered feasible from hadron collider measurements. These projections are included in the EFT-based interpretation of Higgs measurements discussed in the previous section.

4 Supersymmetry

Over the course of the SFB676, the perspective on searches for direct production of new particles and on the determination of their properties changed drastically: In the earlier phases the work was focussed on the prospects for precision measurements on particles which were assumed to be discovered soon at the LHC but the determination of the specific properties and the distinction



(a) (b)

Figure 6: Achieved and achievable precisions on anomalous charged triple gauge couplings at LEP, (HL-)LHC and the ILC. The ATLAS and CMS results correspond to their respective analysis basedon the 8 TeV data. (a) from single-parameter fits (b) from the simultaneous fit of all three couplings, is so far not considered feasible at the LHC. Figures taken from Ref. [5].

of the models was expected to be covered by the LC. With the absence of early discoveries beyond the Higgs boson, the question whether an e^+e^- collider could still discover new particles became of higher and higher relevance. This lead e.g. in 2012 to a comprehensive review of the impact of LHC 8 TeV results and other constraints on the MSSM parameter space and to the definition of new SUSY benchmarks for Linear Collider studies [31]. A recent summary of the BSM opportunities at the ILC, prepared with leading contributions from the SFB-B1 project, can be found in [32]. For an comprehensive review on physics at a LC, providing also on overview about theoretical frameworks, see [1, 33]. In the following, we will highlight a few individual results obtained with this SFB project.

4.1 Determination of particle properties

The challenging task in particle physics —after the observation of new physics signal— is the determination of the underlying new physics model. Since the SM is not only highly consistent with all experimental results so far but also from theoretical point of view, there is no clear direction for a BSM model. Therefore it is even more important to develop strategies how to measure the properties of possible new physics candidates precisely and in a model-independent way. One of the characteristics of several new physics model, as for instance in SUSY or in Universal Extra Dimension (UED) models, is the spin of the new particles.

4.1.1 Spin determination

The spin of supersymmetric particles can be determined unambiguously at e^+e^- colliders. In [34], we showed for a characteristic set of non-colored supersymmetric particles – smuons, selectrons, and charginos/neutralinos, how to determine the spin in a model-independent way via three different steps: analyzing the threshold behavior of the excitation curves for pair production in e^+e^- collisions, the angular distribution in the production process and decay angular distributions, For the production of spin-0 sleptons (for selectrons close to threshold),

Threshold Excitation and Angular Distribution					
SUSY	particle	$\tilde{\mu}$	$\tilde{e}$	$\tilde{\chi}^{\pm}$	$\tilde{\chi}^{0}$
	spin	0	0	1/2	1/2
	σ_{thr}	β^3	β^3	β	β^3
	θ dep.	$\sin^2\theta$	thr: $\sin^2\theta$	thr: isotropic	thr: $1+\kappa\cos^2\theta$
UED	particle	μ_1	e_1	$W_1^{\pm}$	Z_1
	spin	1/2	1/2	1	1
	σ_{thr}	β	β	β	β
	θ dep.	$1+\kappa^2\cos^2\theta$	thr: isotropic	thr: isotropic	thr: isotropic
General	particle	$B[s]$	$B[s,t,u]$	$F_{D,M}[s]$	$F_{D,M}[s,t,u]$
	spin	≥ 1	≥ 1	$\geq 1/2$	$\geq 1/2$
	σ_{thr}	β^3	β	β, β^3	β, β^3
	θ dep.	$1+\kappa\cos^2\theta$	thr: isotropic	$1+\kappa\cos^2\theta$	thr: $1+\kappa\cos^2\theta$

Table 2: The table shows the general characteristics of spin-J particles, the corresponding threshold behavior and the angular distribution in, for instance, SUSY and UED particle pair production processes. B and $F_{D,M}$ generically denote bosons and Dirac, Majorana fermions; The parameters κ [$\kappa \neq -1$] depend on mass ratios and particle velocities β. Measurements of the polar angle distribution in the slepton sector provide unique spin-0 assignments. However, for spin-1/2 particles neither threshold excitation nor angular distributions are sufficient, i.e. also a final state analyses must be performed to determine the quantum numbers. Table reprinted from Ref. [34] with kind permission of The European Physical Journal (EPJ).

it turns out that the $\sin^2\theta$-law for the production is a unique signal of the spin-0 character. However, while the observation of the $\sin^2\theta$-angular-distribution is sufficient for sleptons, the β^3 onset of the excitation curve is a necessary but not a sufficient condition for the spin-0 character. In the case of spin-1/2-particles (chargino/neutralino sector), neither the onset of excitation curves nor the angular distributions in the production processes provide unique signals of the spin quantum numbers. Here, decay angular distributions provide a unique signal for the chargino/neutralino spin $J = 1/2$, albeit at the expense of more involved experimental analyses, cf. Table 2.

4.1.2 Structure of couplings

A specific feature for Supersymmetric models is that the coupling characterics are preserved under SUSY transformations. In order to prove supersymmetry, it is therefore necessary to verify this feature. For instance, the SUSY Yukawa-couplings have to be proven to be identical to the corresponding gauge couplings. In the electroweak sector, it has been shown in [35], that the measurements of polarized cross section serve perfectly well for this purpose. In [36], the study has been extended to the coloured sector and it has been examined whether the quark-squark-gluino Yukawa couplings, can be determined, complementary to LHC analyses, by studying $q - \tilde{q} - \tilde{g}$ and $\tilde{q} - \tilde{q} - g$ and comparing it with the radiation process qqg at a TeV e^+e^- collider. SUSY QCD corrections at NLO have been included. These channels have been investigated to test this fundamental identity between the couplings. While the golden channel measures the $q - \tilde{q} - \tilde{g}$ Yukawa coupling, the radiation processes $\tilde{q} - \tilde{q} - g$ and qqg determine the QCD gauge coupling in the $\tilde{q}$-sector and the standard q-sector for comparison.

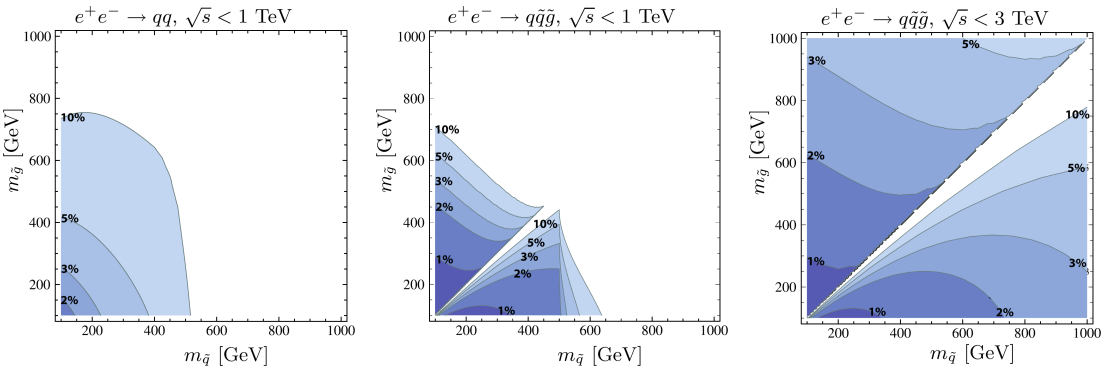
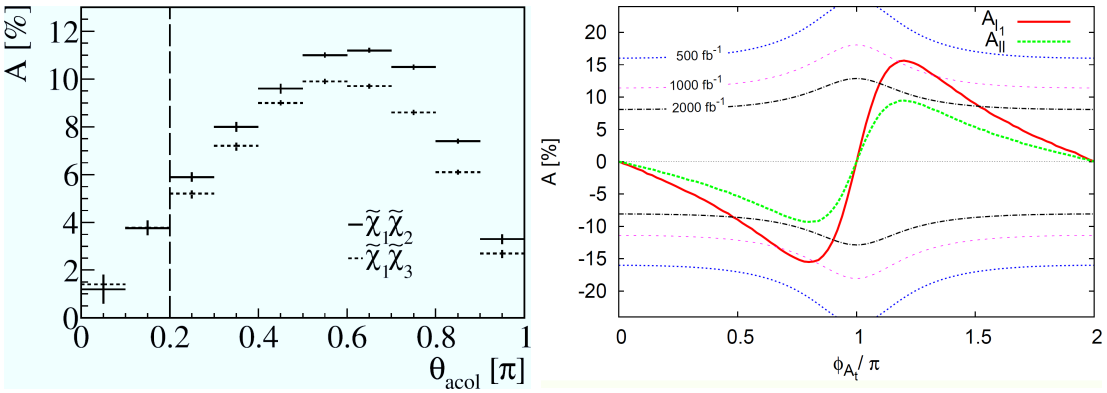


Figure 7: Contour plots of the statistical 1-σ errors of the Yukawa coupling $\Delta\alpha_s/\alpha_s$ in the $[m_{\tilde{q}}, m_{\tilde{g}}]$ mass plane; (a) the indirect channel $e^+e^- \to qq$ at $\sqrt{s} \leq 1$ TeV; the golden direct channel $e^+e^- \to q\tilde{q}\tilde{g}$, corresponding to (b) a maximal ILC $\sqrt{s} \leq 1$ TeV, and (c) up to $\sqrt{s} \leq 3$ TeV for CLIC, respectively. Figures reprinted from Ref. [36] with kind permission of The European Physical Journal (EPJ).

A few percent variation in the Yukawa couplings is observable at e^+e^- colliders, depending on the masses of the squark and gluinos, cf. Figs.7. Such a potential is fully complementary to the respecting potential at the LHC where the production of $\tilde{q}$-pairs in qq collisions provides a stage for the measuriing the SUSY-QCD Yukawa coupling, requiring however, an ensemble of auxiliary measurements of decay branching ratios.

4.1.3 CP properties

Since SUSY offers naturally new sources for CP-violation, required for explaining the baryon-antibaryon asymmetry in our Universe, it is of high importance to work out to which extent these phases could be determined in experiments. The sizes of these phases are constrained by experimental bounds from the electric dipole moments (EDMs). Such experimental limits generally restrict the CP phases to be small, in particular the phase Φ_μ. Cancellations among different contributions to the EDMs can occur so that still large CP phases could happen, causing CP-violating signals at colliders. Thus, direct measurements of SUSY CP-sensitive observables are necessary to determine or constrain the phases independently of EDM measurements. The phases change SUSY particle masses, their cross sections, branching ratios. However, although such CP-even observables are sensitive to the CP phases, CP-odd (T-odd) observables have to be measured for a direct evidence of CP violation. In [37, 38] triple product asymmetries have been studied in an interdisciplinary theo-exp endeavour resulting a first experimentally-oriented analysis based on a full detector simulation with regard to the observation of CP asymmetries, cf. Fig.8 (a): the process $e^+e^- \to \tilde{\chi}_i^0\tilde{\chi}_j^0$ and subsequent leptonic two-body decays $\tilde{\chi}_i^0 \to \tilde{l}_R l, \tilde{l}_R \to \tilde{\chi}_1^0 l$, for $l = e, \mu$ has been calculated and the expected triple product asymmetry between the incoming e^- and final leptons ℓ^+, ℓ^- has been evaluated, including the relevant Standard Model background processes, a realistic beam energy spectrum as well as beam backgrounds. Assuming an integrated luminosity of 500 fb$^-$1 and simultaneous beam polarization of $P_{e^-} = +80\%$ and $P_{e^+} = -60\%$ a relative measurement accuracy of 10%



(a) (b)

Figure 8: (a) The θ_{aco} dependence of the asymmetries of $A\left[\vec{p}_{e-}, \vec{p}_{\ell-N}, \vec{p}_{\ell+F}\right]_{\tilde{\chi}_1^0\tilde{\chi}_2^0}$ (solid) and $A\left[\vec{p}_{e-}, \vec{p}_{\ell-N}, \vec{p}_{\ell+F}\right]_{\tilde{\chi}_1^0\tilde{\chi}_3^0}$ (dashed). The cut value used in our analysis is indicated by the dashed line. In each case 10^7 events were generated and no detector effects are included. Figure reprinted from Ref. [37] with kind permission of The European Physical Journal (EPJ). (b) The asymmetries, originating in stop decays into neutralinos, A_{l_1} and A_{ll}, along with the lines showing the asymmetry required for a 3σ observation at a given integrated luminosity of 500 fb^{-1}, 1000 fb^{-1} and 2000 fb^{-1} at $\sqrt{s} = 1$ TeV in the case of momentum reconstruction. Figure taken from Ref. [39].

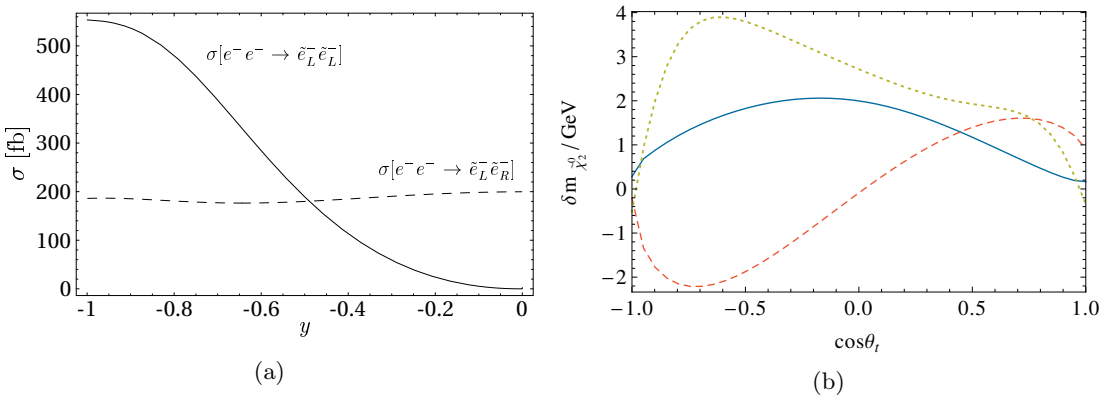
for the CP-sensitive asymmetry is achievable. We demonstrate that our method of signal selection using kinematic reconstruction can be applied to a broad class of scenarios and it allows disentangling processes with similar kinematic properties.

In [39] another channel for exploiting CP-odd observables has been studied: triple product correlations originating from $\tilde{t}_1$ decays into neutrlinos $\tilde{\chi}_2^0$: $T_{l1}^{\mp} = (\vec{p}_{l1} \cdot (\vec{p}_W^{\mp} \times \vec{p}_t)$, $T_{ll}^{\mp} = (\vec{p}_b \cdot (\vec{p}_{l^+} \times \vec{p}_{l^-})$. Assuming a successful momentum reconstruction a maximal asymmetry can be observed with at least 1000 fb^{-1} collected data. The result showed that the CP violating phase ϕ_{A_t} of the trilinear top coupling accounted for a maximal triple product asymmetry of approximately 15.5 %, cf. Fig. 8 (b). Under the assumption of successful momentum reconstruction, this asymmetry could be measured for 2000 fb^{-1} collected data in the region of a maximal CP violating angle, $1.10\pi < \phi_{A_t} < 1.5\pi$. With an integrated luminosity of 1000 fb^{-1} the asymmetry could still be exposed close to the maximum ($1.18\pi < \phi_{A_t} < 1.33\pi$). The results show that a future linear collider with high luminosity is essential.

4.1.4 Majorana character

SUSY offers not only Dirac-type fermions but also Majorana-type massive fermions (where the particle is its own antiparticle). This property is particularly difficult to prove uniquely experimentally, it is affected by the impact of spin correlations in production×three-body decays [40], threshold behaviours [41] and two-body decays [42].

The study [43] addresses the comparison of the production of Majorana-like neutralinos and gluinos in the MSSM with that of Dirac-like neutralinos and gluinos within the framework of $N = 2$ MSSM. Decays of such self-conjugate particles generate charge symmetric ensembles of



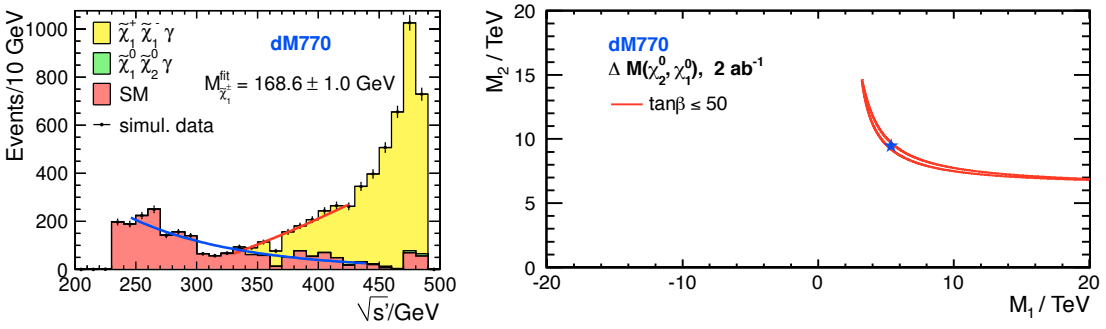
(a) (b)

Figure 9: (a) Partonic cross sections for same-sign selectron production as a functions of the Dirac/Majorana control parameter y, for $\sqrt{s} = 500$ GeV and SPS1a' parameters. Not shown is the cross section for $e^-e^- \to \tilde{e}_L^-\tilde{e}_R^-$, which, apart from the different normalization, shows a similar behavior as the cross section for $e^-e^- \to \tilde{e}_L^-\tilde{e}_L^-$. Reprinted figure with permission from Ref. [43]. Copyright (2008) by the American Physical Society. (b) One-loop corrections to the masses of neutralinos $\tilde{\chi}_2^0$ as a function of the stop mixing angle $\cos\theta_t$, for three scenarios S1 ($(M_1, M_2, \mu) = (125, 250, 180)$ GeV) (blue), S2 ($(M_1, M_2, \mu) = (125, 2000, 180)$ GeV) (red, dashed) and S3 ($(M_1, M_2, \mu) = (106, 212, 180)$ GeV) (green, dotted). Figure reprinted from Ref. [44] with kind permission of The European Physical Journal (EPJ).

final states. The LC offers a unique possibility to adjust the experimental conditions particularly well to specific needs of the theories: the $^-e^-$-mode would offer unique possibilities to test the Majorana- versus Dirac-exchange-character of the involved processes. In the study, it has been analyzed to which extent like-sign dilepton production in the process $e^-e^- \to \tilde{e}^-\tilde{e}^-$ is affected by the exchange of either Majorana or Dirac neutralinos, see Fig. 9 (left panel). Using polarized beams at an e^-e^--LC, the Dirac/Majorana character can be studied experimentally. The 'conclusio generalis' of [43] is that the Majorana theory can be discriminated from the Dirac theory using like-sign dilepton events at the level of more than 10σ.

4.2 Light higgsinos

Another important SUSY example are scenarios with light higgsinos. They can be motivated by naturalness arguments [45], but also occur in hybrid gauge-gravity mediation models motivated by string theory. The latter case has been studied in close collaboration with the A1 project of this SFB [46,47]. Two benchmark points with higgsino mass splittings of 1.6 GeV and 770 MeV, respectively, have been chosen to evaluate the ILC prospects in detailed simulation of the ILD detector concept. This study led to a new awareness within the ILD concept group concerning the importance of designing the detector with sufficient sensitivity to low-momentum particles, and these model-points have become standard benchmarks for the ILD detector optimisation process. Figure 10a shows the recoil mass of a chargino pair against an ISR photon. From the endpoint of the signal distribution the mass of the chargino can be determined with sub-percent precision already from 500 fb^{-1}. Together with the determination of the mass difference to the LSP from the energy distribution of the visible decay products and the polarised cross sections,



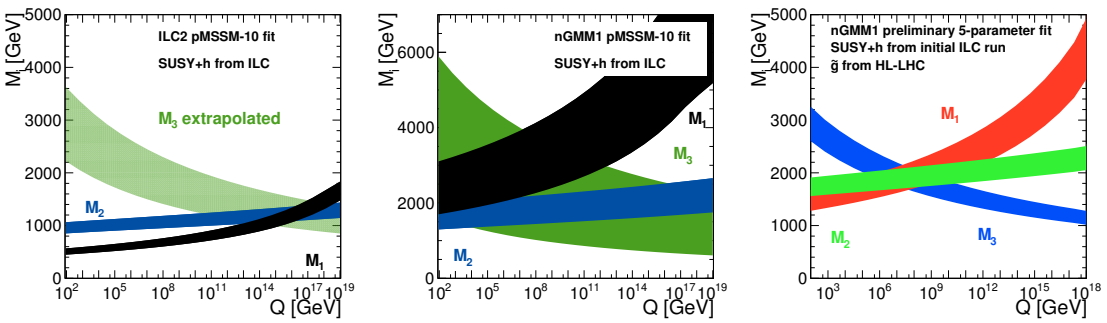
(a) (b)

Figure 10: Light higgsinos with sub-GeV mass differences at the ILC: (a) Measurement of the chargino mass from the recoil against an ISR photon for 500 fb^{-1} at 500 GeV. (b) Constraint on the multi-TeV gaugino mass parameters M_1 and M_2 obtained from higgsino mass and cross section measurements at the 500 GeV ILC, based on an integrated luminosity of 2000 fb^{-1}, split equally between the two opposite-sign beam polarisation states. Figures reprinted from Ref. [46] with kind permission of The European Physical Journal (EPJ).

the higgsino mass parameter μ can be determined, and the gaugino mass parameters can be constrained to a narrow region in the multi-TeV regime, which is shown in Fig. 10b.

In the case of light higgsino scenarios with somewhat larger mass differences of a few GeV, even a full SUSY parameter determination can be carried out. Three different benchmark points with chargino-LSP mass differences of 11, 6 and 2.5 GeV, respectively have been studied in full detector simulation of the ILD concept, and the resulting percent-level precisions on masses and polarised cross sections have been used as inputs to SUSY parameter fits at the weak scale and at the GUT scale [48, 49]. Similar as in case of the STC benchmark series discussed above, also in these cases the masses, or, in case of the coloured sector, mass ranges of the unobserved sparticles can be predicted. The relic density of the LSP can also be well determined, showing in these cases clearly that the LSP provides only a small fraction of the dark matter in the universe, while the rest would need another explanation, like e.g. axions — another important topic in the SFB 676.

Figure 11 goes, however, even one step further: it shows the RGE running of the gaugino mass parameters as determined from a weak-scale pMSSM-10 fit to ILC observables up to the GUT scale. The width of the bands reflects both the uncertainties of the parameter values at the weak scale as well as the uncertainty in the RGE running due to the finite knowledge of the involved SUSY parameters. Three different cases are displayed: Fig. 11a shows the situation in the NUHM2 benchmark with the medium mass differences based on full simulation of the ILD detector. M_3 is extrapolated back down to the weak scale assuming gaugino mass unification at the GUT-scale, with $M_{1/2}$ being determined to about 10% precision from M_1 and M_2. The smallest mass difference case has been studied in a benchmark based on a mirage mediation model and is shown in Fig. 11b. A standard GUT-scale unification of the gaugino masses can be excluded at the 99.9% confidence level. Figure 11c shows the RGE running in the same benchmark, but instead of using the mass and cross section precision obtained from the full simulation study, hypothetical resolutions of 1% on the masses and 3% on the



(a) (b) (c)

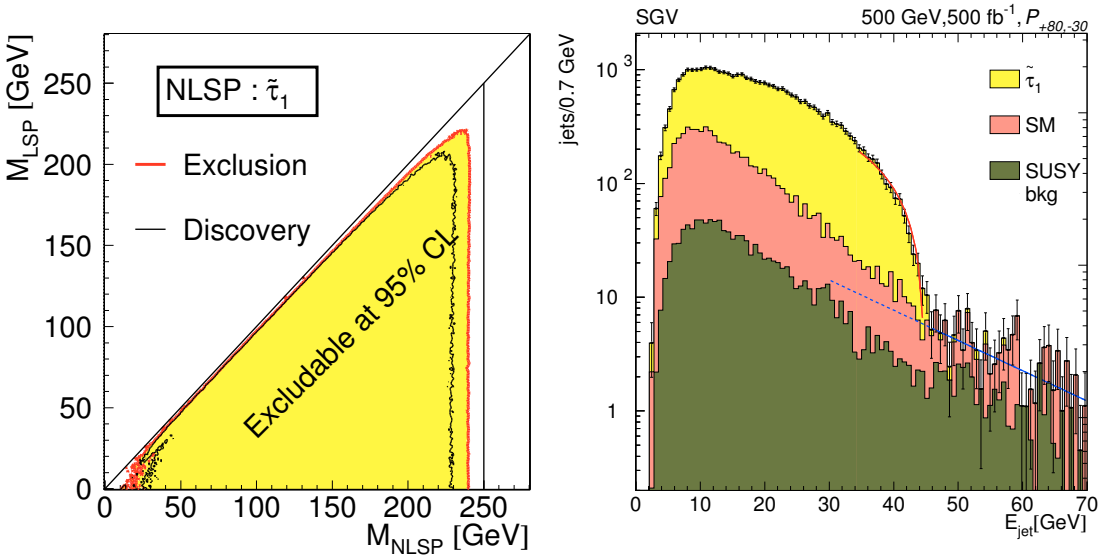
Figure 11: Light higgsinos with few-GeV mass differences at the ILC: (a) RGE running of gaugino mass parameters determined from a weak-scale pMSSM-10 fit to ILC measurements in an NUHM2 benchmark. M_3 is extrapolated back down to the weak scale assuming gaugino mass unification, predicting a gluino at about 3 TeV. (b) Same excercise in case of a mirage mediation benchmark. A standard GUT-scale unification of the gaugino masses can be excluded at the 99.9% confidence level. (c) Same benchmark as in (b), but with more optimistic assumptions described in the text. Figures taken from Ref. [49].

cross sections have been used. This corresponds to about a factor of 2 improvement in the experimental resolutions. In addition, a 10% measurement of the gluino mass at the HL-LHC has been assumed here, and the parameters for the multi-TeV scalars have been fixed. As can be seen from the comparison of Figs. 11b and 11c, such improvements would make a qualitative difference to the determination of the mass unification scale, where the impact of the fixed parameters remains to be quantified. Possibilities to improve the capabilities of the ILD detector are being evaluated by the ILC concept group.

4.3 $\tilde{\tau}$ co-annihilation models

A long term focus of the SFB-B1 project has been the study of SUSY scenarios with a $\tilde{\tau}$ as the next-to-lightest SUSY particle (NLSP), especially when its mass difference to the lightest SUSY particle (LSP) is small. In these cases, the cosmologically observed relic density of dark matter can be explained by co-annihilation between NLSP and LSP. At the same time, the searches for $\tilde{\tau}$'s are very challenging at the LHC, so that currently there is effectively no exclusions beyond the LEP results [50, 51], and also the HL-LHC prospects are very limited [52], in particular for mass differences less than about 100 GeV.

The prospects for discovering any NLSP, but especially also the most difficult case of a $\tilde{\tau}$ NLSP at the ILC have been evaluated in [53]. As can be seen in Fig. 12a, the exclusion and discovery potential in the $\tilde{\tau}$ vs LSP mass plane is highly complementary to (HL-)LHC prospects, since also compressed spectra can be probed up to a few GeV below the kinematic limit already with about an eighth of the total luminosity. This immediately leads to the question of precision spectroscopy, which has been studied originally based on the famous SPS1a' benchmark scenario [54, 55]. These studied showed that production cross sections and masses of $\tilde{\tau}_1$ and $\tilde{\tau}_2$ can be measured to the percent-level, and that the polarisation of the τ's from the $\tilde{\tau}_1$ decay, which gives a handle on the mixings of the $\tilde{\tau}$ and the LSP, can be determined



(a) (b)

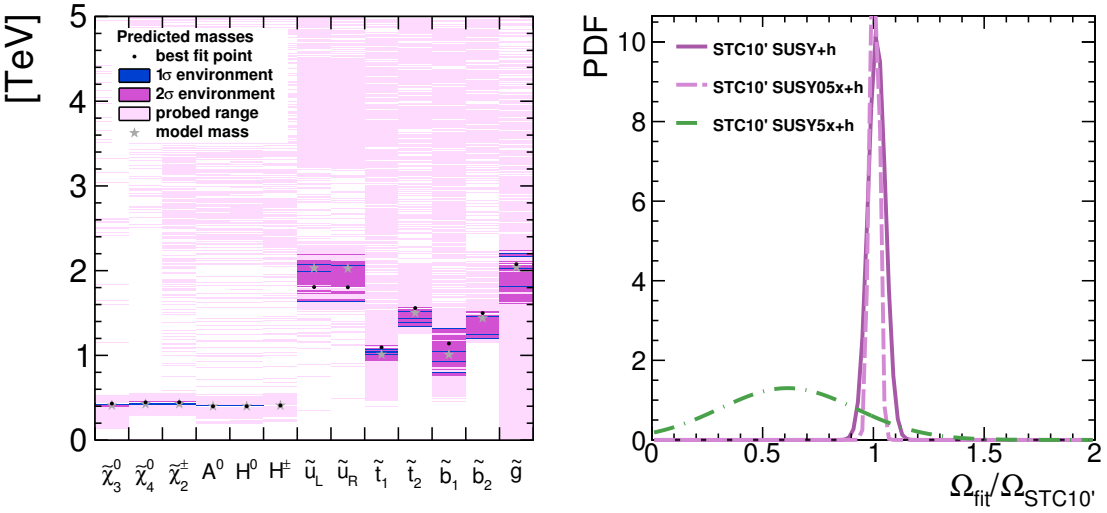
Figure 12: ILC capabilities in the $\tilde{\tau}$ sector from a simulation study of $\tilde{\tau}_1$ pair production based on the ILD detector: (a) exclusion and discovery reach in the $\tilde{\tau}$ vs LSP mass plane for 500 fb^{-1} at 500 GeV, corresponding to about an eighth of the foreseen data set at 500 GeV. Figure taken from Ref. [53]. (b) τ energy spectrum from signal and SUSY and SM backgrounds. The measurement of the endpoint enables a determination of the $\tilde{\tau}$ mass with a precision of 200 MeV. Figures taken from Ref. [56] as update of Ref. [54].

to a few percent. Figure 12b shows the τ energy spectrum as expected from the $\tilde{\tau}_1$ decay which is input to the determination of the $\tilde{\tau}_1$ mass via kinematic edges.

The original SPS1a' scenario had a very light coloured sector, which was quickly excluded after the start of the LHC. Therefore the more recent studied where based on the STC benchmark series from [31] which has a very similar electroweak sector than SPS1a', but a much heavier coloured sector. In a joined study between the SFB-B1 project and the DESY CMS group, the interplay between LHC and ILC was investigated in these benchmarks, as opposed to the by then popular simplified models [56]. This study highlighted the complementarity and synergies between hadron and lepton colliders, even identifying cases where the knowledge of some sparticle masses from the ILC enables the targeted search for heavier states in LHC data. It also showed that in full SUSY models which can include many decays modes and long decay chain, the naive application of limits formulated in simplified models can be misleading.

The final step then was to investigate whether the precisions of masses and cross sections would be sufficient to e.g. identify the LSP as main component of dark matter, to determine the underlying SUSY model and parameters as well as to predict masses of yet unobserved sparticles, which woud provide important input to upgrades of the ILC or the design of e.g. the next high-energy hadron collider [49].

Figure 13a shows the predictions for the masses of the unobserved sparticles obtained from an pMSSM-13 fit to ILC SUSY and Higgs observables, based on a data set of 1000 fb^{-1} at



(a) (b)

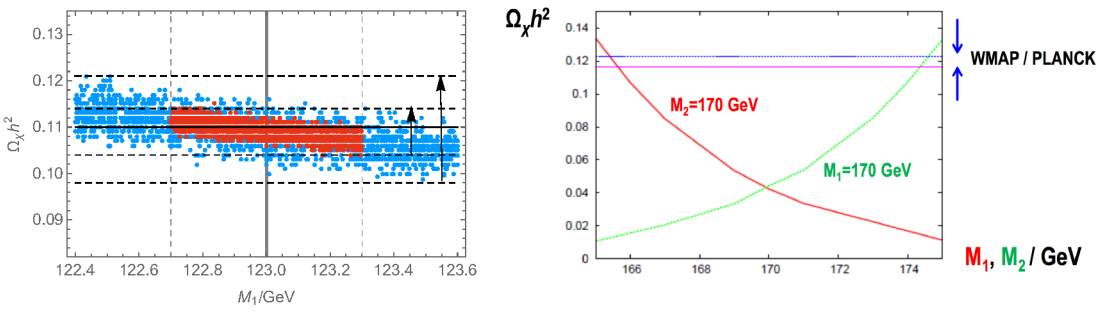
Figure 13: SUSY parameter determination at the ILC: (a) Masses of unobserved sparticles predicted from an pMSSM-13 fit to ILC SUSY and Higgs observables based on 1000 fb^{-1} at 500 GeV in the STC10' benchmark (b) Prediction of the LSP relic density from the same fit, showing also the impact of 5 times worse and 2 times better precisions, whether the latter corresponds to the 4000 fb^{-1} at 500 GeV in the standard H20 running scenario. Figures taken from Ref. [49].

500 GeV, split equally between $\mathcal{P}(e^-e^+) = (\pm 80\%, \mp 30\%)$, corresponding to about a quarter of the foreseen luminosity at 500 GeV. The probability density function for the prediction of the LSP relic density from the same fit is displayed in Fig. 13b, along-side the analogous results for a 5 times worse and a 2 times better resolution. It can be clearly seen that in the worse resolution case it is not possible to constrain the relic density in a satisfactory way, thus the precisions at the percent and for some observables at the permille are essential in order to identify the LSP as the dark matter particle.

4.4 Impact of electroweak loops, in particular on dark matter searches

Since the ILC is designed to perform high precision measurements of masses, cross sections and branching ratios with high accuracy in the per-cent level, such a precision has to be matched from the theoretical side as well and tree-level calculations will not be sufficient. This project focuses on the SUSY Higgs and electroweak sector and the relevant parameters. Since via the loop effects not only the fundamental parameters M_1, M_2, μ, $\tan\beta$ enter, but also other mass parameters of heavier states, the well-known strategies for determining the fundamental SUSY parameters [35] have to be extended. In many models, the lightest and stable SUSY particle is the neutralino $\tilde{\chi}_1^0$, often treated as suitable dark matter candidate. The precise determination of parameters has therefore direct impact on the predicted dark matter contribution as well.

The first step in this project [44, 57, 58] was to incorporate quantum corrections in the theoretical calculation in order to determine the underlying SUSY parameters from measurements



(a) (b)

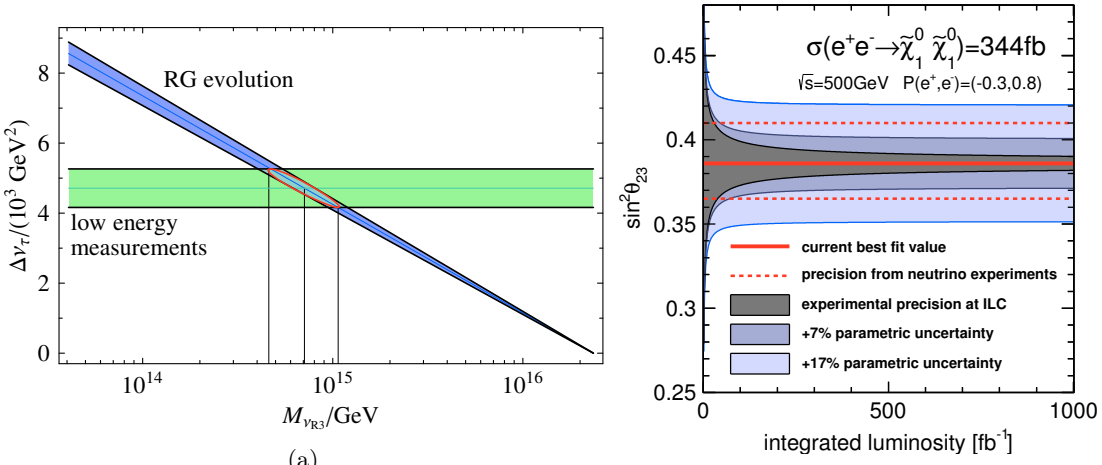
Figure 14: (a) Determination of fundamental SUSY parameters at % level (including evaluation of loop corrections) in scenario S1 either via mass measurements in he continuum (blue area) or via threshold scans (red area) and the resulting uncertainty in the prediction of the dark matter density. (b) Dark matter density caused by the DM candidate $\tilde{\chi}_1^0$ and its strong dependence on the gaugino SUSY parameters. High precision is required for accurate predictions for Ωh^2 [62].

of chargino/neutralino masses and cross sections. The one-loop predictions were fitted to the prospective measurements of cross sections, forward-backward asymmetries and the accessible chargino and neutralino masses. Since the one-loop contributions are dominated by the stop sector, the accurate determination of the desired parameters provides also access to the stop masses and mixing angle. Having determined the fundamental parameters [59–61] using 1-loop corrected observables, we have applied the results to the prediction of the expected dark matter contribution. The impact of the one-loop corrected parameters, in particular M_1 causes up to a 10% correction for the corresponding dark matter contribution in Ωh^2, see Fig. 14.

A particular challenge of this SFB project [57] was to work out consistent renormalization in the on-shall scheme in the complex MSSM. The impact of this quantum corrections has been evaluated in Higgs decays $h(a) \to \tilde{\chi}_i^+ \tilde{\chi}_j^-$, where the Higgs-propagator corrections have been incorporated up to the two-loop level, as well as in chargino production $e^+e^- \to \tilde{\chi}_i^+ \tilde{\chi}_j^-$. Concerning the parameter renormalisation in the chargino and neutralino sector, we have shown that the phases of the parameters in the chargino and neutralino sector do not need to be renormalised at the one-loop level. We have therefore adopted a renormalisation scheme where only the absolute values of the parameters M_1, M_2 and μ are subject to the renormalisation procedure. In order to perform an on-shell renormalisation for those parameters we have worked out the strategy choosing three out of the six masses in the chargino and neutralino sector that are renormalised on-shell, while the predictions for the physical masses of the other three particles receive loop corrections.

4.5 Extended SUSY models

SFB676-B1 project studied also extended SUSY models, as for instance, unification models, models with an extended $U(1)$ sector as well as models with R-parity violation that can explain neutrino mixing scenarios.



(a) (b)

Figure 15: (a) Shift $\Delta_{\nu\tau}$ of the third generation L slepton mass parameter generated by loops involving heavy neutrino R-superfields. The blue area corresponds to the prediction originating from the renormalization group [RG], whereas the green band is determined by low-energy mass measurements. Reprinted figure with permission from Ref. [63]. Copyright (2008) by the American Physical Society. (b) Precision of the measurement of the neutrino mixing angle θ_{23} via $e^+e^- \to \tilde{\chi}_1^0\tilde{\chi}_1^0\gamma$ at the ILC compared with the corresponding achievable precision via neutrino experiments. Figure taken from Ref. [64].

4.5.1 Unification models: supersymmetric SO(10) models

Extrapolations of soft scalar mass parameters in supersymmetric theories can be used to explore elements of the physics scenario near the grand unification scale. In [63] the potential of this method in the lepton sector of SO(10) which incorporates right-handed neutrino superfields has been explored. Two examples have been analyzed in which high-scale parameters in supersymmetric SO(10) models have been connected with experimental observations that could be expected in future high-precision Terascale experiments at LHC and e^+e^- linear colliders: a) the case for a one-step breaking SO(10) $\to$ SM and b) the analysis of two-step breaking SO(10) $\to$ SU(5) $\to$ SM. The renormalization group provides the tool for bridging the gap between the Terascale experiments and the underlying high-scale grand unification theory. Even though it depends on the detailed values of the parameters with which resolution the highscale picture can be reconstructed, a rather accurate result could be established in the example for one-step breaking SO(10) $\to$ SM, including the heavy mass of the right-handed neutrino ν_{R3} expected in the seesaw mechanism. As naturally anticipated, the analysis of two-step breaking SO(10) $\to$ SU(5) $\to$ SM turns out to be significantly more difficult, demanding a larger set of additional assumptions before the parametric analysis can be performed, see Fig.15a.

4.5.2 U(1)-extended SUSY models: light singlets

Motivated by grand unified theories and string theories, there has been analyzed in [65] the general structure of the neutralino sector in the USSM, an extension of the Minimal Supersym-

metric Standard Model that involves a broken extra U(1) gauge symmetry. This supersymmetric U(1)-extended model includes an Abelian gauge superfield and a Higgs singlet superfield in addition to the standard gauge and Higgs superfields of the MSSM. The interactions between the MSSM fields and the new fields are in general weak and the mixing is small, so that the coupling of the two subsystems can be treated perturbatively. Light singlets escaping LEP and LHC bounds, are natural in these models. Prospects for the production channels in cascade decays at the LHC and pair production at e^+e^- colliders have been discussed in this SFB study.

4.5.3 R-Parity violating SUSY: bridge from collider to neutrino physics

Supersymmetry (SUSY) with bilinearly broken R parity (bRPV) does not provide any dark matter candidates, but offers an attractive possibility to explain the origin of neutrino masses and mixings. In such scenarios, the study of neutralino decays at colliders can give access to neutrino parameters. In [64] a full detector simulation for neutralino $\tilde{\chi}_1^0$-pair-production and two-body decays has been performed including Standard Model background processes. As studied parameter point a worst case scenario has been used, where $m_{\tilde{\chi}_1^0} \sim m_{W/Z}$, thus, the signal significantly overlaps with SM background. It has been developed a model-independent selection strategy to disentangle the different event classes involving the two decay modes of the LSP $\tilde{\chi}_1^0 \to \mu^{\pm}W^{\mp}$ and $\tilde{\chi}_1^0 \to \tau^{\pm}W^{\mp}$. The $\mu\mu$ and $\mu\tau$ events have been used to determine the ratio of the two branching ratios $BR(\tilde{\chi}_1^0 \to \mu^{\pm}W_{\mp})/BR(\tilde{\chi}_1^0 \to \tau^{\pm}W_{\mp})$, which is related to the atmospheric neutrino mixing angle $\sin^2\theta_{23}$. For an integrated luminosity of 500 fb^{-1} the total uncertainty on this ratio, including statistical and systematic uncertainties, has been determined to 4%, see Fig.15b. In addition it has been shown that the precision in measuring the atmospheric neutrino mixing angle is in the same range than measurements from neutrino oscillation experiments, even when taking parametric uncertainties due to the unknown parts of the SUSY spectrum into account. Therefore, the International Linear Collider is highly capable to test bRPV SUSY as origin of neutrino masses and mixings.

5 Other extensions of the SM

Although Supersymmetry is one of the best motivated BSM models, explaining several of the remaining open questions of the SM, it is of great importance to study also further BSM models like Little Higgs models as well as models with large extra dimensions or gauge group extended models.

5.1 Automatisation of BSM models

It is of great importance to check new physics models against data of the LHC and of expected data at the ILC. The original purpose of the computing tool CheckMATE, public code to perform collider phenomenology, was to offer theorists a way to quickly test their favourite BSM models against various existing LHC analyses. It consists of an automatised chain of Monte Carlo event generation, detector simulation, event analysis and statistical evaluation and allows to check whether a given parameter point of a BSM model is excluded or not on basis of currently more than 50 individual ATLAS or CMS analyses at both energies $\sqrt{s} = 8$ and 13 TeV [66]. The used recasting procedure is a powerful procedure which applies existing collider results on new theoretical ideas without requiring the full experimental data analysis to be restarted. Theories which share experimentally indistinguishable topologies can be tested

via identical event selection techniques, bearing the advantage that background expectation and the number of observed events stay constant.

We were able to make use of the powerful features of the Monte Carlo event generator Whizard to simulate e^+e^- collisions including the effects of beam polarisation, initial state radiation and beamstrahlung. Furthermore, we continue using the fast detector simulation Delphes to describe the ILD detector. Currently it provides a good approximation of the most relevant acceptance and efficiency factors. Lastly, we extended the set of accessible parameters in CheckMATE, allowing users to test different polarisation and luminosity combinations. This makes it very convenient to discuss the importance of e.g. the lepton polarisation for the overall sensitivity of the experiment to a given BSM hypothesis. CheckMATE fuctionality has been extended to analysis studies for different ILC set-ups, as, for instance, different beam polarization configurations, variable energies etc. Of particular interest are challenging studies for the LHC, as, for instance, monophoton searches for dark matter particles in compressed spectra [67].

5.2 Little Higgs models

Another model that has been checked with the help of CheckMATE against real LHC data at 8 TeV and13 TeV are little Higgs models with T-Parity [67]. We scrutinize the allowed parameter space of Little Higgs models with the concrete symmetry of T-parity by providing comprehensive analyses of all relevant production channels of heavy vectors, top partners, heavy quarks and heavy leptons and all phenomenologically relevant decay channels.

This model is an elegant implementation of global collective symmetry breaking combined with a discrete symmetry to explain the natural lightness of the Higgs boson as a (pseudo-) Nambu-Goldstone boson. This model predicts heavy partners for the Standard Model quarks q_H, leptons ℓ_H, gauge bosons W_H, Z_H, A_H and special partners for the top quark $T^{\pm}$. Constraints on the model will be derived from the signatures of jets and missing energy or leptons and missing energy. Besides the symmetric case, we also study the case of T-parity violation. Furthermore, we give an extrapolation to the LHC high-luminosity phase at 14 TeV. Our results show that, although the Littlest Higgs model with T-parity has been constrained much stronger by LHC run 2 data, it is still a rather natural solution to the shortcomings of the electroweak and scalar sector, and we will need full high-luminosity data from the LHC to decide whether naturalness is actually an issue of the electroweak sector or not. A qualitative improvement of all bounds on the model, particularly in the Higgs sector and the heavy lepton sector, might need the running of a high-energy lepton collider (or a hadron collider at much higher energy).

5.3 Z' models, models with large extra dimensions and contact interaction models

Another class of new physics models are models with an additional Z' boson. Unfortunately up to now no additional $Z-$boson has been found (yet) at LHC. That means, the limits on $m_{Z'}$ are already in the multi-TeV region, depending on the model and on the number of extra dimensions, and it is crucial to determine the sensitivity to such new physics models via measuring deviations of the cross sections from their Standard Model predictions. Due to the clean environment at the ILC, precise measurements of well-known SM processes, as, for instance W^+W^--production and the Z-pole, are predestinated for such searches.

5.3.1 Z' models and models with heavy leptons

In this SFB-B1 study [68], we therefore discuss the expected sensitivity to Z's in $W^{\pm}$-pair production cross sections at the ILC. In particular it is focussed on the potential for distinguishing observable effects of the Z' from analogous ones in competitor models with anomalous trilinear gauge couplings (AGC) that can lead to the same or similar new physics experimental signatures at the ILC. The sensitivity of the ILC for probing the Z-Z' mixing and its capability to distinguish these two new physics scenarios is substantially enhanced when the polarizations of the initial beams and the produced $W^{\pm}$ bosons are considered. A model independent analysis of the Z' effects in the process $e^+e^- \to W^+W^-$ allows to differentiate the full class of vector Z' models from those with anomalous trilinear gauge couplings, with one notable exception: the sequential SM (SSM)-like models can in this process not be distinguished from anomalous gauge couplings. Results of model dependent analysis of a specific Z' are expressed in terms of discovery and identification reaches on the Z-Z' mixing angle and the Z' mass, cf. Fig. 16 (a).

In [69], we extended our Z' searches and explore the effects of neutrino and electron mixing with exotic heavy leptons in the process $e^+e^- \to W^+W^-$ within E_6 models, which also incorporate an additional Z'. We examine the possibility of uniquely distinguishing and identifying such effects of heavy neutral lepton exchange from $Z - Z^0$ mixing within the same class of models and also from analogous ones in competitor models with anomalous trilinear gauge couplings (AGC) that can lead to very similar experimental signatures at the ILC with $\sqrt{s} = 350$, 500 GeV and 1 TeV. A clear identification of the model with respect to is possible by using a certain double polarization asymmetry that requires simultaneously polarized e^- and e^+ beams. In addition, the sensitivity of the ILC for probing exotic-lepton admixture is substantially enhanced when the polarization of the produced $W^{\pm}$ bosons is considered, cf. Fig. 16(b).

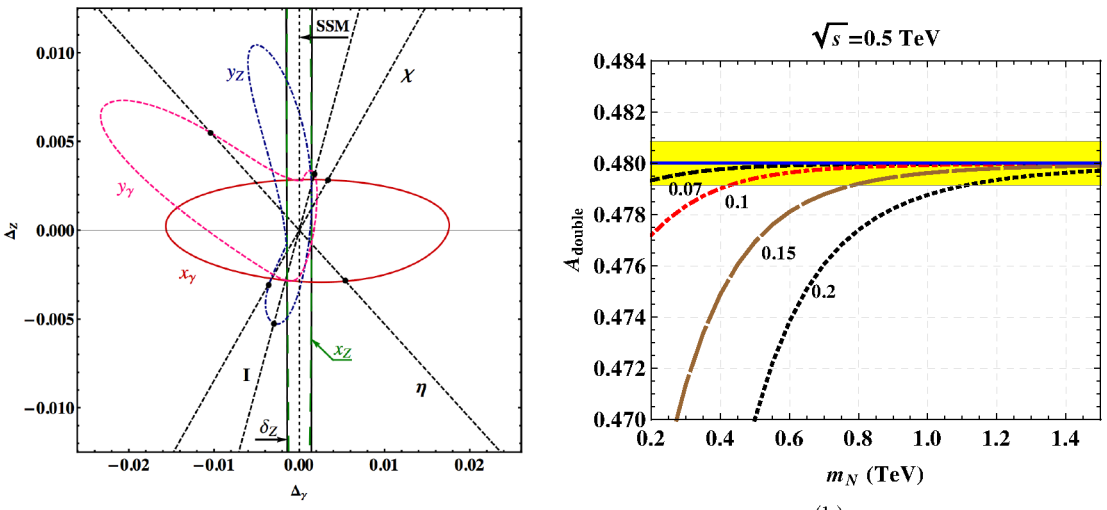
5.3.2 Large extra dimension and contact interactions

Concerning high precision measurements at the Z-pole, both high luminosity and the polarization of both beams are mandatory to achieve a precision in the determination of the electroweak mixing angle, of about one order of magnitude better than at LEP and SLC. In [7] the physics potential at a Z-factory (corresponding to the GigaZ-option at the ILC) has been summarized. This article explains the fundamentals in (beam) polarization and provides an overview of the impact of these spin effects in electroweak precision physics. Measuring the left-right-asymmetry at the Z-pole under these conditions allows to resolve the discrepancy between the experimentally measured values of $sin^2\theta_{\text{eff}}$ derived from A_{LR} and from A_{FB}. The measured value has immediate impact on predictions in the Higgs and beyond Standard Model physics sector.

In [6] the potential of polarized beams has been summarized in searches for contact interactions, for large extra dimensions and SUSY. In many case, the availability of both beams polarized in particular allows in particular the distinction of different models, as for instance, between the RS-model and the ADD-model concerning extra dimension or the model-independent determination of specific contact interactions.

6 Testing of QED processes at e^+e^- colliders

There is also a great potential at future high-energy e^+e^- linear colliders to test nonlinear QED processes. Since the e^- an e^+ beams are both of high energy as well as high intensity,



(a) (b)

Figure 16: (a) Generic Z' models and anomalous gauge coupling models: correponding parameters are assumed to take non-vanishing values, one at a time only: x_γ, x_Z, y_γ, y_Z and δ_Z. Dashed straight lines correspond to specific Z' models (χ, ψ, η, I and LRS). The study was done for $\sqrt{s} = 500$ GeV, $\mathcal{L}_{int} = 500$ fb^{-1} and polarized beams with $P(e^-) = \pm 80\%$, $P(e^+) = \mp 50\%$. Figure reprinted from Ref. [68] with kind permission of The European Physical Journal (EPJ). (b) Double beam polarization asymmety A_{double} in the process $e^+e^- \to W^+W^-$ as function of the neutral heavy lepton mass m_N for different sizes of the couplings at $\sqrt{s} = 500$ GeV and $\mathcal{L}_{\text{int}} = 1$ ab^{-1}. The horizontal line corresponds to $A^{\text{SM}}_{\text{double}} = A^{\text{Z}'}_{\text{double}} = A^{\text{AGC}}_{\text{double}}$ (error band for the SM case at the 1-σ level. Reprinted figure with permission from Ref. [69]. Copyright (2013) by the American Physical Society.

the interaction zone between both beams can be used for testing QED processes: the oncoming beam generates a strong external background field for the incoming e^- beam and it has to be checked under which experimental conditions the electrons have to be treated as dressed stated, the so called Volkov states within the quantum mechanical 'Furry picture', details about this description are given, for instance, in [70].

Within the SFB676-B1project, the impact of such intense beams (high luminosity, high energy) have been analyzed in the beam-beam interaction region, where strong electromagnetic fields occur [71]. The unstable vacuum present at the interaction zone might lead to a regime of nonlinear Quantum Electrodynamics, affecting the processes in the IP area. Such conditions therefore motivate to calculate all probabilities of the physics processes under fully consideration of the external electromagnetic fields affecting the vacuum. At previous lepton colliders, the much weaker external electromagnetic fields at the IPs did not needed to be considered apart for background processes: the first order background processes as beamstrahlung and coherent pair production, the second order incoherent pair production as well. At future linear colliders the external fields would be orders of magnitude higher so an estimate of the effects on all the processes is requested. As we have shown, indeed, the χ parameter, that encodes the dependence of the probabilities on the intensity of the external field at the IP, is up to 3 orders

Machine	LEP II	SLC	ILC-1TeV	CLIC-3TeV
Energy (GeV)	94.5	46.6	500	1500
N (10^{10})	334	4	2	0.37
σ_x, σ_y (μm)	190, 3	2.1, 0.9	0.335, 0.0027	0.045, 0.001
σ_z (mm)	20	1.1	0.225	0.044
$\chi_{average}$	0.00015	0.001	0.27	3.34
χ_{max}	0.00034	0.0019	0.94	10.9

Table 3: Lepton colliders parameters. N is the number of leptons per bunch, σ_x, σ_y are the transversal dimensions of the bunches, σ_z presents the longitudinal dimension. E is the energy of the particles in the bunches. The parameters for ILC-1TeV are taken from a 2011 dataset. Table taken from Ref. [71].

of magnitude higher at ILC and CLIC than at LEP. In particular at CLIC-3TeV, we would have $\chi_{\rm av} \sim 3:34$, describing a critical regime, see Tab.3.

In [72] we compared the Furry picture (FP), which separates the external field from the interaction Lagrangian and requires solutions of the minimally coupled equations of motion, with the Quasi-classical Operator method (QOM), which is an alternative theory in the Heisenberg picture which relies on the limiting case of ultra-relativistic particles. We applied these theories to collider phenomenology for future linear colliders in which two strong non-collinear fields (those of the colliding charge bunches) are present at the interaction point. The FP requires new solutions of the equations of motion, external field propagators and radiative corrections, in the two non-collinear electromagnetic fields. The FP applies to all physics processes taking place at the interaction point. The QOM, however, we showed can be applied to a subset of processes in which the quasi-classical approximation is valid [73].

In [74], we presented a comprehensive investigation of nonlinear lepton-photon interactions in external background fields. The considered strong-field processes were Compton scattering and stimulated electron-positron pair production (nonlinear Breit-Wheeler process). We discuss nonlinear Compton scattering in head-on lepton-photon collisions extended properly to beyond the soft-photon regime. A semi-classical method based on coherent states of radiation allowed us to treat the external background quasi-classically in the ordinary QED action. We discussed in great detail the relevance of these extra terms by applying our general formula to Compton scattering by an electron propagating in a laser-like background and compared our unconstrained phase-space integrand with the one in the soft photon limit. We showed that already the leading term in the soft limit is not sufficient to describe the exact total scattering probability for large energies.

7 Conclusion

In conclusion, this SFB made over the 12 years of its lifetime a huge impact to the evaluation of the physics potential of future electron-positron colliders, and provided important input to the design of the detectors, the accelerator and the running program of such a machine. This would not have been possible without the intense interplay between theory and experiment and the long-term support by the SFB.

After the 12 years of this SFB, which saw the start-up of the LHC, the discovery of the

Higgs boson, and, sadly, strong limits on further new particles, the physics progam of a Linear Collider is more important and timely than ever in the quest for widening the horizon of our knowledge.

References

[1] G. Moortgat-Pick, H. Baer, M. Battaglia, G. Belanger, K. Fujii, J. Kalinowski et al., *Physics at the e^+e^- Linear Collider*, *Eur. Phys. J.* **C75** (2015) 371, [1504.01726].

[2] T. Behnke, J. E. Brau, B. Foster, J. Fuster, M. Harrison, J. M. Paterson et al., *The International Linear Collider Technical Design Report - Volume 1: Executive Summary*, 1306.6327.

[3] M. Berggren, *ILC Beam-Parameters and New Physics*, in *International Linear Collider Workshop (LCWS10 and ILC10) Beijing, China, March 26-30, 2010*, 2010, 1007.3019.

[4] T. Barklow, J. Brau, K. Fujii, J. Gao, J. List, N. Walker et al., *ILC Operating Scenarios*, 1506.07830.

[5] K. Fujii et al., *Physics Case for the 250 GeV Stage of the International Linear Collider*, 1710.07621.

[6] G. Moortgat-Pick, *Impact of polarized e^- and e^+ beams at a future Linear Collider and a Z-factory. Part I: Fundamentals in polarization and electroweak precision physics*, . http://www-library.desy.de/cgi-bin/showprep.pl?desy10-242.

[7] G. Moortgat-Pick, *Impact of polarized e^- and e^+ beams at a future Linear Collider and a Z-factory. Part II: Physics beyond the standard model*, *J.Phys.Conf.Ser.* **298** (2011) 012001.

[8] ILD, SiD Collaborations, J. List, *Beam Polarisation and Triple Gauge Couplings in $e^+e^- \to W^+W^-$ at the ILC*, *PoS* **EPS-HEP2013** (2013) 233.

[9] I. Marchesini, *Triple Gauge Couplings and Polarization at the ILC and Leakage in a Highly Granular Calorimeter*, Ph.D. thesis, Universität Hamburg, 2011. http://www-flc.desy.de/flc/work/group/thesis/thesis_Marchesini.pdf.

[10] R. Karl and J. List, *Polarimetry at the ILC*, in *Proceedings, International Workshop on Future Linear Colliders 2016 (LCWS2016): Morioka, Iwate, Japan, December 05-09, 2016*, 2017, 1703.00214.

[11] K. Fujii et al., *The role of positron polarization for the inital 250 GeV stage of the International Linear Collider*, 1801.02840.

[12] W. Kilian, T. Ohl and J. Reuter, *WHIZARD: Simulating Multi-Particle Processes at LHC and ILC*, *Eur. Phys. J.* **C71** (2011) 1742, [0708.4233].

[13] W. Kilian, F. Bach, T. Ohl and J. Reuter, *WHIZARD 2.2 for Linear Colliders*, in *International Workshop on Future Linear Colliders (LCWS13) Tokyo, Japan, November 11-15, 2013*, 2014, 1403.7433.

[14] M. Beckmann, B. List and J. List, *Treatment of Photon Radiation in Kinematic Fits at Future e+ e- Colliders*, *Nucl.Instrum.Meth.* **A624** (2010) 184–191, [1006.0436].

[15] M. Beckmann, *Verbesserung der WW/ZZ-Unterscheidung am ILC durch Berücksichtigung von Photonabstrahlung in kinematischen Fits*, Ph.D. thesis, Leibniz-Universität Hannover, 2010. 10.3204/DESY-THESIS-2010-014 http://www-library.desy.de/cgi-bin/showprep.pl?desy-thesis-10-014.

[16] C. F. Dürig, *Measuring the Higgs Self-coupling at the International Linear Collider*, Ph.D. thesis, Universität Hamburg, 2016. http://inspirehep.net/record/1493742/files/phd_thesis_duerig.pdf.

[17] C. Dürig, K. Fujii, J. List and J. Tian, *Model Independent Determination of HWW coupling and Higgs total width at ILC*, in *International Workshop on Future Linear Colliders (LCWS13) Tokyo, Japan, November 11-15, 2013*, 2014, 1403.7734.

[18] F. J. Müller, *Development of a Triple GEM Readout Module for a Time Projection Chamber & Measurement Accuracies of Hadronic Higgs Branching Fractions in $\nu\nu H$ at a 350 GeV ILC*, Ph.D. thesis, Universität Hamburg, 2016. 10.3204/PUBDB-2016-02659 http://inspirehep.net/record/1477464/files/Dissertation_Felix_Mueller-1.pdf.

[19] T. Barklow, K. Fujii, S. Jung, R. Karl, J. List, T. Ogawa et al., *Improved Formalism for Precision Higgs Coupling Fits*, *Phys. Rev.* **D97** (2018) 053003, [1708.08912].

[20] P. Drechsel, G. Moortgat-Pick and G. Weiglein, *Sensitivity of the ILC to light Higgs masses*, in *International Workshop on Future Linear Collider (LCWS2017) Strasbourg, France, October 23-27, 2017*, 2018, 1801.09662.

[21] Y. Wang, J. List and M. Berggren, *Search for Light Scalars Produced in Association with Muon Pairs for $\sqrt{s}$ = 250 GeV at the ILC*, in *International Workshop on Future Linear Collider (LCWS2017) Strasbourg, France, October 23-27, 2017*, 2018, 1801.08164.

[22] S. Liebler, G. Moortgat-Pick and G. Weiglein, *Off-shell effects in Higgs processes at a linear collider and implications for the LHC*, *JHEP* **06** (2015) 093, [1502.07970].

[23] F. Bach, B. C. Nejad, A. Hoang, W. Kilian, J. Reuter, M. Stahlhofen et al., *Fully-differential Top-Pair Production at a Lepton Collider: From Threshold to Continuum*, *JHEP* **03** (2018) 184, [1712.02220].

[24] J. Reuter, F. Bach, B. C. Nejad, A. Hoang, W. Kilian, J. Lindert et al., *Exclusive top production at a Linear Collider at and off the threshold*, in *International Workshop on Future Linear Collider (LCWS2017) Strasbourg, France, October 23-27, 2017*, 2018, 1801.08083.

[25] Gfitter Group, M. Baak, J. Cuth, J. Haller, A. Hoecker, R. Kogler, K. Mönig et al., *The global electroweak fit at nnlo and prospects for the lhc and ilc*, *Eur. Phys. J.* **C74** (2014) 3046, [1407.3792].

[26] S. Liebler, G. Moortgat-Pick and A. S. Papanastasiou, *Probing the top-quark width through ratios of resonance contributions of $e^+e^- \to W^+W^-b\bar{b}$*, *JHEP* **03** (2016) 099, [1511.02350].

[27] M. Awramik, M. Czakon, A. Freitas and B. A. Kniehl, *Two-loop electroweak fermionic corrections to $sin^2\theta^{b\bar{b}}_{eff}$*, *Nucl. Phys.* **B813** (2009) 174–187, [0811.1364].

[28] S. Bilokin, R. Pöschl and F. Richard, *Measurement of b quark EW couplings at ILC*, 1709.04289.

[29] A. Rosca, *Measurement of the charged triple gauge boson couplings at the ILC*, *Nucl. Part. Phys. Proc.* **273-275** (2016) 2226–2231.

[30] R. Karl, *Prospects for Electroweak Precision Measurements and Triple Gauge Couplings at a Staged ILC*, *PoS* **EPS-HEP2017** (2017) 763.

[31] H. Baer and J. List, *Post LHC8 SUSY benchmark points for ILC physics*, *Phys.Rev.* **D88** (2013) 055004, [1307.0782].

[32] J. List, *The ILC Potential for Discovering New Particles*, *PoS* **EPS-HEP2017** (2017) 307, [1711.02870].

[33] G. Moortgat-Pick, I. Fleck, S. Riemann, F. Simon, O. Adeyemi et al., *Helmholtz Alliance Linear Collider Forum*, . http://www-library.desy.de/preparch/desy/proc/proc13-02.pdf.

[34] S. Y. Choi, K. Hagiwara, H. U. Martyn, K. Mawatari and P. M. Zerwas, *Spin analysis of supersymmetric particles*, *Eur. Phys. J.* **C51** (2007) 753–774, [hep-ph/0612301].

[35] S. Y. Choi, J. Kalinowski, G. A. Moortgat-Pick and P. M. Zerwas, *Analysis of the neutralino system in supersymmetric theories*, *Eur. Phys. J.* **C22** (2001) 563–579, [hep-ph/0108117]. [Addendum: Eur. Phys. J.C23,769(2002)].

[36] A. Brandenburg, M. Maniatis, M. M. Weber and P. M. Zerwas, *Squarks and gluinos at a TeV e^+e^- collider: Testing the identity of Yukawa and gauge couplings in SUSY-QCD*, *Eur. Phys. J.* **C58** (2008) 291–300, [0806.3875].

[37] O. Kittel, G. Moortgat-Pick, K. Rolbiecki, P. Schade and M. Terwort, *Measurement of CP asymmetries in neutralino production at the ILC*, *Eur.Phys.J.* **C72** (2012) 1854, [1108.3220].

[38] M. Terwort, O. Kittel, G. Moortgat-Pick, K. Rolbiecki and P. Schade, *Measurement of CP Violation in the MSSM Neutralino Sector with the ILD*, in *Helmholtz Alliance Linear Collider Forum: Proceedings of the Workshops Hamburg, Munich, Hamburg 2010-2012, Germany*, (Hamburg), pp. 440–444, DESY, DESY, 2013, 1201.5272.

[39] K. Salimkhani, J. Tattersall and G. Moortgat-Pick, *CP Violating Effects in Stop Decay*, in *Helmholtz Alliance Linear Collider Forum: Proceedings of the Workshops Hamburg, Munich, Hamburg 2010-2012, Germany*, (Hamburg), pp. 445–449, DESY, DESY, 2013, http:/www-flc.desy.de/lcnotes/notes/LC-REP-2012-067.ps.gz.

[40] G. A. Moortgat-Pick and H. Fraas, *Influence of CP and CPT on production and decay of Dirac and Majorana fermions*, *Eur. Phys. J.* **C25** (2002) 189–197, [hep-ph/0204333].

[41] S. Y. Choi, *Probing the Majorana nature and CP properties of neutralinos*, in *Linear colliders. Proceedings, International Conference, LCWS 2004, Paris, France, April 19-23, 2004*, pp. 893–896, 2004, hep-ph/0409050.

[42] S. Y. Choi and Y. G. Kim, *Analysis of the neutralino system in two body decays of neutralinos*, *Phys. Rev.* **D69** (2004) 015011, [hep-ph/0311037].

[43] S. Y. Choi, M. Drees, A. Freitas and P. M. Zerwas, *Testing the Majorana Nature of Gluinos and Neutralinos*, *Phys. Rev.* **D78** (2008) 095007, [0808.2410].

[44] A. Bharucha, J. Kalinowski, G. Moortgat-Pick, K. Rolbiecki and G. Weiglein, *One-loop effects on MSSM parameter determination via chargino production at the LC*, *Eur. Phys. J.* **C73** (2013) 2446, [1211.3745].

[45] H. Baer, V. Barger, P. Huang, A. Mustafayev and X. Tata, *Radiative natural SUSY with a 125 GeV Higgs boson*, *Phys. Rev. Lett.* **109** (2012) 161802, [1207.3343].

[46] M. Berggren, F. Brümmer, J. List, G. Moortgat-Pick, T. Robens et al., *Tackling light higgsinos at the ILC*, *Eur.Phys.J.* **C73** (2013) 2660, [1307.3566].

[47] H. Sert, *Light Higgsinos at the ILC: Precision Measurements and Detector Requirements*, Ph.D. thesis, Universität Hamburg, 2016. http://www-library.desy.de/cgi-bin/showprep.pl?desy-thesis-16-001.

[48] S.-L. Lehtinen, H. Baer, M. Berggren, K. Fujii, J. List, T. Tanabe et al., *Naturalness and light Higgsinos: why ILC is the right machine for SUSY discovery*, *PoS* **EPS-HEP2017** (2017) 306, [1710.02406].

[49] S.-L. Lehtinen, *Supersymmetry parameter determination at the International Linear Collider*, Ph.D. thesis, Universität Hamburg, 2018.

[50] ATLAS Collaboration, G. Aad et al., *Search for the electroweak production of supersymmetric particles in $\sqrt{s}$=8 TeV pp collisions with the ATLAS detector*, *Phys. Rev.* **D93** (2016) 052002, [1509.07152].

[51] CMS Collaboration, *Search for pair production of tau sleptons in $\sqrt{s} = 13$ TeV pp collisions in the all-hadronic final state*, *CMS-PAS-SUS-17-003* (2017) . http://cds.cern.ch/record/2273395.

[52] ATLAS Collaboration, *Prospect for a search for direct stau production in events with at least two hadronic taus and missing transverse momentum at the High Luminosity LHC with the ATLAS Detector*, *ATL-PHYS-PUB-2016-021* (2016) . https://cds.cern.ch/record/2220805.

[53] M. Berggren, *Simplified SUSY at the ILC*, in *Proceedings, Community Summer Study 2013: Snowmass on the Mississippi (CSS2013): Minneapolis, MN, USA, July 29-August 6, 2013*, 2013, 1308.1461.

[54] P. Bechtle, M. Berggren, J. List, P. Schade and O. Stempel, *Prospects for the study of the $\tilde{\tau}$-system in SPS1a' at the ILC*, *Phys.Rev.* **D82** (2010) 055016, [0908.0876].

[55] P. Bechtle, K. Desch, M. Uhlenbrock and P. Wienemann, *Constraining SUSY models with Fittino using measurements before, with and beyond the LHC*, *Eur. Phys. J.* **C66** (2010) 215–259, [0907.2589].

[56] M. Berggren, A. Cakir, D. Krücker, J. List, I. A. Melzer-Pellmann, B. Safarzadeh Samani et al., *Non-simplified SUSY: stau-coannihilation at LHC and ILC*, *Eur. Phys. J.* **C76** (2016) 183, [1508.04383].

[57] A. Bharucha, A. Fowler, G. Moortgat-Pick and G. Weiglein, *Consistent on shell renormalisation of electroweakinos in the complex MSSM: LHC and LC predictions*, *JHEP* **05** (2013) 053, [1211.3134].

[58] A. Bharucha, J. Kalinowski, G. Moortgat-Pick, K. Rolbiecki and G. Weiglein, *MSSM parameter determination via chargino production at the LC: NLO corrections*, 1208.1521.

[59] A. Bharucha, *Chargino Production at a future LC in the MSSM with complex Parameters: NLO Corrections*, in *International Workshop on Future Linear Colliders (LCWS11) Granada, Spain, September 26-30, 2011*, 2012, 1202.6284.

[60] A. Bharucha, *Determining MSSM parameters via chargino production at the LC: a one-loop analysis*, *PoS* **ICHEP2012** (2013) 106, [1212.1921].

[61] A. Bharucha, J. Kalinowski, G. Moortgat-Pick, K. Rolbiecki and G. Weiglein, *One-loop effects on MSSM parameter determination via chargino production at the LC*, . http://inspirehep.net/record/1475539/files/1238328_415-439.pdf.

[62] G. Moortgat-Pick, A. Bharucha, G. Weiglein, J. Kalinowski and K. Rolbiecki, *Impact of electroweak precision measurements for dark matter constraints*, in *Proceedings, 2015 European Physical Society Conference on High Energy Physics (EPS-HEP 2015): Vienna, Austria, July 22-29, 2015*, 2015.

[63] F. Deppisch, A. Freitas, W. Porod and P. M. Zerwas, *Determining Heavy Mass Parameters in Supersymmetric SO(10) Models*, *Phys. Rev.* **D77** (2008) 075009, [0712.0361].

[64] B. Vormwald and J. List, *Bilinear R parity violation at the ILC: neutrino physics at colliders*, *Eur.Phys.J.* **C74** (2014) 2720, [1307.4074].

[65] S. Y. Choi, H. E. Haber, J. Kalinowski and P. M. Zerwas, *The neutralino sector in the U(1)-extended supersymmetric standard model*, *Nucl. Phys.* **B778** (2007) 85–128, [hep-ph/0612218].

[66] D. Dercks and G. Moortgat-Pick, *Automatised ILC-Bounds on Dark Matter Models with CheckMATE*, in *International Workshop on Future Linear Collider (LCWS2017) Strasbourg, France, October 23-27, 2017*, 2018, 1801.08037.

[67] D. Dercks, G. Moortgat-Pick, J. Reuter and S. Y. Shim, *The fate of the Littlest Higgs Model with T-parity under 13 TeV LHC Data*, *JHEP* **05** (2018) 049, [1801.06499].

[68] V. Andreev, G. Moortgat-Pick, P. Osland, A. Pankov and N. Paver, *Discriminating Z' from Anomalous Trilinear Gauge Coupling Signatures in $e^+e^- \to W^+W^-$ at ILC with Polarized Beams*, *Eur.Phys.J.* **C72** (2012) 2147, [1205.0866].

[69] G. Moortgat-Pick, P. Osland, A. Pankov and A. Tsytrinov, *Unique heavy lepton signature at e^+e^- linear collider with polarized beams*, *Phys.Rev.* **D87** (2013) 095017, [1303.3845].

[70] G. Moortgat-Pick, *The Furry picure*, *J.Phys.Conf.Ser.* **198** (2009) 012002.

[71] S. Porto, A. Hartin and G. Moortgat-Pick, *Methods for evaluating physical processes in strong external fields at e^+e^- colliders: Furry picture and quasi-classical approach*, *PoS* **Corfu2012** (2013) 039, [1304.4241].

[72] A. Hartin, G. Moortgat-Pick and S. Porto, *Strong field effects on physics processes at the Interaction Point of future linear colliders*, *PoS* **ICHEP2012** (2013) 480, [1304.2632].

[73] A. Müller, *Nonlinear Compton Scattering: Comparison of two calculation methods*, Master's thesis, Universität Hamburg, 2017.
https://www.physnet.uni-hamburg.de/services/bibliothek/Examensarbeiten/master/master2017.htm.

[74] I. Akal and G. Moortgat-Pick, *Nonlinear lepton-photon interactions in external background fields*, 1602.01057.

Studies of Boosted Topologies and Jet Substructure at the LHC

Johannes Haller[1], *Roman Kogler*[1], *Frank J. Tackmann*[2]

[1]Institut für Experimentalphysik, Universität Hamburg, Germany
[2]DESY, Hamburg, Germany

DOI: http://dx.doi.org/10.3204/PUBDB-2018-00782/B2a

The high centre-of mass energy available in run-2 of CERN's Large-Hadron-Collider (LHC) results in an abundant production of heavy particles with high transverse momenta (p_T). The boosted decay products of these high-p_T particles are collimated in the laboratory system and, in case of hadronic decays, the resulting jets are merged into a single larger jet which features certain characteristics in its substructure. During the last decade, several novel techniques have been developed to study and identify these boosted hadronic decays of heavy particles at the LHC. In this article, we summarize the results of developments on boosted topologies and jet substructure as obtained in the context of the SFB 676 in Hamburg and we discuss a few example results of their application.

1 Introduction

The large LHC datasets collected at $\sqrt{s} = 13$ TeV over the past years, open the possibility to study the yet unexplored region of very high invariant masses of new resonances. An important feature of many BSM scenarios is the abundant production of heavy SM particles (t, W, Z and H) as decay products of these new high-mass resonances. As a result, an increased production rate of these particles compared to the SM prediction can provide direct evidence for new physics. Furthermore, the study of the production of Higgs bosons at large transverse momenta, leading to boosted Higgs decays, is an important ingredient in the determination of properties and couplings of the Higgs boson

The high transverse momentum of the decaying t, W, Z, or H lead to boosted topologies in the final state with non-isolated leptons and merged jets. In the extreme case, all decay products of the decay chain are merged into a single large jet. In classical analyses, these final states cannot be identified and boosted heavy-particle decays cannot be distinguished from the large background of QCD multijet production. For an increased sensitivity, dedicated techniques for the reconstruction of such boosted topologies are required. This implies the development of new methods for the reconstruction and identification of boosted heavy objects, as well as their theoretical description. The key idea, which has long been recognized, is the study of the substructure of the large jets. Jet substructure techniques have become increasingly important both in the standard model as well as in searches for new physics. Often the techniques exploit the properties of a fixed number of subjets. Theoretical predictions at increasingly high precision are needed to match the increasing precision of the data, but are challenging due to the appearance of multiple widely separate physical scales, requiring the development of new

factorization and resummation techniques.

We summarize the results in the area of boosted topologies and jet substructure obtained in the context of the SFB 676 in Hamburg. We present the concepts of the first measurement of an important substructure observable, the distribution of the jet mass in highly boosted $t\bar{t}$ events as performed by the CMS collaboration, followed by an overview of the key features of the HOTVR tagging algorithm. We highlight the theoretical developments of exploiting the N-jettiness observable as a factorization and resummation friendly exclusive cone jet algorithm, and we summarize the developments of novel effective field theories that enable the factorization and resummation of large logarithms appearing in boosted regimes and in the jet-mass spectrum. Finally, example BSM search results of the CMS collaboration are discussed exploiting the techniques of tagging and substructure observables.

2 Measurement of the jet mass in boosted $t\bar{t}$ events

One of the most important jet substructure observables is the jet mass m_{jet}, the invariant mass calculated from the jet constituents[1]. The jet mass of a large jet with a fully merged, highly boosted decay of t, W, Z or H is subject to various contributions, like multiple proton-proton scatterings in one bunch crossing (pileup), additional partonic radiation, multiple parton interactions and hadronisation effects. A detailed understanding and the measurement of the m_{jet} distribution is therefore crucial to test important components of the simulation, needed for LHC analyses of highly boosted topologies in the SM and for searches of new physics. In the case of fully hadronic top quark decays, the distribution of m_{jet} also provides sensitivity to the top quark mass m_t.

Calculations from first principles of the m_{jet} distribution for fully-merged top quark decays are available in soft collinear effective theory in e^+e^- collisions [2, 3] and most recently for the LHC environment [4–6]. As a result, the measurement of the m_{jet} distribution can be used for an independent m_t determination in the boosted regime with the aim of reaching a reliable correspondence between the top quark mass in any well-defined renormalisation scheme and the top quark mass parameter in general-purpose event generators.

While measurements of m_{jet} at particle level had been done by the ATLAS and CMS collaborations for light-quark and gluon jets [7, 8], the measurement of the differential $t\bar{t}$ production cross section as a function of the leading-jet mass for boosted top quark decays has been done for the first time in [1] using the $\sqrt{s} = 8\,\text{TeV}$ data-set recorded by the CMS collaboration. The measurement is performed on $t\bar{t}$ events in which the leading jet includes the three subjets of one hadronic top quark decay, while the other top quark decays in the $l\nu_l b$ mode. The Cambridge–Aachen (CA) jet-clustering algorithm [9, 10] with a distance parameter of $R = 1.2$ and $p_T > 400\,\text{GeV}$ is used for the definition of the highly boosted top quark jets used in the measurement.

In Fig. 1 the m_{jet} distribution unfolded to the particle level and normalised to the fiducial-region total cross section as obtained from the CMS data is shown and compared to the equivalent distributions from Monte-Carlo (MC) simulations. The data distribution agrees with predictions from simulations indicating a high quality of the modelling of the jet mass in the simulation of highly boosted top quark decays. The overall sensitivity of a possible mass measurement derived from this measurement has been determined from a comparison of the data distribution with distributions obtained from simulations with different values of m_t and a

[1] The text presented in this section is based on the text of [1].

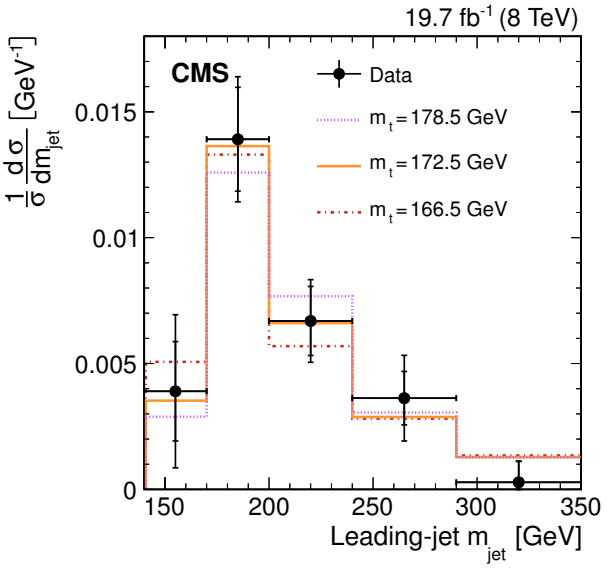


Figure 1: Normalised particle-level $t\bar{t}$ differential cross section as a the function of the leading-jet mass as measured by the CMS collaboration using pp collisions at $\sqrt{s} = 8\,\text{TeV}$. The CMS measurement (data points) is compared to MC predictions for three different values of m_t (solid, dotted and dashed histograms). Figure taken from Ref. [1].

sensitivity of $\pm 9\,\text{GeV}$ has been obtained. The dominating uncertainty results from the limited statistics ($\pm 6.0\,\text{GeV}$), while the experimental systematic uncertainty is $\pm 2.8\,\text{GeV}$. The modelling uncertainty contributes $\pm 4.6\,\text{GeV}$, while the theoretical uncertainty due to missing higher orders in the simulation amounts to $\pm 4.0\,\text{GeV}$.

While the current precision of a m_t determination using this method is not comparable with the precision obtained by other mass measurements, the analysis represents a proof-of-principle of the method. With more data collected at higher centre-of-mass energies the dominating statistical uncertainty of this measurement will drastically improve. In addition, the experimental systematic uncertainties will be significantly reduced through improved techniques in the reconstruction of boosted hadronic top quark decays [11, 12]. Furthermore, the improved statistical precision will allow for stronger constraints on the simulation of boosted top decays, leading to improvements of the modelling uncertainties. Lastly, new generations of MC event generators include full next-to-leading order calculations, which reduce the theoretical uncertainties. Overall, competitive top quark mass measurements using this technique can be envisaged for future data analyses by the LHC collaborations.

3 Identification of heavy hadronically decaying particles at the LHC with the HOTVR tagger

Since the start of the LHC a variety of innovative approaches based on the substructure of jets have been developed to identify decays of heavy hadronically decaying particles from the

overwhelming background of QCD multijet production (see [13] for a list of references)[2]. Most of the developed algorithms are designed for a specific kinematic region (sometimes following an involved algorithmic procedure): either they are optimized for the region of low transverse momentum p_{T}, where the decay products can be resolved, or they provide an optimized performance in the boosted regime of high p_{T}.

During the course of the SFB 676 we developed a new algorithm [14] for the identification of boosted, hadronically decaying, heavy particles which is based on the procedure of jet clustering with variable distance parameter R [15] to adapt the jet size to jet transverse momentum p_{T}. It is the first application of the variable-R jet clustering algorithm for tagging boosted heavy SM decays. The advantage of a shrinking cone size with increasing p_{T} is that contributions of perturbative and non-perturbative effects on jet substructure observables increase with p_{T}, and are compensated by a decreasing jet size. Additionally, the algorithm identifies subjets using a mass jump condition [16]. The resulting algorithm, Heavy Object Tagger with Variable R (HOTVR) [14], has only little algorithmic complexity. It performs the clustering of jets, the identification of subjets and the rejection of soft clusters in a single sequence. While the HOTVR algorithm is in principle applicable for the tagging of any heavy hadronically decaying particle (W, Z, H, t or possible BSM resonances) the focus of past studies [14] has been put on performance studies of the identification of top quark decays for which selection cuts on measureable substructure observables have been studied and optimized.

Certain exemplary features of the performance of the algorithm are illustrated in Fig. 2 where the results of the application of the HOTVR algorithm are shown for two simulated $t\bar{t}$ events in pp collisions at $\sqrt{s} = 13\,\mathrm{TeV}$ at low p_{T} (left) and at high p_{T} (right). The HOTVR algorithm indeed adapts the jet size to the jet p_{T} and it is able to reconstruct correctly the sub-jets (orange/blue) within the larger jets, thereby identifying the initial top quark decay products (red circles) and rejecting soft clusters originating from additional QCD radiation (grey areas) with the mass jump criterion.

Compared to other top tagging algorithms used within the CMS collaboration [17], the HOTVR algorithm was found [14] to demonstrate a remarkably stable performance in a wide range of top quark p_{T}, such that it can be used to cover the regions from nearly resolved decays up to the highly boosted regime with very high efficiency. As result, the HOTVR tagger could be used at the LHC in searches for hypothetical BSM particles decaying to top quarks in the low, the intermediate and the high mass region simultaneously.

While the performance studies of the HOTVR have focused on decays of the top quark so far, the identification of W, Z and H decays or hypothetical BSM resonances remains a potential subject for future studies in this area. Because of its stable performance over a wide range of different kinematic regions and its algorithmic simplicity, the HOTVR tagger will become a helpful ingredient for future boosted analyses at the LHC.

4 N-jettiness as a jet algorithm

As a global event shape, N-jettiness measures the degree to which the hadrons in the final state are aligned along N jet axes or the beam direction [18]. It was originally introduced to veto additional jets in an event, providing a way to define and resum exclusive N-jet cross sections [18–20]. N-jettiness was later adapted to the jet shape N-subjettiness [21, 22], which is an efficient measure to identify N-prong boosted hadronic objects such as top quarks, W/Z

[2]The text presented in this section closely follows the text of [14].

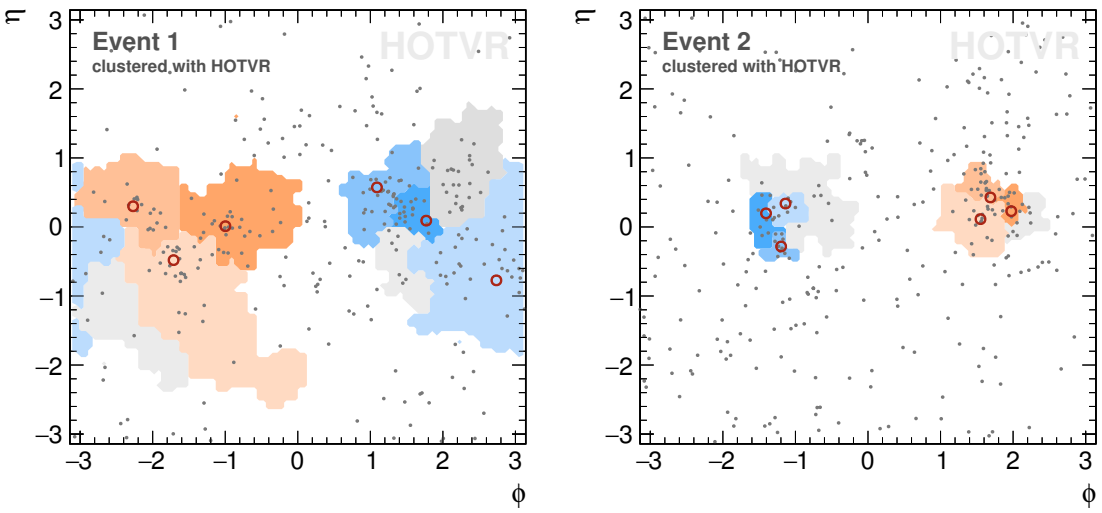


Figure 2: Reconstruction and (sub-)jet identification of simulated $t\bar{t}$ events in pp collisions at $\sqrt{s} = 13\,\text{TeV}$ at low p_T (left) and at high p_T (right) respectively using the HOTVR algorithm. The locations in the plane of the pseudo-rapidity η versus the azimuthal angle ϕ of the two leading jets in the events are shown as coloured areas (orange/blue). The locations of the stable particles (quarks from the top quark decay) are illustrated by grey dots (red circles). The subjets are shaded from light to dark, corresponding to increasing p_T. The grey areas correspond to regions rejected by the mass jump criterion. Figures taken from Ref. [14].

bosons, and Higgs bosons within a larger jet. By minimizing N-(sub)jettiness, one can directly identify N (sub)jet directions. By now, N-subjettiness has become an important jet substructure observable.

While hadronic jets are crucial to connect the observed hadronic final state to the short-distance hard interaction, the definition of a hadronic jet is ambiguous, as there is no unique way to map colour-singlet hadrons to colour-carrying partons. Moreover, different physics applications can benefit from different jet definitions. For these reasons, a wide variety of jet algorithms have been proposed, though currently, most LHC measurements involve jets clustered with the anti-k_T algorithm [23].

The possibility of using N-jettiness as a jet algorithm was already pointed out in [18]. In [12], a new jet algorithm called "XCone" is developed. It is based on minimizing the event shape N-jettiness [18] and uses developments from the jet shape N-subjettiness [21, 22]. The key feature is that N-jettiness defines an *exclusive cone* jet algorithm, i.e, it always returns a predetermined fixed number of jets, relevant for physics applications where the number of jets is known in advance. Like anti-k_T jets, XCone jets are nearly conical for well-separated jets. Typically, when using other jet algorithms, the boosted regime of overlapping jets requires separate analysis strategies using large jets with substructure. In contrast, with XCone the jets remain resolved even when jets are overlapping in the boosted regime. As a result, a key feature of XCone is that it smoothly transitions between the resolved regime where the N signal jets of interest are well separated and the boosted regime where they overlap. The returned value of N-jettiness also provides a quality criterion of how N-jet-like the event looks. In [11], examples

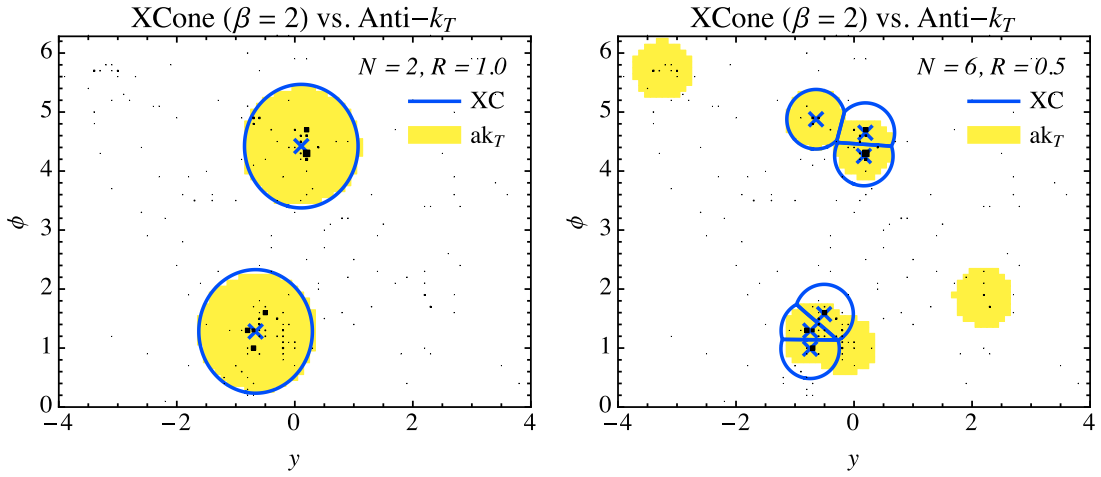


Figure 3: Comparison between the XCone (with its default measure) and anti-k_T for a boosted hadronic $t\bar{t}$ event. Left: Asking for two large-radius jets, the event is characterized by two widely-separated jets. For such jets, XCone yields nearly identical jet regions to anti-k_T. Right: Asking for six small-radius jets, the boosted hadronic top decay topology becomes clearly visible with XCone. Unlike anti-k_T which merges jet regions closer in angle than $\approx R$, XCone allows such jet regions to remain split, making it much more robust against picking up unrelated ISR jets. Figures taken from Ref. [12].

of quasi-boosted kinematics that capitalize on this feature are discussed for dijet resonances, Higgs decays to bottom quarks, and all-hadronic top-quark pairs.

There is considerable flexibility in precisely how one defines N-jettiness, and several different N-jettiness measures yielding different jet regions have been considered before [18, 20–22, 24]. The XCone default is a conical geometric measure that incorporates the insights from the different previous use cases. This measure is based on the dot product between particles and lightlike axes but incorporates an angular exponent β, as well as a beam exponent γ for additional flexibility. Most importantly, it is linear in the particle momenta, which simplifies theoretical calculations, as discussed below. At the same time, and crucially for the purposes of jet finding at the LHC, this measure yields conical jets over a wide rapidity range. Well separated jets are bounded by circles of radius R in the rapidity-azimuth plane, and are nearly identical to anti-k_T jets. This is illustrated in the left panel of Fig. 3. On the other hand, overlapping jet regions automatically form nearest-neighbour clover-like jets, as show in the right panel of Fig. 3. In contrast to anti-k_T, XCone does not merge the overlapping jets even in the boosted regime, making the 3-prong structure of the boosted top decay clearly visible.

The presence of jets makes perturbative QCD calculations challenging and lead to a complicated singularity structure. Furthermore, imposing a fixed number of jets through some kind of direct or indirect veto on additional jets restricts the phase space for additional collinear and soft emissions. This generates logarithms that often dominate the perturbative series and need to be resummed to obtain predictions with the best possible precision. Soft Collinear Effective Theory (SCET) [25–28] provides a framework to systematically carry out the resummation of logarithms to higher orders by factorizing the cross section into hard, collinear, and soft

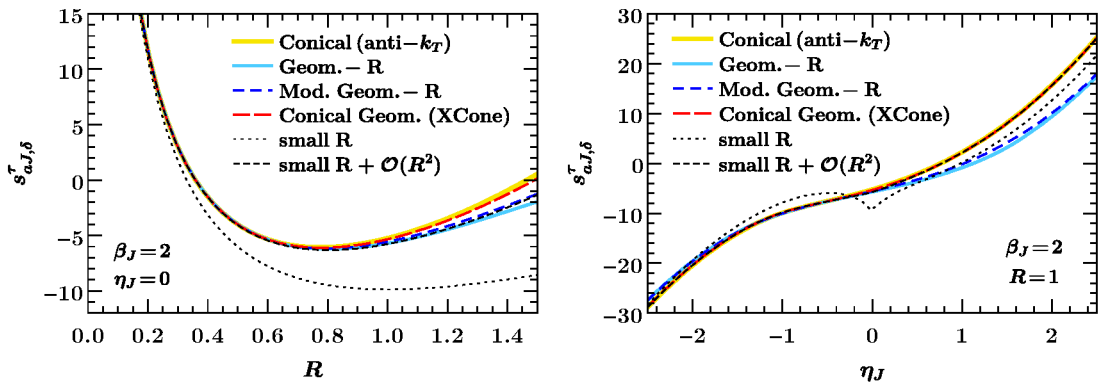


Figure 4: Soft coefficient describing initial-final state soft interference. Left: Jet radius dependence for different jet algorithm distance measures. The dotted and dashed curves show the small-R limit and including the first $O(R^2)$ corrections. Right: Dependence on the jet rapidity for fixed $R = 1$. Figures taken from Ref. [30].

functions, and then exploiting their renormalization group evolution. Schematically, the cross section for $pp \to N$ jets factorizes for many observables in the singular limit as [18, 19]

$$\sigma_N = H_N \times \left[B_a B_b \prod_{i=1}^{N} J_i \right] \otimes S_N, \tag{1}$$

where the hard function H_N contains the virtual corrections to the partonic hard scattering process, the beam functions $B_{a,b}$ contain parton distribution functions and describe collinear initial-state radiation. The jet functions J_i describe final-state radiation collinear to the direction of the hard partons, and the soft function S_N describes wide-angle soft radiation. The resummation of large logarithms is achieved by evaluating each component at its natural scale and then renormalization-group evolving all components to a common scale. The jet and beam functions typically do not depend on the precise definition of the jet regions and algorithm and are known for a variety of jet and beam measurements. Hard functions are also known for many processes at one loop or beyond (see e.g. Ref. [29] and references therein).

In [12, 30], the factorization theorems relevant for various N-jettiness measures, including the XCone default, and jet measurements are determined. The resummation at NNLL requires the soft function at one loop. Compared to the beam and jet functions, the perturbative calculation of the soft function generally requires a more sophisticated setup, since it depends not only on the measurements made in the jet and beam regions, but also on the angles between all jet and beam directions and the precise definition of the jet boundaries, i.e., the considered jet algorithm. In [30] a general method is developed to compute the N-jet soft functions for a wide class of jet algorithms and jet measurements, which so far have been known only for specific cases [20, 31]. Different types of jet vetoes are discussed, including beam thrust, beam C parameter, and a jet-p_T veto. For the jet algorithm of the signal jets, different partitionings are considered, including anti-k_T and XCone. It is found that the one-loop soft function can be written in terms of universal analytic contributions and a set of numerical integrals, which explicitly depend on the partitioning and observable. Fully analytical results can be obtained

in the limit of small jet radius R. Interestingly, it is found that the small-R expansion works remarkably well for the soft function even for moderate values of R, if one includes corrections up to $O(R^2)$. This is illustrated in Fig 4, which shows as an example the contribution to the soft function from soft gluon interference between the incoming and outgoing hard partons.

5 Factorization in boosted regimes and at small jet radius

In multijet events one generically encounters additional hierarchies in the hard kinematics of the jets, namely among the jet energies and/or among the angles between jets. At the LHC, an important class of examples are precisely jet substructure methods to reconstruct boosted heavy objects, which essentially rely on identifying soft or collinear (sub)jets. Another example is cascade decays of heavy new (coloured) particles leading to experimental signatures with jets of widely different p_{T}. There are also cases where additional jets produced by QCD are used to tag or categorize the signal events, a prominent example being the current Higgs measurements. Whenever such kinematic hierarchies arise among QCD-induced jets, in particular in the corresponding background processes, the enhancement of soft and collinear emissions in QCD leads to additional logarithms of the jet kinematics in the cross section. So far, a complete and general factorization framework for multijet processes that allows for a systematic resummation of such kinematic logarithms for generic jet hierarchies has been missing. Current predictions therefore rely on Monte Carlo parton showers and are thus mostly limited to leading-logarithmic (LL) accuracy.

In [32], we developed a general factorization framework called SCET$_+$, which is an extension of standard SCET and allows for a systematic higher-order resummation of such kinematic logarithms for generic jet hierarchies. Compared to the usual soft and collinear emissions present in SCET, in SCET$_+$ the effects of additional intermediate emissions are considered that have both soft and collinear characteristics and describe the production and interaction of hierarchical soft and collinear jets. The resulting factorized cross sections amount to further factorizing the hard and soft functions appearing in the non-hierarchical case in Eq. (1), with the additional factorization ingredients given in terms of collinear splitting amplitudes and soft gluon currents, which fully capture spin and colour correlations.

Special cases have been considered before, in particular SCET$_+$ first appeared in Ref. [33], where its purely collinear regime was constructed to describe the situation of two energetic jets collinear to each other. The purely soft regime of SCET$_+$ was first considered in Ref. [34]. There it was shown that this regime is essential for the resummation of non-global logarithms by explicitly resolving additional soft subjets (see also Refs. [35, 36]).

In [32], the general application to N-jet processes at hadron colliders is derived in detail, considering all relevant representative classes of hierarchies, from which the general case can be built, and it is discussed how to systematically combine the different hierarchical (boosted) and non-hierarchical regimes to obtain a complete description of the kinematic jet phase space. This includes in particular multiple hierarchies that are either strongly ordered in angle or energy or not. Our results pave the way to resum kinematic logarithms appearing in differential jet measurements to NNLL or beyond and systematically improve upon the LL description of kinematic logarithms in parton showers.

As mentioned before, the same type of jet hierarchies also appear in jet substructure measurements, and SCET$_+$ has become the cornerstone of analytic resummation of jet substructure observables. For example, in Ref. [35], SCET$_+$ was used to factorize and resum a two-prong jet

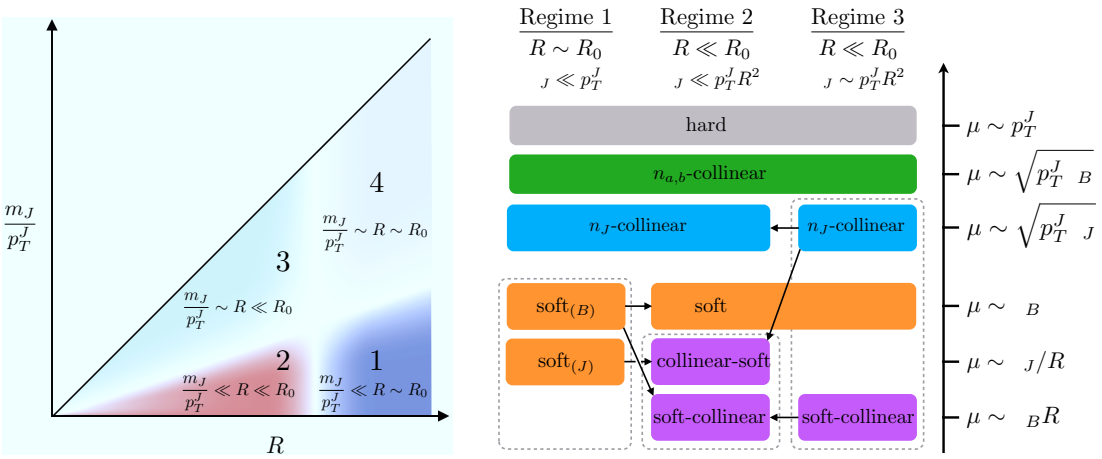


Figure 5: Illustration of the various regimes for jet mass measurements as a function of the jet radius R and p_{T}^J/m_J (left panel) and the resulting physical scales and radiation types that must be considered in the factorization (right panel). Figures taken from Ref. [42].

substructure variable and in Ref. [37] it was used to provide the first resummed hadron-level predictions for a groomed 2-prong jet substructure variable.

A basic and important benchmark observable for studying the radiation inside a jet is the invariant mass m_J of a jet. The jet mass spectrum provides key information about the influence of Sudakov double logarithms and soft radiation in a hadronic environment and probes the dependence on the jet algorithm and jet size R, colour flow, initial and final state partonic channels, hadronization, and underlying event. For this reason, it is a key benchmark observable for jet substructure studies. For example, the utility of the first moment of the jet mass spectrum as a mechanism to disentangle different sources of soft radiation underlying the hard interaction was discussed in Ref. [38]. The best sensitivity to these effects comes from studying jets in their primal state, without using jet-grooming techniques to change the nature of the jet constituents. While useful for tagging studies, jet grooming fundamentally changes the nature of the jet mass observable and reduces its utility as a probe of these physical effects.

To predict the jet mass spectrum at a hadron collider, it is crucial to account for the resummation of logarithms between the transverse momentum p_{T}^J of the jet and its invariant mass m_J. The jet-mass spectrum for N-jettiness jets (defined via the standard geometric N-jettiness measure) was first calculated at NNLL in [24]. Other analytic ungroomed jet-mass calculations have been carried out in Refs. [38–41]. In [42], the analytic description of exclusive jet mass spectra at the LHC is extended to realistic jet algorithms, including both anti-k_T clustering and XCone. A particular focus is on the limit of small jet radius, which turns out to be relevant already for moderately small $R \lesssim 1$ as typically used in experiments. In particular, for small R, the exclusive N-jet cross section contains Sudakov double logarithms of R, in conjunction with logarithms of the jet mass and jet veto. It turns out that the factorization in the small-R limit provides a different application of SCET$_+$, which was already found for the case of jet rates (without a measurement on the jet) in Refs. [43, 44].

As illustrated in Fig. 5, one must in principle distinguish four different regimes with different hierarchies for R and the scales m_J and $p_{\mathrm{T}}^J R$:

- regime 1: large-R jets for small m_J: $m_J \ll p_{\mathrm{T}}^J R \sim p_{\mathrm{T}}^J$
- regime 2: small-R jets for small m_J: $m_J \ll p_{\mathrm{T}}^J R \ll p_{\mathrm{T}}^J$
- regime 3: small-R jets for large m_J: $m_J \sim p_{\mathrm{T}}^J R \ll p_{\mathrm{T}}^J$
- regime 4: large-R jets for large m_J: $m_J \sim p_{\mathrm{T}}^J R \sim p_{\mathrm{T}}^J$.

All of these require distinct effective field theory setups to resum the corresponding logarithms. Specifically, in regimes 1 and 2 these are logarithms of m_J/p_{T}^J, and in regimes 2 and 3 logarithms of R. The factorization for each of the different regimes is discussed, as well as the relations between the different regimes and how to combine them. A particular focus is on regime 2, which has the most phenomenologically interest. Here, by applying SCET_+, all relevant scales associated with m_J, R, the applied jet veto, and the p_{T}^J of the jet are fully factorized, enabling the systematic resummation of jet-radius logarithms in addition to the jet-mass logarithms beyond leading-logarithmic order.

6 Application of boosted techniques in the search for BSM physics at the LHC

From the start of data taking at the LHC, boosted techniques have become a very important tool in searches for new physics. The reason is the much larger accessible resonance mass range compared to previous colliders, which results in more collimated final states. A large number of searches have benefitted from the application of jet substructure algorithms, either in terms of improved sensitivity or by making the search feasible in channels which are not accessible with standard reconstruction methods. In this section, we discuss a few results obtained by the CMS collaboration by using these techniques in the search for BSM physics.

An important example is the search for resonant $t\bar{t}$ production, which is predicted to be mediated by BSM particles with masses of multiple TeVs in a number of new physics models. Analyses that have been carried out during the course of the SFB 676 use the full $\sqrt{s} = 8\,\mathrm{TeV}$ dataset [45, 46] and data with $\sqrt{s} = 13\,\mathrm{TeV}$ recorded in the years 2015 [47] and 2016 [48] by the CMS collaboration. The analyses consider leptonic and fully-hadronic final states. The requirement of a jet from a boosted top quark decay in the lepton+jets channel results in a considerable improvement in sensitivity, compared to traditional reconstruction methods. The analyses of all-hadronic channels, optimized for low and high resonance masses, were only made possible through jet substructure methods, which achieved an impressive reduction of the SM multijet background by more than four orders of magnitude. An crucial aspect of these searches is the determination of the SM multijet background from data since the simulation of multi-parton final states with light quarks and gluons produced through the strong force is not precise enough for the demands of these searches. Jet substructure methods offer a reliable possibility for the determination of these backgrounds through control regions. These can be obtained by inverting criteria on the jet substructure observables used for identifying boosted top quark decays. The jets measured in these control regions have very similar kinematic distributions as the ones in the signal regions, resulting in reliable extrapolations of the SM backgrounds with small uncertainties. The analyses still rely on an accurate modelling of jet substructure observables for the determination of irreducible backgrounds from SM $t\bar{t}$ production and the signal efficiencies.

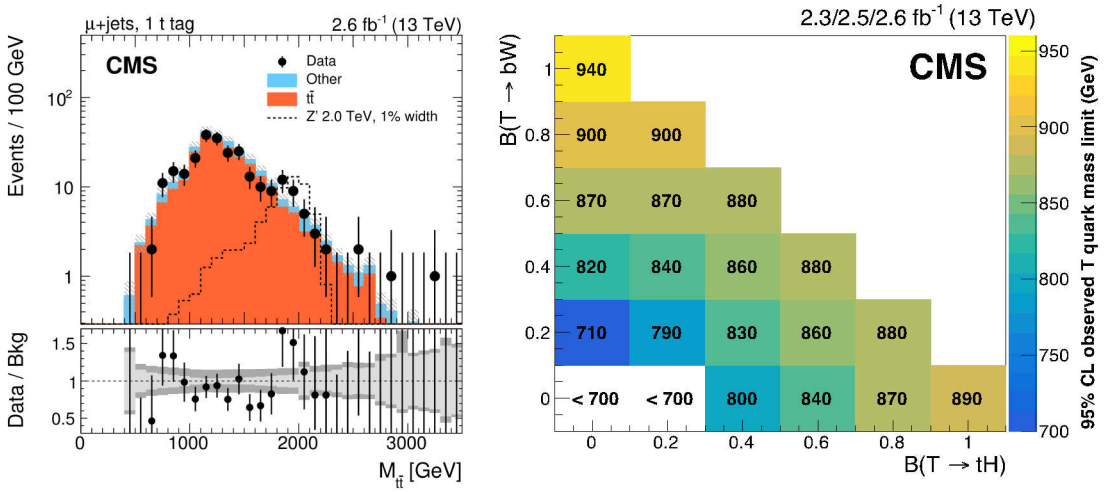


Figure 6: Example results of CMS searches using boosted top quark reconstruction techniques in pp collisions at $\sqrt{s} = 13\,\text{TeV}$: (left) Distribution of the $t\bar{t}$ invariant mass in μ+jets events including a top-tagged jet in the search of $t\bar{t}$ resonances. Shown are the data, the expected SM background contribution as well as the BSM signal normalized to a signal cross section of 1 pb. (right) Observed 95 % CL exclusion limit on the mass of vector-like T quark for a variety of $T \to tH$ and $T \to bW$ branching fraction combinations. Figures taken from Refs. [47] and [49], respectively.

The measured distribution of the mass of the $t\bar{t}$ system in the muon+jets channel with an identified boosted top quark decay is shown in Fig. 6 (left). The dominant background is irreducible SM $t\bar{t}$ production, and a possible BSM signal would be visible as a peak on top of the falling background distribution. The power of jet substructure methods in searches for new physics is demonstrated when comparing the sensitivity of the individual channels. At high resonance masses, analyses in the all-hadronic channels achieve comparable sensitivity to the ones in the lepton+jets channels. When combined, these searches have placed the most stringent constraints on resonant $t\bar{t}$ production in pp collisions at the time of publication.

Another example class of BSM scenarios that can be probed with jet substructure methods are models with vector-like quarks (VLQs), which extend the three generations of SM quarks by a fourth generation with a different chiral structure. These VLQs are expected to be much heavier than the third generation quarks with masses not generated by the BEH mechanism and thus avoiding constraints from H coupling measurements. Possible decay modes of the VLQs are bW, tZ and tH for heavy partners of the top quark (T) and tW, bZ and bH for partners of the bottom quark (B). Pair production of heavy VLQs at the LHC would thus result in complex final states with decays of highly boosted t, W, Z and H.

A search by the CMS collaboration targeting the final states bW and tH has been carried out using data recorded in 2015 with $\sqrt{s} = 13$ TeV [49]. The decay of one VLQ is reconstructed through the leptonic decay of a W boson, thus reducing the SM multijet background. The presence of a second VLQ is surmised through jet substructure methods, requiring a jet with substructure compatible to the fully-merged hadronic decay of a W or H boson. The results of the analysis in terms of VLQ mass exclusion limits are shown in Fig. 6 (right). The sensitivity

of this search could be improved considerably by advanced techniques to identify the highly-boosted W and H decays. This result has been a precursor for a number of VLQ searches using data with $\sqrt{s} = 13$ TeV.

7 Conclusion

In this contribution, we have summarized the results that have been obtained in the context of the SFB 676 in the area of studies of boosted topologies and jet substructure at the LHC. Example results are concepts for the development of the first measurements of the jet mass distribution in boosted $t\bar{t}$ events by the CMS collaboration, the development of the HOTVR tagger, theoretical developments of the exploitation of the N-jettiness observable as a jet algorithm and developments of novel effective field theories that enable the factorization and resummation of large logarithms appearing in boosted regimes and in the jet-mass spectrum. In addition, we discussed a few example results of searches for new physics by the CMS collaboration using boosted reconstruction techniques.

Acknowledgments

J.H. and R.K. would like to thank their collaborators in the CMS collaboration. The work presented here has been supported in parts by the DFG through the SFB 676 "Particles, Strings and the Early Universe" located in Hamburg.

References

[1] CMS Collaboration, A. M. Sirunyan et al., *Measurement of the jet mass in highly boosted $t\bar{t}$ events from pp collisions at $\sqrt{s} = 8$ TeV*, *Eur. Phys. J.* **C77** (2017) 467, [1703.06330].

[2] S. Fleming, A. H. Hoang, S. Mantry and I. W. Stewart, *Jets from massive unstable particles: Top-mass determination*, *Phys. Rev.* **D77** (2008) 074010, [hep-ph/0703207].

[3] S. Fleming, A. H. Hoang, S. Mantry and I. W. Stewart, *Top Jets in the Peak Region: Factorization Analysis with NLL Resummation*, *Phys. Rev.* **D77** (2008) 114003, [0711.2079].

[4] A. H. Hoang, A. Pathak, P. Pietrulewicz and I. W. Stewart, *Hard Matching for Boosted Tops at Two Loops*, *JHEP* **12** (2015) 059, [1508.04137].

[5] M. Butenschoen, B. Dehnadi, A. H. Hoang, V. Mateu, M. Preisser and I. W. Stewart, *Top Quark Mass Calibration for Monte Carlo Event Generators*, *Phys. Rev. Lett.* **117** (2016) 232001, [1608.01318].

[6] A. H. Hoang, S. Mantry, A. Pathak and I. W. Stewart, *Extracting a Short Distance Top Mass with Light Grooming*, 1708.02586.

[7] ATLAS Collaboration, G. Aad et al., *Jet mass and substructure of inclusive jets in $\sqrt{s} = 7$ TeV pp collisions with the ATLAS experiment*, *JHEP* **05** (2012) 128, [1203.4606].

[8] CMS Collaboration, S. Chatrchyan et al., *Studies of jet mass in dijet and W/Z + jet events*, *JHEP* **05** (2013) 090, [1303.4811].

[9] Y. L. Dokshitzer, G. D. Leder, S. Moretti and B. R. Webber, *Better jet clustering algorithms*, *JHEP* **08** (1997) 001, [hep-ph/9707323].

[10] M. Wobisch and T. Wengler, *Hadronization corrections to jet cross-sections in deep inelastic scattering*, in *Monte Carlo generators for HERA physics. Proceedings, Workshop, Hamburg, Germany, 1998-1999*, pp. 270–279, 1998, hep-ph/9907280.

[11] J. Thaler and T. F. Wilkason, *Resolving Boosted Jets with XCone*, *JHEP* **12** (2015) 051, [1508.01518].

[12] I. W. Stewart, F. J. Tackmann, J. Thaler, C. K. Vermilion and T. F. Wilkason, *XCone: N-jettiness as an Exclusive Cone Jet Algorithm*, *JHEP* **11** (2015) 072, [1508.01516].

[13] L. Asquith et al., *Jet Substructure at the Large Hadron Collider : Experimental Review*, 1803.06991.

[14] T. Lapsien, R. Kogler and J. Haller, *A new tagger for hadronically decaying heavy particles at the LHC*, *Eur. Phys. J.* **C76** (2016) 600, [1606.04961].

[15] D. Krohn, J. Thaler and L.-T. Wang, *Jets with Variable R*, *JHEP* **06** (2009) 059, [0903.0392].

[16] M. Stoll, *Vetoed jet clustering: The mass-jump algorithm*, *JHEP* **04** (2015) 111, [1410.4637].

[17] CMS Collaboration, *Top Tagging with New Approaches*, *CMS-PAS-JME-15-002* (2016) . http://cds.cern.ch/record/2126325.

[18] I. W. Stewart, F. J. Tackmann and W. J. Waalewijn, *N-Jettiness: An Inclusive Event Shape to Veto Jets*, *Phys. Rev. Lett.* **105** (2010) 092002, [1004.2489].

[19] I. W. Stewart, F. J. Tackmann and W. J. Waalewijn, *Factorization at the LHC: From PDFs to Initial State Jets*, *Phys. Rev.* **D81** (2010) 094035, [0910.0467].

[20] T. T. Jouttenus, I. W. Stewart, F. J. Tackmann and W. J. Waalewijn, *The Soft Function for Exclusive N-Jet Production at Hadron Colliders*, *Phys. Rev.* **D83** (2011) 114030, [1102.4344].

[21] J. Thaler and K. Van Tilburg, *Identifying Boosted Objects with N-subjettiness*, *JHEP* **03** (2011) 015, [1011.2268].

[22] J. Thaler and K. Van Tilburg, *Maximizing Boosted Top Identification by Minimizing N-subjettiness*, *JHEP* **02** (2012) 093, [1108.2701].

[23] M. Cacciari, G. P. Salam and G. Soyez, *The Anti-k(t) jet clustering algorithm*, *JHEP* **04** (2008) 063, [0802.1189].

[24] T. T. Jouttenus, I. W. Stewart, F. J. Tackmann and W. J. Waalewijn, *Jet mass spectra in Higgs boson plus one jet at next-to-next-to-leading logarithmic order*, *Phys. Rev.* **D88** (2013) 054031, [1302.0846].

[25] C. W. Bauer, S. Fleming and M. E. Luke, *Summing Sudakov logarithms in B —> X(s gamma) in effective field theory*, *Phys. Rev.* **D63** (2000) 014006, [hep-ph/0005275].

[26] C. W. Bauer, S. Fleming, D. Pirjol and I. W. Stewart, *An Effective field theory for collinear and soft gluons: Heavy to light decays*, *Phys. Rev.* **D63** (2001) 114020, [hep-ph/0011336].

[27] C. W. Bauer and I. W. Stewart, *Invariant operators in collinear effective theory*, *Phys. Lett.* **B516** (2001) 134–142, [hep-ph/0107001].

[28] C. W. Bauer, D. Pirjol and I. W. Stewart, *Soft collinear factorization in effective field theory*, *Phys. Rev.* **D65** (2002) 054022, [hep-ph/0109045].

[29] I. Moult, I. W. Stewart, F. J. Tackmann and W. J. Waalewijn, *Employing Helicity Amplitudes for Resummation*, *Phys. Rev.* **D93** (2016) 094003, [1508.02397].

[30] D. Bertolini, D. Kolodrubetz, D. Neill, P. Pietrulewicz, I. W. Stewart, F. J. Tackmann et al., *Soft Functions for Generic Jet Algorithms and Observables at Hadron Colliders*, *JHEP* **07** (2017) 099, [1704.08262].

[31] T. Kasemets, W. J. Waalewijn and L. Zeune, *Calculating Soft Radiation at One Loop*, *JHEP* **03** (2016) 153, [1512.00857].

[32] P. Pietrulewicz, F. J. Tackmann and W. J. Waalewijn, *Factorization and Resummation for Generic Hierarchies between Jets*, *JHEP* **08** (2016) 002, [1601.05088].

[33] C. W. Bauer, F. J. Tackmann, J. R. Walsh and S. Zuberi, *Factorization and Resummation for Dijet Invariant Mass Spectra*, *Phys. Rev.* **D85** (2012) 074006, [1106.6047].

[34] A. J. Larkoski, I. Moult and D. Neill, *Non-Global Logarithms, Factorization, and the Soft Substructure of Jets*, *JHEP* **09** (2015) 143, [1501.04596].

[35] A. J. Larkoski, I. Moult and D. Neill, *Analytic Boosted Boson Discrimination*, *JHEP* **05** (2016) 117, [1507.03018].

[36] D. Neill, *The Edge of Jets and Subleading Non-Global Logs*, 1508.07568.

[37] A. J. Larkoski, I. Moult and D. Neill, *Factorization and Resummation for Groomed Multi-Prong Jet Shapes*, *JHEP* **02** (2018) 144, [1710.00014].

[38] I. W. Stewart, F. J. Tackmann and W. J. Waalewijn, *Dissecting Soft Radiation with Factorization*, *Phys. Rev. Lett.* **114** (2015) 092001, [1405.6722].

[39] M. Dasgupta, K. Khelifa-Kerfa, S. Marzani and M. Spannowsky, *On jet mass distributions in Z+jet and dijet processes at the LHC*, *JHEP* **10** (2012) 126, [1207.1640].

[40] Y.-T. Chien, R. Kelley, M. D. Schwartz and H. X. Zhu, *Resummation of Jet Mass at Hadron Colliders*, *Phys. Rev.* **D87** (2013) 014010, [1208.0010].

[41] Z. L. Liu, C. S. Li, J. Wang and Y. Wang, *Resummation prediction on the jet mass spectrum in one-jet inclusive production at the LHC*, *JHEP* **04** (2015) 005, [1412.1337].

[42] D. W. Kolodrubetz, P. Pietrulewicz, I. W. Stewart, F. J. Tackmann and W. J. Waalewijn, *Factorization for Jet Radius Logarithms in Jet Mass Spectra at the LHC*, *JHEP* **12** (2016) 054, [1605.08038].

[43] Y.-T. Chien, A. Hornig and C. Lee, *Soft-collinear mode for jet cross sections in soft collinear effective theory*, *Phys. Rev.* **D93** (2016) 014033, [1509.04287].

[44] T. Becher, M. Neubert, L. Rothen and D. Y. Shao, *Effective Field Theory for Jet Processes*, *Phys. Rev. Lett.* **116** (2016) 192001, [1508.06645].

[45] CMS Collaboration, S. Chatrchyan et al., *Searches for new physics using the $t\bar{t}$ invariant mass distribution in pp collisions at $\sqrt{s}$=8 TeV*, *Phys. Rev. Lett.* **111** (2013) 211804, [1309.2030]. [Erratum: Phys. Rev. Lett.112,no.11,119903(2014)].

[46] CMS Collaboration, V. Khachatryan et al., *Search for resonant $t\bar{t}$ production in proton-proton collisions at $\sqrt{s} = 8$ TeV*, *Phys. Rev.* **D93** (2016) 012001, [1506.03062].

[47] CMS Collaboration, A. M. Sirunyan et al., *Search for $t\bar{t}$ resonances in highly boosted lepton+jets and fully hadronic final states in proton-proton collisions at $\sqrt{s} = 13$ TeV*, *JHEP* **07** (2017) 001, [1704.03366].

[48] CMS Collaboration, *Search for resonant $t\bar{t}$ production in proton-proton collisions at $\sqrt{s} = 13$ TeV*, *CMS-PAS-B2G-17-017* (2018) . http://cds.cern.ch/record/2621631.

[49] CMS Collaboration, A. M. Sirunyan et al., *Search for pair production of vector-like T and B quarks in single-lepton final states using boosted jet substructure in proton-proton collisions at $\sqrt{s} = 13$ TeV*, *JHEP* **11** (2017) 085, [1706.03408].

Studies of the MSSM Parameter Space at the LHC

Sam Bein[1], *Christian Sander*[2], *Peter Schleper*[1]

[1]Institut für Experimentalphysik, Universität Hamburg, Germany
[2]DESY, Hamburg, Germany

DOI: http://dx.doi.org/10.3204/PUBDB-2018-00782/B2b

Extensions of the Standard Model of particle physics often predict new particles with masses at the electroweak scale or up to a few TeV/c^2. Searches for the decay of such particles at the Large Hadron Collider most often are performed by looking for dedicated final states and by interpreting the results either within a given theoretical model such as Supersymmetry or in a more generic way using so called simplified models. Here we highlight key measurements for Supersymmetry and their usage in parameter scans. Corresponding searches in the data of the CMS experiment are summarized and their interpretation in the framework of the phenomenological MSSM is described.*

1 Supersymmetry at the LHC

Although the Standard Model (SM) of particle physics stands in good agreement with nearly all published results from collider experiments, there remain a number of open questions that are not fully addressed by the SM. Among them are three significant issues for which Supersymmetry (SUSY) may provide a natural solution: the SM does not predict a cold Dark Matter (DM) candidate, which is needed to explain the DM relic abundance observed in cosmology; the gauge couplings do not unify at high energies, as predicted by Grand Unified Theories (GUTs); and finally, radiative corrections to the scalar Higgs mass are expected to be of the order of the Planck scale, up to which the SM is assumed to be valid.

SUSY is an extension of the Poincaré algebra, which introduces a symmetry between fermions and bosons. Invariance under supersymmetry transformations requires that each SM particle is paired with a SUSY partner particle possessing the same quantum numbers except for the spin, which differs by a fundamental unit $\hbar/2$. The scalar partners of the fermions are called squarks ($\tilde{q}$) and sleptons ($\tilde{l}$), while the (gauge) boson partners, the bino ($\tilde{B}$), wino ($\tilde{W}$), gluino ($\tilde{g}$), and higgsino ($\tilde{H}$), mix to form the fermionic chargino ($\tilde{\chi}^{\pm}_{1,2}$) and neutralino ($\tilde{\chi}^{0}_{1,2,3,4}$) states. The lightest neutralino $\tilde{\chi}^{0}_{1}$ is often considered as the lightest SUSY particle (LSP), because in such a case, assuming conservation of R-parity, it is a suitable DM candidate. Since no experimental evidence for these particles has thus far been found, the SUSY partners must be much heavier than the SM particles. The corresponding breaking of SUSY in its most general form involves more than one hundred new parameters, which limits the predictive power of the theory. There are several suggestions for how SUSY might be broken, which often imply assumptions on the breaking parameters at the GUT scale, as for example is the case

*Contribution to "Particles, String and the Early Universe – Research Results of the Collaborative Research Centre SFB 676 in Hamburg".

in the constrained MSSM (cMSSM). Such models usually have a much smaller number of free parameters—just five in the case of the cMSSM—which facilitates a relatively straight-forward interpretation. On the other hand, the assumption of a specific breaking mechanism imposes strong correlations among the SUSY mass parameters, which renders the phenomenology of the models less than fully representative of the broader MSSM.

To overcome this shortcoming, two alternate approaches have been developed. First, simplified models have been used for the interpretation of LHC searches, where only two or three SUSY particles are assumed to be kinematically accessible and all other particles too heavy to have an influence. For example, in the case of sufficiently small squark and LSP masses, the dominant production of SUSY particles at the LHC would be $gg \to \tilde{q}\tilde{q}$ with a subsequent decay $\tilde{q} \to q\tilde{\chi}_1^0$. In such scenarios, the signal event kinematics are governed by only two parameters, namely the masses of the two involved SUSY particles. The interpretation of the LHC data within a comprehensive set of simplified models is a model-independent way to present limits on SUSY masses and production cross sections. This approach allows the results of LHC searches to be applied as constraints on various other models of new physics, provided the models can be represented as a composition of simplified models. A review of SUSY searches from Run 1 and the corresponding interpretations in terms of simplified models can be found in [1].

The second approach is the interpretation of SUSY searches in terms of a so-called full-spectrum SUSY model with a large but manageable number of free parameters and a minimal set of assumptions about the SUSY breaking mechanism. One such model is the phenomenological minimal supersymmetric Standard Model (pMSSM), which imposes a number of assumptions on top of the MSSM that reduce the number of free parameters down to just 19. These assumptions include the restriction that there be no new large sources of CP violation or flavor-changing neutral currents, which are both highly constrained by experimental data. Further, the first two generations of sfermions are assumed to be mass degenerate, and only the trilinear couplings of the third generation are relevant. These assumptions leave the following pMSSM parameters free, where the allowed ranges have been selected to limit the study to a subspace that is kinematically accessible at the LHC [2]:

- three gaugino mass parameters M_1, M_2 and M_3 ($|M_{1,2}| < 3$ TeV, $M_3 < 3$ TeV)
- the ratio $\tan\beta$ of the Higgs vacuum expectation values (from 2 to 60)
- the higgsino mass parameter μ and the pseudoscalar Higgs boson mass m_A ($<$3 TeV)
- ten independent sfermion mass parameters $m_{\tilde{F}}$ with $\tilde{F} = \tilde{Q}_{1,2}$, $\tilde{U}_{1,2}$, $\tilde{D}_{1,2}$, $\tilde{L}_{12}$, $\tilde{E}_{12}$, $\tilde{Q}_3$, $\tilde{U}_3$, $\tilde{D}_3$, $\tilde{L}_3$, $\tilde{E}_3$ ($<$3 TeV)
- three trilinear couplings A_t, A_b, and A_τ ($|A_i| < 7$ TeV).

These parameters are defined at a SUSY mass scale $M_{\text{SUSY}} = \sqrt{m_{\tilde{t}_1} m_{\tilde{t}_2}}$, often called the electroweak symmetry breaking (EWSB) scale, in contrast to the GUT scale. For a given parameter configuration, denoted by θ, a full SUSY model is specified, making predictions for contributions to electroweak precision observables and possible LHC signatures. Those predictions can be tested against experimental data, which serves to constrain the pMSSM parameter space and to identify parameter regions that are not yet excluded.

2 Strategy for the interpretation of LHC searches in the pMSSM

The compatibility of a model with existing data can be expressed by a posterior density of the model parameters θ, given by

$$p(\theta|D^{\mathrm{LHC}}) \propto L(D^{\mathrm{LHC}}|\theta) \cdot p^{\text{non-direct LHC}}(\theta),$$

where D^{LHC} denotes the data from direct searches at the LHC and $L(D^{\mathrm{LHC}}|\theta)$ is the likelihood for the observed dataset given a particular θ. The prior density $p^{\text{non-direct LHC}}(\theta)$ includes several constraints from non-LHC precision measurements like $\mathcal{B}(b \to s\gamma)$, $\mathcal{B}(B_s \to \mu\mu)$, $R(B \to \tau\nu)$, Δa_μ, $\alpha_s(M_Z)$, and $m_b(m_b)$, but also other input from LHC measurements like m_{top}, m_{Higgs}, and the Higgs signal strength μ_{Higgs}. Further factors in the prior density derive from theoretical considerations, such as the requirement that there be no tachyonic particles. Details regarding the measurements employed in the prior density can be found in reference [2].

To scan the 19-dimensional parameter space, a Markov chain Monte Carlo method was used. Approximately 20 million parameter configurations were generated using the ranges for the parameters indicated above. Out of these models, a random sub-sample of about 7200 points was selected for an in-depth study based on an analysis of simulated signal events. Each of the selected model points was used to generate 10000 signal events, which were then processed by a fast simulation of the CMS detector. The resulting event samples were analyzed to estimate the signal acceptance corresponding to various search regions and final states featured in numerous CMS publications, and confronted with the observed yields in real data.

3 Input from LHC searches

A first version of a pMSSM interpretation with CMS data from searches at $\sqrt{s} = 7$ TeV was presented in [3]. For the final interpretation of the full Run 1 data, the expected number of signal events for each incorporated analysis was computed for each model.

A full list of the considered searches is given in [2]. Here, we highlight one of the searches with the highest impact on the pMSSM phase space, which is the search for SUSY in final states with no leptons, multiple jets, and missing transverse momentum $E_{\mathrm{T}}^{\mathrm{miss}}$, targeting the production of squarks and gluinos.

Several iterations of the analysis were published [4–8], and a number of Ph.D. theses documented contributions [9,10]. For the pMSSM interpretation discussed here, the results with the full 7 TeV and 8 TeV data sets are used [5,6]. The searches usually include a light lepton veto and require large transverse hadronic activity H_{T} defined as the scalar sum of the transverse momentum of the jets, in addition to large $E_{\mathrm{T}}^{\mathrm{miss}}$. Further search selections are defined for different jet multiplicities and b-tagged jet multiplicities to increase sensitivity to a broad range of SUSY scenarios.

A particular challenge of searches for new physics is the understanding of the remaining SM background after the applied selections. For this purpose, several data driven techniques have been developed and improved upon over time. In summary, the SM background for this search can be subdivided in four categories: Z($\to \nu\nu$)+jets ("Z to invisible"), W+jets and $t\bar{t}$ with W$\to e/\mu + \nu$ ("lost lepton"), W+jets and $t\bar{t}$ with W$\to \tau + \nu$ ("hadronic tau"), and QCD multi-jet events.

The background from Z to invisible is estimated from Z$\to \ell\bar{\ell}$+jets and γ+jets events, in the latter case making use of the similarity of Z bosons and photons. The background from hadronic tau processes is estimated from events with one isolated muon; lepton universality allows the replacement of the muon by a τ proxy, obtained by smearing the muon four-momentum according to response templates obtained from simulated samples of hadronically-decaying τ leptons. Similarly, the lost lepton background is estimated from events with one isolated lepton, and each event is re-weighted to account for the probability that the lepton is either out of the detector acceptance, not reconstructed, or not isolated. The corresponding efficiencies are taken from or are validated with measurements from data via tag and probe techniques involving $Z \to l^+l^-$ events. Finally, the QCD background is expected to be small, but contributes with a large experimental uncertainty. The large uncertainty is due to fact that $E_{\mathrm{T}}^{\mathrm{miss}}$ in QCD events arises from gross mismeasurements of the energy of one or more jets in an event. This background is estimated using a technique called Rebalance and Smear, which builds a jet response model and applies it to an inclusive sample of multi-jet events (here, inclusive means there is no $E_{\mathrm{T}^{\mathrm{miss}}}$ requirement placed on events). In the first (rebalance) step, the jet momenta are adjusted according to pre-constructed response functions until the event is consistent with a particle-level (perfectly-measured) QCD event with only a small momentum imbalance. In the second step (smearing), the re-balanced jet momenta are smeared according to the response functions, yielding an event sample that can be directly used to derive the prediction for the QCD yield in the signal regions. The response functions are obtained from simulated events but corrected for differences between data and simulation, both for the gaussian core of the jet response and for the non-gaussian tails of the response.

Figure 1 shows the comparison of data and expected background in 36 exclusive search regions of one particular analysis [5], as well as an interpretation in a simplified model of direct squark production. This search was able to exclude squark masses below $\sim$ 780 GeV in the case of 5-fold squark mass degeneracy and assuming a light LSP, Gluino masses were excluded up to 1.2 TeV for small LSP masses in several simplified models. Weaker constraints on the gluino and squark masses are obtained for larger LSP masses, since scenarios with a smaller mass difference of the produced SUSY particles and the LSP lead naturally to lower hadronic activity and MET. These results have been outperformed by recent Run 2 results at $\sqrt{s} = 13$ TeV [7,8], but for the presented pMSSM interpretation they have a large impact since they are among the most sensitive generic SUSY searches from Run 1.

4 Results of the parameter scan

For most of the CMS SUSY searches, the individual analysis teams provided the number of signal events in each signal region for each model point θ. The background count and uncertainty $B \pm \delta B$ were also provided for each search bin. With this information, it is possible to construct a simplified likelihood,

$$L(D^{\mathrm{LHC}}|\theta) = \int \mathrm{Poisson}(N|s(\theta) + b)\; p(b|B, \delta B)\, db,$$

with the number of observed events N, and the number of expected background events b. The number b follows a prior density $p(b|B, \delta B)$, which is modeled as a gamma function with parameters tuned such that the mode and variance are B and $(\delta B)^2$ respectively. Since most searches have more than one exclusive search bin, the results from each bin are combined assuming the

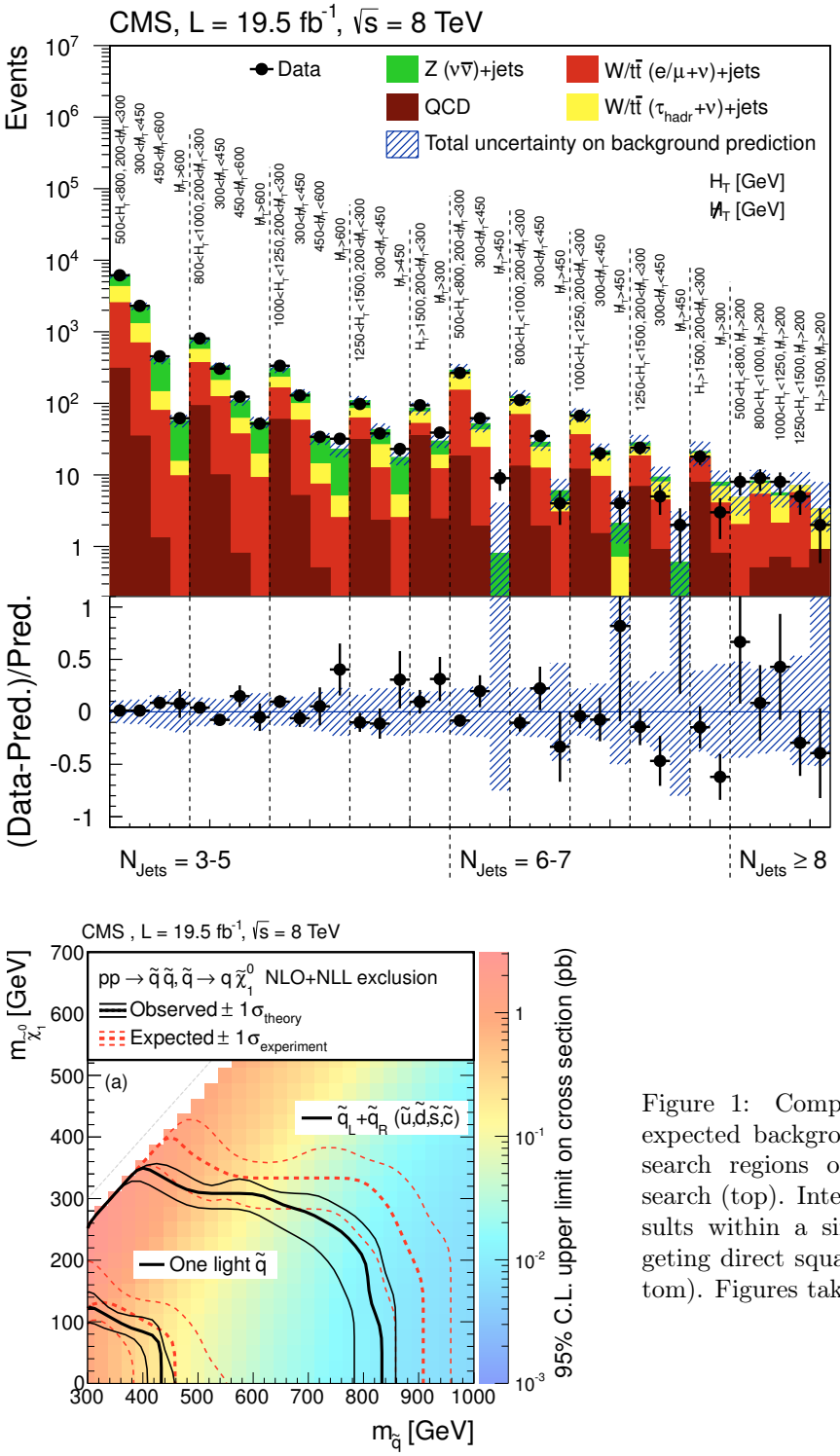


Figure 1: Comparison of data and expected background in 36 exclusive search regions of a jet plus $E_{\mathrm{T}}^{\mathrm{miss}}$ search (top). Interpretation of the results within a simplified model targeting direct squark production (bottom). Figures taken from Ref. [6].

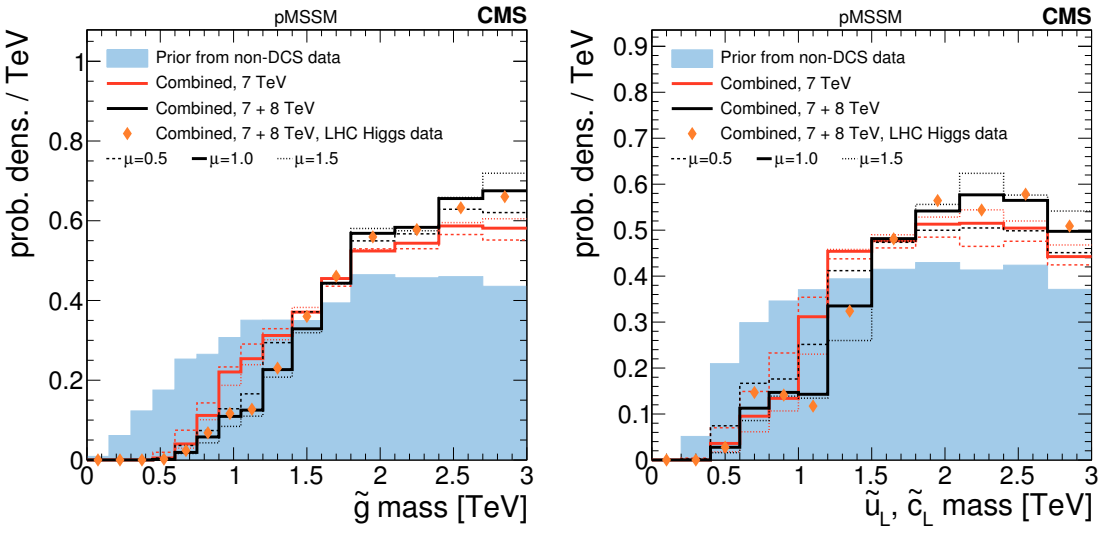


Figure 2: Impact of the direct searches for Supersymmetry on the probability density of the gluino mass (left) and the squark mass (right). The filled blue histogram shows the prior $p^{\text{non-direct LHC}}(\theta)$. The red markers show the impact if LHC Higgs signal strength measurements are included. Figures taken from Ref. [2].

uncertainties for the background to be uncorrelated among the bins, while systematic uncertainties on the signal are treated as fully correlated, leading in general to conservative results. The final agreement of the data with a given hypothesis is quantified by the signal significance

$$Z(\theta) = \text{sign}[\log B_{10}(D,\theta)]\sqrt{2\log B_{10}(D,\theta)},$$

where the local Bayes factor for the data D at a model θ is given by

$$B_{10}(D,\theta) = \frac{L(D|\theta,H_1)}{L(D|H_0)},$$

where $L(D|\theta,H_1)$ and $L(D|H_0)$ are the likelihoods for the signal plus background (H_1) and background-only hypothesis (H_0), respectively. $Z \gg 1$ indicates the presence of signal, while $Z \ll 1$ corresponds to the background-only hypothesis, and a value of $Z(\theta) = -1.64$ corresponds to a 95% C.L. exclusion in a frequentist approach.

Figure 2 shows the results for the posterior density projected into the dimensions of the gluino and squark masses. One can see how the inclusion of 7 TeV and 8 TeV search results are increasingly lowering the probability density for low mass squarks and gluinos. The impact of the inclusion of the direct Higgs signal strength measurements is shown as well. These measurements only mildly influence the examined probability densities, suggesting that in the considered parameter space, the lightest Higgs boson has properties very similar to the SM, as expected in the decoupling limit. Gluino and squark masses below $\sim$ 500 GeV are excluded, which is significantly weaker than the values quoted before for the simplified model interpretation in case of a light LSP. The so-called *survival probability*, defined as the fraction of pMSSM points within a given region of parameter configurations with an observed significance $Z > -1.64$, is shown in Figure 3.

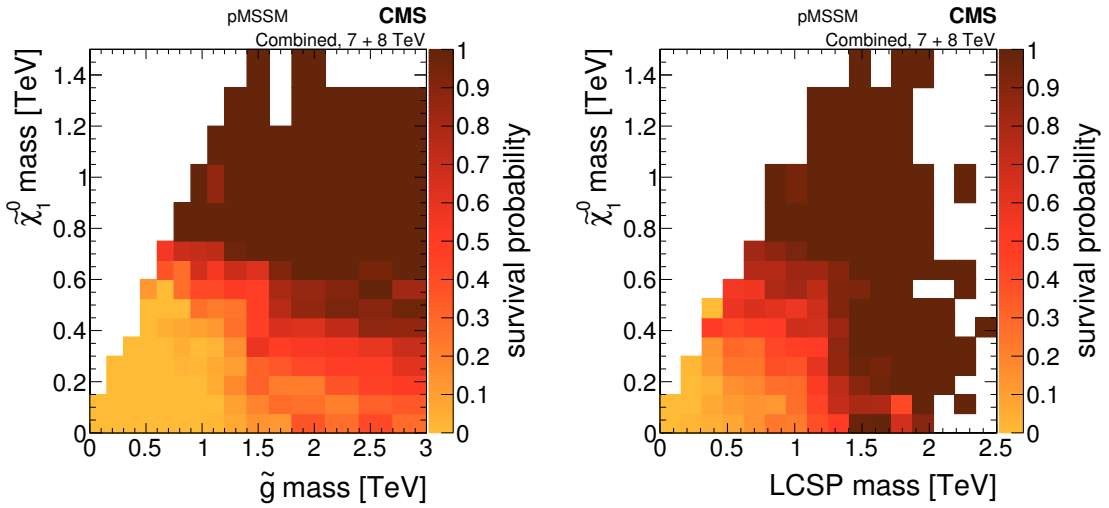


Figure 3: Fraction of pMSSM models surving the combined significance analysis as a function of the LSP and gluino mass (left) and the LSP and squark mass (right). Figures taken from Ref. [2].

Particularly interesting is the fact that a fraction of pMSSM models with rather light squark or gluino masses are not excluded. One reason for this is the limited sensitivity to scenarios with a small mass difference between the produced particle (either squark or gluino) and the LSP. These so-called *compressed* mass scenarios typically predict less hadronic activity and $E_{\mathrm{T}}^{\mathrm{miss}}$ than non-compressed mass scenarios and are difficult to access experimentally.

One of the main purposes of this pMSSM study was to identify regions in the pMSSM parameter space that have evaded exclusion by experimental searches conducted so far. A visualization of the non-excluded parameter space has been prepared in a series of parallel coordinate plots, an example of which is shown in Figure 4. On the first axis, the six most common principal processes are shown for pMSSM models which are not excluded by the considered analyses, and a color is assigned. A process is *principal* if it bears the largest cross section times branching ratio of any process given rise to by a given pMSSM model point. On the following axes, several properties of the models are shown, such as the total cross section, average missing transverse energy, number of jets, and further quantities. One finding from this presentation is the fact that most of the pMSSM models with a large cross section are originating from chargino-neutralino production, which results in low $E_{\mathrm{T}}^{\mathrm{miss}}$, a low number of jets, and even a small number of leptons because of compressed masses. To target such scenarios particular focus must be put on searches with a highly energetic jet from initial state radiation produced in combination with soft leptons.

5 Searches for compressed mass scenarios

To target compressed mass scenarios for chargino-neutralino production in the case that colored superpartners are heavy, a search in final states with taus plus a vector boson fusion (VBF) signature has been performed [11]. Final states with taus are motivated by cosmology, since

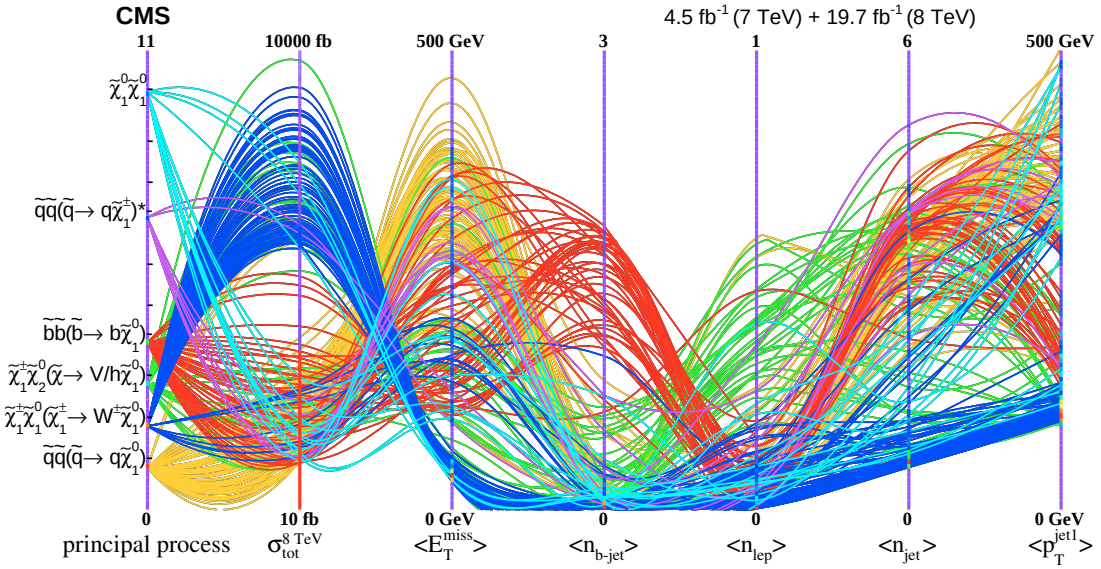


Figure 4: A parallel coordinates display of a subsample of pMSSM model points that survive the Run 1 CMS SUSY searches. Various model properties are given on the vertical axes, and a single pMSSM point is represented by a curved line. Figure taken from Ref. [2].

co-annihilation processes may be key in explaining the observed of relic DM density. The VBF signature allows the threshold on $E_{\mathrm{T}}^{\mathrm{miss}}$ to be lowered at the level of the trigger as well as the offline analysis. This improves the sensitivity to compressed mass scenarios. The inclusion of such a channel in a future pMSSM interpretation may reveal tighter constraints on the allowed phase space.

In pMSSM models with $M_2 \ll M_1, \mu$, longer life times for the charginos are possible, leading to signatures of highly ionizing heavy stable charged particles (HSCPs) or, in case of shorter life times, disappearing tracks. A re-interpretation of existing searches for HSCPs in the pMSSM showed a good sensitivity to a significant fraction of the parameter space with large $c\tau$ values [12]. However, if the long-lived charginos decay after only O($\sim$ 10 cm), the sensitivity diminishes considerably. For that purpose a search for disappearing tracks was developed which used the energy deposits in the most inner pixel detector of CMS to improve the sensitivity to very short-lived HSCPs [13].

6 Gravitino LSP

Further searches have been carried out that probe more selective regions of the pMSSM phase space. Moreover, studies involving particular final states point to opportunities for future versions of the pMSSM analysis to expand in scope. Since the pMSSM assumes the LSP to be the lightest neutralino, other SUSY scenarios in which this is not the case have been studied. In particular, in general gauge mediation (GGM), the LSP is the gravitino. In such models, final states with one or more photons, jets, and $E_{\mathrm{T}}^{\mathrm{miss}}$ are expected, and dedicated searches have been performed [14]. Since no excess above the SM expectation was observed, stringent limits

on the model parameters have been set.

7 Outlook

Searches for SUSY in many different final states have been carried out and interpreted in the context of simplified models and the pMSSM. The differences between the results show the complementary of both approaches in understanding and contextualizing the findings of SUSY searches. A pMSSM interpretation of searches performed on the 13 TeV data will lead to a more global understanding of how the SUSY parameter space is constrained, and will help in the design of new search strategies tailored to overlooked signatures. Of particular interest are searches for compressed mass spectra e.g. through long lived particles of VBF production modes in addition to soft leptons.

Acknowledgements

We are grateful to the German Research Foundation (DFG) for their support of the Collaborative Research Center SFB-676. We thank the German Government for their support of the BMBF-Forschungsschwerpunkt "Physik mit dem CMS Experiment". We appreciate the collaboration with our colleagues at CERN and other institutes in the Compact Muon Solenoid Experiment (CMS).

References

[1] P. Bechtle, T. Plehn and C. Sander, *Supersymmetry*, in *The Large Hadron Collider: Harvest of Run 1* (T. Schörner-Sadenius, ed.), pp. 421–462. Springer International Publishing, Cham, 2015. 1506.03091. DOI.

[2] CMS Collaboration, V. Khachatryan et al., *Phenomenological MSSM interpretation of CMS searches in pp collisions at sqrt(s) = 7 and 8 TeV*, *JHEP* **10** (2016) 129, [1606.03577].

[3] CMS Collaboration, L. Vanelderen, *Phenomenological MSSM interpretation of the CMS 2011 7 TeV 5 fb^{-1} results*, in *Proceedings, 1st Large Hadron Collider Physics Conference (LHCP 2013): Barcelona, Spain, May 13-18, 2013*, vol. 60, p. 20020, 2013, DOI.

[4] CMS Collaboration, S. Chatrchyan et al., *Search for New Physics with Jets and Missing Transverse Momentum in pp collisions at $\sqrt{s} = 7$ TeV*, *JHEP* **08** (2011) 155, [1106.4503].

[5] CMS Collaboration, S. Chatrchyan et al., *Search for new physics in the multijet and missing transverse momentum final state in proton-proton collisions at $\sqrt{s} = 7$ TeV*, *Phys. Rev. Lett.* **109** (2012) 171803, [1207.1898].

[6] CMS Collaboration, S. Chatrchyan et al., *Search for new physics in the multijet and missing transverse momentum final state in proton-proton collisions at $\sqrt{s} = 8$ TeV*, *JHEP* **06** (2014) 055, [1402.4770].

[7] CMS Collaboration, V. Khachatryan et al., *Search for supersymmetry in the multijet and missing transverse momentum final state in pp collisions at 13 TeV*, *Phys. Lett.* **B758** (2016) 152–180, [1602.06581].

[8] CMS Collaboration, A. M. Sirunyan et al., *Search for supersymmetry in multijet events with missing transverse momentum in proton-proton collisions at 13 TeV*, *Phys. Rev.* **D96** (2017) 032003, [1704.07781].

[9] Kristin Goebel, *Probing supersymmetry based on precise jet measurements at the CMS experiment*, Ph.D. thesis, Universität Hamburg, 2015. PhD thesis, February 2015, 10.3204/DESY-THESIS-2015-003 http://www-library.desy.de/cgi-bin/showprep.pl?thesis15-003.

[10] Matthias Schröder, *Quality of Jet Measurements and Impact on a Search for New Physics at CMS*, Ph.D. thesis, Universität Hamburg, 2012. PhD thesis (July 2012) http://www-library.desy.de/cgi-bin/showprep.pl?thesis12-042.

[11] CMS Collaboration, V. Khachatryan et al., *Search for supersymmetry in the vector-boson fusion topology in proton-proton collisions at* $\sqrt{s} = 8$ *TeV*, *JHEP* **11** (2015) 189, [1508.07628].

[12] CMS Collaboration, V. Khachatryan et al., *Constraints on the pMSSM, AMSB model and on other models from the search for long-lived charged particles in proton-proton collisions at sqrt(s) = 8 TeV*, *Eur. Phys. J.* **C75** (2015) 325, [1502.02522].

[13] Teresa Lenz, *A search for new heavy particles in events with highly ionising, short tracks at the CMS experiment*, Ph.D. thesis, Universität Hamburg, 2016. PhD thesis (April 2016), 10.3204/DESY-THESIS-2016-016 https://bib-pubdb1.desy.de/record/300800.

[14] CMS Collaboration, V. Khachatryan et al., *Search for supersymmetry with photons in pp collisions at* $\sqrt{s}$*=8 TeV*, *Phys. Rev.* **D92** (2015) 072006, [1507.02898].

Neutrinos in the Standard Model

Alessandro Mirizzi[1,2]

[1]Dipartimento Interateneo di Fisica "Michelangelo Merlin", Bari, Italy
[2]Istituto Nazionale di Fisica Nucleare – Sezione di Bari, Italy

DOI: http://dx.doi.org/10.3204/PUBDB-2018-00782/B3

The project B3 of the SFB 676 has been focussed on theoretical and experimental aspects of low-energy neutrinos from artificial and astrophysical sources. The experimental part consists in the study of the background induced by cosmic muons in current low-energy neutrino experiments. The theoretical part has been devoted to the flavor conversions of neutrinos emitted during a stellar collapse and in the early universe. The project has also been expanded to study the low-energy neutrino project LAGUNA (European design study Large Apparati for Grand Unification and Neutrino Astrophysics), which is investigating to feasibility of large underground detectors for proton decay searches, the observation of rare galactic supernova and solar neutrinos. Here we briefly review the work carried on in the theoretical part of the B3 project.

1 Introduction

Neutrinos are the most elusive of all elementary particles. The three different kinds (flavors) of neutrinos can convert into each other by their nonzero masses and flavor mixing - a macroscopic quantum effect named neutrino flavor oscillations. The possibility of neutrino flavor oscillations, theoretically suggested more than half a century ago, is now an experimentally established fact. After many years of research with atmospheric, solar, accelerator and reactor neutrinos, we have achieved a mature understanding the oscillation phenomenon, crowned in 2015 with the Nobel Prize in Physics awarded to T. Kajita and A. B. McDonald "... for the discovery of neutrino oscillations which show that neutrinos have mass".

Now that the three-flavor oscillation framework is well determined (apart from the still unknown mass ordering and possible CP violation), neutrino physics enters a new phase, where these particles can be used to probe distant astrophysical and cosmic sources. At this regard, the leading idea of the theory part of the B3 project has been to exploit astrophysical and cosmological environments as laboratories for testing neutrino physics. In particular, it has focussed mainly on the astroparticle theory and phenomenology of neutrinos and on the implications of their observations in current or future experiments. In spite of their weak interactions, there are two environments where neutrino reach thermal equilibrium: a supernova core and the Early Universe. Neutrino thus play a dominant role in the supernova and cosmic evolution. In particular, these two environments offer peculiar conditions to probe neutrino flavor conversions.

Core-collapse supernovae (SNe) represent a unique laboratory to probe neutrino properties in the extreme conditions offered by a stellar gravitational collapse. In this context, B3 project has been devoted in the challenging study of the non-linear equations that describe the neutrino

flavor evolution in the presence of neutrino-neutrino interactions. The characterization of these effects is crucial in the case of SN neutrinos, since in deepest stellar regions the neutrino density is so high that neutrino-neutrino interactions dominate the flavor dynamics. The recent discovery of these effects has dramatically changed the paradigm of neutrino flavor conversions during a stellar collapse, with important consequences on the observable SN neutrino signal and on the core-collapse dynamics.

The study of flavor conversions between active and sterile neutrinos in the Early Universe represents another hot topic, after intriguing but controversial hints for low-mass sterile neutrinos, coming from precision cosmological measurements and laboratory oscillation experiments. In this context in the B3 project have been developed dedicated investigations, performing accurate solutions of the kinetic equations for the evolution of the active-sterile ensemble. These are necessary in order to determine the relic abundance of sterile neutrinos. This task was extremely timely, since cosmological experiments, like the Planck satellite, were releasing precise measurements of the possible extra-radiation in the Early Universe.

A more detailed description of the research accomplishment is presented below. Section 2 is devoted to the theory and phenomenology of SN neutrino flavor conversions. Section 3 deals with the cosmological impact of eV-mass sterile neutrinos. Finally, Section 4 presents a brief outlook.

2 Supernova neutrinos flavor conversions

Neutrinos emitted from core-collapse supernovae (SNe) have been extensively studied as a probe of both fundamental neutrino properties and of core-collapse physics. The detailed features of the neutrino signal may reveal the ordering of the neutrino mass spectrum, necessary to reconstruct the neutrino mass matrix and its possible underlying symmetries. In this context, in the B3 project have been developed different research activities on various theoretical and phenomenological aspects of supernova neutrino flavor conversions.

2.1 Collective neutrino oscillations in dense neutrino gases

The core of the B3 theory research activity has revolved around the very complicated issue of collective flavor oscillations that can emerge in dense neutrino gases. These unusual phenomena are likely to be important in the context of stellar collapse (supernovae) or coalescing neutron stars (short gamma-ray bursts) or the early Universe. In these extreme environments where the neutrino gas is so dense that it becomes itself a "background medium". In these conditions, the flavor evolution equations become highly non-linear, sometimes resulting in surprising phenomena where the entire neutrino system oscillates coherently as a single collective mode. In the context of supernova neutrino flavor evolution, these collective neutrino oscillations can produce new effects in the region of high neutrino density, a few tens of kilometers above the supernova core. The recent discovery of these phenomena, which are currently changing the paradigm of supernova neutrino flavor conversions, triggered a lot of activity to investigate many aspects of these intriguing effects. In particular, it has been found that, taking typical input for the initial neutrino fluxes, supernova neutrinos can have their energy spectra partially swapped during collective oscillations. This effect is sensitive to the (still unknown) neutrino mass ordering (hierarchy). The B3 project gave a significant contribution to the progress of these studies.

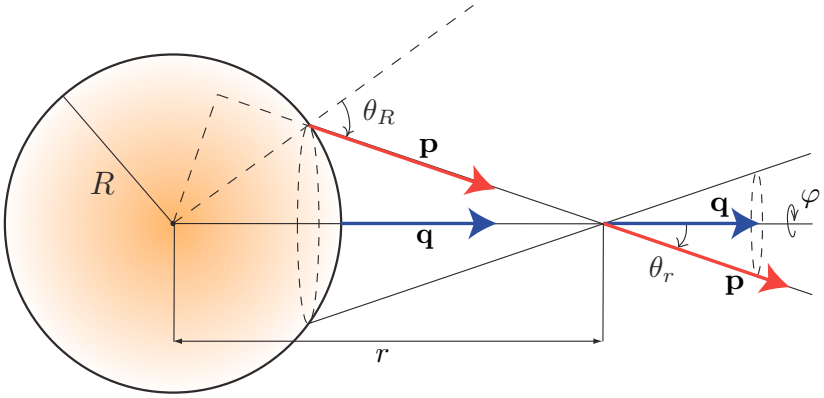


Figure 1: Geometrical picture of the SN neutrino bulb model. Reprinted from Ref. [1] with kind permission of Società Italiana di Fisica.

In particular, there have been developed large-scale numerical simulations and analytical approximations for the characterization of the non-linear neutrino flavor evolution in high-density supernova regions. At this regard, a complication that arises in these simulations is related to the so called "multi-angle effects". These arise since the current-current nature of low-energy weak interactions implies that a factor $1 - \cos\theta$ appears in the neutrino-neutrino interaction strength, where θ is the angle between neutrino trajectories (see Fig. 1). As a consequence, the solution of the SN neutrino equations of motion is extremely challenging, since it requires an advanced numerical approach to simulate accurately the coupling of intersecting neutrino trajectories and the associated multi-angle effects which affect the flavor evolution. The numerical simulations developed in the B3 project, including multi-angle effects in a three-flavor framework, represented the state of the art in the field.

In this context one of the most relevant result has been the investigation of the SN self-induced flavor conversions during the early times accretion phase (at post-bounce times $t_{\rm pb} \lesssim 0.5$ s). This phase would offer the best opportunity to detect effects from neutrino flavor oscillations, since the emitted neutrino fluxes are large with a distinct flavor hierarchy. It has been performed a dedicated study of this problem, characterizing the neutrino emissivity and the SN matter density profile, using results from recent neutrino radiation hydrodynamical simulations. It has been realized that during the accretion phase the matter density, piled-up above the neutrinosphere, is so high that it dominates over the neutrino density. In contrast to what is expected in the presence of only neutrino-neutrino interactions, it has been found that the multi-angle effects associated with the dense ordinary matter suppress collective oscillations (see Fig. 2). The matter suppression implies that neutrino oscillations start outside the neutrino transport region and therefore have a negligible impact on the neutrino heating and the explosion dynamics. Furthermore, the SN neutrino signal during the accretion phase would be processed by the only Mikheyev–Smirnov–Wolfenstein (MSW) matter effect in the SN mantle and by the Earth matter effects [2, 3]. These results already had a strong impact on the description of the SN neutrino flavor conversions and stimulated further independent investigations to confirm them. In order to study these effects, it has been also developed an analytical approach to interpret and predict the outcome of the numerical simulations, based on the stability analysis of the linearized equations of motion (see Ref. [4]). This technique allows

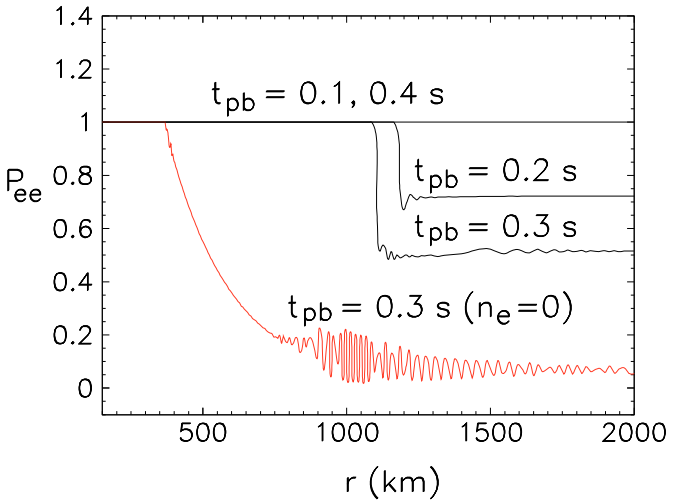


Figure 2: Radial profiles of the $\bar{\nu}_e$ survival probability P_{ee} at selected post-bounce times from multi-angle simulations in matter (black continuous curves) and for $n_e = 0$ (light curve). Reprinted figure with permission from Ref. [2]. Copyright (2011) by the American Physical Society.

one to determine the possible instability of the SN neutrino ensemble versus the self-induced flavor transformations.

Self-induced flavor conversions, even if suppressed during the accretion phase, can still produce sizable effects during the SN cooling phase ($t_{\rm pb} \gtrsim 1.0$ s) when the matter density becomes sub-dominant with respect to the neutrino one. However, the predictions for the initial SN neutrino fluxes at late times are less robust than during the accretion phase. For this reason, it has been interesting to perform a study to determine how different original neutrino fluxes can affect the pattern of the self-induced flavor conversions. Thanks to challenging numerical simulations it has been possible to point out a rich and unexpected phenomenology [5–7]. In particular, multi-angle and three-flavor effects peculiarly affect the development of the self-induced spectral splits in both neutrino and antineutrino spectra. Remarkably, it has been found that some of these spectral splits could occur sufficiently close to the peak energies to produce significant distortions in the observable SN neutrino signal, as shown in Fig. 3. The detection of these signatures at proposed large underground neutrino detectors could give hints about the primary SN neutrino fluxes, as well as on the neutrino mass hierarchy.

It has been also explored the effect of the SN neutrino angular distributions on the development of the self-induced flavor conversions. It has been found that flavor-dependent angular distributions may lead to a new multi-angle instability, that can dramatically affect the SN neutrino oscillations, smearing the splitting features found with trivial neutrino emission models [8, 9].

Finally, it has been devoted attention to the effect of removal of space-time symmetries in the self-induced flavor evolution. In this context, the basic assumptions of the supernova neutrino emission model, namely the azimuthal symmetry in the supernova physical properties, i.e. the physical conditions only depend on the distance r from the center of the star, and the quasi-

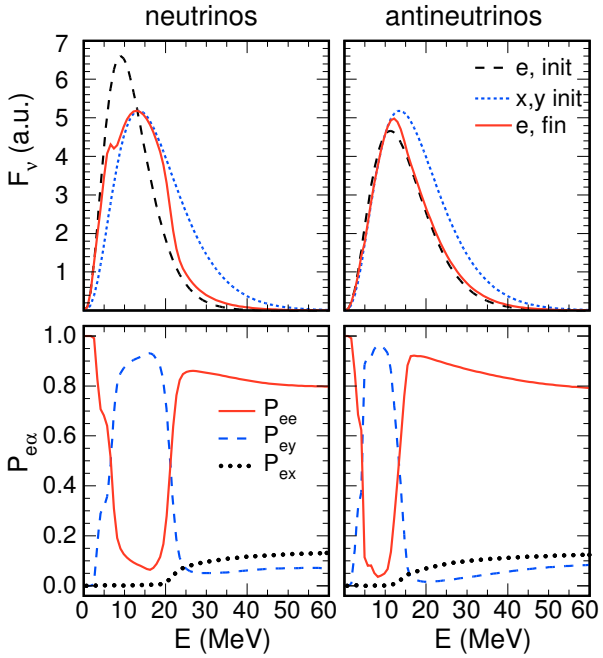


Figure 3: Three-flavor evolution during the SN cooling phase in the multi-angle case and in inverted mass hierarchy for neutrinos (left panels) and antineutrinos (right panels). Upper panels: Initial energy spectra for ν_e (long-dashed curve) and $\nu_{x,y}$ (short-dashed curve) and for ν_e after collective oscillations (solid curve). Lower panels: Probabilities P_{ee} (solid red curve), P_{ey} (dashed blue curve), P_{ex} (dotted black curve). Reprinted figure with permission from Ref. [5]. Copyright (2011) by the American Physical Society.

stationary neutrino emission have been recently questioned. Indeed, it was tacitly assumed that unavoidable small deviations from them do not significantly perturb the flavor evolution. However, we have realized with simple examples that instabilities may grow once assumptions the two assumptions are relaxed, since self-interacting neutrinos can spontaneously break both the azimuthal symmetry [10–12] and the translation symmetry in space and time [13]. The role of density matter turbulence in supernova neutrino flavor conversions has also been investigated [14].

2.2 Supernova neutrino phenomenology

In [15] we proposed to use the rise time of a Galactic supernova $\overline{\nu}_e$ lightcurve, observable at a high-statistics experiment such as the Icecube Cherenkov detector, as diagnostic tool for the neutrino mass hierarchy at "large" 1-3 leptonic mixing angle θ_{13}, as measured few years ago. We showed that, thanks to the combination of matter suppression of collective effects at early post-bounce times on one hand and the presence of the ordinary Mikheyev–Smirnov–Wolfenstein effect in the outer layers of the SN on the other hand, a sufficiently fast rise time on $\mathcal{O}(100)$ ms scale is indicative of an inverted mass hierarchy, as shown in Fig. 4. We investigated results

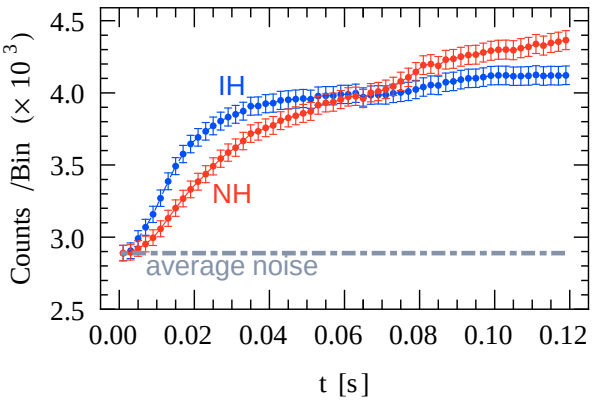


Figure 4: SN $\bar{\nu}_e$ count rate signal in IceCube assuming a distance of 10 kpc in normal (NH) and inverted (IH) mass hierarchy. Reprinted figure with permission from Ref. [15]. Copyright (2012) by the American Physical Society.

from an extensive set of stellar core-collapse simulations, providing a first exploration of the astrophysical robustness of these features.

Neutrino oscillations in the Earth matter may introduce peculiar modulations in the SN neutrino spectra. The detection of this effect has been proposed as diagnostic tool for the neutrino mass hierarchy at "large" θ_{13}. In this context we performed an updated study on the observability of the Earth matter effect at large next-generation underground detectors (i.e., 0.4 Mton water Cherenkov, 50 kton scintillation and 100 kton liquid Argon detectors) based on neutrino fluxes from state-of-the-art SN simulations and accounting for statistical fluctuations via Monte Carlo simulations [16]. Since the average energies predicted by recent simulations are lower than previously expected and a tendency towards the equalization of the neutrino fluxes appears during the SN cooling phase, the detection of the Earth matter effect will be more challenging than expected from previous studies. We found that none of the proposed detectors shall be able to detect the Earth modulation for the neutrino signal of a typical galactic SN at 10 kpc.

We also worked on an improved characterization of the observability of the galactic and diffuse extragalactic SN neutrino fluxes in next generation neutrino detectors. In particular, we focused on water-Cherenkov, scintillator, and liquid argon techniques which are currently investigated in the context of the LAGUNA-LBNO (Large Apparati for Grand Unification and Neutrino Astrophysics–Long Baseline Neutrino Observatory) project.

3 Active-sterile neutrino conversions in the Early Universe

Neutrino flavor conversions in the Early Universe are a fascinating problem involving collisional damping, refractive effects from charged leptons and neutrino self-interactions. At this regard, in the B3 project we have been extensively working on the flavor conversions of active-sterile neutrinos in the Early Universe. In this context, recent analysis from precision cosmology and Big-Bang Nucleosynthesis data seemed to mildly favor the presence of extra radiation in the Universe beyond photons and ordinary neutrinos, lending support to the existence of low-mass

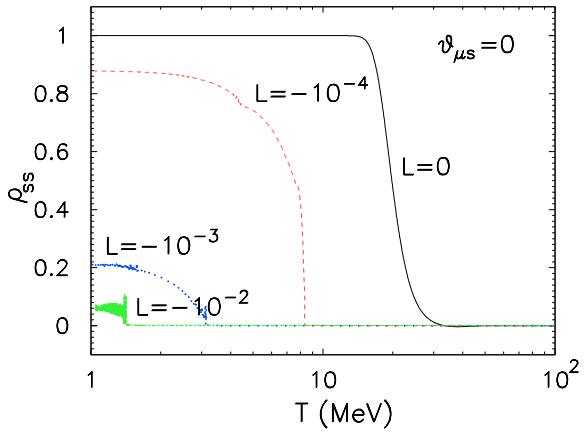


Figure 5: Evolution of the sterile neutrino density matrix element in function of the temperature T for different values of the primordial letpon asymmetry. Reprinted figure with permission from Ref. [17]. Copyright (2012) by the American Physical Society.

sterile neutrinos. At present there are tentative hints for the existence of sterile neutrinos of (sub)-eV mass from a variety of short baseline neutrino experiments. The preferred range of masses and mixing angles leads to almost complete thermalization. Then sterile neutrinos should be present with approximately the same number density as active states. However, this is in disagreement with recent cosmological data analyses, in particular with neutrino mass bounds form the first data release of the Planck experiment, as well as from the data of the structure formation (see Ref. [18]). A possible escape route to reconcile eV-sterile neutrinos with cosmology requires the suppression of their primordial abundance. Different arguments have been proposed, introducing new physics in the particle sector or in cosmology. The most intriguing scenarios discussed so far consists of large lepton asymmetries in the neutrino sector. These would generate a large matter term, that can suppress the effective in-medium mixing angle between active and sterile neutrinos. In this context, we performed a detailed study of the kinetic equations for the ensemble of three active neutrinos plus an eV-sterile neutrino in which we calculated the suppression of the sterile neutrino abundance in function of different neutrino asymmetries, removing several approximations adopted in the previous literature, as shown in Fig. 5 (see Ref. [17]). This goal has required the development of advanced numerical codes in order to simulate the neutrino flavor evolution. Moreover we also investigated possible signatures of active-sterile flavor conversions on the Big-Bang Nucleosynthesis (see Ref. [19]). Another mechanism recently proposed to suppress the sterile abundances, is based on secret interactions in the sterile neutrino sector. If sterile neutrinos are charged under a new gauge group with a light vector boson, this can generate a very strong matter potential for themselves. Unfortunately, also in this case, the reconciliation of sterile neutrino with cosmology is not guaranteed, since the suppression of the sterile species production is associated with significant spectral distortions of the active neutrino species, with potentially interesting cosmological consequences both for BBN, especially for the Deuterium abundance, as we discussed in Ref. [20]. We also investigated nontrivial consequences for the neutrino mass bounds if the mass of the new vector boson is relatively small [21]. The connection of these scenarios with self-interacting dark matter models has been recently pointed out.

4 Outlook

The study of neutrino physics has been always accompanied by surprises. Often our theoretical prejudices have been disproved by experimental results, that required to significantly modify our previous pictures. In this context, supernovae and Early Universe represent two laboratories where amazing effects can still arise. A complete understanding of flavor conversions in supernovae is mandatory in order to interpret the neutrino signal from the next Galactic explosion. This could shed light on the mechanism of a stellar gravitational collapse and on neutrino fundamental properties, like the mass ordering. Early Universe will continue to be an important environment to probe neutrino properties, such as the mass and the possibility of extra sterile neutrinos. The work shortly reviewed here shed the basis for further investigations. These are motivated in order to better understand the neutrino flavor conversions in these high-density media and their impact on cosmology and astrophysics.

Acknowledgments

The work of A.M. is supported by the Italian Istituto Nazionale di Fisica Nucleare (INFN) through the "Theoretical Astroparticle Physics" project and by Ministero dell'Istruzione, Università e Ricerca (MIUR). A.M. warmly thanks his collaborators Enrico Borriello, Sovan Chakraborty and Ninetta Saviano on the projects presented in this report.

The work presented in this report has been supported in part by the DFG through the SFB 676 "Particles, Strings and the Early Universe."

References

[1] A. Mirizzi, I. Tamborra, H.-T. Janka, N. Saviano, K. Scholberg, R. Bollig et al., *Supernova Neutrinos: Production, Oscillations and Detection*, *Riv. Nuovo Cim.* **39** (2016) 1–112, [1508.00785].

[2] S. Chakraborty, T. Fischer, A. Mirizzi, N. Saviano and R. Tomas, *No collective neutrino flavor conversions during the supernova accretion phase*, *Phys. Rev. Lett.* **107** (2011) 151101, [1104.4031].

[3] S. Chakraborty, T. Fischer, A. Mirizzi, N. Saviano and R. Tomas, *Analysis of matter suppression in collective neutrino oscillations during the supernova accretion phase*, *Phys. Rev.* **D84** (2011) 025002, [1105.1130].

[4] N. Saviano, S. Chakraborty, T. Fischer and A. Mirizzi, *Stability analysis of collective neutrino oscillations in the supernova accretion phase with realistic energy and angle distributions*, *Phys. Rev.* **D85** (2012) 113002, [1203.1484].

[5] A. Mirizzi and R. Tomas, *Multi-angle effects in self-induced oscillations for different supernova neutrino fluxes*, *Phys. Rev.* **D84** (2011) 033013, [1012.1339].

[6] B. Dasgupta, A. Mirizzi, I. Tamborra and R. Tomas, *Neutrino mass hierarchy and three-flavor spectral splits of supernova neutrinos*, *Phys. Rev.* **D81** (2010) 093008, [1002.2943].

[7] S. Choubey, B. Dasgupta, A. Dighe and A. Mirizzi, *Signatures of collective and matter effects on supernova neutrinos at large detectors*, 1008.0308.

[8] A. Mirizzi and P. D. Serpico, *Instability in the Dense Supernova Neutrino Gas with Flavor-Dependent Angular Distributions*, *Phys. Rev. Lett.* **108** (2012) 231102, [1110.0022].

[9] A. Mirizzi and P. D. Serpico, *Flavor Stability Analysis of Dense Supernova Neutrinos with Flavor-Dependent Angular Distributions*, *Phys. Rev.* **D86** (2012) 085010, [1208.0157].

[10] A. Mirizzi, *Multi-azimuthal-angle effects in self-induced supernova neutrino flavor conversions without axial symmetry*, *Phys. Rev.* **D88** (2013) 073004, [1308.1402].

[11] S. Chakraborty and A. Mirizzi, *Multi-azimuthal-angle instability for different supernova neutrino fluxes*, *Phys. Rev.* **D90** (2014) 033004, [1308.5255].

[12] S. Chakraborty, A. Mirizzi, N. Saviano and D. d. S. Seixas, *Suppression of the multi-azimuthal-angle instability in dense neutrino gas during supernova accretion phase*, *Phys. Rev.* **D89** (2014) 093001, [1402.1767].

[13] G. Mangano, A. Mirizzi and N. Saviano, *Damping the neutrino flavor pendulum by breaking homogeneity*, *Phys. Rev.* **D89** (2014) 073017, [1403.1892].

[14] E. Borriello, S. Chakraborty, H.-T. Janka, E. Lisi and A. Mirizzi, *Turbulence patterns and neutrino flavor transitions in high-resolution supernova models*, *JCAP* **1411** (2014) 030, [1310.7488].

[15] P. D. Serpico, S. Chakraborty, T. Fischer, L. Hudepohl, H.-T. Janka and A. Mirizzi, *Probing the neutrino mass hierarchy with the rise time of a supernova burst*, *Phys. Rev.* **D85** (2012) 085031, [1111.4483].

[16] E. Borriello, S. Chakraborty, A. Mirizzi, P. D. Serpico and I. Tamborra, *(Down-to-)Earth matter effect in supernova neutrinos*, *Phys. Rev.* **D86** (2012) 083004, [1207.5049].

[17] A. Mirizzi, N. Saviano, G. Miele and P. D. Serpico, *Light sterile neutrino production in the early universe with dynamical neutrino asymmetries*, *Phys. Rev.* **D86** (2012) 053009, [1206.1046].

[18] A. Mirizzi, G. Mangano, N. Saviano, E. Borriello, C. Giunti, G. Miele et al., *The strongest bounds on active-sterile neutrino mixing after Planck data*, *Phys. Lett.* **B726** (2013) 8–14, [1303.5368].

[19] N. Saviano, A. Mirizzi, O. Pisanti, P. D. Serpico, G. Mangano and G. Miele, *Multi-momentum and multi-flavour active-sterile neutrino oscillations in the early universe: role of neutrino asymmetries and effects on nucleosynthesis*, *Phys. Rev.* **D87** (2013) 073006, [1302.1200].

[20] N. Saviano, O. Pisanti, G. Mangano and A. Mirizzi, *Unveiling secret interactions among sterile neutrinos with big-bang nucleosynthesis*, *Phys. Rev.* **D90** (2014) 113009, [1409.1680].

[21] A. Mirizzi, G. Mangano, O. Pisanti and N. Saviano, *Collisional production of sterile neutrinos via secret interactions and cosmological implications*, *Phys. Rev.* **D91** (2015) 025019, [1410.1385].

Unstable Quantum Fields and Higgs Vacuum

Bernd A. Kniehl

II. Institut für Theoretische Physik, Universität Hamburg, Germany

DOI: http://dx.doi.org/10.3204/PUBDB-2018-00782/B4

We summarize the progress of the research performed in project B4 of the SFB 676 and highlight the most important results obtained. Starting from the observation that mixing and instability of elementary particles concur in nature, one central goal was to construct a general renormalization scheme that rigorously incorporates both aspects and to explore its phenomenological consequences in the Standard Model (SM) of elementary particle physics and its most favorable extensions. Another central goal was to significantly improve the analysis of the electroweak vacuum stability and the theoretical concepts necessary for the extraction of the top-quark mass from experimental data.

1 Overview

The research of project B4 was divided into two areas. The first research area, which was continuously worked on during all three funding periods, was dedicated to deepening our understanding of the notions of mixing and instability of elementary particles in the context of quantum field theory and is covered in Sec. 2. The second research area, which was primarily worked on during the third funding period, was devoted to the stability of the electroweak (EW) vacuum and is covered in Sec. 3. Project B4 has produced eighteen journal publications [1–18] and four proceedings contributions [19–22] altogether. Three of these publications made it into *Physical Review Letters* [1, 9, 15]. One [15] of the latter three publications was distinguished as *Editors' Suggestion* and featured by Alexander Kusenko with the article *Viewpoint: Are We on the Brink of the Higgs Abyss?* in *Physics*.[1] A related publication in *Computer Physics Communications* [17], in which the C++ library `mr` for the matching and running of the Standard Model parameters is described, was distinguished there as *Highlighted Article* and featured by Abigail Beall with the article *A time machine to explore the universe*.[2] Key publications in preparation of the second research area include Refs. [23–26]. Project B4 yielded one bachelor thesis [27], one master thesis [28], and one doctoral thesis [29].

[1] `https://physics.aps.org/articles/v8/108`

[2] `https://www.journals.elsevier.com/computer-physics-communications/highlighted-articles/a-time-machine-to-explore-the-universe`

2 Mixing and instability in field theory

2.1 Starting point

The state of the art at the beginning of project B4 may be summarized as follows. An on-shell renormalization scheme had been formulated to all orders for the SM under the simplifying assumptions that all particles are stable, neutrinos are massless, and quark flavors do not mix [30]. A complex-pole scheme of renormalization had been elaborated for the $W^\pm$ [31], Z [32], and Higgs bosons [33, 34]. The complex poles of the propagators of the physical fields in the SM had been shown to be gauge independent via Nielsen identities [35]. Definitions of branching ratios and partial decay widths of unstable particles had been proposed that satisfy the basic principles of additivity and gauge independence to all orders [36, 37]. Various schemes for the renormalization of the Cabibbo–Kobayashi–Maskawa (CKM) mixing matrix of stable quarks had been proposed at one loop, none of which was completely satisfactory and suitable for generalizations to higher orders and the case of instability. The renormalized CKM matrix was either gauge dependent [38], off-shell [39], not unitary [40], or complicated by vertex corrections [41]. Mixing renormalization had also been considered at one loop for mixed systems of stable fermions involving Majorana degrees of freedom [42]. An on-shell renormalization scheme had been formulated to all orders for the EW part of the minimal supersymmetric extension of the SM (MSSM) allowing for the physical particles to be unstable [43], which, however, left room for improvements and extensions.

The central goal to establish a complex-pole scheme of mixing renormalization for unstable particles valid to all orders for the SM and its most attractive extensions requires generalized concepts for flavor-changing propagators and vertices. In the SM with massless neutrinos, these are the propagator matrices of the up- and down-type quarks and their charged-current vertices. This pattern carries over to the lepton sector if the neutrinos are massive Dirac fermions, while things are more complicated in the presence of Majorana degrees of freedom, which typically give rise to flavor-changing vertices involving the Z^0 and Higgs bosons, too. In supersymmetric extensions of the SM, there is additional flavor mixing for the superpartners of the fermions, the spin-zero squarks and sleptons, and for the spin-$\frac{1}{2}$ charginos and neutralinos.

The results on flavor-changing propagators and vertices achieved in project B4 are reported in Secs. 2.2 and 2.3, respectively.

2.2 Flavor-changing propagators

We made significant progress in the SM. We established the all-order renormalization of the propagator matrix of a mixed system of unstable Dirac fermions in three stages: (i) unstable fermion without mixing [3]; (ii) stable fermions with mixing [8]; (iii) general case [9, 11].

In Ref. [3], the concepts of pole mass and width, previously elaborated for scalar [33, 34] and vector bosons [31, 32], were extended to unstable fermions in the general framework of parity-nonconserving gauge theories, such as the SM. In contrast with the conventional on-shell definitions, these concepts are gauge independent and avoid severe unphysical singularities, such as threshold [44, 45] or power-like infrared singularities [46], properties of great importance since most fundamental fermions in nature are unstable particles. General expressions for the unrenormalized and renormalized dressed propagators of unstable fermions and their wave-function renormalization (WFR) constants were presented. It was shown that the masses and widths of the left- and right-handed fermion fields coincide to all orders and that their pole

residues cannot be arranged to be both unity, with a relative phase remaining.

In Ref. [8], we derived general and explicit expressions for the unrenormalized and renormalized dressed propagators of stable Dirac fermions in parity-nonconserving theories with inter-generation mixing. The mass eigenvalues, the corresponding mass counterterms, and the effect of inter-generation mixing on their determination were discussed. Invoking the Aoki–Hioki–Kawabe–Konuma–Muta [47] renormalization conditions and employing a number of very useful relations from Matrix Algebra, we showed explicitly that the renormalized dressed propagators satisfy important physical properties.

In Refs. [9, 11], we showed how to renormalize the propagator matrix of a mixed system of unstable Dirac fermions to all orders in the pole scheme. We presented closed expressions for the pole masses, comprising both the physical masses and total decay widths, and the WFR matrices in terms of the scalar, pseudo-scalar, vector, and axial-vector form factors of the one-particle-irreducible self-energies, and also listed their expansions through two loops, which had not previously been available. We explicitly demonstrated that the poles of the left- and right-handed parts of the dressed propagator matrices coincide as they should, and that the resonating diagonal elements of the latter have unit residues. We identified residual degrees of freedom in the WFR matrices and proposed an additional renormalization condition to exhaust them. As a consequence of instability, the WFR matrices of the in and out states bifurcate in the sense that they are no longer related by Hermitian conjugation, in contrast to text book wisdom. This feature had already been anticipated in a one-loop analysis [48] triggered by the applicant. By contrast, if the WFR of the out state is enforced to be the Hermitian conjugate of that of the in state, then the residues of the left- and right-handed parts of the resonating propagator cannot both be unity, but are related by a phase factor [3]. In contrast to the conventional on-shell scheme, the complex-pole scheme leads to gauge-invariant definitions of the masses and total decay widths of physical particles and avoids severe unphysical singularities, of threshold [33] or power-like infrared [31] nature. In the case of stable Dirac fermions, the well-known one-loop results were recovered [42].

In Ref. [12], generalized the analysis of Refs. [9, 11] to unstable Majorana fermions in a general parity-nonconserving theory. In contrast to the case of unstable Dirac fermions, the WFR matrices of the in and out states are uniquely fixed, while they again bifurcate in the sense that they are no longer related by pseudo-Hermitian conjugation. We again presented closed analytic expressions, as well as their expansions through two loops, for the renormalization constants in terms of the scalar, pseudoscalar, vector, and pseudovector parts of the unrenormalized self-energy matrix. The well-known one-loop results for stable Majorana fermions [42] were reproduced.

To formulate the WFR conditions in the pole scheme underlying Refs. [9, 11, 12], it was necessary to generalize the Dirac equations and spinors in momentum space to free unstable spin-½ fermions taking into account the fundamental requirement of Lorentz covariance. In Ref. [13], we thus derived the generalized adjoint Dirac equations and spinors, and explained the very simple relation that exists, in our formulation, between the unstable and stable cases. As an application of the generalized spinors, we evaluated the probability density. We also discussed the behavior of the generalized Dirac equations under time reversal.

2.3 Flavor-changing vertices

In Refs. [1,2], we developed an explicit on-shell framework to renormalize the CKM quark mixing matrix V_{ij} at the one-loop level. It is based on a novel procedure to separate the external-leg

mixing corrections into gauge-independent self-mass and gauge-dependent WFR contributions, and to adjust non-diagonal mass counterterm matrices $\delta m_{ij}^{U,D}$ to cancel all the divergent self-mass contributions, and also their finite parts subject to constraints imposed by the Hermiticity of the mass matrices $m_{ij}^{U,D}$. It was also shown that the proof of gauge independence and finiteness of the remaining one-loop corrections to $W \to q_i + \overline{q}_j$ reduces to that in the unmixed, single-generation case. Diagonalization of the complete mass matrices $m_{ij}^{U,D} = m_{ij}^{U,D(0)} + \delta m_{ij}^{U,D}$ leads to an explicit CKM counterterm matrix δV_{ij}, which automatically satisfies all the following important properties: it is gauge independent, preserves unitarity, and leads to renormalized amplitudes that are non-singular in the limit in which any two fermions of the same weak isospin become mass degenerate, i.e. for $m_k^U \to m_i^U$ or $m_k^D \to m_j^D$.

In Refs. [5,19], we proposed an alternative, amazingly simple on-shell CKM renormalization scheme that avoids the somewhat cumbersome recalculation of external-leg mixing amplitudes required by operational procedure of Refs. [1, 2]. As in Refs. [1, 2], the counterterm of the mixing matrix is generated in a two-step procedure. One first constructs non-diagonal mass counterterm matrices $\delta m_{ij}^{U,D}$ for the up- and down-type fermions using Nielsen identities [35–37,48,49]. In this way, $\delta m_{ij}^{U,D}$ are automatically gauge independent and satisfy the Hermiticity constraints of the mass matrices $m_{ij}^{U,D}$. In the second step, one diagonalizes the complete mass matrices by bi-unitary transformations as in Refs. [1, 2]. On top of the desirable theoretical properties exhibited by the CKM counterterm matrix of Refs. [1,2] (see above), here also flavor democracy is manifest. To summarize, the renormalized mixing matrix of Refs. [5,19] possesses all conceivable desirable properties: it is ultraviolet finite, gauge independent, unitary, flavor democratic, on-shell, finite in case of fermion mass degeneracy, and expressed in terms of self-energies only. This renormalization prescription is, therefore, superior to previous proposals [38–41] and provides a promising starting point for the generalization to higher orders and the case of instability. This scheme is also very convenient for practical applications because the Lorentz-invariant self-energy functions can be automatically calculated using standard computer algebra packages.

As important phenomenological applications, we investigated the numerical significance of quark mixing renormalization for the extraction of the CKM matrix elements from the partial widths of the top-quark [7] and hadronic W-boson decays [4], and estimated the scheme dependence by using the renormalization prescriptions of Refs. [1,2,5,38,39,41] and the modified minimal-subtraction ($\overline{\rm MS}$) scheme [50] of dimensional regularization.

We generalized the CKM renormalization prescription of Ref. [1] to extended lepton sectors including both Dirac and Majorana neutrinos in the framework of the seesaw mechanism [6]. Important properties of this formulation include the gauge independence of the renormalized lepton mixing matrices and the conservation of the texture zero in the neutrino mass matrix. We also found that the preferable renormalization prescription of Ref. [5] does not in general carry over to such scenarios.

As for generalizations to the MSSM, we received support from principal investigators of projects B1 and B9, who worked out at one loop an on-shell renormalization scheme for the chargino–neutralino sector of the MSSM with complex parameters [51,52]. In particular, they showed that products of imaginary parts arising from MSSM parameters and absorptive parts of loop integrals may contribute to one-loop predictions for physical observables.

3 Electroweak vacuum stability

3.1 Starting point

The SM has been enormously consolidated by the discovery at the CERN Large Hadron Collider of a new weak neutral resonance that, within the present experimental uncertainty, shares the spin (J), parity (P), and charge-conjugation (C) quantum numbers $J^{PC} = 0^{++}$ and the coupling strengths with the SM Higgs boson H, in the absence of convincing signals of new physics beyond the SM. Moreover, its mass of (125.18 ± 0.16) GeV falls well inside the M_H range predicted within the SM through global analyses of EW precision data. Besides completing the SM particle multiplet and confirming the Higgs mechanism of mass generation via the spontaneous breaking of the EW symmetry proposed by Englert, Higgs (The Nobel Prize in Physics 2013), and Brout, this groundbreaking discovery also has fundamental cosmological consequences by allowing conclusions regarding the fate of the Universe via the analysis of the vacuum stability [53]. In fact, owing to an intriguing conspiracy of the SM particle masses, chances are that the Higgs potential develops a second minimum, as deep as the one corresponding to the vacuum with expectation value $v = 2^{-1/4} G_F^{-1/2} = 246$ GeV in which we live, at a field value of the order of the Planck mass $M_P = 1.22 \times 10^{19}$ GeV [23], a scenario of criticality. This would imply that the SM be stable all the way up to the energy scale where the unification with gravity is expected to take place anyways, which would diminish the necessity for grand unified theories at lower scales. EW symmetry breaking might thus be determined by Planck-scale physics [23], and the existence of a relationship between M_P and SM parameters might signify a reduction of fundamental couplings. Of course, experimental facts that the SM fails to explain, such as the smallness of the neutrino masses, the strong CP problem, the existence of dark matter, and the baryon asymmetry in the Universe, would then still call for an extension.

Obviously, the ultimate answer to the existential question whether our vacuum is stable or not crucially depends on the quality of the theoretical analysis as for both conceptual rigor and high precision, and it was a central goal of the second research area in project B4 to significantly push the state of the art by optimally exploiting information that had become available just recently. The technical procedure is as follows. The set of running coupling constants of the full SM, including the $\mathrm{SU}(2)_I$, $\mathrm{U}(1)_Y$, and $\mathrm{SU}(3)_c$ gauge couplings $g(\mu)$, $g'(\mu)$, and $g_s(\mu)$, respectively, the Higgs self-coupling $\lambda(\mu)$, and the Yukawa couplings $y_f(\mu)$, are evolved in the renormalization scale μ from $\mu^{\mathrm{thr}} = O(v)$ to $\mu^{\mathrm{cri}} = O(M_P)$ using the renormalization group (RG) equations. The beta functions appearing therein take a simple polynomial form in the $\overline{\mathrm{MS}}$ scheme. Prior to the third funding period, they were fully known through three loops [54–60] in the approximation of neglecting the Yukawa couplings of the first- and second-generation fermions, and the ones of g_s [61, 62] and y_q [63–65] also at the four-loop order $O(\alpha_s^4)$, the latter being given by the quark mass anomalous dimensions. The initial conditions at $\mu = \mu^{\mathrm{thr}}$ are evaluated from the relevant constants of nature, including Sommerfeld's fine-structure constant α_{Th} defined in Thomson scattering—or, alternatively, Fermi's constant G_F—, the strong-coupling constant $\alpha_s^{(5)}(M_Z)$ at its reference point in QCD with $n_f = 5$ active quark flavors, and the physical particle masses M_i $(i = W, Z, H, f)$ defined via the propagator poles, taking into account threshold corrections [66, 67]. Prior to the third funding period, the latter were known at one loop, at $O(\alpha\alpha_s)$ [23], at $O(\alpha^2)$ in the gaugeless limit [68] and in numerical approximation [69], for g_s at $O(\alpha_s^3)$ [70, 71] and $O(\alpha_s^4)$ [72–74], and for y_q at $O(\alpha_s^3)$ [75–77]. Self-consistency requires that n-loop evolution is combined with $(n-1)$-loop matching.

Key publications that triggered the second research area in project B4 include Refs. [23–26]. In Ref. [23], we rendered the analyses of the vacuum stability bound on M_H significantly more reliable by evaluating the threshold corrections to the top Yukawa coupling y_t and the Higgs self-coupling λ at the two-loop order $\mathcal{O}(\alpha\alpha_s)$. Including also the three-loop corrections to the running of these and the other SM couplings that had recently become available [54–60], we thus elevated the state of the art from one-loop matching/two-loop running to two-loop matching/three-loop running. In support of project B1, we reported the key results of our analysis [23] as LCnote LC–REP–2012–011 to the European Strategy Preparatory Group, emphasizing that a future e^+e^- linear collider (LC) operated as Higgs and top factories will be indispensable to ultimately clarify if the SM vacuum can be stable all the way up to the Planck scale.

In Ref. [25], we recalculated the four-loop RG functions in the two-dimensional nonlinear O(n) σ model using the coordinate space method. The high accuracy of the calculation allowed us to find the analytic forms of the β and γ functions (anomalous dimensions).

The vacuum stability bound on M_H sensitively depends on the input parameter M_t. The mass parameter $M_t^{\rm MC}$ presently reconstructed from the decay products of the top quark is not well defined from the theoretical point of view and, strictly speaking, must not be identified with the pole mass M_t, as is frequently done in the literature, because the Monte Carlo (MC) event generators that are utilized in the experimental data analyses do not even include one-loop radiative corrections. On the other hand, as proposed by the principal investigator of project B11 and his collaborators [78, 79], the total cross section of top-quark pair production allows for a clean determination of the running mass $m_t(\mu)$ of the $\overline{\rm MS}$ scheme [50]. Therefore, the precise knowledge of the relationship $m_t(M_t) - M_t$, including also EW corrections besides the QCD ones, is indispensable for the determination of M_t from a global fit to experimental data. When the $\overline{\rm MS}$ definition of mass is extended from QCD, for which it was originally introduced [50], to the full SM, then all contributing self-energy diagrams, including tadpoles, must be included in order not to generate artificial gauge dependence [67]. This also ensures that the mass anomalous dimensions in the broken phase of the SM coincide with those in the unbroken one [24, 26]. Incidentally, the $\mathcal{O}(\alpha)$ and $\mathcal{O}(\alpha\alpha_s)$ corrections to $m_t(M_t) - M_t$ almost perfectly compensate the familiar -10 GeV shift due to the pure QCD corrections through $\mathcal{O}(\alpha_s^3)$, so that the theoretical uncertainty due to scheme dependence in physical observables that depend on M_t at leading order is dramatically reduced.

The results on threshold corrections and beta functions achieved in project B4 are reported in Sec. 3.2 and those on the EW vacuum stability in Sec. 3.3.

3.2 Threshold corrections and beta functions

In Ref. [10], we studied the relationship between the $\overline{\rm MS}$ Yukawa coupling and the pole mass for the bottom and top quarks at the two-loop EW order $\mathcal{O}(\alpha^2)$ in the gaugeless limit of the SM. We also considered the $\overline{\rm MS}$ to pole mass relationships at this order, which include tadpole contributions to ensure the gauge independence of the $\overline{\rm MS}$ masses. In order to suppress numerically large tadpole contributions, we proposed a redefinition of the running heavy-quark mass in terms of the $\overline{\rm MS}$ Yukawa coupling. We also presented Sirlin's EW parameter Δr in the $\overline{\rm MS}$ scheme at $\mathcal{O}(\alpha^2)$ in the gaugeless limit. As an aside, we also listed the exact two-loop expressions for the mass counterterms of the bottom and top quarks. In Ref. [14], we completed the analysis of Ref. [10] by considering the full set of basic parameters in the SM and by including the full $\mathcal{O}(\alpha^2)$ corrections. To ensure the gauge invariance of the parameters,

in particular of the $\overline{\rm MS}$ masses, we worked in R_ξ gauge and systematically included tadpole contributions. We also considered the gaugeless-limit approximation and compared it with the full two-loop EW calculation. Furthermore, we added the full $\mathcal{O}(\alpha^2)$ correction as the fourth term in

$$m_t(M_t) - M_t = (-10.38 + 11.88 - 0.39 - 0.96)\ \text{GeV} = 0.14\ \text{GeV}, \tag{1}$$

where the first three terms are due to the previously known QCD [75–77, 80], $\mathcal{O}(\alpha)$ [67], and $\mathcal{O}(\alpha\alpha_s)$ [24, 26] corrections, respectively.

As for the QCD parameters, the threshold corrections usually refer to full QCD, with $n_f = 6$ active quark flavors. In the case of y_b, however, this is inconvenient because precision determinations of the bottom quark mass are typically performed in the $n_f = 5$ regime. In Ref. [18], we thus considered EW corrections to the relation between the running $\overline{\rm MS}$ mass m_b of the bottom quark in the $n_f = 5$ QCD×QED effective theory and its counterpart in the SM. As a bridge between the two parameters, we used the pole mass M_b of the bottom quark, which can be calculated in both models. The running mass is not a fundamental parameter of the SM Lagrangian, but the product of the running Yukawa coupling y_b and the Higgs vacuum expectation value v. Since there exist different prescriptions to define the latter, the relations considered in Ref. [18] involve a certain amount of freedom. All the definitions can be related to each other in perturbation theory. Nevertheless, we argued in favor of a certain gauge-independent prescription and provided a relation which can be directly used to deduce the value of y_b at the EW scale from m_b. This approach allows one to resum large logarithms $\ln(m_b/M_t)$ systematically. Numerical analysis showed that, indeed, the corrections to the proposed relation are much smaller than those between y_b and M_b.

In Refs. [16, 22], the beta function of the strong coupling was calculated at four loops in the SM taking into account the top Yukawa and Higgs self-interactions, but neglecting EW gauge couplings. The expression was obtained from gluon self-energy diagrams in the background field gauge, without application of special infrared-rearrangement tricks. Ambiguities due to the treatment of γ_5 were discussed and a particular *reading* prescription for odd Dirac traces was advocated.

In Ref. [17], we presented the C++ program library `mr` that allows us to reliably calculate the values of the running parameters in the SM at high energy scales. The initial conditions are obtained by relating the running parameters in the $\overline{\rm MS}$ renormalization scheme to observables at lower energies with full two-loop precision. The evolution is then performed in accordance with the RG equations with full three-loop precision. Pure QCD corrections to the matching and running are included through four loops. We also provided a Mathematica interface for this program library.

3.3 Electroweak vacuum stability

In Refs. [15, 21], we performed a high-precision analysis of the vacuum stability in the SM incorporating full two-loop threshold corrections [10,14,23,81], three-loop beta functions [54–60], and $O(\alpha_s^3)$ and $O(\alpha_s^4)$ corrections to the matching and running of g_s [61, 62, 70–74] and y_q [63–65, 75–77, 80], and adopting two gauge-independent approaches, one based on the criticality criterion for $\lambda(\mu)$ [23],

$$\lambda(\mu^{\rm cri}) = \beta_\lambda(\mu^{\rm cri}) = 0, \tag{2}$$

and one on a reorganization of Higgs effective potential, so that its minimum is gauge independent order by order [82]. The two-fold criticality condition in Eq. (2) and its counterpart in

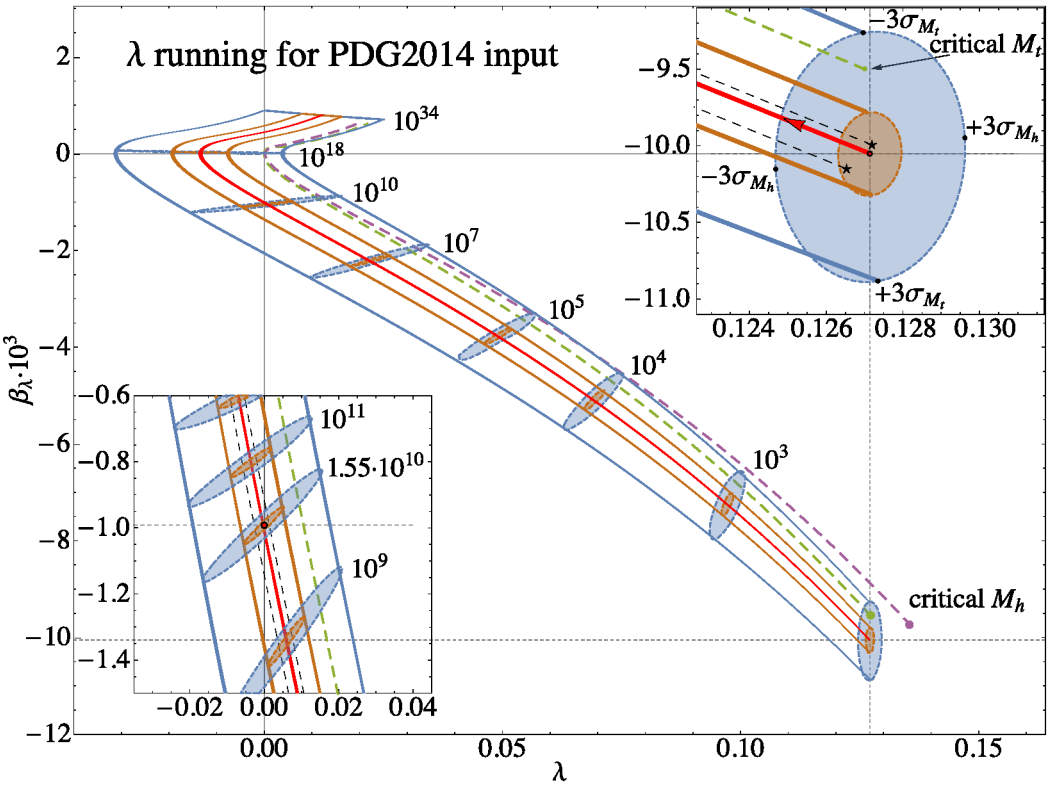


Figure 1: RG evolution of $\lambda(\mu)$ from $\mu^{\rm thr}$ to $\mu^{\rm cri}$ and beyond in the (λ, β_λ) plane for default input values and matching scale (red solid line), effects of 1σ (brown solid lines) and 3σ (blue solid lines) variation in $M_t^{\rm MC}$, theoretical uncertainty due to the variation of $\xi = \mu^{\rm thr}/M_t^{\rm MC}$ from 1/2 to 2 (upper and lower black dashed lines with asterisks in the insets), and results for $M_t^{\rm cri}$ (green dashed line) and $M_H^{\rm cri}$ (purple dashed line). The 1σ (brown ellipses) and 3σ (blue ellipses) contours due to the errors in $M_t^{\rm MC}$ and M_H are indicated for selected values of μ. The insets in the upper right and lower left corners refer to $\mu = M_t^{\rm MC}$ and $\mu = 1.55 \times 10^{10}$ GeV, respectively. Reprinted figure with permission from Ref. [15]. Copyright (2015) by the American Physical Society.

Ref. [82] have gauge-independent solutions for the critical ultrahigh scale $\mu^{\rm cri}$ and one free basic parameter, which we take to be $M_t^{\rm cri}$, the upper bound on the top-quark pole mass M_t, which is much less precisely known than M_H. For comparisons with the literature, we also determined the M_H lower bound $M_H^{\rm cri}$ sloppily using as input the mass parameter $M_t^{\rm MC}$. The results for $\mu^{\rm cri}$ obtained together with $M_t^{\rm cri}$ and $M_H^{\rm cri}$ are denoted as $\mu_t^{\rm cri}$ and $\mu_H^{\rm cri}$, respectively.

In Fig. 1, the RG evolution flow from the starting scale $\mu^{\rm thr}$ to the critical scale $\mu^{\rm cri}$ and beyond is shown in the (λ, β_λ) plane. The propagation with μ of the 1σ and 3σ confidence ellipses with respect to $M_t^{\rm MC} = (173.21 \pm 0.87)$ GeV and $M_H = (125.7 \pm 0.4)$ GeV [83] tells us that the second condition in Eq. (2) is almost automatic, the ellipses for $\mu = 10^{18}$ GeV being approximately degenerated to horizontal lines. For default input values, $\lambda(\mu)$ crosses zero at $\mu = 1.55 \times 10^{10}$ GeV. The contour of $M_t^{\rm cri}$ approximately coincides with the right envelope of

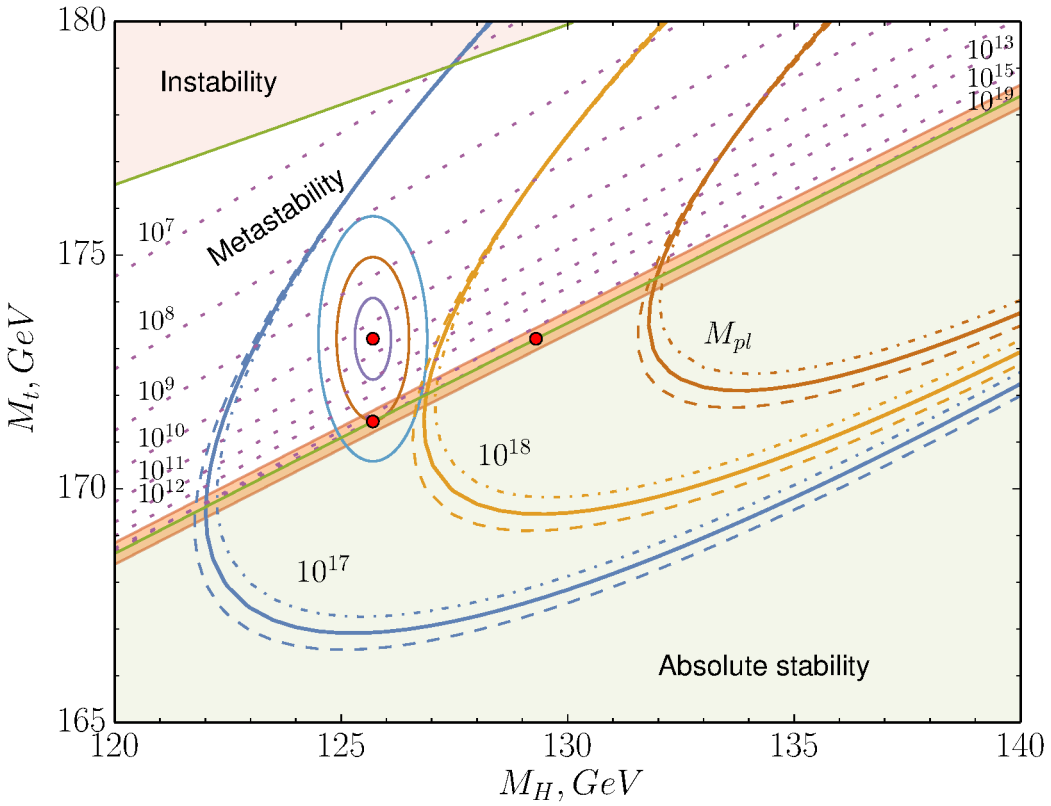


Figure 2: Phase diagram of vacuum stability (light-green shaded area), metastability, and instability (pink shaded area) in the (M_H, M_t) plane, contours of $\lambda(\mu^0) = 0$ for selected values of μ^0 (purple dotted lines), contours of $\beta_\lambda(\mu^0) = 0$ for selected values of μ^0 (solid parabolalike lines) with uncertainties due to 1σ error in $\alpha_s^{(5)}(M_Z)$ (dashed and dot-dashed lines), critical line of Eq. (2) (solid green line) with uncertainty due to 1σ error in $\alpha_s^{(5)}(M_Z)$ (orange shaded band), and critical points with $M_t^{\rm cri}$ (lower red bullet) and $M_H^{\rm cri}$ (right red bullet). The present world average of $(M_t^{\rm MC}, M_H)$ (upper left red bullet) and its 1σ (purple ellipse), 2σ (brown ellipse), and 3σ (blue ellipse) contours are marked for reference. Reprinted figure with permission from Ref. [15]. Copyright (2015) by the American Physical Society.

the 2σ ellipses, while the one of $M_H^{\rm cri}$, which relies on $M_t^{\rm MC}$, is driven outside the 3σ band as μ runs from $\mu_H^{\rm cri}$ to $\mu^{\rm thr}$.

Our upgraded and updated version of the familiar phase diagram [68,69,79,82] is presented in Fig. 2. Besides the boundary of the stable phase defined by Eq. (2), on which the critical points with $M_t^{\rm cri}$ and $M_H^{\rm cri}$ are located, we also show contours of $\lambda(\mu^0) = 0$ and $\beta_\lambda(\mu^0) = 0$. The demarcation line between the metastable phase and the unstable one, in which the lifetime of our vacuum is shorter than the age of the Universe, is evaluated as in Ref. [82]. The customary confidence ellipses with respect to $M_t^{\rm MC}$ and M_H, which are included Fig. 2 for reference, have to be taken with caution because they misleadingly suggest that the tree-level mass parameter

$M_t^{\rm MC}$ and its error [83] identically carry over to M_t, which is actually the real part of the complex pole position upon mass renormalization in the on-shell scheme [3].

For the M_t upper bound we thus obtained

$$M_t^{\rm cri} = (171.54 \pm 0.30\,^{+0.26}_{-0.41})\ {\rm GeV}, \tag{3}$$

where the first error is experimental, due the 1σ variations in the input parameters, and the second one is theoretical, due to the scale, scheme, and truncation uncertainties. This is compatible with the value $M_t = (170.4 \pm 1.2)$ GeV extracted in project B11 via a global analysis of experimental data of $\sigma_{\rm tot}(p\bar{p}, pp \to t\bar{t} + X)$ at next-to-next-to-leading order in QCD [84]. This clearly contradicts the familiar notion [68,69] that our vacuum is metastable. On the contrary, the probability that the Universe exists in a stable state may be greater than previously thought. At face value, this finding actually suggests that the state of the Universe may as well be critical, with all the far-reaching consequences for our understanding of Nature mentioned in Sec. 3.3.

References

[1] B. A. Kniehl and A. Sirlin, *Simple Approach to Renormalize the Cabibbo-Kobayashi-Maskawa Matrix*, *Phys. Rev. Lett.* **97** (2006) 221801, [hep-ph/0608306].

[2] B. A. Kniehl and A. Sirlin, *Simple On-Shell Renormalization Framework for the Cabibbo-Kobayashi-Maskawa Matrix*, *Phys. Rev.* **D74** (2006) 116003, [hep-th/0612033].

[3] B. A. Kniehl and A. Sirlin, *Pole Mass, Width, and Propagators of Unstable Fermions*, *Phys. Rev.* **D77** (2008) 116012, [0801.0669].

[4] A. A. Almasy, B. A. Kniehl and A. Sirlin, *Quark mixing renormalization effects in the determination of the CKM parameters*, *Phys. Rev.* **D79** (2009) 076007, [0811.0355]. [Erratum: Phys. Rev.D82,059901(2010)].

[5] B. A. Kniehl and A. Sirlin, *A Novel Formulation of Cabibbo-Kobayashi-Maskawa Matrix Renormalization*, *Phys. Lett.* **B673** (2009) 208–210, [0901.0114].

[6] A. A. Almasy, B. A. Kniehl and A. Sirlin, *On-shell renormalization of the mixing matrices in Majorana neutrino theories*, *Nucl. Phys.* **B818** (2009) 115–134, [0902.3793].

[7] A. A. Almasy, B. A. Kniehl and A. Sirlin, *Quark mixing renormalization effects in the determination of $|V_{tq}|$*, *Phys. Rev.* **D83** (2011) 096004, [1101.5758].

[8] B. A. Kniehl and A. Sirlin, *Renormalization in general theories with inter-generation mixing*, *Phys. Rev.* **D85** (2012) 036007, [1201.4333].

[9] B. A. Kniehl, *All-Order Renormalization of the Propagator Matrix for Fermionic Systems with Flavor Mixing*, *Phys. Rev. Lett.* **112** (2014) 071603, [1308.3140].

[10] B. A. Kniehl and O. L. Veretin, *Two-loop electroweak threshold corrections to the bottom and top Yukawa couplings*, *Nucl. Phys.* **B885** (2014) 459–480, [1401.1844]. [Erratum: Nucl. Phys.B894,56(2015)].

[11] B. A. Kniehl, *All-order renormalization of propagator matrix for unstable Dirac fermions*, *Phys. Rev.* **D89** (2014) 096005.

[12] B. A. Kniehl, *Propagator mixing renormalization for Majorana fermions*, *Phys. Rev.* **D89** (2014) 116010, [1404.5908].

[13] B. A. Kniehl and A. Sirlin, *Considerations concerning the generalization of the Dirac equations to unstable fermions*, *Phys. Rev.* **D90** (2014) 077901, [1409.5869].

[14] B. A. Kniehl, A. F. Pikelner and O. L. Veretin, *Two-loop electroweak threshold corrections in the Standard Model*, *Nucl. Phys.* **B896** (2015) 19–51, [1503.02138].

[15] A. V. Bednyakov, B. A. Kniehl, A. F. Pikelner and O. L. Veretin, *Stability of the Electroweak Vacuum: Gauge Independence and Advanced Precision*, *Phys. Rev. Lett.* **115** (2015) 201802, [1507.08833].

[16] A. V. Bednyakov and A. F. Pikelner, *Four-loop strong coupling beta-function in the Standard Model*, *Phys. Lett.* **B762** (2016) 151–156, [1508.02680].

[17] B. A. Kniehl, A. F. Pikelner and O. L. Veretin, *mr: a C++ library for the matching and running of the Standard Model parameters*, *Comput. Phys. Commun.* **206** (2016) 84–96, [1601.08143].

[18] A. V. Bednyakov, B. A. Kniehl, A. F. Pikelner and O. L. Veretin, *On the b-quark running mass in QCD and the SM*, *Nucl. Phys.* **B916** (2017) 463–483, [1612.00660].

[19] B. A. Kniehl and A. Sirlin, *Novel formulations of CKM matrix renormalization*, *AIP Conf. Proc.* **1182** (2009) 327–330, [0906.2670].

[20] F. Jegerlehner, M. Yu. Kalmykov and B. A. Kniehl, *Self-consistence of the Standard Model via the renormalization group analysis*, *J. Phys. Conf. Ser.* **608** (2015) 012074, [1412.4215].

[21] A. V. Bednyakov, *An advanced precision analysis of the SM vacuum stability*, *Phys. Part. Nucl.* **48** (2017) 698–703, [1609.02503].

[22] A. V. Bednyakov and A. F. Pikelner, *On the four-loop strong coupling beta-function in the SM*, *EPJ Web Conf.* **125** (2016) 04008, [1609.02597].

[23] F. Bezrukov, M. Yu. Kalmykov, B. A. Kniehl and M. Shaposhnikov, *Higgs Boson Mass and New Physics*, *JHEP* **10** (2012) 140, [1205.2893]. [DESY-PROC-2013-02 (2012) 275].

[24] F. Jegerlehner, M. Yu. Kalmykov and B. A. Kniehl, *On the difference between the pole and the $\overline{MS}$ masses of the top quark at the electroweak scale*, *Phys. Lett.* **B722** (2013) 123–129, [1212.4319].

[25] O. Veretin, *Analytical results for the four-loop RG functions in the 2D non-linear O(n) σ-model on the lattice*, *Phys. Part. Nucl.* **44** (2013) 573–576, [1306.2771].

[26] F. Jegerlehner, M. Yu. Kalmykov and B. A. Kniehl, *About the EW contribution to the relation between pole and MS-masses of the top-quark in the Standard Model*, *PoS* **DIS2013** (2013) 190, [1307.4226].

[27] Gabele, Tim, *All-order renormalization of the fermion propagator*, Bachelor's Thesis, Universität Hamburg, Bachelor's thesis, Universität Hamburg, 2015.

[28] Ernst, Anne, *Towards mixing renormalization at two loops via the Nielsen identities*, Master's thesis, Universität Hamburg, 2015.

[29] Ernst, Anne, *Axion predictions in SO(10)$\times$U(1)$_{PQ}$ models*, Ph.D. thesis, Universität Hamburg, 2018.

[30] E. Kraus, *Renormalization of the Electroweak Standard Model to All Orders*, *Annals Phys.* **262** (1998) 155–259, [hep-th/9709154].

[31] M. Passera and A. Sirlin, *Radiative corrections to W and quark propagators in the resonance region*, *Phys. Rev.* **D58** (1998) 113010, [hep-ph/9804309].

[32] A. Sirlin, *Theoretical considerations concerning the Z0 mass*, *Phys. Rev. Lett.* **67** (1991) 2127–2130.

[33] B. A. Kniehl and A. Sirlin, *Differences between the pole and on-shell masses and widths of the Higgs boson*, *Phys. Rev. Lett.* **81** (1998) 1373–1376, [hep-ph/9805390].

[34] B. A. Kniehl and A. Sirlin, *Mass and width of a heavy Higgs boson*, *Phys. Lett.* **B440** (1998) 136–140, [hep-ph/9807545].

[35] P. Gambino and P. A. Grassi, *The Nielsen identities of the SM and the definition of mass*, *Phys. Rev.* **D62** (2000) 076002, [hep-ph/9907254].

[36] P. A. Grassi, B. A. Kniehl and A. Sirlin, *Width and partial widths of unstable particles*, *Phys. Rev. Lett.* **86** (2001) 389–392, [hep-th/0005149].

[37] P. A. Grassi, B. A. Kniehl and A. Sirlin, *Width and partial widths of unstable particles in the light of the Nielsen identities*, *Phys. Rev.* **D65** (2002) 085001, [hep-ph/0109228].

[38] A. Denner and T. Sack, *Renormalization of the Quark Mixing Matrix*, *Nucl. Phys.* **B347** (1990) 203–216.

[39] P. Gambino, P. A. Grassi and F. Madricardo, *Fermion mixing renormalization and gauge invariance*, *Phys. Lett.* **B454** (1999) 98–104, [hep-ph/9811470].

[40] A. Barroso, L. Brucher and R. Santos, *Renormalization of the Cabibbo-Kobayashi-Maskawa matrix*, *Phys. Rev.* **D62** (2000) 096003, [hep-ph/0004136].

[41] K. P. O. Diener and B. A. Kniehl, *On mass shell renormalization of fermion mixing matrices*, *Nucl. Phys.* **B617** (2001) 291–307, [hep-ph/0109110].

[42] B. A. Kniehl and A. Pilaftsis, *Mixing renormalization in Majorana neutrino theories*, *Nucl. Phys.* **B474** (1996) 286–308, [hep-ph/9601390].

[43] W. Hollik, E. Kraus, M. Roth, C. Rupp, K. Sibold and D. Stockinger, *Renormalization of the minimal supersymmetric standard model*, *Nucl. Phys.* **B639** (2002) 3–65, [hep-ph/0204350].

[44] B. A. Kniehl, C. P. Palisoc and A. Sirlin, *Higgs boson production and decay close to thresholds*, *Nucl. Phys.* **B591** (2000) 296–310, [hep-ph/0007002].

[45] B. A. Kniehl, C. P. Palisoc and A. Sirlin, *Elimination of threshold singularities in the relation between on shell and pole widths*, *Phys. Rev.* **D66** (2002) 057902, [hep-ph/0205304].

[46] B. A. Kniehl and A. Sirlin, *On the field renormalization constant for unstable particles*, *Phys. Lett.* **B530** (2002) 129–132, [hep-ph/0110296].

[47] K. I. Aoki, Z. Hioki, M. Konuma, R. Kawabe and T. Muta, *Electroweak Theory. Framework of On-Shell Renormalization and Study of Higher Order Effects*, *Prog. Theor. Phys. Suppl.* **73** (1982) 1–225.

[48] D. Espriu, J. Manzano and P. Talavera, *Flavor mixing, gauge invariance and wave function renormalization*, *Phys. Rev.* **D66** (2002) 076002, [hep-ph/0204085].

[49] N. K. Nielsen, *On the Gauge Dependence of Spontaneous Symmetry Breaking in Gauge Theories*, *Nucl. Phys.* **B101** (1975) 173–188.

[50] W. A. Bardeen, A. J. Buras, D. W. Duke and T. Muta, *Deep Inelastic Scattering Beyond the Leading Order in Asymptotically Free Gauge Theories*, *Phys. Rev.* **D18** (1978) 3998.

[51] A. C. Fowler and G. Weiglein, *Precise Predictions for Higgs Production in Neutralino Decays in the Complex MSSM*, *JHEP* **01** (2010) 108, [0909.5165].

[52] A. Bharucha, A. Fowler, G. Moortgat-Pick and G. Weiglein, *Consistent on shell renormalisation of electroweakinos in the complex MSSM: LHC and LC predictions*, *JHEP* **05** (2013) 053, [1211.3134].

[53] N. V. Krasnikov, *Restriction of the Fermion Mass in Gauge Theories of Weak and Electromagnetic Interactions*, *Yad. Fiz.* **28** (1978) 549–551.

[54] L. N. Mihaila, J. Salomon and M. Steinhauser, *Gauge Coupling Beta Functions in the Standard Model to Three Loops*, *Phys. Rev. Lett.* **108** (2012) 151602, [1201.5868].

[55] L. N. Mihaila, J. Salomon and M. Steinhauser, *Renormalization constants and beta functions for the gauge couplings of the Standard Model to three-loop order*, *Phys. Rev.* **D86** (2012) 096008, [1208.3357].

[56] K. G. Chetyrkin and M. F. Zoller, *Three-loop β-functions for top-Yukawa and the Higgs self-interaction in the Standard Model*, *JHEP* **06** (2012) 033, [1205.2892].

[57] K. G. Chetyrkin and M. F. Zoller, *β-function for the Higgs self-interaction in the Standard Model at three-loop level*, *JHEP* **04** (2013) 091, [1303.2890]. [Erratum: *JHEP* **09** (2013) 155].

[58] A. V. Bednyakov, A. F. Pikelner and V. N. Velizhanin, *Anomalous dimensions of gauge fields and gauge coupling beta-functions in the Standard Model at three loops*, *JHEP* **01** (2013) 017, [1210.6873].

[59] A. V. Bednyakov, A. F. Pikelner and V. N. Velizhanin, *Yukawa coupling beta-functions in the Standard Model at three loops*, *Phys. Lett.* **B722** (2013) 336–340, [1212.6829].

[60] A. V. Bednyakov, A. F. Pikelner and V. N. Velizhanin, *Higgs self-coupling beta-function in the Standard Model at three loops*, *Nucl. Phys.* **B875** (2013) 552–565, [1303.4364].

[61] T. van Ritbergen, J. A. M. Vermaseren and S. A. Larin, *The Four loop beta function in quantum chromodynamics*, *Phys. Lett.* **B400** (1997) 379–384, [hep-ph/9701390].

[62] M. Czakon, *The Four-loop QCD beta-function and anomalous dimensions*, *Nucl. Phys.* **B710** (2005) 485–498, [hep-ph/0411261].

[63] K. G. Chetyrkin, *Quark mass anomalous dimension to O (alpha-s**4)*, *Phys. Lett.* **B404** (1997) 161–165, [hep-ph/9703278].

[64] K. G. Chetyrkin, *Four-loop renormalization of QCD: Full set of renormalization constants and anomalous dimensions*, *Nucl. Phys.* **B710** (2005) 499–510, [hep-ph/0405193].

[65] J. A. M. Vermaseren, S. A. Larin and T. van Ritbergen, *The four loop quark mass anomalous dimension and the invariant quark mass*, *Phys. Lett.* **B405** (1997) 327–333, [hep-ph/9703284].

[66] A. Sirlin and R. Zucchini, *Dependence of the Quartic Coupling H(m) on M(H) and the Possible Onset of New Physics in the Higgs Sector of the Standard Model*, *Nucl. Phys.* **B266** (1986) 389–409.

[67] R. Hempfling and B. A. Kniehl, *On the relation between the fermion pole mass and MS Yukawa coupling in the standard model*, *Phys. Rev.* **D51** (1995) 1386–1394, [hep-ph/9408313].

[68] G. Degrassi, S. Di Vita, J. Elias-Miro, J. R. Espinosa, G. F. Giudice, G. Isidori et al., *Higgs mass and vacuum stability in the Standard Model at NNLO*, *JHEP* **08** (2012) 098, [1205.6497].

[69] D. Buttazzo, G. Degrassi, P. P. Giardino, G. F. Giudice, F. Sala, A. Salvio et al., *Investigating the near-criticality of the Higgs boson*, *JHEP* **12** (2013) 089, [1307.3536].

[70] K. G. Chetyrkin, B. A. Kniehl and M. Steinhauser, *Strong coupling constant with flavor thresholds at four loops in the MS scheme*, *Phys. Rev. Lett.* **79** (1997) 2184–2187, [hep-ph/9706430].

[71] K. G. Chetyrkin, B. A. Kniehl and M. Steinhauser, *Decoupling relations to O (alpha-s**3) and their connection to low-energy theorems*, *Nucl. Phys.* **B510** (1998) 61–87, [hep-ph/9708255].

[72] Y. Schroder and M. Steinhauser, *Four-loop decoupling relations for the strong coupling*, *JHEP* **01** (2006) 051, [hep-ph/0512058].

[73] K. G. Chetyrkin, J. H. Kuhn and C. Sturm, *QCD decoupling at four loops*, *Nucl. Phys.* **B744** (2006) 121–135, [hep-ph/0512060].

[74] B. A. Kniehl, A. V. Kotikov, A. I. Onishchenko and O. L. Veretin, *Strong-coupling constant with flavor thresholds at five loops in the anti-MS scheme*, *Phys. Rev. Lett.* **97** (2006) 042001, [hep-ph/0607202].

[75] K. G. Chetyrkin and M. Steinhauser, *Short distance mass of a heavy quark at order α_s^3*, *Phys. Rev. Lett.* **83** (1999) 4001–4004, [hep-ph/9907509].

[76] K. G. Chetyrkin and M. Steinhauser, *The Relation between the MS-bar and the on-shell quark mass at order alpha(s)**3*, *Nucl. Phys.* **B573** (2000) 617–651, [hep-ph/9911434].

[77] K. Melnikov and T. v. Ritbergen, *The Three loop relation between the MS-bar and the pole quark masses*, *Phys. Lett.* **B482** (2000) 99–108, [hep-ph/9912391].

[78] U. Langenfeld, S. Moch and P. Uwer, *Measuring the running top-quark mass*, *Phys. Rev.* **D80** (2009) 054009, [0906.5273].

[79] S. Alekhin, A. Djouadi and S. Moch, *The top quark and Higgs boson masses and the stability of the electroweak vacuum*, *Phys. Lett.* **B716** (2012) 214–219, [1207.0980].

[80] P. Marquard, A. V. Smirnov, V. A. Smirnov and M. Steinhauser, *Quark Mass Relations to Four-Loop Order in Perturbative QCD*, *Phys. Rev. Lett.* **114** (2015) 142002, [1502.01030].

[81] A. V. Bednyakov, *On the electroweak contribution to the matching of the strong coupling constant in the SM*, *Phys. Lett.* **B741** (2015) 262–266, [1410.7603].

[82] A. Andreassen, W. Frost and M. D. Schwartz, *Consistent Use of the Standard Model Effective Potential*, *Phys. Rev. Lett.* **113** (2014) 241801, [1408.0292].

[83] PARTICLE DATA GROUP, K. A. Olive et al., *Review of Particle Physics*, *Chin. Phys.* **C38** (2014) 090001.

[84] S. Alekhin, J. Blümlein, S. Moch and R. Placakyte, *Parton distribution functions, α_s, and heavy-quark masses for LHC Run II*, *Phys. Rev.* **D96** (2017) 014011, [1701.05838].

Global SM and BSM Fits using Results from LHC and other Experiments

Emanuele Bagnaschi[1], *Philip Bechtle*[2], *Johannes Haller*[3], *Roman Kogler*[3], *Thomas Peiffer*[4], *Tim Stefaniak*[1], *Georg Weiglein*[1]

[1]DESY, Hamburg, Germany
[2]Physikalisches Institut, Universität Bonn, Germany
[3]Institut für Experimentalphysik, Universität Hamburg, Germany
[4]II. Physikalisches Institut, Universität Göttingen, Germany

DOI: http://dx.doi.org/10.3204/PUBDB-2018-00782/B8

Global fits which confront results of High-Energy-Physics experiments with accurate theoretical predictions can be used to provide indirect constraints on fundamental parameters of the Standard Model of particle physics or new physics models. Important examples are global fits of the electroweak sector of the Standard Model or fits of supersymetric extensions of it. In this article we review the results obtained using the public software tools `Gfitter`, `Fittino`, `MasterCode`, `HiggsBounds` and `HiggsSignals` and we highlight the physics results of global fits in the Standard Model, Supersymmetry and various other beyond-the-Standard-Model theories.

1 Introduction

Models of fundamental physics are characterized by a set of free parameters, which cannot be calculated from fundamental model assumptions, but must be determined experimentally. Each of these parameters affects a large variety of observables because of the effects of radiative corrections. From a detailed comparison of accurate theoretical predictions with experimental observables and direct search results obtained at High-Energy-Physics (HEP) experiments, indirect constraints on the free parameters of particle physics models can be derived, and the overall consistency of these models with the data can be studied. Such comparisons enable insights into the model in mass regions even higher than the centre-of-mass energy available in the respective HEP experiments because of the effects of radiative corrections.

Often, these comparisons are performed with so-called global fits using software frameworks which provide tool-kits of sophisticated statistical methods for the interpretation of the fit results. These software tools provide implementations of accurate theoretical calculations or software interfaces to calculations implemented in external software. Furthermore, tools for model independent interpretations of measurements and search results can be integrated into the global fit frameworks, or applied by themselves to check the agreement of a certain physics model with the measurements.

In this article, a review is given of the results obtained using the software tools `Gfitter`, `Fittino`, `MasterCode`, `HiggsBounds` and `HiggsSignals` which have been developed in parts during the course of the SFB 676. We discuss the physics results in the Standard Model

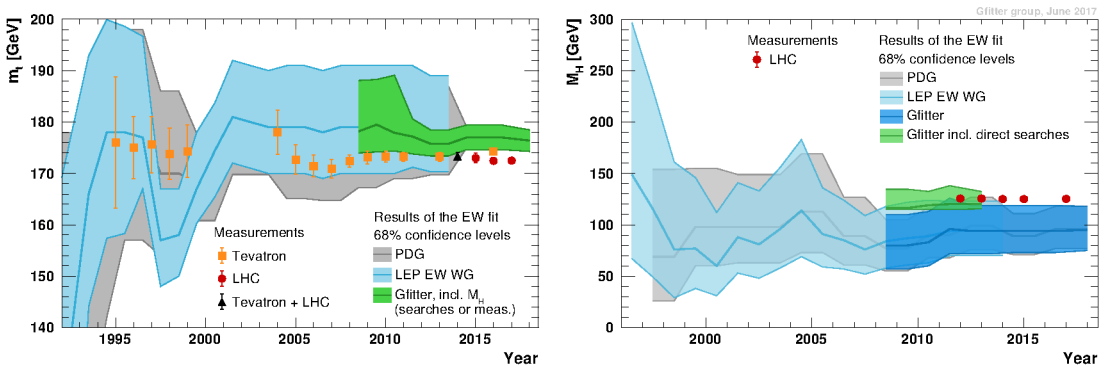


Figure 1: Prediction of the top quark mass (left) and the Higgs boson mass (right) within the Standard Model as a function of time as obtained by various analysis groups using electroweak precision data (grey [3], light blue [2], green [4]). Direct mass measurements after the top quark and Higgs boson discoveries are displayed by the data points. Figures taken from Ref. [11].

of particle physics (SM) and models of new physics with particular emphasis on supersymetric models and models with an extended Higgs sector. Furthermore, we highlight the developments during the last decade in this area, with a major impact arising from the discovery of a Higgs boson in 2012 at CERN's LHC.

2 Global fits of the electroweak sector of the SM

During the last decades, tremendous progress has been made in the experimental techniques to measure crucial observables of the SM as well as in theoretical calculations that have led to precise predictions of these observables within the SM. In particular, the precise measurements of electroweak data obtained during the 1990ies in e^+e^- collisions at the Z pole by the LEP collaborations and the SLD collaboration [1] have allowed the application of the techniques of global fits to obtain impressive results in the electroweak sector of the SM [2–5]. For an historical review of the results of global fits of the electroweak sector of the SM and a discussion of their perspectives the reader is referred to Ref. [6]. Results on the subject obtained within the SFB 676 using the `Gfitter` framework can be found in Ref. [7–13].

For a long time, these global fits have been used to derive indirect constraints on yet experimentally undetermined SM parameters. An impressive example of this kind is the correct indirect determination of the mass of the top quark m_t before its direct discovery at the Tevatron in 1995 [14, 15] as shown in Fig. 1 (left) where the indirect prediction of m_t as obtained in global fits by several groups is shown as a function of time as well as results from direct m_t measurements. Later, the discovery of the top quark and the measurement of its mass enabled the indirect determination of the mass of the Higgs boson M_H within the SM using global fits before the direct discovery of a Higgs boson at the LHC. The development of the M_H predictions obtained by several groups in global fits is shown in Fig. 1 (right) as a function of time. The combination of precise theoretical calculations, electroweak precision data, information on m_t and results from direct Higgs boson searches at LEP and the Tevatron have led to an indirect

prediction of $M_H = 120^{+12}_{-5}$ GeV in 2011 [8] which was in impressive agreement with the direct discovery of a Higgs boson by the LHC collaborations in 2012 [16,17] and their combined mass measurement of $M_H = 125.09 \pm 0.21 \pm 0.11$ GeV using the LHC run-1 data-set [18] .

With an interpretation of the discovered Higgs boson as the Higgs boson of the SM and with the measurement of its mass, the electroweak sector of the SM is complete and all fundamental SM parameters are directly measured. In this situation, global fits are a powerful tool for tests of the internal consistency of the SM, for the prediction of SM parameters with high precision, and for the derivation of constraints of theories describing physics beyond the SM (cf. Sect. 5). In the following we restrict ourselves to the discussion of the most recent results as obtained in this field of research within the SFB 676 by the `Gfitter` group [11] using latest experimental results and theoretical predictions. Earlier `Gfitter` results [7–10] are only mentioned to highlight recent changes and improvements.

The data used in the fits are the electroweak precision data at the Z pole and their correlations as measured by the LEP and SLD collaborations [1], the width [19] and the mass [11] of the W boson including information from measurements at LEP [20], Tevatron [21] and most recently from the ATLAS experiment [22], the world average values for the running quark masses [19], a measurement of the effective leptonic electroweak mixing angle by the Tevatron experiments [23], an up-to-date determination of the five-quark vacuum polarisation contribution to $\alpha(M_Z^2)$, $\Delta\alpha^{(5)}_{\rm had}(M_Z^2)$ [24], an average [11] of the top quark mass measurements as obtained by ATLAS and CMS in the run-1 data-set of the LHC and the combined ATLAS and CMS measurement of the Higgs boson mass [18]. The electroweak fit makes use of the most up-to-date theoretical calculations of the electroweak observables, mostly at NNLO accuracy. For a detailed list of calculations used in the fit, the reader is referred to [11].

Using these input data and theoretical calculations with the free fit parameters M_H, M_Z, m_c, m_b m_t, $\Delta\alpha^{(5)}_{\rm had}(M_Z^2)$ and α_S (plus ten additional theoretical uncertainty (*nuisance*) parameters), the global fit converges at a minimum χ^2 value of 18.6 for 15 degrees of freedom, which corresponds to a p-value of 0.23. In Fig. 2 (left), the difference between the global fit result as well as the input measurement with the indirect determination (obtained from a global fit excluding the experimental measurement of the observable in question) for each observable are shown in units of the total uncertainty (quadratic sum of uncertainties of indirect determination and input measurement). Analogue results for the indirect determinations, trivially centered around zero, are shown to illustrate the impact of their uncertainties on the total uncertainties. In general, a nice agreement is observed, with only few observables featuring deviations of more than 2σ. The strongest deviation is observed for the forward-backward asymmetry of b quarks, $A^{0,b}_{\rm FB}$, which is extensively discussed in the literature.

The experimental observables provide sensitivity to constrain the Higgs boson mass with different strength because of different impacts in the contribution of radiative corrections in their theoretical prediction. In Fig. 2 (right), the indirect determinations of M_H in the SM using the four observables providing the strongest M_H constraints are compared to the fit result including all data except the direct M_H measurement which results in $M_H = 90^{+21}_{-18}$ GeV and is in agreement with the direct M_H measurement within 1.7 standard deviations.

The indirect result for the mass of the W boson provided by the gobal fit is $M_W = 80.354 \pm 0.007_{\rm tot}$ GeV [11] which represents the most precise determination of M_W in the SM, even outperforming the direct measurement. The total uncertainty is not dominated by a single source but results from many different contributions of similar impact. The most important contributions are the theoretical uncertainty of M_W (contributing ± 0.0040 GeV to the

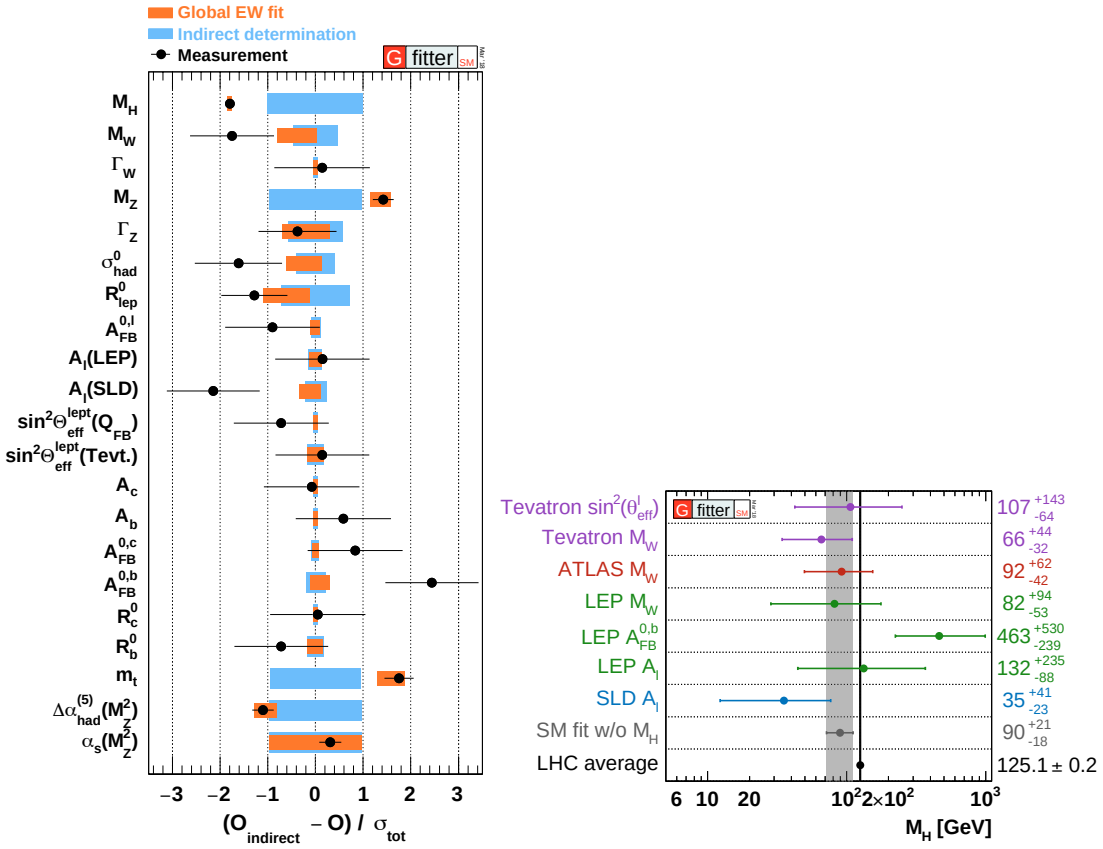


Figure 2: Results of the global electroweak fit: (left) comparison of the fit results and the input measurements with the indirect determinations in units of the total uncertainties for all observables used in the fit. (right) Comparison of the indirect prediction of M_H obtained from individual observables with the indirect global fit result and the LHC measurement of M_H. Figures taken from Ref. [11].

total uncertainty), the theoretical uncertainty on m_t (contributing $\pm 0.0030\,\text{GeV}$), the experimental uncertainty on m_t (contributing $\pm 0.0027\,\text{GeV}$), the uncertainty on M_Z (contributing $\pm 0.0026\,\text{GeV}$), the uncertainty of α_S (contributing $\pm 0.0026\,\text{GeV}$) and the uncertainty on $\Delta\alpha_{\text{had}}$ (contributing $\pm 0.0024\,\text{GeV}$).

Likewise, the indirect result of the global fit for the effective leptonic weak mixing angle is $\sin^2\theta^l_{\text{eff}} = 0.23153 \pm 0.00006_{\text{tot}}$ with dominating uncertainties resulting from the determination of $\Delta\alpha_{\text{had}}$ (± 0.000035) and from the theoretical uncertainty on $\sin^2\theta^l_{\text{eff}}$ (± 0.000040).

Other highlights of the physics results of the global fit are the indirect fit result for the mass of the top quark, $m_t = 176.4 \pm 2.1\,\text{GeV}$, and the indirect fit result for the strong coupling strength at the scale of the Z boson mass, $\alpha_S(M_Z^2) = 0.1194 \pm 0.0029$, which is determined at full NNLO for electroweak and strong contributions and partially at NNNLO for strong corrections.

With a simultaneous two-dimensional indirect determination of m_t and M_W the internal

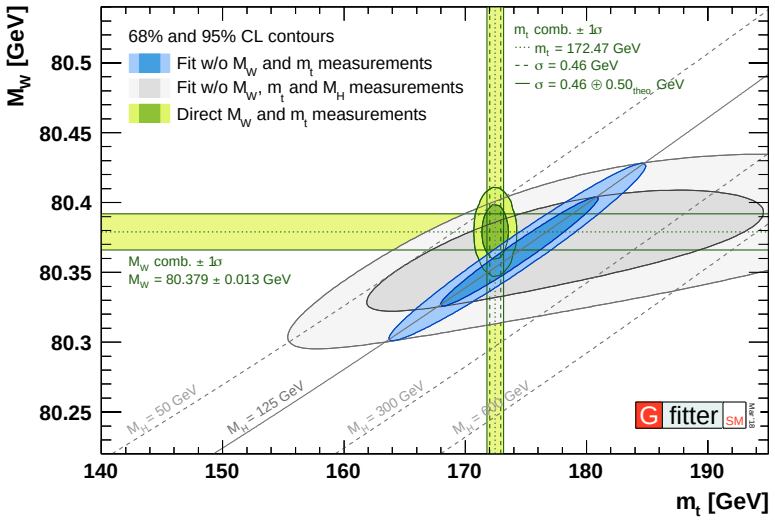


Figure 3: Internal consistency of the electroweak sector of the SM: allowed regions in the M_W versus m_t plane for the global fit including (blue) and excluding (grey) the LHC M_H measurement. The direct measurements of M_W and m_t are excluded from the fits. The fit results are compared to the direct measurements shown as green vertical and horizontal 1σ bands and two-dimensional 1σ and 2σ ellipses. Figure taken from Ref. [11].

consistency of the SM can be tested. In Fig. 3, the 68 % and 95 % confidence level (CL) allowed regions in the plane M_W versus m_t are shown for the global fit including all data except the direct m_t and M_W measurements (blue) and for a global fit excluding in addition the M_H measurement (grey). The strong impact of the precise M_H measurement is clearly visible by a huge reduction of the allowed parameter space. The fit results are compared to average values of the direct measurements of m_t and M_W shown in green error bands and ellipses. Good agreement between direct measurements and indirect determinations are observed.[1]

While the electroweak precision data measured in e^+e^- collisions at LEP and SLD still have a crucial importance for global fits of the electroweak sector, experimental results obtained during the last decades at hadron colliders have continuously improved the fit performance: notably, the precise measurements of the top quark mass and the W boson mass at the Tevatron and at the LHC, and, most importantly, the LHC determination of the mass of the Higgs boson. While future improved measurements of M_W and m_t can be expected at the LHC, the International Linear Collider (ILC) with GigaZ option will provide even better precision for these mass parameters, together with improved values for the partial decay width of the Z boson, R_l^0 and for $\sin^2\theta_{\text{eff}}^f$ from measurements of the left-right asymmetry A_{LR}. With these experimental improvements together with projected improvements in the theoretical calculations, a significant increase in the predictive power of the fit is found [10], where in particular the ILC/GigaZ scenario provides excellent sensitivity to indirect new physics.

[1] An additional theoretical uncertainty of 0.5 GeV is attributed to the average of the kinematic m_t measurements at the LHC due to the ambiguity in kinematic top quark mass definition, the colour structure of the fragmentation process and the perturbative relation between pole and $\overline{MS}$ mass.

3 Constraints from Higgs searches and measurements

Since the discovery of a Higgs boson [16, 17] one of the most important aims of HEP is to understand this particle in utmost detail, and to contrast its measured properties with the predictions of the SM and its possible new physics extensions. However, already before, the limits from collider searches both for a SM-like Higgs boson and for other more exotic scalar bosons posed important constraints on Higgs boson properties which had a large impact on the construction of alternatives and extensions of the SM. The same is true after the discovery of a SM-like Higgs boson for searches for additional scalar bosons. The constraints on their properties obtained from search limits continue to play an important role in model building and phenomenology.

In this section, we introduce two tools developed in parts in the context of the SFB 676. The code `HiggsBounds` deals with model independent exclusion limits on SM-like Higgs bosons and other scalar bosons. It incorporates the legacy of exclusion limits from searches at the LEP and Tevatron experiments. `HiggsSignals`, on the other hand, incorporates the experimental measurements of the discovered Higgs boson's properties, including its mass, production and decay rates, and kinematical information in the form of Simplified Template Cross Section (STXS) results.

3.1 HiggsBounds

Before the LHC, the most stringent limits on a SM-like Higgs boson were set by the LEP experiments [25]. Also the Tevatron searches showed sensitivity for a SM Higgs boson interpretation, especially around a Higgs boson mass of $m_{\mathrm{h}} \approx 2m_{\mathrm{W}} \approx 160\,\mathrm{GeV}$ [26]. In addition, a variety of searches for non-standard Higgs bosons were carried out at LEP [27] and the Tevatron, where the latter ones resulted in important constraints on 2HDM or SUSY interpretations for large $\tan\beta$ (see e.g. [28, 29]). The experimental searches, previously at LEP and the Tevatron and nowadays at the LHC, are carried out in many different channels. For instance, already at LEP the search for a neutral Higgs boson was performed in Higgsstrahlung, in WW and ZZ fusion, in the Yukawa process, and in pair production. The final states of the searches at LEP, the Tevatron and the LHC incorporate SM Higgs decays such as $h \to \gamma\gamma, ZZ, WW, gg, b\bar{b}, \tau\tau, \mu\mu$, as well decay modes that are motivated by new physics scenarios, e.g. into invisible particles. In addition, new physics models like the 2HDM and MSSM feature a charged Higgs boson giving rise to further decay signatures. In total, a plethora of different search results has been obtained, most of which have been presented both in specific model interpretations and as model-independent limits on the signal cross section for a specific Higgs mass and a specific combination of the production and decay modes. Making use of this wealth of experimental information to constrain the parameter space of different models is a non-trivial task.

With `HiggsBounds` [30–32] a common tool is provided which deals with the problems of finding the most significant limit and of deciding whether a particular search limit is valid for any given new physics model containing an arbitrary number of neutral and charged scalar bosons. The theoretical input of `HiggsBounds` is provided in terms of physical quantities predicted by the new physics model, i.e. the number of charged and neutral Higgs bosons, their masses, total decay widths, production and decay rates. The production rates can either be approximated in the code from effective couplings, or directly specified at the partonic or hadronic level. Similarly, the decay rates are estimated from effective couplings or given directly by the user. In this way, `HiggsBounds` is independent of the internal details of the new physics

model, and applicable to basically any model.

A first challenge occurs in tests of a model against several observed limits at a specific CL in parallel. For instance, for limits given at 95% CL the chance to wrongfully exclude a signal model is $\leq 5\%$ for each tested limit, and after n tests the true CL of the model exclusion might be as low as $1 - 0.95^n$. While such a dilution of the CL is not intended, it was often ignored in phenomenological studies. However, a proper statistical combination of various limits usually requires more information (e.g. correlations between systematic uncertainties) than is typically publicly available. The procedure implemented in `HiggsBounds` is a test of the model only against the limit of the most sensitive search which represents a well-defined, conservative and CL preserving statistical procedure. The sensitivity of a search can be determined by comparing the model predictions with the expected exclusion limit.

A second challenge arises from the validity of a given limit in a certain model. A typical example are the assumptions made in the derivation of published limits on the composition of Higgs production and decay modes, like in combined searches for a SM Higgs boson at LEP, Tevatron or the LHC, where it is assumes that all combined search channels contribute to the signal in the same fraction as predicted by the SM. In order to test whether such a limit is valid in a certain model, `HiggsBounds` checks whether the model-predicted signal fractions of the relevant channels, weighted with their absolute size, are within a very small (user configurable) band around the assumption used for the limit generation [33].

In addition to the exclusion test with respect to a fixed 95 % CL, an improved implementation of exclusions is possible if the full likelihood of the exclusion fit is available. Since `HiggsBounds` version 4.1 [33] an approximate likelihood function for the LEP exclusions is provided. After the Higgs discovery, these exclusions are still highly relevant for new physics models that contain an additional lighter Higgs boson. Assuming Gaussian behaviour, the likelihood approximation is provided as a χ^2 contribution for every mass point and for every signal strength parameter $\mu = [0.001, 1]$ for which the CL_{s+b} value has been retained in the LEP model independent limits. Such an (approximate) likelihood for exclusions from Higgs searches is useful in global fits, and it would be desirable to have more such likelihoods available, in particular for the recent LHC results.

The first publication of model-independent likelihoods instead of 95% CL limits at the LHC was performed by the CMS experiment in the search for non-standard (heavy) Higgs bosons in the $\tau^+\tau^-$ final state [35], using a single scalar narrow resonance (ϕ) toy model. In Ref. [34] a description is given of the `HiggsBounds` procedure for the reconstruction of the exclusion likelihood from this data for arbitrary Higgs models and its application on MSSM benchmark models. The likelihood information allows a statistically consistent combination of the information on limits from searches for additional Higgs bosons with the measurements of the observed SM-like Higgs boson. The tools `HiggsBounds` and `HiggsSignals` (see below) provide a framework for this task and can be applied to arbitrary models with scalars. Figure 4 exemplifies the use of the likelihood information from the CMS $pp \to \phi \to \tau^+\tau^-$ search. In Fig. 4 (left) one example of the likelihood values is shown for fixed Higgs mass $m_\phi = 300\,\mathrm{GeV}$ as a function of the cross sections of the two main production modes, gluon fusion ($gg \to \phi$) and b-associated Higgs production ($b\bar{b} \to \phi$). Many models of new physics change the ratio of these cross sections. This three-dimensional grid of likelihood values is then interpolated in `HiggsBounds` and allows one to reproduce the model dependent limit in the m_h^{max} benchmark scenario to very high accuracy, as shown in Fig. 4 (right).

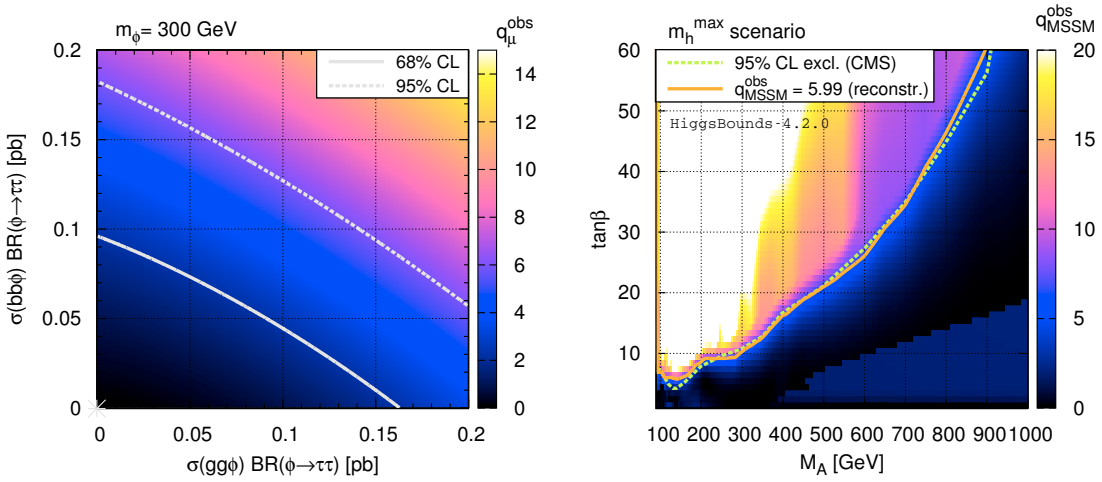


Figure 4: Input and validation of the exclusion likelihood reconstructed by `HiggsBounds` [34] for the CMS search for $pp \to \phi \to \tau^+\tau^-$ [35]. The likelihood input (left) is provided for a single scalar narrow resonance (ϕ) toy model for varying masses m_ϕ and cross sections in the dominant production modes $gg \to \phi$ and $bb \to \phi$. The implementation is validated by comparing the likelihood-based exclusion (right) in the m_h^{max} benchmark scenario with the official CMS limit, yielding excellent agreement. Figures taken from Ref. [34].

3.2 HiggsSignals

Since any new physics extension of the SM has to feature a particle with properties consistent with the measured properties of the Higgs boson, an important task is a comparison of the model predictions with the Higgs boson measurements at the LHC. While a large amount of sensitive model interpretations have been published by ATLAS and CMS (see e.g. Ref. [36] for the LHC run-1 results), not every new physics model can be tested against these results as these are based on specific model assumptions. The aim of `HiggsSignals` [32, 37–39] is the usage of model-independent experimental results — the mass measurements and the signal strength measurements (or, equivalently, absolute signal rate measurements) — in each individual search channel and kinematical configuration studied by the experiments. `HiggsSignals` calculates a χ^2 value that quantifies the level of (dis-)agreement between model predictions and measurements by decomposing the given uncertainties on the rate measurements into all theoretical sources of systematic errors, all known correlated experimental systematic errors, and a remainder that contains the statistical uncertainty and remaining publicly inseparable experimental systematic uncertainties. This decomposition enables the code to take into account the major correlations among the measurements. Furthermore, `HiggsSignals` incorporates all available information on the sub-channel composition of each rate measurement, which depends on the relative efficiency of the different Higgs production and possibly decay modes in the experimentally analysed search channel. If public information on these efficiencies is available, it is included by default.

The current public version [32] offers in addition the implementation of Simplified Template Cross Section (STXS) [40] results which contain experimental results binned in kinematical configurations which promise sensitivity on the vertex structure of the Higgs boson production

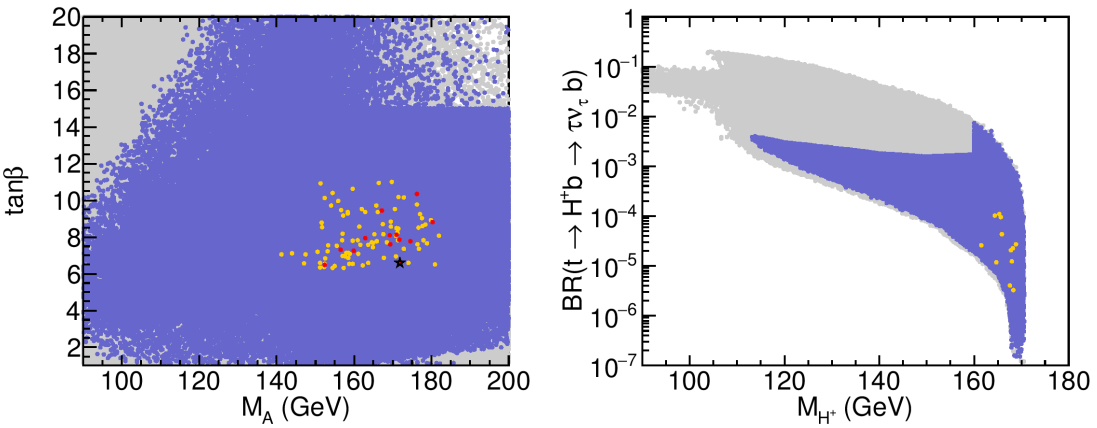


Figure 5: Result from a scan of the phenomenological MSSM with eight parameters using `HiggsBounds` and `HiggsSignals` for the case where the heavier CP even Higgs boson H is identified with the observed Higgs boson at $m_{\mathrm{H}} = 125\,\mathrm{GeV}$ [41]. The red and yellow points correspond to the 1 and 2σ-level, respectively, while allowed points outside the 2σ region are indicated in blue. The left plot shows the allowed points in the $(M_A, \tan\beta)$ parameter plane, while the right plot shows the combined branching fraction for the top quark decaying to a charged Higgs boson $H^\pm$ and a b-quark, and $H^\pm$ decaying to $\tau\nu_\tau$. Figures taken from Ref. [41].

through e.g. the transverse momentum spectrum of the Higgs boson or additional objects in the event.

The power of combining `HiggsBounds` and `HiggsSignals` is e.g. illustrated in the study of the parameter space of the eight-dimensional phenomenological MSSM [41], where different possible interpretations have been identified: Either the light Higgs boson h can be identified with the observed particle at 125 GeV, and the other Higgs particles are heavy ("decoupling limit"), or one of the neutral CP even Higgs bosons becomes SM-like despite the further Higgs spectrum being light ("alignment without decoupling"). The latter happens within the MSSM only in a rather specific parameter region, and provides the possibilities that either the lighter or the heavier CP even Higgs boson can be identified with the SM-like state at 125 GeV. Interestingly, the heavier Higgs boson (H) interpretation of the signal is still allowed after taking into account all LHC run-1 Higgs measurements and limits from ATLAS and CMS, as well as constraints from flavour physics. Some scan results for this interpretation are shown in Fig. 5. Fig. 5 (left) illustrates in the $(M_A, \tan\beta)$ parameter plane that the allowed points (in yellow and red) are clustered in a very restricted parameter space, as they are constrained from many complementary searches. The branching fraction for top quarks decaying into a light charged Higgs boson $H^\pm$ with successive decay to $\tau\nu_\tau$ is shown in Fig. 5 (right), indicating that the remaining viable parameter points are located at the kinematic threshold (or beyond) of this decay such that they escape the exclusion limit. It should be noted that the situation where the SM-like Higgs boson at 125 GeV is not the lightest state in the Higgs spectrum occurs generically in extensions of the SM with an additional Higgs singlet as it is the case in the NMSSM, see e.g. Refs. [42, 43].

The exploration of the mechanism of electroweak symmetry breaking via precision investigations in the Higgs sector will continue to be one of the prime topics of elementary particle

physics during the next decades. The prospective improvements in the experimental precision in combination with corresponding efforts on the theory side will significantly enhance the sensitivity for discovering small deviations from the SM. Tools like `HiggsBounds` and `HiggsSignals` will continue to play an important role in this research field, enabling quick and rather precise tests of new physics models with any number of scalars against the experimental results thus allowing to easily identify the phenomenologically relevant parameter space of the model.

4 Global fits of supersymmetric models

For tests of the compatibility of the experimental data with scenarios of physics beyond the SM, it is of high interest to study well-motivated complete and renormalizable extensions of the SM, like Supersymmetry, which provide a more fundamental theory beyond the SM with a broader range of explained features of nature. The ability to calculate loop corrections to a wide variety of precision measurements, like the properties of electroweak symmetry breaking and the Higgs boson, and the ability to calculate cosmological predictions, increases the predictive power and accordingly the falsifiability of such a theory dramatically.

Besides many strong theoretical arguments for supersymmetric extensions of the SM, at least two observations which indicate deviations from the SM prediction could be a first experimental hint towards the realisation of SUSY in nature: First, the observed dark matter (DM) content in the universe [44], which is naturally explained by a neutral particle with a weak coupling and a mass near the electroweak scale, and second, the measurement of the anomalous magnetic moment of the muon $(g-2)_\mu$ which deviates from the SM prediction [45]. On the other hand, no SUSY particles have been found so far. Thus, it is interesting to contrast these experimental constraints and the electroweak precision measurements, including the measurement of the Higgs boson mass, with the limits from direct searches for SUSY particles by means of global fits. In the next sections we introduce the global fitting tools `Fittino` and `MasterCode` which have partially been developed and extensively used within this project.

Since SUSY can be implemented in a wide variety of theoretical models with a large number of free parameters, it is desirable to start its investigation in global fits with models which are constrained by additional theoretical assumptions and symmetries leading to a more restricted number of free parameters. One of the models studied extensively in the following, is the constrained Minimal Supersymmetric Standard Model (cMSSM or CMSSM), which is defined by only four parameters, three of which are specified at the grand unification scale, and a sign. Other models studied are the so-called Phenomenological MSSM with 10 (pMSSM10) [46] and 11 (pMSSM11) [47] parameters, the NUHM1(2) in which universality is relaxed for both together (each separately) of the soft SUSY-breaking contributions to the masses-squared of the Higgs multiplets (see references in [48, 49]), a SU(5)-GUT inspired scenario [50] and a scenario with Anomaly Mediated Supersymmetry Breaking (mAMSB) (see references in [51]).

4.1 Fittino

`Fittino` [52] is a global fitting tool for models beyond the SM (in particular SUSY) aiming at the LHC era and the yet-to-begin era of precision measurements of new physics at a high-energy e^+e^- collider. A list of citations to other global fit tools in this area is given in [53]. A global SUSY fit is sensitive to observables from SM precision measurements, cosmological measurements like the DM relic density, results from astroparticle physics (like direct and

indirect DM annihilation and detection results), Higgs boson limits and properties, results from flavour physics, and exclusion limits from direct SUSY particle searches. In a series of publications [54–57] the impact of these experimental results on SUSY models was explored and projections for future colliders [58] have been obtained.

The results showed two consistent constraints pushing the cMSSM into the region of high sparticle mass scales: The relatively high Higgs boson mass requires large third generation squark masses to generate large enough loop effects on the Higgs mass, to lift it from its maximally allowed tree level value of m_Z up to around 125 GeV. At the same time, the direct LHC searches push the first generation squark masses above 1 TeV.

In the attempt to exclude the cMSSM [53] the `Fittino` collaboration faced a number of conceptual and technical challenges. First, SUSY exclusions are typically derived by defining a CL of e.g. CL < 0.05 as a criterion for exclusion, where the CL is derived from a hypothesis test consisting of a likelihood ratio between two competing hypotheses: the null hypothesis, often the SM, and the alternative hypothesis, often SUSY. This approach works for a comparison of isolated features of a model, such as the search for a set of sparticles, or the search for an extended Higgs boson sector. However, for an attempt of a global exclusion of a SUSY model the null hypothesis would trivially fail the test since the DM relic density simply can't be explained in the SM. Of course, SUSY could be tested against the SM with an ad-hoc-assumption of some unexplained solution for DM. But since SUSY decouples, the cMSSM trivially becomes a SM with DM, if the SUSY mass scale is driven to infinity, and the two models in the hypothesis test would be asymptotically identical. For this reason, the remaining solution is to give up on the sensitivity of the Neyman-Pearson approach of likelihood-ratio based hypothesis tests, and just trivially test the goodness-of-fit of the cMSSM global fit to the data.

For most SUSY fits cited above, a Markov Chain Monte Carlo (MCMC) based approach, or other stochastic alternatives, for efficient scans of the parameter space are used. For an overview and comparison of approaches, see [59]. For a model with four continuous SUSY parameters and a few SM parameters, such as the cMSSM, about one billion scanning points with a valid SUSY sparticle spectrum are required to make a meaningful statement about the uncertainties, which represents a significant obstacle for the determination of the goodness of fit using a toy-Monte-Carlo based approach, since the computer codes for the calculation of the observables (see e.g. [60–63]) easily use about 20 seconds per SUSY parameter points. A toy-Monte-Carlo based approach is however indispensable for determining the goodness-of-fit, as a very large number of scan points is needed because of the behaviour of the model: The dependence of the observables on the parameters is highly irregular. The fit spans regions from low-scale SUSY with gauginos and sleptons in the $\mathcal{O}(100\,\text{GeV})$ range, where the LHC exclusion can change rapidly within a few GeV, up to the decoupling regime where the prediction becomes independent of the parameter value. In addition, the prediction of the DM density depends critically on the interplay between different SUSY particles, and the fit covers different co-annihilation and focus-point regions [53], all with different relations between parameters and observables. Finally, the fit behaviour can change rapidly between regions with a physical spectrum and a forbidden tachyonic spectrum, or between the neutral lightest SUSY particle and the charged lightest SUSY particle.

In [53] a high-statistics toy fit of the cMSSM was performed for the first time. The goodness-of-fit test in Fig. 6 (right) sees the cMSSM just excluded at CL < 0.05. In the figure, the smooth line shows the χ^2 distribution expected for fully gaussian uncertainties and fully linear relations between all observables and all parameters. However, the histogram illustrates the influence of non-gaussian errors, non-linearities and the effect of one-sided limits which distort the real

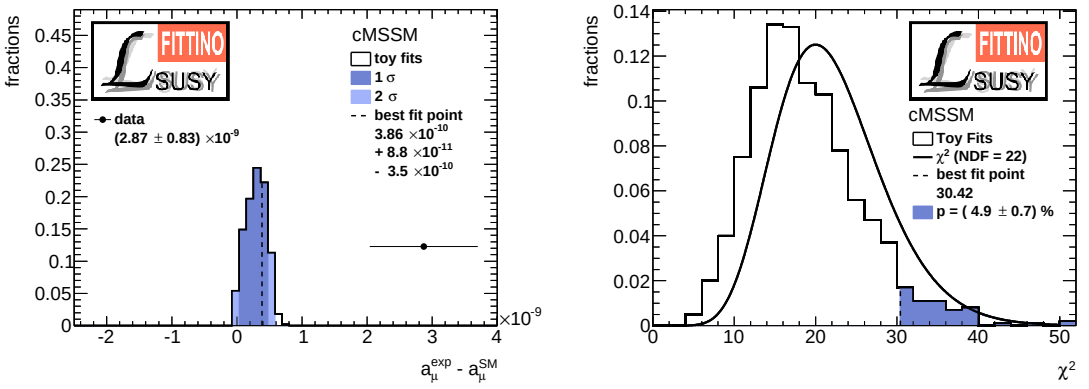


Figure 6: Results from the cMSSM exclusion: the tension between the prediction of $(g-2)_\mu$ and the experimental result (left) and the result of the toy-experiment based χ^2 distribution, which emanates from the inability of the fit to both accommodate $(g-2)_\mu$ and the negative LHC search results (right). Figures taken from Ref. [53].

toy-Monte-Carlo based distribution.

The observed CL critically depends on the choice of observables, much more so than when discussing parameter estimations. In the latter case, if one parameter affects several separate observables in a correlated way, it makes no difference whether all separate observables are fitted directly, or whether the separate observables are first combined and then a fit to the combined experimental result is performed. However, in the former case, the splitting of the sensitivity over many observables for which the theory prediction is largely correlated dilutes the goodness-of-fit test, since meaningful deviations between best fit and observations drown with respect to many random variations. In reality, it is not straightforward to optimize the observable selection while avoiding a bias on the result. The possible inputs to the global fit are discussed in [53], and some extreme choices do not allow an exclusion of the cMSSM with CL < 0.05. However, it is not possible to shed new light on this question before the muon anomalous moment $(g-2)_\mu$ is measured with better precision, and before its theory uncertainty does not decrease, as illustrated in Fig. 6 (left), where the uncertainty range of the toy-Monte-Carlo based fits is shown in the coloured distribution, and the measurement of $(g-2)_\mu$ is shown in the data point with experimental and theoretical uncertainty. The fit results fulfill the constraints of the LHC sparticle mass exclusions and the SM-like Higgs-boson properties, and thus no room is left to explain one of its two main motivations. Effectively, the cMSSM has become a SM with DM, forced to do so by the LHC results.

Ongoing work focuses on making global fits with a very large number of scanned SUSY parameter points in models beyond the cMSSM as flexible as possible. While a number of fits of the pMSSM exists (see e.g. Section 4.2), each model typically either requires its own implementation of parametrisations of LHC limits, or is limited to a small number of scan points, many orders of magnitude lower than the order of 1 billion required for realistic uncertainty estimates. One possible solution to this problem is presented in the code `SCYNet` [64]. Under the assumption that the dependence of the exclusion likelihood (cf. Fig. 4 (left)) on the relevant parameters is typically much more smooth and regular than the dependence of the global fit likelihood ratio or χ^2 on the parameters, the LHC sparticle exclusion likelihood can

Nuisance parameters	**Electroweak precision observables**
M_Z, M_T, $\Delta\alpha_{\rm had}$	M_W, A_b, A_c, $A_{FB}^{0,b}$,$A_{FB}^{0,c}$, $A_{FB}^{0,l}$, $A_l(P_\tau)$, $A_l(SLD)$, Γ_Z, R_b^0, R_c^0, R_l^0, $\sigma_{\rm had}^0$, $\sin^2\theta_{\rm eff}^l(Q_{FB}^{\rm had})$, a_μ
Higgs physics	**Flavour Constraints**
h_{125} properties $A/H \to \tau^\pm\tau^\mp$ searches	${\rm BR}_{B\to X_s ll}$, ${\rm BR}_{K\to l\nu}$, ${\rm BR}_{K\to\pi\nu\bar{\nu}}$, ${\rm BR}_{B\to X_s\gamma}$ ΔM_{B_s}, $\frac{\Delta M_{B_s}}{\Delta M_{B_d}}$, ${\rm BR}_{B_{s,d}\to\mu^\pm\mu^\mp}$, ϵ_k
Collider	**Dark Matter**
LEP, LHC run-1, LHC run-2	$\Omega_{CDM}h^2$, $\sigma_p^{\rm SI}$, $\sigma_p^{\rm SD}$

Table 1: Overview of the constraints included in a typical `MasterCode` analysis.

be parametrised independently of the rest of the global fit, using a much smaller number of scanning points. In `SCYNet`, this is explored using a deep Neural Net to perform a regression on the likelihood ratio output of a significant number of SUSY searches at ATLAS and CMS, implemented in a fast detector simulation and event selection using the tool `CheckMATE` [65]. Presently, a precision of the neural-net based regression compared to the simulation of the order of $-2\Delta\ln\mathcal{L} \approx \chi^2 \approx 1$ is achieved. At least the 2σ allowed range is described sufficiently precisely.

Based on such and other competing approaches, more complex models can be studied in the future. Currently, no direct positive experimental hint for SUSY beyond the tried-and-tested cosmological DM and $(g-2)_\mu$ has arisen. However, flavour physics holds the promise of anomalies (see e.g. [66] for an overview), which yet are waiting for a consistent interpretation in a UV-complete model.

4.2 MasterCode

`MasterCode` is a frequentist global-fitting framework which interfaces several different codes that provide state-of-the-art predictions for a wide range of observables of phenomenological interest using `SLHALib` [67,68]. Among these codes, we mention: the spectrum generator `SoftSUSY` [69]; `FeynHiggs` [63, 70–73], `HiggsBounds` [30, 31, 33, 34] and `HiggsSignals` [38, 39] (see above) for the Higgs sector observables and search limits; `micrOMEGAs` [74] and `SSARD`[2] for DM observables; `SuFla` [75,76] and `SuperISO` [61,77,78] for the flavour sector; `FeynWZ` [79–81] for the Electroweak Precision Observables (EWPOs). The sampling of the multidimensional parameter space of the model under analysis is performed using the `MultiNest` algorithm [82–84]. For an easy deployment of the framework on batch clusters a container-based approach with the `udocker` middleware [85] is used. An overview of constraints used in a typical `MasterCode` analysis is given in Tab. 1.

[2]SSARD is a private code developed by K. Olive and collaborators.

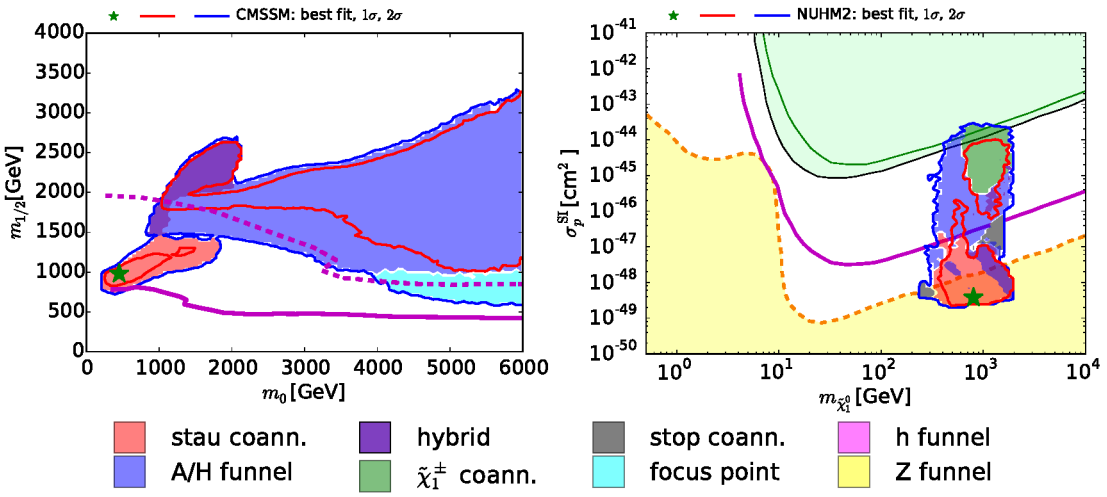


Figure 7: The relevant mechanisms to obtain the observed DM relic density (colour shadings), at 95%CL, in the m_0-$m_{1/2}$ plane of the CMSSM (left) and in the $m_{\tilde{\chi}_1^0}$-σ_p^{SI} of NUHM2 (right). In the left plot, the solid purple contour represents the LHC run-1 95% CL exclusion from $E_{T,\text{miss}}$ searches, while the dashed purple contour shows the prospective 5σ discovery reach for $E_{T,\text{miss}}$ searches at the LHC with 3000/fb at 14 TeV, corresponding approximately to the 95% CL exclusion sensitivity with 300/fb at 14 TeV. In the right plot, the black and green lines show the sensitivity of XENON100 and LUX back in 2015, while the purple one is the projected 95% exclusion sensitivity for LZ. Figures taken from Ref. [86].

4.2.1 Scenarios with specific SUSY-breaking patterns

While GUT-inspired scenarios and minimal Anomaly-Mediated Supersymmetry Breaking (mAMSB) provide theoretically inspired and elegant approaches towards possible UV completions, these models are all unable to explain the observed deviation from the SM prediction in the $(g-2)_\mu$ measurement. Nevertheless we consider the study of these scenarios an interesting and worthwhile effort, since the scientific community is still in the process of verifying the significance of this anomaly, both from the theory and experimental sides.

In [86] we have reappraised our CMSSM, NUHM1 and NUHM2 studies, with the aim of studying in more detail the DM phenomenology of these scenarios. Specifically, we were interested in the mechanisms which allow a recovery of the observed DM relic density. We started from the samples obtained in the study presented in refs. [48, 49] and then, in a given mass-plane, for each point selected after likelihood profiling we inferred the relevant process from the spectrum configuration. In other words, we defined a set of phenomenological "dark matter measures" to classify the points. For instance, points for which the relation $\left(m_{\tilde{\tau}_1}/m_{\tilde{\chi}_1^0}\right) < 0.15$ is satisfied were assigned to the process "stau co-annihilation". We cross-checked our approach with the explicit computation from `micrOMEGAs`, verifying that these DM measures are accurate in the vast majority of the cases. Two example results obtained in this analysis are illustrated in Fig. 7 where the m_0-$m_{1/2}$ plane in the CMSSM (left) and the $m_{\tilde{\chi}_1^0}$-σ_p^{SI} plane in the NUHM2 scenario (right) is shown. From this kind of results, one may appreciate how different mechanisms characterize the different allowed regions of the two models. Moreover, the study points

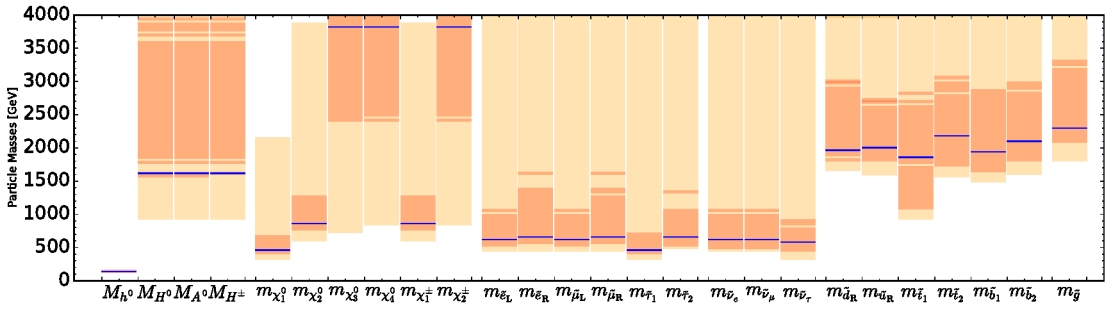


Figure 8: The allowed mass ranges at 68% CL (dark peach) and 95% CL (bright peach) in the SU(5)-GUT inspired scenario. The mass values corresponding to the best fit point are shown as horizontal blue lines. Figure taken from Ref. [87].

out the complementarity of information obtained from collider and direct detection experiments in these two scenarios.

We extended our studies with an analysis of an SU(5)-GUT inspired scenario [87] and an analysis of mAMSB [51]. In these papers the relevant constraints on superpartners production coming from LHC runs at 13 TeV have been implemented for the first time. For the sampling of the parameter space, the likelihood has been modelled following the `FastLim` [88] approach. In this approach, the relevant topologies for a given model have been identified and for each one of them the upper-limit on the cross-section at 95% CL provided by the experiments has been compared with the actual cross-section of the point being sampled, using a simple rescaling law to model the likelihood. In this way, a full MC simulation is avoided, since the elements needed (ie. the cross-section and the relevant branching ratio) can be computed using dedicated computer codes, such as `NLL-fast` [89,90], with very high performances. Higgs searches are implemented with a similar approach, using the cross-section times branching-ratio values computed by `FeynHiggs`.

The SU(5)-GUT study has revealed that, in contrast to the CMSSM/NUHM1/NUHM2 scenarios, also the co-annihilation mechanisms with either a $\tilde{\nu}_\tau$ or with $\tilde{u}_R$ or $\tilde{c}_R$ play a role because of the different pattern of the boundary conditions for the soft SUSY-breaking masses. In Fig. 8 the allowed mass range for the BSM particles in the SU(5)-GUT scenarios, at 68% CL (dark peach) and at 95% CL (bright peach) is shown as a typical outcome of a global `MasterCode` analysis. The mass values of the best fit point are indicated as horizontal blue lines. The figure illustrates the impact of the LHC results in providing stronger lower bounds for the coloured superpartners and for the other Higgs states of the MSSM. On the other hand, the allowed mass range of purely electroweakly interacting sparticles is less dependent on LHC search results.

The mAMSB study showed that a Wino-like or an Higgsino-like neutralino can fulfil the role of a DM candidate, with an upper bound on the neutralino mass of $m_{\tilde{\chi}_1^0} \lesssim 3$ TeV to avoid violating the bound coming from the observed DM relic density. Fig. 9 shows the two-dimensional likelihood profiles in the m_0-$m_{3/2}$ plane (left) and in the $m_{\tilde{\chi}_1^0}$-$m_{\tilde{\chi}_1^0}$ plane (right). In both cases, the colour shading reflects the nature of the neutralino. The left plot shows that the LSP is Wino-like only for a restricted range of $m_{3/2}$ values, while the Higgsino case is allowed for a larger range. The right plot displays the strict correlation between the neutralino nature and its mass, required by the relic density constraint.

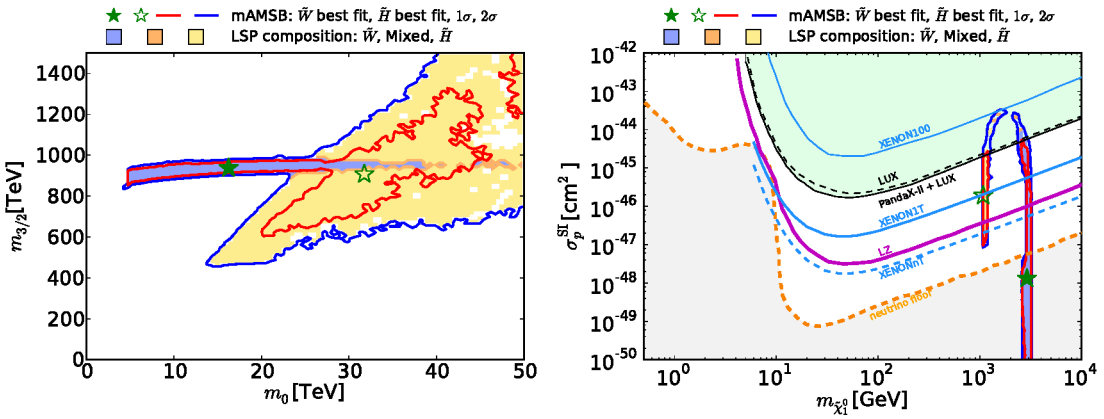


Figure 9: On the left (right), we show the two-dimensional likelihood profiles at 68% CL and at 95% CL in the m_0-$m_{3/2}$ ($m_{\tilde{\chi}_1^0}$-$\sigma_p^{\rm SI}$) plane in mAMSB. The colour shadings reflect the nature of the LSP, which can be either Wino-like (blue), Higgsino-like (yellow) or an admixture of the two (orange). Figures taken from Ref. [51].

In addition, a study of the CMSSM was performed in the so called "sub-GUT" flavour [91] in which the input scale of the soft SUSY-breaking terms, $M_{\rm in}$, is one of the parameters over which the sampling is performed and it is not fixed to be the GUT-scale. The one-dimensional likelihood profile for $\log(M_{\rm in})$ shown in Fig. 10 (left) features a slight preference, at the level of $\Delta\chi^2 \simeq 3$ for $M_{\rm in} \simeq 10^5$ GeV and for $M_{\rm in} \simeq 10^9$ GeV with respect to the case $M_{\rm in} \simeq M_{GUT}$ (i.e. the usual CMSSM scenario). The reason for this preference for lower $M_{\rm in}$ is a better compatibility with the latest BR($B_{s,d} \to \mu^\pm\mu^\mp$) measurements. The two-dimensional likelihood profiles in the $\log(M_{\rm in})$-m_0 plane show the non-trivial dependence of m_0 on the scale $M_{\rm in}$.

4.2.2 Phenomenological scenarios

Besides studies of MSSM scenarios with definite SUSY-breaking patterns, phenomenological scenarios have been studied which are able to explain the observed $(g-2)_\mu$ anomaly. Moreover, allowing for lighter SUSY-spectra, they can be used to assess the possibility of a MSSM discovery at future LHC runs or at a future e^+e^- collider. We have focused our attention to the pMSSM10 and pMSSM11.

The pMSSM10 is indeed able to fit $(g-2)_\mu$, differently from various GUT scenarios, as can be seen from a comparison of the likelihoods displayed in Fig. 11 (left). Fig. 11 (right) display the two-dimensional likelihood profiles in the $m_{\tilde{\chi}_1^0}$-σ_p^{SI} plane. The most significant features are an upper-bound $m_{\tilde{\chi}_1^0} \lesssim 500$ GeV, required to satisfy $(g-2)_\mu$, a lower-bound on the chargino co-annihilation region at $m_{\tilde{\chi}_1^0} \simeq 103$ GeV from LEP limits and the light-Higgs- and Z-funnel regions at $m_{\tilde{\chi}_1^0} \simeq 62$ GeV and $m_{\tilde{\chi}_1^0} \simeq 45$ GeV respectively.

In the pMSSM11 scenario, an extended study of the impact of LHC run-2 constraints and of $(g-2)_\mu$ on the allowed parameter space has been performed [47]. Moreover, for the first time LHC run-2 constraints on electroweakinos have been included, still using a `FastLim`-like approach and a recently developed tool, `EWKFast` [92], which allows the fast computation of electroweakino production cross-sections at NLO-QCD. The one additional free parameter

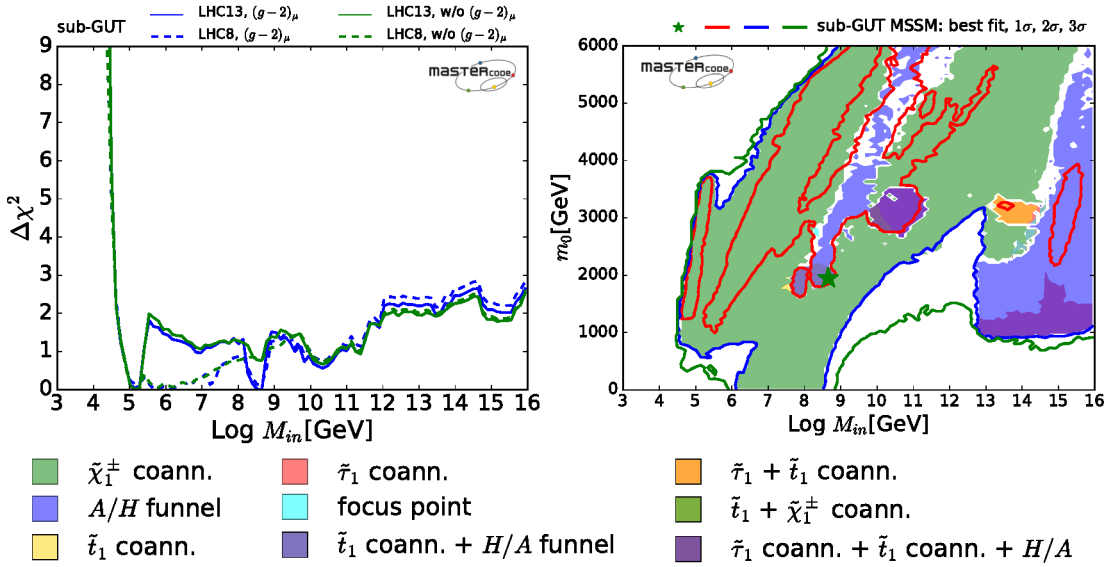


Figure 10: On the left, we show the one-dimensional likelihood profiles for the input scale $M_{\rm in}$ of the soft SUSY-breaking terms. We show four different profiles, with (solid) and without (dashed) the constraints coming from the direct searches for coloured superpartners and heavy Higgses at LHC run-2 and with (blue) and without (green) the constraint coming from the $(g-2)_\mu$ anomaly. On the right, we display the two-dimensional likelihood profiles at 68%/95%/99% CL in the $\log(M_{\rm in})$-m_0 plane, with the full constraint set applied. The colour shadings indicate the dominant mechanism which moves the CDM density into the allowed range from cosmological observations. Figures taken from Ref. [91].

with respect to the pMSSM10 (the soft SUSY-breaking mass terms for the $\tilde{\tau}$) changed the phenomenology by introducing a new relic density mechanism, slepton co-annihilation.

Fig. 12 (left) shows again the one-dimensional likelihood profile for the SUSY contribution to $(g-2)_\mu$, with and without the constraints from searches of SUSY particles at the LHC at 13 TeV and with and without imposing the $(g-2)_\mu$ constraint. In the pMSSM11 the displayed range of values can be covered, including the region consistent with the experimental measurement. Fig. 12 (right) shows the $m_{\tilde{\chi}_1^0}$-σ_p^{SI} plane *without* imposing the $(g-2)_\mu$ constraint. The best fit region moves to larger masses, where the neutralino has a mas of $\simeq$ 1 TeV and it is Higgsino-like. This change in the location of the preferred region is a result of an improved compatibility with the flavour constraints, especially BR($B_{s,d} \to \mu^\pm\mu^\mp$).

Since phenomenological scenarios such as the pMSSM11 have more room for light SUSY spectra, it is interesting to study the impact of the LHC run-2 results and the most recent direct detection experiments. Fig. 13 (left) shows the change in $m_{\tilde{q}_{1,2}}$-$m_{\tilde{g}}$ plane after including the aforementioned results. The shift from LHC searches performed at 8 TeV to the ones at the 13 TeV produces a marked change in the likelihood contours, shifting the lowest allowed mass for the first two-generation squarks and the gluino by a sizable amount, excluding completely the compressed region at low squark-/gluino-mass which was allowed by the LHC run-1 results and shifting the boundaries of the non-compressed region by $\simeq$ 500-1000 GeV. Fig. 13 (right)

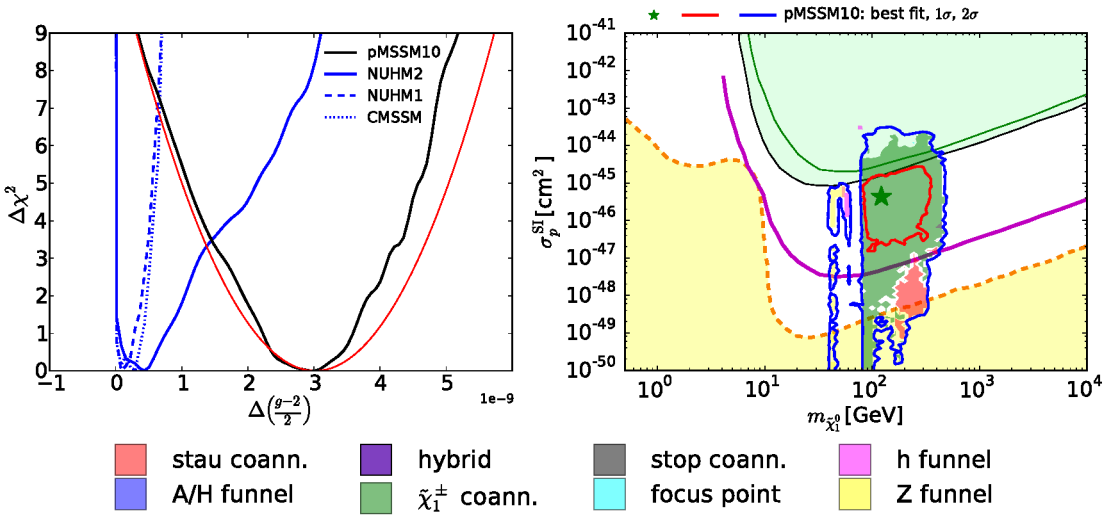


Figure 11: On the left, the one-dimensional likelihood profile for the SUSY contribution to $\Delta((g-2)/2)$ in the pMSSM10 and the CMSSM, NUHM1 and NUHM2. On the right, the two-dimensional likelihood profiles in the pMSSM10 in the $m_{\tilde{\chi}_1^0}$-σ_p^{SI} plane. The colour shadings indicate the dominant mechanism which moves the CDM density into the allowed range from cosmological observations. Figures taken from Refs. [46] and [86], respectively.

shows the same result without using the $(g-2)_\mu$ constraint. Lower masses are allowed in this case since larger neutralino masses are allowed and more compressed spectra are possible which evade the LHC bounds.

5 Fits of other BSM models

5.1 Oblique parameters from the global electroweak fit

New physics effects from virtual particles in loops can contribute through vacuum polarization corrections to the electroweak precision observables if the scale of new physics is larger than the electroweak scale. These effects are conveniently parametrised by the three self-energy parameters S, T, and U [93,94] describing the difference between the oblique vacuum corrections as determined from the experimental data and the corrections expected in a reference SM (with fixed reference values of m_t and M_H). The parameters S and T describe new physics contributions to neutral weak currents and to the difference between neutral and charged weak current processes, respectively. The U parameter is only constrained by the W boson mass and width, it is predicted to be small in most new physics models and often set to zero. The S, T, and U parameters are normalised such that the expected BSM contributions are of order $\mathcal{O}(1)$. The global electroweak fit can be used to determine S, T and U. Significant deviation of the results from zero are an unambiguous hint for new physics.

For reference values of $M_{H,\mathrm{ref}} = 125\,\mathrm{GeV}$ and $m_{t,\mathrm{ref}} = 172.5\,\mathrm{GeV}$ the following values are obtained [11] using the `Gfitter` framework: $S = 0.04 \pm 0.11$, $T = 0.09 \pm 0.14$, $U = -0.02 \pm 0.11$ with correlation coefficients of $+0.92$ between S and T, -0.68 between S and

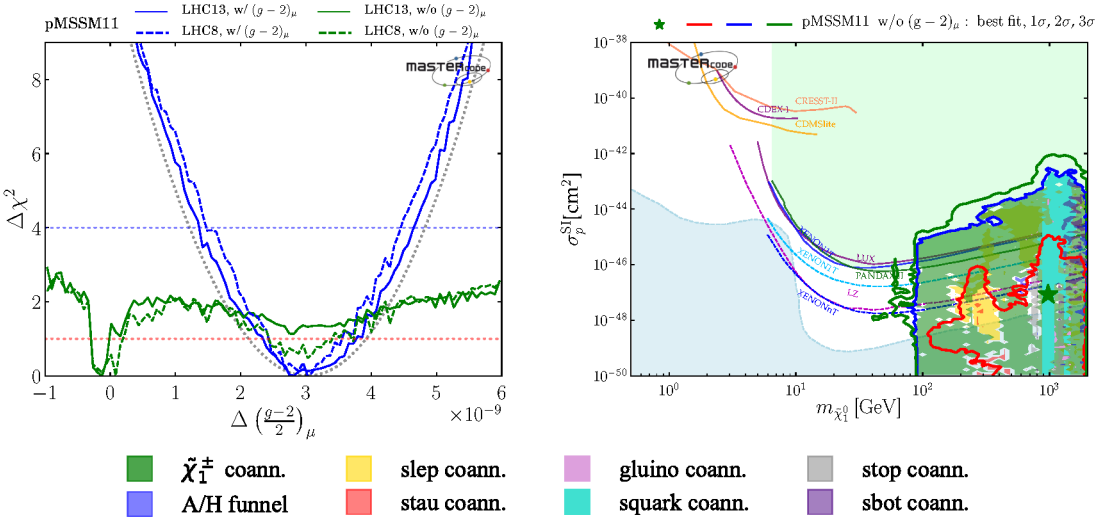


Figure 12: On the left, the one-dimensional likelihood profile for the SUSY contribution to $\Delta((g-2)/2)$ in the pMSSM11. We show four different profiles, with (solid) and without (dashed) the constraints coming from the direct searches for coloured superpartners at LHC run-2 and with (blue) and without (green) the constraint coming from $(g-2)_\mu$. On the right, the two-dimensional likelihood profiles in the pMSSM11 in the $m_{\tilde{\chi}_1^0}$-σ_p^{SI} plane. The colour shadings indicate the dominant mechanism which moves the CDM density into the allowed range from cosmological observations. Figures taken from Ref. [47].

U and -0.87 between T and U. The 68 % and 95 % CL allowed regions on S and T for a fixed value of $U = 0$ are shown in Fig.14. The constraints obtained for individual observables with strongest sensitivities are compatible with each other and their combination yields allowed regions in agreement with the prediction of the reference SM. These results on the oblique parameters are used by analyses to constrain the allowed parameter regions of new physics models. Example results for such analyses before the Higgs boson discovery are derived in [8] for a fourth fermion generation, two Higgs doublet, inert Higgs and littlest Higgs models, models with large, universal or warped extra dimensions and technicolour.

5.2 Global fits of two-Higgs-doublet models

A popular extension of the minimal Higgs sector, as implemented in the SM, are Two-Higgs-doublet models (2HDM) [95] which only introduce an additional $SU(2)_L \times U(1)_Y$ Higgs doublet field with hypercharge $Y = 1$, leading to five physical Higgs bosons h, H, A, H^+, and H^-. The neutral h can be identified with the 125 GeV Higgs boson as discovered at the LHC. Free model parameters of the 2HDM are the masses of these boson states M_{A^0}, M_{h^0}, M_{H^0} and $M_{H^\pm}$, the ratio of the vacuum expectation values of the two Higgs doublets $\tan\beta = v_2/v_1$ and the angle α describing the mixing of the two neutral Higgs fields h and H. In general, the 2HDM may lead to flavour-changing neutral currents (FCNCs) and CP violating interactions which can be avoided by fixing the Higgs boson couplings for up-type quarks, down-type quarks and leptons to specific values [95, 96]. Most popular CP conserving 2HDM scenarios include the *Type-I*

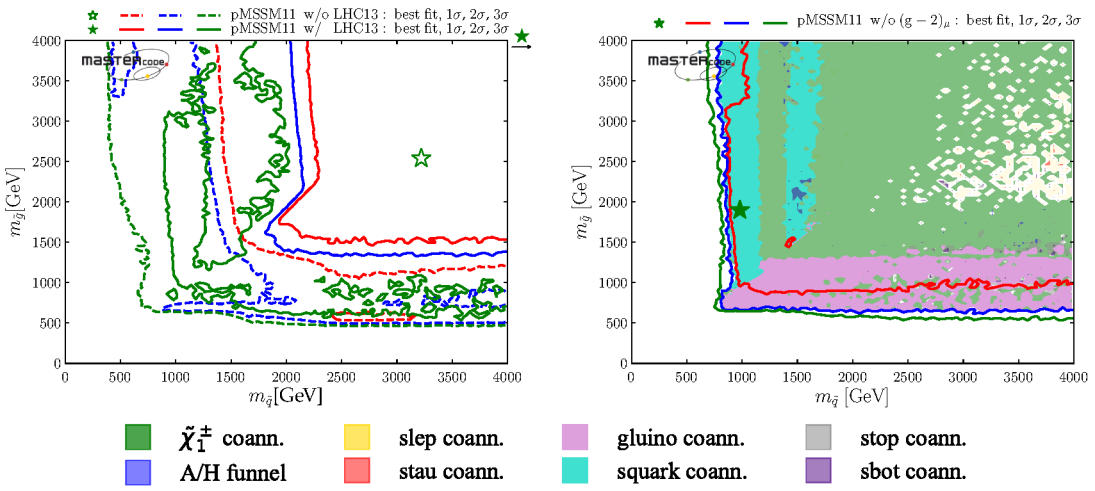


Figure 13: On the left, we show the two-dimensional likelihood profiles in the $m_{\tilde{q}_{1,2}}$-$m_{\tilde{g}}$ plane before (dashed lines) and after (solid lines) applying the constraints coming from LHC run-2 results, including flavour, and from the results of direct detection experiments after 2015. On the right, we display the same plane, with the full constraint set applied but for $(g-2)_\mu$. The colour shadings represent the dominant DM mechanism, with the colour coding defined in the legend below the plots. Figures taken from Ref. [47].

scenario, the *Type-II* scenario, the *lepton specific* scenario, and the *flipped* scenario.

Measurements of observables with sensitivity to the existence of the additional 2HDM Higgs bosons via quantum corrections can be used in global fits to constrain the allowed ranges of the Higgs boson masses and mixing angles in these scenarios. Within this project we performed several 2HDM analyses using the `Gfitter` framework. A first analysis before the Higgs discovery [7] was restricted to the Type-II scenario and only included observables sensitive to corrections from the exchange of a charged Higgs boson. At the time, the most stringent constraints have been obtained from rare radiative and leptonic decays of B and K mesons in which the charged Higgs boson replaces a SM W boson in the charged current process. A second 2HDM analysis [8] showed that constraints from the oblique parameters (cf. Sec. 5.1) do not allow a determination of any of the free 2HDM parameters independently of the values of the other parameters. A third analysis [11] after the Higgs boson discovery used individually the data from Higgs boson coupling measurements, from flavour observables (mainly branching fractions of B, D and K mesons), the anomalous magnetic moment of the muon, and the electroweak precision data via the oblique parameters and combined them in a global fit. In the following only results of this most recent study are discussed.

By construction of the four 2HDM scenarios considered, FCNC transitions are forbidden at tree-level and flavour violation can only arise at loop level by the exchange of a charged Higgs boson with strength depending on $M_{H^\pm}$ and $\tan\beta$. Example constraints obtained from the individual flavour observables are shown in Fig. 15 (left) where the excluded parameter regions (95 % CL) in the Type-II scenario are shown in the plane of these two sensitive parameters. Most stringent constraints are obtained from the branching fraction $\mathcal{B}(b \to X_s\gamma)$ which allows to exclude $M_{H^\pm} < 590\,\text{GeV}$. It is interesting to note that the measurements of the semileptonic

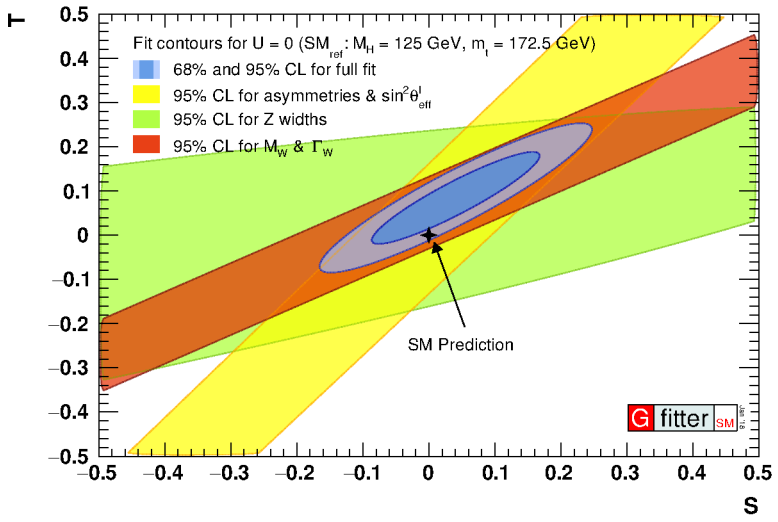


Figure 14: Allowed regions of the oblique parameters S and T, with the U parameter fixed to zero, as obtained from the global electroweak fit using all observables (blue) and for individual sensitive observables (yellow, green, red). Figure taken from Ref. [11].

decay ratios of neutral B mesons $R(D)$ and $R(D^*)$ which differ from their SM predictions [97] only feature a compatible parameter region in the Type-II scenario which is however excluded by several other observables (not shown in the figure).

Example constraints for the Type-II scenario from the combined analysis of Higgs coupling measurements, flavour observables, magnetic moment of the muon and the oblique parameters are shown in Fig. 15 (right) where the resulting 68 % and 95 % CL allowed regions in the M_A versus M_H plane are shown for a fixed charged Higgs boson mass of 750 GeV. All other 2HDM parameters are allowed to vary freely. A strong alignment of either the H or the A boson mass with the mass of the $H^\pm$ can be observed (this is true for all 2HDM scenarios considered) as a result of constraints on $\beta - \alpha$ obtained from the Higgs coupling strength measurements. For the Type-II scenario (and the flipped scenario, not shown) pairs of (H, A) masses below $\sim$ 400 GeV are excluded as indicated by the hatched regions where also results of different statistical interpretations are illustrated by red and green lines. However, our analysis also demonstrated that no absolute mass limits can be derived with current data for the Type-I and lepton specific scenarios.

5.3 Constraints on Higgs physics-relevant $d = 6$ operators

If new physical effects stay elusive and direct searches for new physics at the LHC continue to produce null results, this could point towards high-scale new physics. While no new states would be observable at energy scales reachable at the LHC, this nevertheless can lead to subtle deviations from SM expectations which might still be observable. In this scenario, not a single measurement alone would lead to a discovery, but small hints would emerge in a number of different channels.

Under this predicament, the most promising avenue for finding new physics are precision

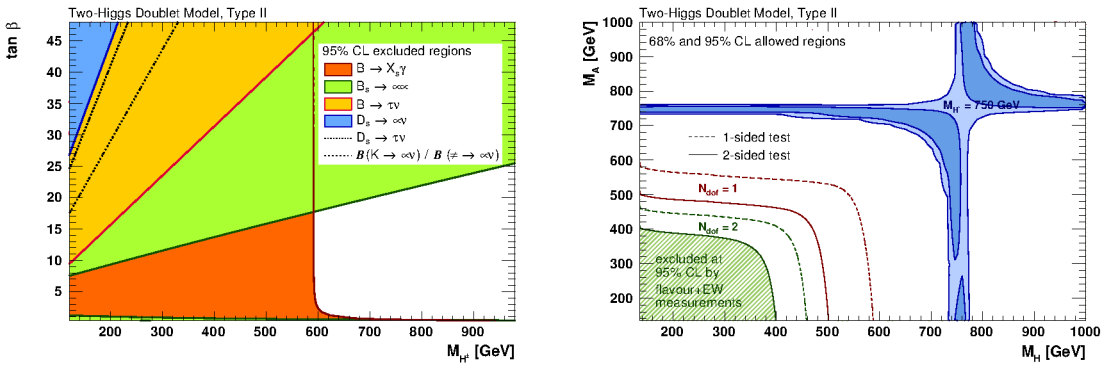


Figure 15: Results of fits of 2HDM models of Type II: (left) excluded parameter regions in the $\tan\beta$ versus $M_{H^\pm}$ plane as obtained from individual flavour observables; (right) allowed regions in the M_A versus M_H plane as obtained from a combined fit of constraints from the Higgs boson coupling strength measurements, flavour observables, muon anomalous magnetic moment and electroweak precision data. Figures taken from Ref. [11].

studies of Higgs production, which is the least constraint sector of the SM. This motivates the extension of the Lagrangian of the Higgs sector by dimension six ($d = 6$) operators

$$\mathcal{L}_{\text{Higgs}} = \mathcal{L}^{\text{SM}}_{\text{Higgs}} + \sum_i \frac{c_i}{\Lambda^2} O_i \tag{1}$$

to capture new interactions beyond the Standard Model (BSM) in a model-independent way. The first term on the right-hand side of Eq. 1 is the SM Lagrangian of the Higgs sector, while the second term denotes BSM contributions from $d = 6$ operators O_i, which scale with the Wilson coefficients c_i over the square of the scale of new physics Λ^2. This extension assumes that all unknown states have been integrated out and only the effect of the resulting $d = 6$ operators are observable at present colliders. An important question that arises is the extent to which it will be possible to probe the presence of such interactions. Or equivalently, what are realistic estimates of Wilson coefficient constraints that can be expected after LHC run-2 and LHC run-3 or after the high luminosity phase of the LHC (HL-LHC) if direct hints for new physics will remain elusive?

To study this question the set of operators known as the strongly interacting light Higgs (SILH) Lagrangian in bar convention [98] has been considered in global analyses using the `Gfitter` framework [12, 13]. Focusing on the Higgs sector with flavour-diagonal dimension six effects and respecting constraints from oblique corrections to LEP data through the S and T parameters, the number of relevant operators is eight. Using LHC run-1 Higgs data from ATLAS and CMS two coefficients, $\bar{c}_g$ and $\bar{c}_\gamma$, can be reliably constrained in a global fit at 95% CL:

$$\begin{aligned} \bar{c}_g &\in [\,-0.64,\, 0.43\,] \times 10^{-4} \\ \bar{c}_\gamma &\in [\,-7.8,\, 4.3\,] \times 10^{-4}\,, \end{aligned} \tag{2}$$

where the constraints from the likelihood scan of $\bar{c}_g$ are shown in Fig. 16 (left). There are no noteworthy constraints on the other six operators from LHC run-1 data, which is only partially

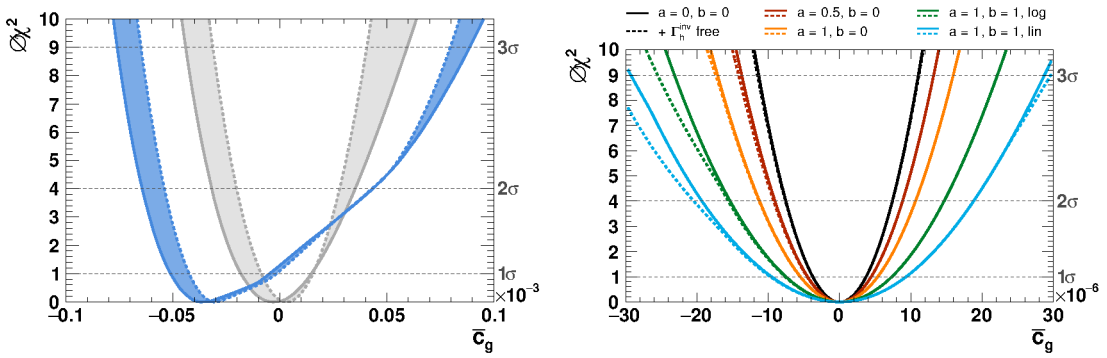


Figure 16: Constraints of the Wilson coefficient $\bar{c}_g$: results as obtained from the LHC run-1 dataset (left). The solid (dashed) line corresponds to a fit with theoretical uncertainties included (excluded). The grey band denotes the individual constraints on $\bar{c}_g$, and blue refers to the marginalised result; sensitivity projection for HL-LHC using differential Higgs p_T distributions (right). Figures taken from Refs. [12] and [13], respectively.

due to the insufficient precision of these data. When projecting to the expected precision achieved after the HL-LHC, still a number of operators cannot be constrained in a global fit [12] due to so-called flat directions in the multi-dimensional parameter space, which are due to effects from new physics that cancel out on inclusive Higgs observables and hence lead to unobservable BSM contributions.

These flat directions can be lifted by including measurements of differential distributions of Higgs boson production, most notably the Higgs boson transverse momentum p_T. The reason for this is the large effect of BSM contributions to the tails of the p_T distributions. When including measurements in all observable Higgs production modes and decay channels at the LHC, the effects of the various $d = 6$ operators do not cancel out fully anymore leading to the prospect of constraints on all operators, albeit the constraints on the Higgs-fermion operators will stay weaker than the ones on the Higgs boson ones. The likelihood scans shown in Fig. 16 (right) show the constraints on $\bar{c}_g$ obtained from pseudo data extrapolated to the HL-LHC precision. The different colours denote assumptions on the theoretical uncertainties, and dashed lines have been obtained in a scenario where an additional unobservable contribution to the total width of the Higgs boson from light degrees of freedom has been taken into account. While there are differences of up to a factor of two on the sensitivity at 95% CL for different assumptions, even with overly pessimistic theoretical uncertainties in the tails of the distributions ($a = 1$, $b = 1$, lin), stronger bounds can be obtained than by considering signal strength measurements only [13]. In this sense, differential measurements of Higgs boson production can help to improve the physics potential of the LHC when combined in a global fit with inclusive data.

6 Conclusions

We have summarized the highlight results of the project B8 of the SFB 676: developments of the software tools `Gfitter`, `Fittino`, `MasterCode`, `HiggsBounds` and `HiggsSignals` as well as physics results obtained from the application of these tools in global fits of the SM, supersym-

metric models and further extensions of the SM.

The experimental results used in the global fits consist of measurements of electroweak precision observables, measurements of the properties of the Higgs signal at 125 GeV, limits from searches for additional Higgs bosons and further states of physics scenarios beyond the SM, results from flavor physics, the dark matter relic density and further astrophysical data. If the results of the dark matter relic density and the magnetic moment of the muon are discarded from the considered data set, the SM with a Higgs boson at 125 GeV is compatible with the experimental results at the present level. However, the same is true, even after including the dark matter relic density and the magnetic moment of the muon, for various supersymmetric extensions of the SM and further scenarios of new physics. We have determined the parameter regions that are preferred by the current data, for a variety of models, which represent attractive alternatives to the SM and are based on fundamentally different physics assumptions.

The identification of the mechanism of electroweak symmetry breaking and more generally the structure of the electroweak and strong interactions will continue to be a prime target of particle physics research during the next decades. The prospective improvements in experimental precision in combination with corresponding efforts in theoretical calculations will significantly enhance the sensitivity for discriminating between different realisations of the underlying dynamics, and global fits will be of crucial importance for accomplishing this task. The results of this project constitute a significant progress in this area and provide the foundations for future analyses.

Acknowledgements

E. B. and G. W. would like to thank their collaborators on the `MasterCode` project, J.C. Costa, M. Borsato, O. Buchmueller, R. Cavanaugh, M. Citron, A. De Roeck, M.J. Dolan, J.R. Ellis, H. Flächer, S. Heinemeyer, G. Isidori, M. Lucio, D. Martínez Santos, K.A. Olive, A. Richards, K. Sakurai and K.J. De Vries. J. H., R. K. and T. P. would like to thank the current and past members of the `Gfitter` group for their collaboration and support, M. Baak, J. Cuth, H. Flächer, M. Goebel, A. Hoecker, D. Kennedy, K. Mönig, M. Schott and J. Stelzer. P. B. and T. S. would like to thank the current and past members of the `Fittino` group, K. Desch, H. Dreiner, M. Hamer, M. Krämer, B. O'Leary, W. Porod, B. Sarrazin, M. Uhlenbrock and P. Wienemann. P. B., T. S. and G. W. would like to thank the current and past members of the `HiggsBounds` and `HiggsSignals` projects for their collaboration and support, O. Brein, S. Heinemeyer, O. Stål, K.E. Williams. We would furthermore like to thank H. Haber, A. Weiler and L. Zeune for fruitful collaboration.

The work presented in this report has been supported in part by the DFG through the SFB 676 "Particles, Strings and the Early Universe".

References

[1] SLD Electroweak Group, DELPHI, ALEPH, SLD, SLD Heavy Flavour Group, OPAL, LEP Electroweak Working Group, L3, S. Schael et al., *Precision electroweak measurements on the Z resonance*, *Phys. Rept.* **427** (2006) 257–454, [hep-ex/0509008].

[2] The yearly reports of the LEP Electroweak Working Group can be found at http://lepewwg.web.cern.ch/LEPEWWG/stanmod.

[3] All versions of the PDG particle listings and reviews can be found at http://pdg.lbl.gov/2016/html/rpp_archives.html.

[4] Gfitter Group. Results at http://cern.ch/gfitter.

[5] HEPFIT GROUP. Results at http://hepfit.roma1.infn.it.

[6] M. Baak, J. Haller and K. Mönig, *Global Fits of the Electroweak Standard Theory: Past, Present and Future*, *Adv. Ser. Direct. High Energy Phys.* **26** (2016) 215–229.

[7] GFITTER GROUP, H. Flacher, M. Goebel, J. Haller, A. Hocker, K. Monig and J. Stelzer, *Revisiting the Global Electroweak Fit of the Standard Model and Beyond with Gfitter*, *Eur. Phys. J.* **C60** (2009) 543–583, [0811.0009]. [Erratum: *Eur. Phys. J.* **C71** (2011) 1718].

[8] GFITTER GROUP, M. Baak, M. Goebel, J. Haller, A. Hoecker, D. Ludwig, K. Moenig et al., *Updated Status of the Global Electroweak Fit and Constraints on New Physics*, *Eur. Phys. J.* **C72** (2012) 2003, [1107.0975].

[9] GFITTER GROUP, M. Baak, M. Goebel, J. Haller, A. Hoecker, D. Kennedy, R. Kogler et al., *The Electroweak Fit of the Standard Model after the Discovery of a New Boson at the LHC*, *Eur. Phys. J.* **C72** (2012) 2205, [1209.2716].

[10] GFITTER GROUP, M. Baak, J. Cúth, J. Haller, A. Hoecker, R. Kogler, K. Mönig et al., *The global electroweak fit at NNLO and prospects for the LHC and ILC*, *Eur. Phys. J.* **C74** (2014) 3046, [1407.3792].

[11] GFITTER GROUP, J. Haller, A. Hoecker, R. Kogler, K. Mönig, T. Peiffer and J. Stelzer, *Update of the global electroweak fit and constraints on two-Higgs-doublet models*, *Eur. Phys. J.* **C78** (2018) 675, [1803.01853].

[12] C. Englert, R. Kogler, H. Schulz and M. Spannowsky, *Higgs coupling measurements at the LHC*, *Eur. Phys. J.* **C76** (2016) 393, [1511.05170].

[13] C. Englert, R. Kogler, H. Schulz and M. Spannowsky, *Higgs characterisation in the presence of theoretical uncertainties and invisible decays*, *Eur. Phys. J.* **C77** (2017) 789, [1708.06355].

[14] D0 Collaboration, S. Abachi et al., *Observation of the top quark*, *Phys. Rev. Lett.* **74** (1995) 2632–2637, [hep-ex/9503003].

[15] CDF Collaboration, F. Abe et al., *Observation of top quark production in $\bar{p}p$ collisions*, *Phys. Rev. Lett.* **74** (1995) 2626–2631, [hep-ex/9503002].

[16] ATLAS Collaboration, G. Aad et al., *Observation of a new particle in the search for the Standard Model Higgs boson with the ATLAS detector at the LHC*, *Phys. Lett.* **B716** (2012) 1–29, [1207.7214].

[17] CMS Collaboration, S. Chatrchyan et al., *Observation of a new boson at a mass of 125 GeV with the CMS experiment at the LHC*, *Phys. Lett.* **B716** (2012) 30–61, [1207.7235].

[18] ATLAS, CMS Collaborations, G. Aad et al., *Combined Measurement of the Higgs Boson Mass in pp Collisions at $\sqrt{s} = 7$ and 8 TeV with the ATLAS and CMS Experiments*, *Phys. Rev. Lett.* **114** (2015) 191803, [1503.07589].

[19] PARTICLE DATA GROUP, C. Patrignani et al., *Review of Particle Physics*, *Chin. Phys.* **C40** (2016) 100001.

[20] DELPHI, OPAL, LEP ELECTROWEAK, ALEPH, L3 Collaborations, S. Schael et al., *Electroweak Measurements in Electron-Positron Collisions at W-Boson-Pair Energies at LEP*, *Phys. Rept.* **532** (2013) 119–244, [1302.3415].

[21] CDF, D0 Collaborations, T. E. W. Group, *2012 Update of the Combination of CDF and D0 Results for the Mass of the W Boson*, 1204.0042.

[22] ATLAS Collaboration, M. Aaboud et al., *Measurement of the W-boson mass in pp collisions at $\sqrt{s} = 7$ TeV with the ATLAS detector*, *Eur. Phys. J.* **C78** (2018) 110, [1701.07240].

[23] CDF, D0 Collaborations, T. A. Aaltonen et al., *Tevatron Run II combination of the effective leptonic electroweak mixing angle*, *Phys. Rev.* **D97** (2018) 112007, [1801.06283].

[24] M. Davier, A. Hoecker, B. Malaescu and Z. Zhang, *Reevaluation of the hadronic vacuum polarisation contributions to the Standard Model predictions of the muon $g-2$ and $\alpha(m_Z^2)$ using newest hadronic cross-section data*, *Eur. Phys. J.* **C77** (2017) 827, [1706.09436].

[25] OPAL, DELPHI, LEP WORKING GROUP FOR HIGGS BOSON SEARCHES, ALEPH, L3, R. Barate et al., *Search for the standard model Higgs boson at LEP*, *Phys. Lett.* **B565** (2003) 61–75, [hep-ex/0306033].

[26] CDF, D0 Collaborations, T. T. E. V. N. P. H. W. Group, *Combined CDF and D0 Upper Limits on Standard Model Higgs-Boson Production with up to 6.7 fb^{-1} of Data*, in *Proceedings, 35th International Conference on High energy physics (ICHEP 2010): Paris, France, July 22-28, 2010*, 2010, 1007.4587.

[27] DELPHI, OPAL, ALEPH, LEP WORKING GROUP FOR HIGGS BOSON SEARCHES, L3, S. Schael et al., *Search for neutral MSSM Higgs bosons at LEP*, *Eur. Phys. J.* **C47** (2006) 547–587, [hep-ex/0602042].

[28] D0 Collaboration, V. M. Abazov et al., *Search for Higgs bosons of the minimal supersymmetric standard model in $p\bar{p}$ collisions at $\sqrt{(}s) = 1.96$ TeV*, *Phys. Lett.* **B710** (2012) 569–577, [1112.5431].

[29] CDF Collaboration, T. Aaltonen et al., *Search for Higgs bosons predicted in two-Higgs-doublet models via decays to tau lepton pairs in 1.96-TeV p anti-p collisions*, *Phys. Rev. Lett.* **103** (2009) 201801, [0906.1014].

[30] P. Bechtle, O. Brein, S. Heinemeyer, G. Weiglein and K. E. Williams, *HiggsBounds: Confronting Arbitrary Higgs Sectors with Exclusion Bounds from LEP and the Tevatron*, *Comput. Phys. Commun.* **181** (2010) 138–167, [0811.4169].

[31] P. Bechtle, O. Brein, S. Heinemeyer, G. Weiglein and K. E. Williams, *HiggsBounds 2.0.0: Confronting Neutral and Charged Higgs Sector Predictions with Exclusion Bounds from LEP and the Tevatron*, *Comput. Phys. Commun.* **182** (2011) 2605–2631, [1102.1898].

[32] P. Bechtle, O. Brein, S. Heinemeyer, O. Stal, T. Stefaniak, G. Weiglein et al. code available from http://higgsbounds.hepforge.org/.

[33] P. Bechtle, O. Brein, S. Heinemeyer, O. Stål, T. Stefaniak, G. Weiglein et al., HiggsBounds – 4*: Improved Tests of Extended Higgs Sectors against Exclusion Bounds from LEP, the Tevatron and the LHC*, *Eur. Phys. J.* **C74** (2014) 2693, [1311.0055].

[34] P. Bechtle, S. Heinemeyer, O. Stal, T. Stefaniak and G. Weiglein, *Applying Exclusion Likelihoods from LHC Searches to Extended Higgs Sectors*, *Eur. Phys. J.* **C75** (2015) 421, [1507.06706].

[35] CMS Collaboration, V. Khachatryan et al., *Search for neutral MSSM Higgs bosons decaying to a pair of tau leptons in pp collisions*, *JHEP* **10** (2014) 160, [1408.3316].

[36] ATLAS, CMS Collaborations, G. Aad et al., *Measurements of the Higgs boson production and decay rates and constraints on its couplings from a combined ATLAS and CMS analysis of the LHC pp collision data at $\sqrt{s} = 7$ and 8 TeV*, *JHEP* **08** (2016) 045, [1606.02266].

[37] P. Bechtle, S. Heinemeyer, O. Stal, T. Stefaniak, G. Weiglein and L. Zeune, *MSSM Interpretations of the LHC Discovery: Light or Heavy Higgs?*, *Eur. Phys. J.* **C73** (2013) 2354, [1211.1955].

[38] P. Bechtle, S. Heinemeyer, O. Stål, T. Stefaniak and G. Weiglein, *HiggsSignals: Confronting arbitrary Higgs sectors with measurements at the Tevatron and the LHC*, *Eur. Phys. J.* **C74** (2014) 2711, [1305.1933].

[39] P. Bechtle, S. Heinemeyer, O. Stål, T. Stefaniak and G. Weiglein, *Probing the Standard Model with Higgs signal rates from the Tevatron, the LHC and a future ILC*, *JHEP* **11** (2014) 039, [1403.1582].

[40] LHC HIGGS CROSS SECTION WORKING GROUP, D. de Florian et al., *Handbook of LHC Higgs Cross Sections: 4. Deciphering the Nature of the Higgs Sector*, 1610.07922.

[41] P. Bechtle, H. E. Haber, S. Heinemeyer, O. Stål, T. Stefaniak, G. Weiglein et al., *The Light and Heavy Higgs Interpretation of the MSSM*, *Eur. Phys. J.* **C77** (2017) 67, [1608.00638].

[42] F. Domingo and G. Weiglein, *NMSSM interpretations of the observed Higgs signal*, *JHEP* **04** (2016) 095, [1509.07283].

[43] P. Drechsel, L. Galeta, S. Heinemeyer and G. Weiglein, *Precise Predictions for the Higgs-Boson Masses in the NMSSM*, *Eur. Phys. J.* **C77** (2017) 42, [1601.08100].

[44] PLANCK Collaboration, P. A. R. Ade et al., *Planck 2013 results. XVI. Cosmological parameters*, *Astron. Astrophys.* **571** (2014) A16, [1303.5076].

[45] MUON G-2 COLLABORATION, G. Bennett et al., *Final Report of the Muon E821 Anomalous Magnetic Moment Measurement at BNL*, *Phys.Rev.* **D73** (2006) 072003, [hep-ex/0602035].

[46] K. J. de Vries et al., *The pMSSM10 after LHC Run 1*, *Eur. Phys. J.* **C75** (2015) 422, [1504.03260].

[47] E. Bagnaschi et al., *Likelihood Analysis of the pMSSM11 in Light of LHC 13-TeV Data*, *Eur. Phys. J.* **C78** (2018) 256, [1710.11091].

[48] O. Buchmueller et al., *The CMSSM and NUHM1 after LHC Run 1*, *Eur. Phys. J.* **C74** (2014) 2922, [1312.5250].

[49] O. Buchmueller et al., *The NUHM2 after LHC Run 1*, *Eur. Phys. J.* **C74** (2014) 3212, [1408.4060].

[50] M. Cannoni, J. Ellis, M. E. Gómez, S. Lola and R. Ruiz de Austri, *Supersymmetry Searches in GUT Models with Non-Universal Scalar Masses*, *JCAP* **1603** (2016) 041, [1511.06205].

[51] E. Bagnaschi et al., *Likelihood Analysis of the Minimal AMSB Model*, *Eur. Phys. J.* **C77** (2017) 268, [1612.05210].

[52] P. Bechtle, K. Desch and P. Wienemann, *Fittino, a program for determining MSSM parameters from collider observables using an iterative method*, *Comput. Phys. Commun.* **174** (2006) 47–70, [hep-ph/0412012].

[53] P. Bechtle et al., *Killing the cMSSM softly*, *Eur. Phys. J.* **C76** (2016) 96, [1508.05951].

[54] P. Bechtle, K. Desch, M. Uhlenbrock and P. Wienemann, *Constraining SUSY models with Fittino using measurements before, with and beyond the LHC*, *Eur. Phys. J.* **C66** (2010) 215–259, [0907.2589].

[55] P. Bechtle, B. Sarrazin, K. Desch, H. K. Dreiner, P. Wienemann, M. Kramer et al., *What if the LHC does not find supersymmetry in the $\sqrt{s} = 7$ TeV run?*, *Phys. Rev.* **D84** (2011) 011701, [1102.4693].

[56] P. Bechtle et al., *Constrained Supersymmetry after two years of LHC data: a global view with Fittino*, *JHEP* **06** (2012) 098, [1204.4199].

[57] M. Kramer et al., *Constrained supersymmetric models in the light of LHC exclusions, precision measurements and astroparticle physics*, *Frascati Phys. Ser.* **54** (2012) 258–266.

[58] A. De Roeck et al., *From the LHC to Future Colliders*, *Eur. Phys. J.* **C66** (2010) 525–583, [0909.3240].

[59] GAMBIT Collaboration, G. D. Martinez, J. McKay, B. Farmer, P. Scott, E. Roebber, A. Putze et al., *Comparison of statistical sampling methods with ScannerBit, the GAMBIT scanning module*, *Eur. Phys. J.* **C77** (2017) 761, [1705.07959].

[60] W. Porod and F. Staub, *SPheno 3.1: Extensions including flavour, CP-phases and models beyond the MSSM*, *Comput.Phys.Commun.* **183** (2012) 2458–2469, [1104.1573].

[61] F. Mahmoudi, *SuperIso v2.3: A Program for calculating flavor physics observables in Supersymmetry*, *Comput.Phys.Commun.* **180** (2009) 1579–1613, [0808.3144].

[62] G. Belanger, F. Boudjema, A. Pukhov and A. Semenov, *MicrOMEGAs: A Program for calculating the relic density in the MSSM*, *Comput.Phys.Commun.* **149** (2002) 103–120, [hep-ph/0112278].

[63] S. Heinemeyer, W. Hollik and G. Weiglein, *FeynHiggs: A Program for the calculation of the masses of the neutral CP even Higgs bosons in the MSSM*, *Comput. Phys. Commun.* **124** (2000) 76–89, [hep-ph/9812320].

[64] P. Bechtle, S. Belkner, D. Dercks, M. Hamer, T. Keller, M. Krämer et al., *SCYNet: Testing supersymmetric models at the LHC with neural networks*, *Eur. Phys. J.* **C77** (2017) 707, [1703.01309].

[65] M. Drees, H. Dreiner, D. Schmeier, J. Tattersall and J. S. Kim, *CheckMATE: Confronting your Favourite New Physics Model with LHC Data*, *Comput. Phys. Commun.* **187** (2015) 227–265, [1312.2591].

[66] J. Albrecht, F. Bernlochner, M. Kenzie, S. Reichert, D. Straub and A. Tully, *Future prospects for exploring present day anomalies in flavour physics measurements with Belle II and LHCb*, 1709.10308.

[67] P. Z. Skands et al., *SUSY Les Houches accord: Interfacing SUSY spectrum calculators, decay packages, and event generators*, *JHEP* **07** (2004) 036, [hep-ph/0311123].

[68] T. Hahn, *SUSY Les Houches Accord 2 I/O made easy*, *Comput. Phys. Commun.* **180** (2009) 1681–1693, [hep-ph/0605049].

[69] B. C. Allanach, *SOFTSUSY: a program for calculating supersymmetric spectra*, *Comput. Phys. Commun.* **143** (2002) 305–331, [hep-ph/0104145].

[70] S. Heinemeyer, W. Hollik and G. Weiglein, *The Masses of the neutral CP - even Higgs bosons in the MSSM: Accurate analysis at the two loop level*, *Eur. Phys. J.* **C9** (1999) 343–366, [hep-ph/9812472].

[71] G. Degrassi, S. Heinemeyer, W. Hollik, P. Slavich and G. Weiglein, *Towards high precision predictions for the MSSM Higgs sector*, *Eur. Phys. J.* **C28** (2003) 133–143, [hep-ph/0212020].

[72] M. Frank et al., *The Higgs Boson Masses and Mixings of the Complex MSSM in the Feynman-Diagrammatic Approach*, *JHEP* **02** (2007) 047, [hep-ph/0611326].

[73] T. Hahn et al., *High-Precision Predictions for the Light CP -Even Higgs Boson Mass of the Minimal Supersymmetric Standard Model*, *Phys. Rev. Lett.* **112** (2014) 141801, [1312.4937].

[74] G. Belanger, F. Boudjema, A. Pukhov and A. Semenov, *micrOMEGAs_3: A program for calculating dark matter observables*, *Comput. Phys. Commun.* **185** (2014) 960–985, [1305.0237].

[75] G. Isidori and P. Paradisi, *Hints of large tan(beta) in flavour physics*, *Phys. Lett.* **B639** (2006) 499–507, [hep-ph/0605012].

[76] G. Isidori, F. Mescia, P. Paradisi and D. Temes, *Flavour physics at large tan(beta) with a Bino-like LSP*, *Phys. Rev.* **D75** (2007) 115019, [hep-ph/0703035].

[77] F. Mahmoudi, *SuperIso: A Program for calculating the isospin asymmetry of B —> K* gamma in the MSSM*, *Comput. Phys. Commun.* **178** (2008) 745–754, [0710.2067].

[78] D. Eriksson, F. Mahmoudi and O. Stal, *Charged Higgs bosons in Minimal Supersymmetry: Updated constraints and experimental prospects*, *JHEP* **11** (2008) 035, [0808.3551].

[79] S. Heinemeyer, W. Hollik, D. Stockinger, A. M. Weber and G. Weiglein, *Precise prediction for M(W) in the MSSM*, *JHEP* **08** (2006) 052, [hep-ph/0604147].

[80] S. Heinemeyer, W. Hollik, A. M. Weber and G. Weiglein, *Z Pole Observables in the MSSM*, *JHEP* **04** (2008) 039, [0710.2972].

[81] S. Heinemeyer, W. Hollik, G. Weiglein and L. Zeune, *Implications of LHC search results on the W boson mass prediction in the MSSM*, *JHEP* **12** (2013) 084, [1311.1663].

[82] F. Feroz and M. P. Hobson, *Multimodal nested sampling: an efficient and robust alternative to MCMC methods for astronomical data analysis*, *Mon. Not. Roy. Astron. Soc.* **384** (2008) 449, [0704.3704].

[83] F. Feroz, M. P. Hobson and M. Bridges, *MultiNest: an efficient and robust Bayesian inference tool for cosmology and particle physics*, *Mon. Not. Roy. Astron. Soc.* **398** (2009) 1601–1614, [0809.3437].

[84] F. Feroz, M. P. Hobson, E. Cameron and A. N. Pettitt, *Importance Nested Sampling and the MultiNest Algorithm*, 1306.2144.

[85] J. Gomes, I. Campos, E. Bagnaschi, M. David, L. Alves, J. Martins et al., *Enabling rootless Linux Containers in multi-user environments: the udocker tool*, *Comput. Phys. Commun.* **232** (2018) 84–97, [1711.01758].

[86] E. A. Bagnaschi et al., *Supersymmetric Dark Matter after LHC Run 1*, *Eur. Phys. J.* **C75** (2015) 500, [1508.01173].

[87] E. Bagnaschi et al., *Likelihood Analysis of Supersymmetric SU(5) GUTs*, *Eur. Phys. J.* **C77** (2017) 104, [1610.10084].

[88] M. Papucci, K. Sakurai, A. Weiler and L. Zeune, *Fastlim: a fast LHC limit calculator*, *Eur. Phys. J.* **C74** (2014) 3163, [1402.0492].

[89] W. Beenakker, M. Kramer, T. Plehn, M. Spira and P. M. Zerwas, *Stop production at hadron colliders*, *Nucl. Phys.* **B515** (1998) 3–14, [hep-ph/9710451].

[90] W. Beenakker, C. Borschensky, M. Krämer, A. Kulesza, E. Laenen, S. Marzani et al., *NLO+NLL squark and gluino production cross-sections with threshold-improved parton distributions*, *Eur. Phys. J.* **C76** (2016) 53, [1510.00375].

[91] J. C. Costa et al., *Likelihood Analysis of the Sub-GUT MSSM in Light of LHC 13-TeV Data*, *Eur. Phys. J.* **C78** (2018) 158, [1711.00458].

[92] E. Bagnaschi, P. Michele, K. Sakurai, W. A. and L. Zeune, *EWKFast: a fast calculator for EWKino production processes at the LHC*, *In preparation,* (2018) .

[93] M. E. Peskin and T. Takeuchi, *A New constraint on a strongly interacting Higgs sector*, *Phys. Rev. Lett.* **65** (1990) 964–967.

[94] M. E. Peskin and T. Takeuchi, *Estimation of oblique electroweak corrections*, *Phys. Rev.* **D46** (1992) 381–409.

[95] H. E. Haber, G. L. Kane and T. Sterling, *The Fermion Mass Scale and Possible Effects of Higgs Bosons on Experimental Observables*, *Nucl. Phys.* **B161** (1979) 493–532.

[96] G. C. Branco, P. M. Ferreira, L. Lavoura, M. N. Rebelo, M. Sher and J. P. Silva, *Theory and phenomenology of two-Higgs-doublet models*, *Phys. Rept.* **516** (2012) 1–102, [1106.0034].

[97] HFLAV Collaboration, Y. Amhis et al., *Averages of b-hadron, c-hadron, and τ-lepton properties as of summer 2016*, *Eur. Phys. J.* **C77** (2017) 895, [1612.07233].

[98] G. F. Giudice, C. Grojean, A. Pomarol and R. Rattazzi, *The Strongly-Interacting Light Higgs*, *JHEP* **06** (2007) 045, [hep-ph/0703164].

Probing the Nature of Higgs Physics and Electroweak Symmetry Breaking with Results from the LHC

Alexei Raspereza[1], *Peter Schleper*[2], *Kerstin Tackmann*[1,2], *Georg Weiglein*[1]

[1]DESY, Hamburg, Germany
[2]Institut für Experimentalphysik, Universität Hamburg, Germany

DOI: http://dx.doi.org/10.3204/PUBDB-2018-00782/B9

The discovery of a Higgs signal at the LHC marks the beginning of a new era of particle physics. The prime goal now is to identify the underlying physics of the new state and to determine the mechanism of electroweak symmetry breaking. Some of the results obtained in this project are highlighted, covering both the period before and after the discovery. In particular, the properties of the new state have been investigated in close cooperation between experiment and theory and the possible interpretations of the observed signal have been analysed. Confronting the experimental results on the signal as well as from the search limits with model predictions, the resulting constraints on the parameter space of different models and their phenomenological implications have been demonstrated.*

1 Introduction

Identifying the physics that is responsible for providing elementary particles with the property of mass is one of the key issues in the quest for a better understanding of the fundamental interactions of nature. Within the present experimental and theoretical uncertainties the properties of the signal that was detected in the Higgs searches at the LHC are compatible with the predictions of the Standard Model (SM) of particle physics, but also with a wide variety of other possibilities, corresponding to very different underlying physics.

In this project the nature of Higgs physics and electroweak symmetry breaking has been probed in a joint effort between experiment and theory. In the following a brief account of some of the achieved results is given, comprising Higgs searches, property determinations, appropriate model predictions, as well as the discrimination between different interpretations of the experimental results.

*Contribution to "Particles, String and the Early Universe – Research Results of the Collaborative Research Centre SFB 676 in Hamburg".

2 Theoretical studies preceding the Higgs boson discovery

2.1 Light NMSSM Higgs bosons in SUSY cascade decays at the LHC

An interesting feature of the next-to-minimal supersymmetric extension of the Standard Model (NMSSM) is that one or more Higgs bosons may be comparably light ($M_{H_i} < M_Z$) without being in conflict with current experimental bounds. Due to a large singlet component, their direct production in standard channels at the Large Hadron Collider (LHC) is suppressed. In Ref. [1] good prospects for observing such a light Higgs boson in decays of heavy supersymmetric (SUSY) particles at the LHC were demonstrated.

Considering an example scenario with 20 GeV $< M_{H_1} < M_Z$, it was shown that a large fraction of cascade decays of gluinos and squarks would involve the production of at least one Higgs boson. Performing a Monte Carlo analysis at the level of fast detector simulation, it was demonstrated how the Higgs signal can be separated from the main backgrounds, see Fig. 1, where the simulation has been done for SUSY scales of $M_{\mathrm{SUSY}} = 750$ GeV (left column) and $M_{\mathrm{SUSY}} = 1$ TeV (right column). Besides the SM $t\bar{t}$ background also SUSY background from other SUSY processes has been taken into account. The impact of various kinematical variables on discriminating between the inclusive SUSY signal (including events both with and without a Higgs boson in the cascade) and the SM background from $t\bar{t}$ production has been investigated. A set of simple cuts has been devised that turned out to be efficient for establishing the inclusive SUSY signal. It should be noted that no specific knowledge about the background from SUSY background from events without a Higgs in the cascades was assumed. Accordingly, besides favoring events containing the light H_1 by selecting the combination minimizing $\Delta R(bb)$ in configurations with multiple b-jets, no particular cuts for suppressing the SUSY background have been applied.

It was pointed out in Ref. [1] that the analysis of the resulting $b\bar{b}$ mass spectrum according to Fig. 1 opened up an opportunity for the discovery of a light Higgs boson already with 5 fb^{-1} of LHC data at 7 TeV. In the considered scenario with rather light SUSY particles a statistical significance for the H_1 mass peak of $S/\sqrt{B} \approx 4$ was found for $M_{\mathrm{SUSY}} = 1$ TeV at $\sqrt{s} = 7$ TeV (the gluino mass parameter was set to 1 TeV), which increased to $S/\sqrt{B} \approx 8$ for $M_{\mathrm{SUSY}} = 750$ GeV at 7 TeV and reached a level of almost 30 for both values of M_{SUSY} at 14 TeV with the very modest integrated luminosity of just 5 fb^{-1} for LHC running both at 7 TeV and 14 TeV. The presented results are rather insensitive to the precise value of M_{H_1}. Since the production relies on the decay of heavier SUSY states, with branching ratios largely independent of M_{H_1}, the Higgs production rates remain similar for the whole mass range $M_{H_1} < M_Z$.

The observation of a light Higgs boson in this channel would give direct access to the Yukawa coupling of the Higgs state to bottom quarks. While compared to the experimental situation that was analysed in Ref. [1] the limits from SUSY searches have meanwhile become much stronger, there is still ample room for one or more light Higgs bosons with suppressed couplings to gauge bosons, as will be discussed in more detail below.

The phenomenological investigation carried out in Ref. [1] triggered an experimental activity that is described in Sec. 6.5 below. It resulted in the CMS analysis of Ref. [2].

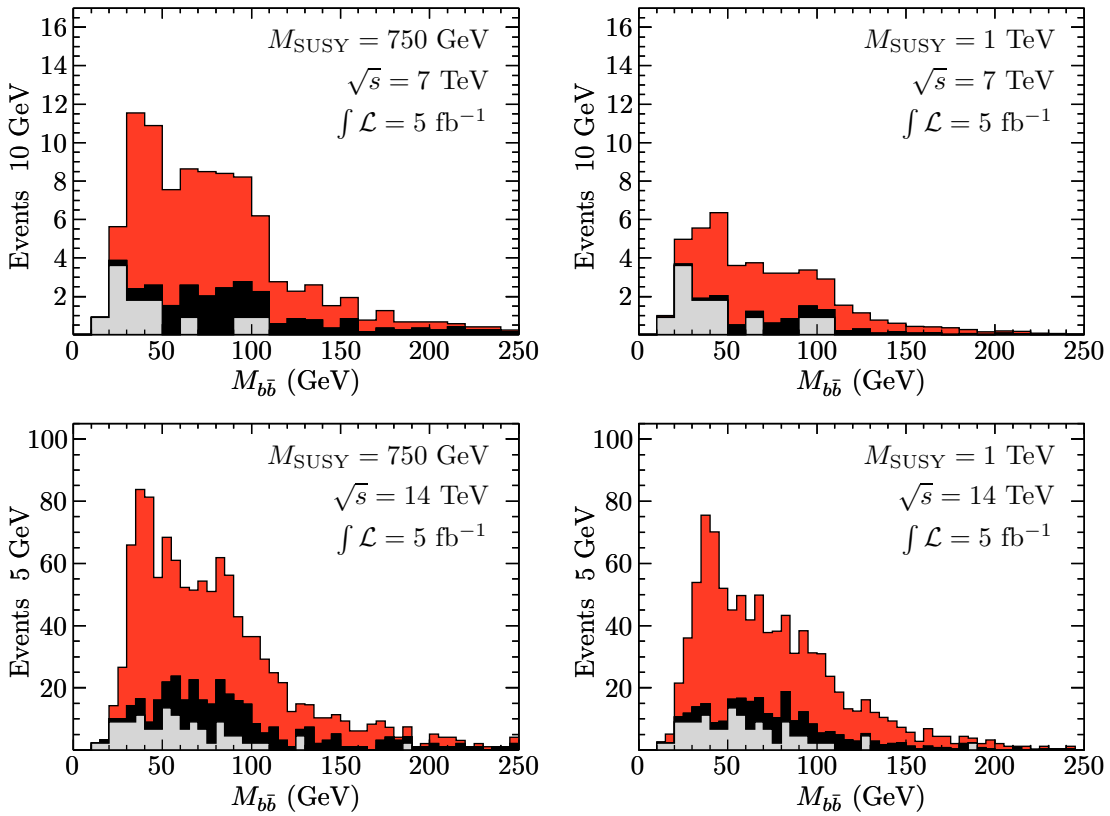


Figure 1: Invariant mass of b-jet pairs for SUSY signal (red), SUSY background (black) and SM $t\bar{t}$ background (light gray) in the considered benchmark scenario with $M_{\mathrm{SUSY}} = 750$ GeV (left column) and $M_{\mathrm{SUSY}} = 1$ TeV (right column) at 7 TeV (upper row) and 14 TeV (lower row) for an integrated luminosity of 5 fb^{-1}. Figures taken from Ref. [1].

2.2 Interpreting the LHC Higgs search results in the MSSM

In view of the excess observed at about 125 GeV in the Higgs searches at the LHC in December 2011, in Ref. [3] the implications of a possible Higgs signal were discussed within the context of the minimal supersymmetric Standard Model (MSSM), taking into account previous limits from Higgs searches at LEP, the Tevatron and the LHC. It was pointed out that the observed excess with a mass of about 125 GeV was well compatible with the predictions of the MSSM, while the observation of a SM-like Higgs boson with a mass above about 135 GeV would have unambiguously ruled out the MSSM with TeV-scale SUSY particles (but would have been viable in the SM and in non-minimal supersymmetric extensions of it). Interpreting the observed excess as signal within the MSSM, the consequences for the remaining MSSM parameter space were investigated. Under the assumption of a Higgs signal new lower bounds on the tree-level parameters of the MSSM Higgs sector were derived. Both the possibilities of associating the observed excess with the light CP-even Higgs boson of the MSSM, h, and the the heavier CP-even Higgs boson H, were investigated. It was demonstrated that also the somewhat exotic

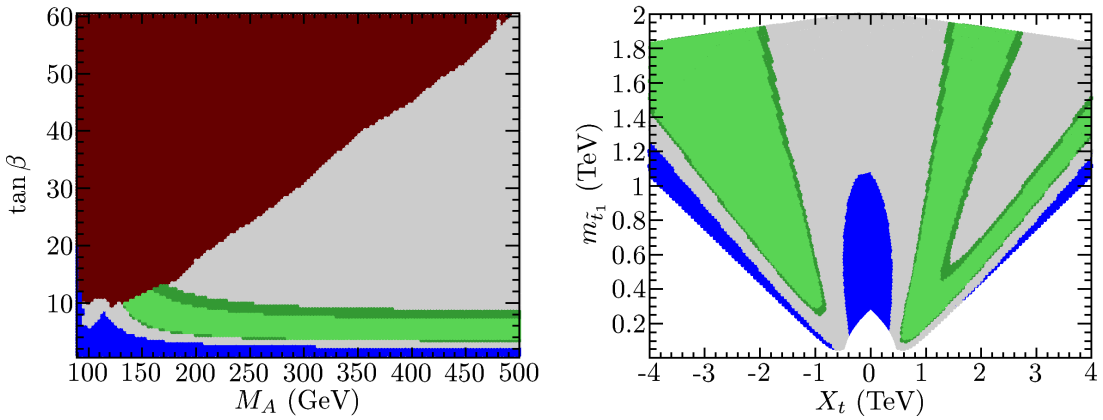


Figure 2: Left: Tree-level Higgs sector parameters (M_A, $\tan\beta$) for the case where the parameters governing the higher-order corrections are chosen such that a maximum value for M_h is obtained ($m_h^{\max}$ benchmark scenario). The different colours correspond to the regions excluded by LEP (blue) and Tevatron/LHC (red). The gray area is the allowed parameter space prior to the observation of an excess at the LHC. The green band shows the region where M_h is compatible with the observed excess. Right: Constraints on the MSSM stop sector from the assumed Higgs signal. The allowed ranges are shown in the (X_t, $M_{\rm SUSY}$) plane (left) and the (X_t, $m_{\tilde{t}_1}$) plane (right) for $M_A = 1$ TeV, $\tan\beta = 20$. The colour coding is as in the left plot. Figures taken from Ref. [3].

possibility that the observed excess was in fact caused by the heavier CP-even Higgs boson (while the lighter one escaped the search limits) was compatible with the data.

Results for the interpretation of the observed excess in terms of the light CP-even Higgs boson of the MSSM are displayed in Fig. 2, showing that there is a significant parameter space of the MSSM compatible with this interpretation. In the left plot of Fig. 2 the parameters that enter via the (in general) numerically large higher-order corrections in the MSSM Higgs sector were set to their values in the $m_h^{\max}$ benchmark scenario, which maximizes the upward shift in M_h as compared to the tree-level value. In this way conservative lower limits on the parameters governing the M_h prediction at tree level, M_A and $\tan\beta$, could be obtained. Taking into account conservatively estimated theoretical uncertainties from unknown higher orders as well as the most important parametric uncertainties arising from the experimental error on the top-quark mass, compatibility with the observed excess yields the lower bounds $M_A > 133$ GeV and $\tan\beta > 3.2$ (for $M_{\rm SUSY} = 1$ TeV). The bound on M_A translates directly into a lower limit $M_{H^\pm} > 155$ GeV, which restricts the kinematic window for MSSM charged Higgs production in the decay of top quarks.

The approach followed in the right plot of Fig. 2 was to choose values for M_A and $\tan\beta$ in the decoupling region and to investigate the constraints on the scalar top and bottom sector of the MSSM from the required compatibility with the observed excess. It was found that a lightest stop mass as light as $m_{\tilde{t}_1} \sim 100$ GeV was still compatible with the observed excess. The bound on $m_{\tilde{t}_1}$ raises to $m_{\tilde{t}_1} \gtrsim 250$ GeV if one restricts to the negative sign of the stop mixing parameter $X_t \equiv A_t - \mu/\tan\beta$, which in general yields better compatibility with the constraints from BR($b \to s\gamma$).

Concerning the interpretation of the observed excess in terms of the heavier CP-even Higgs boson, a scan over M_A, $\tan\beta$, $M_{\rm SUSY}$ and X_t was performed, yielding an allowed area at low M_A and moderate $\tan\beta$. A SM-like rate for production and decay of the heavier CP-even Higgs in the relevant search channels at the LHC is possible for large values of μ and large mixing in the stop sector. It is interesting to note that in the scenario where the assumed Higgs signal is interpreted in terms of the heavier CP-even Higgs boson H the mass of the lighter Higgs, M_h, always comes out to be *below* the SM LEP limit of 114.4 GeV (with reduced couplings to gauge bosons so that the limits from the LEP searches for non-SM like Higgs bosons are respected). It was pointed out that the fact that scenarios of this kind are phenomenologicall viable should serve as a strong motivation for extending the LHC Higgs searches, most notably in the $\gamma\gamma$ final states, also to the mass region below 100 GeV.

3 The discovery and properties of the Higgs boson

3.1 The discovery

Simulation studies performed before the start of data taking had estimated that more than $10\,\text{fb}^{-1}$ collected at $\sqrt{s} = 14\,\text{TeV}$ would be needed to reach a discovery significance of $5\,\sigma$ for a Standard Model Higgs boson with a mass of 125 GeV [4]. In fact, with about $4.8\,\text{fb}^{-1}$ collected at $\sqrt{s} = 7\,\text{TeV}$ in 2011 and about $5.8\,\text{fb}^{-1}$ collected at $\sqrt{s} = 8\,\text{TeV}$, the observed (expected) significance for an excess of events near 126 GeV was $4.5\,\sigma$ ($2.5\,\sigma$) in the $H \to \gamma\gamma$ channel and $5.9\,\sigma$ ($4.9\,\sigma$) after combination with the $H \to ZZ^* \to 4\ell$ and $H \to WW^* \to 2\ell 2\nu$ decay channels in the ATLAS experiment [5]. When considering the look-elsewhere-effect, the observed significance was reduced to $5.1\,\sigma$. Very similar results were obtained by the CMS experiment [6], finding an observed (expected) significance of $5.0\,\sigma$ ($5.8\,\sigma$). With these results, the two experiments had discovered a new particle with properties consistent with those expected from a SM Higgs boson.

The analysis in the $H \to \gamma\gamma$ decay channel employed event categorisation, which improved the sensitivity of the analysis by more than 20%. The categorisation was based on the kinematic properties of the photon candidates, on whether or not the photon candidates were reconstructed as converted photons, and on the event topology, defining also two categories with topology as expected from vector boson fusion production. The event categorisation in Fig. 3 shows the weighted invariant mass spectrum at the time of the discovery. The weighting gives a visual representation of the effect of the categorisation on the analysis.

3.2 Property studies of the new particle

After the discovery, the focus turned to studies of the properties of the new particle to determine whether or not they are consistent with the properties expected from the SM. This included studies of the spin and CP properties, as well as measurements of cross sections and branching ratios, which are sensitive to the coupling of the Higgs boson to SM particles.

3.2.1 Search for and discovery of Higgs boson decays to τ leptons

The discovery had been made in Higgs decays to two bosons, and one important outstanding question was whether or not the mass of fermions is generated by Yukawa couplings. One important channel to study the Higgs couplings to fermions is the Higgs boson decay to two

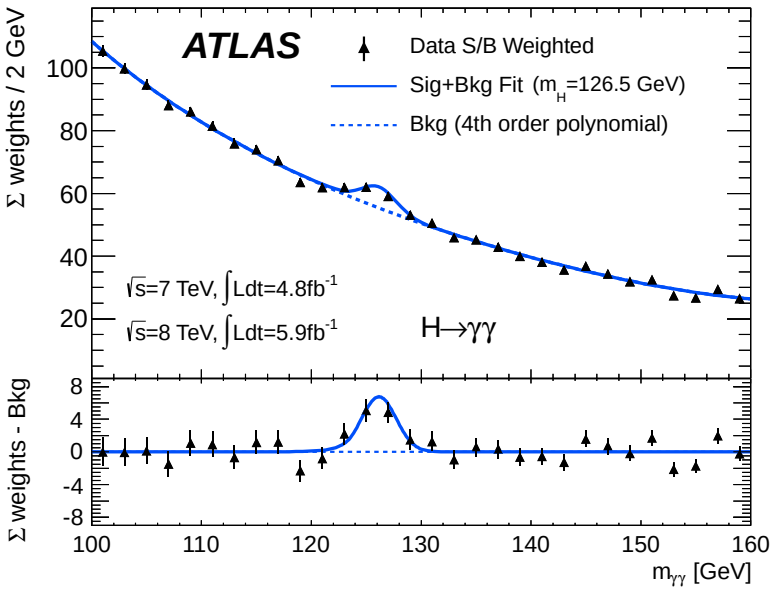


Figure 3: Invariant diphoton mass distribution from the $H \to \gamma\gamma$ discovery analysis. The weight w_i for events in category i is defined to be $\ln(1+S_i/B_i)$, where S_i is 90% of the expected signal for $m_H = 126.5\,\text{GeV}$, and B_i is the integral in the smallest window containing S_i signal events. Figure taken from Ref. [5].

τ leptons. Evidence for the Higgs boson decay to τ leptons was first established with LHC Run 1 data, and the decay was then observed with statistical significance of 5.9 standard deviations after combining Run 1 and Run 2 LHC data collected with the CMS detector [7,8]. The invariant di-tau mass distribution from the observation of the Higgs decay to τ leptons is shown in Fig. 4.

3.2.2 Simplified template cross sections – development and measurements

In the LHC Run 1, the production processes were measured inclusively, i.e. in the full phase space, and as signal strengths, i.e. as the ratio of the measured and the predicted cross section. It is virtually impossible to update the signal strength measurement of the different Higgs production processes performed in Run 1 when improved theoretical predictions become available. In addition, the interpretation of the measurements would greatly benefit from more differential information. This motivated the discussions and work to develop the Simplified Template Cross Section (STXS) framework in a collaborative effort between theory and experiment [9,10]. The framework defines kinematic regions for each production process ("bins"), in which the cross section for the given production process will be measured. The definition of the bins is motivated by the goals to reduce the theoretical uncertainties that are folded into the measurement, and to provide measurements useful for reinterpretation, including bins that are particularly sensitive to BSM effects. Different "stages" are defined to allow for measurements with different granularity. In addition, schemes for the parametrisation of the theoretical uncertainties were developed [11].

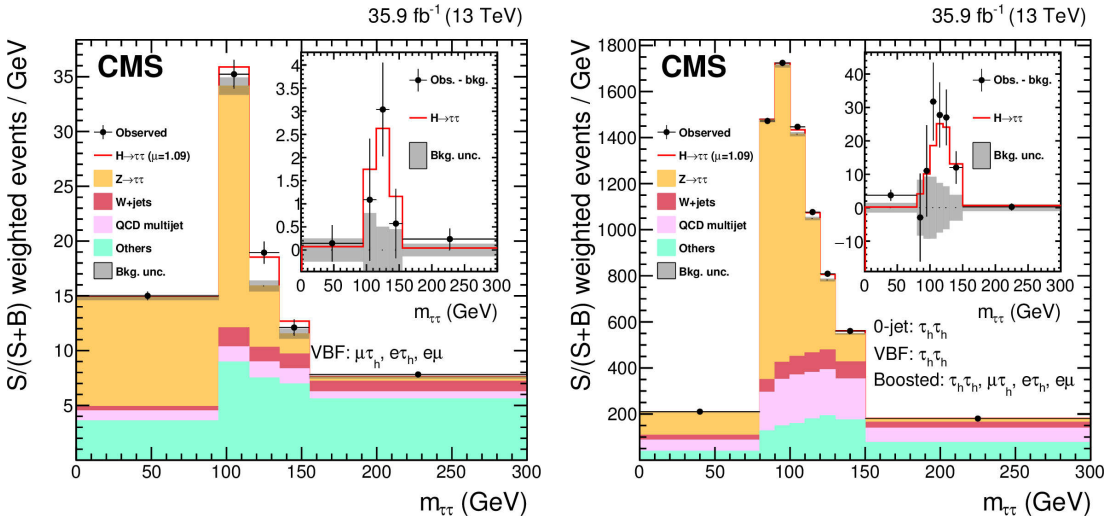


Figure 4: Invariant di-tau mass distribution from the $H \to \tau\tau$ analysis. Figure taken from Ref. [8].

Figure 5 (left) shows "merged stage-1" STXS measurements from $H \to \gamma\gamma$ decays using $80\,\text{fb}^{-1}$ collected with the ATLAS detector [12]. The categories defined to target $t\bar{t}H$ production also contributed to the discovery of the $t\bar{t}H$ production process [13]. Figure 5 (right) shows "merged stage-1" STXS measurements obtained from a combination of results obtained in the $H \to \gamma\gamma$ and $H \to 4\ell$ decay channels using $36\,\text{fb}^{-1}$ collected with the ATLAS detector [14]. With the dataset collected in Run 2 so far, several bins in jet multiplicity and Higgs boson transverse momentum could be measured for gluon fusion production, as well as bins sensitive to vector boson fusion production.

3.3 Property determinations (theory)

On the theory side, contributions were made to the determination of the spin and CP properties of the detected state [15], to the analysis of off-shell effects [16, 17], and to the determination of Higgs-boson couplings [15, 18, 19].

Concerning the coupling determination, in general a modification of a coupling with respect to the SM prediction may give rise to a change of both the coupling strength and the tensor structure of the coupling, where the latter will affect the CP properties of the coupling. Accordingly, the tasks of determining the couplings and CP properties of the observed signal are in fact closely related to each other. In order to reduce the complexity of the analyses for determining coupling properties during Run 1, an "interim framework" has been introduced in Ref. [18]. It was adopted by the LHC Higgs Cross Section Working Group [19] and used by the ATLAS and CMS collaborations for their experimental analyses. The developed framework consists of a parametrisation of small deviations from SM-like behaviour of the couplings for various benchmark scenarios, based on several simplifying assumptions, in particular: the signals observed in the different search channels are assumed to originate from a single resonance; the width of the observed particle is neglected, so that the predicted rate for a given channel can be decomposed

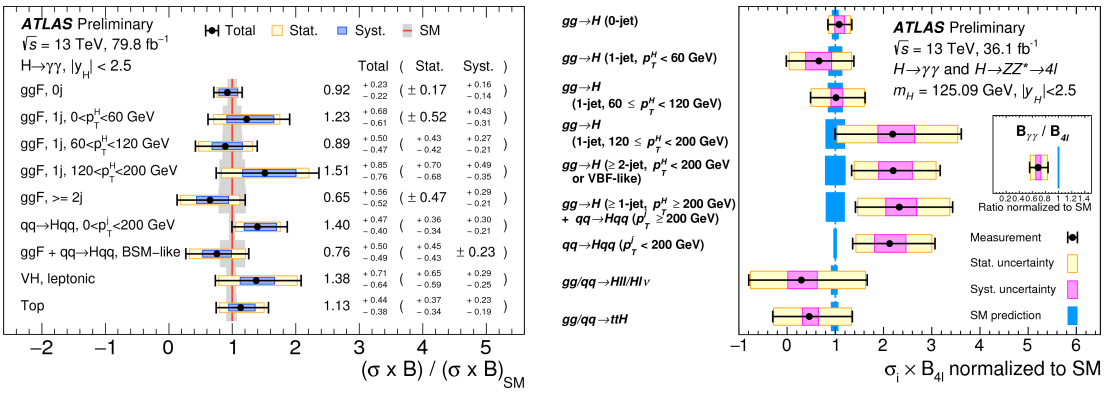


Figure 5: STXS measurements using a "merged stage-1" scheme in the $H \to \gamma\gamma$ decay channel with $80\,\text{fb}^{-1}$ (left), and obtained from combining measurements in $H \to \gamma\gamma$ and $H \to 4\ell$ with $36\,\text{fb}^{-1}$ (right). Figures taken from Refs. [12] and [14], respectively.

into the production and decay contributions, $\sigma \cdot \text{B}(i \to H \to f) = \sigma_i \cdot \Gamma_f / \Gamma_H$, where σ_i is the production cross section through the initial state i, B and Γ_f are the branching ratio and partial decay width into the final state f, respectively, and Γ_H is the total width of the Higgs boson; only modifications of coupling strengths are considered, while the tensor structure of the couplings is assumed to be the same as in the Standard Model – this assumption implies in particular that the observed state is assumed to be a CP-even scalar.

Coupling scale factors κ_j were defined in such a way that the cross sections σ_j and the partial decay widths Γ_j associated with the SM particle j scale with κ_j^2 compared to the SM prediction. By definition, the best available SM predictions for all $\sigma \cdot \text{B}$, including higher-order QCD and electroweak corrections, are recovered when all $\kappa_j = 1$. Since the LHC measurements always involve a combination of Higgs couplings from the production and the decay processes and since there is limited access to the total Higgs-boson width, without further theoretical assumptions only ratios of couplings can be measured at the LHC rather than absolute values of the couplings. The different proposed benchmark scenarios correspond to different assumptions on which of the couplings are fixed to their SM values and for which of them deviations from their SM strengths are considered.

4 Possible interpretations of the detected Higgs signal

4.1 Confronting supersymmetric models with the Higgs signal observed at the LHC

In Ref. [20] the experimental information on the discovered new state was confronted with the predictions in the MSSM and the NMSSM. Performing a scan over the relevant regions of parameter space in both models it was analysed in particular to what extent a significant enhancement of the $\gamma\gamma$ rate of the new particle with respect to the SM prediction could occur in the two models.

Enhancements of this kind are indeed possible in view of limits on the parameter space arising from theoretical constraints as well as from the limits from direct searches for super-

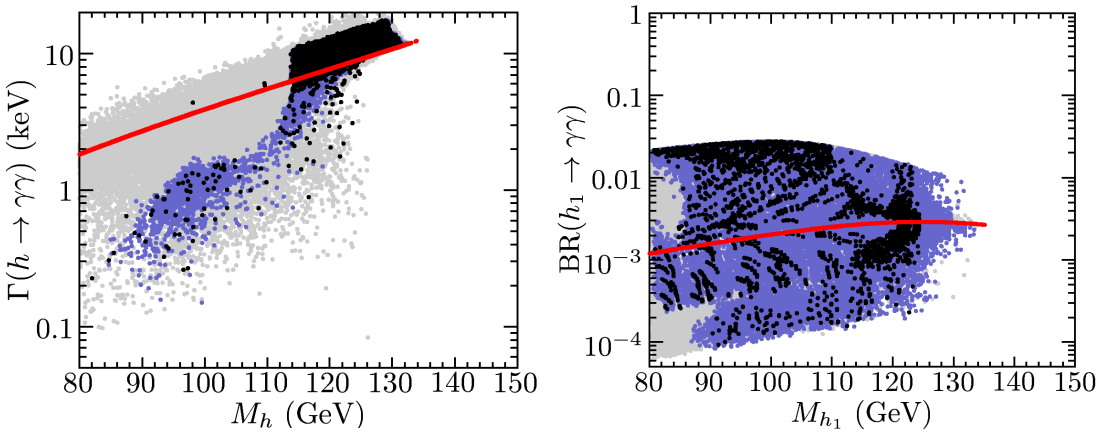


Figure 6: Results from parameter scans in the MSSM (left) and the NMSSM (right) for the decay of the lightest CP-even Higgs boson of the model into a pair of photons. The full result of the scan (all points allowed by the theoretical constraints and the direct search limits for sparticles) is shown in grey. The blue points are compatible with the direct Higgs search limits at that time (from `HiggsBounds 3.6.1`, which included LHC results up to the year 2011), while the black points in addition give a result in agreement with $(g-2)_\mu$ and $\mathrm{BR}(b \to s\gamma)$. The left plot shows the partial decay width $\Gamma(h \to \gamma\gamma)$ in the MSSM, while the right plot shows the branching ratio $\mathrm{BR}(h_1 \to \gamma\gamma)$ in the NMSSM. The solid (red) curve shows the respective quantities evaluated in the SM. Figures reprinted from Ref. [20] with kind permission of The European Physical Journal (EPJ).

symmetric particles, from the Higgs searches at LEP, the Tevatron and the LHC (incorporating the limits known at that time), from electroweak precision observables and from flavour physics, as can be seen in Fig. 6. Mechanisms that can lead to an enhanced $\gamma\gamma$ rate in comparison to the SM prediction have been analysed in the two models. Within the MSSM, besides the presence of light scalar taus, in particular a suppression of the $b\bar{b}$ decay mode results in an enhanced $\gamma\gamma$ rate. This suppression can either be caused by Higgs-boson propagator corrections entering the effective mixing angle, or by non-decoupling SUSY corrections affecting the relation between the bottom quark mass and the bottom Yukawa coupling. Within the NMSSM the same mechanisms as in the MSSM can be realised. In addition, there exist mechanisms that are genuine for the NMSSM. It was pointed out that in particular the doublet-singlet mixing can result in a substantial suppression of the $b\bar{b}$ mode and an associated enhancement of the $\gamma\gamma$ rate.

The possible interpretation of the discovered Higgs signal in terms of either the light or the heavy CP-even Higgs boson of the MSSM has been investigated in detail in Refs. [21,22]. MSSM fits have been performed of the various rates of cross section times branching ratio as measured by the LHC and Tevatron experiments under the hypotheses of either the light or the heavy CP-even Higgs boson being the new state around 125 GeV, with and without the inclusion of further low-energy observables. An overall good quality of the fits has been found, in the case of the interpretation in terms of the light CP-even Higgs even slightly better than for the SM [21]. Besides the decoupling limit, also the possibility of alignment without decoupling has been investigated. It has furthermore been demonstrated that also the heavy CP-even Higgs

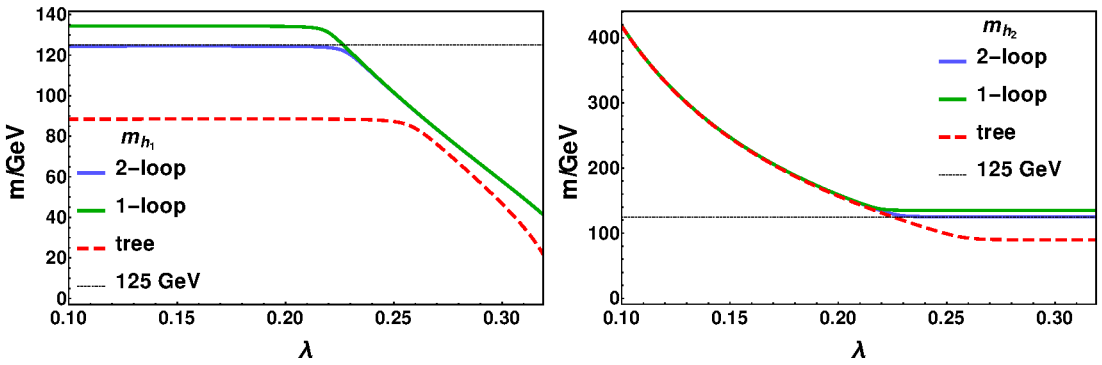


Figure 7: Mass predictions for the lightest and next-to lightest CP-even Higgs-states, m_{h_1} (left), and m_{h_2} (right), of the NMSSM at tree-level, one-loop and two-loop order. Figures taken from Ref. [23].

boson continues to be a viable candidate to explain the Higgs signal – albeit only in a highly constrained parameter region, which is probed by LHC searches for the CP-odd Higgs boson and the charged Higgs boson. The SUSY fits have been carried out in close cooperation with the B8 project of the SFB 676 on global fits.

While as explained above the case where the signal at 125 GeV is not the lightest Higgs boson in the spectrum is tightly constrained in the MSSM, it is important to notice that such a scenario is a quite typical feature of many other extensions of the SM. For instance, in the NMSSM an additional light Higgs boson arises generically if the mass scale of the singlet is lower than the one of the doublets. Such a light Higgs boson is only very weakly constrained by present experimental bounds. In Ref. [23] precise predictions for Higgs-boson masses of the NMSSM were obtained. Figure 7 shows predictions for the masses of the lightest and next-to lightest CP-even Higgs-states at tree-level, one-loop and two-loop order as a function of the NMSSM parameter λ. One can see that the variation of λ gives rise to a "cross-over" behaviour between the doublet-like and the singlet-like Higgs state.

Figure 8 shows results of a parameter scan in the NMSSM for the two lightest neutral Higgs bosons [24]. The state at 125 GeV in Fig. 8 has a small singlet component and can be identified with the Higgs signal observed at the LHC. The model predicts an additional lighter Higgs boson, which has a mass of about 105 GeV in this case, with a large singlet component giving rise to suppressed couplings to the gauge bosons and fermions of the SM. The coloured regions with the indicated best-fit points are in agreement with the experimental results on the Higgs signal and with the limits from Higgs searches as implemented in the public tools `HiggsSignals` [21, 25, 26] and `HiggsBounds` [27, 28].

4.2 Benchmark scenarios for MSSM Higgs searches after the discovery of a Higgs-like particle

In view of the discovered signal new low-energy benchmark scenarios have been proposed for MSSM Higgs searches in Ref. [29]. Those benchmarks are over a wide parameter range compatible with the mass and production rates of the observed signal. The proposed scenarios also exhibit interesting phenomenology for the MSSM Higgs sector. They comprise in particular a

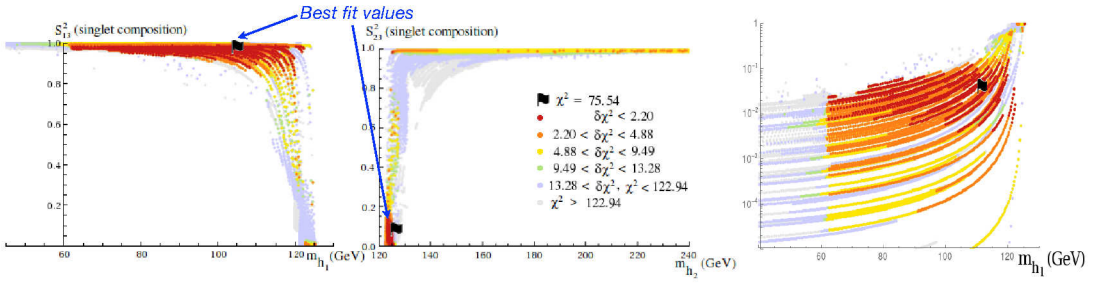


Figure 8: Results of a parameter scan in the NMSSM for the two lightest neutral Higgs bosons. The regions that are preferred by the fit in the vicinity of the indicated best points are shown in red. The plots show the singlet composition of the lightest two states (left) and the squared coupling of the lightest Higgs state to gauge bosons, normalised to the SM value. Figures taken from Ref. [24].

slightly modified version of the well-known $m_h^{\max}$ scenario, called m_h^{mod}, where the light CP-even Higgs boson can be interpreted as the LHC signal in large parts of the M_A–$\tan\beta$ plane, see Fig. 9. Furthermore, a light stop scenario leading to a suppression of the lightest CP-even Higgs gluon fusion rate, a light stau scenario with an enhanced decay rate of h to $\gamma\gamma$ at large $\tan\beta$, and a τ-phobic Higgs scenario in which the lightest Higgs boson can have suppressed couplings to down-type fermions have been defined. The importance of investigating different values of both signs of the parameter μ has been emphasized. For the default value of $\mu = 200$ GeV sizeable branching ratios of the heavy Higgs bosons into charginos and neutralinos occur, see Fig. 9. In addition to the scenarios where the lightest CP-even Higgs boson is interpreted as the LHC signal, also a low–M_H scenario has been proposed, where instead the heavy CP-even Higgs boson corresponds to the new state around 125 GeV (see above). See Ref. [30] for a recent update of the MSSM benchmark scenarios.

5 Precise predictions for Higgs physics in supersymmetric models

A particular effort in the research activities has been devoted to precise predictions for Higgs physics in supersymmetric models. In this context in particular the public code `FeynHiggs`[†] [31–37] has been further developed, including an ongoing effort of extending the predictions from the MSSM to the NMSSM [23,38,39]. In the following only a few examples of the accomplished results will be mentioned.

5.1 Improved two-loop predictions in the MSSM with complex parameters

In Refs. [40] and [41] improved two-loop results for the Higgs-boson masses of the MSSM have been obtained for the general case of arbitrary complex parameters. The corresponding self-energies and their renormalization have been obtained in the Feynman-diagrammatic approach.

[†]see `www.feynhiggs.de`

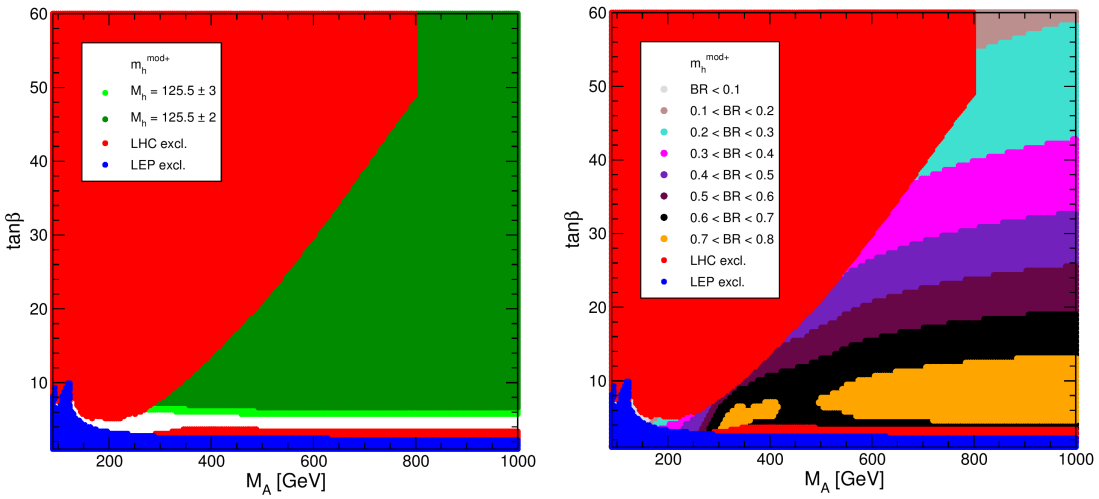


Figure 9: The M_A–$\tan\beta$ plane in the $m_h^{\mathrm{mod+}}$ scenario. The excluded regions from LEP and the LHC as obtained from `HiggsBounds` [27,28] at the time of writing [29] are indicated in blue and red, respectively. In the left plot the favoured region $M_h = 125.5 \pm 2(3)$ GeV is shown in green, while in the right plot the colour coding in the allowed region indicates the average total branching ratio of H and A into charginos and neutralinos. Figures reprinted from Ref. [29] with kind permission of The European Physical Journal (EPJ).

In Ref. [40] the corrections of $\mathcal{O}\left(\alpha_{\mathrm{t}}^2 + \alpha_{\mathrm{t}}\alpha_{\mathrm{b}} + \alpha_{\mathrm{b}}^2\right)$ from the Yukawa sector in the gauge-less limit have been calculated, while in Ref. [41] the complete two-loop QCD contributions to the mass of the lightest Higgs boson in the MSSM have been obtained.

In the result of Ref. [41] the full dependence on the external momentum and all relevant mass scales has been taken into account at the two-loop level without any approximation. The evaluation of the involved two-loop two-point integrals with up to five different mass scales was carried out with numerical methods. The impact of the new contributions on the Higgs spectrum can be seen in Fig. 10. In the left plot the prediction for M_{h_1} as a function of $\tan\beta$ is compared in an $m_h^{\mathrm{mod+}}$-like scenario with the previous result including and excluding the $\mathcal{O}\left(\alpha_{\mathrm{b}}\alpha_{\mathrm{s}}\right)$ terms that are known in the MSSM with real parameters. While the effect of the latter is small, the formally sub-leading two-loop contributions in our new result yield an upward shift of about 0.85 GeV compared to the previous result over a wide range of $\tan\beta$ values. In the right plot the prediction for M_{h_1} is shown as function of the gluino phase ϕ_{M_3}. The plot shows a sensitive dependence on the gluino phase, which enters at the two-loop level, and again a sizeable upward shift of the new result as compared to the previous result.

5.2 Combination of fixed-order results and effective field theory methods for precise Higgs-mass predictions

The precisely measured experimental value of the detected Higgs state can be confronted with models like supersymmetric extensions of the Standard Model where the mass of the state that is identified with the observed signal can be predicted from the other model parameters. This

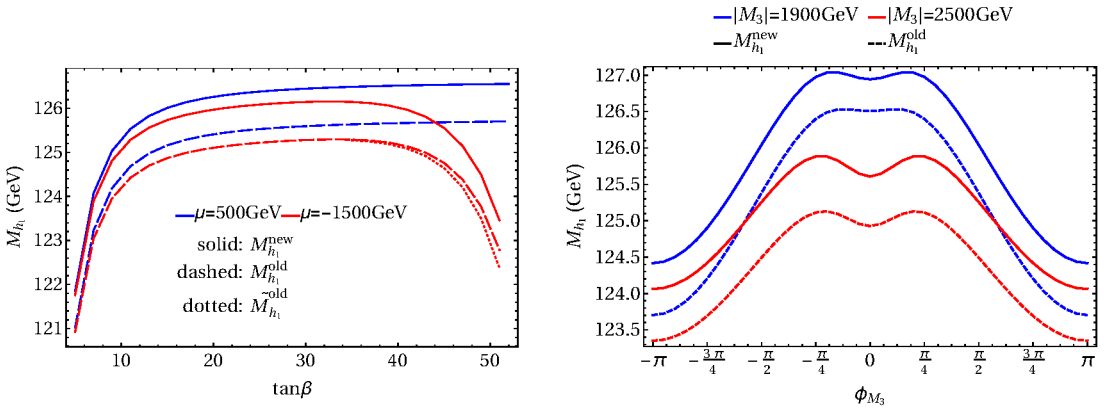


Figure 10: Prediction for the light Higgs-boson mass M_{h_1} as a function of $\tan\beta$ (left) and as a function of the gluino phase ϕ_{M_3} (right). In the left plot the new result (solid) is compared with the previous result (dashed) in an $m_h^{\rm mod+}$-like scenario for two values of μ. The dotted line shows the case where the previous result is supplemented with the $\mathcal{O}(\alpha_b\alpha_s)$ terms that are known in the MSSM with real parameters. In the right plot the new result (solid) is compared with the previous result (dashed) in a scenario with $\tan\beta = 50$ for two values of $|M_3|$. Figures taken from Ref. [41].

confrontation of the experimental value with the model prediction yields sensitive constraints on the parameter space of each model and plays a crucial role in the quest to discriminate between different models. A very high precision of the theoretical predictions is required in order to exploit the high accuracy of the measured mass value. The relatively high value of about 125 GeV of the detected Higgs signal together with the existing limits from direct searches for SUSY particles has led to various investigations where some or all of the SUSY particles are in the multi-TeV range or above. In case of large hierarchies between the electroweak and the SUSY scale a resummation of large logarithmic contributions via effective field theory (EFT) methods is necessary in order to obtain accurate theoretical predictions.

In Ref. [35] a "hybrid approach" improving the prediction for the SM-like state in the MSSM has been developed. It combines the fixed-order result, comprising the full one-loop and leading and subleading two-loop corrections, with a resummation of the leading and subleading logarithmic contributions from the scalar top sector to all orders obtained from solving the two-loop renormalisation group equations. Particular care was taken in this context to consistently match these two different types of corrections. In this way for the first time a high-precision prediction for the mass of the light CP-even Higgs boson in the MSSM was obtained that is valid from the electroweak scale up to the multi-TeV region of the relevant supersymmetric particles. The results were implemented into the public code `FeynHiggs`. In Fig. 11 the pure fixed-order result as a function of the SUSY scale, for two values of the parameter X_t controlling the mixing in the scalar top sector, is compared with the result including the resummation of leading and next-to-leading logarithmic contributions to all orders. Furthermore, the results of an analytic solution of the renormalisation group equations at the 3-loop to 7-loop level are also shown. While the impact of the higher-order logarithmic contributions is relatively small for SUSY scales around 1 TeV, they give rise to large effects for higher values of M_S.

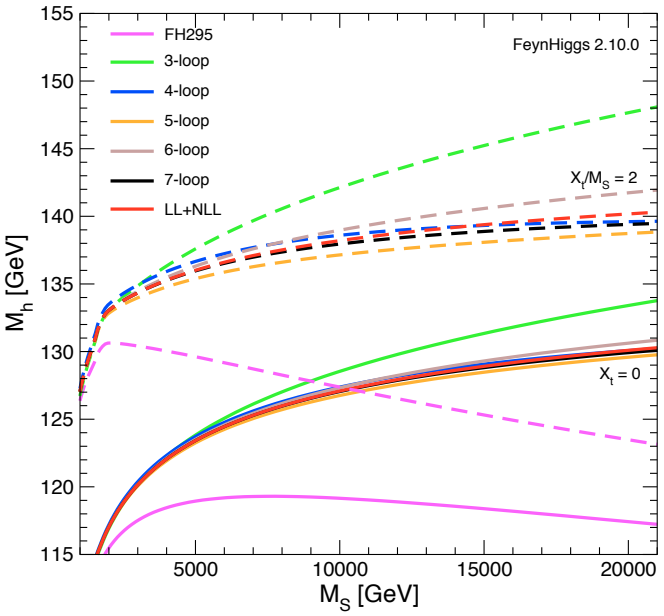


Figure 11: Prediction for the light Higgs-boson mass M_h as a function of the SUSY scale M_S for $X_t = 0$ (solid) and $X_t/M_S = 2$ (dashed). The full result including a resummation of logarithmic contributions ("LL+NLL") is compared with results containing the logarithmic contributions up to the 3-loop, ..., 7-loop level and with the previous fixed-order result ("FH295"). Reprinted figure with permission from Ref. [35]. Copyright (2014) by the American Physical Society.

The predictions obtained in the hybrid approach have been further improved by including the full next-to-leading-logarithmic (NLL) and a partial next-to-NLL (NNLL) resummation of the large logarithmic corrections. In Ref. [37] a detailed analytical comparison of the hybrid approach and the pure EFT approach has been carried out, and the numerical results of `FeynHiggs` have been confronted with the ones of the EFT code `SUSYHD` [42]. The sources of several discrepancies that were previously reported in the literature could be resolved, and the remaining deviations were discussed.

6 Searches for rare and non-SM decays of the detected Higgs boson and for non-SM Higgs bosons

6.1 Search for decays to two muons

The simple relation

$$g_{Hff} = \sqrt{2}\frac{m_f}{v}$$

between the mass m_f of a fermion, the Higgs–fermion coupling g_{Hff}, and the vacuum expectation value v is one of the central assumptions of the Standard Model. Experimentally however, this could be tested up to now only for the heavy fermions of the third generation. Since the

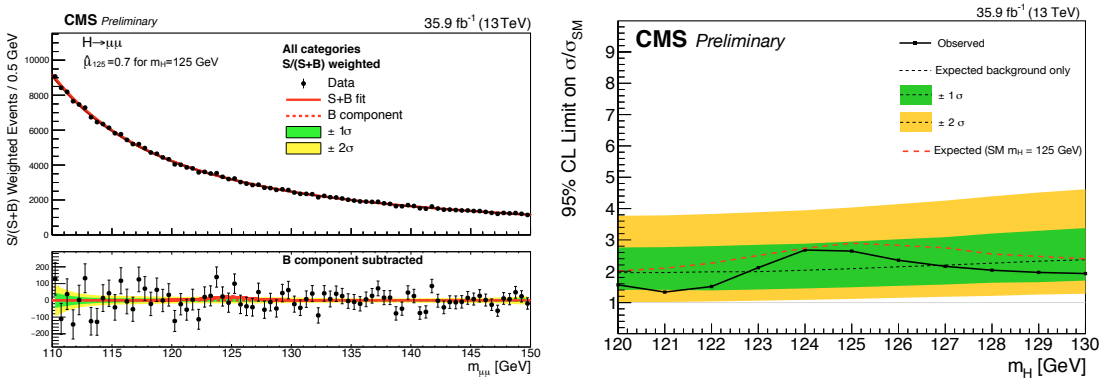


Figure 12: Left: Weighted distribution of measured invariant masses of $\mu^+\mu^-$ pairs in comparison to the sum of fits of signal and background to all event categories. Right: Limit on the cross section in relation to the Standard Model prediction. Figures taken from Ref. [43].

branching ratios $H \to f\bar{f}$ depend on g^2_{Hff} the only hope to probe this prediction for the other generations are $H \to c\bar{c}$ decays, where however the background from other processes is vast, and $H \to \mu^+\mu^-$ decays. For the latter case the background consists mostly of Drell-Yan events with off-shell Z/γ and of leptonic decays of W^+W^-- and $t\bar{t}$-pairs. This background is way lower than for the $c\bar{c}$ case, but due to the expected small branching ratio $\mathrm{B}(H \to \mu^+\mu^-) = 2.18 \times 10^{-4}$ still much larger than the signal process. For a search conducted by the CMS collaboration [43] the excellent invariant mass resolution of the $\mu^+\mu^-$ pair is employed. Using observables uncorrelated to $m_{\mu^+\mu^-}$ a boosted decision tree is used to classify events according to the Higgs production topology. The resulting weighted event disctribution is shown in Fig. 12. In combination with previous data obtained at lower centre of mass energy this search leads to an observed (expected) limit on the cross section times branching ratio, which is a factor 2.92 (2.16) larger than the Standard Model prediction.

A future aim of this analysis is to measure for the first time a Higgs coupling to second generation fermions by including data from 2017 and 2018.

6.2 Search for lepton-flavour violating decays

In many extensions of the Standard Model and in particular in classes of two-Higgs doublet models the fermion–Higgs couplings do not have to be flavour diagonal but allow for lepton flavour violating decays such as $H \to \tau^\pm\mu^\mp$, $H \to \tau^\pm e^\mp$, $H \to \mu^\pm e^\mp$ (cf. references in Ref. [44]). The emerging final states have a striking signature at the LHC with low Standard Model background, so that sensitivities to the corresponding couplings can be reached which are much stricter than those obtained from searches for rare or forbidden decays such as $\tau \to \mu\gamma$, etc. In an early search for the most promising decay $H \to \tau^\pm\mu^\mp$ using 7 TeV data from CMS, a small excess was observed [45]. This triggered much theoretical work but also searches for the other decay modes using much larger data sets at higher centre of mass energies [44, 46].

In Fig. 13 the event distributions of the most recent data are shown in comparison to various background sources and for a Higgs at a mass of 125 GeV with a branching ratio of 10% into $\tau^\pm\mu^\mp$. As the data for this larger sample agree with the background only expectation, an upper

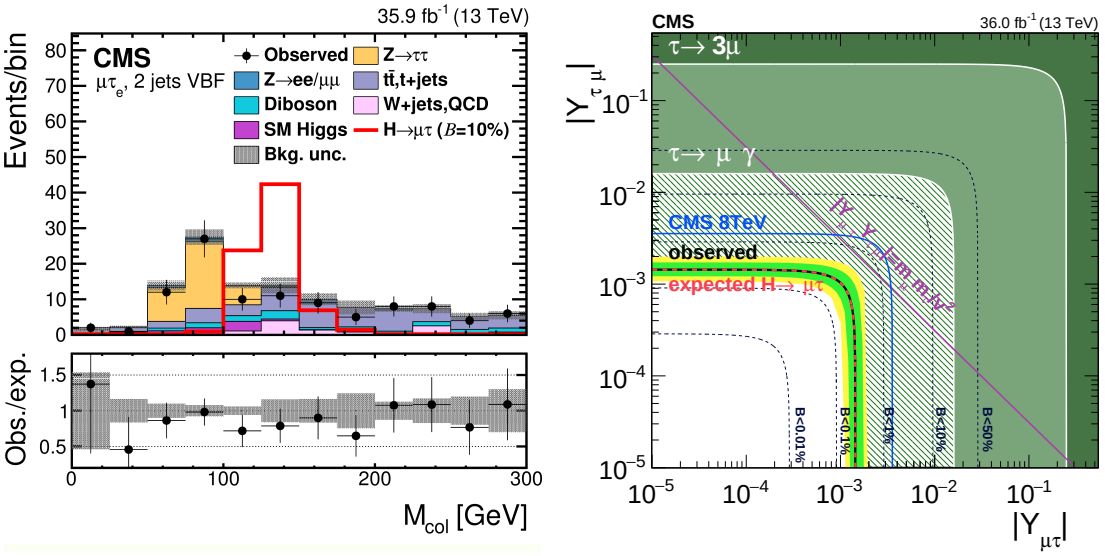


Figure 13: Left: Measured distribution of collinear masses for $H \to \tau^{\pm}\mu^{\mp}$ with the τ decaying into an electron and neutrinos and two further jets to tag vector boson fusion processes. The expected rate for $H \to \tau^{\pm}\mu^{\mp}$ is shown for a branching ratio of 10%. Close to the Higgs mass the background is dominated by $t\bar{t}$ production. Right: Combining analysis for different Higgs production and τ decay modes the limit on the Higgs branching ratio is converted into a limit on the Higgs couplings in the mixing matrix, $Y_{\mu\tau}$ and $Y_{\tau\mu}$. The observed limit is about one order of magnitude stronger than the one from indirect constraints ($\tau \to \mu\gamma$). Figures taken from Ref. [44].

limit on the branching ratio of $\mathrm{B}(H \to \tau^{\pm}\mu^{\mp}) \geq 0.25\%$ was derived.

6.3 Search for decays to $Z\gamma$

In the SM, the Higgs boson decay to $Z\gamma$ proceeds through a loop process, similar to the $H \to \gamma\gamma$ decay. As such, it is sensitive to contributions from physics beyond the SM that could contribute to the loop. In the SM, the branching ratio for the $Z\gamma$ decay is predicted to be $(1.54 \pm 0.09) \times 10^{-3}$, comparable to that for the decay into two photons, but the number of reconstructed events is significantly reduced by considering Z boson decays into electrons or muons, to benefit from a good invariant mass resolution. The search with the data collected in 2015 and 2016 by the ATLAS experiment set an upper limit on $\sigma(pp \to H) \cdot \mathrm{B}(H \to Z\gamma)$ of 6.6 times the SM prediction at the 95% confidence level (CL) [47], corresponding to an upper limit on the branching ratio of Higgs boson decays to $Z\gamma$ of 1% when assuming SM Higgs boson production. The expected 95% CL limit on $\sigma(pp \to H) \cdot \mathrm{B}(H \to Z\gamma)$ assuming SM Higgs boson decay to $Z\gamma$ was 5.2 times the SM prediction.

A future extension of this analysis is a search for the Higgs boson decays into $\gamma^*\gamma$, which is an experimentally more challenging signature since the two leptons have an invariant mass different from the Z-boson mass.

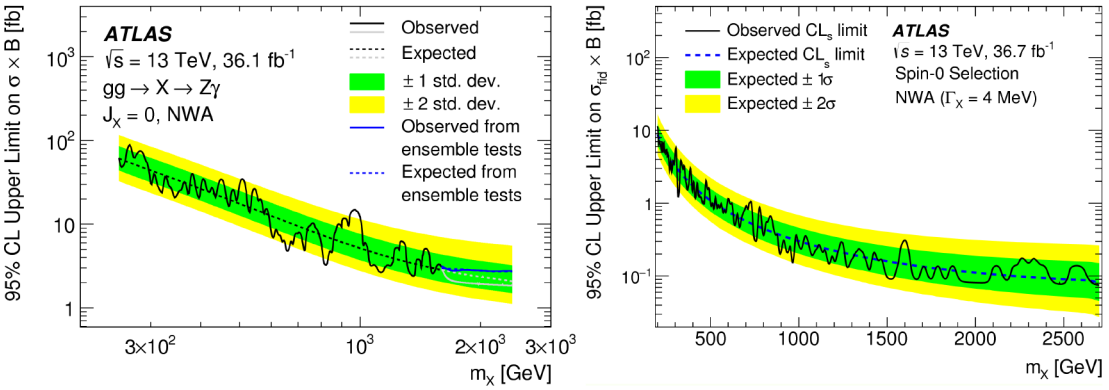


Figure 14: Limits on the cross section times branching ratio for heavy spin-0 particles decaying into $Z\gamma$ (left) or $\gamma\gamma$ (right). Figures taken from Refs. [47] and [48], respectively.

6.4 Search for heavy Higgs bosons decaying to $Z\gamma$ or $\gamma\gamma$

Many extensions of the SM introduce new heavy bosons, for example as extensions of the Higgs sector. Searching for these potential new heavy bosons in decays to $Z(\to \ell\ell)\gamma$ or $\gamma\gamma$ profits from the good invariant mass resolution of these final states, as well as moderate backgrounds. Figure 14 shows the exclusion limits on the cross section times branching ratio for the production of heavy spin-0 particles decaying into $Z\gamma$ or $\gamma\gamma$ at the 95% CL from the analyses performed with the 2015+2016 dataset collected by the ATLAS experiment [47, 48].

Should a new heavy resonance be found at the LHC, one of the first questions to answer would be whether it is produced in gluon or quark initial states. Good sensitivity to identify the initial state can be achieved in a model-independent way by using a tight veto on hadronic jets produced in association with a heavy resonance to divide the data into two mutually exclusive samples, with and without hadronic jets [49], as can be seen in Fig. 15.

6.5 Search for further supersymmetric Higgs bosons

Additional Higgs particles are predicted for example by Two-Higgs-Doublet-Models such as the Minimal Supersymmetric Standard Model (MSSM). Experimental searches for decays of such Higgs particles into Standard Model particles are carried out in a variety of final states. Their relative importance depends of course on the fundamental parameters of the underlying theory.

For heavy neutral Higgs particles (H) in the range $250 \leq M_H \leq 350$ GeV, i.e. above twice the mass of the discovered Higgs boson (h with $m_h = 125$ GeV) and below twice the mass of the top-quark, decays $H \to hh$ often have a large branching ratio. The subsequent final state with one h decaying into $h \to bb$ and the other into $h \to \tau\tau$ has the advantage of a rather large combined branching ratio and well detectable b-quarks and τ-leptons. Furthermore this final state is kinematically overconstrained once the low mass to momentum ratio of the tau leptons is employed to constrain the direction of the neutrinos in the tau decays. A dedicated kinematic fit was developed which in addition makes use of the known value of m_h and of transverse momentum balance in order to drastically improve the resolution for m_H [50]. The analysis of the CMS data using this method actually was able to basically exclude heavy Higgs particles in the MSSM in the stated mass range [51] for low $\tan\beta$.

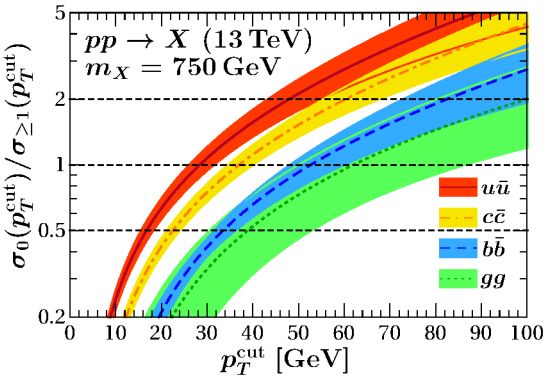


Figure 15: Ratio of the cross section of events produced without hadronic jets to the cross section for events with at least one hadronic jet for different initial states. Reprinted figure with permission from Ref. [49]. Copyright (2016) by the American Physical Society.

Of particular interest are also decay modes of neutral heavy Higgs bosons into pairs of tau leptons. The background estimation techniques and analysis tools developed in the course of the aforementioned studies of the discovered Higgs boson are applicable here as well. Searches performed at different centre of mass energies [52, 53] revealed no signal, and results of the analyses have been used to set upper limits on the Higgs boson production cross section times branching ratio B($H \to \tau\tau$) as well as to put stringent constraints on the model parameters. Within several MSSM benchmark scenarios, results of the search have been translated into exclusion contours in the $(M_A, \tan\beta)$ plane. Typically, values of $\tan\beta$ above 60 are excluded for $M_A > 1.7$ TeV in scenarios where the lightest scalar boson is compatible with the measured properties of the discovered 125 GeV Higgs boson. Figure 16 shows the example of the $m_h^{\rm mod+}$ benchmark scenario [29], see Sec. 4.2. A crucial ingredient to these measurements is the understanding of the τ identification and momentum scale for hadronically decaying τ leptons in the kinematic phase space not accessible via the $Z \to \tau\tau$ standard candle. Their measurement has been done for τ leptons with transverse momentum exceeding 100 GeV in the sample of highly virtually W bosons decaying into τ lepton and neutrino [54].

Searches for heavy neutral supersymmetric Higgs bosons dacaying into b-quarks have also been performed. Since the inclusive search for this signature has low sensitivity because of overwhelming QCD multijet background, Higgs boson production in association with further b-quarks was investigated. This production mode is characterised by an enhanced rate at large values of $\tan\beta$. The analysis has been facilitated by specialized multijet triggers. No signal was found in the searches performed [55, 56]. The results are thus interpreted in a model-independent way by placing upper limits on the product of signal production cross section and branching ratio of decays into b-quarks on $\tan\beta$ as a function of M_A within several MSSM benchmark scenarios. The study has yielded the best world sensitivity to date to the MSSM Higgs bosons in the $H \to bb$ decay mode.

In the Next-to-Minimal Supersymmetric Standard Model (NMSSM) a further singlet is assumed to solve the μ problem. In particular there are scenarios in which a light scalar boson with $M_h < M_Z$ has a large singlet component so that its couplings to the SM particles are suppressed. Therefore conventional present and past searches targeting either gluon-gluon

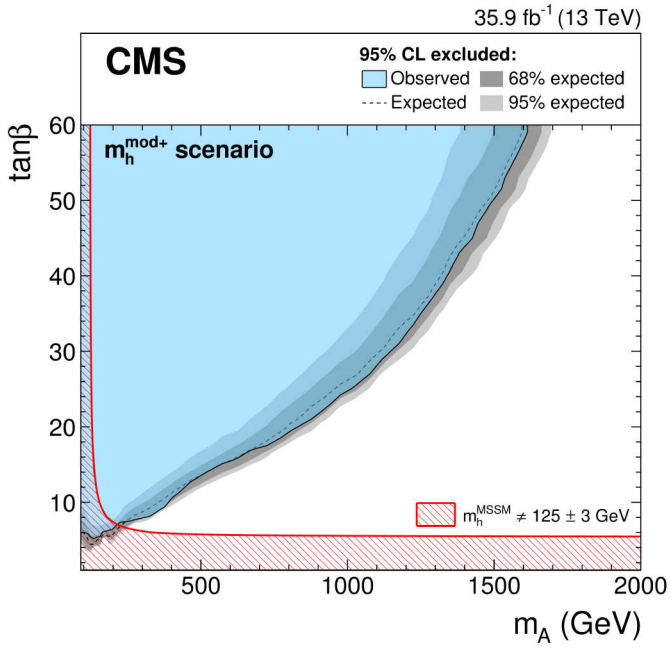


Figure 16: Exclusion bounds from CMS searches for heavy Higgs bosons decaying into a pair of tau leptons in the $(M_A, \tan\beta)$ plane of the MSSM for the $m_h^{\text{mod+}}$ benchmark scenario [29]. Figure taken from Ref. [53].

fusion or b-quark associated production at hadron colliders or Higgs-strahlug process at electron-positron colliders, could miss such a state. Instead it was suggested to search for this light state in cascade decays of coloured SUSY particles [1]. Experimentally the signal was searched for in multijet final state with two b-quarks resulting from the decay of the searched light scalar boson, and therefore exhibiting resonance structure in its invariant mass distribution. No signal was found, and results of the analysis were translated into constraints on the NMSSM parameters. The results of these studies have been presented in Ref. [2].

Also a search for a very light pseudoscalar Higgs boson produced in decays of the 125 GeV boson and decaying into tau lepton pairs was performed. The study probed masses of the pseudoscalar boson in the range $4 \leq m_a \leq 8$ GeV, where the decay of a into a pair of tau leptons dominates at high values of $\tan\beta$. No evidence for a signal has been established, and upper limits on the 125 GeV Higgs boson production cross section times branching ratio of the searched decay, $\text{B}(H \to aa \to 4\tau)$, have been devised as a function of m_a [57].

6.6 Impact of interference effects in the search for additional Higgs bosons

As shown in Ref. [58], interference and mixing effects between neutral Higgs bosons in the MSSM with complex parameters can have a significant impact on the interpretation of LHC searches for additional supersymmetric Higgs bosons. Complex MSSM parameters introduce mixing between the CP-even and CP-odd Higgs states h, H, A into the mass eigenstates h_1, h_2, h_3

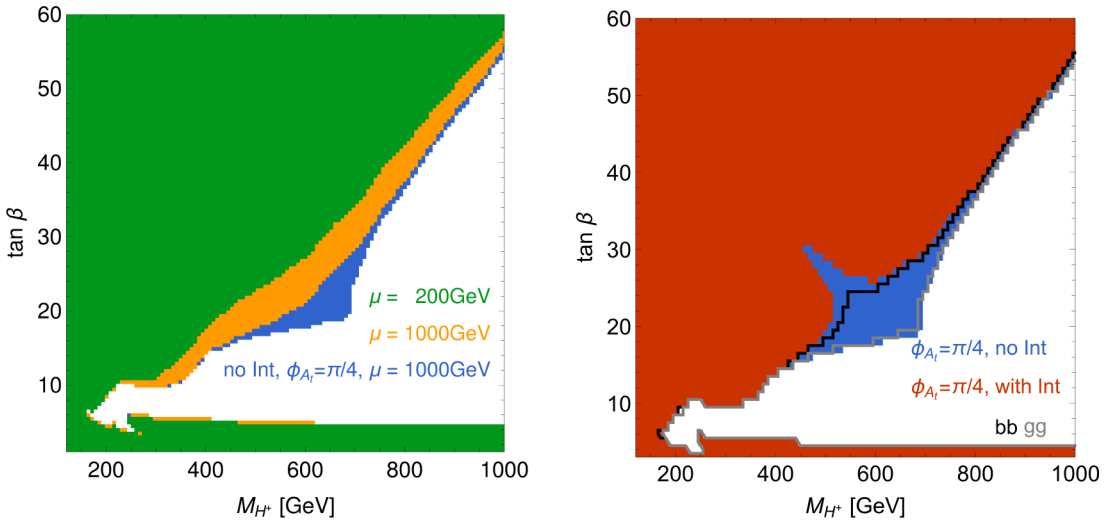


Figure 17: Exclusion bounds in the $(M_{H^\pm}, \tan\beta)$ plane of the MSSM obtained with `HiggsBounds` [27, 28]. The left plot shows the results for the $m_h^{\mathrm{mod}+}$ benchmark scenario [29] with real parameters for $\mu = 200$ GeV (green) and $\mu = 1$ TeV (orange) as well as the exclusion bound that would be obtained in the corresponding scenario with $\phi_{A_t} = \pi/4$ and $\mu = 1$ TeV for the incoherent sum of cross sections with 3×3 mixing but without the interference contribution (blue). The blue area is the same in the right plot, where it is compared with the result taking into account the interference contribution in both the $b\bar{b}$ and the gg processes (red). For illustration also the cases where the interference contribution is included only in the $b\bar{b}$ (black line) and only in the gg (grey line) process are shown. Figures taken from Ref. [58].

and generate CP-violating interference terms. Both effects are enhanced in the case of almost degenerate states. Such a situation is typically realised in an extended Higgs sector with a SM-like Higgs state at about 125 GeV, since in the decoupling limit the additional Higgs bosons tend to be heavy and nearly mass-degenerate.

Employing as an example an extension of the $m_h^{\mathrm{mod}+}$ benchmark scenario [29] by a non-zero phase ϕ_{A_t}, the interference contributions for the production of neutral Higgs bosons in gluon-fusion and in association with b-quarks followed by the decay into a pair of τ-leptons have been obtained in Ref. [58]. While the resonant mixing increases the individual cross sections for the two heavy Higgs bosons h_2 and h_3, strongly destructive interference effects between the contributions involving h_2 and h_3 leave a considerable parameter region unexcluded that would appear to be ruled out if the interference effects were neglected. This is shown in Fig. 17, where the exclusion limits obtained from `HiggsBounds` [27,28] are compared with the result that would be obtained if the interference contributions were neglected. The interference contributions give rise to the unexcluded "fjord" in the right plot of Fig. 17 (red area). The chosen scenario with $\mu = 1$ TeV and $\phi_{A_t} = \pi/4$ is compared with the $m_h^{\mathrm{mod}+}$ benchmark scenario [29] with real parameters for $\mu = 200$ GeV and $\mu = 1$ TeV in the left plot of Fig. 17.

7 Conclusions

In this report we have summarized some of the results that have been obtained in the project B9 of the SFB 676, in which the underlying physics of electroweak symmetry breaking has been probed in a joint effort between experimental activities in ATLAS and CMS and theoretical investigations. The presented results comprise theoretical studies preceding the Higgs boson discovery, experimental contributions to the Higgs boson discovery, the determination of properties of the detected state in close interplay between experiment and theory, precise theory predictions and possible interpretations of the detected Higgs signal, as well as experimental and theoretical aspects of searches for physics beyond the Standard Model in the Higgs sector.

The quest to identify the dynamics that is responsible for the generation of the property of mass of elementary particles is one of the most important goals of current fundamental science. The discovery of a Higgs boson has opened up a new window to the exploration of the mechanism of electroweak symmetry breaking and of the structure of the vacuum. In this project, this unique window has been exploited, and a lot of progress has been made within this vibrant field. Future data on searches and precision measurements that can be obtained at the LHC and beyond together with corresponding activities on the theory side provide excellent prospects for further breakthroughs in this area of research.

Acknowledgements

We would also like to thank H. Bahl, P. Bechtle, R. Benbrik, N. Berger, S. Borowka, M. Carena, F. Domingo, P. Drechsel, M. Duehrssen-Debling, M. A. Ebert, P. Francavilla, E. Fuchs, L. Galeta, M. Gomez Bock, N. Greiner, H. Haber, T. Hahn, S. Heinemeyer, W. Hollik, S. Liebler, G. Moortgat-Pick, I. Moult, S. Paßehr, S. Patel, H. Rzehak, O. Stål, T. Stefaniak, I. W. Stewart, F. J. Tackmann, C.E.M. Wagner, and L. Zeune for fruitful collaboration on the results presented in this report. We appreciate the collaboration with our colleagues at CERN and other institutes in the ATLAS and CMS experiments. The work presented in this report has been supported in part by the DFG through the SFB 676 "Particles, Strings and the Early Universe".

References

[1] O. Stål and G. Weiglein, *Light NMSSM Higgs bosons in SUSY cascade decays at the LHC*, *JHEP* **01** (2012) 071, [1108.0595].

[2] CMS Collaboration, *Search for a light NMSSM Higgs boson produced in supersymmetric cascades and decaying into a b-quark pair*, Tech. Rep. CMS-PAS-HIG-14-030, CERN, Geneva, 2015.

[3] S. Heinemeyer, O. Stål and G. Weiglein, *Interpreting the LHC Higgs Search Results in the MSSM*, *Phys. Lett.* **B710** (2012) 201–206, [1112.3026].

[4] ATLAS Collaboration, *Expected Performance of the ATLAS Experiment - Detector, Trigger and Physics*, 0901.0512.

[5] ATLAS Collaboration, *Observation of a new particle in the search for the Standard Model Higgs boson with the ATLAS detector at the LHC*, *Phys. Lett.* **B716** (2012) 1–29, [1207.7214].

[6] CMS Collaboration, *Observation of a new boson at a mass of 125 GeV with the CMS experiment at the LHC*, *Phys. Lett.* **B716** (2012) 30–61, [1207.7235].

[7] CMS Collaboration, *Evidence for the 125 GeV Higgs boson decaying to a pair of τ leptons*, *JHEP* **05** (2014) 104, [1401.5041].

[8] CMS Collaboration, *Observation of the Higgs boson decay to a pair of τ leptons with the CMS detector*, *Phys. Lett.* **B779** (2018) 283–316, [1708.00373].

[9] J. R. Andersen et al., *Les Houches 2015: Physics at TeV Colliders Standard Model Working Group Report*, in *9th Les Houches Workshop on Physics at TeV Colliders (PhysTeV 2015) Les Houches, France, June 1-19, 2015*, 2016, 1605.04692, http://lss.fnal.gov/archive/2016/conf/fermilab-conf-16-175-ppd-t.pdf.

[10] LHC Higgs Cross Section Working Group, D. de Florian et al., *Handbook of LHC Higgs Cross Sections: 4. Deciphering the Nature of the Higgs Sector*, 1610.07922. 10.23731/CYRM-2017-002.

[11] J. R. Andersen et al., *Les Houches 2017: Physics at TeV Colliders Standard Model Working Group Report*, in *10th Les Houches Workshop on Physics at TeV Colliders (PhysTeV 2017) Les Houches, France, June 5-23, 2017*, 2018, 1803.07977, http://lss.fnal.gov/archive/2018/conf/fermilab-conf-18-122-cd-t.pdf.

[12] ATLAS Collaboration, *Measurements of Higgs boson properties in the diphoton decay channel using 80 fb^{-1} of pp collision data at $\sqrt{s}$ = 13 TeV with the ATLAS detector*, Tech. Rep. ATLAS-CONF-2018-028, CERN, Geneva, 2018.

[13] ATLAS Collaboration, ATLAS Collaboration, *Observation of Higgs boson production in association with a top quark pair at the LHC with the ATLAS detector*, *Phys. Lett.* **B784** (2018) 173–191, [1806.00425].

[14] ATLAS Collaboration, *Combined measurements of Higgs boson production and decay in the $H \to ZZ^* \to 4\ell$ and $H \to \gamma\gamma$ channels using $\sqrt{s}$ = 13 TeV pp collision data collected with the ATLAS experiment*, Tech. Rep. ATLAS-CONF-2017-047, CERN, Geneva, 2017.

[15] K. Jakobs, G. Quast and G. Weiglein, *Higgs-Boson Physics at the LHC*, in *The Large Hadron Collider: Harvest of Run 1* (T. Schorner-Sadenius, ed.), pp. 195–258. Springer, Cham, 2015. DOI.

[16] S. Liebler, G. Moortgat-Pick and G. Weiglein, *Off-shell effects in Higgs processes at a linear collider and implications for the LHC*, *JHEP* **06** (2015) 093, [1502.07970].

[17] N. Greiner, S. Liebler and G. Weiglein, *Interference contributions to gluon initiated heavy Higgs production in the Two-Higgs-Doublet Model*, *Eur. Phys. J.* **C76** (2016) 118, [1512.07232].

[18] LHC Higgs Cross Section Working Group, A. David, A. Denner, M. Duehrssen, M. Grazzini, C. Grojean, G. Passarino et al., *LHC HXSWG interim recommendations to explore the coupling structure of a Higgs-like particle*, 1209.0040.

[19] LHC Higgs Cross Section Working Group, J. R. Andersen et al., *Handbook of LHC Higgs Cross Sections: 3. Higgs Properties*, 1307.1347. 10.5170/CERN-2013-004.

[20] R. Benbrik, M. Gomez Bock, S. Heinemeyer, O. Stål, G. Weiglein and L. Zeune, *Confronting the MSSM and the NMSSM with the Discovery of a Signal in the two Photon Channel at the LHC*, *Eur. Phys. J.* **C72** (2012) 2171, [1207.1096].

[21] P. Bechtle, S. Heinemeyer, O. Stål, T. Stefaniak, G. Weiglein and L. Zeune, *MSSM Interpretations of the LHC Discovery: Light or Heavy Higgs?*, *Eur. Phys. J.* **C73** (2013) 2354, [1211.1955].

[22] P. Bechtle, H. E. Haber, S. Heinemeyer, O. Stål, T. Stefaniak, G. Weiglein et al., *The Light and Heavy Higgs Interpretation of the MSSM*, *Eur. Phys. J.* **C77** (2017) 67, [1608.00638].

[23] P. Drechsel, L. Galeta, S. Heinemeyer and G. Weiglein, *Precise Predictions for the Higgs-Boson Masses in the NMSSM*, *Eur. Phys. J.* **C77** (2017) 42, [1601.08100].

[24] F. Domingo and G. Weiglein, *NMSSM interpretations of the observed Higgs signal*, *JHEP* **04** (2016) 095, [1509.07283].

[25] P. Bechtle, S. Heinemeyer, O. Stål, T. Stefaniak and G. Weiglein, *HiggsSignals: Confronting arbitrary Higgs sectors with measurements at the Tevatron and the LHC*, *Eur. Phys. J.* **C74** (2014) 2711, [1305.1933].

[26] P. Bechtle, S. Heinemeyer, O. Stål, T. Stefaniak and G. Weiglein, *Probing the Standard Model with Higgs signal rates from the Tevatron, the LHC and a future ILC*, *JHEP* **11** (2014) 039, [1403.1582].

[27] P. Bechtle, O. Brein, S. Heinemeyer, G. Weiglein and K. E. Williams, *HiggsBounds: Confronting Arbitrary Higgs Sectors with Exclusion Bounds from LEP and the Tevatron*, *Comput. Phys. Commun.* **181** (2010) 138–167, [0811.4169].

[28] P. Bechtle, O. Brein, S. Heinemeyer, G. Weiglein and K. E. Williams, *HiggsBounds 2.0.0: Confronting Neutral and Charged Higgs Sector Predictions with Exclusion Bounds from LEP and the Tevatron*, *Comput. Phys. Commun.* **182** (2011) 2605–2631, [1102.1898].

[29] M. Carena, S. Heinemeyer, O. Stål, C. E. M. Wagner and G. Weiglein, *MSSM Higgs Boson Searches at the LHC: Benchmark Scenarios after the Discovery of a Higgs-like Particle*, *Eur. Phys. J.* **C73** (2013) 2552, [1302.7033].

[30] H. Bahl, E. Fuchs, T. Hahn, S. Heinemeyer, S. Liebler, S. Patel et al., *MSSM Higgs Boson Searches at the LHC: Benchmark Scenarios for Run 2 and Beyond*, 1808.07542.

[31] S. Heinemeyer, W. Hollik and G. Weiglein, *The Masses of the neutral CP - even Higgs bosons in the MSSM: Accurate analysis at the two loop level*, *Eur.Phys.J.* **C9** (1999) 343–366, [hep-ph/9812472].

[32] S. Heinemeyer, W. Hollik and G. Weiglein, *FeynHiggs: A Program for the calculation of the masses of the neutral CP even Higgs bosons in the MSSM*, *Comput.Phys.Commun.* **124** (2000) 76–89, [hep-ph/9812320].

[33] G. Degrassi, S. Heinemeyer, W. Hollik, P. Slavich and G. Weiglein, *Towards high precision predictions for the MSSM Higgs sector*, *Eur.Phys.J.* **C28** (2003) 133–143, [hep-ph/0212020].

[34] M. Frank, T. Hahn, S. Heinemeyer, W. Hollik, H. Rzehak et al., *The Higgs Boson Masses and Mixings of the Complex MSSM in the Feynman-Diagrammatic Approach*, *JHEP* **0702** (2007) 047, [hep-ph/0611326].

[35] T. Hahn, S. Heinemeyer, W. Hollik, H. Rzehak and G. Weiglein, *High-Precision Predictions for the Light CP -Even Higgs Boson Mass of the Minimal Supersymmetric Standard Model*, *Phys. Rev. Lett.* **112** (2014) 141801, [1312.4937].

[36] H. Bahl and W. Hollik, *Precise prediction for the light MSSM Higgs boson mass combining effective field theory and fixed-order calculations*, *Eur. Phys. J.* **C76** (2016) 499, [1608.01880].

[37] H. Bahl, S. Heinemeyer, W. Hollik and G. Weiglein, *Reconciling EFT and hybrid calculations of the light MSSM Higgs-boson mass*, *Eur. Phys. J.* **C78** (2018) 57, [1706.00346].

[38] F. Domingo, P. Drechsel and S. Paßehr, *On-Shell neutral Higgs bosons in the NMSSM with complex parameters*, *Eur. Phys. J.* **C77** (2017) 562, [1706.00437].

[39] F. Domingo, S. Heinemeyer, S. Paßehr and G. Weiglein, *Decays of the neutral Higgs bosons into SM fermions and gauge bosons in the $\mathcal{CP}$-violating NMSSM*, 1807.06322.

[40] S. Paßehr and G. Weiglein, *Two-loop top and bottom Yukawa corrections to the Higgs-boson masses in the complex MSSM*, *Eur. Phys. J.* **C78** (2018) 222, [1705.07909].

[41] S. Borowka, S. Paßehr and G. Weiglein, *Complete two-loop QCD contributions to the lightest Higgs-boson mass in the MSSM with complex parameters*, *Eur. Phys. J.* **C78** (2018) 576, [1802.09886].

[42] J. Pardo Vega and G. Villadoro, *SusyHD: Higgs mass Determination in Supersymmetry*, *JHEP* **07** (2015) 159, [1504.05200].

[43] CMS Collaboration, A. M. Sirunyan et al., *Search for the Higgs boson decaying to two muons in proton-proton collisions at $\sqrt{s} = 13$ TeV*, 1807.06325. submitted to Phys. Rev. Lett.

[44] CMS Collaboration, A. M. Sirunyan et al., *Search for lepton flavour violating decays of the Higgs boson to $\mu\tau$ and $e\tau$ in proton-proton collisions at $\sqrt{s} = 13$ TeV*, *JHEP* **06** (2018) 001, [1712.07173].

[45] CMS Collaboration, V. Khachatryan et al., *Search for Lepton-Flavour-Violating Decays of the Higgs Boson*, *Phys. Lett.* **B749** (2015) 337–362, [1502.07400].

[46] CMS Collaboration, V. Khachatryan et al., *Search for lepton flavour violating decays of the Higgs boson to $e\tau$ and $e\mu$ in proton–proton collisions at $\sqrt{s} = 8$ TeV*, *Phys. Lett.* **B763** (2016) 472–500, [1607.03561].

[47] ATLAS Collaboration, *Searches for the $Z\gamma$ decay mode of the Higgs boson and for new high-mass resonances in pp collisions at $\sqrt{s} = 13$ TeV with the ATLAS detector*, *JHEP* **10** (2017) 112, [1708.00212].

[48] ATLAS Collaboration, *Search for new phenomena in high-mass diphoton final states using 37 fb^{-1} of proton–proton collisions collected at $\sqrt{s} = 13$ TeV with the ATLAS detector*, *Phys. Lett.* **B775** (2017) 105–125, [1707.04147].

[49] M. A. Ebert, S. Liebler, I. Moult, I. W. Stewart, F. J. Tackmann, K. Tackmann et al., *Exploiting jet binning to identify the initial state of high-mass resonances*, *Phys. Rev.* **D94** (2016) 051901, [1605.06114].

[50] Malte Hoffmann, *Search for the decay of a heavy Higgs boson decaying to two light Higgs bosons using a kinematic fit*, Ph.D. thesis, Universität Hamburg, 2016.
http://ediss.sub.uni-hamburg.de/volltexte/2016/8244.

[51] CMS Collaboration, V. Khachatryan et al., *Searches for a heavy scalar boson H decaying to a pair of 125 GeV Higgs bosons hh or for a heavy pseudoscalar boson A decaying to Zh, in the final states with $h \to \tau\tau$*, *Phys. Lett.* **B755** (2016) 217–244, [1510.01181].

[52] CMS Collaboration, V. Khachatryan et al., *Search for neutral MSSM Higgs bosons decaying to a pair of tau leptons in pp collisions*, *JHEP* **10** (2014) 160, [1408.3316].

[53] CMS Collaboration, A. M. Sirunyan et al., *Search for additional neutral MSSM Higgs bosons in the $\tau\tau$ final state in proton-proton collisions at $\sqrt{s} = 13$ TeV*, 1803.06553. submitted to JHEP.

[54] CMS Collaboration, *Performance of reconstruction and identification of tau leptons in their decays to hadrons and tau neutrino in LHC Run-2*, Tech. Rep. CMS-PAS-TAU-16-002, CERN, Geneva, 2016.

[55] CMS Collaboration, V. Khachatryan et al., *Search for neutral MSSM Higgs bosons decaying into a pair of bottom quarks*, *JHEP* **11** (2015) 071, [1506.08329].

[56] CMS Collaboration, A. M. Sirunyan et al., *Search for beyond the standard model Higgs bosons decaying into a $\mathrm{b\bar{b}}$ pair in pp collisions at $\sqrt{s} = 13$ TeV*, *JHEP* **08** (2018) 113, [1805.12191].

[57] CMS Collaboration, V. Khachatryan et al., *Search for a very light NMSSM Higgs boson produced in decays of the 125 GeV scalar boson and decaying into τ leptons in pp collisions at $\sqrt{s} = 8$ TeV*, *JHEP* **01** (2016) 079, [1510.06534].

[58] E. Fuchs and G. Weiglein, *Impact of CP-violating interference effects on MSSM Higgs searches*, *Eur. Phys. J.* **C78** (2018) 87, [1705.05757].

Top-Quark Physics at the LHC

Sven-Olaf Moch[1], *Jürgen Reuter*[2]

[1]II. Institut für Theoretische Physik, Universität Hamburg, Germany
[2]DESY, Hamburg, Germany

DOI: http://dx.doi.org/10.3204/PUBDB-2018-00782/B11

We report on the precision determination of the top-quark mass to next-to-next-to-leading order in QCD in well-defined renormalization schemes using data from the Large Hadron Collider for single-top and top-quark pair production. We also discuss the calibration of the so-called Monte Carlo top-quark mass parameter which is determined from a comparison to events with top-quark decay products. The implications of the measured value of the top-quark mass for conclusions about the stability of the electroweak vacuum state of our Universe are illustrated. At future lepton colliders, we provide for the first time matched exclusive calculations valid both at the top threshold and in the continuum, also fully differentially. In addition, we calculate fully off-shell top-pair production (also with an associated Higgs boson) at next-to-leading order in QCD, which allows to extract the top-Yukawa coupling with an unprecedented precision.

1 Introduction

Top-quark production features among the processes with the largest cross sections at the Large Hadron Collider (LHC). So far, the LHC has collected high quality data at collision energies up to $\sqrt{s} = 13$ TeV to be confronted with the high precision theory predictions of the Standard Model (SM) of particle physics. For the latter, the current state-of-art is based on the Quantum Chromodynamics (QCD) corrections up to the next-to-next-to-leading order (NNLO) in the strong coupling constant α_s, which can be used to determine the top-quark mass m_t at this theoretical accuracy. After the confirmation of the Higgs boson's existence, these measured values of the SM parameters m_t and α_s play a decisive role in addressing questions currently in focus of the scientific community and related to the Higgs boson's implications for our Universe at very early times and the stability of the electroweak vacuum. Altogether this makes top-quark physics at the moment one of the most interesting areas in particle physics and precision predictions for processes at present and future colliders are a necessary prerequisites.

In this article we begin with a brief review of the present theory predictions for the production of single top-quarks and top-quark pairs at the LHC. Then we report on the precision determination of the top-quark mass $m_t(\mu_r)$ to NNLO in QCD in the $\overline{\rm MS}$ scheme at a chosen renormalization scale μ_r from measured cross sections at various center-of-mass energies at the LHC. Related, we also discuss the procedure for the calibration of the Monte Carlo top-quark mass parameter used in the kinematic reconstruction of events with top-quark decay products. Finally, we apply the measured values of m_t and α_s together with their present uncertainties to the running of the Higgs boson's self-coupling at large scales, which indicates stability of the ground state of the electroweak theory.

	$\sqrt{s} = 7$ TeV	$\sqrt{s} = 8$ TeV	$\sqrt{s} = 13$ TeV
$\sigma_{pp\to t\bar{t}}$ [pb]	$171.8^{+0.1}_{-5.3} \pm 3.4$	$247.5^{+0.0}_{-7.5} \pm 4.6$	$831.4^{+0.0}_{-23.1} \pm 14.5$

Table 1: Cross section for top-quark pair production at NNLO in QCD with errors shown as $\sigma + \Delta\sigma_{\text{scale}} + \Delta\sigma_{\text{PDF}}$ at various center-of-mass energies of the LHC using $m_t(m_t) = 160.9$ GeV in the $\overline{\text{MS}}$ scheme and the ABMP16 PDF set [1]. The scale uncertainty $\Delta\sigma_{\text{scale}}$ is based on the shifts for the choices $\mu_r = \mu_f = m_t(m_t)/2$ and $\mu_r = \mu_f = 2m_t(m_t)$ and $\Delta\sigma_{\text{PDF}}$ is the 1σ combined PDF+α_s+m_t error.

At future electron-positron colliders, such as the planned International Linear Collider (ILC), the top-quarks can be copiously produced by operating at center-of-mass energies around the threshold to top-quark pair production. With the large statistics collected under such conditions and the significantly reduced uncertainties due to experimental systematics in collisions with electrons and positrons, the ILC is ideally suited for an improved precision measurement of m_t as well as for investigating possible deviations from SM predictions in the top-quark related processes. These aspects are detailed in the final section of this article.

2 Top-quark physics at the LHC

2.1 Inclusive top-quark hadro-production

The theoretical description of both top-quark pair production and single-top production has reached a very high level of accuracy. According to the standard QCD factorization the cross section is given as

$$\sigma_{pp\to X}(s, m_t^2) = \sum_{ij} f_i(\mu_f^2) \otimes f_j(\mu_f^2) \otimes \hat{\sigma}_{ij\to X}\left(\alpha_s(\mu_r), s, m_t^2, \mu_f^2\right) \ , \tag{1}$$

where μ_f and μ_r are the factorization and renormalization scale and s is the center-of-mass energy. The parton distribution functions (PDFs) in the proton are denoted by f_i ($i = q, \bar{q}, g$) and $\hat{\sigma}_{ij\to X}$ is the (hard) subprocess cross section for parton types i and j to produce the final state X, which can be a single top-quark or a $t\bar{t}$ pair. Both, PDFs and the partonic cross sections in Eq. (1) are subject to the standard convolution in the parton momentum fractions, denoted as "$\otimes$". The top-quark mass in Eq. (1) requires the choice of a renormalization scheme, which we take to be the $\overline{\text{MS}}$ scheme, that is using $m_t(\mu_r)$.

The hadro-production of $t\bar{t}$ pairs is a QCD process at Born level, i.e., the leading order contributions to $\hat{\sigma}_{ij\to t\bar{t}}$ are proportional to α_s^2 and the gluon-gluon-fusion process $gg \to t\bar{t}$ driven by the gluon PDF dominates. Higher order corrections to the respective inclusive partonic cross sections have been calculated up to the NNLO in perturbative QCD [2–5] and the result shows good apparent convergence of the perturbative expansion and greatly reduced sensitivity with respect to variations of the scales μ_r and μ_f. The latter is conventionally taken as an estimate of the residual theoretical uncertainty.

In Tab. 1 we quote results for the inclusive $t\bar{t}$ cross section at NNLO accuracy in QCD using the `Hathor` code [6] with the PDF set ABMP16 [1] for various center-of-mass energies of the LHC, $\sqrt{s} = 7, 8$, and 13 TeV. The top-quark mass taken in the $\overline{\text{MS}}$ scheme is set to

$m_t(m_t) = 160.9$ GeV and the strong coupling to $\alpha_s^{(n_f=5)}(M_Z) = 0.1147$. The PDF uncertainties quoted represent the combined symmetric 1σ uncertainty $\Delta\sigma(\text{PDF} + \alpha_s + m_t)$ arising from the variation of the PDF parameters, α_s and m_t in 29 PDF sets of ABMP16. Thanks to the high precision LHC data used in the ABMP16 fit and NNLO accuracy in QCD the overall cross section uncertainty is significantly reduced.

Single-top production on the other hand generates the top-quark in an electroweak interaction at Born level. This proceeds predominantly in a vertex with a W-boson, top- and bottom-quark and its orientation assigns single-top production diagrams to different channels. At the LHC, the t-channel process (Fig. 1b) dominates, while the cross section for Wt-production (Fig. 1c) is typically smaller by one order of magnitude and the s-channel contribution (Fig. 1a) is negligible.

Higher order QCD corrections to the inclusive parton cross sections $\hat{\sigma}_{ij\to t}$ for the single-top production in the t-channel are known to NNLO in the so-called structure function approximation [7] (see also Ref. [8]), which separately accounts for the QCD corrections to the light- and heavy-quark lines, see Fig. 1b, neglecting dynamical cross-talk between the two quark lines, which is expected to be small due to color suppression. Moreover, the known NNLO QCD corrections to $\hat{\sigma}_{ij\to t}$ are quite small. For the inclusive cross section Ref. [7] has reported the ratios $\sigma^{\text{NNLO}}_{pp\to t}/\sigma^{\text{NLO}}_{pp\to t} \simeq -1.6\%$ and $\sigma^{\text{NNLO}}_{pp\to \bar{t}}/\sigma^{\text{NLO}}_{pp\to \bar{t}} \simeq -1.3\%$ at $\sqrt{s} = 8$ TeV for a pole mass $m_t^{\text{pole}} = 173.2$ GeV.

The cross sections for t-channel single-top production are directly proportional to the light quark PDFs. These are nowadays well constrained by data on the measured charged lepton asymmetries from $W^{\pm}$ gauge-boson production at the LHC [9]. Therefore data on cross sections for t-channel production of single top-quarks offers the interesting possibility for a determination of m_t, which is not subject to strong correlations between m_t, α_s and the gluon PDF as is the case for the cross section for $t\bar{t}$-pair production.

In Figs. 2 and 3 we display the cross sections $\sigma_{pp\to\bar{t}}$ and $\sigma_{pp\to\bar{t}}$ at next-to-leading order (NLO) in QCD (computed with the `Hathor` library [6, 10]) for LHC energies of $\sqrt{s} = 7$ and 8 TeV, respectively, using $m_t(m_t) = 160.9$ GeV with scale choice $\mu_r = \mu_f = m_t(m_t)$ and compare with data from ATLAS [11] and CMS [12]. We use the NNLO PDF sets of ABMP16 [1]. CT14 [13], MMHT14 [14], and NNPDF3.1 [15] and central value for each PDF set is complemented by the symmetrized PDF uncertainty. Within the current large experimental uncertainties all predictions in Figs. 2 and 3 agree with the data.

In the ratio of the cross sections $R_t = \sigma_{pp\to\bar{t}}/\sigma_{pp\to\bar{t}}$ on the other hand many theoretical and experimental uncertainties cancel as shown in Fig. 4. This quantity is thus a very sensitive probe for the ratio of d/u quark PDFs at large x. While still all predictions for R_t with the various PDF sets agree with the data there are systematic shifts visible so that with improved statistics for single-top production at $\sqrt{s} = 13$ TeV, this reaction might serve as a standard candle process in the future, cf. Ref. [9].

2.2 Top-quark mass determination

The available high precision theory predictions for the inclusive top-quark hadro-production can be used to extract the top-quark mass when confronted with accurate measurements of those cross sections at the LHC. See, e.g., Ref. [1] for a recent compilation of the respective LHC data sets and Ref. [17] for a review of earlier work on precise heavy-quark mass determinations, including charm and bottom.

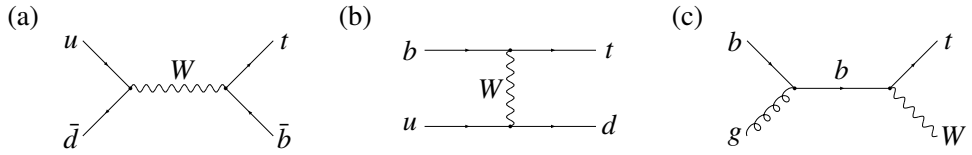


Figure 1: Representative leading order Feynman diagrams for single top-quark production: (a) s-channel; (b) t-channel; (c) in association with a W boson. Figures taken from Ref. [16].

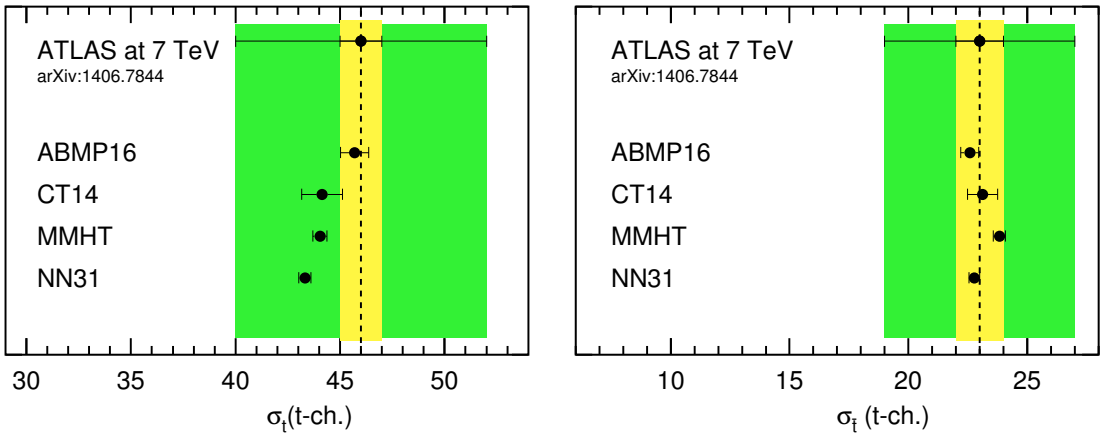


Figure 2: Cross sections together with their 1σ PDF uncertainties for the t-channel production of single (anti)top-quarks in pp collision at $\sqrt{s} = 7$ TeV in comparison to ATLAS data [11] for a $\overline{\text{MS}}$ mass $m_t(m_t) = 160.9$ GeV at the scale $\mu_r = \mu_f = m_t(m_t)$ with PDF sets are taken at NNLO. The inner (yellow) band denotes the statistical uncertainty and the outer (green) band the combined uncertainty due to statistics and systematics.

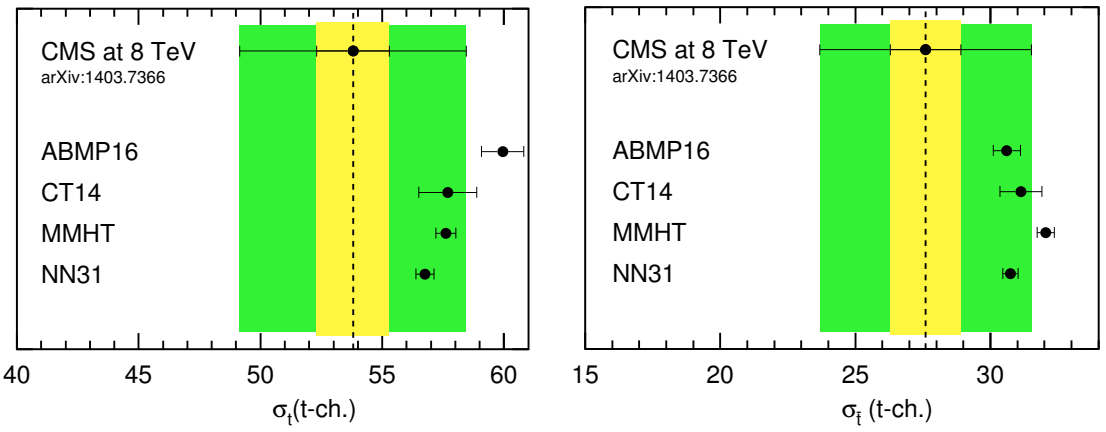


Figure 3: Same as Fig. 2 for pp collision at $\sqrt{s} = 8$ TeV in comparison to CMS data [12].

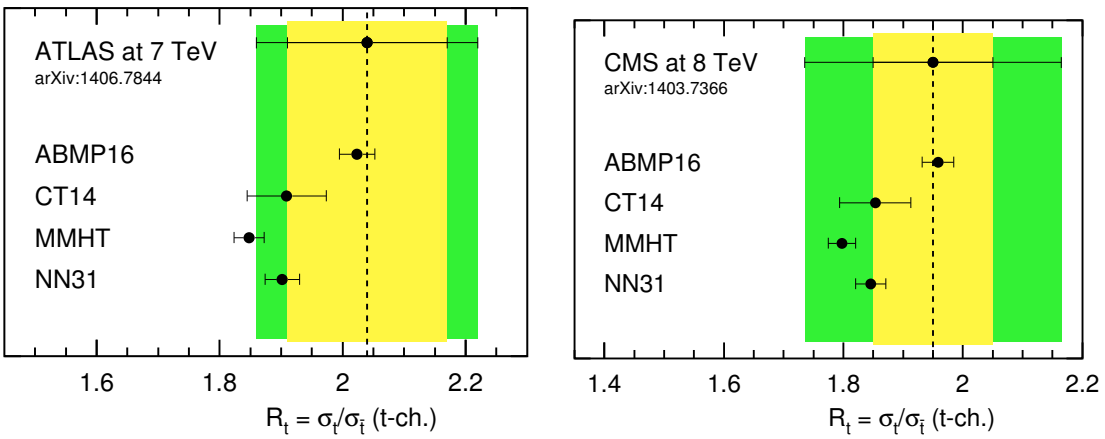


Figure 4: Same as in Figs. 2 and 3 for the ratio of cross sections $R_t = \sigma_{pp\to t\bar{t}}/\sigma_{pp\to\bar{t}}$ in comparison to ATLAS data [11] at $\sqrt{s} = 7$ TeV (left) and to CMS data [12] at $\sqrt{s} = 8$ TeV (right).

To that end, it is important to keep in mind that quark masses are not physical observables, so that the determination of m_t relies on comparing the parametric dependence of the theory prediction $\sigma_{\rm th}(m_t)$ with the experimentally measured cross section value $\sigma_{\rm exp}$. The accuracy of the extracted top-quark mass is intrinsically limited by the sensitivity $\mathcal{S}$ of $\sigma_{\rm th}(m_t)$ to m_t,

$$\left|\frac{\Delta\sigma}{\sigma}\right| = \mathcal{S} \times \left|\frac{\Delta m_t}{m_t}\right| . \tag{2}$$

For the processes under consideration the sensitivity $\mathcal{S} \simeq 5$ for $t\bar{t}$ hadro-production and $\mathcal{S} \simeq 1.5$ for single-top production in the t-channel [10].

Next, the theory computation for $\sigma_{\rm th}(m_t)$ is performed at a given order in perturbation theory and requires the choice of a renormalization scheme for m_t. The most common choice are the on-shell scheme with the pole mass $m_t^{\rm pole}$ and the $\overline{\rm MS}$ scheme with the running top-quark mass $m_t(\mu_r)$, which are then extracted at a given order in perturbation theory. The different mass definition can be related to each other in perturbation theory, see, e.g., Ref. [18] and Ref. [19] for a review of relations between these and other renormalization schemes such as the so-called MSR mass.

Finally, it is important to address the correlation of the m_t dependence in $\sigma_{\rm th}(m_t)$ with all other input parameters, most prominently the PDFs in the proton and the strong coupling constant α_s. To account for those correlations any extraction of m_t from hadro-production cross sections should be performed as a global fit of m_t, the PDFs and α_s simultaneously [1]. Shifts in m_t for a given choice of a fixed value of α_s in variants of the global fit performed in Ref. [1] are illustrated in Fig. 5. As can be seen, these are sizable and easily exceed the experimental uncertainty on m_t indicated by the vertical bars.

Using the theory predictions with a running top-quark mass $m_t(\mu_r)$ at NNLO for $t\bar{t}$ production [20] and for single-top production [16] the global analysis of Ref. [1] determines n the $\overline{\rm MS}$ scheme at NNLO the value

$$m_t(m_t) \quad = \quad 160.9 \pm 1.1 \ \ {\rm GeV} . \tag{3}$$

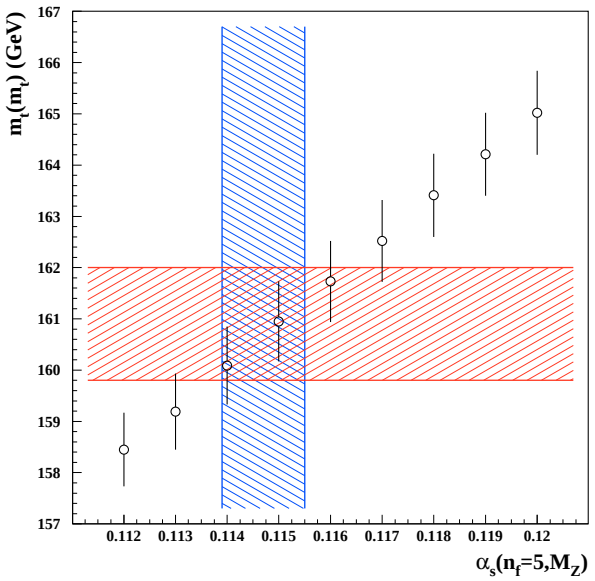


Figure 5: The $\overline{\rm MS}$ value of $m_t(m_t)$ obtained in the variants of the ABMP16 analysis with the value of $\alpha_s^{(n_f=5)}(M_Z)$ fixed in comparison with the 1σ bands for $m_t(m_t)$ and $\alpha_s^{(n_f=5)}(M_Z)$ obtained in the nominal ABMP16 fit (left-tilted and right-tilted hatch, respectively). Reprinted figure with permission from Ref. [1]. Copyright (2017) by the American Physical Society.

The top-quark mass in Eq. (3) has been extracted in a well-defined renormalization scheme with direct relation to the parameter in the QCD Lagrangian. A commonly used experimental procedure, on the other hand, performs a fit of the top-quark mass parameter used in Monte Carlo simulations of events with top-quark decays, when comparing those simulations to the kinematic measurement of the top-quark decay products. The mass determined in this way is therefore often referred to as the so-called top-quark Monte Carlo mass and the calibration of this mass parameter has been a long-standing problem, since no renormalization schemes has been specified in those Monte Carlo event generators.

To overcome this problem, Ref. [21] has proposed a method to establish experimentally the relation between the top-quark mass $m_t^{\rm MC}$ as implemented in a given Monte-Carlo generator and the Lagrangian mass parameter m_t in a theoretically well-defined renormalization scheme. The method proceeds through a simultaneous fit of $m_t^{\rm MC}$ and an observable with sensitivity to m_t, such as the inclusive $t\bar{t}$ cross section $\sigma_{pp\to t\bar{t}}$ discussed above. In particular, this approach does not rely on any prior assumptions about the relation between m_t and $m_t^{\rm MC}$, since the measured observable, e.g., $\sigma_{pp\to t\bar{t}}$ is independent of $m_t^{\rm MC}$ and can be used subsequently for a determination of m_t.

In Fig.6 the analysis strategy has been illustrated with a two parameter likelihood fit for the measured Monte Carlo mass $m_t^{\rm MC}$ and the inclusive $t\bar{t}$ production cross section $\sigma_{pp\to t\bar{t}}$. Using the measured value for $\sigma_{pp\to t\bar{t}}$ it is the possible to extract, e.g., the pole mass $m_t^{\rm pole}$ in a subsequent step and to determine the off-set $\Delta_m = m_t^{\rm pole} - m_t^{\rm MC}$. Examples from inclusive

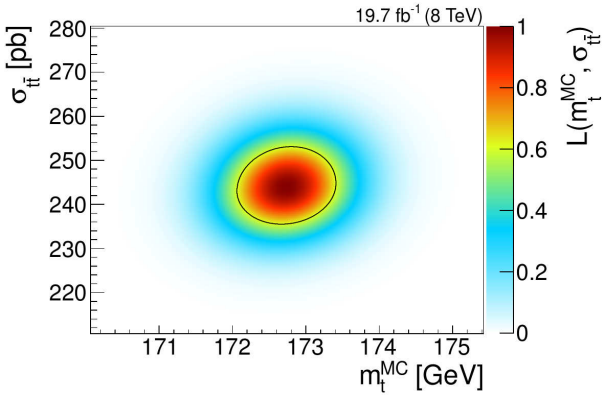


Figure 6: Likelihood L for the measured Monte Carlo mass m_t^{MC} and the $t\bar{t}$ production cross section $\sigma_{pp\to t\bar{t}}$ at a center-of-mass energy of $\sqrt{s} = 8$ TeV with the 1σ uncertainty denoted by the black contour. Reprinted figure with permission from Ref. [21]. Copyright (2016) by the American Physical Society.

and differential cross sections for hadro-production of top-quarks considered in Ref. [21] have led to $\Delta_m \simeq \mathcal{O}(2)$ GeV, depending on details of the analysis, of course.

2.3 Stability of the electroweak vacuum

In the light of the recent high-precision measurements of the Higgs boson mass $m_H = 125.09 \pm 0.24$ GeV [22], the measured values for the strong coupling α_s and the top-quark mass m_t, i.e., the Yukawa coupling of the top-quark to the Higgs boson give rise to an intriguing coincidence. The scalar potential $V(\phi)$ of the Higgs boson field ϕ, given by

$$V(\phi) = -\frac{m_\phi^2}{2}\phi^\dagger\phi + \lambda(\phi^\dagger\phi)^2\,, \tag{4}$$

is controlled by the scalar self-coupling $\lambda(\mu_r)$ and the quadratic Higgs mass parameter proportional to m_ϕ with the normalization $m_\phi = m_H$ at tree level, which combine in the expectation value of the electroweak vacuum as $v(\mu_r) = \sqrt{m_\phi^2(\mu_r)/(2\lambda(\mu_r))}$. It is possible for the Higgs potential to develop a second minimum at field values as large as the Planck scale $M_{Pl} \simeq 10^{19}$ GeV in addition to $v = 246$ GeV in which we live.

Investigations of the stability of the electroweak vacuum are therefore important to answer the question, if the SM can be extended to very high scales, where unification with gravity is expected. Requiring $\lambda(\mu_r) \geq 0$ at all scales up to the Planck scale M_{Pl} allows to formulate the condition for the vacuum stability as a lower bound on the mass of the Higgs boson as follows [23]

$$\begin{aligned} m_H \;=\; & 129.6 \;\text{GeV} \\ & +1.8 \times \left(\frac{m_t^{\mathrm{pole}} - 173.34\;\text{GeV}}{0.9}\right) - 0.5 \times \left(\frac{\alpha_s^{(n_f=5)}(M_Z) - 0.1184}{0.0007}\right) \text{GeV} \pm 0.3\;\text{GeV}\,, \end{aligned} \tag{5}$$

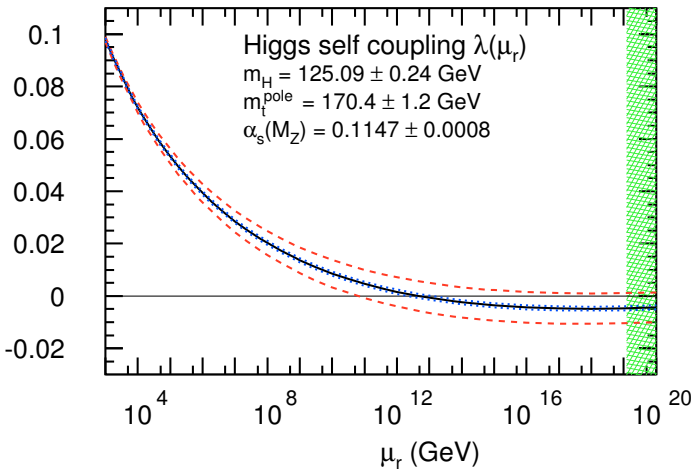


Figure 7: The renormalization group evolution of the Higgs boson self-coupling λ as a function of scale μ_r. The dashed (red) lines denote the combined 1σ uncertainty for $\alpha_s^{(n_f=5)}(M_Z)$ and $m_t^{\rm pole}$ and the dotted (blue) lines the 1σ uncertainty in the value of $m_H = 125.09 \pm 0.24$. The range of scales $\mu_r \geq M_{Pl}$ is indicated by the hatched (green) band on the right. Reprinted figure with permission from Ref. [1]. Copyright (2017) by the American Physical Society.

where m_t and α_s are to be taken in the on-shell and $\overline{\rm MS}$ schemes, respectively, and the uncertainty of $\pm 0.3\,$GeV appears due to missing higher-order corrections (see also Ref. [24]).

With the values determined in Ref. [1] at NNLO in QCD for the strong coupling, $\alpha_s^{(n_f=5)}(M_Z) = 0.1147 \pm 0.0008$ and the running top-quark mass $m_t(m_t)$, cf. Eq. (3), we are in a position to update previous work [25]. The value of m_t in Eq. (3) correspond to the pole mass $m_t^{\rm pole} = 170.4 \pm 1.2$ GeV at NNLO so that Eq. (5) leads to the bound

$$m_H \;=\; 126.3 \pm 2.5 \;\; \text{GeV}\,, \tag{6}$$

where all uncertainties have been added in quadrature. Thus, within its 1σ uncertainty this lower bound is compatible with the measured value $m_H = 125.09 \pm 0.24$ GeV [22] for the Higgs boson mass, allowing for stability up to the scale M_{Pl}.

In a complementary way this is illustrated in Fig. 7 showing the running of the Higgs boson self-coupling $\lambda(\mu_r)$ in full three-loop accuracy and with α_s and m_t obtained in Ref. [1] as the input parameters. The computation has been performed with the code `mr`, which implements matching and running of the SM parameters [26]. Clearly, a vanishing Higgs self-coupling $\lambda = 0$ at M_{Pl} remains a scenario which is compatible with the current values of α_s, m_t and m_H within their 1σ uncertainties. In addition, as follows from our analysis the value of $\lambda(\mu_r)$ remains strictly positive up to scales $\mu_r \sim \mathcal{O}(10^{12}\,\text{GeV})$, so that no new physics needs to be invoked in order to stabilize the electroweak vacuum.

2.4 Beyond the SM top-quark physics

Most models beyond the Standard Model treat the top-quark special as it is the heaviest known particle and couples most strongly to the electroweak symmetry breaking sector. We

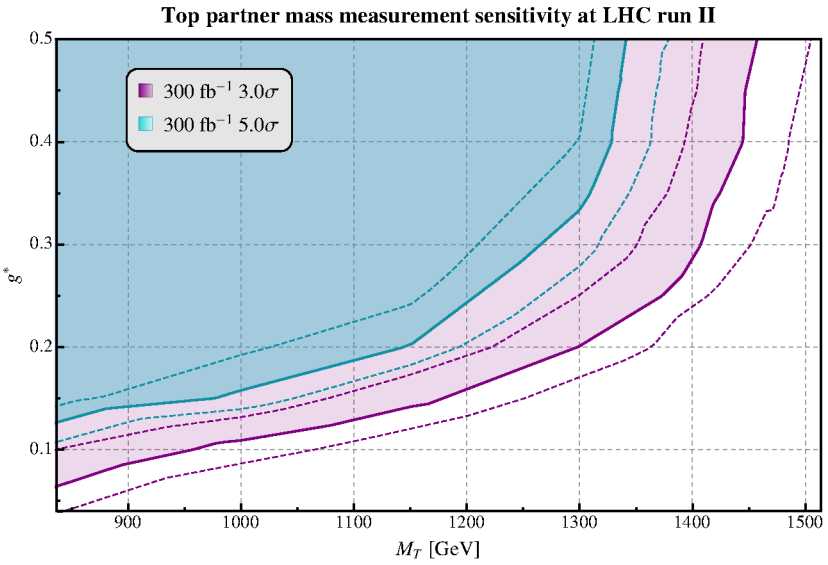


Figure 8: Sensitivity to top-partners at LHC Run 2 with $\sqrt{s} = 13\,\text{TeV}$ and $300\,\text{fb}^{-1}$ of integrated luminosity using the $T \to tZ$ channel with hadronic boosted top reconstruction. Figure taken from Ref. [27].

just discuss here one particular aspect of new physics in the top-sector, namely the search for so-called heavy top-partners at the LHC and the possible measurements of their properties. These particles are predicted in many models to compensate the large radiative corrections to the Higgs potential from the SM top-quark. We focus here on fermionic top partners (denoted here as T), where searches in specific decay channels of these particles into the SM top-quark and a Z-boson, i.e., the decay $T \to tZ$, have been studied [27]. This channel has been studied for hadronically decaying top-quarks by means of so-called boosted top tagging techniques. As there is a huge mass gap expected between the top-partner and the SM top-quark, the SM top-quark gets a considerable boost which allows it to be treated with jet substructure techniques. Due to the leptonically decaying Z boson, this channel allows to fully reconstruct the mass of the top-partner particle in case of a discovery.

This has been studied in the context of simplified models, where only the top-partner and its electroweak and QCD couplings to SM particles are considered. Typical scenarios for such top-partners are models with composite Higgs boson or Little Higgs models, which have also been studied specifically in this context, cf. [28–30].

Possible discoveries of a top-partner have been quantified as a function of its mass and its universal electroweak coupling g^*. The sensitivity curves for 3σ evidence as well as for 5σ discovery are shown in Fig. 8. The shown bands include a possible additional non-statistical uncertainty of 30% on the visible cross section of the involved processes, e.g., from the experimental systematics in detection efficiencies. If a signal peak is observed, a measurement of the top-partner's invariant mass is possible with a resolution of $\Delta m_T = \pm 75$ GeV around the peak, at worst.

Another project focusing on new physics in the top-quark sector studied single-top production at the LHC as a means to measure possible anomalous charged-current contact interactions

in the top-quark sector [31]. This relies on an effective-field theory approach which parameterizes the effect of new physics in a model-independent way in the form of higher-dimensional four-fermion operators for $tbff'$ contact interactions whose Wilson coefficients can be interpreted as anomalous top-quark couplings. Here, binned likelihood distributions over specific kinematic observables have been studied to gain sensitivity on the Wilson coefficients. As a result it was found that for new physics scale $\Lambda_{\rm np}$ of $\Lambda_{\rm np} = 3$ TeV the LHC with $\sqrt{s} = 14$ TeV and 100 fb^{-1} integrated luminosity reaches a sensitivity of the order $\mathcal{O}(0.01 - 1)$ for the Wilson coefficients. Angular distributions can serve as spin analyzers for the top-quark and allow to resolve ambiguities in the parameter determination.

3 Top-quark physics at the ILC and CLIC

Top-quark physics represents together with Higgs boson precision measurements and the search for new physics one of the three cornerstones of the physics program of any future electron-positron collider. The ILC baseline design [32, 33] contains runs at center-of-mass energies of both $\sqrt{s} = 350$ GeV and 500 GeV, respectively, while the baseline design of the Compact Linear Collider (CLIC) [34, 35] contains stages at $\sqrt{s} = 380$ GeV, 1.4 TeV and 3 TeV, respectively. The new staging scenario foresees a long run of the ILC at $\sqrt{s} = 250$ GeV before an energy upgrade [36] containing the top-quark physics program. The work carried out for this top-quark physics program within this project encompasses fixed-order NLO QCD corrections for the fully off-shell leptonic top-decays, without and with an additional Higgs boson in the final state, i.e., the processes

$$e^+e^- \to e^+\nu_e\mu^-\bar{\nu}_\mu b\bar{b}(+H)\,, \tag{7}$$

see [37], as well as the matching of the fully exclusive resummed non-relativistic threshold corrections within non-relativistic QCD (NRQCD) at next-to-leading logarithmic accuracy (NLL) to the above mentioned continuum (NLO QCD) calculation [38]. Both calculations have been relying on the framework for automated NLO QCD calculations within the Monte-Carlo event generator `WHIZARD` [39] which has been developed during the final phase of the SFB 676.

In Ref. [37], top-pair production and top-pair production in association with a Higgs boson have been calculated at three different levels of off-shellness. First, for the on-shell processes,

$$e^+e^- \to t\bar{t}(H)\,, \tag{8}$$

second, with decaying top-quarks,

$$e^+e^- \to W^-bW^+\bar{b}(H)\,, \tag{9}$$

and, third, with leptonic W-boson decays,

$$e^+e^- \to e^+\nu_e\mu^-\bar{\nu}_\mu b\bar{b}(H)\,. \tag{10}$$

For top-pair production, the main results are shown in Fig. 9. The left panel shows the total cross section at LO and NLO QCD for the full energy range up to the maximal energy of the CLIC project of $\sqrt{s} = 3$ TeV. The two panels at the bottom show the K-factor (the ratio between NLO and LO total sections), as well as the ratio of the off-shell to the on-shell process. This ratio is rising from unity close to threshold up to a factor of two, demonstrating that the non-resonant irreducible background becomes more and more important at higher energy.

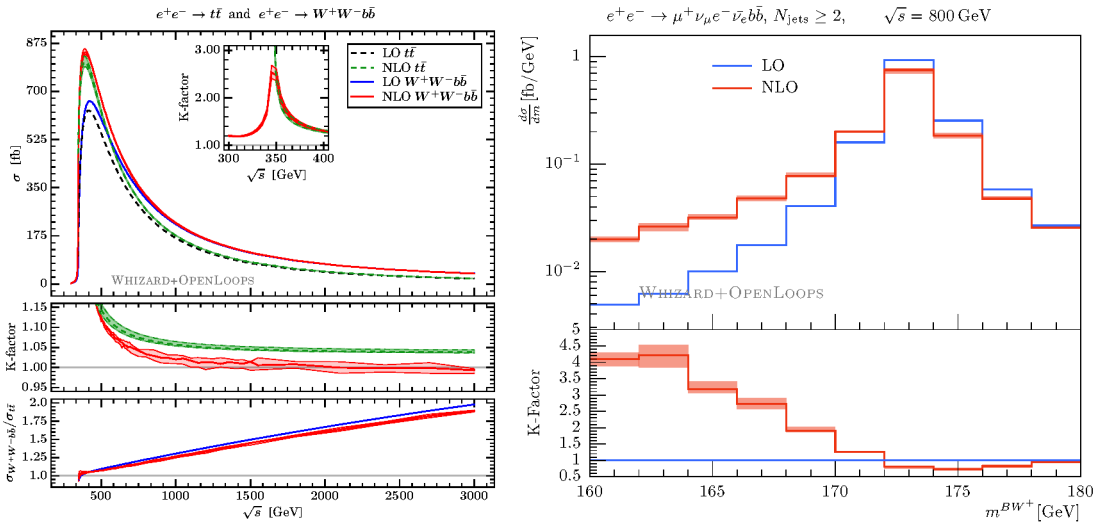


Figure 9: Left panel: Total cross section for $e^+e^- \to W^+bW^-\bar{b}$ at leading order (LO) QCD (blue) and NLO QCD (red), respectively. Dashed curves show the on-shell process $e^+e^- \to t\bar{t}$. The ratio plots show the K-factor (NLO QCD over LO QCD) and the off-shell over the on-shell process. The inset shows the K-factor close to threshold. Right panel: Differential distribution for the invariant mass of the b-jet and the W^+ for $e^+e^- \to e^+\nu_e\mu^-\bar{\nu}_\mu b\bar{b}$ at LO QCD (blue) and NLO QCD (red), respectively. The red band shows the scale uncertainties for $m_t/2 < \mu < 2m_t$ around the central scale $\mu = m_t$. Figures taken from Ref. [37].

The inset shows the K-factor in the proximity of the top-quark threshold, where fixed-order perturbation theory is not a good approximation any more due to the strong QCD binding effects of the non-relativistic top-quark pair. The right panel shows the differential distribution of the invariant mass of the b-jet and the W^+ at LO and NLO QCD, with the K-factor being clearly not constant over the phase space. In Fig. 10, the corresponding total cross section for off-shell top pair production in association with a Higgs boson is shown in the left panel. All curves have the corresponding meaning compared to Fig. 9. The right panel shows the total cross section for the off-shell process

$$e^+e^- \to W^+bW^-\bar{b}H\,, \tag{11}$$

as a function of the signal strength modifier $\xi_t = y_t/y_t^{SM}$ for the top-Yukawa coupling. It shows that the dependence on this modifier differs between LO and NLO QCD. The results from this NLO QCD calculation have been used by the CLICdp collaboration for the assessment on the precision with which the top-Yukawa coupling can be measured at CLIC for 1.4 TeV center-of-mass energy [40].

The most precise method known to measure the top-quark mass with an ultimate precision of $\Delta m_t = 30 - 70$ MeV is a template fit of the top threshold scan for the total inclusive cross section. The main uncertainties in addition to the unknown higher order corrections beyond next-to-next-to-next-to-leading order (NNNLO) in QCD are theoretical background uncertainties, systematic uncertainties due to selection efficiencies and uncertainties from the

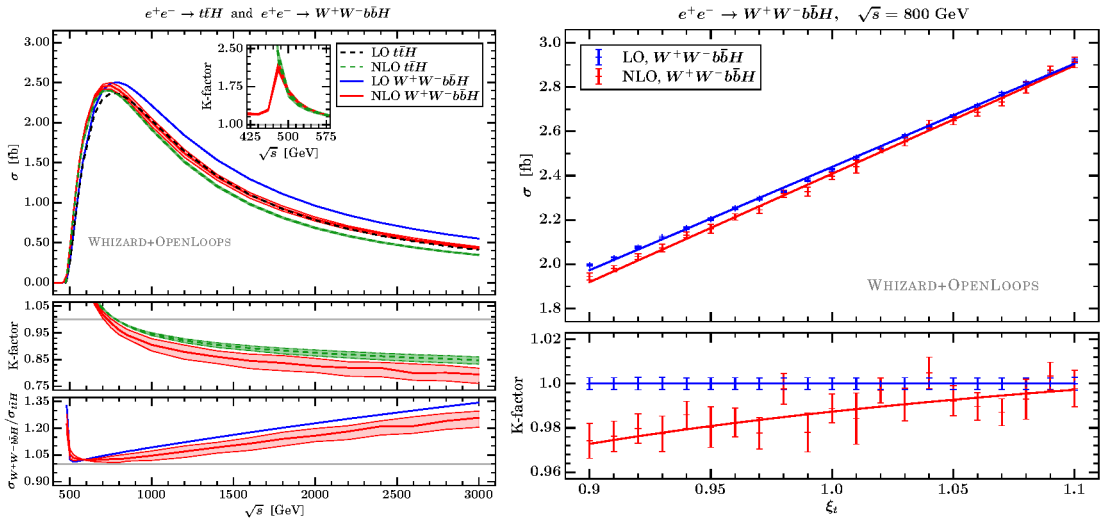


Figure 10: Left panel: Total cross section for $e^+e^- \to W^+bW^-\bar{b}H$ at LO QCD (blue) and NLO QCD (red), respectively. Dashed curves show the on-shell process $e^+e^- \to t\bar{t}H$. The ratio plots show the K-factor (NLO QCD over LO QCD) and the off-shell over the on-shell process. The inset shows the K-factor close to threshold. Right panel: Dependence of the total cross section for $e^+e^- \to W^+bW^-\bar{b}H$ at LO QCD (blue) and NLO QCD (red), respectively, on the signal strength modifier for the top-Yukawa coupling, $\xi_t = y_t/y_t^{SM}$. Figures taken from Ref. [37].

beam spectrum. All of the last three ones can be addressed with the work from [38]. The main difficulty is to properly match the non-relativistic effective-field theory calculation using NRQCD that is best suited right at the threshold with the relativistic NLO QCD calculation at the continuum. For that purpose, a factorized calculation in double-pole approximation with on-shell projection has been devised in [38] to subtract the double-counting of α_s corrections from both approaches, thereby maintaining full electroweak gauge invariance. The left panel of Fig. 11 shows the fully exclusive matched threshold scan for the process

$$e^+e^- \to W^+bW^-\bar{b}\,. \tag{12}$$

The blue curve shows the fixed-order NLO QCD calculation including scale variations, while the red curve shows the fully matched calculation. The red band includes uncertainties from the soft and hard NRQCD scale variations, the relativistic NLO QCD scale variations, variations over the details of the switch-off of the non-relativistic contributions in the continuum. (The dashed black line shows how the non-relativistic threshold calculation fails to describe top pair production properly in the continuum.) To be more conservative, scale variations are also symmetrized with respect to the central value line as the NRQCD scale variations are highly asymmetric. The plot includes the effects from an all-order resummation of soft-collinear QED photons from initial-state radiation as well as hard-collinear photons up to third order in α. The matched exclusive calculation provided in [38] allows for the first time to study differential top-quark distributions in the vicinity of the top threshold. This is shown in the right panel of Fig. 11 for the invariant mass of the b-jet and the W^+ boson. The blue curve shows the NLO QCD result, while the red curve shows the matched calculation.

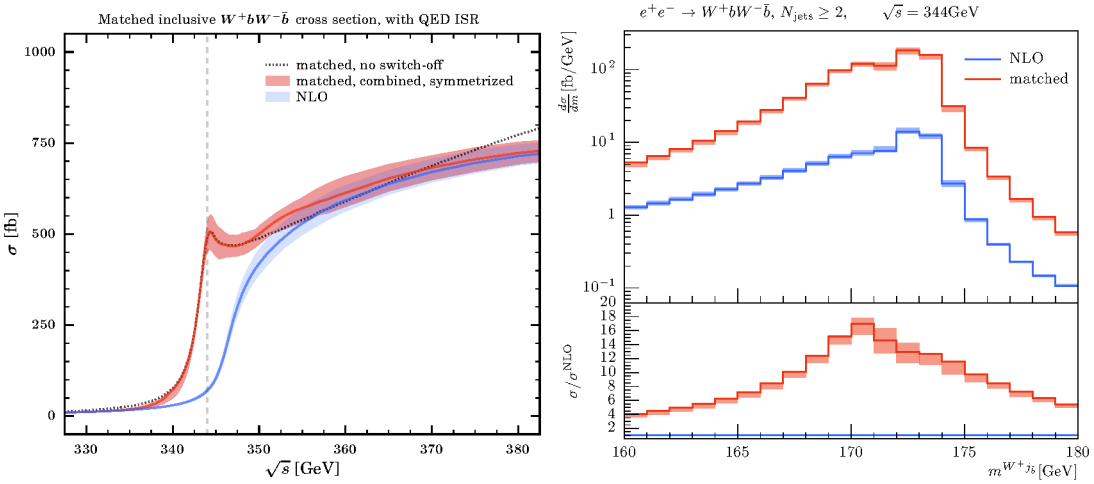


Figure 11: Left panel: Threshold scan for the exclusive process $e^+e^- \to W^+bW^-\bar{b}$ matched at NLL NRQCD (threshold) to NLO QCD (continuum), including full all-order QED initial state radiation effects. Right panel: Differential distribution for the invariant mass of the b-jet and the $W+$ boson at fixed order NLO QCD (blue) and fully matched (red), respectively. Figures taken from Ref. [38].

4 Conclusions

Top-quark physics is one the major fields in particle physics, both to study the properties of the heaviest known particle in Nature, as well as using it as a means to search for new physics. In this project, forefront precision calculations have been performed for the studies of the properties of the top-quark at the running LHC as well as for future lepton colliders. The calculations made in this project are very important for the measurement of the mass of the top-quark, the strong coupling constant, the top-Yukawa coupling and the width of the top-quark, as well as for a better understanding of the parton distribution functions of the proton. In addition, top-quark physics has been used as a tool for searches for new physics, e.g. for the search of heavy top-like new quarks, so-called top-partner particles.

Acknowledgments

S. M. gratefully acknowledges collaborations with S. Alekhin, J. Blümlein, J. Kieseler, K. Lipka, R. Placakyte and S. Thier; and J. R. R. wants to thank for collaborations with A.H. Hoang, W. Kilian, J. Lindert and S. Pozzorini.

References

[1] S. Alekhin, J. Blümlein, S. Moch and R. Placakyte, *Parton distribution functions, α_s, and heavy-quark masses for LHC Run II*, *Phys. Rev.* **D96** (2017) 014011, [1701.05838].

[2] P. Bärnreuther, M. Czakon and A. Mitov, *Percent Level Precision Physics at the Tevatron: First Genuine NNLO QCD Corrections to $q\bar{q} \to t\bar{t} + X$*, *Phys. Rev. Lett.* **109** (2012) 132001, [1204.5201].

[3] M. Czakon and A. Mitov, *NNLO corrections to top-pair production at hadron colliders: the all-fermionic scattering channels*, *JHEP* **12** (2012) 054, [1207.0236].

[4] M. Czakon and A. Mitov, *NNLO corrections to top pair production at hadron colliders: the quark-gluon reaction*, *JHEP* **01** (2013) 080, [1210.6832].

[5] M. Czakon, P. Fiedler and A. Mitov, *Total Top-Quark Pair-Production Cross Section at Hadron Colliders Through $O(\alpha_s^4)$*, *Phys. Rev. Lett.* **110** (2013) 252004, [1303.6254].

[6] M. Aliev, H. Lacker, U. Langenfeld, S. Moch, P. Uwer and M. Wiedermann, *HATHOR: HAdronic Top and Heavy quarks crOss section calculatoR*, *Comput. Phys. Commun.* **182** (2011) 1034–1046, [1007.1327].

[7] M. Brucherseifer, F. Caola and K. Melnikov, *On the NNLO QCD corrections to single-top production at the LHC*, *Phys. Lett.* **B736** (2014) 58–63, [1404.7116].

[8] E. L. Berger, J. Gao, C. P. Yuan and H. X. Zhu, *NNLO QCD Corrections to t-channel Single Top-Quark Production and Decay*, *Phys. Rev.* **D94** (2016) 071501, [1606.08463].

[9] S. Alekhin, J. Blümlein, S. Moch and R. Placakyte, *Isospin asymmetry of quark distributions and implications for single top-quark production at the LHC*, *Phys. Rev.* **D94** (2016) 114038, [1508.07923].

[10] P. Kant, O. M. Kind, T. Kintscher, T. Lohse, T. Martini, S. Mölbitz et al., *HatHor for single top-quark production: Updated predictions and uncertainty estimates for single top-quark production in hadronic collisions*, *Comput. Phys. Commun.* **191** (2015) 74–89, [1406.4403].

[11] ATLAS Collaboration, G. Aad et al., *Comprehensive measurements of t-channel single top-quark production cross sections at $\sqrt{s} = 7$ TeV with the ATLAS detector*, *Phys. Rev.* **D90** (2014) 112006, [1406.7844].

[12] CMS Collaboration, V. Khachatryan et al., *Measurement of the t-channel single-top-quark production cross section and of the $| V_{tb} |$ CKM matrix element in pp collisions at $\sqrt{s}$= 8 TeV*, *JHEP* **06** (2014) 090, [1403.7366].

[13] S. Dulat, T.-J. Hou, J. Gao, M. Guzzi, J. Huston, P. Nadolsky et al., *New parton distribution functions from a global analysis of quantum chromodynamics*, *Phys. Rev.* **D93** (2016) 033006, [1506.07443].

[14] L. A. Harland-Lang, A. D. Martin, P. Motylinski and R. S. Thorne, *Parton distributions in the LHC era: MMHT 2014 PDFs*, *Eur. Phys. J.* **C75** (2015) 204, [1412.3989].

[15] NNPDF Collaboration, R. D. Ball et al., *Parton distributions from high-precision collider data*, *Eur. Phys. J.* **C77** (2017) 663, [1706.00428].

[16] S. Alekhin, S. Moch and S. Thier, *Determination of the top-quark mass from hadro-production of single top-quarks*, *Phys. Lett.* **B763** (2016) 341–346, [1608.05212].

[17] S. Moch, *Precise heavy-quark masses*, *Nucl. Part. Phys. Proc.* **261-262** (2015) 130–139.

[18] P. Marquard, A. V. Smirnov, V. A. Smirnov, M. Steinhauser and D. Wellmann, *$\overline{\text{MS}}$-on-shell quark mass relation up to four loops in QCD and a general $SU(N)$ gauge group*, *Phys. Rev.* **D94** (2016) 074025, [1606.06754].

[19] S. Moch et al., *High precision fundamental constants at the TeV scale*, 1405.4781.

[20] U. Langenfeld, S. Moch and P. Uwer, *Measuring the running top-quark mass*, *Phys. Rev.* **D80** (2009) 054009, [0906.5273].

[21] J. Kieseler, K. Lipka and S.-O. Moch, *Calibration of the Top-Quark Monte Carlo Mass*, *Phys. Rev. Lett.* **116** (2016) 162001, [1511.00841].

[22] ATLAS, CMS Collaborations, G. Aad et al., *Combined Measurement of the Higgs Boson Mass in pp Collisions at $\sqrt{s} = 7$ and 8 TeV with the ATLAS and CMS Experiments*, *Phys. Rev. Lett.* **114** (2015) 191803, [1503.07589].

[23] D. Buttazzo, G. Degrassi, P. P. Giardino, G. F. Giudice, F. Sala, A. Salvio et al., *Investigating the near-criticality of the Higgs boson*, *JHEP* **12** (2013) 089, [1307.3536].

[24] A. V. Bednyakov, B. A. Kniehl, A. F. Pikelner and O. L. Veretin, *Stability of the Electroweak Vacuum: Gauge Independence and Advanced Precision*, *Phys. Rev. Lett.* **115** (2015) 201802, [1507.08833].

[25] S. Alekhin, A. Djouadi and S. Moch, *The top quark and Higgs boson masses and the stability of the electroweak vacuum*, *Phys. Lett.* **B716** (2012) 214–219, [1207.0980].

[26] B. A. Kniehl, A. F. Pikelner and O. L. Veretin, *mr: a C++ library for the matching and running of the Standard Model parameters*, *Comput. Phys. Commun.* **206** (2016) 84–96, [1601.08143].

[27] J. Reuter and M. Tonini, *Top Partner Discovery in the $T \to tZ$ channel at the LHC*, *JHEP* **01** (2015) 088, [1409.6962].

[28] J. Reuter and M. Tonini, *Can the 125 GeV Higgs be the Little Higgs?*, *JHEP* **02** (2013) 077, [1212.5930].

[29] J. Reuter, M. Tonini and M. de Vries, *Littlest Higgs with T-parity: Status and Prospects*, *JHEP* **02** (2014) 053, [1310.2918].

[30] D. Dercks, G. Moortgat-Pick, J. Reuter and S. Y. Shim, *The fate of the Littlest Higgs Model with T-parity under 13 TeV LHC Data*, *JHEP* **05** (2018) 049, [1801.06499].

[31] F. Bach and T. Ohl, *Anomalous top charged-current contact interactions in single top production at the LHC*, *Phys. Rev.* **D90** (2014) 074022, [1407.2546].

[32] H. Baer, T. Barklow, K. Fujii, Y. Gao, A. Hoang, S. Kanemura et al., *The International Linear Collider Technical Design Report - Volume 2: Physics*, 1306.6352.

[33] K. Fujii et al., *Physics Case for the International Linear Collider*, 1506.05992.

[34] L. Linssen, A. Miyamoto, M. Stanitzki and H. Weerts, *Physics and Detectors at CLIC: CLIC Conceptual Design Report*, 1202.5940.

[35] P. Lebrun, L. Linssen, A. Lucaci-Timoce, D. Schulte, F. Simon, S. Stapnes et al., *The CLIC Programme: Towards a Staged e+e- Linear Collider Exploring the Terascale : CLIC Conceptual Design Report*, 1209.2543.

[36] T. Barklow, J. Brau, K. Fujii, J. Gao, J. List, N. Walker et al., *ILC Operating Scenarios*, 1506.07830.

[37] B. Chokoufé Nejad, W. Kilian, J. M. Lindert, S. Pozzorini, J. Reuter and C. Weiss, *NLO QCD predictions for off-shell $t\bar{t}$ and $t\bar{t}H$ production and decay at a linear collider*, *JHEP* **12** (2016) 075, [1609.03390].

[38] F. Bach, B. C. Nejad, A. Hoang, W. Kilian, J. Reuter, M. Stahlhofen et al., *Fully-differential Top-Pair Production at a Lepton Collider: From Threshold to Continuum*, *JHEP* **03** (2018) 184, [1712.02220].

[39] W. Kilian, T. Ohl and J. Reuter, *WHIZARD: Simulating Multi-Particle Processes at LHC and ILC*, *Eur. Phys. J.* **C71** (2011) 1742, [0708.4233].

[40] CLICDP Collaboration, H. Abramowicz et al., *Top-Quark Physics at the CLIC Electron-Positron Linear Collider*, 1807.02441.

SUSY Phenomenology—From the Early Universe to the LHC Era

Jörn Kersten

Department of Physics and Technology, University of Bergen, Norway

DOI: http://dx.doi.org/10.3204/PUBDB-2018-00782/N1

If supersymmetry exists around the TeV scale, it affects not only experiments at the LHC but also searches for rare processes, astroparticle physics and cosmology. The goal of the project was to combine information from all these sources in order to learn as much as possible about processes in the early universe and about physics at very high energies that are inaccessible to colliders. Examples include the impact of relatively late decaying particles on big bang nucleosynthesis, supersymmetry breaking and the origin of the observed flavor structures.

1 Introduction

While low-energy supersymmetry (SUSY) remains the most elegant solution of the hierarchy problem, it is being pressured on a number of fronts. In addition to the classical problems like the flavor and gravitino problem, the lack of a signal for superparticles at the LHC becomes an increasingly severe issue, which might be dubbed the SUSY discovery problem. This may imply that SUSY is not realized in nature after all. However, it may also imply that the realization of SUSY chosen by nature has somewhat unusual features that limit the effectiveness of the LHC searches.

One such feature is the nature of the lightest SUSY particle (LSP). If it is the neutralino, as is usually assumed, the gravitino is unstable. Due to its extremely weak interactions, it has a relatively long lifetime of up to several years. In this case, the energetic decay products created by gravitino decays in the early universe destroy nuclei produced by big bang nucleosynthesis (BBN) [1–3]. The observed abundances of primordial light elements therefore either require a gravitino mass $m_{3/2} \gg 1\,\mathrm{TeV}$ or a reheating temperature after inflation $T_\mathrm{R} \lesssim 10^6\,\mathrm{GeV}$ [4]. The former constraint implies a quite unnatural mass spectrum in most scenarios of SUSY breaking, whereas the latter one prevents thermal leptogenesis [5] without fine-tuning [6]. This motivates scenarios where the gravitino is the LSP and thus stable [7]. For SUSY at the TeV scale and $T_\mathrm{R} \sim 10^9\,\mathrm{GeV}$, thermal production shortly after inflation yields a gravitino density that is consistent with the observed dark matter density, if the gravitino has a mass of some tens of GeV [8, 9]. Thus, a relatively heavy gravitino LSP is a viable cold dark matter candidate. In this case the next-to-LSP (NLSP) becomes long-lived in the absence of R-parity violation, as the only superparticle it can decay into is the gravitino with its superweak interactions. So even in this scenario we have to worry about the effect of late decays on BBN [10]. Charged NLSPs are further constrained since they form bound states with nuclei, which alters BBN reaction rates [11]. Consequently, the gravitino problem is present also in gravitino LSP scenarios but

significantly alleviated.

Given the nature of the constraints from late decays, there are three logical possibilities to tackle the problem. First, we can minimize the impact of decays by choosing an NLSP whose decay products interact only weakly; the classical example is the sneutrino, which is mostly harmless for BBN [12] but also difficult to probe at the LHC [13, 14]. Second, we can minimize the density of decaying particles by either choosing regions in parameter space with enhanced annihilation or by modifying the thermal history of the universe. Third, we can minimize the lifetime of the NLSP in order to let it decay before decisive BBN processes set in, either by making it quite heavy or by opening new decay channels.

With a gravitino LSP, the LHC phenomenology is determined by the properties of the NLSP and quite different from the standard neutralino LSP case, which may alleviate the discovery problem.

The appearance of unacceptably large flavor and CP violation in a generic SUSY scenario is a problem that can be tackled by the mechanism mediating SUSY breaking from the hidden to the visible sector, family symmetries, or a high overall superparticle mass scale. Vice versa, measurements of rare processes where flavor or CP is violated, are a promising way to probe SUSY and other new physics scenarios.

2 Gravitino LSP scenarios at the LHC

For gravitino masses in the cosmologically motivated mass range, the NLSP is effectively stable on timescales relevant for collider experiments. Leaving aside BBN constraints for the time being, this is especially interesting for an electrically charged NLSP like the stau because it leaves a spectacular signature at LHC experiments, charged tracks leaving the detector and no missing transverse energy. Searches for heavy stable charged particles (HSCP) at the LHC test this possibility.

Considering the production of staus via the Drell–Yan process $p\bar{p} \to \gamma, Z \to \tilde{\tau}^+\tilde{\tau}^-$, which depends only on the stau mass and mixing angle, the luminosity required for discovering or excluding a stau NLSP in an HSCP search at the LHC can be determined as a function of its mass alone. The main experimental limitation is the discrimination of metastable staus from muons by measuring the particle velocity, which is usually smaller for staus due to their heavy mass. Employing a conservative but realistic estimate for the background rejection factor due to the velocity discrimination, which was based on discussions with experimentalists from project B2 of the SFB, and a careful statistical treatment using Poisson statistics, which is appropriate due to the small number of events, the LHC reach for stau NLSPs from Drell–Yan production was determined in [15]. For example, with a luminosity of $300\,\mathrm{fb}^{-1}$ and a center-of-mass energy of 14 TeV, the LHC can discover such staus with masses up to roughly 750 GeV. The results were later largely confirmed by ATLAS and CMS [16, 17], which however were able to exclude higher masses since the experimental performance exceeded the conservative assumptions in the theoretical analysis.

The limits from Drell–Yan production are the most model-independent and conservative ones possible because they depend only on the properties of the stau itself. If other superparticles are not much heavier, their production and subsequent decay to staus will extend the mass reach of HSCP searches, in particular for the initial production of squarks or gluinos via the strong interaction. Of course, this increases the number of free parameters. In order to enable an analysis without assumptions about a model for SUSY breaking despite this obstacle, a

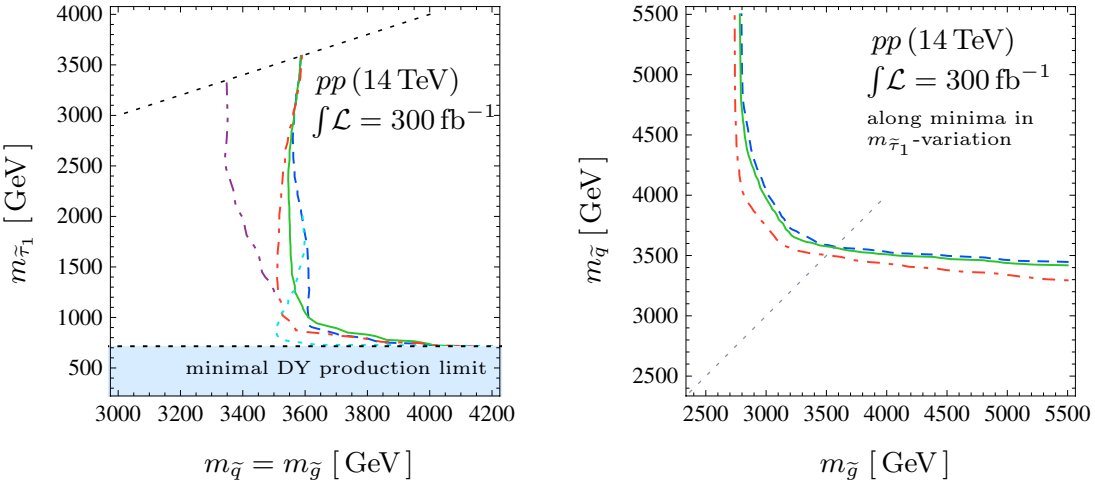


Figure 1: Projected LHC sensitivity (95% $\mathrm{CL_s}$ exclusion and approximate 5σ discovery reach) for the simplified models with a metastable stau NLSP in the case of a common squark mass $m_{\tilde{q}}$. In the right panel the curves represent the minima in the sensitivity with respect to the variation of $m_{\tilde{\tau}_1}$. Reprinted figures with permission from Ref. [18]. Copyright (2012) by the American Physical Society.

simplified model approach was proposed in [18]. A total of six simplified models were introduced, covering the possibilities of mass-degenerate squarks and a light stop, and in each case three limiting cases for the masses of the intermediate superparticles in the decay chain from the originally produced squark or gluino to the stau, capturing the phenomenology of any realistic spectrum within the long-lived stau scenario. Each model contains the three free parameters $m_{\tilde{\tau}_1}$, $m_{\tilde{g}}$ and either the common squark mass $m_{\tilde{q}}$ or $m_{\tilde{t}_1}$. As an example, Fig. 1 shows the potential of Run 3 of the LHC for the case of a common squark mass.

The simplified model approach turned out to work even better than in searches for SUSY with a neutralino LSP, although the number of relevant parameters is larger at first sight. It is possible to cover the whole parameter space with a small number of selection criteria that yield both a high signal efficiency and a very good background rejection, enabling a model-independent analysis. The direct Drell–Yan contribution to stau production prevents a loss of sensitivity for a large mass difference between the stau and the colored superparticles, in which case both staus in a cascade event are typically too fast to be identified. As a consequence, there are no regions in parameter space where the scenario can hide from detection, so the exclusion bounds expected if the LHC does not find a signal are in fact more robust than in the neutralino LSP case.

3 Supersymmetry in the early universe

The effect of stau decays on primordial element abundances is less severe than that of neutralino decays due to the smaller hadronic branching ratio. However, due to their electric charge they form bound states with light nuclei, which leads to a drastic change of some BBN reaction rates

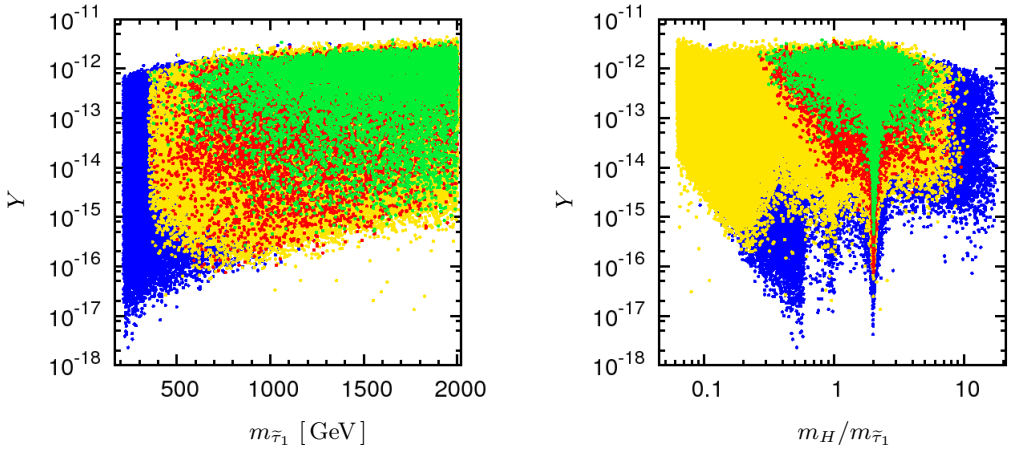


Figure 2: Stau yields in a 17-parameter pMSSM scan as a function of the stau mass (left) and the ratio $m_H/m_{\tilde{\tau}_1}$ (right). The green points pass all the constraints. The blue points are excluded by LHC searches for long-lived particles. The yellow points are rejected by HIGGSBOUNDS [25], are inconsistent with the measured W mass, or violate flavor physics constraints. At the red points, charge- or color-breaking minima may occur in the scalar potential. Readers of the black and white version can identify colors by noting that in the left panel the sequence of dominating colors from left to right is blue-yellow-red-green. Figures taken from Ref. [24].

resulting in an overproduction of ^{6}Li [11]. Consequently, a viable stau NLSP has to have either a lifetime smaller than about 10^3 sec or a very small yield $Y \equiv n/s \lesssim 10^{-15}$ [19,20], where n is the stau number density just before its decay and s is the entropy density.

Generically, the production of staus by thermal freeze-out in the early universe yields $Y \sim 10^{-13}$ for a mass around 100 GeV [21]. Thus, BBN requires an exceptional suppression of the yield for long-lived staus. This is indeed possible, for example, for particular values of the stau mass parameters that lead to an enhanced stau-Higgs coupling and thereby to a strongly enhanced stau annihilation cross section [22,23]. More generally, the parameter space of the MSSM can be classified according to the stau yield [24]: a bulk region with generic abundance, an electroweakino co-annihilation region with a reduction by up to two orders of magnitude, gluino and squark co-annihilation regions with a yield reduction by around one order of magnitude, as well as Higgs final state, Higgs resonant and third-generation squark co-annihilation regions with a reduction by up to four orders of magnitude.

Performing a scan in the phenomenological MSSM (pMSSM) with 17 free parameters, these regions were constrained by all available experimental and theoretical limits [24]. A careful inclusion of the HSCP searches at Run 1 of the LHC was emphasized, refining and extending the methods developed in [15,18]. For instance, the production of staus via decays of initially produced neutralinos and charginos as well as via intermediate Higgs particles ($pp \to h, H \to \tilde{\tau}_1\tilde{\tau}_1$) was included. Further relevant constraints stem from Higgs measurements (mass, rates, searches for heavy Higgses), searches for metastable particles different from the stau, the W mass, flavor observables, and charge- or color-breaking minima in the scalar potential. The impact of these constraints on the stau relic abundance is shown in Fig. 2. We see that suppressed abundances are still viable. The smallest values require enhanced stau-Higgs couplings and stau annihila-

No.	Requirement	Comment
i	$T_\phi^{\rm dec} < T_{\rm NLSP}^{\rm fo}$	to have effect on $\Omega_{\rm NLSP}$
ii	$T_\phi^{\rm dec} > T_{\rm BBN}$	not to spoil BBN
iii	$\frac{\rho_\phi}{\rho_{\rm rad}}(T_\phi^{\rm dec}) > 1$	$\mathcal{O}(10) < \Delta < 10^4$
iv	$\frac{\rho_\phi}{\rho_{\rm rad}}(T_{\rm NLSP}^{\rm fo}) < 1$	for standard NLSP freeze-out
v	${\rm BR}(\phi \to {\rm NLSP} + \ldots) \simeq 0$	from NLSP decay problem
vi	${\rm BR}(\phi \to {\rm gravitino} + \ldots) \simeq 0$	from overproduction ($\Omega_{3/2}^{\rm tp} \simeq \Omega_{\rm DM}$)
vii	e.g., $\tau_{3/2} \gg t_0$	compatibility with gravitino dark matter
viii	ii) and v)–vii)	for by-products; no new problems

Table 1: Requirements for a viable scenario of entropy production by decays of a long-lived particle ϕ that dilutes the NLSP density. Reprinted table with permission from Ref. [28]. Copyright (2010) by the American Physical Society.

tion via the exchange of a heavy Higgs H^0 in resonance, as demonstrated by the narrow region of green points at $m_H \simeq 2\, m_{\tilde\tau_1}$ in the right panel of the figure. The lowest viable stau yield is about 2×10^{-16}. The very tip of this peak is excluded by HSCP searches, to a large extent due to the resonant production of staus via the heavy Higgs.

Extending the scan parameters by the gravitino mass, the reheating temperature can be calculated from the observed dark matter density [26]. Points with $T_{\rm R} > 10^9\,{\rm GeV}$ are allowed in the Higgs resonant region where $m_H \simeq 2\, m_{\tilde\tau_1}$. Consequently, the gravitino problem can be solved and thermal leptogenesis can occur within the R-parity-conserving MSSM. In the corresponding parameter space points, the staus produced at the LHC tend to be very slow. Their discovery would hence be facilitated by an extended buffering of the tracker data in the detectors [18].

Generic stau or neutralino NLSP yields can be made compatible with BBN by modifying the thermal history of the early universe compared to the standard scenario. If a long-lived particle ϕ dominates the energy density for a short period between the NLSP's freeze-out at temperature $T_{\rm NLSP}^{\rm fo}$ and BBN, its decays at $T_\phi^{\rm dec}$ increase the entropy by a factor Δ, which can dilute the NLSP density below the upper limit from BBN [27]. However, the baryon asymmetry is diluted as well, which has to be compensated by a larger heavy neutrino mass M_1 and a correspondingly higher reheating temperature in thermal leptogenesis. As washout processes reduce the efficiency of leptogenesis for very large M_1, this mass cannot be increased arbitrarily. Consequently, entropy generation is limited from above. The upper bound was estimated as $\Delta \lesssim 10^4$ [28], but it could possibly be larger by up to an order of magnitude [29]. As a consequence, constraints on the NLSP remain, which were studied in detail for the neutralino in [28].

An overview of the criteria that the entropy-producing particle has to satisfy [28] is given in Tab. 1. Although they are satisfied quite generically in any scenario with long-lived particles, it is non-trivial to find a candidate that satisfies all criteria in a natural way. For example, the axion supermultiplet contains the saxion as a weakly coupled, massive scalar field. The version of the scenario where thermal saxion production dominates is very predictive but not

able to generate a sufficient amount of entropy. Besides, the axino causes severe problems. Decoupling saxion production and decay by assuming production in coherent oscillations, which is generically expected anyway, these difficulties can be overcome, enabling a scenario with a completely consistent cosmology. The biggest price to pay from the point of view of naturalness is a saxion mass around 10 GeV, which is somewhat lighter than generically expected.

Late decays can also quite naturally produce dark radiation, i.e., relativistic particles different from photons and Standard Model neutrinos, which contribute to the effective number of neutrino species N_{eff}. Together with indications for a larger N_{eff} than expected in the Standard Model [30–32],[1] this motivated the first systematic study of particle decay as the origin of dark radiation [35]. In the simplest scenario, a non-relativistic "mother" particle decays into two "daughters". The lighter daughter acts as dark radiation. Depending on how close in mass the heavier daughter is to the mother, it can contribute to dark radiation as well, but it could also form the dark matter or a component thereof in principle. It turned out that the heavier daughter acts as hot dark matter if the amount of dark radiation is non-negligible; consequently, it can form a subdominant component of the dark matter at most. However, this leaves the interesting possibility that the heavier daughter could mimic the effect of non-vanishing neutrino masses in cosmological observations, which could explain a contradiction with laboratory experiments if that should arise in the future.

If the mother has two possibilities to decay, either into a pair of light daughters or into a pair of heavy daughters, the relative branching fraction between these decay modes is an additional free parameter that allows for new possibilities. In the most interesting case, the lighter daughter again forms the dark radiation. The heavier daughter can now form all of the observed dark matter. What is more, its free-streaming length can be adjusted such that the missing satellite problem of structure formation [36, 37] is solved.

The scenario is predictive because the amount of dark radiation determines the energy density of the mother at the time of decay. It is therefore possible to determine bounds on the involved branching ratios and mass hierarchies as functions of the lifetime of the long-lived particle, employing constraints from BBN, the cosmic microwave background and structure formation. As an example, Fig. 3 shows limits on the branching fraction of the decaying particle into photons and electron-positron pairs, which could arise from off-shell or loop-induced processes. Note that the thinner lines in the figure ("strongest bounds") correspond to a very large dark radiation density that is now ruled out.

A particular realization of the scenario is a model with mixed axion and axino dark matter [42]. The axino has a mass below a keV and is the LSP, while the gravitino with a mass of order 100 GeV is the NLSP. In this case the superpartners of the Standard Model particles decay into axino and photon before BBN, which realizes the third possibility of avoiding BBN problems mentioned in the introduction (although strictly speaking now the particle whose decays could be problematic is the next-to-NLSP). The gravitino decays after BBN but before the creation of the cosmic microwave background into axino and axion, which do not affect the light element abundances due to their weak couplings. However, these particles are created as dark radiation and thus contribute to N_{eff} [43]. The increase of this quantity is of order one for expected (natural) masses and a reheating temperature around 10^{10} GeV. This makes the model more easily testable but also leads to a new upper bound on the reheating temperature four orders of magnitude stronger than the one derived in [42].

[1] These indications were not confirmed by the Planck satellite, but a sizable amount of dark radiation remains allowed [33]. There are even hints that late decays to dark radiation are preferred by current cosmological data [34].

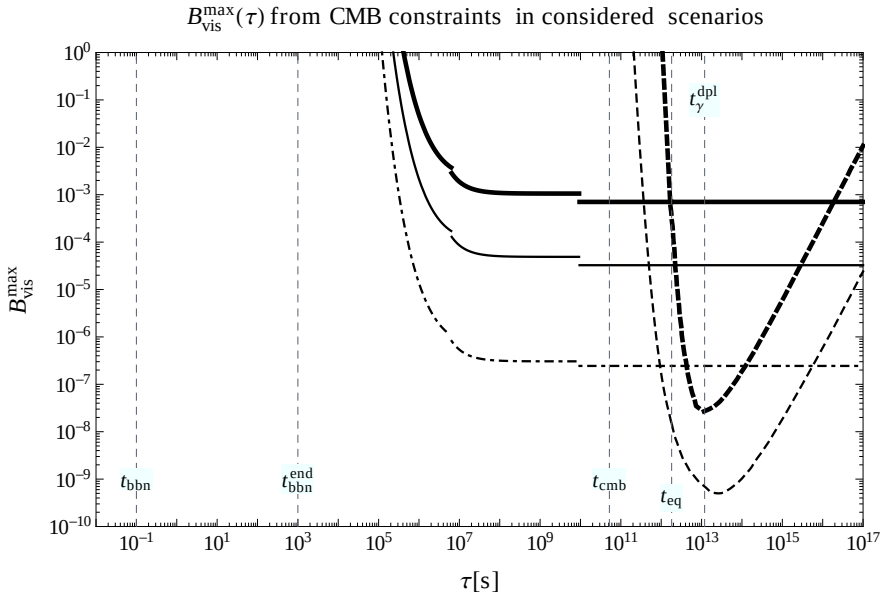


Figure 3: Upper bounds from the cosmic microwave background on the branching ratio of a decaying particle as a function of its lifetime τ in the scenario of particle decay as the origin of dark radiation. Thick and thin solid curves represent the weakest and the strongest bounds, respectively, on the branching ratio into photons that can be derived from CMB spectral distortions [38, 39]. The dash-dotted curve indicates the discovery reach of the proposed PIXIE experiment [40] if $\Delta N_{\rm eff} = 1$. Thick and thin dashed curves represent weakest and strongest bounds on the branching ratio into electrons, positrons and photons, which were obtained from the ionization history of the universe [41]. Figure reprinted from Ref. [35]. © 2013 IOP Publishing Ltd and Sissa Medialab srl.

Another way to reduce the lifetime of potentially dangerous particles is introducing a small violation of R parity. This causes the NLSP to decay mainly into Standard Model particles before BBN and thus satisfies the constraints [44]. The cosmological bounds on the axion multiplet in this scenario were determined in [45]. We systematically considered different axion models and NLSP candidates and compared the standard scenario with R parity conservation to the one with R parity violation as well as a setup with both R parity violation and late-time entropy production. The faster NLSP decay turned out to be the most important effect of R parity violation. It allows the axino, whose decays produce NLSPs, to decay shortly before BBN, relaxing the stringent lower bound on its mass in the standard scenario. Also decays of the saxion are allowed to produce NLSPs at any time before BBN, and its mass is virtually unconstrained. Consequently, generically expected spectra are allowed where both saxion and axino mass are of the same order of magnitude as the other superparticle masses. It is thus fair to conclude that R parity violation not only solves the gravitino problem but also makes it easier to solve the strong CP problem via the Peccei–Quinn mechanism [46].

Finally, applying the formalism of late-decaying particles to decays before BBN, it was shown that moduli from string theory compactifications could leave traces in the gravitational wave background [47].

4 FCNCs, CP violation and the fermionic flavor structure

Extensions of the Standard Model typically contain new sources of flavor and CP violation. Therefore, they are testable and constrained not only by direct searches for new particles at colliders but also by indirect searches for flavor-changing neutral currents (FCNCs) and CP violation.

A CP- and T-violating triple spin correlation in muon to electron conversion in nuclei is generally of order one in left-right symmetric theories, offering hope of observing CP violation in this lepton-flavor-violating (LFV) process [48]. Such a measurement might even enable a determination of the Majorana phases in the lepton mixing matrix in case neutrinos are Majorana particles.

Indirect new physics searches, in particular employing the mass differences of neutral kaons and B mesons as well as CP violation in these systems, also yield the most important constraints on the scale of left-right symmetry restoration in the minimal left-right symmetric model. A combined analysis [49] yielded $M_{W_\mathrm{R}} \gtrsim 3.5\,\mathrm{TeV}$ and $M_{W_\mathrm{R}} \gtrsim 2.5\,\mathrm{TeV}$, respectively, where the two limits correspond to two ways of defining the parity symmetry. The signatures at the LHC were studied as well, in particular same-sign dileptons from the decay of the heavy right-handed neutrino, demonstrating the complementarity between direct and indirect searches. Even in the minimal case, it is possible to observe both the charged and the neutral gauge boson at the LHC, if their masses are sufficiently close to the lower limits.

Lepton flavor violation can also be used to probe models with light fermionic $\mathrm{SU}(2)_\mathrm{L}$ triplets that are motivated by a minimal extension of the SU(5) grand unified theory [50]. The most relevant constraint comes from a search for the transition of a muon to an electron inside a gold nucleus. In the minimal case of a single triplet, the constraints on muonic transitions are precise enough to forbid an observation of a transition in the tau sector, at least in the foreseeable future. In non-minimal cases with several triplets, this restriction disappears. The follow-up work [51] examined leptogenesis in the model, including a more complete treatment of flavor effects.

In the case of SUSY, the non-observation of larger flavor and CP violation than predicted in the Standard Model is a long-standing problem. A very interesting approach are non-Abelian family symmetries introduced in order to understand the observed fermion masses and mixings. They can also restrict the soft SUSY breaking parameters to conserve flavor and CP [52, 53]. The breaking of a family symmetry leads to suppressed flavor- and CP-violating soft parameters, which are in principle calculable. In this way, one could not only solve the SUSY flavor problem but also obtain an additional experimental test of models with family symmetries. Unfortunately, it turned out that the predictivity for the SUSY breaking parameters is in fact more limited than previously assumed [54]. The reason is that the predictions depend on unknown details of the messenger sector, which is needed to generate couplings between the Standard Model fermions and the flavons breaking the family symmetry. Depending on the model, it can be possible to improve the predictivity by a change of the messenger sector.

A different route to suppress FCNCs and CP violation in supersymmetric models was followed in [55]. The study considered a scenario derived from string theory, the G_2-MSSM [56], where only the gauginos have masses below a TeV while the other superparticles are heavier than about 20 TeV. The trilinear scalar couplings are large as well and in general not proportional to the Yukawa couplings. Analyzing the flavor- und CP-violating observables, the largest sensitivity to new physics was found in the neutral kaon system. While the change of the kaon mass difference is very small, a sizable contribution to the CP-violating parameter ϵ_K

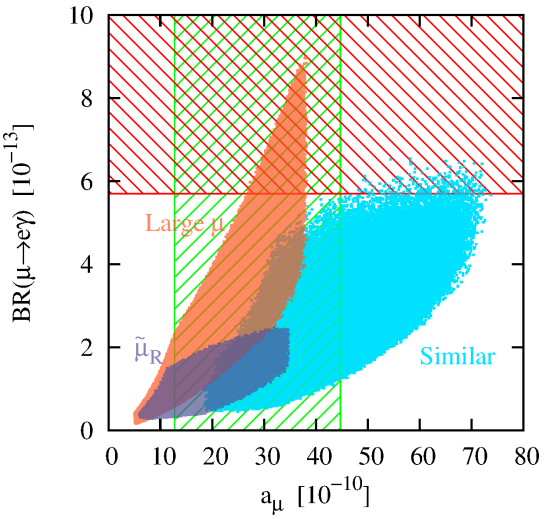


Figure 4: Supersymmetric contribution to the anomalous magnetic moment of the muon, $a_\mu = (g-2)_\mu/2$, versus $\mathrm{BR}(\mu \to e\gamma)$ for similar SUSY masses, large μ and heavy left-handed sleptons (dark region labeled "$\tilde{\mu}_\mathrm{R}$"), respectively. In each case, $\delta_\mathrm{LL} = \delta_\mathrm{RR} = 2 \times 10^{-5}$ and $\tan\beta = 50$. The vertical hatched band corresponds to the experimentally favored 2σ range for a_μ, while the horizontal band marks the region excluded by MEG [61]. Figure taken from Ref. [62].

is possible, which turned out to depend sensitively on the choice of trilinear couplings. Thus, heavy scalars alone do not guarantee the absence of flavor and CP problems. Nevertheless, parts of the parameter space of the G_2-MSSM are compatible with the observed value of ϵ_K, thanks largely to the theoretical uncertainty of the Standard Model prediction.

Subsequently, [57] improved the calculation of flavor- and CP-violating observables in scenarios where the gauginos have masses around a TeV while either all sfermions or only those of the first and second generation are much heavier. The latter option, known as natural SUSY, is also motivated by the relatively heavy observed Higgs mass and the SUSY discovery problem [58]. The results are thus useful not only for constructing models like the G_2-MSSM or family symmetries but also for constraining supersymmetric scenarios that currently are receiving a lot of attention. We analyzed the flavor- und CP-violating observables in the neutral kaon system, taking into account QCD corrections at the next-to-leading order. Working in the mass insertion approximation, we derived limits on the heavy squark masses and on the flavor-violating parameters that govern the mixing between the first and second squark generation.

If the deviation of the measured value of the muon's anomalous magnetic moment $(g-2)_\mu$ from the Standard Model prediction is due to SUSY, this may enable predictions for the LFV decay $\mu \to e\gamma$, since the Feynman diagrams leading to both processes in supersymmetric models are closely related. In short, the value of $(g-2)_\mu$ sets the scale of superpartner masses that enters into the branching ratio for $\mu \to e\gamma$. Thus, the only unknowns in the latter process are the actual LFV parameters δ_LL and δ_RR. They can then be constrained using the experimental upper limit and determined after a discovery of the decay in the future. However, a clear correlation between the two processes requires that a single Feynman diagram dominate both processes [59, 60].

If this is not the case, the correlation is weakened by significant cancellations between diagrams in large parts of the parameter space. However, the order of magnitude of $\mathrm{BR}(\mu \to e\gamma)$ for a fixed flavor-violating parameter can often be predicted [62]. Consider for example the region labeled "Similar" in Fig. 4, which was obtained by randomly varying the seven relevant SUSY mass parameters between 300 GeV and 600 GeV while fixing $\delta_{\mathrm{LL}} = \delta_{\mathrm{RR}} = 2 \times 10^{-5}$ such that the experimental limit $\mathrm{BR}(\mu \to e\gamma) < 5.7 \times 10^{-13}$ [61] is satisfied. We can see that for a fixed SUSY contribution to $(g-2)_\mu$, the branching ratio varies by a factor of 10 at most. This allows to determine a limit $\delta_{\mathrm{LL}} \lesssim 2 \times 10^{-5}$ below which $\mathrm{BR}(\mu \to e\gamma)$ is guaranteed to satisfy the experimental bound if the relevant SUSY masses vary by up to 30 % around a mass scale M chosen such that we obtain the best-fit value of $(g-2)_\mu$ for all masses equal to M.

A strong correlation between the two observables is realized, for example, in the case of neutralino-$\tilde{\mu}_{\mathrm{R}}$ dominance, which occurs for very heavy left-handed sleptons and $M_1, m_{\tilde{\ell}_{\mathrm{R}}} < M_2, |\mu|$ [62]. This is illustrated by the dark region labeled "$\tilde{\mu}_{\mathrm{R}}$" in Fig. 4. A special case occurs for large values of μ and $\tan\beta$, which do cause a single Feynman diagram to dominate and a significant correlation, as evidenced by the "Large μ" region in the figure. However, in this case LFV is not governed by δ_{LL} or δ_{RR} but by a different combination of parameters. In such regions with characteristic mass hierarchies and strong correlations, the experimental limit on $\mathrm{BR}(\mu \to e\gamma)$ can yield severe constraints on LFV parameters that cannot be evaded by raising the overall SUSY mass scale, since it is fixed by the measured value of $(g-2)_\mu$.

Acknowledgements

I would like to acknowledge financial support and hospitality from the Fine Theoretical Physics Institute at the University of Minnesota and the Meltzer Research Fund during the writing of this summary.

References

[1] I. V. Falomkin et al., *Low-energy $\bar{p}\,{}^4He$ annihilation and problems of the modern cosmology, GUT and SUSY models*, *Nuovo Cim.* **A79** (1984) 193–204. [Yad. Fiz. **39** (1984), 990].

[2] M. Y. Khlopov and A. D. Linde, *Is It Easy to Save the Gravitino?*, *Phys. Lett.* **B138** (1984) 265–268.

[3] J. R. Ellis, J. E. Kim and D. V. Nanopoulos, *Cosmological Gravitino Regeneration and Decay*, *Phys. Lett.* **B145** (1984) 181.

[4] M. Kawasaki, K. Kohri, T. Moroi and Y. Takaesu, *Revisiting Big-Bang Nucleosynthesis Constraints on Long-Lived Decaying Particles*, *Phys. Rev.* **D97** (2018) 023502, [1709.01211].

[5] M. Fukugita and T. Yanagida, *Baryogenesis without grand unification*, *Phys. Lett.* **B174** (1986) 45.

[6] W. Buchmüller, P. Di Bari and M. Plümacher, *Cosmic microwave background, matter-antimatter asymmetry and neutrino masses*, *Nucl. Phys.* **B643** (2002) 367–390, [hep-ph/0205349].

[7] M. Bolz, W. Buchmüller and M. Plümacher, *Baryon asymmetry and dark matter*, *Phys. Lett.* **B443** (1998) 209–213, [hep-ph/9809381].

[8] M. Bolz, A. Brandenburg and W. Buchmüller, *Thermal production of gravitinos*, *Nucl. Phys.* **B606** (2001) 518–544, [hep-ph/0012052].

[9] J. Pradler and F. D. Steffen, *Thermal gravitino production and collider tests of leptogenesis*, *Phys. Rev.* **D75** (2007) 023509, [hep-ph/0608344].

[10] T. Moroi, H. Murayama and M. Yamaguchi, *Cosmological constraints on the light stable gravitino*, *Phys. Lett.* **B303** (1993) 289–294.

[11] M. Pospelov, *Particle physics catalysis of thermal Big Bang Nucleosynthesis*, *Phys. Rev. Lett.* **98** (2007) 231301, [hep-ph/0605215].

[12] M. Fujii, M. Ibe and T. Yanagida, *Upper bound on gluino mass from thermal leptogenesis*, *Phys. Lett.* **B579** (2004) 6–12, [hep-ph/0310142].

[13] L. Covi and S. Kraml, *Collider signatures of gravitino dark matter with a sneutrino NLSP*, *JHEP* **08** (2007) 015, [hep-ph/0703130].

[14] T. Figy, K. Rolbiecki and Y. Santoso, *Tau-Sneutrino NLSP and Multilepton Signatures at the LHC*, *Phys. Rev.* **D82** (2010) 075016, [1005.5136].

[15] J. Heisig and J. Kersten, *Production of long-lived staus in the Drell-Yan process*, *Phys. Rev.* **D84** (2011) 115009, [1106.0764].

[16] CMS Collaboration, S. Chatrchyan et al., *Searches for long-lived charged particles in pp collisions at $\sqrt{s}$=7 and 8 TeV*, *JHEP* **07** (2013) 122, [1305.0491].

[17] ATLAS Collaboration, G. Aad et al., *Searches for heavy long-lived charged particles with the ATLAS detector in proton-proton collisions at $\sqrt{s}$=8 TeV*, *JHEP* **01** (2015) 068, [1411.6795].

[18] J. Heisig and J. Kersten, *Long-lived staus from strong production in a simplified model approach*, *Phys. Rev.* **D86** (2012) 055020, [1203.1581].

[19] K. Jedamzik, *Bounds on long-lived charged massive particles from Big Bang nucleosynthesis*, *JCAP* **03** (2008) 008, [0710.5153].

[20] M. Kawasaki, K. Kohri, T. Moroi and A. Yotsuyanagi, *Big-bang nucleosynthesis and gravitinos*, *Phys. Rev.* **D78** (2008) 065011, [0804.3745].

[21] T. Asaka, K. Hamaguchi and K. Suzuki, *Cosmological gravitino problem in gauge mediated supersymmetry breaking models*, *Phys. Lett.* **B490** (2000) 136–146, [hep-ph/0005136].

[22] M. Ratz, K. Schmidt-Hoberg and M. W. Winkler, *A Note on the primordial abundance of stau NLSPs*, *JCAP* **10** (2008) 026, [0808.0829].

[23] J. Pradler and F. D. Steffen, *Thermal relic abundances of long-lived staus*, *Nucl. Phys.* **B809** (2009) 318–346, [0808.2462].

[24] J. Heisig, J. Kersten, B. Panes and T. Robens, *A survey for low stau yields in the MSSM*, *JHEP* **04** (2014) 053, [1310.2825].

[25] P. Bechtle, S. Heinemeyer, O. Stål, T. Stefaniak and G. Weiglein, *HiggsSignals: Confronting arbitrary Higgs sectors with measurements at the Tevatron and the LHC*, *Eur. Phys. J.* **C74** (2014) 2711, [1305.1933].

[26] J. Heisig, *Gravitino LSP and leptogenesis after the first LHC results*, *JCAP* **04** (2014) 023, [1310.6352].

[27] W. Buchmüller, K. Hamaguchi, M. Ibe and T. T. Yanagida, *Eluding the BBN constraints on the stable gravitino*, *Phys. Lett.* **B643** (2006) 124–126, [hep-ph/0605164].

[28] J. Hasenkamp and J. Kersten, *Leptogenesis, Gravitino Dark Matter and Entropy Production*, *Phys. Rev.* **D82** (2010) 115029, [1008.1740].

[29] M. N. Breistein, *Late Time Entropy Production in Leptogenesis Scenarios*, Master's thesis, University of Bergen, 2016. http://hdl.handle.net/1956/15532.

[30] Y. I. Izotov and T. X. Thuan, *The primordial abundance of 4He: evidence for non-standard big bang nucleosynthesis*, *Astrophys. J.* **710** (2010) L67–L71, [1001.4440].

[31] J. Dunkley et al., *The Atacama Cosmology Telescope: Cosmological Parameters from the 2008 Power Spectra*, *Astrophys. J.* **739** (2011) 52, [1009.0866].

[32] R. Keisler et al., *A Measurement of the Damping Tail of the Cosmic Microwave Background Power Spectrum with the South Pole Telescope*, *Astrophys. J.* **743** (2011) 28, [1105.3182].

[33] PLANCK Collaboration, P. A. R. Ade et al., *Planck 2015 results. XIII. Cosmological parameters*, *Astron. Astrophys.* **594** (2016) A13, [1502.01589].

[34] T. Bringmann, F. Kahlhoefer, K. Schmidt-Hoberg and P. Walia, *Converting nonrelativistic dark matter to radiation*, *Phys. Rev.* **D98** (2018) 023543, [1803.03644].

[35] J. Hasenkamp and J. Kersten, *Dark radiation from particle decay: cosmological constraints and opportunities*, *JCAP* **08** (2013) 024, [1212.4160].

[36] A. A. Klypin, A. V. Kravtsov, O. Valenzuela and F. Prada, *Where are the missing Galactic satellites?*, *Astrophys. J.* **522** (1999) 82–92, [astro-ph/9901240].

[37] B. Moore et al., *Dark matter substructure within galactic halos*, *Astrophys. J.* **524** (1999) L19–L22, [astro-ph/9907411].

[38] W. Hu and J. Silk, *Thermalization constraints and spectral distortions for massive unstable relic particles*, *Phys. Rev. Lett.* **70** (1993) 2661–2664.

[39] J. Chluba and R. A. Sunyaev, *The evolution of CMB spectral distortions in the early Universe*, *Mon. Not. Roy. Astron. Soc.* **419** (2012) 1294–1314, [1109.6552].

[40] A. Kogut et al., *The Primordial Inflation Explorer (PIXIE): a nulling polarimeter for cosmic microwave background observations*, *JCAP* **07** (2011) 025, [1105.2044].

[41] T. R. Slatyer, *Energy injection and absorption in the cosmic dark ages*, *Phys. Rev.* **D87** (2013) 123513, [1211.0283].

[42] T. Asaka and T. Yanagida, *Solving the gravitino problem by axino*, *Phys. Lett.* **B494** (2000) 297–301, [hep-ph/0006211].

[43] J. Hasenkamp, *Dark radiation from the axino solution of the gravitino problem*, *Phys. Lett.* **B707** (2012) 121–128, [1107.4319].

[44] W. Buchmüller, L. Covi, K. Hamaguchi, A. Ibarra and T. Yanagida, *Gravitino dark matter in R-parity breaking vacua*, *JHEP* **03** (2007) 037, [hep-ph/0702184].

[45] J. Hasenkamp and J. Kersten, *Dark and visible matter with broken R-parity and the axion multiplet*, *Phys. Lett.* **B701** (2011) 660–666, [1103.6193].

[46] R. Peccei and H. R. Quinn, *CP Conservation in the Presence of Instantons*, *Phys. Rev. Lett.* **38** (1977) 1440–1443.

[47] R. Durrer and J. Hasenkamp, *Testing Superstring Theories with Gravitational Waves*, *Phys. Rev.* **D84** (2011) 064027, [1105.5283].

[48] B. Bajc, M. Nemevšek and G. Senjanović, *Probing leptonic CP phases in LFV processes*, *Phys. Lett.* **B684** (2010) 231–235, [0911.1323].

[49] A. Maiezza, M. Nemevšek, F. Nesti and G. Senjanović, *Left-Right Symmetry at LHC*, *Phys. Rev.* **D82** (2010) 055022, [1005.5160].

[50] J. F. Kamenik and M. Nemevšek, *Lepton flavor violation in type I + III seesaw*, *JHEP* **11** (2009) 023, [0908.3451].

[51] D. Aristizabal Sierra, J. F. Kamenik and M. Nemevšek, *Implications of Flavor Dynamics for Fermion Triplet Leptogenesis*, *JHEP* **10** (2010) 036, [1007.1907].

[52] S. Abel, S. Khalil and O. Lebedev, *Additional stringy sources for electric dipole moments*, *Phys. Rev. Lett.* **89** (2002) 121601, [hep-ph/0112260].

[53] G. G. Ross and O. Vives, *Yukawa structure, flavor and CP violation in supergravity*, *Phys. Rev.* **D67** (2003) 095013, [hep-ph/0211279].

[54] K. Kadota, J. Kersten and L. Velasco-Sevilla, *Supersymmetric Musings on the Predictivity of Family Symmetries*, *Phys. Rev.* **D82** (2010) 085022, [1007.1532].

[55] K. Kadota, G. Kane, J. Kersten and L. Velasco-Sevilla, *Flavour issues for string-motivated heavy scalar spectra with a low gluino mass: the G_2-MSSM case*, *Eur. Phys. J.* **C72** (2012) 2004, [1107.3105].

[56] B. S. Acharya, K. Bobkov, G. L. Kane, J. Shao and P. Kumar, *G_2-MSSM: An M theory motivated model of particle physics*, *Phys. Rev.* **D78** (2008) 065038, [0801.0478].

[57] J. Kersten and L. Velasco-Sevilla, *Flavor constraints on scenarios with two or three heavy squark generations*, *Eur. Phys. J.* **C73** (2013) 2405, [1207.3016].

[58] M. Papucci, J. T. Ruderman and A. Weiler, *Natural SUSY Endures*, *JHEP* **09** (2012) 035, [1110.6926].

[59] M. Graesser and S. D. Thomas, *Supersymmetric relations among electromagnetic dipole operators*, *Phys. Rev.* **D65** (2002) 075012, [hep-ph/0104254].

[60] Z. Chacko and G. D. Kribs, *Constraints on lepton flavor violation in the MSSM from the muon anomalous magnetic moment measurement*, *Phys. Rev.* **D64** (2001) 075015, [hep-ph/0104317].

[61] MEG Collaboration, J. Adam et al., *New constraint on the existence of the $\mu^+ \to e^+\gamma$ decay*, *Phys. Rev. Lett.* **110** (2013) 201801, [1303.0754].

[62] J. Kersten, J.-h. Park, D. Stöckinger and L. Velasco-Sevilla, *Understanding the correlation between $(g-2)_\mu$ and $\mu \to e\gamma$ in the MSSM*, *JHEP* **08** (2014) 118, [1405.2972].

Section C

Cosmology

Axions and other WISPs

Dieter Horns[1], *Andreas Ringwald*[2], *Le Hoang Nguyen*[1], *Andrei Lobanov*[1,3]

[1]Institut für Experimentalphysik, Universität Hamburg, Germany
[2]DESY, Hamburg, Germany
[3]Max-Planck-Institut für Radioastronomie, Bonn, Germany

DOI: http://dx.doi.org/10.3204/PUBDB-2018-00782/C1

The project C1 of the SFB 676 concentrated on very weakly interacting slim (i.e., ultra-light) particles (WISPs). The possible occurrence of particular WISP examples such as axions or hidden photons in well-motivated extensions of the Standard Model (SM) was explored. It was shown that WISPs are natural dark matter candidates. Extensive phenomenological, astrophysical, and cosmological studies were performed and WISP experiments were proposed and carried out.

1 Introduction

There are many proposed dark matter particle candidates, spanning a wide parameter range in masses and couplings. Two classes stand out because of their convincing physics case and the variety of experimental and observational probes: WIMPs (Weakly Interacting Massive Particles), such as neutralinos in the minimal supersymmetric standard model (MSSM), and WISPs [1], such as the axion in models solving the strong CP problem. Another candidate is a hidden photon – a new Abelian gauge boson mixing kinetically with the photon. Axions, axion-like particles (ALPs), and hidden photons (HPs) occur naturally in extensions of the SM occurring from string compactifications, cf. Sec. 2. Stars are very efficient sources of WISPs. Therefore, strong constraints on WISPs arise from stellar cooling considerations, cf. Sec. 3. Photons and WISPs may oscillate into each other when propagating through the interstellar and intergalactic medium. This propagation effects may modify photon spectra from astrophysical sources, cf. Sec. 4. Bosonic WISPs are naturally produced in the early universe via the vacuum-realignment mechanism and behave as cold dark matter, cf. Sec. 5. There are several promising techniques to search for WISPs in terrestrial experiments, cf. Sec. 6.

2 WISPs from well-motivated UV completions of the SM

2.1 SM – Axion – Seesaw – Higgs portal inflation (SMASH)

One prominent example of a WISP is the axion [2, 3] – the particle excitation of the phase of a complex scalar field (dubbed Peccei–Quinn field) which gets a vacuum expectation value from the spontaneous breaking of a global chiral $U(1)_{\rm PQ}$ symmetry canceling the CP-violating θ-term in the QCD Lagrangian and thus solving the strong CP problem [4]. In Ref. [5], a minimal extension of the Standard Model (SM) was constructed by adding three right-handed

SM-singlet neutrinos and a vector-like quark, all of them being charged under a global lepton number and Peccei–Quinn (PQ) U(1) symmetry which is spontaneously broken by the vacuum expectation value $v_\sigma \sim 10^{11}\,\mathrm{GeV}$ of a SM-singlet complex scalar field. It was observed that this model solves many problems of the SM in one stroke – neutrino masses and mixing (by the seesaw mechanism), baryogenesis (by leptogenesis), dark matter (by axions), strong CP problem (by axions). In Refs. [6, 7] it was found, that this model automatically also solves the problem of inflation. Indeed, a linear combination of the Peccei–Quinn scalar and the Higgs represents a viable inflaton candidate if the quartic coupling of the former is small, $\lambda_\sigma \sim 10^{-10}$ and the coupling to the Ricci scalar is bounded from below, $\xi_\sigma \gtrsim 10^{-2}$. The model was dubbed "SMASH" (Standard Model*Axion*Seesaw*Higgs portal inflation). It predicts the dark matter axion mass in the range $30\,\mu\mathrm{eV} \lesssim m_A \lesssim 130\,\mathrm{meV}$. It can be probed decisively by upcoming cosmic microwave background and axion dark matter experiments (cf. Sec. 6). First steps towards a GUT SMASH variant are promising [8].

2.2 WISPs from string compactifications

The low-energy limit of string compactifications yields an effective field theory with promising QCD axion candidates [9–12], or even an 'axiverse' containing a plethora of light ALPs with a logarithmically hierarchical mass spectrum [13]. Reference [14] was devoted to the search for closed string axions and ALPs in IIB string flux compactifications. For natural values of the background fluxes and TeV scale gravitino mass, it was found that the moduli stabilisation mechanism of the LARGE Volume Scenario predicts the existence of a QCD axion candidate with intermediate scale decay constant, $f_a \sim 10^{9-12}\,\mathrm{GeV}$, associated with the small cycles wrapped by the branes hosting the visible sector, plus a nearly massless and nearly decoupled ALP associated with the LARGE cycle. In setups where the visible sector branes are wrapping more than the minimum number of two intersecting cycles, there are more ALPs which have approximately the same decay constant and coupling to the photon as the QCD axion candidate, but which are exponentially lighter, realising an axiverse scenario. Models with additional light ALPs where constructed which may explain some intriguing astrophysical anomalies (cf. Secs. 3 and 4), and could be searched for in the next generation of axion helioscopes and light-shining-through-a-wall experiments (cf. Sec. 6).

Axions and ALPs do not exhaust the WISP candidates from string compactifications. Of particular interest are extra "hidden" U(1) gauge bosons which seem to occur frequently in all three major paradigms for string phenomenology – compactifications of the heterotic string, of type II strings with D-branes, and of F-theory [15–18]. They present a window to very large energy scales, since hidden U(1) gauge bosons can mix kinetically with the visible sector hypercharge U(1) gauge boson, leading to a term of mass dimension four in the low-energy effective Lagrangian [19], $\mathcal{L} \supset -\frac{\chi}{2} F_{\mu\nu} X^{\mu\nu}$, where F (X) is the visible (hidden) sector U(1) field strength. Correspondingly, the dimensionless kinetic mixing parameter χ is not necessarily parametrically small, even if the messengers are ultra-heavy. Moreover, on the mass dimension two level, there is also the possibility of Stückelberg mass mixing between hidden U(1)s and the hypercharge U(1). References [20, 21] investigated the masses and the kinetic mixing of hidden U(1)s in LARGE volume compactifications of IIB string theory. It was found that in these scenarios the hidden photons can be naturally light and that their kinetic mixing with the ordinary electromagnetic photon can be of a size interesting for near future experiments and observations (cf. Sec. 6).

3 WISP constraints and hints from stellar cooling

WISPs are produced in hot astrophysical plasmas and can thus transport energy out of stars. Their couplings with SM particles is bounded by the constraint that stellar lifetimes or energy-loss rates should not conflict with observation [22]. Intriguingly, however, stars in different stages in their evolution, notably red giants, horizontal branch stars, and white dwarfs, show a mild preference for a cooling excess beyond the SM. This exotic cooling could be provided by WISPs, produced in the hot stellar cores and escaping the star. In Ref. [23], the cooling hints were analyzed in terms of ALPs, HPs, minicharged particles, and neutrino anomalous magnetic moments. Among them, the ALP or a massless HP appear to represent the best solution. Interestingly, the hinted ALP parameter space is accessible to the next generation proposed ALP searches, such as ALPS II and IAXO (cf. Sec. 6) and the massless HP requires a multi TeV energy scale of new physics that might be accessible at the LHC. In Ref. [24] it was explored whether the best fit to the cooling anomalies can be obtained in particular axion models. It was found that both a DFSZ-type as well as a KSVZ-type axion/majoron model allow a good global fit to the data, preferring an axion mass around 10 meV. An axion in this mass range can also be the main constituent of dark matter (cf. Sec. 5).

4 ALP constraints from photon $\leftrightarrow$ ALP conversion in astrophysical magnetic fields

The constraints from stellar evolution (see previous section) are necessarily limited to the case of photon-ALP mixing in a *high density environment* where the background plasma influences the two photon-ALP mixing. In the case of photon propagation in the interstellar or intergalactic medium as well as in light-shining through wall experiments in vacuum (cf. Sec. 6), the mixing takes place in well-approximated vacuum conditions. The resulting phenomenology may very well differ from the high density environment in stellar interior [25].

The calculation of the probability of converting a photon into an axion-like particle state $p_{\gamma\leftrightarrow a}$ is based upon the term of the Lagrangian

$$\mathcal{L}_{a\gamma} = -\frac{1}{4} g_{a\gamma} a F_{\mu\nu} \tilde{F}^{\mu\nu} = g_{a\gamma} a \mathrm{E} \cdot \mathrm{B} \,. \tag{1}$$

For a polarized beam of photons with energy E propagating along the z-direction, the linearized set of equations takes the form [26]

$$\left(i\frac{d}{dz} + E + \mathcal{M}_0 \right) \begin{pmatrix} A_x(z) \\ A_y(z) \\ a(z) \end{pmatrix} = 0 \,. \tag{2}$$

For our purposes, we limit the discussion to the simple case of a homogeneous magnetic field which is oriented along the y-axis ($\mathbf{B} = B_T \hat{\mathbf{e}}_y$; for the more general treatment of the problem [27]). In this case, the matrix is commonly written down in the following form:

$$\mathcal{M}_0 = \begin{pmatrix} \Delta_\perp & \Delta_R & 0 \\ \Delta_R & \Delta_\parallel & \Delta_{a\gamma} \\ 0 & \Delta_{a\gamma} & \Delta_a \end{pmatrix} , \tag{3}$$

the elements $\Delta_\perp = \Delta_{\rm pl} + \Delta_\perp^{CM}$, $\Delta_\parallel = \Delta_{\rm pl} + \Delta_\parallel^{CM}$, $\Delta_{a\gamma} = g_{a\gamma} B_T/2$, $\Delta_a = -m_a^2/(2E)$ describe the expected activity of the medium via Δ_R (Faraday rotation) and the birefringence of the medium via the Cotton–Mouton effect leading to $|\Delta_\perp^{CM} - \Delta_\parallel^{CM}|^2 \propto B_T^2$ [26]. For the photon energies considered here, we can neglect the Δ_R term. The presence of free charges in the plasma with volume number density n_e leads to the characteristic plasma frequency for electrons

$$\omega_{\rm pl} = \sqrt{4\pi\alpha n_e m_e^{-1}} \simeq 1.17 \times 10^{-14} \left(\frac{n_e}{10^{-7}\ {\rm cm}^{-3}}\right)^{0.5}\ {\rm eV}\,. \tag{4}$$

With the given choice of the transverse magnetic field, the polarization amplitudes are either parallel to the magnetic field $A_y(z) = A_\parallel(z)$ or perpendicular $A_x(z) = A_\perp(z)$. The matrix $\mathcal{M}$ describing a decoupled $A_\perp$, while $A_\parallel$ and a are evolving via mixing through the off-diagonal element $\Delta_{a\gamma}$. The solution to the coupled differential equation is obtained via rotation with the angle

$$\tan(2\theta) = \frac{2\Delta_{a\gamma}}{\Delta_{\rm pl} - \Delta_a}, \quad \sin(2\theta) = \frac{2\Delta_{a\gamma}}{\Delta_{\rm osc}}\,. \tag{5}$$

This is a very similar situation to the two-flavor mixing of propagating neutrino states, with the probability of oscillating from one state to the other over a distance d:

$$p_{a\gamma} = p_{\gamma a} = \sin^2(2\theta)\sin^2\left(\frac{\Delta_{\rm osc}\ d}{2}\right), \tag{6}$$

with

$$\Delta_{\rm osc} = \sqrt{(\Delta_a - \Delta_{\rm pl})^2 + 4\Delta_{a\gamma}^2}\,, \tag{7}$$

or re-written with the definition

$$E_c \equiv \frac{E|\Delta_a - \Delta_{\rm pl}|}{2\Delta_{a\gamma}}\,, \tag{8}$$

$$\Delta_{\rm osc} = 2\Delta_{a\gamma}\sqrt{1 + \left(\frac{E_c}{E}\right)^2}\,. \tag{9}$$

The energy E_c basically separates two regimes of photon-ALPs mixing: For $E \ll E_c$, the mixing angle $\theta = \Delta_{a\gamma}/\Delta_{\rm osc} \ll 1$ leads to very inefficient and rapid mixing except for a resonance when $\Delta_a = \Delta_{\rm pl}$. For $E \simeq E_c$, the mixing becomes energy-dependent, while at $E \gg E_c$, the mixing angle $\theta = \pi/4$ leads to maximum mixing without any dependence on the energy.

The range of possible astrophysical observations relating to propagation of photons and effects of photon-ALPs mixing is naturally very wide-reaching. However, the approaches fall typically into three categories:

1. Polarization
2. Disappearance channel
3. Appearance channel

All three approaches have been used within the recent years to interpret observations at various wavelengths including radio/UV (birefringence), high-energy gamma-rays (disappearance channel), and very high energy gamma-rays (appearance channel).

4.1 Polarization/dichroism

The coupling of $A_\parallel$ via $\Delta_{a\gamma}$ leads for $\Delta_{\rm osc} d \ll 1$ to a reduction of the polarization of $A_\parallel$, while $A_\perp$ remains unchanged. Under the assumption that birefringence can be ignored, we can observe a dichroic effect, changing the angle of polarization $\phi(z)$:

$$\phi(z) = \phi_0 + \arctan\left(\frac{A_\parallel(z)}{A_\perp(z)}\right). \tag{10}$$

We have carried out a study with 8 radio galaxies with measured polarization angle. The sources are located at redshift values between 2.34 and 3.57. The polarization angle is measured with respect to the orientation of the observed radio jet. The observed polarization angles are close to 90 degrees which is expected under the assumption that the emission is produced by electrons in the magnetic field aligned with the jet axis.

Since the magnetic field structure of the intervening medium is not well constrained, a simulation of single domains, randomly aligned with the line of sight is carried out and the resulting distribution of polarization angle changes is compared with the measurement. In a maximum-likelihood method, we were able to constrain $B_T g_{a\gamma} \lesssim 10^{-11}\mathrm{GeV}^{-1}$ nG for ultralight ALPS of $m_a \lesssim 10^{-15}$ eV$\approx \omega_{\rm pl}$. Further details are given in [28].

4.2 Disappearance channel

The mixing of photons and ALPs in a transverse magnetic field leads to the apparent disappearance of photons whenever the distance traveled $d \approx \Delta_{\rm osc}$ and the energy of the photon is $E \gtrsim E_c$. For a typical Galactic magnetic field configuration, large scale and ordered field structures exist aligned with the spiral arms. The halo of the Galaxy is magnetized and the field strength is estimated to be in the range of a few μG. Therefore, the critical energy

$$E_c \simeq 2.5\ \mathrm{GeV}\frac{|m_a^2 - \omega_{\rm pl}^2|}{\mathrm{neV}}\left(\frac{B_T}{\mu\mathrm{G}}\right)^{-1}\left(\frac{g_{a\gamma}}{10^{-11}\ \mathrm{GeV}^{-1}}\right)^{-1}, \tag{11}$$

is within the reach of the *Fermi*-LAT instrument which has been observing the entire gamma-ray sky in the energy range between 100 MeV and several TeV since August 2008. The oscillation length for $E \gg E_c$ is

$$l_{\rm osc} = \frac{2\pi}{\Delta_{\rm osc}/2} \approx 32\ \mathrm{kpc}\left(\frac{B_T}{\mu\mathrm{G}}\right)^{-1}\left(\frac{g_{a\gamma}}{10^{-11}\ \mathrm{GeV}^{-1}}\right)^{-1}. \tag{12}$$

For typical values of the Galactic magnetic field, we can therefore expect to observe conversion and even re-conversion of photons when propagating along a line of sight that intersects spiral arms with a large pitch angle. We have therefore analyzed the energy spectra of suitable sources obtained with *Fermi*-LAT. Since the distance of the objects needs to be known, we focused on Galactic gamma-ray pulsars. The gamma-ray spectra of pulsars share a similar shape (they follow a power-law with an exponential suppression at the high energy end). Furthermore, the well-known and nearby (200 pc) Vela pulsar serves as a calibration source to verify that indeed the spectrum of this object does not show any energy-dependent modulation.

In a recent publication [29], we have demonstrated the method and its application to a sample of six gamma-ray pulsars. The most distant object in the sample PSR J2021+3651 is poorly fit with a standard pulsar spectrum - the residuals indicate structures at GeV-energies

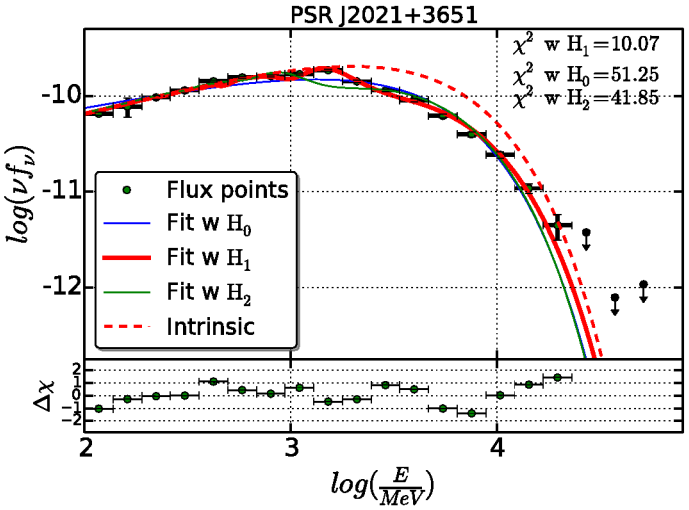


Figure 1: As an example of the studied pulsars' spectra: the spectral energy distribution of PSR J2021+3651, a young gamma-ray pulsar at a distance of ≈ 10 kpc. A smooth power-law with exponential cut-off spectrum (blue line, marked H_0), does not reproduce the spectrum well, while a fit with photon-ALPs coupling (red solid line, marked H_1) provides a significant improvement. The red dashed line indicates the shape of the emitted spectrum. Figure taken from Ref. [30].

which result in a poor fit of a smooth spectrum (see Fig. 1). We have carried out a combined analysis and found an improvement of the spectral fits of all six objects with a combined significance of 4.6 σ for a choice of $m_a = (3.6^{+0.5_{\rm stat}}_{-0.2_{\rm stat}} \pm 0.2_{\rm sys})$ neV and $g_{a\gamma} = (2.3^{+0.3_{\rm stat}}_{-0.4_{\rm stat}} \pm 0.4_{\rm sys}) \times 10^{-11}$ GeV^{-1}. In addition to the six objects in the Galactic plane presented in [29], we have in addition investigated twelve suitable and bright pulsars off the Galactic plane. Even though these sources have very different directions of lines of sight and distances, the resulting improvement of the fit when assuming a photon-ALPs coupling is significant and constrains the parameters in a consistent range (for details, see [30]).

4.3 Appearance channel

In the mixing matrix given in Eqn. 3, the absorption of photons is not considered. For energetic photons ($E = \mathcal{O}(\text{TeV})$), pair-production of photons on the optical/infra-red photons of the extra-galactic medium leads to a suppression of the observed flux for sources at cosmological distances. This process is included in the mixing matrix via an additional term:

$$\mathcal{M} = \mathcal{M}_0 - i\frac{\Gamma}{2}\begin{pmatrix} 1 & 0 & 0 \\ 0 & 1 & 0 \\ 0 & 0 & 0 \end{pmatrix}, \tag{13}$$

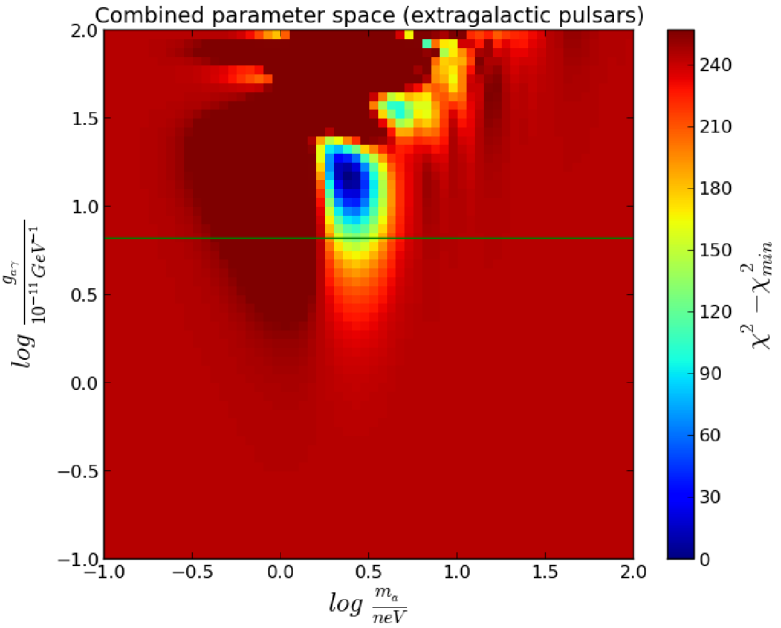


Figure 2: The combination of 12 pulsars located off the Galactic plane: the color-scale indicates the value of $\Delta\chi^2 = \chi^2 - \chi^2_{\rm min}$. For vanishing coupling ($g_{a\gamma} \to 0$), the fit is significantly worse than for the choice of the best-fitting mass m_a and coupling $g_{a\gamma}$ which we estimate to be $m_a \approx 3$ neV and $g_{a\gamma} \approx 10^{-10}$ GeV^{-1}. Figure taken from Ref. [30].

with Γ as the interaction rate calculated from the assumed isotropic background photon field with differential number density $dn = n_{\rm bck}(\epsilon)d\epsilon$:

$$\Gamma(E) = \int\limits_{m_e^2/E}^{\infty} d\epsilon n_{\rm bck}(\epsilon) \int\limits_{-1}^{1-\frac{2m_e^2}{E\epsilon}} d\mu \frac{1-\mu}{2} \sigma_{\gamma\gamma}(\beta)\,, \tag{14}$$

where the cross section above threshold depends on the electron/positron velocity in the center of momentum system $\beta = \sqrt{1 - 2m_e^2(E\epsilon(1-\mu))^{-1}}$:

$$\sigma_{\gamma\gamma} = \sigma_0(1-\beta^2)\left[2\beta(\beta^2-2) + (3-\beta^4)\log\frac{1+\beta}{1-\beta}\right]. \tag{15}$$

At gamma-ray energies, the polarization state is not measured and therefore, the propagated state is described as a density matrix ρ which is propagated across domains of constant magnetic field with random orientation. Further details are discussed in [31].

For the sake of simplicity, we consider the following case similar to the one discussed in [32]: Assuming that the source emits a beam with $a = 0$ and the source is embedded in a region of sufficiently large and turbulent magnetic field (e.g., the intra-cluster medium of a galaxy cluster or group), the photon beam leaving the magnetized source region will be mixed in such a way, that the normalized amplitudes $A_1 + A_2 \approx 2/3$. The beam will propagate through

the intergalactic medium where mixing is rather inefficient given the small magnetic field. However, the photonic part of the beam will get depleted by the absorption by some factor $e^{-\tau}$, where τ is the optical depth $\tau = \Gamma d$. The beam will finally propagate through the Galactic magnetic field, where on average $A_1 + A_2 \approx 2\exp(-\tau)/3 + 1/9$ will be detected. Conversely, once $\tau \gtrsim \ln(6) \approx 1.79$, the additional contribution from the back-converted ALPs-flux starts to dominate over the absorbed flux. Given the monotonic nature of $\Gamma \propto E^{\alpha}$ with $\alpha = -s+1$ for a power-law background field $n_{\rm bck} \propto \epsilon^s$, the effect of *appearance* of gamma-rays subject to large optical depth is most pronounced for sources at large distance and large energies. In a first-time study of the effect and its visibility in gamma-ray spectra from extra-galactic TeV-photon sources, we have demonstrated, that the observed flux above the energy where $\tau(E,z) > 2$ is systematically larger than in the case of a minimum background radiation field [33]. Here, we present an update of that initial analysis, where the data-sample has been expanded and a different method has been used to probe for deviations from the absorption-only picture.

We consider the spectral data-points from the same sample of energy spectra as listed in [34]. For each pair of differential measurements of a source with index j at redshift z_j at energies E_i and $E_{i+1} > E_i$ $f_{ij} = f(E_i, z_j)$ and $f_{i+1,j} = f(E_{i+1}, z_j)$ we calculate the differential slope

$$\alpha_{ij} \equiv \frac{\ln(f_{i+1,j}) - \ln(f_{i,j})}{\ln(E_{i+1}) - \ln(E_i)} = \frac{\Delta \ln(f)}{\Delta \ln(E)} \,. \tag{16}$$

Subsequently, we calculate the average $\langle\alpha\rangle_\tau = \sum w_{ij}\alpha_{ij} / \sum w_{ij}$ where the sum runs over all i, j where τ falls into intervals of width $\Delta\tau$. The averaging takes into account the measurement uncertainties σ_{ij} in an unbiased way via $w_{ij} = \sigma_{ij}^{-2}$. This way, we consider the average slope in bins of optical depth and can analyze the change of α with optical depth. In order to calculate $\tau(E,z)$, a particular model of $n_{\rm bck}$ is used.

The result is shown in Fig. 3 for two different models of the background photon field. The model according to Dominguez [35] is a phenomenological model which provides a prediction of the background field, while the model according to [34] is derived from the gamma-ray spectra (assuming no photon-ALPs mixing). The observed average slope is marked in green while the red points are the calculated slopes $\tilde{\alpha} = (\ln(\tilde{f}_{i+1,j}) - \ln(\tilde{f}_{i,j}))/\Delta\ln(E)$ with $\tilde{f}_{ij} = f_{ij}\ \exp(\tau_{ij})$. In both considered cases, the observed spectra show an upturn for an optical depth of $\tau \gtrsim 1.5$, roughly in line with the expectation considered above. The observed slope hardens monotonically for increasing optical depth. This trend is even more prominent when considering the values of $\tilde{\alpha}$ (red points). For both sets of points a smoothed curve is overlaid to guide the eye. The green shaded region indicates the observable slope that would lead to an intrinsic value of $\tilde{\alpha}$ fixed at the value for optical depth $\tau = 0$. This would be the expectation where the intrinsic slope does not depend on the observed optical depth (the source does not *know*, at which optical depth it is being observed).

In a related study, we have estimated the allowed minimum coupling $g_{a\gamma}$ under the assumption that the magnetic field is not exceeding other bounds [36].

5 WISPy dark matter

It was shown in Ref. [37] that bosonic WISPs, such as ALPs or HPs, are inevitably non-thermally produced in the early universe via the vacuum realignment mechanism and survive as a cold dark matter population until today. It was found that a large part of the parameter range probed by the next generation of experimental WISP searches – exploiting haloscopes (direct

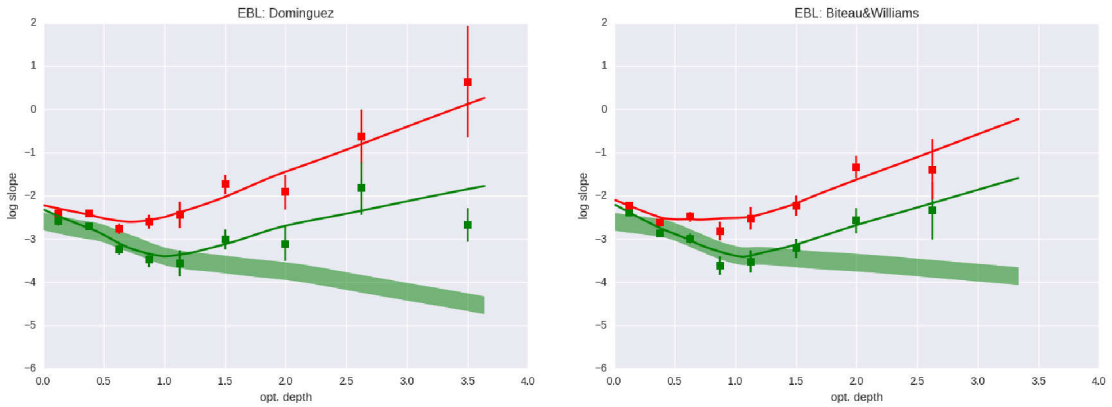


Figure 3: For a sample of extra-galactic TeV sources with redshifts in the range of $z = 0.03 \ldots 1$, the average logarithmic slope of the differential flux measurements (see text for further details) in intervals of optical depth: the green points are the measured (apparent) slopes, while the red points indicate the slopes after correcting for the absorption. In both considered models of the absorbing photon field, an unexpected upturn of slope for optical depth $\tau \gtrsim 1.5$ is apparent that is not expected without an effect related to the propagation of photons. The green shaded region indicates the expected slope of the spectra.

dark matter searches), helioscopes (searches for solar ALPs or HPs), or light-shining-through-a-wall techniques, cf. Sec. 6 – is consistent with the parameter space occupied by WISPy dark matter.

6 WISP searches in terrestrial laboratories

6.1 Light-shining-through-a-wall search: ALPS experiment

The vacuum oscillation of pseudoscalars in vacuum was already introduced in Eqn. (6). In the considered astrophysical settings, the resulting probability is typically $p_{a\leftrightarrow\gamma} \approx 0.5(g_{a\gamma} B_T d)^2 \approx 0.05(B_{T,\mu\mathrm{G}}\ g_{-10}\ d_{\mathrm{kpc}})^2$, with $B_T = B_{T,\mu\mathrm{G}}\ \mu$G, $g_{a\gamma} = g_{-10} \times 10^{-10}$ GeV^{-1}, $d = d_{\mathrm{kpc}}$ kpc. In laboratory settings, the corresponding probability $p_{a\leftrightarrow\gamma} \approx 10^{-13}$ when considering a distance of 10 m with a magnetic field of 10 T. In an experiment where the appearance of light behind a wall is considered, the probability is $p_{\gamma\to\gamma} = p^2_{a\leftrightarrow\gamma} \approx 10^{-26}$ for the re-appearance of light.

This approach was exploited in the pioneering ALPS-experiment [38], which used a single dipole magnet and an optical cavity. The setup reached a sensitivity to detect a re-appearance probability of $\approx 10^{-25}$ with a magnetic field of 5 T and $d = 4$ m, resulting in a sensitivity for a coupling $g_{a\gamma} < 7 \times 10^{-8}$ GeV^{-1}. The successor experiment, planned to start taking data in 2020, will increase the length to almost 100 m and add a cavity for the enhanced recovery of the beam after the wall. The proposed experiment [39] is designed to reach a sensitivity to the coupling $g_{a\gamma}$ improved by a factor of ≈ 3000 compared to the previous setup, covering the range of coupling preferred in the astrophysical scenarios discussed earlier.

6.2 Helioscope: Solar Hidden Photon Search (SHIPS)

The production and release of hidden photons from the sun provides an additional energy-loss mechanism that is globally constrained by the evolution of the sun. A more direct approach is the observation of hidden photons produced in the sun's interior [40]. The kinetic mixing couples this light particle with the normal photon. The Lagrangian density is

$$\mathcal{L} = -\frac{1}{4}F_{\mu\nu}F^{\mu\nu} - \frac{1}{4}X_{\mu\nu}X^{\mu\nu} + \frac{m_\chi^2}{2}X_\mu X^\mu - \frac{\chi}{2}F_{\mu\nu}X^{\mu\nu}, \tag{17}$$

where the angle $\chi \ll 1$ parameterizes the kinetic mixing between the two fields. Inside the sun, the coupling with the plasma modes and absorption need to be considered in order to derive the hidden photon flux at Earth. The resulting spectrum (including both resonant and off-resonant production dominating for photon energies above the maximum plasma frequency $\omega_P^2 = 4\pi\,\alpha\,n_e\,m_e^{-1} \approx 0.3$ keV for the central region of the sun). The resonant production takes place in the layers of the sun where the plasma frequency $\omega_P = \omega$ matches the produced photon frequency ω. The bulk of the emitted power is produced in the layers close to the photosphere where the electron density drops fastest. The hidden photon luminosity of the sun scales with $\chi^2 m_\chi^2$.

So-called *helioscopes* are sensitive to the hidden photon flux. The generic setup consists of an evacuated tube (the density should be sufficiently lowered such that $\omega_P < \omega$ and kinetic mixing takes place in vacuum conditions) and a low-background detector sensitive in the relevant energy range. In the case of the sun, the spectrum is dominated by optical emission such that e.g., a cooled photomultiplier tube can be used. If the diameter of the tube is larger than the diameter of the photosensitive surface of the detector, additional optical elements (e.g., a lens) can be used to increase the collection efficiency.

Such a helioscope experiment was designed, built, and operated at the Hamburg observatory under the name of *SHIPS* (solar hidden photon search) [41,42]. The experiment took 330 hours of data, pointing the tube to the sun (a similar time was used to estimate the background rate). The limit on the rate of photons generated was $\approx 5 \times 10^{-3}$ s^{-1} which translates into a limit on $\chi m_\chi \lesssim 10^{-10}$ eV for the mass range $10^{-4} \lesssim m_\chi/\text{eV} \lesssim 3$.

6.3 Haloscopes

Experiments which are sensitive to a local (Galactic halo) component of nonbaryonic and aphotic (dark) matter, usually are constructed following the haloscope approach. In the case of the QCD axion [43, 44], the guaranteed coupling to two-photon states via the Primakoff effect leads to detectable signals that can be picked up with a haloscope [45]. The original idea takes advantage of a resonator which enhances the oscillating electromagnetic field produced in a strong and external magnetic field. The resulting signal scales for a fixed dark matter energy density in the halo with the volume of the cavity, the energy density of the external magnetic field, and the quality factor of the resonator. The mode-overlap with the oscillating field is usually parameterized with a form-factor which in the ideal case is close to unity, for further details see, e.g., [46].

The resonant frequency ω is determined by the dimension of the cavity: in the case of a pill-box cavity with radius R, the most important $TM_{0,1,0}$ mode has a frequency $\omega \approx 2.405\,cR^{-1} \approx$ 72 GHz $R_{\rm cm}^{-1}$, with $R = R_{\rm cm}$ cm. The quality factor of a cavity is given by the ratio of its volume to the product of surface and skin depth. The latter scales with $\omega^{-1/2}$. Therefore,

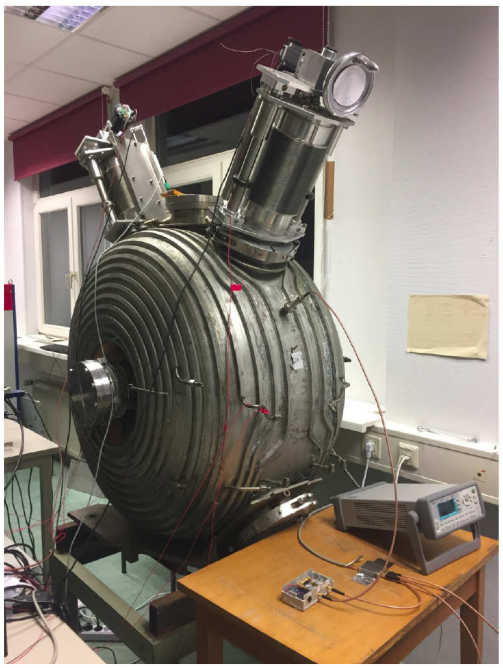


Figure 4: A photo of the WISPDMX setup including the two plunging tuners mounted on top of the cavity. The setup is operated at room temperature.

power generated in a haloscope increases non-linearly with decreasing frequency (or mass of the WISP) (roughly with $R^{7/2}$). This in turn makes it more difficult to detect axions with large mass as compared to smaller masses.
On the other hand, for an axion-haloscope, the entire volume needs to be filled with a strong magnetic field, leading to a fast rise of the expenses when constructing large volume bore magnets. For hidden photon searches however, the measurable power of the cavity does not depend on external magnetic fields. Therefore, hidden-photon haloscopes with large volume detectors are feasible and reach favorable sensitivity.

6.3.1 WISPDMX

Following this notion, we have developed and operated a large cavity experiment (WISPDMX: WISP Dark Matter eXperiment) using a spare resonator cavity of the HERA proton synchrotron accelerator (see Fig. 4). The cavity is operated without a magnetic field and is therefore only sensitive to a hidden-photon type dark matter. The cavity is excited via (neglecting higher order terms in χ)

$$\partial_\mu \partial^\mu A^\nu = m_\chi^2 \, \chi X^\nu , \tag{18}$$

with the field of the hidden photon $|\mathbf{X}| = \rho_{\mathrm{dm}} m_\chi / 2$ related to the local dark matter density $\rho_{\mathrm{dm}} \approx (0.04\ \mathrm{eV})^4$ (in natural units). The resulting power that can be measured with an antenna coupling to the cavity mode with a sub-critical efficiency $\kappa < 0.5$ is then given by

$$\dot{U} = \kappa \, \chi^2 \, m_\chi \, \rho_{dm} \, Q \, V G \, , \tag{19}$$

where G is the form factor of the mode and Q, V are the quality factor and volume of the cavity respectively. When using values characteristic for the WISPDMX setup, we find for the

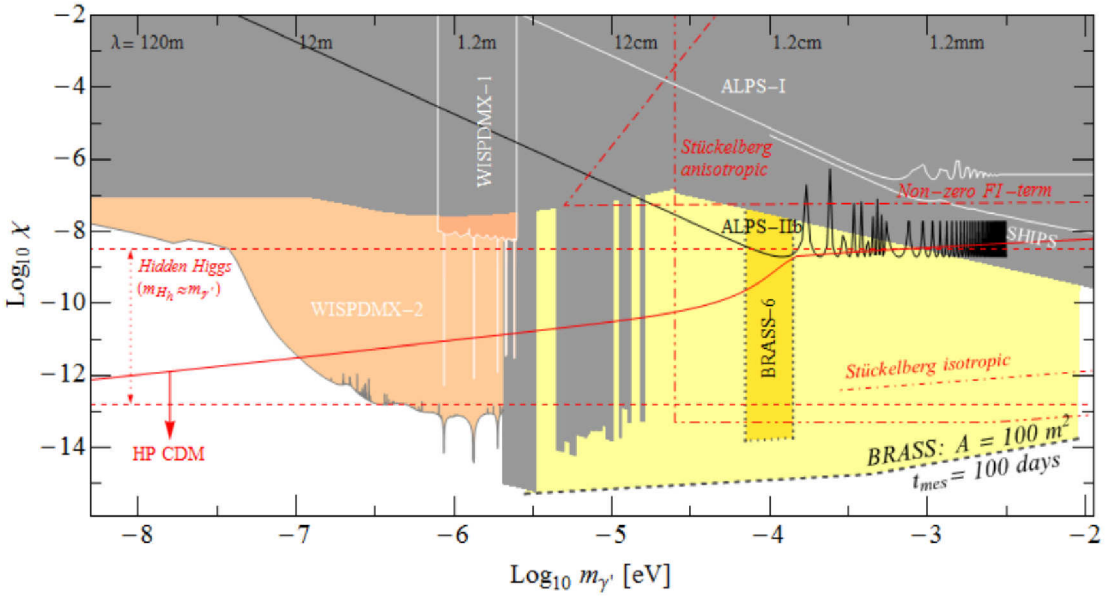


Figure 5: The parameters of mixing χ and mass of the hidden photon m'_γ: The previously existing limits are marked in gray. The preliminary WISPDMX limits are shown in orange. Future limits achievable with the planned non-resonating BRASS experiment are shown in yellow. Theoretically predicted ranges are indicated with red lines.

power (in the case of an isotropic distribution of the vector field $\mathbf{X}$ [47]):

$$\dot{U} \approx 1.63 \times 10^{-16}\ \mathrm{W} \left(\frac{\chi}{10^{-12}}\right)^2 \frac{\kappa}{0.1} \frac{Q}{50\,000} \frac{V}{447\ \mathrm{l}} \frac{G}{0.3} \frac{m_\chi}{\mu\mathrm{eV}} \frac{\rho_0}{\mathrm{GeV\ cm^{-3}}} \,. \tag{20}$$

The experimental setup consists of the cavity, two plunger units for tuning, a set of sensors for temperature, two loop-type antennae, and a low-noise amplification and digitization setup. The setup is operated at room temperature. The amplified signal from the antenna is read-out continuously and streamed to the host computer for 10 seconds via a fast digitizer with 10^9 samples per second. The spectra are then processed in parallel to the next read-out cycle with a GPU card. The system operates nearly in real-time; the resetting of the digitizer card after each cycle leads to a dead time of 4 seconds per cycle. This dead time reduces slightly our sensitivity. We process the spectra with a resolution of 50 Hz per channel. This is sufficient to oversample the expected signal shape at higher frequencies and slightly undersample the signal for lower frequencies.

We have completed the first science run end of 2017. The preliminary result on constraints of the mixing angle χ in the mass range below 2.08 μeV is presented in Fig. 5. The constraints cover a previously unexplored part of the parameter space. The combination of resonant and off-resonant searches demonstrates that a much broader mass range can be constrained with this type of read-out system.

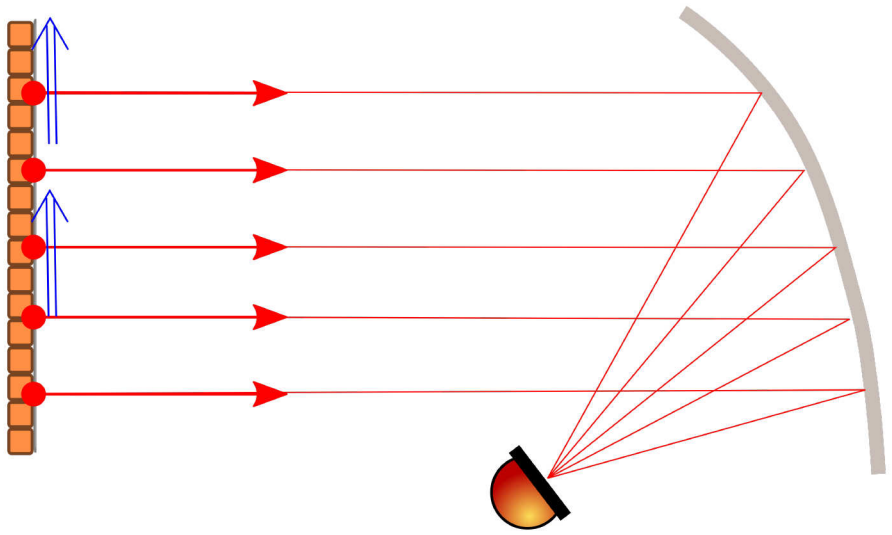


Figure 6: A schematic of the BRASS experiment: The converter surface consist of a layer of permanent magnets arranged in a Halbach-type configuration. The emission is then concentrated via a parabolic reflector into the detection system.

6.3.2 Dish approach

In order to mitigate the inherent problems with cavity-type haloscopes (see the beginning of this section) at high frequencies, a non-resonant approach was suggested [48]. In this approach, the oscillating field at the boundary to a conductor leads to the emission of a propagating wave parallel to the surface normal. This method does not have a resonant enhancement but the large surface area allows to compensate the missing resonance. Also, there is no tuning required and a broad-band search is possible. In this way, we can probe the mass range up to several 100 meV, limited only by the surface quality and detector available. The power radiated of a surface element is given by [48], assuming that the vector dark matter field $\mathbf{X}$ is isotropic:

$$\frac{\dot{U}}{\mathrm{m}^2} = 10^{-23}\ \mathrm{W} \left(\frac{\chi}{2.5 \times 10^{-14}} \right)^2 \frac{\rho_0}{\mathrm{GeV\ cm}^{-3}} \,. \tag{21}$$

In case of a pseudoscalar dark matter field (ALPs or the QCD axion), the dish needs to be magnetized with a predominantly parallel field component $B_\parallel$. The resulting power is therefore [48]:

$$\frac{\dot{U}}{\mathrm{m}^2} = 10^{-23}\ \mathrm{W} \left(\frac{m_a}{0.1\ \mathrm{meV}} \right)^{-2} \frac{\langle B_\parallel^2 \rangle}{\mathrm{T}^2} \left(\frac{g_{a\gamma\gamma}}{10^{-11}\ \mathrm{GeV}^{-1}} \right)^2 \frac{\rho_0}{\mathrm{GeV\ cm}^{-3}} \,. \tag{22}$$

A possible setup of a dish-type haloscope is shown in Fig. 6. In this particular scheme, a surface formed with permanent magnets is used as radiator, illuminating a secondary optic that is viewed by a receiver. A similar scheme is planned for the BRASS experiment.

References

[1] J. Jaeckel and A. Ringwald, *The Low-Energy Frontier of Particle Physics*, *Ann.Rev.Nucl.Part.Sci.* **60** (2010) 405–437, [1002.0329].

[2] S. Weinberg, *A New Light Boson?*, *Phys. Rev. Lett.* **40** (1978) 223–226.

[3] F. Wilczek, *Problem of Strong p and t Invariance in the Presence of Instantons*, *Phys. Rev. Lett.* **40** (1978) 279–282.

[4] R. D. Peccei and H. R. Quinn, *CP Conservation in the Presence of Instantons*, *Phys. Rev. Lett.* **38** (1977) 1440–1443.

[5] A. G. Dias, A. C. B. Machado, C. C. Nishi, A. Ringwald and P. Vaudrevange, *The Quest for an Intermediate-Scale Accidental Axion and Further ALPs*, *JHEP* **06** (2014) 037, [1403.5760].

[6] G. Ballesteros, J. Redondo, A. Ringwald and C. Tamarit, *Unifying Inflation with the Axion, Dark Matter, Baryogenesis, and the Seesaw Mechanism*, *Phys. Rev. Lett.* **118** (Feb, 2017) 071802, [1608.05414].

[7] G. Ballesteros, J. Redondo, A. Ringwald and C. Tamarit, *Standard Model—axion—seesaw—Higgs portal inflation. Five problems of particle physics and cosmology solved in one stroke*, *JCAP* **1708** (2017) 001, [1610.01639].

[8] A. Ernst, A. Ringwald and C. Tamarit, *Axion Predictions in $SO(10) \times U(1)_{\rm PQ}$ Models*, *JHEP* **02** (2018) 103, [1801.04906].

[9] E. Witten, *Some Properties of O(32) Superstrings*, *Phys. Lett.* **149B** (1984) 351–356.

[10] J. P. Conlon, *The QCD axion and moduli stabilisation*, *JHEP* **05** (2006) 078, [hep-th/0602233].

[11] P. Svrcek and E. Witten, *Axions In String Theory*, *JHEP* **06** (2006) 051, [hep-th/0605206].

[12] K.-S. Choi, I.-W. Kim and J. E. Kim, *String compactification, QCD axion and axion-photon-photon coupling*, *JHEP* **03** (2007) 116, [hep-ph/0612107].

[13] A. Arvanitaki, S. Dimopoulos, S. Dubovsky, N. Kaloper and J. March-Russell, *String Axiverse*, *Phys. Rev.* **D81** (2010) 123530, [0905.4720].

[14] M. Cicoli, M. Goodsell and A. Ringwald, *The type IIB string axiverse and its low-energy phenomenology*, *JHEP* **1210** (2012) 146, [1206.0819].

[15] S. A. Abel, J. Jaeckel, V. V. Khoze and A. Ringwald, *Illuminating the Hidden Sector of String Theory by Shining Light through a Magnetic Field*, *Phys. Lett.* **B666** (2008) 66–70, [hep-ph/0608248].

[16] S. A. Abel, M. D. Goodsell, J. Jaeckel, V. V. Khoze and A. Ringwald, *Kinetic Mixing of the Photon with Hidden U(1)s in String Phenomenology*, *JHEP* **07** (2008) 124, [0803.1449].

[17] M. Goodsell and A. Ringwald, *Light Hidden-Sector U(1)s in String Compactifications*, *Fortsch.Phys.* **58** (2010) 716–720, [1002.1840].

[18] M. Goodsell, S. Ramos-Sanchez and A. Ringwald, *Kinetic Mixing of U(1)s in Heterotic Orbifolds*, *JHEP* **1201** (2012) 021, [1110.6901].

[19] B. Holdom, *Two U(1)'s and Epsilon Charge Shifts*, *Phys. Lett.* **166B** (1986) 196–198.

[20] M. Goodsell, J. Jaeckel, J. Redondo and A. Ringwald, *Naturally Light Hidden Photons in LARGE Volume String Compactifications*, *JHEP* **0911** (2009) 027, [0909.0515].

[21] M. Cicoli, M. Goodsell, J. Jaeckel and A. Ringwald, *Testing String Vacua in the Lab: From a Hidden CMB to Dark Forces in Flux Compactifications*, *JHEP* **1107** (2011) 114, [1103.3705].

[22] G. G. Raffelt, *Stars as laboratories for fundamental physics: The astrophysics of neutrinos, axions, and other weakly interacting particles*. University of Chicago Press, Chicago, USA, 1996.

[23] M. Giannotti, I. Irastorza, J. Redondo and A. Ringwald, *Cool WISPs for stellar cooling excesses*, *JCAP* **1605** (2016) 057, [1512.08108].

[24] M. Giannotti, I. G. Irastorza, J. Redondo, A. Ringwald and K. Saikawa, *Stellar Recipes for Axion Hunters*, *JCAP* **1710** (2017) 010, [1708.02111].

[25] J. Jaeckel, E. Masso, J. Redondo, A. Ringwald and F. Takahashi, *The Need for Purely Laboratory-Based Axion-Like Particle Searches*, *Phys. Rev.* **D75** (2007) 013004, [hep-ph/0610203].

[26] G. Raffelt and L. Stodolsky, *Mixing of the photon with low-mass particles*, *Physical Review D* **37** (Mar., 1988) 1237–1249.

[27] A. De Angelis, O. Mansutti, M. Persic and M. Roncadelli, *Photon propagation and the VHE gamma-ray spectra of blazars: how transparent is really the Universe?*, *Mon. Not. Roy. Astron. Soc.* **394** (2009) L21–L25, [0807.4246].

[28] D. Horns, L. Maccione, A. Mirizzi and M. Roncadelli, *Probing axion-like particles with the ultraviolet photon polarization from active galactic nuclei in radio galaxies*, *Phys. Rev.* **D85** (2012) 085021, [1203.2184].

[29] J. Majumdar, F. Calore and D. Horns, *Search for gamma-ray spectral modulations in Galactic pulsars*, *JCAP* **1804** (2018) 048, [1801.08813].

[30] J. Majumdar, *Astrophysical phenomenology of axions and other very weakly interacting sub-eV particles*, Ph.D. thesis, Universität Hamburg, 2018. http://ediss.sub.uni-hamburg.de/volltexte/2018/9220.

[31] A. Mirizzi and D. Montanino, *Stochastic conversions of TeV photons into axion-like particles in extragalactic magnetic fields*, *JCAP* **0912** (2009) 004, [0911.0015].

[32] D. Horns, L. Maccione, M. Meyer, A. Mirizzi, D. Montanino et al., *Hardening of TeV gamma spectrum of AGNs in galaxy clusters by conversions of photons into axion-like particles*, *Phys.Rev.* **D86** (2012) 075024, [1207.0776].

[33] D. Horns and M. Meyer, *Indications for a pair-production anomaly from the propagation of VHE gamma-rays*, *JCAP* **1202** (2012) 033, [1201.4711].

[34] J. Biteau and D. A. Williams, *The extragalactic background light, the Hubble constant, and anomalies: conclusions from 20 years of TeV gamma-ray observations*, *Astrophys. J.* **812** (2015) 60, [1502.04166].

[35] A. Domínguez et al., *Extragalactic Background Light Inferred from AEGIS Galaxy SED-type Fractions*, *Mon. Not. Roy. Astron. Soc.* **410** (2011) 2556, [1007.1459].

[36] M. Meyer, D. Horns and M. Raue, *First lower limits on the photon-axion-like particle coupling from very high energy gamma-ray observation*, *Phys.Rev.* **D87** (2013) 035027, [1302.1208].

[37] P. Arias, D. Cadamuro, M. Goodsell, J. Jaeckel, J. Redondo et al., *WISPy Cold Dark Matter*, *JCAP* **1206** (2012) 013, [1201.5902].

[38] K. Ehret, M. Frede, S. Ghazaryan, M. Hildebrandt, E.-A. Knabbe et al., *New ALPS Results on Hidden-Sector Lightweights*, *Phys.Lett.* **B689** (2010) 149–155, [1004.1313].

[39] R. Bähre et al., *Any light particle search II —Technical Design Report*, *JINST* **8** (2013) T09001, [1302.5647].

[40] J. Redondo and G. Raffelt, *Solar constraints on hidden photons re-visited*, *JCAP* **1308** (2013) 034, [1305.2920].

[41] M. Schwarz, *The Solar Hidden Photon Search (SHIPS)*, Ph.D. thesis, Universität Hamburg, 2015. http://ediss.sub.uni-hamburg.de/volltexte/2015/7320.

[42] M. Schwarz, E.-A. Knabbe, A. Lindner, J. Redondo, A. Ringwald, M. Schneide et al., *Results from the Solar Hidden Photon Search (SHIPS)*, *JCAP* **1508** (2015) 011, [1502.04490].

[43] R. D. Peccei and H. R. Quinn, *CP Conservation in the Presence of Pseudoparticles*, *Physical Review Letters* **38** (June, 1977) 1440–1443.

[44] F. Wilczek, *Problem of Strong P and T Invariance in the Presence of Instantons*, *Physical Review Letters* **40** (Jan., 1978) 279–282.

[45] P. Sikivie, *Experimental Tests of the "Invisible" Axion*, *Physical Review Letters* **51** (Oct., 1983) 1415–1417.

[46] P. Arias, D. Cadamuro, M. Goodsell, J. Jaeckel, J. Redondo and A. Ringwald, *WISPy Cold Dark Matter*, *JCAP* **1206** (2012) 013, [1201.5902].

[47] J. A. R. Cembranos, C. Hallabrin, A. L. Maroto and S. J. N. Jareno, *Isotropy theorem for cosmological vector fields*, *Phys. Rev.* **D86** (2012) 021301, [1203.6221].

[48] D. Horns, J. Jaeckel, A. Lindner, A. Lobanov, J. Redondo et al., *Searching for WISPy Cold Dark Matter with a Dish Antenna*, *JCAP* **1304** (2013) 016, [1212.2970].

Dark Matter Searches

Marcus Brüggen[1], *Dieter Horns*[2], *Christian Spiering*[3], *Janis Kummer*[1], *Chao Zhang*[2]

[1]Hamburger Sternwarte, Universität Hamburg, Germany
[2]Institut für Experimentalphysik, Universität Hamburg, Germany
[3]DESY, Zeuthen, Germany

DOI: http://dx.doi.org/10.3204/PUBDB-2018-00782/C2

The search for dark matter particles with astrophysical methods and observations includes diverse methods and approaches. Here, we consider three approaches: the indirect searches for self-annihilating and decaying dark matter particles at keV to TeV mass, observations sensitive to the self-interaction cross-section of dark matter particles, and finally, searches for rare and ultra-massive particles with the IceCube large volume detector. The sensitivity of the observations and methods is sufficient to probe regions of parameter space relevant for non-baryonic dark matter.

1 Introduction

In the past decades, a number of key and major facilities have started operation. This includes the high-energy physics experiments CMS [1] and ATLAS [2] at the Large Hadron Collider [3], large scale direct dark matter search experiments (the strongest constraints are currently delivered by dual phase Xenon detectors like XENON 1t [4], LUX [5], PANDA X-II [6]), as well as gamma-ray telescopes (from ground the upgraded H.E.S.S. array in Namibia [7]; in orbit, the *Fermi* large area telescope [8]), and the AMS-02 experiment at the international space station. So far, neither the ongoing searches at the LHC experiments have revealed any candidate particle for dark matter nor have any of the searches for dark matter particles lead to the discovery of dark matter particles in the solar environment, from various sources including the center of the Galaxy, dwarf spheroidal galaxies, galaxy clusters, and the interstellar medium. Some of the existing constraints are discussed in the following sections.

Besides the aforementioned searches for dark matter particles which are commonly considered *weakly interacting massive particles* (WIMPs), two additional candidates are targeted here: keV-mass dark matter (e.g., as a sterile neutrino or an axion) and magnetic monopoles. Finally, the astrophysical ramifications of a more complicated dark sector including self-interacting dark matter are investigated via simulations.

2 Indirect searches for dark matter

2.1 Searches for decaying light dark matter

Sterile (right-handed) neutrinos are straight-forward extensions of the standard model of particle physics. In the simplest manifestation of these models, singlet neutrinos are added to

the weak doublet eigenstates. The three singlets could naturally explain anomalies of neutrino flavor oscillations, non-baryonic dark matter as well as the tiny masses of the left handed neutrinos via a see-saw mechanism [9]. The intermediate sterile neutrino would be a dark matter particle and would be produced most likely via resonant mixing [10].

The unknown parameters of sterile neutrino dark matter (SNDM) are the mixing angle ϑ with the active neutrinos and the mass $m_{\nu,R}$ of the particle. The mixing angle is constrained in a model-dependent way for resonant production by the actual relic density observed today. The mass of the SNDM is bound to be at least above the 100 eV range in order to match the Tremaine–Gunn bound derived from the phase-space density distribution for fermions in e.g., dwarf spheroidal galaxies.

Further constraints on the mixing angle for a fixed mass of the SNDM can be obtained through the decay of the sterile neutrino ν_R into its active partner ν_L

$$\nu_R \rightarrow \gamma + \nu_L,$$

which leads to the production of observable and mono-energetic photons at $E_\gamma = m_{\nu,R}/2$ (assuming that $m_{\nu,R} \gg m_{\nu,L}$). The decay rate $\Gamma(\nu_R \rightarrow \gamma + \nu_L)$ of a Majorana sterile neutrino is directly linked to the mixing angle

$$\Gamma(\nu_R \rightarrow \gamma + \nu_L) = \frac{9\alpha G_F^2}{1024\ \pi^4} \sin^2(2\vartheta)\ m_{\nu,R}^5,$$

the Dirac neutrino would have a rate reduced by a factor two.

The observation of a narrow, line-like feature in the X-ray spectra is therefore a signature of SNDM. Various approaches have been suggested. The idea common to all approaches is to use X-ray observations of objects which have a large abundance of dark matter in comparison with visible matter. In the case of a non-detection, an upper limit on the mixing angle ϑ can be derived under the assumption of the dark matter density and its spatial distribution in the target object.

In the past years, spurious X-ray line signals have been found with controversial claims about their interpretation. The most extensive episode has been the claim for a detection of a feature in the stacked X-ray spectra of various galaxy clusters [11]. The line-like feature was initially unidentified and later found to be most likely associated with a charge exchange reaction involving sulphur ions that have been measured to be at an energy of 3.47 ± 0.06 keV [12], well consistent with the observed line at 3.5 keV from Galaxy clusters.

The line emission has not been seen from the interstellar medium of our Galaxy. An archival search for X-ray line emission from an accumulated data set taken with the XMM-*Newton* satellite has been investigated [13]. The data set is complementary to the observations of Galaxy clusters as the astrophysical foreground emission is distinctly different (the temperature of the hot phase of the interstellar medium is below the temperature of the hot intra-cluster gas).

In our study, we have combined different observations with the PN instrument [14] after subtracting the detected X-ray point sources in the respective fields of view. We have carefully modeled and disentangled the instrumental and astrophysical background. The resulting background subtracted spectra (see Fig. 1 for an example of a deep observation of an object in the Galactic bulge) do not show any unknown X-ray lines. Under the assumption of different Galactic dark matter density distribution functions, we have converted the non-detection of lines (at a flux limit of $\approx 10^{-6}$ cm^{-2}s^{-1}) into a limit on $\sin^2(2\vartheta)$. The resulting limit shown

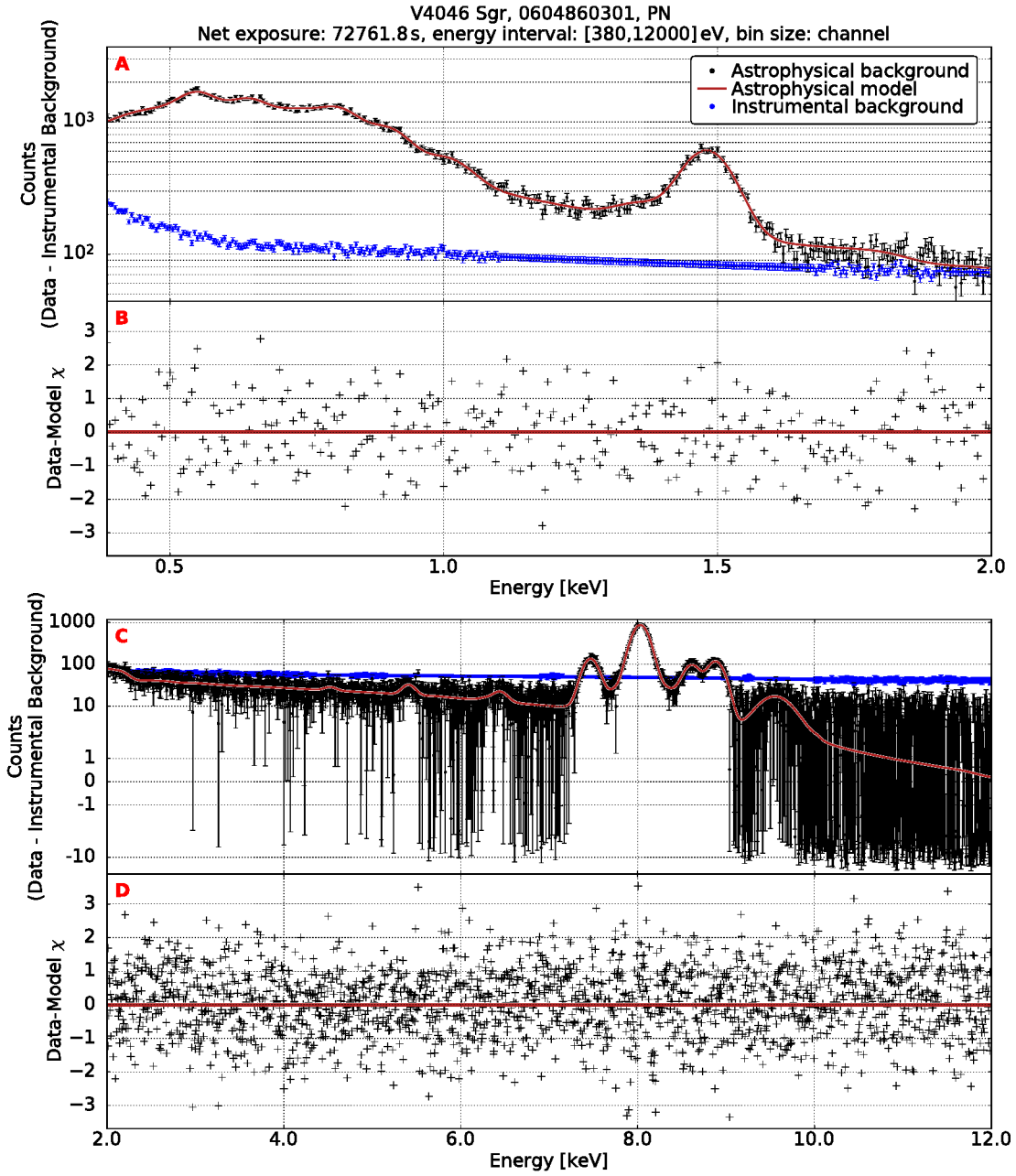


Figure 1: Upper panel: count spectra for the energy range from 0.38 keV to 2 keV, lower panel, energy range from 2 keV to 12 keV. The count spectra from one particular field of view towards the Galactic bulge, together with the instrumental and astrophysical background. Note, the very good match of the modeled background with the data. Figure reprinted from Ref. [13]. © 2017 IOP Publishing Ltd and Sissa Medialab.

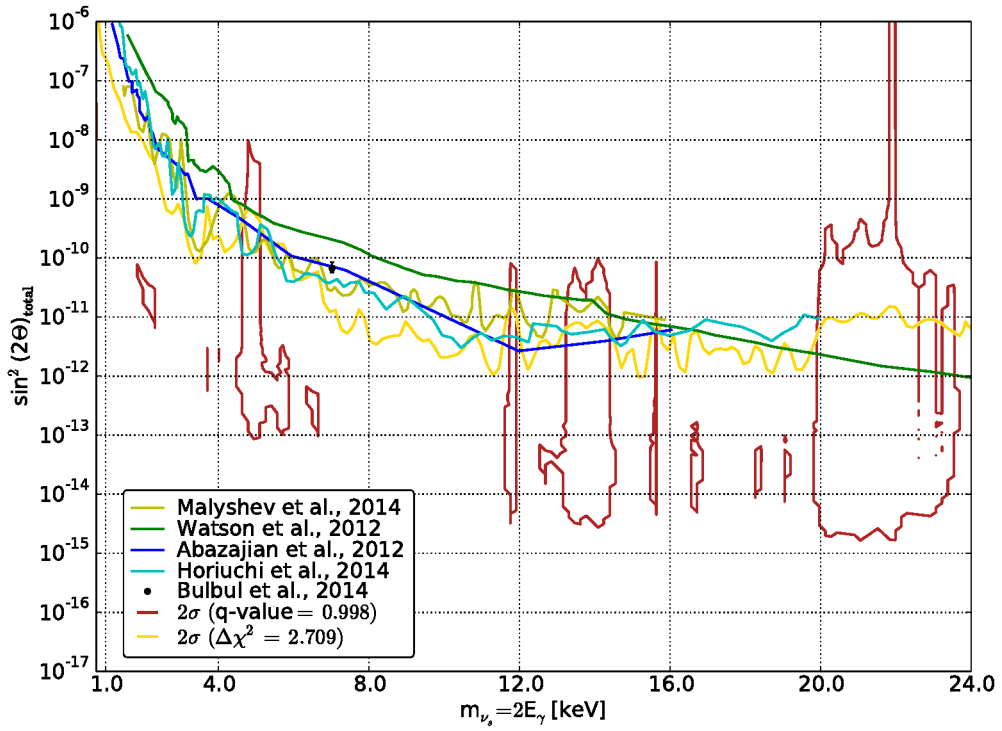


Figure 2: The constraints on the mixing angle with a sterile neutrino for the entire accessible mass range in comparison with previous constraints as well as the spurious detection discussed in the text at $m_{\nu,R} \approx 7$ keV. Figure reprinted from Ref. [13]. © 2017 IOP Publishing Ltd and Sissa Medialab.

in Fig. 2 is almost invariant under the choice of the dark matter density distribution. In addition to the constraint in the form of an upper limit, we also include the 2σ contours where an additional line would be slightly favored.

The same constraint on X-ray line emission can also be used to constrain the two-photon coupling of axion-like particles to be $g_{a\gamma\gamma} < \mathcal{O}(10^{-18})$ GeV^{-1} for particle masses between 4 and 24 keV (see Ref. [13] for further details).

2.2 Indirect WIMP searches

2.2.1 Dwarf galaxies and Galactic center

The indirect searches for WIMPs generically relies on self-annihilation or decay of massive particles which are not part of the standard model of particle physics (for a recent review see Ref. [15]). We are mainly concerned with the annihilation process which is naturally linked to the thermal production of WIMPs in the young and hot universe.

The approach shared by all indirect WIMP searches is to use the fact that $\langle \sigma v \rangle$ is fixed by the relic density and therefore provides a guaranteed annihilation rate per volume that scales with the dark matter particle density $(\rho_{\mathrm{DM}}/m_{\mathrm{DM}})^2$, with ρ_{DM} the actual energy density and

$m_{\rm DM}$ the particle mass.

During the past decade, the indirect WIMP searches have reached sufficient sensitivity to close in on the so-called thermal cross-section of $\langle\sigma v\rangle \approx 10^{-26}$ cm^{3}s^{-1} which provides the observed relic abundance via the *WIMP-miracle* [16].

While the Galactic center has been considered for a long time to be the best choice to search for gamma-ray emission produced in annihilation reactions, it has become clear that the gamma-ray emission produced by astrophysical processes provides a strong and difficult to disentangle background limiting the sensitivity for dark-matter searches from the Galactic center.

As an example, consider the controversial interpretation of a claimed GeV excess from the Galactic center. In recent studies, the gamma-ray emission detected at GeV energies has been finally identified to be produced by a population of point sources [17–19], most likely spun-up pulsars, often found in globular clusters and suspected to be present in the Galactic bulge as well.

The very-high energy (up to 10 TeV) emission from Galactic center remains however unidentified and has been considered to be produced in self-annihilating heavy dark matter with reasonable values of dark matter density and its spatial distribution [20]. An important clue to the origin of the gamma-ray emission can be obtained through observations of variability (so far, not found, see e.g., [21]) or even searches for time-dependent eclipsing of a compact gamma-ray source (e.g., linked to Sgr A* [22]).

Besides the aforementioned spurious detections, the non-detection of gamma-rays from dwarf galaxies provides solid constraints on the value of $\langle\sigma v\rangle$. The most recent manifestation of indirect limits is collected in Fig. 3. The summary presented there is not complete, but it highlights three important features:

(i) The achievements of the last decade have lead to a substantial improvement on the sensitivity of the cross section (using the same instrumentation) via new observational strategies (new dwarf galaxies identified, observation of the inner Galactic halo); compare e.g., the bounds obtained by [28] from classical dwarf spheroidal galaxies, and more recent bounds with the same instrument from the inner halo [25].

(ii) Gamma-ray observations cover a wide range of different objects (with different velocity distributions and mass-to-light ratios) at a large range of masses, going from a few GeV to hundreds of TeV.

(iii) Finally, the sensitivity of future instruments does not improve substantially on the current limits when conservative assumptions on the background and dark matter distribution are made. Compare, e.g., the projected sensitivity of CTA [29] with the one already obtained with H.E.S.S. [25]. The sensitivity is not limited by statistics but rather by systematic effects related to galactic diffuse emission as well as cosmic-ray background (note, however previous estimates of the CTA sensitivity were much more optimistic, see e.g., [34]).

2.2.2 Dark subhalo objects

The most common approaches to search indirectly for dark matter with gamma-ray telescopes rely on additional (model dependent) knowledge of the dark matter distribution in dark matter dominated objects. For dwarf galaxies, the challenging observation of the dynamics of member stars leaves us with some degeneracy on the underlying halo model. The resulting uncertainties

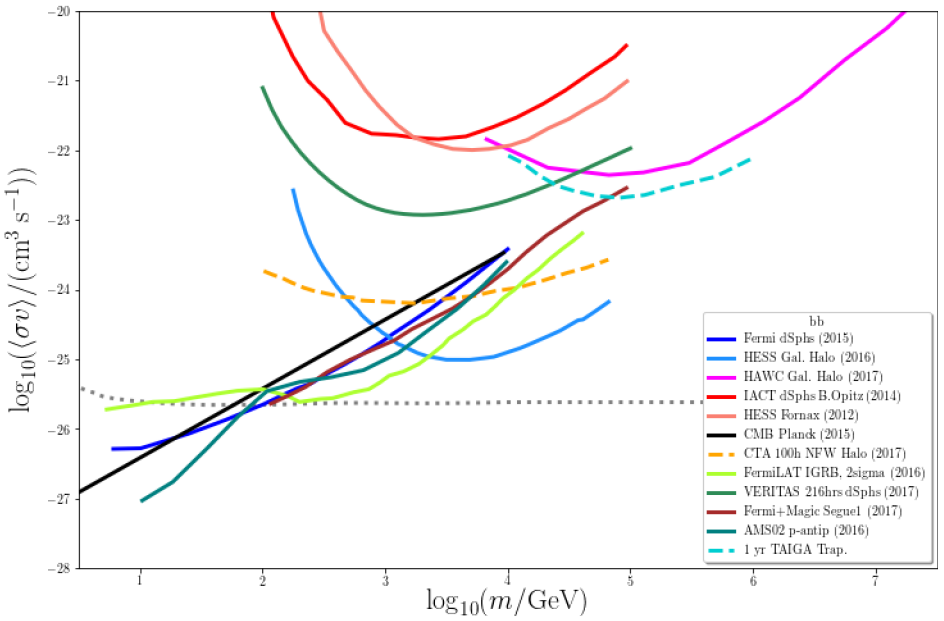


Figure 3: A collection of bounds (final state $b\bar{b}$) from existing instruments and observations (solid lines) as well as bounds from future installations (dashed lines)- compared with the cross section to match the relic density in standard thermal decoupling scenarios (dotted line) [16]. The most constraining limits are obtained with *Fermi*-LAT observations of dwarf galaxies [23] and (more model-dependent) from the intergalactic gamma-ray background [24]. At the TeV-mass range, H.E.S.S. observations of the Galactic halo are most constraining [25], while observations of dwarf galaxies fall behind [26–28]. The CTA sensitivity for observations from the inner Galactic halo from [29], using a similar method as in [25], is obviously rather conservative. At even higher energies, the air shower arrays HAWC [30] and TAIGA [31] provide the best sensitivity. Complementary to the gamma-ray observations, measurements of the anti-proton component of cosmic rays (AMS-02, [32]) and constraints from the CMB with Planck data [33] provide excellent constraints at the low mass end.

are reasonably well understood and included in the upper limit calculations [23,28,35]. However, in the case of galaxy clusters, the uncertainty on the subhalo structure leaves us with an uncertainty on the boost factor of two orders of magnitude [28,36].

Alternative to these approaches, we have considered a new strategy which is less dependent on the assumed dark matter distribution and could provide us with a clear, smoking gun signature for dark matter annihilation on small scale.

We have considered the possibility that dark matter satellites in our Galaxy are truly dark, without any star formation and baryonic activity. These subhalo objects would appear mainly as gamma-ray sources without any striking counterpart at other wavelengths (with the exception of detectable radio-synchrotron emission [37] - however, the expected flux depends on largely unknown particle propagation and magnetic field structure in these objects). The discovery of unidentified sources from the *Fermi*-LAT sky survey which share a unique energy spectrum and appear spatially extended could be interpreted in terms of dark matter annihilation [38,39]. The

initial searches carried out on the first two releases of the *Fermi*-LAT source catalogs revealed however a substantial problem with source confusion. Within the astrometric uncertainty, the faintest gamma-ray detected (and mostly unidentified) sources in the catalog are expected to line up per chance with at least one faint radio sources which presumably could be counterparts (most likely of active galactic nucleus nature). Nevertheless, we explored the possibility to study the extension of these objects and calculated the expected number of objects that can be expected to be found for a given sensitivity of the observation [38, 39].

This approach has been considered further in the literature, with the most recent study showing that the sensitivity of this approach is similar to other approaches [40].

2.3 Constraining BSM physics with combined fitting

With the various channels that are being used to search for dark matter and dark matter candidates, there are obviously opportunities to combine the informations. One of the earliest approaches towards a more general scheme of fitting parameters of a constrained SUSY model was the *AstroFit* [41] extension of the *fittino* [42] package. The concept was proven to function well and demonstrated with the first data release of the LHC experiments, that the combination of astrophysical constraints (indirect searches), direct searches with collider data could help to constrain parameters of constrained SUSY models [43]. Recently, the approach has been carried further with the so-called *Gambit* package [44], which aims at a modular and generic approach to constrain theories beyond the standard model.

In the context of the SFB 676, we have considered simplified and less model-dependent approaches to obtain insights into the potential reach of indirect detection methods. We have extended upon previous work with a generic scenario where a heavy mediator with free spin properties and coupling is used to build models that are consistent with relic density, direct search, collider and indirect search data. In addition, we also consider the reach of the international linear collider. The resulting type of study is shown in Fig. 4, where the mediator mass and the dark matter particle mass are constrained in a complementary way by collider experiments, direct search experiments and by the requirement to produce thermally the correct relic density. At very low ($m_{\mathrm{DM}} < 10$ GeV) the collider bounds rule out the favored combination with the mediator mass of 100–1000 GeV. At slightly higher mass of the dark matter particle, the direct search bounds dominate. Only at $m_{\mathrm{DM}} > 10$ TeV, the current constraints are not sufficient to rule out this type of generic models [45].

3 Rare-event searches with the IceCube neutrino telescope

Among the hypothetical particles which might *contribute* to dark matter are magnetic monopoles. In classical electrodynamics, their existence would symmetrize Maxwell's equations with respect to the sources of the electromagnetic field [52]. Magnetic monopoles would carry a quantized magnetic charge – integer multiples of the Dirac charge $g_D \approx 68.5\,e$. However, they do not appear automatically in that framework, different to Grand Unified Theories (GUTs) [53] where magnetic monopoles appear as stable, finite energy solutions of the field equations [54, 55]. The predicted masses range from 10^5 GeV to 10^{17} GeV (see e.g. Ref. [56]).

Superheavy monopoles with masses at the GUT scale may have been created during the phase transition associated with the spontaneous breakdown of the unified gauge symmetry in the early universe [57]. Since magnetic monopoles are stable, they should still be present

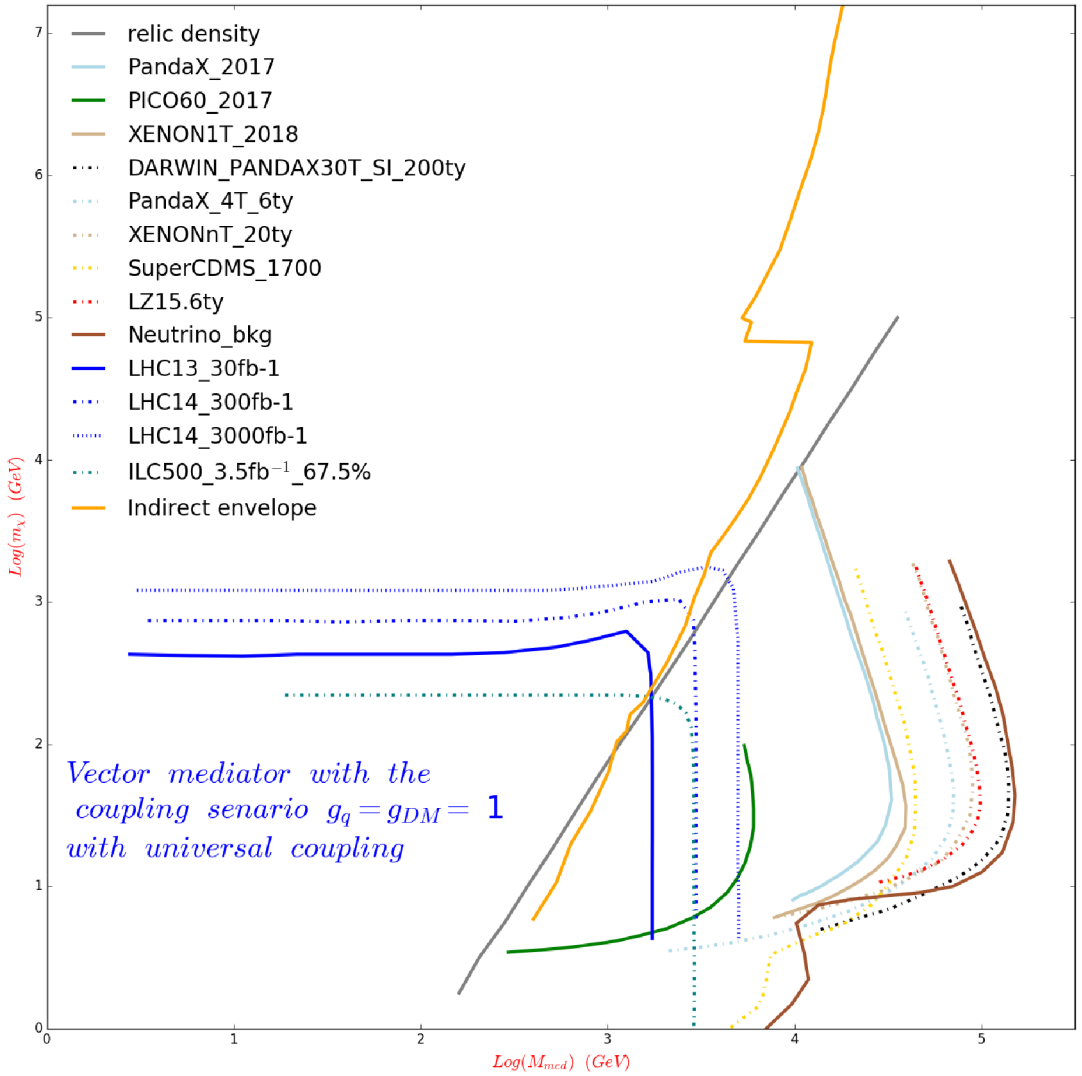


Figure 4: Example for an effective model with a vector mediator, universal coupling: The constraints from direct searches, indirect searches, relic density, and collider searches are included. Only a small region at high (> 10 TeV) and very low mass (< 10 GeV) is consistent with the constraints from [45]. Here we have used the ILC sensitivity (dashed) from [46] and LHC constraints (solid) and sensitivities (dashed) from [47]. For indirect detection, we have combined the constraints in Fig. 3. For the relic density, we have use the data from the Planck collaboration [48]. For direct detection, we have collected all the constraints (solid, spin-independent cross sections) and sensitivities (dashed) with data from Refs. [49–51]. The results on direct detections are similar to those of Ref. [47].

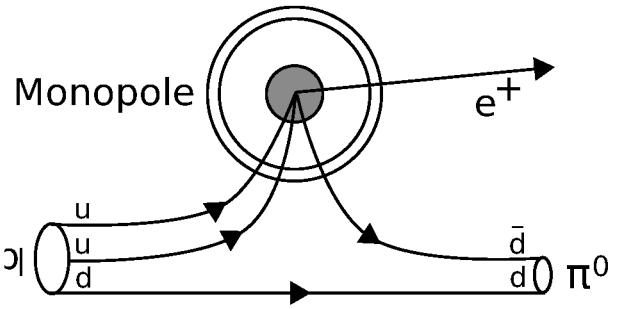


Figure 5: Illustration of a proton decay into a positron and a neutral pion catalyzed by a GUT monopole. Figure taken from Ref. [65].

in cosmic rays. The number density today depends on the existence of an inflationary epoch and on the time of creation, which could be before, during or after this epoch [58]. Since then, monopoles have been accelerated by large-scale cosmic magnetic fields, with a maximum kinetic-energy gain of the order of 10^{14} GeV [56]. Consequently, monopoles with masses at or above this energy scale should be non-relativistic.

Based on the propagation of magnetic monopoles in the Galactic magnetic field an upper bound on the monopole flux can be calculated, assuming the magnetic field does not decrease faster than it can be regenerated. This assumption constrains the monopole flux to be less than $10^{-15}\,\mathrm{cm}^{-2}\,\mathrm{s}^{-1}\,\mathrm{sr}^{-1}$, which is called the Parker Bound [57]. The current best limits for magnetic monopoles constrain their flux to more than two orders of magnitude below the Parker bound depending on the monopole speed and interaction mechanism [59–61]. Consequently, searches for magnetic monopoles require very large detectors. In our case, we use the IceCube Neutrino Observatory at the South Pole, which detects the Cherenkov light from electrically-charged particles [62]. IceCube consists of 5160 optical modules (OMs) arranged at 86 strings, each equipped with 60 OMs. The array covers a full cubic kilometer of highly transparent Antarctic ice, at depths of 1450 to 2450 meters. The horizontal distance between the strings is 125 m; only for the very central part (called DeepCore) it is much smaller, resulting in a higher light collection efficiency.

For relativistic monopoles IceCube would detect the Cherenkov light from the monopole itself (which is about 8300 times brighter than that of single electric charges – $(n_{\mathrm{water}} \times 68.5)^2$, with $n_{\mathrm{water}} = 1.33$ being the refraction index of water). Non-relativistic monopoles at the GUT scale can catalyse the decay of nucleons. They can be detected by the Cherenkov light from electrically charged secondary particles produced in subsequent nucleon decays along the monopole trajectory (via the so-called Rubakov-Callan effect [63, 64]. Figure 5 illustrates the catalysis of a proton decay by $M + p \longrightarrow M + \pi^0 + e^+$.

Current estimates for the catalysis cross sections are of the order of $10^{-27}\,\mathrm{cm}^2$ to $10^{-21}\,\mathrm{cm}^2$. The work within the SFB focused on the search for such non-relativistic magnetic monopoles. It would also have signaled the passage of super-symmetric Q-balls (another hypothetical super-heavy component of dark matter [66]) and the passage of "strange quark matter" – a hypothetical form of matter with equal numbers of up, down and strange quark and mass numbers between a few hundred GeV and the mass of a neutron star [67] – each which its own problems to translate a non-detection to a flux limit. Naturally, such translation problem applies also to the case of GUT monopoles: the emergent flux limits are conditional to an assumed catalysis cross section

and also depend on the velocity.

The search for particles moving with typical virial velocities about $10^{-3}\,c$ is complicated by several facts. The passing time through the full IceCube volume is about 3 ms, not 3 μs, like for relativistic particles. The IceCube data acquisition system and the analysis framework (triggers, filters, Monte-Carlo simulation, reconstruction etc.) are tailored to relativistic particles, e.g. to the μs scale. This does not allow to use any of the standard analysis tools of the experiment but requires an approach "from scratch". Secondly, within 3 ms several thousand noise hits and a few muon tracks appear in the detector and constitute an enormous challenge to identify hits from a particle moving slowly through the detector.

The results of the work done within the SFB have been published in [65]. This paper is based on two data samples. The first sample was taken from May 2009 until May 2010, making use of the full volume of the configuration installed in 2009 (59 strings) and using standard IceCube triggers. These triggers – as mentioned above – are not very effective for monopoles (except for those with a very high light emission, i.e. a very high catalysis cross section). The second sample was taken from May 2011 until May 2012 with a meanwhile installed dedicated slow-particle trigger which, however, acts only on the data taken with DeepCore, the small inner part of IceCube. Compared to the first analysis, this analysis is much more effective for monopoles with low light emission (i.e. a small catalysis cross section at a given velocity); for the brightest monopoles it cannot fully compete with first analysis due to the smaller volume of DeepCore.

The IceCube-59 analysis has yield one event, for an expected background of 4.8 ± 0.7 events. This event contains multiple coincident muons, which renders it compatible with a background event. The filters of the Deep-Core analysis, which was based on data of the slow-particle trigger, were passed by no event, while the number of expected background events was estimated to 3.2 ± 1.4. With no monopole candidate in both analyses, the limits on the flux of non-relativistic magnetic monopoles catalysing proton decay could be improved by about one to two orders of magnitude in comparison to MACRO [59, 60] for most of the investigated parameter space and reach down to about three orders of magnitude below the Parker limit. Figure 6 summarizes the results.

The publication of slow-monopole results in [65] has timely complemented the publication on *relativistic* monopoles with IceCube [68]. The limits from the latter have meanwhile been considerably improved [69]. Within a PhD thesis, also the limits on slow monopoles have recently been improved. This thesis is based on the methods developed [65]; results will be published at the end of 2018.

4 Self-interacting dark matter

The paradigm of collision-less cold dark matter (CDM) predicts the large-scale structure of the universe remarkably well. But on small scales simulations and observations do not agree with each other.

Self-interacting dark matter (SIDM) was suggested by [70] to address the small-scale issues.

The typical cross-section needed to solve these problems are of the order of magnitude $\sigma_{\rm SI}/m_{\rm DM} \sim 1\ {\rm cm}^2/{\rm g}$.

In numerical studies these scattering processes of dark matter particles with themselves are mostly modeled as isotropic contact interactions. In order to avoid the evaporation constraints, these processes have to be rare because the momentum transfer can be large. But there is

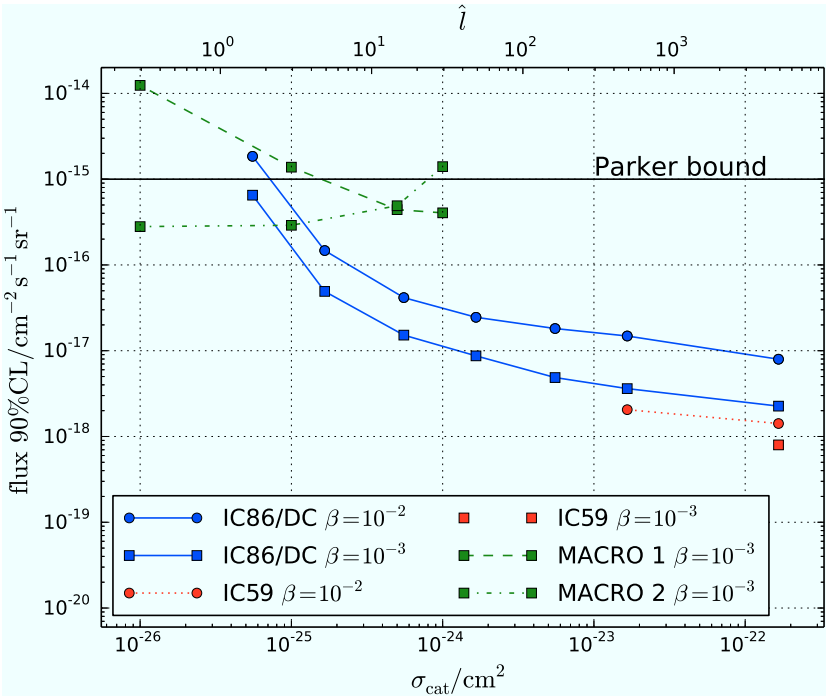


Figure 6: Upper limits on the flux of non-relativistic magnetic monopoles depending on the speed $\beta = v/c$ and catalysis cross section σ_{cat} of the IC-59 analysis and the IC-86/DeepCore analysis. The dashed lines are limits published by the MACRO experiment [59, 60]. Here, MACRO 1 is an analysis developed for monopoles catalyzing the proton decay. MACRO 2 is the standard-MACRO-analysis, which is sensitive to monopoles ionizing the surrounding matter. Additionally, the IceCube limits are shown as a function of l which is proportional to the averaged Cherenkov photon yield per nucleon decay (not valid for MACRO limits). Figure taken from Ref. [65].

another limit which we explored in this project. If the momentum transfer is small, it is possible to have frequent self-scatterings.

The most stringent bounds on DM self-interactions originate from evaporation constraints in merging galaxy clusters. Basically from the assumption that an infalling DM halo should not lose more that 20–30% of its mass during the merging process [71]. We can formulate that statement in terms of the number of expulsive collisions (following [72]). Consider such a system of a subcluster falling into a lager cluster with a relative velocity v_0. As a result of expulsive collisions the velocity of both colliding particles (one from the subcluster scattering with one from the main cluster) exceeds the escape velocity of the subcluster. Thus both are leaving the halo and the subcluster effectively loses particles. The fraction of evaporated DM particles can be expressed as

$$\frac{\Delta N}{N} = 1 - \exp\left(-\frac{\Sigma \sigma_{\mathrm{SI}} f}{m_{\mathrm{DM}}}\right), \tag{1}$$

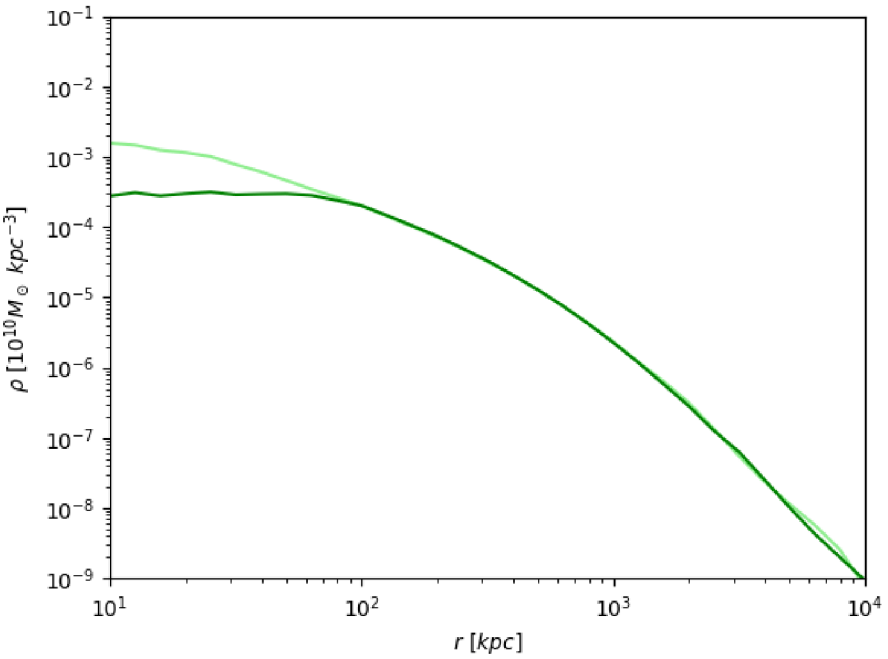


Figure 7: Density profile after $t = 9$ Gyr of the DM halo (Hernquist profile with $M = 10^{15}$ $M_\odot$ and $a = 1$ Mpc).

where Σ is the integrated background density, $\sigma_{\rm SI}/m_{\rm DM}$ the self-interaction cross-section over DM mass and $f = (1 - v_{\rm esc}^2/v_0^2)/(1 + v_{\rm esc}^2/v_0^2)$ the fraction of expulsive collisions (expression valid for isotropic contact interactions) with $v_{\rm esc}$ being the escape velocity of the subcluster. Here we observe that there are in principle two limits in which $\Delta N/N$ gets large. The first is $f \approx 1$ and $\Sigma\sigma_{\rm SI}/m_{\rm DM} \approx 1$. Which means rare self-interactions with a large fraction of expulsive collisions (e.g. Refs. [73, 74]). The second limit with $f \ll 1$ and $\Sigma\sigma_{\rm SI}/m_{\rm DM} \gg 1$ describes frequent self-interactions with a small fraction of expulsive collisions. The momentum transfer has to be small in order to keep the evaporation rate sufficiently low. As a result the differential cross-section must be strongly peaked in the forward direction. For simulations in this limit we cannot consider single scattering processes. The particles scatter multiple times during a single simulation timestep.

The idea of the project was to develop an effective description for simulations of isolated DM haloes in the limit of frequent self-interactions. The deceleration due to these frequent scattering events can be described with an effective description such as a drag force. This effect is particularly important for mergers of galaxy clusters. In order to include the energy transport due to self-scattering we developed a hybrid description. Using a hydrodynamical description we treat the DM particles as collisionless and implement the energy transport by solving a heat diffusion equation. We have implemented such a hybrid description for the energy transfer in the publicly available N-body code GADGET-2 [75]. As an application of this model, we studied the evolution of a cuspy DM halo described by a Hernquist profile under the influence of frequent DM self-interactions. Details will be published in a forthcoming paper.

An example for the effect of self-interactions in the frequent collision limits in an isolated

DM halo is shown in Fig. 7. Efficient heat conduction leads to a reduction of the central density of a DM halo.

The figure shows the formation of a core and using this formalism inside a cosmological simulation will yield to direct constraints on the self-interaction cross-section from observed cluster profiles.

5 Conclusion and outlook

The DM searches are ongoing, but start to saturate in sensitivity: direct searches approach the solar neutrino background scattering rate and indirect searches are subject to systematic uncertainties. Collider experiments may still lead to the discovery of new particles, but ultimately both direct and indirect search experiments are only able to identify DM particles.

Meanwhile, there is a vigorous debate as to whether the current ΛCDM model fits the observations of astrophysical structure, especially on the small scales. Hence, despite the frustration that the DM particle keeps eluding our detectors, these are interesting times since there is a renaissance of a plethora of DM models. Some of those have been studied in this project and this has led to sustained collaborations across disciplines and institutes.

In the future, we will engage in axion detection experiments, continue our efforts in indirect detection through gamma-ray observations and keep studying DM properties through cosmological simulations.

Acknowledgments

DH thanks his former PhD students Milton Fernandes, Alexander Gewering-Peine, Moritz Habermehl, Björn Opitz, Manuel Meyer, Nelly Nguyen, Hannes Zechlin, and former students Friederike Albrecht, Katharina Borm, Stefanie Januschek, Jianqiang Lai, Cameo Lance, Nils Plambeck, Faruk Sellami, and Henrik Edler for their contributions to the SFB project. Many thanks to T. Bringmann, J. List, and P. Sala for discussions on parts of the project, and finally G. Heinzelmann for setting the stage in the initial funding period. MB and JK thank F. Kahlhoefer and K. Schmidt-Hoberg for valuable insights as well as Dr. Klaus Dolag for invaluable help with the GADGET code. CS thanks his former postdoc M.L. Benabderrahmane for his contribution to the SFB project.

References

[1] CMS Collaboration, S. Chatrchyan et al., *The CMS Experiment at the CERN LHC*, *JINST* **3** (2008) S08004.

[2] ATLAS Collaboration, G. Aad et al., *The ATLAS Experiment at the CERN Large Hadron Collider*, *JINST* **3** (2008) S08003.

[3] L. Evans and P. Bryant, *LHC Machine*, *JINST* **3** (2008) S08001.

[4] XENON Collaboration, E. Aprile et al., *The XENON1T Dark Matter Experiment*, *Eur. Phys. J.* **C77** (2017) 881, [1708.07051].

[5] LUX Collaboration, D. S. Akerib et al., *Results from a search for dark matter in the complete LUX exposure*, *Phys. Rev. Lett.* **118** (2017) 021303, [1608.07648].

[6] PandaX-II Collaborations, X. Cui et al., *Dark Matter Results From 54-Ton-Day Exposure of PandaX-II Experiment*, *Phys. Rev. Lett.* **119** (2017) 181302, [1708.06917].

[7] P. Vincent, *H.E.S.S. Phase II*, *International Cosmic Ray Conference* **5** (2005) 163.

[8] FERMI-LAT Collaborations, W. B. Atwood et al., *The Large Area Telescope on the Fermi Gamma-ray Space Telescope Mission*, *Astrophys. J.* **697** (2009) 1071–1102, [0902.1089].

[9] S. Dodelson and L. M. Widrow, *Sterile-neutrinos as dark matter*, *Phys. Rev. Lett.* **72** (1994) 17–20, [hep-ph/9303287].

[10] K. Enqvist, K. Kainulainen and J. Maalampi, *Resonant neutrino transitions and nucleosynthesis*, *Phys. Lett.* **B249** (1990) 531–534.

[11] E. Bulbul, M. Markevitch, A. Foster, R. K. Smith, M. Loewenstein and S. W. Randall, *Detection of An Unidentified Emission Line in the Stacked X-ray spectrum of Galaxy Clusters*, *Astrophys. J.* **789** (2014) 13, [1402.2301].

[12] C. Shah, S. Dobrodey, S. Bernitt, R. Steinbrügge, J. R. C. López-Urrutia, L. Gu et al., *Laboratory measurements compellingly support charge-exchange mechanism for the 'dark matter' ∼3.5 keV X-ray line*, *Astrophys. J.* **833** (2016) 52, [1608.04751].

[13] A. Gewering-Peine, D. Horns and J. H. M. M. Schmitt, *A sensitive search for unknown spectral emission lines in the diffuse X-ray background with XMM-Newton*, *JCAP* **1706** (2017) 036, [1611.01733].

[14] L. Struder et al., *The European Photon Imaging Camera on XMM-Newton: The pn-CCD camera*, *Astron. Astrophys.* **365** (2001) L18–26.

[15] J. Conrad and O. Reimer, *Indirect dark matter searches in gamma and cosmic rays*, *Nature Phys.* **13** (2017) 224–231, [1705.11165].

[16] G. Steigman, B. Dasgupta and J. F. Beacom, *Precise Relic WIMP Abundance and its Impact on Searches for Dark Matter Annihilation*, *Phys. Rev.* **D86** (2012) 023506, [1204.3622].

[17] R. Bartels, S. Krishnamurthy and C. Weniger, *Strong support for the millisecond pulsar origin of the Galactic center GeV excess*, *Phys. Rev. Lett.* **116** (2016) 051102, [1506.05104].

[18] S. K. Lee, M. Lisanti, B. R. Safdi, T. R. Slatyer and W. Xue, *Evidence for Unresolved γ-Ray Point Sources in the Inner Galaxy*, *Phys. Rev. Lett.* **116** (2016) 051103, [1506.05124].

[19] O. Macias, C. Gordon, R. M. Crocker, B. Coleman, D. Paterson, S. Horiuchi et al., *Galactic bulge preferred over dark matter for the Galactic centre gamma-ray excess*, *Nat. Astron.* **2** (2018) 387–392, [1611.06644].

[20] D. Horns, *TeV gamma-radiation from dark matter annihilation in the Galactic center*, *Phys. Lett.* **B607** (2005) 225–232, [astro-ph/0408192]. [Erratum: *Phys. Lett.* **B611** (2005) 297].

[21] H.E.S.S. Collaborations, F. Aharonian, *Simultaneous H.E.S.S. and Chandra observations of Sagittarius A* during an X-ray flare*, *Astron. Astrophys.* **492** (2008) L25, [0812.3762].

[22] A. Abramowski, S. Gillessen, D. Horns and H. S. Zechlin, *Locating the VHE source in the Galactic Centre with milli-arcsecond accuracy*, *Mon. Not. Roy. Astron. Soc.* **402** (2010) 1342A, [1002.2364].

[23] FERMI-LAT Collaborations, M. Ackermann et al., *Searching for Dark Matter Annihilation from Milky Way Dwarf Spheroidal Galaxies with Six Years of Fermi Large Area Telescope Data*, *Phys. Rev. Lett.* **115** (2015) 231301, [1503.02641].

[24] FERMI-LAT Collaborations, M. Di Mauro, *Isotropic diffuse and extragalactic γ-ray background: emission from extragalactic sources vs dark matter annihilating particles*, *J. Phys. Conf. Ser.* **718** (2016) 042019, [1601.04322].

[25] H.E.S.S. Collaborations, H. Abdallah et al., *Search for dark matter annihilations towards the inner Galactic halo from 10 years of observations with H.E.S.S*, *Phys. Rev. Lett.* **117** (2016) 111301, [1607.08142].

[26] FERMI-LAT, MAGIC Collaborations, M. L. Ahnen et al., *Limits to dark matter annihilation cross-section from a combined analysis of MAGIC and Fermi-LAT observations of dwarf satellite galaxies*, *JCAP* **1602** (2016) 039, [1601.06590].

[27] VERITAS Collaborations, S. Archambault et al., *Dark Matter Constraints from a Joint Analysis of Dwarf Spheroidal Galaxy Observations with VERITAS*, *Phys. Rev.* **D95** (2017) 082001, [1703.04937].

[28] B. H. B. Opitz, *Searches for dark matter self-annihilation signals from dwarf spheroidal galaxies and the Fornax galaxy cluster with imaging air Cherenkov telescopes*, Ph.D. thesis, Universität Hamburg, 2014. http://www-library.desy.de/cgi-bin/showprep.pl?thesis14-028.

[29] C. Balázs, J. Conrad, B. Farmer, T. Jacques, T. Li, M. Meyer et al., *Sensitivity of the Cherenkov Telescope Array to the detection of a dark matter signal in comparison to direct detection and collider experiments*, *Phys. Rev.* **D96** (2017) 083002, [1706.01505].

[30] HAWC Collaboration, A. U. Abeysekara et al., *A Search for Dark Matter in the Galactic Halo with HAWC*, *JCAP* **1802** (2018) 049, [1710.10288].

[31] H. Edler, "Indirect searches for gamma rays from self annihilation of heavy dark matter particles with the taiga experiment." Bachelor's thesis, Universität Hamburg 2018. updated in internal note (TAIGA).

[32] B.-Q. Lu and H.-S. Zong, *Limits on dark matter from AMS-02 antiproton and positron fraction data*, *Phys. Rev.* **D93** (2016) 103517, [1510.04032].

[33] PLANCK Collaboration, P. A. R. Ade et al., *Planck 2015 results. XIII. Cosmological parameters*, *Astron. Astrophys.* **594** (2016) A13, [1502.01589].

[34] CTA CONSORTIUM Collaborations, M. Doro et al., *Dark Matter and Fundamental Physics with the Cherenkov Telescope Array*, *Astropart. Phys.* **43** (2013) 189–214, [1208.5356].

[35] H.E.S.S. Collaborations, A. Abramowski et al., *Search for dark matter annihilation signatures in H.E.S.S. observations of Dwarf Spheroidal Galaxies*, *Phys. Rev.* **D90** (2014) 112012, [1410.2589].

[36] H.E.S.S. Collaborations, A. Abramowski et al., *Search for Dark Matter Annihilation Signals from the Fornax Galaxy Cluster with H.E.S.S*, *Astrophys. J.* **750** (2012) 123, [1202.5494]. [Erratum: *Astrophys. J.* **783** (2014) 63].

[37] S. Colafrancesco, M. Regis, P. Marchegiani, G. Beck, R. Beck, H. Zechlin et al., *Probing the nature of Dark Matter with the SKA*, *PoS* **AASKA14** (2015) 100, [1502.03738].

[38] H. S. Zechlin, M. V. Fernandes, D. Elsaesser and D. Horns, *Dark matter subhaloes as gamma-ray sources and candidates in the first Fermi-LAT catalogue*, *Astron. Astrophys.* **538** (2012) A93, [1111.3514].

[39] H.-S. Zechlin and D. Horns, *Unidentified sources in the Fermi-LAT second source catalog: the case for DM subhalos*, *JCAP* **1211** (2012) 050, [1210.3852]. [Erratum: *JCAP* **1502** (2015) E01].

[40] F. Calore, V. De Romeri, M. Di Mauro, F. Donato and F. Marinacci, *Realistic estimation for the detectability of dark matter sub-halos with Fermi-LAT*, *Phys. Rev.* **D96** (2017) 063009, [1611.03503].

[41] N. Nguyen, D. Horns and T. Bringmann, *AstroFit: An Interface Program for Exploring Complementarity in Dark Matter Research*, in *Proceedings, 13th ICATPP Conference on Astroparticle, Particle, Space Physics and Detectors for Physics Applications (ICATPP 2011): Como, Italy, October 3-7, 2011*, pp. 1025–1030, 2012, 1202.1385, DOI.

[42] P. Bechtle, K. Desch and P. Wienemann, *Fittino, a program for determining MSSM parameters from collider observables using an iterative method*, *Comput. Phys. Commun.* **174** (2006) 47–70, [hep-ph/0412012].

[43] P. Bechtle et al., *Constrained Supersymmetry after two years of LHC data: a global view with Fittino*, *JHEP* **06** (2012) 098, [1204.4199].

[44] GAMBIT Collaboration, P. Athron et al., *GAMBIT: The Global and Modular Beyond-the-Standard-Model Inference Tool*, *Eur. Phys. J.* **C77** (2017) 784, [1705.07908]. [Addendum: *Eur. Phys. J.* **C78** (2018) 98].

[45] C. Zhang, *Dark matter searches in effective field theory*, Ph.D. thesis, Universität Hamburg, 2018.

[46] T. Barklow, J. Brau, K. Fujii, J. Gao, J. List, N. Walker et al., *Ilc operating scenarios*, *arXiv preprint arXiv:1506.07830* (2015) .

[47] S. A. Malik et al., *Interplay and Characterization of Dark Matter Searches at Colliders and in Direct Detection Experiments*, *Phys. Dark Univ.* **9-10** (2015) 51–58, [1409.4075].

[48] VIRGO, LIGO SCIENTIFIC Collaborations, B. P. Abbott et al., *Observation of Gravitational Waves from a Binary Black Hole Merger*, *Phys. Rev. Lett.* **116** (2016) 061102, [1602.03837].

[49] PANDAX-II Collaborations, X. Cui et al., *Dark Matter Results From 54-Ton-Day Exposure of PandaX-II Experiment*, *Phys. Rev. Lett.* **119** (2017) 181302, [1708.06917].

[50] PICO Collaboration, C. Amole et al., *Dark Matter Search Results from the PICO-60 C_3F_8 Bubble Chamber*, *Phys. Rev. Lett.* **118** (2017) 251301, [1702.07666].

[51] J. Liu, X. Chen and X. Ji, *Current status of direct dark matter detection experiments*, *Nature Phys.* **13** (2017) 212–216, [1709.00688].

[52] P. A. M. Dirac, *Quantized Singularities in the Electromagnetic Field*, *Proc. Roy. Soc. Lond.* **A133** (1931) 60–72.

[53] H. Georgi and S. L. Glashow, *Unity of All Elementary Particle Forces*, *Phys. Rev. Lett.* **32** (1974) 438–441.

[54] G. 't Hooft, *Magnetic Monopoles in Unified Gauge Theories*, *Nucl. Phys.* **B79** (1974) 276–284.

[55] A. M. Polyakov, *Particle Spectrum in the Quantum Field Theory*, *JETP Lett.* **20** (1974) 194–195.

[56] S. D. Wick, T. W. Kephart, T. J. Weiler and P. L. Biermann, *Signatures for a cosmic flux of magnetic monopoles*, *Astropart. Phys.* **18** (2003) 663–687, [astro-ph/0001233].

[57] M. S. Turner, E. N. Parker and T. J. Bogdan, *Magnetic Monopoles and the Survival of Galactic Magnetic Fields*, *Phys. Rev.* **D26** (1982) 1296.

[58] J. Preskill, *Magnetic Monopoles*, *Ann. Rev. Nucl. Part. Sci.* **34** (1984) 461–530.

[59] MACRO Collaboration, M. Ambrosio et al., *Final results of magnetic monopole searches with the MACRO experiment*, *Eur. Phys. J.* **C25** (2002) 511–522, [hep-ex/0207020].

[60] MACRO Collaboration, M. Ambrosio et al., *Search for nucleon decays induced by GUT magnetic monopoles with the MACRO experiment*, *Eur. Phys. J.* **C26** (2002) 163–172, [hep-ex/0207024].

[61] IceCube Collaborations, M. G. Aartsen et al., *The IceCube Neutrino Observatory Part IV: Searches for Dark Matter and Exotic Particles*, in *Proceedings, 33rd International Cosmic Ray Conference (ICRC2013): Rio de Janeiro, Brazil, July 2-9, 2013*, 2013, 1309.7007.

[62] IceCube Collaborations, J. Ahrens et al., *Sensitivity of the IceCube detector to astrophysical sources of high energy muon neutrinos*, *Astropart. Phys.* **20** (2004) 507–532, [astro-ph/0305196].

[63] V. A. Rubakov, *Adler-Bell-Jackiw Anomaly and Fermion Number Breaking in the Presence of a Magnetic Monopole*, *Nucl. Phys.* **B203** (1982) 311–348.

[64] C. G. Callan, Jr., *Monopole Catalysis of Baryon Decay*, *Nucl. Phys.* **B212** (1983) 391–400.

[65] IceCube Collaborations, M. G. Aartsen et al., *Search for non-relativistic Magnetic Monopoles with IceCube*, *Eur. Phys. J.* **C74** (2014) 2938, [1402.3460].

[66] A. Kusenko, *Solitons in the supersymmetric extensions of the standard model*, *Phys. Lett.* **B405** (1997) 108, [hep-ph/9704273].

[67] A. De Rujula and S. L. Glashow, *Nuclearites: A Novel Form of Cosmic Radiation*, *Nature* **312** (1984) 734–737.

[68] IceCube Collaborations, R. Abbasi et al., *Search for Relativistic Magnetic Monopoles with IceCube*, *Phys. Rev.* **D87** (2013) 022001, [1208.4861].

[69] IceCube Collaborations, M. G. Aartsen et al., *Searches for Relativistic Magnetic Monopoles in IceCube*, *Eur. Phys. J.* **C76** (2016) 133, [1511.01350].

[70] D. N. Spergel and P. J. Steinhardt, *Observational Evidence for Self-Interacting Cold Dark Matter*, *Physical Review Letters* **84** (Apr., 2000) 3760–3763, [astro-ph/9909386].

[71] S. W. Randall, M. Markevitch, D. Clowe, A. H. Gonzalez and M. Bradač, *Constraints on the Self-Interaction Cross Section of Dark Matter from Numerical Simulations of the Merging Galaxy Cluster 1E 0657-56*, *ApJ* **679** (June, 2008) 1173–1180, [0704.0261].

[72] F. Kahlhoefer, K. Schmidt-Hoberg, M. T. Frandsen and S. Sarkar, *Colliding clusters and dark matter self-interactions*, *MNRAS* **437** (Jan., 2014) 2865–2881, [1308.3419].

[73] A. Robertson, R. Massey and V. Eke, *Cosmic particle colliders: simulations of self-interacting dark matter with anisotropic scattering*, *MNRAS* **467** (June, 2017) 4719–4730, [1612.03906].

[74] S. Y. Kim, A. H. G. Peter and D. Wittman, *In the wake of dark giants: new signatures of dark matter self-interactions in equal-mass mergers of galaxy clusters*, *MNRAS* **469** (Aug., 2017) 1414–1444, [1608.08630].

[75] V. Springel, *The cosmological simulation code GADGET-2*, *MNRAS* **364** (Dec., 2005) 1105–1134, [astro-ph/0505010].

Leptogenesis and Dark Matter

Wilfried Buchmüller
DESY, Hamburg, Germany

DOI: http://dx.doi.org/10.3204/PUBDB-2018-00782/C3

We briefly review the work carried out in project C3 of the SFB 676. The main topics are *Quantum Leptogenesis*, the treatment of thermal leptogenesis with nonequilibrium field theory, and *gravitino dark matter*. In a *minimal supersymmetric model* with cosmological $B-L$ breaking, a consistent picture is obtained of inflation, preheating and the transition to the hot early universe by entropy production, including the generation of matter and dark matter.

1 Introduction

During the past thirty years leptogenesis [1] has become one of the leading candidates for explaining the origin of the matter-antimatter asymmetry of the universe. For more than a decade electroweak baryogenesis was considered superior to leptogenesis, based on the hope to understand the baryon asymmetry within the Standard Model. But with increasing lower bounds on the Higgs boson mass and the discovery of neutrino masses in atmospheric neutrino oscillations consistent with leptogenesis, the connection between the baryon asymmetry and neutrino masses became the favoured mechanism. In fact, based on leptogenesis, the smallness of neutrino masses had been anticipated [2].

At the beginning of the project leptogenesis had already been established as a quantitatively successful theory of the baryon asymmetry, based on numerical and semi-analytical solutions of Boltzmann equations. However, this approach has severe conceptual deficiencies. The Boltzmann equations are classical equations for number densities. On the other hand, the employed kernels are zero-temperature S-matrix elements that involve quantum interferences in a crucial manner. Hence, one might worry that in the thermal plasma any generated baryon asymmetry is washed out. During the first phase of the project these concerns led to a detailed study of leptogenesis based on nonequilibrium field theory at finite temperature (Section 2). A second major topic has been the connection between leptogenesis and dark matter in supersymmetric theories (Section 3). For standard WIMP dark matter the high reheating temperature required for leptogenesis leads to a *gravitino problem*, the production of too much entropy from decays of unstable gravitinos after primordial nucleosynthesis (BBN). It was shown that this problem can be avoided for gravitino dark matter, if the gravitino is the lightest superparticle (LSP).

In supersymmetric theories there is a natural connection between leptogenesis and hybrid inflation. In the second phase of the project this led to a series of papers where this connection was studied in detail. It is intriguing that for typical leptogenesis parameters one obtains a reheating temperature after inflation, which is consistent with gravitino dark matter. Moreover, the scale of supersymmetry breaking is important for the gravitino mass as well as for the

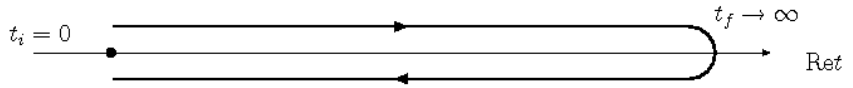


Figure 1: Path in the complex time plane for non-equilibrium Green's functions. Reprinted from Ref. [5], with permission from Elsevier.

scalar spectral index which is obtained from the cosmic microwave background (CMB). Hybrid inflation, together with reheating and entropy production leads to a characteristic spectrum of primordial gravitational waves (Section 4). In the outlook we describe the prospects for testing leptogenesis with further observations in cosmology and at the Large Hadron Collider (LHC). It is impossible to give adequate references to all the work that motivated and stimulated the research carried out within the project C3. Reviews of basics and recent developments of leptogenesis are, for example [3, 4] where also extensive references can be found. Beyond that we refer the reader to the references given in the papers described below.

2 Quantum leptogenesis

Leptogenesis is an out-of-equilibrium process during the very early high-temperature phase of the universe. In its simplest version it is dominated by the CP violating interactions of the lightest of the heavy Majorana neutrinos, the seesaw partners of the ordinary neutrinos, with lepton doublets and the Higgs doublet. These standard model fields have gauge interactions, and therefore they are in thermal equilibrium. On the contrary, the weakly coupled heavy neutrino is out of thermal equilibrium. Its decay width is small compared to the interaction rates of particles in thermal equilibrium. This departure from thermal equilibrium, together with a CP violating quantum interference, generates a lepton asymmetry and, via sphaleron processes, also a baryon asymmetry.

A rigorous description of this subtle effect requires nonequilibrium field theory for which one can use the Schwinger–Keldysh formalism. Here the basic objects are Green's functions on a path in the complex time plane, see Fig. 1. To study the approach to thermal equilibrium, we first considered a scalar field theory [5, 6]. The Schwinger–Dyson equation for a path ordered Green's function on the contour C reads

$$(\Box_1 + m^2)\Delta_C(x_1, x_2) + \int_C d^4x' \Pi_C(x_1, x')\Delta_C(x', x_2) = -i\delta_C(x_1 - x_2)\,,$$

where the self-energy Π_C describes the interaction with the thermal bath. It is convenient to decompose the path ordered Green's function into the spectral function Δ^- and the statistical propagator Δ^+,

$$\Delta^-(x_1, x_2) = i\langle[\Phi(x_1), \Phi(x_2)]\rangle\ , \quad \Delta^+(x_1, x_2) = \frac{1}{2}\langle\{\Phi(x_1), \Phi(x_2)\}\rangle\,.$$

Δ^- carries information about the spectrum of the system and satisfies a homogeneous equation, whereas Δ^+ satisfies an inhomogeneous equation, which encodes the interaction with the

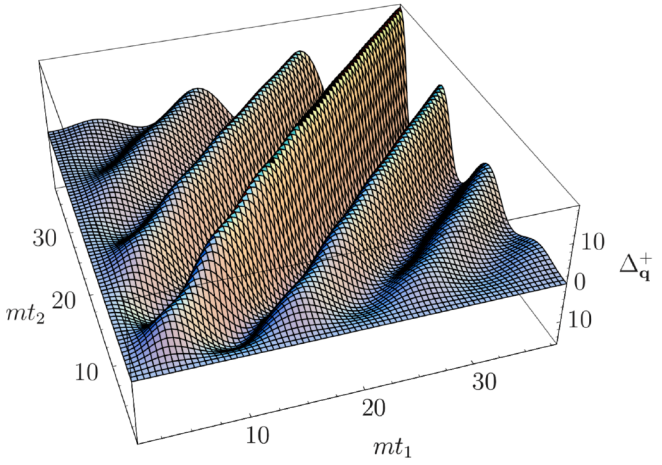


Figure 2: Statistical propagator $\Delta^+_{\mathbf{q}}(t_1, t_2)$ for $\mathbf{q} = 0$. Reprinted from Ref. [5], with permission from Elsevier.

thermal bath. For a homogeneous system the Fourier transform $\Delta^+_{\mathbf{q}}(t_1, t_2)$ depends on two time coordinates. The statistical propagator also depends on initial conditions. The general solution was obtained in [5]. Starting from vanishing mean values of Φ and $\dot{\Phi}$ one obtains the result plotted in Fig. 2. One sees damped oscillations in $t_1 - t_2$ with a frequency given by the mass m of Φ and an approach to equilibrium in $t_1 + t_2$, which is controlled by the width Γ of Φ. For $t_1 + t_2 > 1/\Gamma$ the memory of the initial conditions is lost. For a dilute, weakly coupled gas the Boltzmann equation can be recovered as first term in a derivative expansion. Neglecting memory effects one finds

$$\Delta^+_{\mathbf{q}}(t_1, t_2) \propto f(t, |\mathbf{q}|)\,, \quad t = \frac{t_1 + t_2}{2}\,,$$

where $f(t, |\mathbf{q}|)$ is the Boltzmann distribution function for quanta of the field Φ.

Armed with the knowledge of the Green's function describing the departure from thermal equilibrium, one can attack the treatment of leptogenesis in nonequilibrium field theory [7–9]. The starting point is the Lagrangian

$$\begin{aligned}\mathcal{L} =& \frac{1}{2}\overline{N} i\gamma^\mu \partial_\mu N + \overline{l_{Li}}\widetilde{\phi}\lambda^*_{i1} N + N^T \lambda_{i1} C l_{Li}\phi - \frac{1}{2} M N^T C N \\ &+ \frac{1}{2}\eta_{ij} l^T_{Li}\phi C l_{Lj}\phi + \frac{1}{2}\eta^*_{ij}\overline{l_{Li}}\widetilde{\phi} C \overline{l_{Lj}}^T \widetilde{\phi}\,,\end{aligned}$$

which describes the interaction of a Majorana neutrino N of mass M with lepton doublets l_{Li} and the Higgs doublet ϕ; C is the charge conjugation matrix. Integrating out the two heavier Majorana neutrinos with masses M_2 and M_3 yields the effective dimension-5 coupling

$$\eta_{ij} = \sum_{k>1} \lambda_{ik} \frac{1}{M_k} \lambda^T_{kj}\,.$$

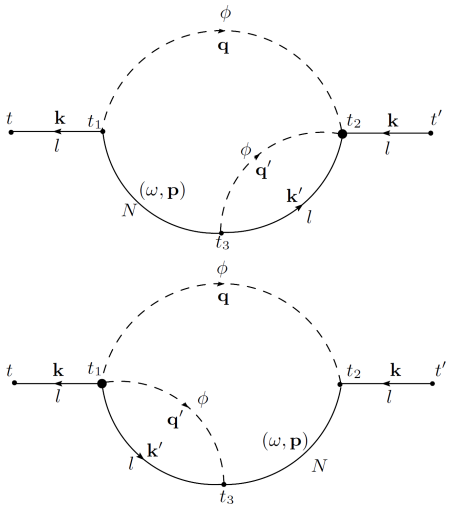


Figure 3: Two-loop contributions to the lepton self-energies $\Pi^{\pm}_{\mathrm{k}}$, which lead to non-zero lepton number densities. Reprinted figures with permission from Ref. [7]. Copyright (2010) by the American Physical Society.

Using this effective coupling has the advantage that vertex- and self-energy contributions to the CP asymmetry in the heavy neutrino decay are obtained from a single graph. For lepton doublets and Higgs doublet equilibrium Green's functions can be used whereas the heavy neutrino N is described by a non-equilibrium Green's function similar to the one described above.

The generated CP asymmetry is obtained from the two-loop graphs shown in Fig. 3. The calculated lepton asymmetry $L_{\mathbf{k}ii}$ is the quantum analog of the difference of Boltzmann distribution functions $f_{Li}(t,k) = f_{li}(t,k) - f_{\bar{l}i}(t,k)$. Including also thermal damping widths γ for lepton doublets and Higgs doublet, the full expression for the quantum asymmetry $L_{\mathbf{k}ii}$ significantly simplifies. In the zero-with approximation for the heavy neutrino, $\gamma \gg \Gamma$, one finds

$$L_{\mathbf{k}ii}(t,t) = -\epsilon_{ii}\; 16\pi \int_{\mathbf{q},\mathbf{q}'} \frac{k\cdot k'}{kk'\omega_{\mathbf{p}}} \frac{\gamma\gamma'}{((\omega_{\mathbf{p}}-k-q)^2+\gamma^2)((\omega_{\mathbf{p}}-k'-q')^2+\gamma'^2)} \times f_{l\phi}(k,q) f_{l\phi}(k',q') f^{eq}_N(\omega_{\mathbf{p}}) \frac{1}{\Gamma}\left(1-e^{-\Gamma t}\right) \;,$$

where ϵ_{ii} is the CP asymmetry in the heavy Majorana neutrino decay for flavour i, and $f_{l\phi}(k,q) = 1 - f_l(k) + f_\phi(q)$. Compared to the result obtained from Boltzmann equations, $L_{\mathbf{k}ii}(t,t)$ contains corrections due to off-shell effects, thermal damping effects and quantum statistical factors. Amazingly, these corrections partially compensate each other, so that the conventional Boltzmann equations provide a rather accurate prediction of the lepton asymmetry. It is straightforward to incorporate washout effects into the presented formalism. A complete *theory of leptogenesis* would also require to include the more subtle effect of spectator processes. The connection between the Schwinger–Keldysh formalism and kinetic equations for quasiparticles was studied in [10].

Leptogenesis crucially depends on the CP violating phases in the couplings of the heavy Majorana neutrinos to lepton doublets and the Higgs doublet. It is remarkable that leptoge-

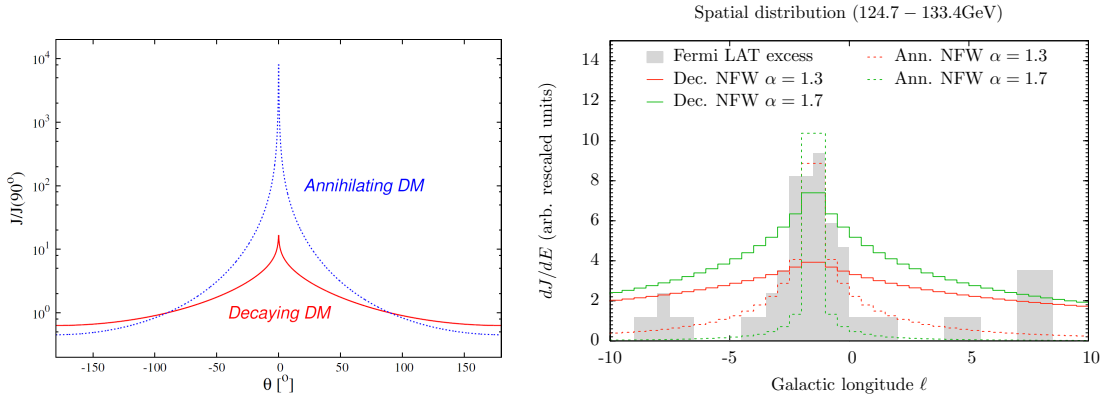


Figure 4: Decaying vs. annihilating dark matter. Left: Angular profile of the gamma-ray signal as function of the angle θ to the centre of the galaxy for decaying DM, solid (red) line, compared to the case of self-annihilating DM, dashed (blue) line. Figure reprinted from Ref. [18]. © 2007 IOP Publishing Ltd and SISSA. Right: Angular profile of the gamma-ray signal from a section of the galactic plane for decaying DM (full lines) and self-annihilating DM (dashed lines), compared with a tentative Fermi-LAT excess. Figure reprinted from Ref. [19]. © 2012 IOP Publishing Ltd and Sissa Medialab srl.

nesis is consistent with our present knowledge of neutrino masses [11]. On the other hand, the predictivity of this mechanism is restricted by the fact that extensions of the SM typically contain a number of CP violating phases. As a consequence, the CP phases relevant for leptogenesis are generically unrelated to other CP phases at low energies [12, 13]. Constraints on the CP phases can be obtained from flavour symmetries, for instance a flavour structure of Frogatt–Nielsen type [14]. In principle, the Majorana neutrino masses can vary significantly. Note that an almost decoupled Majorana neutrino with a mass $\mathcal{O}(100\ \mathrm{GeV})$ is a potential dark matter candidate [15]. It is also interesting that for Majorana neutrinos quantum corrections imply a lower bound on the lightest neutrino mass [16]. So far we have concentrated on the thermal production of heavy Majorana neutrinos. In general, however, heavy neutrinos can also be produced nonthermally, for instance in inflaton decays [17].

3 Leptogenesis and gravitino dark matter

Typical values for the smallest Majorana neutrino mass M_1 and the leptogenesis temperature T_L are $M_1 \sim T_L \sim 10^{10}$ GeV. In supersymmetric theories such high reheating temperatures cause a *gravitino problem* for heavy unstable gravitinos, which leads to an inconsistency with standard WIMP dark matter [20]. However, if the gravitino is the lightest superparticle (LSP), this problem can become a virtue since for superparticle masses of the electroweak scale, thermal production of gravitinos can explain the observed amount of dark matter [21,22]. The dominant contribution from QCD processes is given by

$$\Omega_{3/2}h^2 = C\left(\frac{T_L}{10^{10}\,\mathrm{GeV}}\right)\left(\frac{100\,\mathrm{GeV}}{m_{3/2}}\right)\left(\frac{m_{\tilde{g}}}{1\,\mathrm{TeV}}\right)^2, \quad C \sim 0.5\,,$$

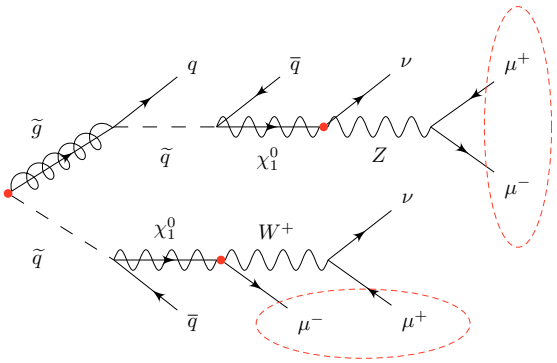


Figure 5: Typical R-parity violating decay chain at the LHC. The primary vertex and the secondary vertices are highlighted. Figure taken from Ref. [31].

where $m_{\tilde{g}}$ is the gluino mass. Clearly, $\Omega_{3/2}h^2 \sim 0.1$ is a natural value for typical superparticle masses in supergravity models.

With the gravitino being the LSP, one has to worry about late decays of the next-to-lightest superparticle (NLSP). A simple and elegant solution is given by a small breaking of R-parity, which can be easily consistent with BBN and leptogenesis [23]. The gravitino decay width is given by

$$\Gamma(\psi_{3/2} \to \gamma\nu) = \frac{1}{32\pi}|U_{\tilde{\gamma}\nu}|^2 \frac{m_{3/2}^3}{M_{\rm P}}\,,$$

where $U_{\tilde{\gamma}\nu}$ is the gravitino-photon-neutrino matrix element. For sufficiently small couplings, needed to avoid the washout of the baryon asymmetry, one can obtain a lifetime much longer then the age of the universe ($M_{\rm P} = 2.4 \times 10^{18}$GeV),

$$\tau_{3/2}^{2-\rm body} \simeq 3.8 \times 10^{27}{\rm s} \left(\frac{|U_{\tilde{\gamma}\nu}|}{10^{-8}}\right)^{-2} \left(\frac{m_{3/2}}{10{\rm GeV}}\right)^{-3}\,.$$

Decaying gravitino dark matter has a number of interesting astrophysical signatures. First of all, it leads to monochromatic gamma-ray lines, with an angular spectrum much less peaked around the galactic center compared to self-annihilating dark matter [18, 24], see Fig. 4, left panel. Moreover, there are interesting signatures in cosmic rays for antimatter [25–28] and the cosmic neutrino flux [29, 30].

Partly motivated by the attractive possibility of decaying dark matter, an intense search for gamma-ray lines was carried out for the Fermi-LAT data, by observers and also by theorists [32–36]. The subject of decaying gravitino dark matter became very topical when in 2012 a gamma-ray signal was identified in the Fermi-LAT data as a 4σ effect. Unfortunately, the angular spectrum of the signal was inconsistent with decaying dark matter, see Fig. 4, right panel, and from the energy spectrum also annihilating higgsino or wino dark matter could be excluded [19]. With increasing statistics the signal faded away. Also important are internal bremsstrahlung signatures [37] and the spin-dependent sensitivity in direct searches [38]. Note that in the supersymmetric standard model asymmetric dark matter can be produced from spontaneous cogenesis [39].

In addition to gravitino decays, R-parity breaking also implies R-violating NLSP decays. These could be stau decays [40] or neutralino decays. Particularly interesting are neutralino NLSP decays, $\chi_1^0 \to W^\pm \mu^\mp$, shown in Fig. 5. In this case the gravitino decay width and the neutralino decay width are governed by the same parameter ζ [41, 42],

$$\Gamma_{3/2} \propto \zeta^2 \frac{m_{3/2}^3}{M P^2} , \qquad \Gamma_{\chi_1^0} \propto \zeta^2 m_{\chi_1^0} .$$

This leads to a very interesting connection between indirect detection and collider searches for dark matter. The observation of a gamma-ray line would determine the gravitino mass and provide information on the parameter ζ. Correspondingly, at the LHC one could observe events with two $\mu^+\mu^-$ pairs, jets and missing energy [31, 43].

Leptogenesis implies an upper bound on superparticle masses since the thermal production cross section for light gravitinos increases $\propto m_{\tilde{g}}^2$. In models with gravity mediation and universal scalar and gaugino masses, one expects bino masses below 600 GeV, stau masses below 500 GeV, gluino masses below 3 GeV and gravitino masses in the range 10 GeV $< m_{3/2} <$ 500 GeV [44]. By now, much of the parameter space has been excluded by searches at the LHC. On the other hand, R-parity violating decays of long-lived neutralinos could still be discovered at the LHC. Most of them will decay outside the detector but due to the characteristic signature a small sample may be sufficient for a discovery [31, 43].

4 Leptogenesis, inflation and gravitational waves

Successful leptogenesis, independent of initial conditions, favours the mass window 10^{-3} eV $\lesssim m_i \lesssim$ 0.1 eV for the light neutrino masses. For an effective neutrino mass $\widetilde{m}_1 = (m_D^\dagger m_D)_{11}/M_1 \sim 0.01$ eV, with m_D the Dirac neutrino mass matrix, the decay width of the heavy Majorana neutrino N_1 becomes

$$\Gamma_{N_1} = \frac{\widetilde{m}_1}{8\pi} \left(\frac{M_1}{v_{\rm EW}} \right)^2 \sim 10^3 \, \text{GeV} .$$

Here we have used $M_1 \sim 10^{10}$ GeV and $v_{\rm EW} = 174$ GeV for the vacuum expectation value (VEV) of electroweak symmetry breaking. If the hot phase of the early universe is initiated by the decays of particles with decay width Γ, the reheating temperature T_R is given by

$$T_R = \left(\frac{90}{\pi^2 g_*} \right)^{1/4} \sqrt{\Gamma M_{\rm P}} ,$$

where $g_* \sim 200$ is the effective number of relativistic degrees of freedom. If reheating occurs through the decay of N_1 neutrinos, one obtains

$$T_R \sim \sqrt{\Gamma_{N_1}^0 M_{\rm P}} \sim 10^{10} \text{ GeV} ,$$

which is indeed the temperature needed for thermal leptogenesis and gravitino dark matter. This observation raises the question, whether in the thermal bath produced by heavy Majorana neutrino decays both, the matter-antimatter asymmetry and gravitino dark matter, can be simultaneously generated [45].

The following example demonstrates that this is indeed possible [46–48]. Consider the supersymmetric standard model with right-handed neutrinos and spontaneous $B-L$ breaking, described by the superpotential

$$W = \frac{\sqrt{\lambda}}{2}\,\Phi\,(v_{B-L}^2 - 2\,S_1 S_2) + \frac{1}{\sqrt{2}} h_i^n n_i^c n_i^c S_1 + h_{ij}^\nu \mathbf{5}_i^* n_j^c H_u + W_{\rm MSSM}\,.$$

Here S_1 and S_2 are the chiral superfields containing the superfield S that breaks $B-L$ at the scale v_{B-L}, Φ contains an inflaton ϕ, a complex scalar field driving inflation, and n_i^c denote the superfields containing the charge conjugates of the right-handed neutrinos; h and λ are coupling constants, and $W_{\rm MSSM}$ is the superpotential of the minimal supersymmetric standard model with quarks, leptons and Higgs fields. Note that spontaneous $B-L$ breaking requires a gauge singlet Φ, which automatically leads to the familar superpotential of hybrid inflation. The requirement of successful inflation fixes the scale of $B-L$ breaking to a value close to the GUT scale, $v_{B-L} = 5 \times 10^{15}$ GeV. The superfields are arranged in $SU(5)$ multiplets, i.e. $\mathbf{5}_i^* = (d_i^c,\, l_i)$, $i = 1, 2, 3$, and the colour triplet partners of the electroweak Higgs doublets H_u and H_d are projected out. The VEVs $v_u = \langle H_u \rangle$ and $v_d = \langle H_d \rangle$ break the electroweak symmetry. The Yukawa couplings can be conveniently parametrized in terms of Froggatt–Nielsen flavour charges, which also govern the hierarchy of quark and lepton masses and mixings.

The most important parameters for the reheating process are the masses and vacuum decay widths of S and N_1. Inflation ends in tachyonic preheating where the energy density of the inflationary phase is mostly converted into the energy density of a nonrelativistic gas of $B-L$ Higgs bosons S. The initial conditions of the matter dominated phase after inflation are determined by the process of tachyonic preheating. The reheating process is dominated by decays of the $B-L$ Higgs bosons S into heavy neutrinos and their subsequent decays into SM particles and their superpartners (see Fig. 6, upper panel). After inflation the time evolution of the system is described by a network of Boltzmann equations. As a detailed analysis shows, the competition between heavy neutrino decays and the cosmic expansion leads to an intermediate plateau of approximately constant *reheating temperature* $T_{\rm RH}(M_1, \widetilde{m}_1)$ (see Fig. 6, lower panel). Note that the effective reheating temperature T_R takes the dynamics of the reheating process into account. Hence, it depends on the decay rates of S and N_1, and consequently on M_1 and $\widetilde{m}_1$.

Successful leptogenesis implies lower bounds on M_1 and $T_{\rm RH}(M_1, \widetilde{m}_1)$, which can be obtained by solving the relevant set of Boltzmann equations. One also obtains a lower bound on the gravitino mass as function of the effective neutrino mass $\tilde{m}_1$ of about 10 GeV, for a gluino mass of $m_{\tilde{g}} = 1$ TeV, see Fig. 7, left panel (for the current LHC bound $m_{\tilde{g}} > 2$ TeV, the lower bound on the gravitino mass increases to $m_{\tilde{G}} \equiv m_{3/2} > 40$ GeV). The reheating process described above can also be consistent if a higgsino or a wino is the LSP [49]. Thermally produced heavier gravitinos can then decay before BBN yielding neutralino dark matter. This leads to upper bounds on higgsino and wino masses, and to a lower bound on the gravitino mass. These bounds are shown in Fig. 7, right panel.

The superpotential for $B-L$ breaking also describes F-term hybrid inflation. In order to obtain the measured scalar spectral index it is crucial to add to the supersymmetric part of the scalar potential a supersymmetry breaking term proportional to the gravitino mass [50] ,

$$V(\phi) = V_{\rm SUSY}(\phi) - \lambda v_{B-L}^2 m_{3/2}(\phi + \phi^*)\,.$$

As a consequence, hybrid inflation becomes a two-field model of inflation, which allows for inflationary trajectories with the correct scalar spectral index. During inflation the $U(1)_{B-L}$

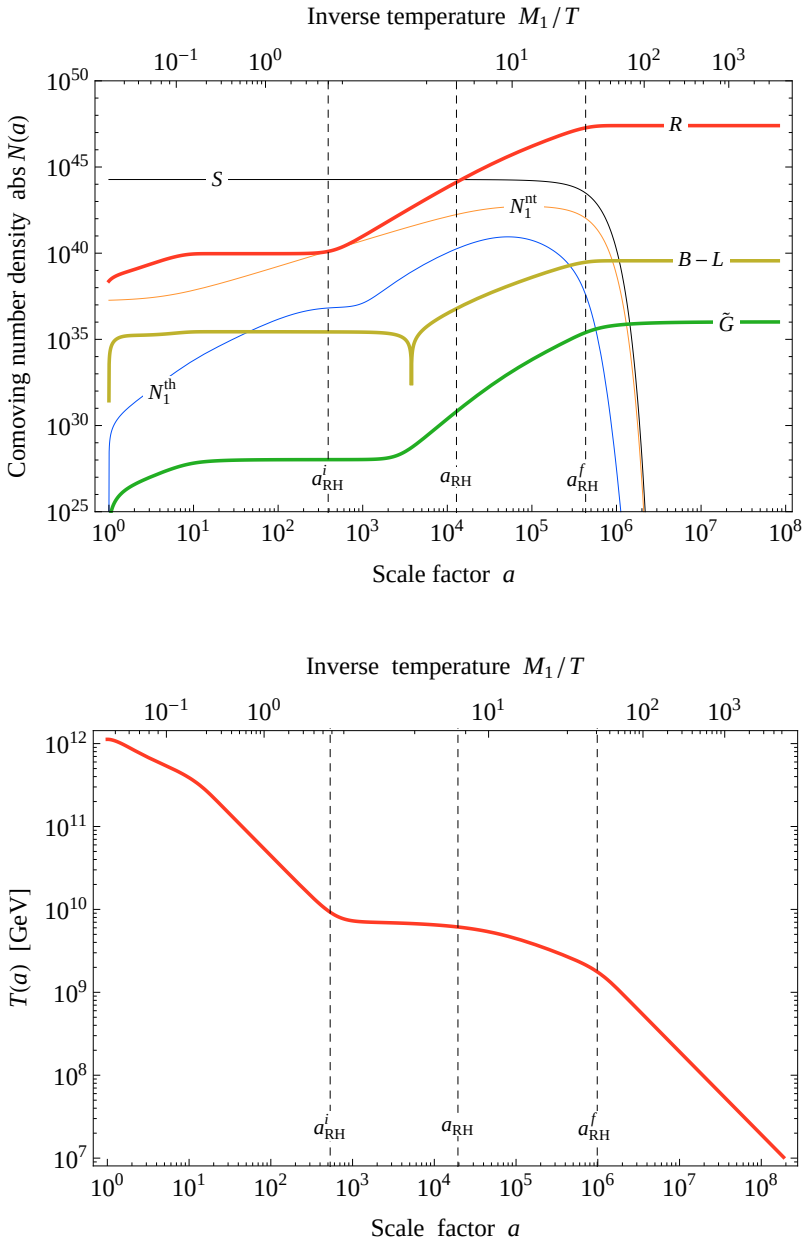


Figure 6: Upper panel: Comoving number densities of Higgs bosons (S), thermally and non-thermally produced heavy neutrinos ($N_1^{\rm th}$, $N_1^{\rm nt}$), radiation (R), lepton asymmetry ($B-L$) and gravitinos ($\widetilde{G}$). Lower panel: Emergent plateau of approximately constant reheating temperature. Input parameters: Heavy neutrino mass $M_1 = 1 \times 10^{11}$ GeV, effective neutrino mass $\widetilde{m}_1 = 4 \times 10^{-2}$ eV. The $B-L$ scale is fixed by requiring consistency with hybrid inflation, $v_{B-L} = 5 \times 10^{15}$ GeV. Reprinted from Ref. [49], with permission from Elsevier.

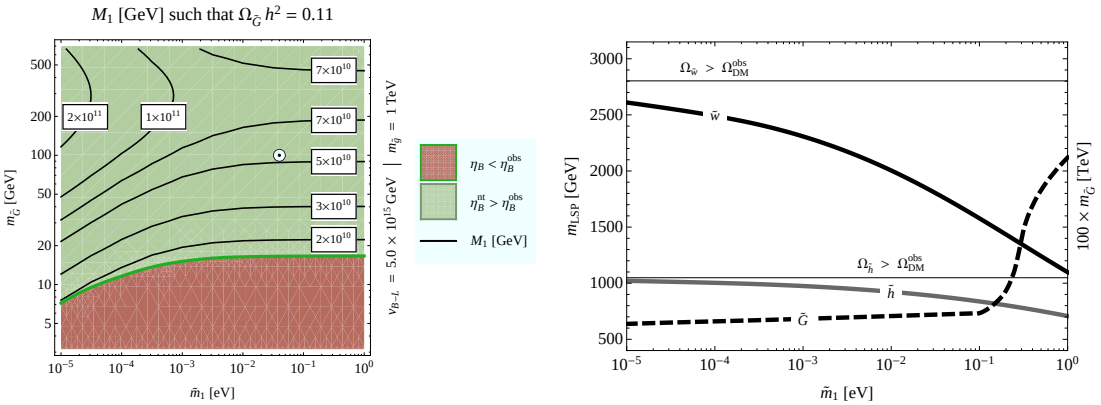


Figure 7: Lower and upper bounds on superparticle masses. Left: Countour plots of the Majorana neutrino mass M_1 as function of the effective neutrino mass $\tilde{m}_1$ and the gravitino mass $m_{\tilde{G}}$ such that the relic density of dark matter is accounted for by gravitinos. Reprinted from Ref. [47], with permission from Elsevier. Right: Upper bounds on wino ($\tilde{w}$) and higgsino ($\tilde{h}$) LSP masses imposed by successful leptogenesis, and a lower bound on the gravitino mass implied by BBN as functions of the effective neutrino mass $\tilde{m}_1$. Reprinted from Ref. [49], with permission from Elsevier.

symmetry is unbroken. It is spontaneouly broken during the process of tachyonic preheating. Hence, cosmic strings are formed in this transition. The time evolution of the string network can be described either by lattice gauge theory simulations for an Abelian Higgs model or, in the zero-width limit, by simulations of Nambu–Goto strings. Unfortunately, the results differ significantly. The CMB and the stochastic gravitational wave background imply an upper bound on the allowed string tension. In the performed analysis the conservative CMB bound of the Planck Collaboration has been used. The results of a detailed two-field inflation analysis are summarized in Fig. 8, where the green band indicates the parameter range of successful inflation. It is remarkable that the allowed gravitino masses include the range 10 GeV $< m_{3/2} <$ 100 TeV, which is consistent with leptogenesis for either gravitino dark matter or higgsino/wino dark matter. In this way, the supersymmetric standard model, supplemented by right-handed neutrinos and spontaneous $B-L$ breaking, yields a *minimal supersymmetric model of particle physics and the early universe* [51].

In addition to F-term hybrid inflation also D-term hybrid inflation was studied, using a superconformal Kähler potential [52]. This model has the intriguing property to coincide with the successful Starobinsky model in the large field regime [53]. An important question is then the consistency with moduli stabilization [54, 55]. The Starobinsky model can also be obtained from Higgs inflation [56]. The severe bounds on the cosmic string tension can be avoided in supergravity inflation [57] where, however, monopole production has to be considered [58]. The density fluctuations produced during inflation are also crucial for the formation of large scale structure, which was analyzed in cosmological perturbation theory [59, 60].

Hybrid inflation in the complex plane predicts a tensor-to-scalar ratio $r \simeq 2 \times 10^{-6}$ [50]. This result was obtained at about the same time when the BICEP Collaboration announced the discovery of B-modes in the CMB, with a value $r \simeq 0.1$. This led to the investigation of several

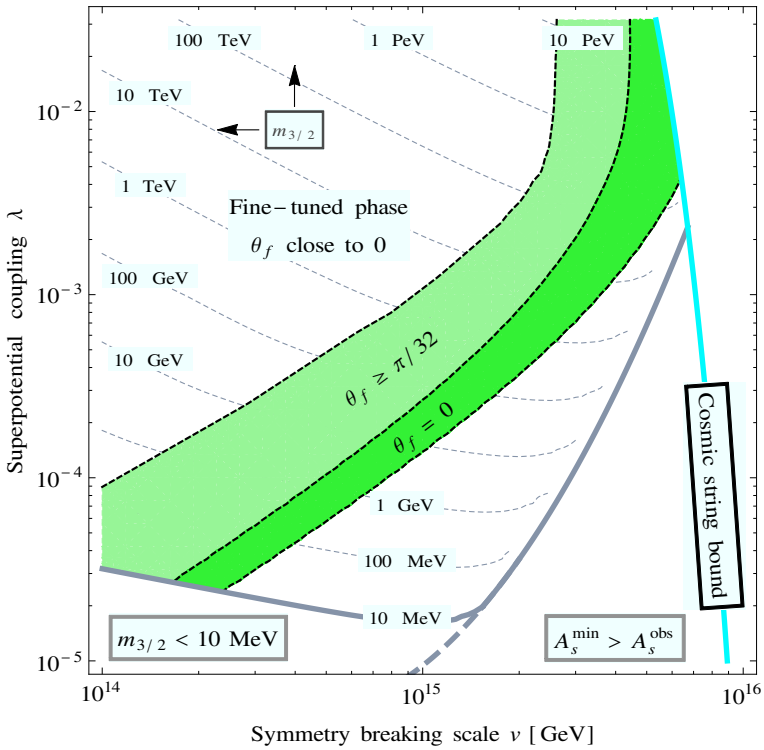


Figure 8: Constraints on the model parameters of hybrid inflation, v, λ and $m_{3/2}$, imposed by the measured values for the inflationary observables and the cosmic string bound (light-blue curve). For each (v, λ) pair, the gravitino mass is adjusted, as indicated by the grey contour lines, such that the scalar amplitude A_s comes out right. Along the solid black line, the best-fit value for the scalar spectral index is reproduced, with the green band indicating the corresponding 2σ confidence interval. Figure taken from Ref. [50].

large field models of inflation. One interesting possibility is *subcritical hybrid inflation* where the inflationary phase extends beyond the point of tachyonic instability [61, 62], leading to a flattened version of chaotic inflation. In large field inflation models the consistency with moduli stabilization is a serious issue and leads to severe constraints on the scale of supersymmetry breaking [63–65].

The presented *minimal model of the early universe* includes all eras of the early universe: inflation, tachyonic preheating, reheating with the generation of baryon asymmetry and dark matter, and the transition to the standard radiation dominated era. This history is imprinted on the, yet unobserved, stochastic gravitational background. An effort has therefore been made to compute the entire gravitational wave (GW) spectrum of all periods [66, 67], which is shown in Fig. 9, in comparision with the sensitivities of current and future gravitational wave interferometers. Particularly exciting is the possibility to measure, at least in principle, the *leptogenesis temperature*, the maximal temperature of the early universe [66, 68].

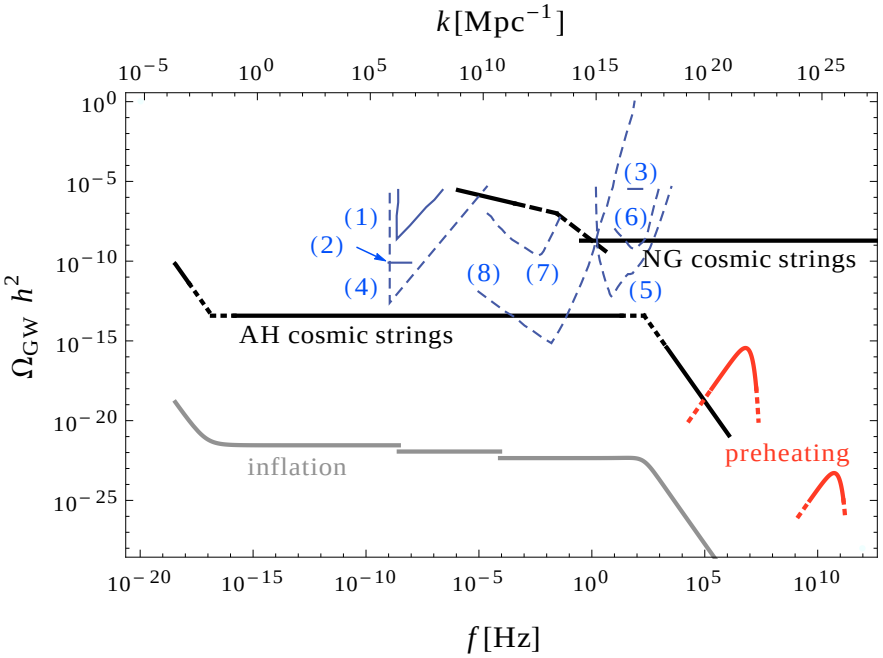


Figure 9: Predicted GW spectrum and the (expected) sensitivity of current and upcoming experiments. The GW spectrum due to inflation (gray), preheating (red) as well as Abelian Higgs and Nambu–Goto cosmic strings (black) is shown for $v_{B-L} = 5 \times 10^{15}$ GeV, $M_1 = 10^{11}$ GeV, $m_S = 3 \times 10^{13}$ GeV, and $\alpha = 10^{-12}$. This corresponds to a reheating temperature of $T_{\rm RH} = 4.9 \times 10^9$ GeV. The current bounds on the stochastic GW spectrum from (1), (2) millisecond pulsar timing and (3) LIGO are marked by solid blue lines. The dashed blue lines mark the expected sensitivity of some planned experiments: (4) SKA, (5) ET, (6) advanced LIGO, (7) eLISA, and (8) BBO and DECIGO. Figure reprinted from Ref. [66]. © 2013 IOP Publishing Ltd and Sissa Medialab srl.

5 Outlook

Leptogenesis is one of the leading candidates for explaining the origin of the cosmological baryon asymmetry. This is mostly due to the remarkable consistency or thermal leptogenesis with the observed small neutrino masses. Moreover, within a framework of grand unification, one obtains Dirac and Majorana neutrino mass matrices, which naturally account for the observed magnitude of the baryon asymmetry. Since leptogenesis is a subtle effect, based on CP violation, departure from thermal equilibrium and quantum interference in a thermal bath, it has been a major topic of project C3 to study this mechanism based on nonequilibrium field theory, going beyond the classical Boltzmann equations. For the first time, the departure from thermal equilibrium and the evaluation of the lepton asymmetry were treated based on Green's functions in the Schwinger–Keldysh formalism. It is reassuring that the results are consistent with previous studies based on Boltzmann equations. The developed techniques can be applied to low-scale leptogenesis or flavoured leptogenesis. Further progress is needed to obtain a *theory of leptogenesis*. In particular, a resummation of gauge interaction with the thermal bath has to

be performed, and also spectator processes have to be taken into account.

There is a tension between thermal leptogenesis and low scale supersymmetry, due to the needed large reheating temperature. Already at the beginning of the project it was know that standard WIMP dark matter is inconsistent with thermal leptogenesis – so far a successful prediction of leptogenesis! It was also known that in principle gravitino dark matter might be an alternative. During the project this possibility was studied in detail. It turned out that gravitino dark matter with small R-parity breaking is indeed consistent with all observational constraints, and that it leads to interesting signatures in cosmic rays as well as collider experiments. A viable alternative are thermally or nonthermally produced higgsinos. So far, there are no experimental hints for R-parity breaking supersymmetry, but there is still room for a discovery of monochromatic gamma-rays from decaying gravitinos and for the observation of R-parity violating decays of long-lived higgsinos at the LHC.

The spontaneous breaking of $B-L$, leptogenesis and gravitino dark matter are naturally related to hybrid inflation. It is remarkable that, given the parameters of the fundamental Lagrangian, the observables of the CMB, entropy production, baryon asymmetry and dark matter can all be explained as consequences of the cosmological evolution, starting from a state of unbroken $B-L$ symmetry. The corresponding history of the early universe is then imprinted on the spectrum of primordial gravitational waves. It is fascinating that one day even the leptogenesis temperature may be measured! In our analysis the CMB bounds on the cosmic string tension were used. In the future, the more stringent bounds from gravitational waves should be taken into account, which may require a revision of the inflationary model. An interesting candidate for an improved analysis may be a version of superconformal D-term inflation, which leads to the Starobinsky model at large field values.

References

[1] M. Fukugita and T. Yanagida, *Baryogenesis Without Grand Unification*, *Phys. Lett.* **B174** (1986) 45–47.

[2] W. Buchmüller and M. Plümacher, *Baryon asymmetry and neutrino mixing*, *Phys. Lett.* **B389** (1996) 73–77, [hep-ph/9608308].

[3] W. Buchmüller, R. D. Peccei and T. Yanagida, *Leptogenesis as the origin of matter*, *Ann. Rev. Nucl. Part. Sci.* **55** (2005) 311–355, [hep-ph/0502169].

[4] C. S. Fong, E. Nardi and A. Riotto, *Leptogenesis in the Universe*, *Adv. High Energy Phys.* **2012** (2012) 158303, [1301.3062].

[5] A. Anisimov, W. Buchmüller, M. Drewes and S. Mendizabal, *Nonequilibrium Dynamics of Scalar Fields in a Thermal Bath*, *Annals Phys.* **324** (2009) 1234–1260, [0812.1934].

[6] M. Drewes, *Quantum aspects of early universe thermodynamics*, Ph.D. thesis, Universität Hamburg, 2010. 10.3204/DESY-THESIS-2010-010 http://inspirehep.net/record/852627/files/desy-thesis-10-010.pdf.

[7] A. Anisimov, W. Buchmüller, M. Drewes and S. Mendizabal, *Leptogenesis from Quantum Interference in a Thermal Bath*, *Phys.Rev.Lett.* **104** (2010) 121102, [1001.3856].

[8] A. Anisimov, W. Buchmüller, M. Drewes and S. Mendizabal, *Quantum Leptogenesis I*, *Annals Phys.* **326** (2011) 1998–2038, [1012.5821].

[9] S. Mendizabal Cofre, *Quantum mechanics of leptogenesis*, Ph.D. thesis, Universität Hamburg, 2010. http://www-library.desy.de/cgi-bin/showprep.pl?thesis10-029.

[10] T. Frossard, M. Garny, A. Hohenegger, A. Kartavtsev and D. Mitrouskas, *Systematic approach to thermal leptogenesis*, *Phys.Rev.* **D87** (2013) 085009, [1211.2140].

[11] W. Buchmüller, *Leptogenesis: Theory and Neutrino Masses*, *Nucl.Phys.Proc.Suppl.* **235-236** (2013) 329–335, [1210.7758].

[12] W. Buchmüller, L. Covi, D. Emmanuel-Costa and S. Wiesenfeldt, *CP Violation and Neutrino Masses and Mixings from Quark Mass Hierarchies*, *JHEP* **0712** (2007) 030, [0709.4650].

[13] W. Buchmüller, *Baryogenesis: 40 Years Later*, in *Proceedings on 13th International Symposium on Particles, strings, and cosmology (PASCOS 2007): London, UK, July 2-7, 2007*, 2007, 0710.5857.

[14] W. Buchmüller, V. Domcke and K. Schmitz, *Predicting θ_{13} and the Neutrino Mass Scale from Quark Lepton Mass Hierarchies*, *JHEP* **1203** (2012) 008, [1111.3872].

[15] A. Anisimov and P. Di Bari, *Cold Dark Matter from heavy Right-Handed neutrino mixing*, *Phys.Rev.* **D80** (2009) 073017, [0812.5085].

[16] I. Rues, *Constraints from the see-saw mechanism and leptogenesis on the minimal neutrino mass*, Master's thesis, Universität Hamburg, 2012.

[17] M. Erbe, *Gravitino dark matter in the leptogenesis environment via inflaton decay*, diploma thesis, Universität Hamburg, 2009.

[18] G. Bertone, W. Buchmüller, L. Covi and A. Ibarra, *Gamma-Rays from Decaying Dark Matter*, *JCAP* **0711** (2007) 003, [0709.2299].

[19] W. Buchmüller and M. Garny, *Decaying vs Annihilating Dark Matter in Light of a Tentative Gamma-Ray Line*, *JCAP* **1208** (2012) 035, [1206.7056].

[20] W. Buchmüller, *Leptogenesis and Gravitino Dark Matter*, *AIP Conf.Proc.* **903** (2007) 56–64, [hep-ph/0611368].

[21] W. Buchmüller, L. Covi, J. Kersten and K. Schmidt-Hoberg, *Dark Matter from Gaugino Mediation*, *JCAP* **0611** (2006) 007, [hep-ph/0609142].

[22] K. Schmidt-Hoberg, *Superpartner mass spectrum and cosmological implications from orbifolds*, Ph.D. thesis, Universität Hamburg, 2007. 10.3204/DESY-THESIS-2007-022 http://www-spires.fnal.gov/spires/find/books/www?cl=DESY-THESIS-2007-022.

[23] W. Buchmüller, L. Covi, K. Hamaguchi, A. Ibarra and T. Yanagida, *Gravitino Dark Matter in R-Parity Breaking Vacua*, *JHEP* **0703** (2007) 037, [hep-ph/0702184].

[24] A. Ibarra and D. Tran, *Gamma Ray Spectrum from Gravitino Dark Matter Decay*, *Phys. Rev. Lett.* **100** (2008) 061301, [0709.4593].

[25] A. Ibarra and D. Tran, *Antimatter Signatures of Gravitino Dark Matter Decay*, *JCAP* **0807** (2008) 002, [0804.4596].

[26] W. Buchmüller, A. Ibarra, T. Shindou, F. Takayama and D. Tran, *Probing Gravitino Dark Matter with PAMELA and Fermi*, *JCAP* **0909** (2009) 021, [0906.1187].

[27] D. Tran, *Indirect signatures of gravitino dark matter in models with R-parity violation*, diploma thesis, Universität Hamburg, 2008. http://inspirehep.net/record/792904/files/david.pdf.

[28] W. Buchmüller, *Gravitino Dark Matter*, *AIP Conf.Proc.* **1200** (2010) 155–164, [0910.1870].

[29] L. Covi, M. Grefe, A. Ibarra and D. Tran, *Unstable Gravitino Dark Matter and Neutrino Flux*, *JCAP* **0901** (2009) 029, [0809.5030].

[30] M. Grefe, *Neutrino signals from gravitino dark matter with broken R-parity*, diploma thesis, Universität Hamburg, 2008. 10.3204/DESY-THESIS-2008-043 http://inspirehep.net/record/802265/files/desy-thesis-08-043.pdf.

[31] S. Bobrovskyi, W. Buchmüller, J. Hajer and J. Schmidt, *Quasi-stable neutralinos at the LHC*, *JHEP* **1109** (2011) 119, [1107.0926].

[32] G. Vertongen and C. Weniger, *Hunting Dark Matter Gamma-Ray Lines with the Fermi LAT*, *JCAP* **1105** (2011) 027, [1101.2610].

[33] T. Bringmann, F. Calore, G. Vertongen and C. Weniger, *On the Relevance of Sharp Gamma-Ray Features for Indirect Dark Matter Searches*, *Phys.Rev.* **D84** (2011) 103525, [1106.1874].

[34] X. Huang, G. Vertongen and C. Weniger, *Probing Dark Matter Decay and Annihilation with Fermi LAT Observations of Nearby Galaxy Clusters*, *JCAP* **1201** (2012) 042, [1110.1529].

[35] X. Huang, G. Vertongen and C. Weniger, *Galaxy Clusters and Gamma-Ray Lines: Probing Gravitino Dark Matter with the Fermi LAT*, 1110.6236.

[36] C. Weniger, T. Bringmann, F. Calore and G. Vertongen, *Spectral cutoffs in indirect dark matter searches*, *J.Phys.Conf.Ser.* **375** (2012) 012034, [1111.6998].

[37] M. Garny, A. Ibarra, M. Pato and S. Vogl, *Internal bremsstrahlung signatures in light of direct dark matter searches*, *JCAP* **1312** (2013) 046, [1306.6342].

[38] M. Garny, A. Ibarra, M. Pato and S. Vogl, *On the spin-dependent sensitivity of XENON100*, *Phys.Rev.* **D87** (2013) 056002, [1211.4573].

[39] K. Kamada and M. Yamaguchi, *Asymmetric Dark Matter from Spontaneous Cogenesis in the Supersymmetric Standard Model*, *Phys.Rev.* **D85** (2012) 103530, [1201.2636].

[40] J. Hajer, *Gravitino and scalar tau-lepton decays in supersymmetric models with broken R-parity*, diploma thesis, Universität Hamburg, 2010. 10.3204/DESY-THESIS-2010-021 http://bib-pubdb1.desy.de/record/288929.

[41] S. Bobrovskyi, W. Buchmüller, J. Hajer and J. Schmidt, *Broken R-Parity in the Sky and at the LHC*, *JHEP* **1010** (2010) 061, [1007.5007].

[42] S. Bobrovskyi, *Gravitinos and hidden supersymmetry at the LHC*, Ph.D. thesis, Universität Hamburg, 2012. 10.3204/DESY-THESIS-2012-032 http://www-library.desy.de/cgi-bin/showprep.pl?thesis12-032.

[43] J. Hajer, *Long-lived neutralinos as probes of gravitino dark matter*, Ph.D. thesis, Universität Hamburg, 2013. http://www-library.desy.de/cgi-bin/showprep.pl?thesis13-031.

[44] W. Buchmüller, M. Endo and T. Shindou, *Superparticle Mass Window from Leptogenesis and Decaying Gravitino Dark Matter*, *JHEP* **0811** (2008) 079, [0809.4667].

[45] W. Buchmüller, K. Schmitz and G. Vertongen, *Matter and Dark Matter from False Vacuum Decay*, *Phys.Lett.* **B693** (2010) 421–425, [1008.2355].

[46] W. Buchmüller, K. Schmitz and G. Vertongen, *Entropy, Baryon Asymmetry and Dark Matter from Heavy Neutrino Decays*, *Nucl.Phys.* **B851** (2011) 481–532, [1104.2750].

[47] W. Buchmüller, V. Domcke and K. Schmitz, *Spontaneous B-L Breaking as the Origin of the Hot Early Universe*, *Nucl.Phys.* **B862** (2012) 587–632, [1202.6679].

[48] K. Schmitz, *The B-L Phase Transition: Implications for Cosmology and Neutrinos*, Ph.D. thesis, Universität Hamburg, 2012. 1307.3887. http://www-library.desy.de/cgi-bin/showprep.pl?thesis12-039.

[49] W. Buchmüller, V. Domcke and K. Schmitz, *WIMP Dark Matter from Gravitino Decays and Leptogenesis*, *Phys.Lett.* **B713** (2012) 63–67, [1203.0285].

[50] W. Buchmüller, V. Domcke, K. Kamada and K. Schmitz, *Hybrid Inflation in the Complex Plane*, *JCAP* **1407** (2014) 054, [1404.1832].

[51] W. Buchmüller, V. Domcke, K. Kamada and K. Schmitz, *A Minimal Supersymmetric Model of Particle Physics and the Early Universe*, 1309.7788.

[52] W. Buchmüller, V. Domcke and K. Schmitz, *Superconformal D-Term Inflation*, *JCAP* **1304** (2013) 019, [1210.4105].

[53] W. Buchmüller, V. Domcke and K. Kamada, *The Starobinsky Model from Superconformal D-Term Inflation*, *Phys.Lett.* **B726** (2013) 467–470, [1306.3471].

[54] W. Buchmüller, V. Domcke and C. Wieck, *No-scale D-term inflation with stabilized moduli*, *Phys. Lett.* **B730** (2014) 155–160, [1309.3122].

[55] W. Buchmüller, C. Wieck and M. W. Winkler, *Supersymmetric Moduli Stabilization and High-Scale Inflation*, *Phys. Lett.* **B736** (2014) 237–240, [1404.2275].

[56] K. Kamada, T. Kobayashi, T. Takahashi, M. Yamaguchi and J. Yokoyama, *Generalized Higgs inflation*, *Phys.Rev.* **D86** (2012) 023504, [1203.4059].

[57] K. Kamada, Y. Miyamoto and J. Yokoyama, *Evading the pulsar constraints on the cosmic string tension in supergravity inflation*, *JCAP* **1210** (2012) 023, [1204.3237].

[58] K. Kamada, K. Nakayama and J. Yokoyama, *Phase transition and monopole production in supergravity inflation*, *Phys.Rev.* **D85** (2012) 043503, [1110.3904].

[59] D. Blas, M. Garny and T. Konstandin, *On the non-linear scale of cosmological perturbation theory*, *JCAP* **1309** (2013) 024, [1304.1546].

[60] D. Blas, M. Garny and T. Konstandin, *Cosmological perturbation theory at three-loop order*, *JCAP* **1401** (2014) 010, [1309.3308].

[61] W. Buchmüller, V. Domcke and K. Schmitz, *The Chaotic Regime of D-Term Inflation*, *JCAP* **1411** (2014) 006, [1406.6300].

[62] W. Buchmüller and K. Ishiwata, *Grand Unification and Subcritical Hybrid Inflation*, *Phys. Rev.* **D91** (2015) 081302, [1412.3764].

[63] W. Buchmüller, E. Dudas, L. Heurtier and C. Wieck, *Large-Field Inflation and Supersymmetry Breaking*, *JHEP* **09** (2014) 053, [1407.0253].

[64] W. Buchmüller, E. Dudas, L. Heurtier, A. Westphal, C. Wieck and M. W. Winkler, *Challenges for Large-Field Inflation and Moduli Stabilization*, *JHEP* **04** (2015) 058, [1501.05812].

[65] C. Wieck, *Stability of Extra Dimensions in the Inflating Early Universe*, Ph.D. thesis, Universität Hamburg, 2015. https://bib-pubdb1.desy.de/record/222293.

[66] W. Buchmüller, V. Domcke, K. Kamada and K. Schmitz, *The Gravitational Wave Spectrum from Cosmological $B - L$ Breaking*, *JCAP* **1310** (2013) 003, [1305.3392].

[67] V. Domcke, *Matter, Dark Matter and Gravitational Waves from a GUT-Scale U(1) Phase Transition*, Ph.D. thesis, Universität Hamburg, 2013. 10.3204/DESY-THESIS-2013-037 http://www-library.desy.de/cgi-bin/showprep.pl?thesis13-037.

[68] W. Buchmüller, *Baryogenesis, Dark Matter and the Maximal Temperature of the Early Universe*, *Acta Phys.Polon.* **B43** (2012) 2153–, [1212.3554].

Supernovae Type Ia & Dark Energy

Peter Hauschildt

Hamburger Sternwarte, Universität Hamburg, Germany

DOI: http://dx.doi.org/10.3204/PUBDB-2018-00782/C5

In project C5 of the SFB 676, we simulated the spectra of cosmological Type Ia supernovae in detail. We use state-of-the-art (3D) NLTE spectral synthesis to analyze the observed multi-wavelength spectra of SNe found in the archives, and make predictions for future observations. This helps us to unlock the mystery of the dark energy.

For this work, we have extended our general model atmosphere code PHOENIX to simulate SN Ia spectra and light curves. For this we have developed a 3D time-dependent radiative transfer module and a number of additional modules (line opacities, equation of state, non-LTE) to create a PHOENIX/3D package [1]. This package allows for the same micro-physics as the PHOENIX/1D mode, so that we are in the rather unique position to investigate both 1D and 3D light-curve models with the same micro-physics as main ingredients.

1 Introduction

The main goal of this project was to improve the accuracy of *d*irect cosmological distance determinations using type Ia supernovae (SNe Ia). These supernovae have been used as standardized candles to measure the history of the expansion of the universe. Their results indicate that the universe does not contain enough matter to stop the expansion that began with the Big Bang and, more surprisingly, that the expansion is speeding up. Under the current standard model for cosmology this is best explained by the presence of a heretofore unknown dark energy.

However, SNe Ia are not perfect standard candles and it is observationally known that they show individually quite different spectra and light curves. This is presently empirically corrected for, however this obviously increases the systematic errors in the determined distances and thus the cosmological parameters determined from the direct supernova channel. Therefore, understanding the differences between individual type Ia supernovae in terms of basic physics is important not only for the history of supernovae (and thus nucleosynthesis) in the universe but also to establish reliable systematic errors and improved cosmological parameters from SN Ia studies.

This project had 2 main work areas:

1. Spectrum synthesis and detailed light curve modeling to compare to observations
2. 3D radiative transfer for SN Ia

In the first part we have completed the development of a 1D NLTE light curve modeling extension of our `PHOENIX/1D` code. This part of the project was part of the PhD thesis of Dennis

Jack (completed 2009). For this project we first developed a time dependent version of our 1D+3D relativistic radiative transfer code [2–4]. The code uses an fully implicit discretization of the DI/Dt term so that there are no significant time step restrictions for this method. It can handle problems such as quickly varying input light sources, flashes running through the atmosphere, etc. This allows us to model variations that occur on very small time scales. The time dependent transfer also allows for time dependent treatment of multi-level transfer problems.

Furthermore, we have developed a time evolution code that follows the time development of the SN Ia atmosphere [4]. This code can be applied to the free expansion phase on the supernova evolution and calculations non-grey, NLTE light curves. We have verified the code operation in a number of tests and have calculated a light curves for a number of different starting hydro models. The calculations show significant differences in the resulting light curves and time dependent spectra so that we will be able to better understand how different predicted SN Ia structures map to different temporal spectra evolution.

In the second part of the project, we have completed the development of a full 3D Lagrangian radiative transfer code for applications to SNe Ia. This was originally intended as a PhD thesis project, however, in became clear during the initial development that this task is too much for a PhD project and required an experienced postdoc for efficient progress. Therefore, we have instead used the available funds to fund a postdoc for 1/2 of the total grant time, with extremely good results.

We have started with the 3D radiative transfer (3DRT) framework discussed in [5] and [6] and extended it to periodic boundary conditions [7] and to 3D spherical and cylindrical coordinates [8]. The former is of particular interest for SN Ia modeling as the structures from 3D hydro models are roughly spherical in shape (the strongest density variations along the radial coordinate with significant fluctuations in polar angle and azimuth). For supernovae we have to be able to consider the relativistic velocity fields in the 3D ejecta with the same accuracy as in the 1D case. For this we have to address two points: (1) the velocity field in the 3D ejecta of a SN Ia will be homologous only to a first approximations, in realistic simulations it will have non-radial components and non-monotonic radial fluctuations. (2) In the standard 1D numerical solution of the radiative transfer equation in the Lagrangian frame the characteristics are *curved*. In 1D this can be easily and accurately done, however, in 3D this method is computationally very inconvenient. In [9] we have addressed the first problem by developing a fully implicitly formal solution (and corresponding operator splitting method) that is highly parallelized. This make the code so efficient that it is in 1D basically as fast (on a given number of CPUs) as the code restricted to monotonic velocity fields. This method can be applied to 3D configuration, see below. In order to address the second problem we have developed an affine parameter method [10] that transforms the wavelength to an affine parameter so that the characteristics remain geodesics (and thus in flat space-times just straight lines). This method can be applied to the 3D case, we have developed such a code and demonstrated its accuracy in [11].

Dr. Dennis Jack developed first a time-dependent 3D radiative transfer module that forms the basis of the 3D light curve simulations [3]. For this he used the developments from the 1D time dependent radiative transfer as blueprints for the 3D code. In extensive tests we discovered that for a numerically correct and stable calculation the fully per-characteristic intensities are needed for the implicit discretization of the time derivative. This "sub-voxel" method gives accuracy in agreement with the 1D algorithm, whereas the much simpler "voxel averaged" intensity time discretization gives substantially less accurate results (and is, therefore, not used

for production calculations). In addition, we have developed a 3D radiative transfer algorithm to treat monotonic velocity fields (e.g., radially symmetric monotonically increasing velocities that are classical results from 1D explosion models) and a more general algorithm that for arbitrary velocity fields (e.g., resulting from non-radially symmetric explosions or when parts of the ejecta collide with slower material). Both algorithms work in the Lagrangian (co-moving) frame which has massive accuracy and technical advantages for the high velocities encountered in Type Ia supernovae (henceforth SNe Ia).

In the Lagrangian 3D radiative transfer it is important to include effects of special relativity for accurate modeling (the situation is identical to the 1D version where relativistic effects are important if the bulk velocities are larger than a few per-cent of the speed of light). In 1D we originally chose a Lagrangian coordinate system in which the light paths (characteristics) are curved but the wavelength derivative is trivially simple. This approach is impractical for 3D calculations as the curvatures of the characteristics would lead to extremely complex algorithms. We have, therefore, developed an affine parameter method in which we chose a Lagrangian coordinate system with straight characteristics and a more complex transformation of the wavelength space. This was first tested in 1D modeling [12,13] and then implemented in the 3D radiative transfer modules. It retains its characteristic properties also in the 3D case, so that monotonic velocity fields can be treated by a method that solves one wavelength after the other (which limits the parallelization due to the filling of the "wavelength pipeline"). For arbitrary velocity fields we need to solve for all wavelength points at once, this allows (and demands) much higher degrees of parallelism as for monotonic velocity fields. In some cases if may be more efficient to use the arbitrary velocity field algorithm even for monotonic fields as it easily scales to several 100k processes and thus can lead to much higher performance as the specialized algorithm.

An additional module, the 3D NLTE module, was also added to the PHOENIX/3D package [14]. This module is necessary for the conditions found in SNe Ia and recently finished. With these packages for PHOENIX/3D we can compute 3D light-curve models for SNe Ia. The models are extremely computer resource intensive and, therefore, we can only run test models at the present time.

2 Time dependent 3D radiative transfer

The material in this section was originally published in Ref. [3].

In the following subsection, we describe the method we use to solve the time dependent 3D radiative transfer. The test calculations are presented in to verify that the implementation functions correctly In the tests, we include scattering and investigate atmospheres with time dependent inner boundary conditions.

2.1 Transfer equation

Ref. [10] presents an approach to solve the radiative transfer equation in a flat space-time and in the comoving-frame. The radiative transfer equation written in terms of an affine parameter ξ, Eq. (18) from [10], is given by

$$\frac{\partial I_\lambda}{\partial \xi} + \left(\frac{\mathrm{d}\lambda}{\mathrm{d}\xi}\right) \frac{\partial I_\lambda}{\partial \lambda} = -\left(\chi_\lambda \frac{h}{\lambda} + \frac{5}{\lambda}\frac{\mathrm{d}\lambda}{\mathrm{d}\xi}\right) I_\lambda + \eta_\lambda \frac{h}{\lambda}. \tag{1}$$

The description of the $\partial I/\partial\lambda$-discretization for homologous velocity fields has been presented in [9]. We use this discretization method and extend it to include the $\partial I/\partial t$ time dependence in the solution of the radiative transfer.

The time dependent 3D radiative transfer equation along a characteristic is a modification of Eq. (15) in [9] and given by

$$\frac{\partial I_{\lambda,t}}{\partial s} + a(s)\frac{\partial}{\partial\lambda}(\lambda I_{\lambda,t}) + a(t)\frac{\partial}{\partial t}I_{\lambda,t} + 4a(s)I_{\lambda,t} = -\chi_\lambda f(s)I_{\lambda,t} + \eta_\lambda f(s), \tag{2}$$

where the factor $a(t)$ is simply

$$a(t) = \frac{1}{c}. \tag{3}$$

The path length along a characteristic is represented by s, the intensity $I_{\lambda,t}$ is a function of the wavelength λ and time t along the characteristic. For the detailed derivation of $f(s)$ and $a(t)$ see [9].

The fully implicit discretization of equation (1) in both wavelength and time is given by

$$\frac{\mathrm{d}I_\lambda}{\mathrm{d}s} + \left[a(s)\frac{\lambda_l}{\lambda_l - \lambda_{l-1}} + \frac{a(t)}{\Delta t} + 4a(s) + \chi_\lambda f(s)\right] \tag{4}$$

$$= a(s)\frac{\lambda_{l-1}I_{\lambda_{l-1}}}{\lambda_l - \lambda_{l-1}} + \eta_\lambda f(s). \tag{5}$$

Following Ref. [9], this leads to a modification of the effective optical length $\hat{\chi}$, which is now defined by

$$\mathrm{d}\tau = -\left(\chi_\lambda f(s) + 4a(s) + \frac{a(s)\lambda_l}{\lambda_l - \lambda_{l-1}} + \frac{a(t)}{\Delta t}\right)\mathrm{d}s \equiv \hat{\chi}\mathrm{d}s. \tag{6}$$

The modified source function $\hat{S}_\lambda$ is then defined by

$$\frac{\mathrm{d}I_\lambda}{\mathrm{d}\tau} = I_\lambda + \frac{\chi_\lambda}{\hat{\chi}_\lambda}\left(S_\lambda f(s) + \frac{a(s)}{\chi_\lambda}\frac{\lambda_{l-1}I_{\lambda_{l-1}}}{\lambda_l - \lambda_{l-1}} + \frac{a(t)}{\chi_\lambda}\frac{1}{\Delta t}I_{t-1}\right) \tag{7}$$

$$\equiv I_\lambda + \hat{S}_\lambda. \tag{8}$$

This approach to include time dependence in the 3D RT framework is similar to the first discretization method for the 1D case as described in [4]. The discretization of the $\partial I/\partial t$ term modifies the generalized optical depth and adds an additional term to the generalized source function. To verify the code, we have calculated the solution for a number of simple parameterized test cases. The inner boundary condition was made time dependent to simulate radiation waves traveling through an atmosphere. All these perturbations move through the atmosphere as expected. We also computed a test case with a sinosoidically varying inner light bulbs. We compared the results of the 3D time dependent radiative transfer to the results of our well tested 1D spherical symmetric radiative transfer program and found excellent agreement. In a scattering dominated atmosphere, it takes more time for the radiation to move through an atmosphere. All tests indicate that the new implementations works as intended.

3 Theoretical light curves of SNe Ia

The material in this section was originally published in Ref. [15].

We have developed a new approach for a energy solver which can be applied to expanding SN Ia envelopes to compute SN Ia model light curves. Test calculations confirm that the implemented code works properly. We applied the energy solver to calculate SN Ia model light curves during the free expansion phase.

We obtained the first `PHOENIX/1D` light curves of type Ia supernovae in different photometric bands. At first, we solved the radiative transfer equation with the assumption of the atmosphere being in LTE. The model light curves were in decent agreement with the observed ones at early times. However, in the infrared I band, the theoretical light curves do not fit the observed light curves. The authors of Ref. [16] had the same deviations in their model light curves compared to observations. Their light curve in the I band is also too bright and further rising, even after the maximum in observed light curves. The author of Ref. [17] presented a detailed study of SN Ia light curves in the near IR. His I band light curve fits the observations better. He also showed how variable and dependent on different parameters the light curves in the near infrared can be.

Three different dynamical models were compared to observed SN Ia light curves. The delayed detonation model DD 16 is unlikely to be the best explosion model because the model light curves are too faint to fit the observed light curves due to the low ^{56}Ni mass. The results of the W7 model are the best fit to the observed light curves.

For the later phase of the light curves, especially in the infrared, we need the atmosphere to be considered in NLTE. We showed that NLTE model light curves computed with an LTE temperature structure leads to improvements in the model light curves. For future work more investigation of the infrared model light curves and the NLTE needs to be performed. The focus has to lie on the influence of line scattering on the shape of the light curves.

4 Near-infrared light curves of type Ia supernovae

The material in this section was originally published in Ref. [18].

We applied our time-dependent model atmosphere code `PHOENIX/1D` to model light curves of Type Ia supernovae in the near-infrared wavelength range. In a first approach with a constant LTE line scattering parameter ϵ in the radiative transfer, we reproduced the observed light curves during the first phase quite well. However, the model light curves during the later phase were too bright and we could not reproduce the secondary maximum.

We show that a more detailed treatment of IR line scattering is very important for the modeling of the later phase of the near-infrared light curves of SNe Ia. We used as an approximation an LTE line scattering parameter that decreases in time. This is a good approach, because the atmosphere becomes thinner as expansion goes on and scattering becomes more important. We use this approximation to obtain fits to the observed light curves of SN 1999ee and SN 2002bo, improving our model light curves significantly. Compared to [17], our fits are quite accurate in all near-infrared bands. The time varying scattering parameter does not significantly effect the optical light curves. The next step is to treat the atmosphere in full non-LTE, where the temperature needs to adapt to the non-LTE condition, which requires substantial time on parallel supercomputers.

The secondary maximum in each band of the near-infrared was quite accurate reproduced

by our model light curves with varied ϵ. We investigated the spectral evolution and found that the I band secondary maximum arises due to recombination of Fe III to Fe II. An Fe II feature emerges in this band and increases the brightness. For the secondary maximum in the J band, a mix of Fe II and Co II lines emerges and causes the rise to a secondary maximum in the model light curve. The bands H and K also show a secondary maximum. This is caused by the recombination of Co III to Co II. We confirmed that ionization stage changes in iron group elements are responsible for the secondary maximum as [17] claimed. Furthermore, we could explicitly assign lines of different elements to different bands. These results also show how important the treatment of Fe and Co in non-LTE is and should be used in future work, when faster computers are available.

Acknowledgments

The calculations presented here were performed at the RRZ of the Universität Hamburg, at the Höchstleistungs Rechenzentrum Nord (HLRN), and at the National Energy Research Supercomputer Center (NERSC), which is supported by the Office of Science of the U.S. Department of Energy under Contract No. DE-AC03-76SF00098. We thank all these institutions for a generous allocation of computer time.

References

[1] P. H. Hauschildt and E. Baron, *A 3D radiative transfer framework. VI. PHOENIX/3D example applications*, A&A **509** (Jan., 2010) A36+, [0911.3285].

[2] D. Jack, P. H. Hauschildt and E. Baron, *Time-dependent radiative transfer with PHOENIX (Corrigendum)*, A&A **549** (Jan., 2013) C1.

[3] D. Jack, P. H. Hauschildt and E. Baron, *A 3D radiative transfer framework. IX. Time dependence*, A&A **546** (Oct., 2012) A39, [1209.5788].

[4] D. Jack, P. H. Hauschildt and E. Baron, *Time-dependent radiative transfer with PHOENIX*, A&A **502** (Aug., 2009) 1043–1049, [0907.1441].

[5] P. H. Hauschildt and E. Baron, *A 3D radiative transfer framework. I. Non-local operator splitting and continuum scattering problems*, A&A **451** (May, 2006) 273–284, [astro-ph/0601183].

[6] E. Baron and P. H. Hauschildt, *A 3D radiative transfer framework. 2. Line transfer problems*, *Astron. Astrophys.* **468** (2007) 255–261, [astro-ph/0703437].

[7] P. H. Hauschildt and E. Baron, *A 3D radiative transfer framework. III. Periodic boundary conditions*, A&A **490** (Nov., 2008) 873–877, [0808.0601].

[8] P. H. Hauschildt and E. Baron, *A 3D radiative transfer framework. IV. Spherical and cylindrical coordinate systems*, A&A **498** (May, 2009) 981–985, [0903.1949].

[9] E. Baron, P. H. Hauschildt and B. Chen, *A 3D radiative transfer framework. V. Homologous flows*, A&A **498** (May, 2009) 987–992, [0903.2486].

[10] B. Chen, R. Kantowski, E. Baron, S. Knop and P. H. Hauschildt, *Steps for solving the radiative transfer equation for arbitrary flows in stationary space-times*, MNRAS **380** (Sept., 2007) 104–112, [arXiv:astro-ph/0603251].

[11] E. Baron, P. H. Hauschildt, B. Chen and S. Knop, *A 3D radiative transfer framework. X. Arbitrary velocity fields in the comoving frame*, A&A **548** (Dec., 2012) A67, [1210.6679].

[12] S. Knop, P. H. Hauschildt and E. Baron, *A new formal solution of the radiative transfer in arbitrary velocity fields*, A&A **496** (Mar., 2009) 295–298, [0902.1876].

[13] S. Knop, P. H. Hauschildt and E. Baron, *Comoving-frame radiative transfer in arbitrary velocity fields – II. Large scale applications*, *Astron. Astrophys.* **501** (2009) 813, [0909.4264].

[14] P. H. Hauschildt and E. Baron, *A 3D radiative transfer framework. XI. Multi-level NLTE*, A&A **566** (June, 2014) A89, [1404.4376].

[15] D. Jack, P. H. Hauschildt and E. Baron, *Theoretical light curves of type Ia supernovae*, A&A **528** (Apr., 2011) A141+, [1105.3330].

[16] S. I. Blinnikov, F. K. Röpke, E. I. Sorokina, M. Gieseler, M. Reinecke, C. Travaglio et al., *Theoretical light curves for deflagration models of type Ia supernova*, A&A **453** (July, 2006) 229–240, [astro-ph/0603036].

[17] D. Kasen, *Secondary Maximum in the Near-Infrared Light Curves of Type Ia Supernovae*, ApJ **649** (Oct., 2006) 939–953, [astro-ph/0606449].

[18] D. Jack, P. H. Hauschildt and E. Baron, *Near-infrared light curves of type Ia supernovae*, A&A **538** (Feb., 2012) A132, [1201.1723].

Scalar Fields in Cosmology: Inflation, Dark Matter, Dark Energy

Jan Louis[1], *Alexander Westphal*[2]

[1]II. Institut für Theoretische Physik, Universität Hamburg, Germany
[2]DESY, Hamburg, Germany

DOI: http://dx.doi.org/10.3204/PUBDB-2018-00782/C6

During the 12 years of project C6 of the SFB 676 it has achieved a set of significant contributions to our understanding of the dynamics of scalar fields in early universe cosmology and its connection to string theory. In this contribution we describe our results at this interface between theoretical cosmology and fundamental high-energy theory in their impacts on 'string inflation' consequences of multi-field inflation in string theory inspired random potentials', 'pole inflation, $f(R)$-gravity, and exponential inflationary plateaus', the 'phenomenological consequences of features before and during inflation', 'false-vacuum tunneling and its consequences for the initial conditions of inflation', connections between slow-rolling scalar fields and electroweak symmetry breaking due to couplings between the Standard Model (SM) Higgs field and inflation, 'moduli stabilization and de Sitter (dS) vacua in string theory', as well as the connection of dS vacua to 'sequestering as a solution to the cosmological constant problem', and on the connection between measurements of ΛCDM parameters from the CMB as well as local data such as the local H_0 determinations, and effects from large-scale structure such as weak gravitational lensing. We finish in section with a summary of a review by one of the PIs on the topic of 'String cosmology – Large field inflation in string theory'.

1 String inflation

Our study of models of inflation in string theory focused on two classes of inflaton candidates. Inflation in string theory can be driven by the slow-roll evolution of volume/Kähler moduli, of open-string moduli, or of axion fields. Both are generically present in 4D compactifications of string theory.

Here we first discuss models where inflation is driven by string moduli scalar fields. In our projects we analyzed the possibility of realizing inflation with a subsequent dS vacuum [1] in the Kähler uplifting scenario [2,3] while building on [4]. The inclusion of several quantum corrections to the 4d effective action evades previous no-go theorems and allows for construction of simple and successful models of string inflation. The predictions of several benchmark models are in accord with current observations, i.e., a red spectral index, negligible non-Gaussianity, and spectral distortions similar to the simplest models of inflation. A particularly interesting subclass of models are "left-rolling" ones, where the overall volume of the compactified dimensions shrinks during inflation. We call this phenomenon "inflation by deflation" (IBD), where deflation refers to the internal manifold. This subclass has the appealing features of being

insensitive to initial conditions, avoiding the overshooting problem, and allowing for observable running $\alpha \sim 0.012$ and enhanced tensor-to-scalar ratio $r \sim 10^{-5}$. The latter results differ significantly from many string inflation models.

In large-field exponential plateau models one focus were the Large Volume Scenario (LVS) [5] of IIB Calabi–Yau flux compactifications. We constructed inflationary models from higher derivative α'^3-corrections [6]. In this case inflation is driven by a Kähler modulus whose potential arises from the aforementioned corrections, while we used the inclusion of string loop effects just to ensure the existence of a graceful exit when necessary. The effective inflaton potential takes a Starobinsky-type form $V = V_0(1 - e^{-\nu\phi})^2$, where we obtained one set-up with $\nu = -1/\sqrt{3}$ and one with $\nu = 2/\sqrt{3}$ corresponding to inflation occurring for increasing or decreasing ϕ respectively. The inflationary observables are thus in perfect agreement with PLANCK, while the two scenarios remain observationally distinguishable via slightly varying predictions for the tensor-to-scalar ratio r. Both set-ups yield $r \simeq (2 \dots 7) \times 10^{-3}$. They hence realise inflation with moderately large fields ($\Delta\phi \sim 6\, M_{Pl}$) without saturating the Lyth bound. Control over higher corrections relies in part on tuning underlying microscopic parameters, and in part on intrinsic suppressions. The intrinsic part of control arises as a leftover from an approximate effective shift symmetry at parametrically large volume.

The leading order dynamics of the type IIB Large Volume Scenario is characterised by the interplay between α' and non-perturbative effects which fix the overall volume and all local blow-up modes leaving (in general) several flat directions. We showed [7] that, in an arbitrary Calabi–Yau compactification with at least one blow-up mode resolving a point-like singularity, any remaining flat directions can be lifted at sub-leading order by the inclusions of higher derivative α' corrections. We also focused on simple fibred cases with one remaining flat direction which can behave as an inflaton if its potential is generated by both higher derivative α' and winding loop corrections. Natural values of the underlying parameters give a spectral index in agreement with observational data and a tensor-to-scalar ratio of order $r = 0.01$ which could be observed by forthcoming CMB experiments. Dangerous corrections from higher dimensional operators are suppressed due to the presence of an approximate non-compact shift symmetry [7].

These fibre inflation models [8] are built in a specific string theory construction based on the large volume scenario that produces an inflationary plateau. We outlined its relation to α-attractor models for inflation, with the cosmological sector originating from certain string theory corrections leading to $\alpha = 2$ and $\alpha = 1/2$ [9]. Above a certain field range, the steepening effect of higher-order corrections leads first to the breakdown of single-field slow-roll and after that to the onset of 2-field dynamics: the overall volume of the extra dimensions starts to participate in the effective dynamics. Finally, we proposed effective supergravity models of fibre inflation based on an $\overline{D3}$ uplift term with a nilpotent superfield. Specific moduli dependent $\overline{D3}$ induced geometries lead to cosmological fibre models but have in addition a de Sitter minimum exit. These supergravity models motivated by fibre inflation are relatively simple, stabilize the axions and disentangle the Hubble parameter from supersymmetry breaking.

We also discussed how α-attractors [10] may generalize to truly multi-field situations including the open-string moduli sector of D-branes [11]. We started the discussion from the observation, that a second order pole in the scalar kinetic term can lead to a class of inflation models with universal predictions referred to as pole inflation or α-attractors. While this kinetic structure is ubiquitous in supergravity effective field theories, realizing a consistent UV complete model in e.g. string theory is a non-trivial task. For one, one expects quantum corrections arising in the vicinity of the pole which may spoil the typical attractor dynamics.

As a conservative estimate of the range of validity of supergravity models of pole inflation we employ the weak gravity conjecture (WGC) [12]. We found that this constrains the accessible part of the inflationary plateau by limiting the decay constant of the axion partner. For the original single complex field models, the WGC does not even allow the inflaton to reach the inflationary plateau region. We proposed addressing these problems by evoking the assistance of N scalar fields from the open string moduli [11]. This improves radiative control by reducing the required range of each individual field. Furthermore, it relaxes the WGC bound allowing to inflate on the plateau, although remaining at finite distance from the pole. Finally, we outlined steps towards an embedding of pole N-flation in type IIB string theory on fibred Calabi–Yau manifolds.

Finally, we connected the structure and phenomenology of fibre inflation as string theory versions of α-attractors to the data from CMB observations. In particular, the Planck satellite may have observed a lack of power on large scales ($\ell < 40$). We argued that this putative feature can be explained by a phase of fast roll at the onset of inflation [13]. We showed that in the context of single field models what is required is an asymmetric inflection point model of which fibre inflation is a string motivated example. We studied the ability of fibre inflation to generate a suppression of the CMB 2-point function power at low l, finding that the potential derived from string loops is not steep enough for this purpose. We introduced a steeper contribution to the potential, that dominates away from the inflationary region, and show that if properly tuned it can indeed lead to a spectrum with lack of power at large scales.

We now move to the discussion of axion fields arising from the higher-dimensional p-form gauge fields of string theory as inflaton candidates. Two relevant classes of such models involve either an axion decay constant alignment mechanism for a few axions [14], or monodromy extending the field range of the single axion [15–17]. Such extensions of the axion field range are necessary, as there are no known cases of weakly coupled string theories with axions acquiring a super-Planckian axion decay constant (and hence super-Planckian field range).

We proposed a new field theory mechanism for generating an effective trans-Planckian decay constant from sub-Planckian ones [18]. Using the minimal two axions and a hierarchy between two axion decay constants is sufficient for realizing inflation through non-perturbative effects only and with minimal tuning. The inflationary motion is kept entirely within a sub-Planckian domain. We outlined possible strategies of embedding the model in a string theory setup.

Moving from axion decay constant hierarchies to alignment, we provided type IIB string embeddings of two axion variants of natural inflation [19]. We used a combination of RR 2-form axions as the inflaton field and had its potential generated by non perturbative effects in the superpotential. Besides giving rise to the inflation, the models developed took into account the stabilization of the compact space, both in the scenario by Kachru, Kallosh, Linde and Trivedi (KKLT) [20] and the LVS regime, an essential condition for any semi-realistic model of string inflation.

Flux couplings to string theory axions yield super-Planckian field ranges along which the axion potential energy grows. At the same time, other aspects of the physics remain essentially unchanged along these large displacements, respecting a discrete shift symmetry with a sub-Planckian period. We presented new classes of specific models of monodromy inflation, with monomial potentials $\mu^{4-p}\phi^p$ [21]. A key simplification in these models is that the inflaton potential energy plays a leading role in moduli stabilization during inflation. The resulting inflaton-dependent shifts in the moduli fields lead to an effective flattening of the inflaton potential, i.e. a reduction of the exponent from a fiducial value p_0 to $p < p_0$. We focued on examples arising in compactifications of type IIB string theory on products of tori or Riemann

surfaces, where the inflaton descends from the NS–NS two-form potential B_2, with monodromy induced by a coupling to the R–R field strength F_1. In this setting we exhibited models with $p = 2/3, 4/3, 2$, and 3, corresponding to predictions for the tensor-to-scalar ratio of $r \approx 0.04, 0.09, 0.13$, and 0.2, respectively. Using mirror symmetry, we also motivated a second class of examples with the role of the axions played by the real parts of complex structure moduli, with fluxes inducing monodromy.

In this scenario, we also studied the pattern of oscillations in the primordial power spectrum in axion monodromy inflation [22], accounting for drifts in the oscillation period that can be important for comparing to cosmological data [23]. In these models the potential energy has a monomial form over a super-Planckian field range, with superimposed modulations whose size is model-dependent. The amplitude and frequency of the modulations are set by the expectation values of moduli fields. We showed that during the course of inflation, the diminishing energy density can induce slow adjustments of the moduli, changing the modulations. We provided templates capturing the effects of drifting moduli, as well as drifts arising in effective field theory models based on softly broken discrete shift symmetries, and we estimated the precision required to detect a drifting period. A non-drifting template suffices over a wide range of parameters, but for the highest frequencies of interest, or for sufficiently strong drift, it is necessary to include parameters characterizing the change in frequency over the e-folds visible in the CMB. We used these templates to perform a preliminary search for drifting oscillations in a part of the parameter space in the Planck nominal mission data.

We now move to analyzing questions of backreaction from stabilized moduli fields on the mechanism of axion monodromy inflation. For this purpose, we start with analyzing the interplay between Kähler moduli stabilization and chaotic inflation in string theory based supergravity models [24]. While heavy moduli decouple from inflation in the supersymmetric limit, supersymmetry breaking generically introduces non-decoupling effects. These lead to inflation driven by a soft mass term, $m_\varphi^2 \sim m m_{3/2}$, where m is a supersymmetric mass parameter. This scenario needs no stabilizer field, but the stability of the moduli during inflation imposes a large supersymmetry breaking scale, $m_{3/2} \gg H$, and a careful choice of initial conditions. This iss illustrated in three prominent examples of moduli stabilization: KKLT stabilization, Kähler Uplifting, and the Large Volume Scenario. Remarkably, all models have a universal effective inflaton potential which is flattened compared to quadratic inflation. Hence, they share universal predictions for the CMB observables, in particular a lower bound on the tensor-to-scalar ratio, $r \gtrsim 0.05$.

Next, we address questions concerning the build-up of 3-brane and 5-brane charge in models of axion monodromy built in warped double-throat geometries. We constructed a simple explicit local geometry providing a 'bifid throat' for 5-brane axion monodromy [25]. A bifid throat is a throat that splits into two daughter throats in the IR, containing a homologous 2-cycle family reaching down into each daughter throat. Our example consists of a deformed $\mathbb{Z}_3 \times \mathbb{Z}_2$ orbifold of the conifold, which provides us with an explicit holographic dual of the bifid throat including D3-branes and fractional 5-branes at the toric singularities of our setup. Having the holographic description in terms of the dual gauge theory allowed us to address the effect of 5-brane-antibrane pair backreaction including the warping effects. This leads to the size of the backreaction being small and controllable after imposing proper normalization of the inflaton potential and hence the warping scales.

Based on these explicit double-throat geometries, we presented a particularly simple model of axion monodromy [26]: Our axion is the lowest-lying KK-mode of the RR-2-form-potential C_2 in the standard Klebanov-Strassler throat. One can think of this inflaton candidate as being

defined by the integral of C_2 over the S^2 cycle of the throat. It obtains an exponentially small mass from the IR-region in which the S^2 shrinks to zero size both with respect to the Planck scale and the mass scale of local modes of the throat. Crucially, the S^2 cycle has to be shared between two throats, such that the second locus where the S^2 shrinks is also in a warped region. Well-known problems like the potentially dangerous back-reaction of brane/antibrane pairs and explicit supersymmetry breaking are not present in our scenario. However, the inflaton back-reaction starts to deform the geometry strongly once the field excursion approaches the Planck scale. We derived the system of differential equations required to treat this effect quantitatively. We find it interesting that such a simple and explicit stringy monodromy model allows an originally sub-Planckian axion to go through many periods with full quantitative control before back-reaction becomes strong. Also, the mere existence of our ultra-light throat mode (with double exponentially suppressed mass) is noteworthy.

Finally, we return the impact of general quantum gravity constraints such as the weak gravity conjecture in the context of axion monodromy inflation. Axions with broken discrete shift symmetry (axion monodromy) have played a central role both in the discussion of inflation and the 'relaxion' approach to the hierarchy problem. We suggested a very minimalist way to constrain such models by the weak gravity conjecture for domain walls [27]: While the electric side of the conjecture is always satisfied if the cosine-oscillations of the axion potential are sufficiently small, the magnetic side imposes a cutoff, $\Lambda^3 \sim mfM_{pl}$, independent of the height of these 'wiggles'. We compared our approach with the recent related proposal by Ibañez, Montero, Uranga and Valenzuela [28]. We also discussed the non-trivial question which version, if any, of the weak gravity conjecture for domain walls should hold. In particular, we showed that string compactifications with branes of different dimensions wrapped on different cycles lead to a 'geometric weak gravity conjecture' relating volumes of cycles, norms of corresponding forms and the volume of the compact space. Imposing this 'geometric conjecture', e.g. on the basis of the more widely accepted weak gravity conjecture for particles, provides at least some support for the (electric and magnetic) conjecture for domain walls.

2 Consequences of multi-field inflation in string theory inspired random potentials

We determined the frequency of regions of small-field inflation in the Wigner landscape [29, 30] as an approximation to random supergravities/type IIB flux compactifications [31]. We showed that small-field inflation occurs exponentially more often than large-field inflation. The power of primordial gravitational waves from inflation is generically tied to the scale of inflation. As for small-field models this is below observational reach, their exponential enhancement seems to indicate a tendency towards small tensor-to-scalar ratio r. However, cosmologically viable inflationary regions must provide for a successful exit from inflation into a meta-stable dS minimum. Hence there is a need to determine the 'graceful exit likelihood' before any statement about the statistically expected level of tensor modes r is possible.

In order to determine this 'graceful exit likelihood' we needed to describe the transition probability for a non-equilibrium ensemble of Wigner matrices to relax back to its equilibrium configuration via the stochastic process of Dyson Brownian Motion. We presented an analytic method for calculating the transition probability between two random Gaussian matrices with given eigenvalue spectra in the context of Dyson Brownian motion [32]. We showed that in the Coulomb gas language, in large N limit, memory of the initial state is preserved in the form of

a universal linear potential acting on the eigenvalues. We computed the likelihood of any given transition as a function of time, showing that as memory of the initial state is lost, transition probabilities converge to those of the static ensemble.

We then applied this general result to small-field inflation in a Wigner random landscape. For this purpose, we developed a stochastic description of small-field inflationary histories with a graceful exit in a random potential whose Hessian is a Gaussian random matrix as a model of the unstructured part of the string landscape [33]. The dynamical evolution in such a random potential from a small-field inflation region towards a viable late-time de Sitter (dS) minimum maps to the dynamics of Dyson Brownian motion describing the relaxation of non-equilibrium eigenvalue spectra in random matrix theory. We analytically computed the relaxation probability in a saddle point approximation of the partition function of the eigenvalue distribution of the Wigner ensemble describing the mass matrices of the critical points. When applied to small-field inflation in the landscape, this leads to an exponentially strong bias against small-field ranges and an upper bound $N \ll 10$ on the number of light fields N participating during inflation from the non-observation of negative spatial curvature.

Moving beyond the inflationary dynamics, we discussed the structure of the phenomenological consequences such as the CMB observables in multifield random landscape inflation. This leads us to rather strong large-N universality governing the CMB observables. For this purpose, we constructed ensembles of random scalar potentials for N_f interacting scalar fields using non-equilibrium random matrix theory, and used these to study the generation of observables during small-field inflation [34]. For $N_f = \mathcal{O}(\text{few})$, these heavily featured scalar potentials give rise to power spectra that are highly non-linear, at odds with observations. For $N_f \gg 1$, the super-horizon evolution of the perturbations is generically substantial, yet the power spectra simplify considerably and become more predictive, with most realisations being well approximated by a linear power spectrum. This provides proof of principle that complex inflationary physics can give rise to simple emergent power spectra. We explained how these results can be understood in terms of large N_f universality of random matrix theory.

Extending this analysis, we studied inflation in models with many interacting fields subject to randomly generated scalar potentials. We used methods from non-equilibrium random matrix theory to construct the potentials and an adaption of the 'transport method' to evolve the two-point correlators during inflation. This construction allows for an explicit study of models with up to 100 interacting fields supporting a period of 'approximately saddle-point' inflation [35]. We determined the statistical predictions for observables by generating over 30,000 models with 2–100 fields supporting at least 60 efolds of inflation. These studies lead us to seven lessons: i) Many-field inflation is not single-field inflation, ii) The larger the number of fields, the simpler and sharper the predictions, iii) Planck compatibility is not rare, but future experiments may rule out this class of models, iv) The smoother the potentials, the sharper the predictions, v) Hyperparameters can transition from stiff to sloppy, vi) Despite tachyons, isocurvature can decay, vii) Eigenvalue repulsion drives the predictions. We conclude that many of the 'generic predictions' of single-field inflation can be emergent features of complex inflation models.

3 Pole inflation, $f(R)$-gravity, and inflationary plateaus

Our next topic deals with the study of α-attractor/pole inflation models and their connection to $f(R)$ models of inflation, mainly using the bottom-up 4D effective description.

We studied a model of inflation with terms quadratic and logarithmic in the Ricci scalar,

where the gravitational action is $f(R) = R + \alpha R^2 + \beta R^2 \ln R$ [36]. These terms are expected to arise from one loop corrections involving matter fields in curved space-time. The spectral index n_s and the tensor to scalar ratio yield $10^{-4} \lesssim r \lesssim 0.03$ and $0.94 \lesssim n_s \lesssim 0.99$, i.e. r is an order of magnitude bigger or smaller than the original Starobinsky model which predicted $r \sim 10^{-3}$. Further enhancement of r gives a scale invariant $n_s \sim 1$ or higher. Other inflationary observables are $dn_s/d\ln k \gtrsim -5.2 \times 10^{-4}$, $\mu \lesssim 2.1 \times 10^{-8}$, $y \lesssim 2.6 \times 10^{-9}$.

We discussed the general structure and observational consequences of some of the simplest versions of chaotic inflation in supergravity in relation to the data by Planck 2013 and BICEP2 [37]. We showed that minimal modifications to the simplest quadratic potential are sufficient to provide a controllable tensor mode signal and a suppression of CMB power at large angular scales.

Inflationary attractors predict the spectral index and tensor-to-scalar ratio to take specific values that are consistent with Planck. An example is the universal attractor for models with a generalized non-minimal coupling, leading to Starobinsky inflation. We demonstrated that it also predicts a specific relation between the amplitude of the power spectrum and the number of e-folds [38]. The length and height of the inflationary plateau are related via the non-minimal coupling: in a wide variety of examples, the observed power normalization leads to at least 55 flat e-foldings. Prior to this phase, the inflationary predictions vary and can account for the observational indications of power loss at large angular scales.

Motivated by UV realisations of Starobinsky-like inflation models, we studied generic exponential plateau-like potentials to understand whether an exact $f(R)$-formulation may still be obtained when the asymptotic shift-symmetry of the potential is broken for larger field values [39]. Potentials which break the shift symmetry with rising exponentials at large field values only allow for corresponding $f(R)$-descriptions with a leading order term R^n with $1 < n < 2$, regardless of whether the duality is exact or approximate. The R^2-term survives as part of a series expansion of the function $f(R)$ and thus cannot maintain a plateau for all field values. We further found a lean and instructive way to obtain a function $f(R)$ describing $m^2\phi^2$-inflation which breaks the shift symmetry with a monomial, and corresponds to effectively logarithmic corrections to an $R + R^2$ model. These examples emphasise that higher order terms in $f(R)$-theory may not be neglected if they are present at all. Additionally, we related the function $f(R)$ corresponding to chaotic inflation to a more general Jordan frame set-up. In addition, we considered $f(R)$-duals of two given UV examples, both from supergravity and string theory. Finally, we outlined the CMB phenomenology of these models which show effects of power suppression at low-ℓ.

We also studied universality properties of inflationary models with a singular non-canonical kinetic term: a Laurent expansion of the kinetic function translates into a potential with a nearly shift-symmetric plateau in canonical fields. The shift symmetry can be broken at large field values by including higher-order poles, which need to be hierarchically suppressed in order not to spoil the inflationary plateau. The resulting corrections to the inflationary dynamics and predictions were shown to be universal at lowest order and possibly induce power loss at large angular scales [40]. At lowest order there are no corrections from a pole of just one order higher and we argued that this phenomenon is related to the well-known extended no-scale structure arising in string theory scenarios. We also outlined which other corrections may arise from string loop effects.

A generic non-minimal coupling can push any higher-order terms of the scalar potential sufficiently far out in field space to yield observationally viable plateau inflation. We provided analytic and numerical evidence that this generically happens for a non-minimal coupling strength

ξ of the order N_e^2 [41]. In this regime, the non-minimally coupled field is sub-Planckian during inflation and is thus protected from most higher-order terms. For larger values of ξ, the inflationary predictions converge towards the sweet spot of PLANCK. The latter includes $\xi \simeq 10^4$ obtained from CMB normalization arguments, thus providing a natural explanation for the inflationary observables measured.

4 Phenomenological consequences of features before and during inflation

In this section we analyze the impact of the features in the inflaton kinetic term or structure in the inflationary scalar potential, either right before the observable $\mathcal{O}(60)$ e-folds of slow-roll, or as periodic features along the scalar potential, on the CMB phenomenology, such as the 2-point or 3-point correlation functions ('non-Gaussianity') of the curvature perturbations. We begin with two observations, which show degeneracies in the shape function of non-Gaussianity between DBI inflation [42] and axion monodromy with a spectrum of periodic corrections, as well the curvature perturbation 2-point function of two suitably related models of canonical and non-canonical inflation.

As an example of the first kind, we discussed the effect of superimposing multiple sources of resonant non-Gaussianity, which arise for instance in models of axion inflation [43]. The resulting sum of oscillating shape contributions can be used to "Fourier synthesize" different non-oscillating shapes in the bispectrum. As an example we reproduced an approximately equilateral shape from the superposition of $\mathcal{O}(10)$ oscillatory contributions with resonant shape. This implies a possible degeneracy between the equilateral-type non-Gaussianity typical of models with non-canonical kinetic terms, such as DBI inflation, and an equilateral-type shape arising from a superposition of resonant-type contributions in theories with canonical kinetic terms. The absence of oscillations in the 2-point function together with the structure of the resonant N-point functions, imply that detection of equilateral non-Gaussianity at a level greater than the PLANCK sensitivity of $f_{NL} \sim \mathcal{O}(5)$ will rule out a resonant origin. We commented on the questions arising from possible embeddings of this idea in a string theory setting.

Next, we looked for potential observational degeneracies between canonical and non-canonical models of inflation of a single field ϕ [44]. Non-canonical inflationary models are characterized by higher than linear powers of the standard kinetic term X in the effective Lagrangian $p(X, \phi)$ and arise for instance in the context of the Dirac–Born–Infeld (DBI) action in string theory. An on-shell transformation was introduced that transforms non-canonical inflationary theories to theories with a canonical kinetic term. The 2-point function observables of the original non-canonical theory and its canonical transform were found to match in the case of DBI inflation.

We then moved towards features of the inflationary scalar potential such as 'steepening' just outside the field range corresponding to the last observable $\simeq 60$ e-folds of slow-roll. We showed that models of 'just enough' inflation, where the slow-roll evolution lasted only 50–60 e-foldings, feature modifications of the CMB power spectrum at large angular scales [45]. We performed a systematic and model-independent analysis of any possible non-slow-roll background evolution prior to the final stage of slow-roll inflation. We found a high degree of universality since most common backgrounds like fast-roll evolution, matter or radiation-dominance give rise to a power loss at large angular scales and a peak together with an oscillatory behavior at scales around the value of the Hubble parameter at the beginning of slow-roll inflation. Depending on the

value of the equation of state parameter, different pre-inflationary epochs lead instead to an enhancement of power at low-ℓ, and so seem disfavored by the observational hints for a lack of CMB power at $\ell \lesssim 40$. We also commented on the importance of initial conditions and the possibility to have multiple pre-inflationary stages.

Besides features in the scalar potential itself, the presence of a spectrum of 'spectator' scalar fields during inflation can significantly modify the properties of the curvature perturbation n-point functions. We presented a complete framework for numerical calculation of the power spectrum and bispectrum in canonical inflation with an arbitrary number of light or heavy fields [46]. Our method includes all relevant effects at tree-level in the loop expansion, including (i) interference between growing and decaying modes near horizon exit; (ii) correlation and coupling between species near horizon exit and on super-horizon scales; (iii) contributions from mass terms; and (iv) all contributions from coupling to gravity. We tracked the evolution of each correlation function from the vacuum state through horizon exit and the superhorizon regime, with no need to match quantum and classical parts of the calculation; when integrated, our approach corresponds exactly with the tree-level Schwinger or 'in-in' formulation of quantum field theory. We gave the equations necessary to evolve all two- and three-point correlation functions together with suitable initial conditions. The final formalism is suitable to compute the amplitude, shape, and scale dependence of the bispectrum in models with $|f_{NL}|$ of order unity or less, which are a target for galaxy surveys such as Euclid, DESI and LSST. As an illustration we applied our framework to a number of examples, obtaining quantitatively accurate predictions for their bispectra.

We also discussed a particular source of deviations from standard slow-roll inflation which arise when the asymptotic past vacuum state of quantum fields during inflation itself gets modified. When modeling inflaton fluctuations as a free quantum scalar field, the initial vacuum is conventionally imposed at the infinite past. This is called the Bunch–Davies (BD) vacuum. If however an asymptotically Minkowskian past does not exist, this requires modifications. We derived corrections to the scalar spectral index n_s and the tensor tilt n_t descending from arbitrary mixed states or from explicit non-BD initial conditions [47]. The former may stem from some pre-inflationary background and can redshift away whereas the latter are induced by a time-like hypersurface parametrizing a physical cut-off. In both cases, we found that corrections scale in parts or fully as $\mathcal{O}(\epsilon)$ where ϵ is the first slow-roll parameter. The precise observational footprint is hence dependent on the model driving inflation. Further, we showed how the inflationary consistency relation is altered. We thus provided an analytic handle on possible high scale or pre-inflationary physics.

5 False-vacuum tunneling and its consequences for the initial conditions of inflation

The string landscape relies on tunneling processes as a cosmological dynamics to physically populate its set of discrete meta-stable vacua. One such process is Coleman–De Luccia (CDL) tunneling in QFT on curved space-time [48]. As this instanton is ubiquitous (though not always the dominant tunneling instanton) in the string landscape, we analyzed its consequence for the initial conditions of a stage of slow-roll inflation taking place after tunneling inside a bubble of lowered vacuum energy formed by the CDL process.

At first, we showed the absence of the usual parametrically large overshoot problem of small-field inflation if initiated by a CDL tunneling transition from an earlier vacuum in the

limit of small inflationary scale compared to the tunneling scale [49] building on prior results of [50]. For low-power monomial exit potentials $V(\phi) \sim \phi^n$, $n < 4$, we derived an expression for the amount of overshoot. This is bounded from above by the width of the steep barrier traversed after emerging from tunneling and before reaching a slow-roll region of the potential. For $n \geq 4$ we showed that overshooting is entirely absent. We extended this result through binomials to a general potential written as a series expansion, and to the case of arbitrary finite initial speed of the inflaton. This places the phase space of initial conditions for small-field and large-field inflation on the same footing in a landscape of string theory vacua populated via CDL tunneling.

Next, we presented exact bounce solutions and amplitudes for tunneling in i) a piecewise linear-quartic potential and ii) a piecewise quartic-quartic potential [51]. We cross checked their correctness by comparing with results obtained through the thin-wall approximation and with a piecewise linear-linear potential.

We close this discussion with an analysis of the effects of the kinks in using kinked scalar potential for deriving exact CDL solutions. This is due to the fact, that Coleman tunneling in a general scalar potential with two non-degenerate minima is known to have an approximation in terms of a piecewise linear triangular-shaped potential with sharp 'kinks' at the place of the local minima. This approximate potential has a regime where the existence of the bounce solution needs the scalar field to 'wait' for some amount of Euclidean time at one of the 'kinks'. We discussed under which conditions a kink approximation of locally smooth 'cap' regions provides a good estimate for the bounce action [52].

6 From slow-rolling scalar fields to the EW vacuum – implications of inflaton-Higgs portal couplings and string theory constraints

Models of axions with large field ranges in string theory based on axion monodromy may provide both for models of inflation including portal-like couplings to the Standard Model (SM) Higgs sector, and relaxation-like slow-roll dynamics which may explain the electroweak (EW) hierarchy [53]. We analyzed phenomenological consequences of such setups for the stability of the EW vacuum as well as possible UV completion of Higgs relaxation dynamics in string theory.

Within the Standard Model, the Higgs and top quark data favor metastability of the electroweak vacuum, although the uncertainties are still significant. The true vacuum is many orders of magnitude deeper than ours and the barrier separating the two is tiny compared to the depth of the well. This raises a cosmological question: how did the Higgs field get trapped in the shallow minimum and why did it stay there during inflation? The Higgs initial conditions before inflation must be fine-tuned to about one part in 10^8 in order for the Higgs field to end up in the right vacuum. We show that these problems can be resolved if there is a small positive coupling between the Higgs and the inflaton [54].

We examined the relaxion mechanism [53] in string theory. An essential feature is that an axion winds over $N \gg 1$ fundamental periods. In string theory realizations via axion monodromy, this winding number corresponds to a physical charge carried by branes or fluxes. We showed that this monodromy charge backreacts on the compact space, ruining the structure of the relaxion action. In particular, the barriers generated by strong gauge dynamics have

height $\propto e^{-N}$, so the relaxion does not stop when the Higgs acquires a vev [55]. Backreaction of monodromy charge can therefore spoil the relaxion mechanism.

7 Moduli stabilization and de Sitter vacua in string theory

Here we report on a series of works, which established both a very general necessary condition for de Sitter (dS) vacua in 4D $\mathcal{N} = 1$ supergravity, and derived explicitly sufficient conditions from the leading-order quantum corrected Kähler moduli spaces in the context of a class of moduli stabilized Calabi–Yau compactifications of type IIB and heterotic string theory.

We started by performing a general analysis on the possibility of obtaining metastable vacua with spontaneously broken N=1 supersymmetry and non-negative cosmological constant in the moduli sector of string models [56]. More specifically, we studied the condition under which the scalar partners of the Goldstino are non-tachyonic, which depends only on the Kähler potential. This condition is not only necessary but also sufficient, in the sense that all of the other scalar fields can be given arbitrarily large positive square masses if the superpotential is suitably tuned. We considered both heterotic and orientifold string compactifications in the large-volume limit and showed that the no-scale property shared by these models severely restricts the allowed values for the 'sGoldstino' masses in the superpotential parameter space. We found that a positive mass term may be achieved only for certain types of compactifications and specific Goldstino directions. Additionally, we showed how sub-leading corrections to the Kähler potential which break the no-scale property may allow to lift these masses.

Next, we extended our discussion of necessary conditions for dS vacua in supergravity to the related case of slow-roll inflation. For this purpose, we performed a general algebraic analysis on the possibility of realizing slow-roll inflation in the moduli sector of string models [57]. This problem turned out to be very closely related to the characterization of models admitting metastable vacua with non-negative cosmological constant. In fact, we showed that the condition for the existence of viable inflationary trajectories is a deformation of the condition for the existence of metastable de Sitter vacua. This condition depends on the ratio between the scale of inflation and the gravitino mass and becomes stronger as this parameter grows. After performing a general study within arbitrary supergravity models, we analyzed the implications of our results in several examples. More concretely, in the case of heterotic and orientifold string compactifications on a Calabi–Yau in the large volume limit we showed that there may exist fully viable models, allowing both for inflation and stabilization. Additionally, we showed that sub-leading corrections breaking the no-scale property shared by these models always allow for slow-roll inflation but with an inflationary scale suppressed with respect to the gravitino scale. A scale of inflation larger than the gravitino scale can also be achieved under more restrictive circumstances and only for certain types of compactifications.

After studying the necessary conditions for dS vacua in 4D $\mathcal{N} = 1$ supergravity, we generalized the analysis to extended supersymmetry. Hence, we studied the stability of vacua with spontaneously broken supersymmetry in N=2 supergravity theories with only hypermultiplets [58]. Focusing on the projection of the scalar mass matrix along the sGoldstino directions, we were able to derive a universal upper bound on the lowest mass eigenvalue. This bound only depends on the gravitino mass and the cosmological constant, but not on the details of the quaternionic manifold spanned by the scalar fields. Comparing with the Breitenlohner–Freedman bound showed that metastability requires the cosmological constant to be smaller than a certain negative critical value. Therefore, only AdS vacua with a sufficiently negative

cosmological constant can be stable, while Minkowski and dS vacua necessarily have a tachyonic direction.

In a first step towards handling dS vacua in string theory, we developed a method for constructing metastable de Sitter vacua in N=1 supergravity models describing the no-scale volume moduli sector of Calabi–Yau string compactifications [59]. We considered both heterotic and orientifold models. Our main guideline was the necessary condition for the existence of metastable vacua coming from the Goldstino multiplet, which constrains the allowed scalar geometries and supersymmetry-breaking directions. In the simplest non-trivial case where the volume is controlled by two moduli, this condition simplifies and turns out to be fully characterised by the intersection numbers of the Calabi–Yau manifold. We analyzed this case in detail and showed that once the metastability condition is satisfied it is possible to reconstruct in a systematic way the local form of the superpotential that is needed to stabilize all the fields. We applied this procedure to construct some examples of models where the superpotential takes a realistic form allowed by flux backgrounds and gaugino condensation effects, for which a viable vacuum arises without the need of invoking corrections to the Kähler potential breaking the no-scale property or uplifting terms. We also discussed the prospects of constructing potentially realistic models along these lines.

Based on this analysis of necessary conditions for dS vacua in supergravity, we moved on to construct two classes of explicit dS vacua based on Calabi–Yau compactifications of type IIB and of heterotic string theory. The structure of the leading quantum corrections to the Kähler moduli space of these string compactifications played a crucial role here.

For the first class of dS vacua, we derived a sufficient condition for realizing them within type IIB string theory flux compactifications with spontaneously broken supersymmetry [60]. There are a number of 'lamp post' constructions of de Sitter vacua in type IIB string theory and supergravity. We showed that one of them – the method of 'Kähler uplifting' by F-terms from an interplay between non-perturbative effects and the leading α'-correction [2, 3] – allows for a more general parametric understanding of the existence of de Sitter vacua. The result is a condition on the values of the flux induced superpotential and the topological data of the Calabi–Yau compactification, which guarantees the existence of a meta-stable de Sitter vacuum if met. Our analysis explicitly included the stabilization of all moduli, i.e. the Kähler, dilaton and complex structure moduli, by the interplay of the leading perturbative and non-perturbative effects at parametrically large volume.

Next, we constructed an explicit example of a de Sitter vacuum in type IIB string theory that realizes the proposal of Kähler uplifting [61]. As the large volume limit in this method depends on the rank of the largest condensing gauge group we carried out a scan of gauge group ranks over the Kreuzer–Skarke set of toric Calabi–Yau three-folds. We found large numbers of models with the largest gauge group factor easily exceeding a rank of one hundred. We constructed a global model with Kähler uplifting on a two-parameter model on $\mathbb{CP}^4_{11169}$, by an explicit analysis from both the type IIB and F-theory point of view. The explicitness of the construction lies in the realization of a D7 brane configuration, gauge flux and RR and NS flux choices, such that all known consistency conditions are met and the geometric moduli are stabilized in a metastable de Sitter vacuum with spontaneous GUT scale supersymmetry breaking driven by an F-term of the Kähler moduli.

We then studied in detail the exhaustive construction method of all flux vacua of the Green–Plesser invariant subsector of a Calabi–Yau consistent with tadpole constraints. To do so, we explicitly constructed all supersymmetric flux vacua of a particular Calabi–Yau compactification of type IIB string theory for a small number of flux carrying cycles and a given D3-brane

tadpole [62]. The analysis was performed in the large complex structure region by using the polynomial homotopy continuation method, which allows to find all stationary points of the polynomial equations that characterize the supersymmetric vacuum solutions. The number of vacua as a function of the D3 tadpole is in agreement with statistical studies in the literature. We calculated the available tuning of the cosmological constant from fluxes and extrapolate to scenarios with a larger number of flux carrying cycles. We also verified the range of scales for the moduli and gravitino masses found for a single explicit flux choice giving a Kähler uplifted de Sitter vacuum in the same construction.

We also constructed a class of dS vacua in the context of the heterotic $E_8 \times E_8'$ string compactified on Calabi–Yau manifolds or their orbifold limits. For this purpose, we performed a systematic analysis of moduli stabilization for weakly coupled heterotic string theory compactified on manifolds which are Calabi–Yau up to α'-effects [63]. We reviewed how to fix all geometric and bundle moduli in a supersymmetric way by fractional fluxes, the requirement of a holomorphic gauge bundle, and D-terms [64], using the addition of higher order perturbative contributions to W, non-perturbative and threshold effects. We then showed that α'-corrections to K lead to new stable Minkowski (or dS) vacua where the complex structure moduli Z and the dilaton are fixed supersymmetrically, while the fixing of the Kähler moduli at a lower scale leads to spontaneous SUSY breaking. The minimum lies at moderately large volumes of all geometric moduli, at a perturbative string coupling and at the right value of the GUT coupling. We also gave a dynamical derivation of anisotropic compactifications which allow for gauge coupling unification around 10^16 GeV. The gravitino mass can be anywhere between the GUT and TeV scale depending on the fixing of the Z-moduli. In general, these are fixed by turning on background fluxes, leading to a gravitino mass around the GUT scale since the heterotic 3-form flux does not contain enough freedom to tune W to small values. Moreover accommodating the observed value of the cosmological constant (CC) was a challenge. Low-energy SUSY could instead be obtained in particular situations where the gauge bundle is holomorphic only at a point-like sub-locus of Z-moduli space, or where the number of Z-moduli is small (like orbifold models), since in these cases one may fix all moduli without turning on any quantized flux. However tuning the CC is even more of a challenge in these cases.

The above heterotic de Sitter vacua utilize the presence of certain quantum corrections to the Kähler moduli sector at $\mathcal{O}(\alpha'^2)$. A similar type of corrections appears in the type IIB context as well. We analyzed this new $\mathcal{N} = 1$ string tree level correction at $\mathcal{O}(\alpha'^2)$ to the Kähler potential of the volume moduli of type IIB Calabi–Yau flux compactification and its impact on the moduli potential [65]. We found that it imposes a strong lower bound the Calabi–Yau volume in the Large Volume Scenario of moduli stabilization. For KKLT-like scenarios we found that consistency of the action imposes an upper bound on the flux superpotential $|W_0| \lesssim 10^{-3}$, while parametrically controlled survival of the KKLT minimum needs extreme tuning of W_0 close to zero. We also analyzed the Kähler uplifting mechanism showing that it can operate on Calabi–Yau manifolds where the new correction is present and dominated by the 4-cycle controlling the overall volume if the volume is stabilized at values $\mathcal{V} \gtrsim 10^3$. We discussed the phenomenological implication of these bounds on $\mathcal{V}$ in the various scenarios.

In a next step we performed a thorough analysis of the higher-derivative corrections to the Kähler moduli sector arising at $\mathcal{O}(\alpha'^3$ in string theory [66]. For this purpose, we started by reviewing the ghost-free four-derivative terms for chiral superfields in $\mathcal{N} = 1$ supersymmetry and supergravity. These terms induce cubic polynomial equations of motion for the chiral auxiliary fields and correct the scalar potential. We discussed the different solutions and argue that only one of them is consistent with the principles of effective field theory. Special attention

was paid to the corrections along flat directions which can be stabilized or destabilized by the higher-derivative terms. We then computed these higher-derivative terms explicitly for the type IIB string compactified on a Calabi–Yau orientifold with fluxes via Kaluza–Klein reducing the $(\alpha')^3 R^4$ corrections in ten dimensions for the respective $\mathcal{N} = 1$ Kähler moduli sector. We proved that together with flux and the known $(\alpha')^3$-corrections [67] the higher-derivative term stabilizes all Calabi–Yau manifolds with positive Euler number, provided the sign of the new correction is negative.

Based on these results, a full matching between the structure of the 10D $\mathcal{O}(\alpha'^3)$ R^4 correction and the 4D effective higher superspace derivative terms requires knowledge of the full structure of such 4D higher superspace derivative operators allowed in supergravity. The supersymmetric completion of such higher-derivative operators often requires introducing corrections to the scalar potential. Hence, we studied these corrections systematically in the context of theories with $\mathcal{N} = 1$ global and local supersymmetry in $D = 4$ focusing on ungauged chiral multiplets [68]. In globally supersymmetric theories the most general off-shell effective scalar potential can be captured by a dependence of the Kähler potential on additional chiral superfields. For supergravity we found a much richer structure of possible corrections. In this context we classified the leading order and next-to-leading order superspace derivative operators and determine the component forms of a subclass thereof. Moreover, we presented an algorithm that simplifies the computation of the respective on-shell action. As particular applications we studied the structure of the supersymmetric vacua for these theories and commented on the form of the corrections to shift-symmetric no-scale models. These results are relevant for the computation of effective actions for string compactifications and, in turn, for moduli stabilization and string inflation.

Models of 4D $\mathcal{N} = 1$ supergravity coupled to chiral multiplets with vanishing or positive scalar potential have been denoted as no-scale. Of particular interest in the context of string theory are models which additionally possess a shift-symmetry. In this case there exists a dual description of chiral models in terms of real linear multiplets. We classified all ungauged shift-symmetric no-scale supergravities in both formulations and verified that they match upon dualization [69]. Additionally, we commented on the realizations within effective supergravities descending from string compactifications.

We return to the topic of backreaction, but now in the context of meta-stable dS vacua. The historically first class of dS vacua in string theory relies on using an anti-D3-brane in a warped region of the Calabi–Yau manifold as a tunable source of SUSY breaking and positive vacuum energy on top of supersymmetric AdS vacuum where the volume moduli are stabilized using non-perturbative quantum effects. Using a 10D lift of non-perturbative volume stabilization in type IIB string theory we study the limitations for obtaining de Sitter vacua. Based on this we found that the simplest KKLT vacua with a single Kähler modulus stabilized by a gaugino condensate cannot be uplifted to de Sitter. Rather, the uplift flattens out due to stronger backreaction on the volume modulus than has previously been anticipated, resulting in vacua which are meta-stable and SUSY breaking, but that are always AdS [70]. However, we also showed that setups such as racetrack stabilization can avoid this issue. In these models it is possible to obtain supersymmetric AdS vacua with a cosmological constant that can be tuned to zero while retaining finite moduli stabilization. In this regime, it seems that de Sitter uplifts are possible with negligible backreaction on the internal volume. We exhibited this behavior also from the 10D perspective.

Finally, we come full circle to study the structure of the supersymmetric moduli spaces of $\mathcal{N} = 1$ and $\mathcal{N} = 2$ supergravity theories in AdS_4 backgrounds [71]. These moduli spaces underlie

all of the dS constructions discussed throughout this section. In the $\mathcal{N} = 1$ case, the moduli space cannot be a complex submanifold of the Kähler field space, but is instead real with respect to the inherited complex structure. In $\mathcal{N} = 2$ supergravity the same result holds for the vector multiplet moduli space, while the hypermultiplet moduli space is a Kähler submanifold of the quaternionic-Kähler field space. These findings are in agreement with AdS/CFT considerations.

8 Sequestering as solution to the cosmological constant problem

Stringy solutions to the cosmological constant (CC) problem rely on a variant of Weinberg's anthropic reasoning enabled by a very large landscape of discrete meta-stable dS vacua with varying vacuum energy. The landscape argument draws its strength in part from Weinberg's no-go theorem, which poses a stringent test for any form of adjustment or self-tuning solution to the CC problem. However, subtle non-local modifications of Einstein gravity coupled to shift and scale symmetry arguments similar to those which help protecting inflation models from dangerous quantum corrections may provide avenues for viable 4D models of 'sequestering' of the perturbative contributions to the vacuum energy.

In a series of papers Kaloper and Padilla proposed such a mechanism to sequester standard model vacuum contributions to the cosmological constant, see e.g. [72, 73]. We studied the consequences of embedding their proposal into a fully local quantum theory. In the original work, the bare cosmological constant Λ and a scaling parameter λ are introduced as global fields. We found that in the local case the resulting Lagrangian is that of a spontaneously broken conformal field theory where λ plays the role of the dilaton [74]. A vanishing or a small cosmological constant is thus a consequence of the underlying conformal field theory structure.

Kaloper and Padilla also proposed a mechanism of vacuum energy sequester as a means of protecting the observable cosmological constant from quantum radiative corrections. The original proposal was based on using global Lagrange multipliers, but later a local formulation was provided [73]. Subsequently other interesting claims of a different non-local approach to the cosmological constant problem were made, based again on global Lagrange multipliers. Given this situation, we examined some of these proposals and find their mutual relationship. We explained that the proposals which do not treat the cosmological constant counterterm as a dynamical variable require fine tunings to have acceptable solutions [75]. Furthermore, the counterterm often needs to be retuned at every order in the loop expansion to cancel the radiative corrections to the cosmological constant, just like in standard GR. These observations are an important reminder of just how the proposal of vacuum energy sequester avoids such problems.

9 Large-scale structure, lensing effects and the determination of H_0

In this series of works we discuss the effects which perturbation-induced stochastic luminosity-distance dispersion and gravitational weak lensing have on the precision determination of cosmological parameters such as e.g. H_0 which underlie our current test of models of dark energy or cosmological inflation.

Starting from the luminosity-redshift relation given up to second order in the Poisson gauge, we calculated the effects of the realistic stochastic background of perturbations of the so-called concordance model on the combined light-cone and ensemble average of various functions of the luminosity distance, and on their variance, as functions of redshift [76]. We applied a gauge-invariant light-cone averaging prescription which is free from infrared and ultraviolet divergences, making our results robust with respect to changes of the corresponding cutoffs. Our main conclusions were that such inhomogeneities not only cannot avoid the need for dark energy, but also cannot prevent, in principle, the determination of its parameters down to an accuracy of order $10^{-3} \dots 10^{-5}$, depending on the averaged observable and on the regime considered for the power spectrum. However, taking into account the appropriate corrections arising in the non-linear regime, we predicted an irreducible scatter of the data approaching the 10% level which, for limited statistics, will necessarily limit the attainable precision. The predicted dispersion appears to be in good agreement with current observational estimates of the distance-modulus variance due to Doppler and lensing effects (at low and high redshifts, respectively), and represents a challenge for future precision measurements.

The (absence of detecting) lensing dispersion of Supernovae type Ia (SNIa) can be used as an extremely efficient probe of cosmology. In this example we analyzed its consequences for the primordial power spectrum [77]. The main setback is the knowledge of the power spectrum in the non-linear regime, $1\mathrm{Mpc}^{-1} < k < 10^2 \dots 10^3 \mathrm{Mpc}^{-1}$ up to redshift of about unity. By using the lensing dispersion and conservative estimates in this regime of wave numbers, we showed how the current upper bound $\sigma_\mu(z = 1) < 0.12$ on existing data gives strong indirect constraints on the primordial power spectrum. The probe extends our handle on the spectrum to a total of 12–15 inflation e-folds. These constraints are so strong that they are already ruling out a large portion of the parameter space allowed by PLANCK for running $\alpha = dn_s/d\ln k$ and running $\beta = d^2 n_s/d\ln k^2$. The bounds follow a linear relation to a very good accuracy. A conservative bound disfavors any enhancement above the line $\beta(k_0) = 0.036 - 0.42\alpha(k_0)$ and a realistic estimate disfavors any enhancement above the line $\beta(k_0) = 0.022 - 0.44\alpha(k_0)$.

Local measurements of the Hubble expansion rate are affected by structures like galaxy clusters or voids. We presented a fully relativistic treatment of this effect, studying how clustering modifies the mean distance (modulus)-redshift relation and its dispersion in a standard ΛCDM universe [78]. The best estimates of the local expansion rate stem from supernova observations at small redshifts ($0.01 < z < 0.1$). It is interesting to compare these local measurements with global fits to data from cosmic microwave background anisotropies. In particular, we argued that cosmic variance (i.e. the effects of the local structure) is of the same order of magnitude as the current observational errors and must be taken into account in local measurements of the Hubble expansion rate.

Probing the primordial power spectrum at small scales is crucial for discerning inflationary models. We demonstrated this necessity by briefly reviewing single small field models that give a detectable gravitational waves signal, thus being degenerate with large field models on CMB scales [79]. A distinct prediction of these small field models is an enhancement of the power spectrum at small scales, lifting up the degeneracy. We proposed a way to detect this enhancement, and more generally, different features in the power spectrum at small scales $1 \lesssim k \lesssim 10^2 \dots 10^3\,\mathrm{Mpc}^{-1}$ by considering the existing data of lensing dispersion in Type Ia supernovae. We showed that for various deviations from the simplest $n_s \simeq 0.96$ the lensing dispersion cuts considerably into the allowed parameter space by PLANCK and constrains the spectrum to smaller scales beyond the reach of other current data sets.

We studied soft limits of correlation functions for the density and velocity fields in the theory

of structure formation [80]. First, we re-derived the (resummed) consistency conditions at unequal times using the eikonal approximation. These are solely based on symmetry arguments and are therefore universal. Then, we explore the existence of equal-time relations in the soft limit which, on the other hand, depend on the interplay between soft and hard modes. We scrutinize two approaches in the literature: The time-flow formalism, and a background method where the soft mode is absorbed into a locally curved cosmology. The latter has been used to set up (angular averaged) 'equal-time consistency relations'. We explicitly demonstrated that the time-flow relations and 'equal-time consistency conditions' are only fulfilled at the linear level, and fail at next-to-leading order for an Einstein–de Sitter universe. While applied to the velocities both proposals break down beyond leading order, we found that the 'equal-time consistency conditions' quantitatively approximates the perturbative results for the density contrast. Thus, we generalized the background method to properly incorporate the effect of curvature in the density and velocity fluctuations on short scales, and discussed the reasons behind this discrepancy.

Local measurements of the Hubble expansion rate are affected by structures like galaxy clusters or voids. We presented a fully relativistic treatment of this effect, studying how clustering modifies the dispersion of the mean distance (modulus)-redshift relation in a standard ΛCDM universe [81]. Our findings were that cosmic variance (i.e. the effects of the local structure) is, for supernova observations at small redshifts ($0.01 < z < 0.1$), of the same order of magnitude as the current observational errors. The cosmic variance has to be taken into account in local measurements of the Hubble expansion rate and it reduces the tension with the CMB measurement.

We provided predictions on small-scale cosmological density power spectrum from supernova lensing dispersion [82]. Parameterizing the primordial power spectrum with running α and running of running β of the spectral index, we exclude large positive α and β parameters which induce too large lensing dispersions over current observational upper bound. We ran cosmological N-body simulations of collisionless dark matter particles to investigate non-linear evolution of the primordial power spectrum with positive running parameters. The initial small-scale enhancement of the power spectrum is largely erased when entering into the non-linear regime. For example, even if the linear power spectrum at $k > 10h \times \mathrm{Mpc}^{-1}$ is enhanced by 1 to 2 orders of magnitude, the enhancement much decreases to a factor of 2 to 3 at late time ($z \leq 1.5$). Therefore, the lensing dispersion induced by the dark matter fluctuations weakly constrains the running parameters. When including baryon-cooling effects (which strongly enhance the small-scale clustering), the constraint is comparable or tighter than the PLANCK constraint, depending on the UV cut-off.

10 PhD-theses and review articles

This work described above was also part of a number of PhD-theses. These are [83–86].

Furthermore, our work has been supplemented by a short review of string cosmology [87]. We wish to connect string-scale physics as closely as possible to observables accessible to current or near-future experiments. Our possible best hope to do so is a description of inflation in string theory. The energy scale of inflation can be as high as that of Grand Unification (GUT). If this is the case, this is the closest we can possibly get in energy scales to string-scale physics. Hence, GUT-scale inflation may be our best candidate phenomenon to preserve traces of string-scale dynamics. Our chance to look for such traces is the primordial gravitational wave, or

tensor mode signal produced during inflation. For GUT-scale inflation this is strong enough to be potentially visible as a B-mode polarization of the cosmic microwave background (CMB). Moreover, a GUT-scale inflation model has a trans-Planckian excursion of the inflaton scalar field during the observable amount of inflation. Such large-field models of inflation have a clear need for symmetry protection against quantum corrections. This makes them ideal candidates for a description in a candidate fundamental theory like string theory. At the same time the need of large-field inflation models for UV completion makes them particularly susceptible to preserve imprints of their string-scale dynamics in the inflationary observables, the spectral index n_s and the fractional tensor mode power r. Hence, we focussed in this review on axion monodromy inflation as a mechanism of large-field inflation in string theory.

References

[1] I. Ben-Dayan, S. Jing, A. Westphal and C. Wieck, *Accidental inflation from Kähler uplifting*, *JCAP* **1403** (2014) 054, [1309.0529].

[2] V. Balasubramanian and P. Berglund, *Stringy corrections to Kahler potentials, SUSY breaking, and the cosmological constant problem*, *JHEP* **11** (2004) 085, [hep-th/0408054].

[3] A. Westphal, *de Sitter string vacua from Kahler uplifting*, *JHEP* **03** (2007) 102, [hep-th/0611332].

[4] A. D. Linde and A. Westphal, *Accidental Inflation in String Theory*, *JCAP* **0803** (2008) 005, [0712.1610].

[5] V. Balasubramanian, P. Berglund, J. P. Conlon and F. Quevedo, *Systematics of moduli stabilisation in Calabi-Yau flux compactifications*, *JHEP* **03** (2005) 007, [hep-th/0502058].

[6] B. J. Broy, D. Ciupke, F. G. Pedro and A. Westphal, *Starobinsky-Type Inflation from α'-Corrections*, *JCAP* **1601** (2016) 001, [1509.00024].

[7] M. Cicoli, D. Ciupke, S. de Alwis and F. Muia, *α'-Inflation: moduli stabilisation and observable tensors from higher derivatives*, *JHEP* **09** (2016) 026, [1607.01395].

[8] M. Cicoli, C. P. Burgess and F. Quevedo, *Fibre Inflation: Observable Gravity Waves from IIB String Compactifications*, *JCAP* **0903** (2009) 013, [0808.0691].

[9] R. Kallosh, A. Linde, D. Roest, A. Westphal and Y. Yamada, *Fibre Inflation and α-attractors*, *JHEP* **02** (2018) 117, [1707.05830].

[10] R. Kallosh, A. Linde and D. Roest, *Superconformal Inflationary α-Attractors*, *JHEP* **11** (2013) 198, [1311.0472].

[11] M. Dias, J. Frazer, A. Retolaza, M. Scalisi and A. Westphal, *Pole N-flation*, 1805.02659.

[12] N. Arkani-Hamed, L. Motl, A. Nicolis and C. Vafa, *The String landscape, black holes and gravity as the weakest force*, *JHEP* **06** (2007) 060, [hep-th/0601001].

[13] F. G. Pedro and A. Westphal, *Low-ℓ CMB power loss in string inflation*, *JHEP* **04** (2014) 034, [1309.3413].

[14] J. E. Kim, H. P. Nilles and M. Peloso, *Completing natural inflation*, *JCAP* **0501** (2005) 005, [hep-ph/0409138].

[15] E. Silverstein and A. Westphal, *Monodromy in the CMB: Gravity Waves and String Inflation*, *Phys. Rev.* **D78** (2008) 106003, [0803.3085].

[16] L. McAllister, E. Silverstein and A. Westphal, *Gravity Waves and Linear Inflation from Axion Monodromy*, *Phys. Rev.* **D82** (2010) 046003, [0808.0706].

[17] N. Kaloper and L. Sorbo, *A Natural Framework for Chaotic Inflation*, *Phys. Rev. Lett.* **102** (2009) 121301, [0811.1989].

[18] I. Ben-Dayan, F. G. Pedro and A. Westphal, *Hierarchical Axion Inflation*, *Phys. Rev. Lett.* **113** (2014) 261301, [1404.7773].

[19] I. Ben-Dayan, F. G. Pedro and A. Westphal, *Towards Natural Inflation in String Theory*, *Phys. Rev.* **D92** (2015) 023515, [1407.2562].

[20] S. Kachru, R. Kallosh, A. D. Linde and S. P. Trivedi, *De Sitter vacua in string theory*, *Phys. Rev.* **D68** (2003) 046005, [hep-th/0301240].

[21] L. McAllister, E. Silverstein, A. Westphal and T. Wrase, *The Powers of Monodromy*, *JHEP* **09** (2014) 123, [1405.3652].

[22] R. Flauger, L. McAllister, E. Pajer, A. Westphal and G. Xu, *Oscillations in the CMB from Axion Monodromy Inflation*, *JCAP* **1006** (2010) 009, [0907.2916].

[23] R. Flauger, L. McAllister, E. Silverstein and A. Westphal, *Drifting Oscillations in Axion Monodromy*, *JCAP* **1710** (2017) 055, [1412.1814].

[24] W. Buchmuller, E. Dudas, L. Heurtier, A. Westphal, C. Wieck and M. W. Winkler, *Challenges for Large-Field Inflation and Moduli Stabilization*, *JHEP* **04** (2015) 058, [1501.05812].

[25] A. Retolaza, A. M. Uranga and A. Westphal, *Bifid Throats for Axion Monodromy Inflation*, *JHEP* **07** (2015) 099, [1504.02103].

[26] A. Hebecker, J. Moritz, A. Westphal and L. T. Witkowski, *Towards Axion Monodromy Inflation with Warped KK-Modes*, *Phys. Lett.* **B754** (2016) 328–334, [1512.04463]. [Erratum: Phys. Lett.B767,493(2017)].

[27] A. Hebecker, F. Rompineve and A. Westphal, *Axion Monodromy and the Weak Gravity Conjecture*, *JHEP* **04** (2016) 157, [1512.03768].

[28] L. E. Ibanez, M. Montero, A. Uranga and I. Valenzuela, *Relaxion Monodromy and the Weak Gravity Conjecture*, *JHEP* **04** (2016) 020, [1512.00025].

[29] A. Aazami and R. Easther, *Cosmology from random multifield potentials*, *JCAP* **0603** (2006) 013, [hep-th/0512050].

[30] D. Marsh, L. McAllister and T. Wrase, *The Wasteland of Random Supergravities*, *JHEP* **03** (2012) 102, [1112.3034].

[31] F. G. Pedro and A. Westphal, *The Scale of Inflation in the Landscape*, *Phys. Lett.* **B739** (2014) 439–444, [1303.3224].

[32] F. G. Pedro and A. Westphal, *Nonequilibrium random matrix theory: Transition probabilities*, *Phys. Rev.* **E95** (2017) 032144, [1606.07768].

[33] F. G. Pedro and A. Westphal, *Inflation with a graceful exit in a random landscape*, *JHEP* **03** (2017) 163, [1611.07059].

[34] M. Dias, J. Frazer and M. C. D. Marsh, *Simple emergent power spectra from complex inflationary physics*, *Phys. Rev. Lett.* **117** (2016) 141303, [1604.05970].

[35] M. Dias, J. Frazer and M. c. D. Marsh, *Seven Lessons from Manyfield Inflation in Random Potentials*, *JCAP* **1801** (2018) 036, [1706.03774].

[36] I. Ben-Dayan, S. Jing, M. Torabian, A. Westphal and L. Zarate, $R^2 \log R$ *quantum corrections and the inflationary observables*, *JCAP* **1409** (2014) 005, [1404.7349].

[37] R. Kallosh, A. Linde and A. Westphal, *Chaotic Inflation in Supergravity after Planck and BICEP2*, *Phys. Rev.* **D90** (2014) 023534, [1405.0270].

[38] B. J. Broy, D. Roest and A. Westphal, *Power Spectrum of Inflationary Attractors*, *Phys. Rev.* **D91** (2015) 023514, [1408.5904].

[39] B. J. Broy, F. G. Pedro and A. Westphal, *Disentangling the* $f(R)$ *- Duality*, *JCAP* **1503** (2015) 029, [1411.6010].

[40] B. J. Broy, M. Galante, D. Roest and A. Westphal, *Pole inflation – Shift symmetry and universal corrections*, *JHEP* **12** (2015) 149, [1507.02277].

[41] B. J. Broy, D. Coone and D. Roest, *Plateau Inflation from Random Non-Minimal Coupling*, *JCAP* **1606** (2016) 036, [1604.05326].

[42] M. Alishahiha, E. Silverstein and D. Tong, *DBI in the sky*, *Phys. Rev.* **D70** (2004) 123505, [hep-th/0404084].

[43] R. Gwyn, M. Rummel and A. Westphal, *Resonant non-Gaussianity with equilateral properties*, *JCAP* **1304** (2013) 040, [1211.0070].

[44] R. Gwyn, M. Rummel and A. Westphal, *Relations between canonical and non-canonical inflation*, *JCAP* **1312** (2013) 010, [1212.4135].

[45] M. Cicoli, S. Downes, B. Dutta, F. G. Pedro and A. Westphal, *Just enough inflation: power spectrum modifications at large scales*, *JCAP* **1412** (2014) 030, [1407.1048].

[46] M. Dias, J. Frazer, D. J. Mulryne and D. Seery, *Numerical evaluation of the bispectrum in multiple field inflation?the transport approach with code*, *JCAP* **1612** (2016) 033, [1609.00379].

[47] B. J. Broy, *Corrections to n_s and n_t from high scale physics*, *Phys. Rev.* **D94** (2016) 103508, [1609.03570]. [Addendum: Phys. Rev.D94,no.10,109901(2016)].

[48] S. R. Coleman and F. De Luccia, *Gravitational Effects on and of Vacuum Decay*, *Phys. Rev.* **D21** (1980) 3305.

[49] K. Dutta, P. M. Vaudrevange and A. Westphal, *The Overshoot Problem in Inflation after Tunneling*, *JCAP* **1201** (2012) 026, [1109.5182].

[50] B. Freivogel, M. Kleban, M. Rodriguez Martinez and L. Susskind, *Observational consequences of a landscape*, *JHEP* **03** (2006) 039, [hep-th/0505232].

[51] K. Dutta, C. Hector, P. M. Vaudrevange and A. Westphal, *More Exact Tunneling Solutions in Scalar Field Theory*, *Phys.Lett.* **B708** (2012) 309–313, [1110.2380].

[52] K. Dutta, C. Hector, T. Konstandin, P. M. Vaudrevange and A. Westphal, *Validity of the kink approximation to the tunneling action*, *Phys.Rev.* **D86** (2012) 123517, [1202.2721].

[53] P. W. Graham, D. E. Kaplan and S. Rajendran, *Cosmological Relaxation of the Electroweak Scale*, *Phys. Rev. Lett.* **115** (2015) 221801, [1504.07551].

[54] O. Lebedev and A. Westphal, *Metastable Electroweak Vacuum: Implications for Inflation*, *Phys.Lett.* **B719** (2013) 415–418, [1210.6987].

[55] L. McAllister, P. Schwaller, G. Servant, J. Stout and A. Westphal, *Runaway Relaxion Monodromy*, *JHEP* **02** (2018) 124, [1610.05320].

[56] L. Covi et al., *de Sitter vacua in no-scale supergravities and Calabi-Yau string models*, *JHEP* **06** (2008) 057, [0804.1073].

[57] L. Covi et al., *Constraints on modular inflation in supergravity and string theory*, *JHEP* **08** (2008) 055, [0805.3290].

[58] M. Gomez-Reino, J. Louis and C. A. Scrucca, *No metastable de Sitter vacua in N=2 supergravity with only hypermultiplets*, *JHEP* **02** (2009) 003, [0812.0884].

[59] L. Covi, M. Gomez-Reino, C. Gross, G. A. Palma and C. A. Scrucca, *Constructing de Sitter vacua in no-scale string models without uplifting*, *JHEP* **03** (2009) 146, [0812.3864].

[60] M. Rummel and A. Westphal, *A sufficient condition for de Sitter vacua in type IIB string theory*, *JHEP* **1201** (2012) 020, [1107.2115].

[61] J. Louis, M. Rummel, R. Valandro and A. Westphal, *Building an explicit de Sitter*, *JHEP* **1210** (2012) 163, [1208.3208].

[62] D. Martinez-Pedrera, D. Mehta, M. Rummel and A. Westphal, *Finding all flux vacua in an explicit example*, *JHEP* **1306** (2013) 110, [1212.4530].

[63] M. Cicoli, S. de Alwis and A. Westphal, *Heterotic Moduli Stabilisation*, *JHEP* **10** (2013) 199, [1304.1809].

[64] L. B. Anderson, J. Gray, A. Lukas and B. Ovrut, *Stabilizing All Geometric Moduli in Heterotic Calabi-Yau Vacua*, *Phys. Rev.* **D83** (2011) 106011, [1102.0011].

[65] F. G. Pedro, M. Rummel and A. Westphal, *Extended No-Scale Structure and α'-Corrections to the Type IIB Action*, 1306.1237.

[66] D. Ciupke, J. Louis and A. Westphal, *Higher-Derivative Supergravity and Moduli Stabilization*, *JHEP* **10** (2015) 094, [1505.03092].

[67] K. Becker, M. Becker, M. Haack and J. Louis, *Supersymmetry breaking and alpha-prime corrections to flux induced potentials*, *JHEP* **06** (2002) 060, [hep-th/0204254].

[68] D. Ciupke, *Scalar Potential from Higher Derivative $\mathcal{N} = 1$ Superspace*, 1605.00651.

[69] D. Ciupke and L. Zarate, *Classification of Shift-Symmetric No-Scale Supergravities*, *JHEP* **11** (2015) 179, [1509.00855].

[70] J. Moritz, A. Retolaza and A. Westphal, *Toward de Sitter space from ten dimensions*, *Phys. Rev.* **D97** (2018) 046010, [1707.08678].

[71] S. de Alwis, J. Louis, L. McAllister, H. Triendl and A. Westphal, *Moduli spaces in AdS_4 supergravity*, *JHEP* **05** (2014) 102, [1312.5659].

[72] N. Kaloper and A. Padilla, *Sequestering the Standard Model Vacuum Energy*, *Phys. Rev. Lett.* **112** (2014) 091304, [1309.6562].

[73] N. Kaloper, A. Padilla, D. Stefanyszyn and G. Zahariade, *Manifestly Local Theory of Vacuum Energy Sequestering*, *Phys. Rev. Lett.* **116** (2016) 051302, [1505.01492].

[74] I. Ben-Dayan, R. Richter, F. Ruehle and A. Westphal, *Vacuum energy sequestering and conformal symmetry*, *JCAP* **1605** (2016) 002, [1507.04158].

[75] G. D'Amico, N. Kaloper, A. Padilla, D. Stefanyszyn, A. Westphal and G. Zahariade, *An Ètude on global vacuum energy sequester*, *JHEP* **09** (2017) 074, [1705.08950].

[76] I. Ben-Dayan, M. Gasperini, G. Marozzi, F. Nugier and G. Veneziano, *Average and dispersion of the luminosity-redshift relation in the concordance model*, *JCAP* **1306** (2013) 002, [1302.0740].

[77] I. Ben-Dayan and T. Kalaydzhyan, *Constraining the primordial power spectrum from SNIa lensing dispersion*, *Phys. Rev.* **D90** (2014) 083509, [1309.4771].

[78] I. Ben-Dayan, R. Durrer, G. Marozzi and D. J. Schwarz, *The value of H_0 in the inhomogeneous Universe*, *Phys. Rev. Lett.* **112** (2014) 221301, [1401.7973].

[79] I. Ben-Dayan, *Lensing dispersion of SNIa and small scales of the primordial power spectrum*, in *Proceedings, 49th Rencontres de Moriond on Cosmology: La Thuile, Italy, March 15-22, 2014*, pp. 95–100, 2014, 1408.3004.

[80] I. Ben-Dayan, T. Konstandin, R. A. Porto and L. Sagunski, *On Soft Limits of Large-Scale Structure Correlation Functions*, *JCAP* **1502** (2015) 026, [1411.3225].

[81] G. Marozzi, I. Ben-Dayan, R. Durrer and D. J. Schwarz, *Impact of cosmic variance on the local measurement of H_0*, *PoS* **FFP14** (2016) 087.

[82] I. Ben-Dayan and R. Takahashi, *Constraints on small-scale cosmological fluctuations from SNe lensing dispersion*, *Mon. Not. Roy. Astron. Soc.* **455** (2016) 552–562, [1504.07273].

[83] C. Gross, *De Sitter vacua and inflation in no-scale string models*, Ph.D. thesis, Universität Hamburg, 2009. http://www-library.desy.de/cgi-bin/showprep.pl?thesis09-029.

[84] M. Rummel, *Vacua and Inflation in String Theory and Supergravity*, Ph.D. thesis, Universität Hamburg, 2013. http://www-library.desy.de/cgi-bin/showprep.pl?thesis13-026.

[85] B. J. Broy, *Inflation and Effective Shift Symmetries*, Ph.D. thesis, Universität Hamburg, 2016. 10.3204/PUBDB-2016-03859 http://ediss.sub.uni-hamburg.de/volltexte/2016/7986/.

[86] D. Ciupke, *Higher-Derivative Supergravity and String Cosmology*, Ph.D. thesis, Universität Hamburg, 2016. 10.3204/PUBDB-2016-03670 http://inspirehep.net/record/1501333/files/phd_thesis_final_pub.pdf.

[87] A. Westphal, *String cosmology – Large-field inflation in string theory*, *Int. J. Mod. Phys.* **A30** (2015) 1530024, [1409.5350].

Thermodynamics of Quantum Fields in Nonstationary Spacetimes

Klaus Fredenhagen[1], *Thomas-Paul Hack*[2], *Nicola Pinamonti*[3]

[1]II. Institut für Theoretische Physik, Universität Hamburg, Germany
[2]Institut für Theoretische Physik, Universität Leipzig, Germany
[3]Department of Mathematics, University of Genova, Italy and INFN, Sez. Genova, Italy

DOI: http://dx.doi.org/10.3204/PUBDB-2018-00782/C7

Quantum field theory (QFT) on non-stationary spacetimes is well understood from the side of the algebra of observables. The state space, however, is largely unexplored, due to the non-existence of distinguished states (vacuum, scattering states, thermal states). Project C7 of the SFB 676 was focused on characterisations of states by asymptotic conditions, e.g. holography (in case the boundary has sufficiently many symmetries), on a precise version of an approximate particle interpretation (for instance in Robertson–Walker spacetimes) and on the determination in terms of expectation values of locally covariant fields. Additionally, the backreaction of quantum matter fields on the curvature as well as the perturbative quantisation of the Einstein–Klein–Gordon system in the case of a cosmological background have been investigated. Finally, a detailed analysis and construction of equilibrium states for interacting field theories has been performed.

1 Introduction

Quantum field theory and General Relativity are two of the most successful physical theories ever developed. Their combination in a unified body is however still problematic. In spite of the many attempts, no universally accepted theory of quantum gravity is available in the literature. In the recent years many interesting features of an eventual theory of quantum gravity have been discovered by analysing the unification of the two theories in approximated regimes like semiclassical gravity. In quantum field theory on curved spacetime, gravity is still described by a classical curved spacetime while matter is modeled by quantum fields which propagate on that classical spacetime. In first approximation, their backreaction can be taken into account by means of the semiclassical Einstein equation

$$G_{ab} = 8\pi \langle T_{ab} \rangle_\omega$$

which is formally similar to the ordinary Einstein equation where the stress tensor of the classical matter is substituted with the expectation value of the stress tensor of quantum matter in a suitable state ω. This equation is meaningful only if the fluctuations of the stress tensor are small. Interesting and well known effects like Hawking radiation for black holes or particle creation in cosmology can be obtained in this approximation.

A physical scenario where these ideas can be tested is cosmology. Due to the homogeneity and isotropy hypothesis applicable in this case, the manifold describing the spacetime is $M = I \times \Sigma$ where I is a real interval representing time and Σ is the three dimensional manifold of space. The geometry is described by the Friedmann–Lemaître–Robertson–Walker (FLRW) metric

$$ds^2 = -dt^2 + a(t)^2 \left(\frac{1}{1-\kappa r^2} dr^2 + r^2 d\theta^2 + r^2 \sin\theta^2 d\varphi^2 \right) \tag{1}$$

where $\kappa \in \{-1, 0, 1\}$ distinguishes between open, flat or closed spatial sections and the scale factor $a(t)$ describes the way in which the universe evolves with respect to cosmological time. At present our spacetime appears to be almost spatially flat, for this reason we shall consider the case $\kappa = 0$ only. Due to the time-dependence present in the metric, concepts like temperature, energy, particles and vacuum states cannot be used – one is forced to rethink all of them.

In order to fully understand the behavior of quantum matter in cosmological spacetimes, as part of the SFB Project we have analysed the construction of regular states and discussed some of their thermodynamical aspects [1–3]. We have furthermore analysed the backreaction of quantum matter on curvature in the semiclassical approximation [4–6]. As a subsequent step, we have investigated the quantisation of the fluctuation of the matter-gravity system (Einstein–Klein–Gordon system) in the linear regime [7] and beyond [8]. We have discussed the form of gauge-invariant observables associated to this system when the background is chosen to be an FLRW spacetime [9]. Finally, more recently, we have rigorously constructed equilibrium states for perturbatively constructed interacting field theories [10, 11].

The project has been carried out using methods of Algebraic Quantum Field Theory. In this approach, quantisation is formulated in two steps. The first consists in the determination of the set of observables and of the algebraic relations among them. In particular, the commutation relations of the theory are implemented at this level. The second steps consists in the analysis of the form of physically relevant states of the system. While the first step is well under control at least for the case of free theories, the choice of a physically relevant state is more difficult and cannot be done using local properties of the spacetime only. The problem of finding regular states also on cosmological spacetimes based on their global properties is not straightforward and was the first point of the analysis performed in this project.

In the next chapter, we briefly outline the obtained results regarding the construction of regular states based on asymptotic spacetime properties and on the local notion of vacuum states. In the third chapter we review the results obtained in this project concerning the backreaction of quantum matter on the curvature induced by the semiclassical Einstein equation. The forth chapter contains a brief recollection of results obtained regarding the perturbative quantisation of the Einstein–Klein–Gordon system. Finally, we present the construction of equilibrium states for interacting field theory recently obtained in the framework of perturbative algebraic quantum field theory in the fifth chapter.

2 Regular states on curved spacetimes

In order to compute correlation functions on a curved spacetime and to analyse their thermal behavior it is necessary to have control on the state of the system. In particular, expectation values of local fields and their fluctuations need to be finite. This requirement constrains the possible quantum states and the class of Hadamard states satisfy this constraint [12]. It is

however not clear how to construct these states starting from initial conditions at some fixed time if the spacetime is not a-priori known.

In this section we discuss various methods developed within this project to construct regular states for a free quantum scalar field ϕ on curved backgrounds (M, g) which are globally hyperbolic spacetimes [13]. Similar results hold for more general types of fields [6]. The field we have in mind satisfies the equation

$$P\phi := -\Box\phi + \xi R\phi + m^2\phi = 0$$

where $\Box = \nabla_a\nabla^a$ is the d'Alembert operator, ξ is the coupling to the scalar curvature R and m is the mass of the field. The $*-$algebra of observables $\mathcal{A}$ associated to this field is generated by "smeared fields" $\phi(f)$ where $f \in \mathcal{D}(M)$, the set of compactly supported smooth functions. The product is such that it satisfies the canonical commutation relations

$$[\phi(f), \phi(h)] = i\Delta(f, h)$$

where $\Delta = \Delta_R - \Delta_A$ is the causal propagator of the theory which is equal to the retarded-minus-advanced fundamental solution of P, both of which are characterised by $P\Delta_{R/A}(f) = f$, $\mathrm{supp}\Delta_{R/A}(f) \subset J^{+/-}(\mathrm{supp}f)$. We recall that the fundamental solutions exist and are unique on globally hyperbolic spacetimes, see e.g. [14]. Since the field is uncharged, the involution $*$ coincides with the complex conjugation

$$\phi(f)^* = \phi(\overline{f}).$$

The algebra $\mathcal{A}$ is called on-shell if $\phi(Pf) = 0$ for every $f \in \mathcal{D}(M)$. If this is not the case, the algebra is said to be off-shell. In the latter case, the on-shell projection can be realised by restricting the physically relevant states of the system to those which satisfy the equation of motion

$$\omega(\phi(f_1)\dots\phi(Pg)\dots\phi(f_n)) = 0.$$

In the case of a free scalar field, a state ω is characterised by its $n-$point functions which are elements of $\mathcal{D}'(M^n)$, the set of distributions on smooth compactly supported functions, defined as

$$\omega_n(x_1, \dots, x_n) := \omega(\phi(x_1)\dots\phi(x_n)).$$

For Gaussian states, also called quasi-free states, the $n-$point functions with odd n vanish while those with even n are obtained from the two-point function as

$$\omega_{2n}(x_1, \dots, x_{2n}) = \sum_{i\in P_{2n}} \omega_2(x_{i_1}, x_{i_2})\dots\omega_2(x_{i_{2n-1}}, x_{i_{2n}})$$

where the sum is taken over all possible ordered sequences P_{2n} of $\{1, \dots, 2n\}$. A sequence i is said to be ordered and thus contained in P_n if $i_{2k-1} < i_{2k}$ and $i_{2k'-3} < i_{2k'-1}$ for $k \in \{1, \dots, n\}$ and $k' \in \{2, \dots, n\}$.

Here we shall concentrate our attention on Gaussian states and thus we have to care only about the two-point function

$$\omega_2(x_1, x_2) = \omega(\phi(x_1)\phi(x_2)).$$

As said before, the states we are considering need to be sufficiently regular to admit an extension to the algebra of local Wick polynomials which are pointlike products of fields and are realised

extending the test functions $(f_1, \ldots, f_n) \in \prod C_0^\infty(M)$ to distributions supported on the diagonal in M^n. Furthermore, the fluctuations of these fields need to be finite. In order to have these properties under control a sufficient condition is to require the state to be of Hadamard form.

A state of a free scalar field theory is of Hadamard form if on every normal neighborhood its two-point function can be expanded in the following way

$$\omega_2(x_1, x_2) = \lim_{\epsilon \to 0} \frac{U(x_1, x_2)}{\sigma_\epsilon(x_1, x_2)} + V(x_1, x_2) \log \sigma_\epsilon(x_1, x_2) + W(x_1, x_2) \tag{2}$$

where U, V are smooth functions on M^2 which are universal and depend only on the geometry and on the parameters present in the equation of motion, while W is a smooth function which characterises the state. Furthermore, $\sigma_\epsilon(x_1, x_2) = \sigma(x_1, x_2) + i\epsilon(T(x_1) - T(x_2))$ and σ is one half of the square of the geodesic distance taken with sign while T is any time function.

It is important to notice that Hadamard states are equivalently characterised by their wave front set. The wave front set of a distribution encodes its singular structure. In particular, it is a subset of the cotangent space whose projection on the spacetime gives the singular support of the distribution while the points in the fiber determine the directions of non-rapid decrease of the Fourier transform of the distribution localised in any neighborhood of the corresponding base point. The precise definition can be found in the book of Hörmander and it is used in the celebrated Hörmander criterion of multiplication of distributions.

The Hadamard state satisfies the "microlocal spectrum condition", namely, its wave front set is such that

$$WF(\omega_2) = \{(x_1, x_2; k_1, k_2) \in T^*M^2 \setminus \{0\} | (x_1, k_1) \sim (x_2, -k_2), k_1 \triangleright 0\} \tag{3}$$

where $(x_1, k_1) \sim (x_2, -k_2)$ if x_1 and x_2 are joined by a null geodesic and $g^{-1}k_1$ and $-g^{-1}k_2$ are the corresponding tangent vector with respect to an affine parametrisation. Furthermore, $k_1 \triangleright 0$ if k_1 is future directed. Radzikowski proved in [15] that a state is of Hadamard form if and only if it satisfies the microlocal spectrum condition. A generalisation of the microlocal spectrum condition to higher order Wick polynomials can be found in [16]. The microlocal spectrum condition can be understood as a covariant remnant of the spectrum condition usually employed in the case of vacuum states for quantum theories on flat spacetimes. It is a remarkable fact that this covariant remnant fixes the singular structure of the two-point function.

The characterisation of Hadamard states by means of the wave front set of the two-point function is quite useful. It is actually much easier to check if a state satisfies the microlocal spectrum condition, then to precisely control the singular structure of its two-point function. Standard results of microlocal analysis like Hörmander's propagation of singularity theorems can in fact be successfully employed.

2.1 States from asymptotic properties

As mentioned above it is not straightforward to get Hadamard states out of initial values if the spacetime is not known a priori. The problem is simpler when the initial values are given on null surface (characteristic initial value problem). In fact, in this situation the positive frequency condition present in the microlocal spectrum condition can be tested directly for the initial values. This is the basic idea at the heart of the construction of Hadamard states based on asymptotic initial values when the asymptotic past infinity (or more generally the asymptotic past boundary) is a causal cone. In the following we discuss these basic ideas in a more rigorous

form. Consider a spacetime M whose past boundary is a null cone $\mathcal{C}$ in another (conformally related) larger spacetime $\tilde{M}$. Due to the well-posedness of the Goursat problem, it is known that giving initial values on $\mathcal{C}$ fixes uniquely a solution of any hyperbolic equation in M.

As an application of the time slice axiom [17], we may thus construct a map from the on-shell algebra $\mathcal{A}(M) \to \mathcal{A}(C)$ which is an injective $*-$homomorphism. This is essentially done at the level of generators of the algebra $\mathcal{A}(M)$ and

$$\iota\phi(f) = \Psi(f_{\mathcal{C}}), \qquad f_{\mathcal{C}} = \Delta(f)|_{\mathcal{C}}$$

where the causal propagator Δ is seen in $\tilde{M}$ and $\Psi(f)$ are the generators of $\mathcal{A}(C)$. On C there is a notion of causality, it is thus possible to construct states which look like a vacuum, meaning that their spectrum contains only positive frequencies with respect to causal directions on $\mathcal{C}$. If we indicate such a state by Ω^+, it turns out that its pullback

$$\omega(A) = \iota^*\Omega^+(A) = \Omega^+(\iota(A))$$

defines a state in M which is an Hadamard state.

This idea has been used in various physical situation in order to determine the singular structure of known states:

- in the case of asymptotically flat spacetime to check the Hadamard property of asymptotically vacuum states for massless particles [18];
- in the case of asymptotically de Sitter spacetimes [1,2] to discuss the Hadamard properties of Bunch–Davies-like states;
- in the case of spacetimes possessing a null big bang scenario to control asymptotically vacuum states [19];
- in the case of Schwarzschild spacetime to prove that the Unruh state is of Hadamard form [20].

For a cosmological spacetime (M, g) with g as in (1), pure Gaussian states which are invariant under the spatial isometries of the metric have a two-point function of the form:

$$\omega_2(x_1, x_2) := \lim_{\epsilon\to 0^+} \frac{1}{8\pi^3 a(t_1)a(t_2)} \int_{\mathbb{R}^3} \chi_k(t_1)\overline{\chi_k(t_2)} e^{i\mathbf{k}\cdot(\mathbf{x}_1-\mathbf{x}_2)} e^{-k\epsilon} d\mathbf{k} \tag{4}$$

whereby $k = |\mathbf{k}|$ and the mode functions $\chi_k(\tau)$ satisfy the equation

$$\chi_k'' + (m^2a^2 + k^2)\chi_k + (6\xi - 1)\frac{a''}{a}\chi_k = 0,$$

where $'$ denotes the derivative with respect to conformal time τ obtained by integrating the relation $dt = ad\tau$, and the modes are normalised such that the following Wronskian condition

$$\overline{\chi_k}'\chi_k - \overline{\chi_k}\chi_k' = i$$

holds. The latter condition ensures that the antisymmetric part of ω_2 is proportional to the causal propagator of the theory [21]. As discussed above, it is not easy to find the modes χ_k for which ω_2 as in (4) correspond to an Hadamard state. The states which are asymptotic vacuum

states constructed with the pullback of ι discussed above, are usually quasi-free states of the from (4) and the modes have the asymptotic form

$$\chi_k(\tau) \underset{\tau\to-\infty}{\longrightarrow} \frac{e^{ik\tau}}{\sqrt{2k}}.$$

The construction of asymptotic vacuum states can be generalised to construct approximate KMS states. In particular, if the boundary state is a KMS state with respect to the characteristic translation, the obtained state in the bulk can be interpreted as an approximate KMS state and its two-point function is

$$\omega_2(x_1,x_2) := \lim_{\epsilon\to 0^+} \frac{1}{8\pi^3 a(t_1)a(t_2)} \int_{\mathbb{R}^3} \left(\frac{\overline{\chi_k(t_1)}\chi_k(t_2)}{1-e^{-\beta k_0}} + \frac{\chi_k(t_1)\overline{\chi_k(t_2)}}{e^{\beta k_0}-1} \right) e^{i\mathbf{k}\cdot(\mathbf{x}_1-\mathbf{x}_2)} e^{-k\epsilon} d\mathbf{k} \quad (5)$$

with $k_0 := |\mathbf{k}|$. Other approximate KMS states can now be constructed considering $k_0 := \sqrt{k^2+m^2a_F^2}$ for a fixed constant a_F. Further comments on this can be found in [3].

2.2 States of low energy

Olbermann proposed in [22] a way to select the mode functions χ_k in (4) in order to obtain a state which satisfies the microlocal spectrum condition. The idea is to find the modes which minimise the energy density smeared in a chosen smooth way along a fixed time interval.

For this reason these states are called states of low energy. Although they depend on the chosen smooth smearing function they can be interpreted as approximate vacuum states. Excitations of these states are natural candidates for approximate particle states, and first results have already been obtained in [23]. An interesting observation is that the number of particles is oscillating during the cosmological evolution. Whether this is an artefact of the approximation or a genuine physical effect has to be clarified.

Within this project, a further extension of these ideas to states which are locally in equilibrium has been discussed in the PhD thesis of Küskü [24].

2.3 Sorkin–Johnston states and generalisations thereof

On a static spacetime, the two-point function of the vacuum state of the theory can be obtained from the spectral decomposition of the causal propagator and its restriction to the positive part of the spectrum. A local version of this construction was proposed by Sorkin–Johnston, see [25] and reference therein. The basic difference between their idea and the above is to construct a local vacuum starting from the spectral decomposition of the causal propagator localised in some double cone region. Unfortunately, in general, the states obtained in this way do not satisfy the microlocal spectrum condition.

Within the present project, Brum and Fredenhagen in [26] showed that a smoothly smeared version of the Sorkin–Johnston construction results in a state which is of Hadamard form. To construct these states, one mollifies the sharp localisation of the causal propagator to a double cone $N \subset M$ by choosing a real-valued $f \in \mathcal{D}(M)$ such that f is equal to 1 on N. This function is then used to construct the operator

$$A := if\Delta f$$

which can be extended to act on the Hilbert space $L^2(M, d\mu_g)$. The operator obtained in this way is, at least on static and on FLRW spacetimes, bounded and self-adjoint, hence, by means of standard functional calculus, it is possible to extract its positive part

$$A^+ := \Pi^+ A$$

where Π^+ is the spectral projection on the interval $[0, |A|]$. The generalised Sorkin–Johnston state is now obtained by considering the quasifree state characterised by the two-point function associated to A^+:

$$\omega_2(h_1, h_2) := \left(h_1, A^+ h_2\right), \qquad h_i \in \mathcal{D}(N).$$

The state obtained in this way turns out to be a Hadamard state.

3 Semiclassical gravity

At first approximation, the influence of quantum matter on the curvature can be taken into account by means of the semiclassical Einstein equation

$$G_{ab} = \langle T_{ab} \rangle_\omega$$

whereby gravity is described by a classical curved spacetime. This equation is formally similar to the classical Einstein equation where the stress tensor of the classical matter is substituted with the expectation value of a the stress-tensor of some quantum field propagating on a curved background.

In the cosmological case, if the conservation equation of the stress tensor

$$\nabla^a \langle T_{ab} \rangle_\omega = 0$$

holds, the semiclassical Einstein equation is equivalent to

$$-R_a{}^a = 8\pi \langle T_a{}^a \rangle_\omega$$

up to an initial condition which fixes the amount of radiation present in the solution. In the expectation value $T = \langle T_a{}^a \rangle_\omega$ of the trace of the stress tensor we can recognize three contributions

$$-R_a{}^a = 8\pi \left(T_{state} + T_{anomalous} + T_{ren.freed.}\right)$$

corresponding to a state dependent part, an anomalous contribution due to the requirement of covariant conservation, see e.g. [27–29], and a contribution which can be interpreted as renormalisation freedom [30]. In the case of $\xi = 1/6$, the anomalous contribution is

$$T_{anomalous} = \frac{1}{8\pi^2}\left(\frac{1}{360}\left(C_{abcd}C^{abcd} + R_{ab}R^{ab} - \frac{R^2}{3} + \Box R\right) + \frac{m^4}{4}\right)$$

with the Weyl tensor C_{abcd}. The renormalisation freedom is

$$T_{ren.freed.} = \alpha m^4 + \beta m^2 R + \gamma \Box R,$$

whereas the state dependent contribution is

$$T_{state} = \frac{1}{8\pi^2} m^2 [W]$$

with $[W]$ indicating the coinciding point limit of the smooth part of the state's two-point function (2). With the choice $\gamma = 0$ and a suitable assumption on the state dependent contribution (considering it to be vanishing like in zeroth-order adiabatic states) and in the case of massive, conformally coupled fields, the equation for the trace is an ordinary differential equation

$$\dot{H}(H^2 - H_0^2) = -H^4 + 2H^2H_0^2 + M; \tag{6}$$

where $H = \dot{a}/a$ is the Hubble parameter and $\dot{\bullet}$ denotes a derivative with respect to cosmological time. The constants

$$H_0^2 = 180\pi \left(\frac{1}{G} - 8\pi m^2 \beta \right), \qquad M = \frac{15}{2} m^4 - 240\pi m^4 \alpha$$

depend on the renormalisation freedom. β can be interpreted as a renormalisation of the Newton constant and for this reason it can be fixed to be 0, α represents a renormalisation of the cosmological constant and can be set to model the present value of the measured constant.

The solution space of the differential equation (6) can be easily obtained. We notice in particular that there are two stable solutions, the first of which could describe the phase of rapid expansion present in the beginning of the universe, whereas the second one can model the present universe and its recent past. However, in this simplified model there is no mechanism which permits to exit the phase of rapid expansion. The oversimplifications present in the model are the following: the considered matter field is a free field, the role of higher derivatives which are present in the equation for a different choice of γ could have an important role and the state dependent contribution is not taken into account properly.

The results presented in this section are summarised in the paper [4]. Within this project it has been shown that similar results hold also when the matter is described by other fields like Dirac fields [6]. In particular, the trace anomaly, the form of stress tensor and the extended algebra of fields for Dirac fields has been analyzed in [5].

3.1 Rigorous analysis of the semiclassical equation

The state dependent contribution present in the trace makes the dynamical problem much more complicated, essentially because it is difficult to fix the state with a universal prescription that does not depend on the particular spacetime.

This problem has been rigorously studied in two cases. The first case considered were cosmological spacetimes which possess an initial null big bang phase. In fact, when the past boundary of M is a null surface, it is possible to use similar techniques like the ones discussed above in section 2.1. In this way it has been proved in [19] that the semiclassical Einstein equation leads to a well-posed initial value problem. This means that solutions exists and are unique, at least for small amounts of time after the null big bang.

Relaxing the request of having full Hadamard states, but considering adiabatic states of order 0 as given in [21] at a fixed time t_0, it was possible to extend the proof of existence also to this situation. The corresponding results have been summarised in [31], where it is proved that solutions of the semiclassical Einstein equation exist and are unique up to future infinity or up to the occurrence of a future blowup of the scale factor (big rip).

4 Quantum gravity and cosmological fluctuations

To go beyond the semiclassical approximation presented above, and to quantise the degrees of freedom of both matter and gravity fields, we have analyzed the quantisation of the fluctuations of the coupled Einstein–Klein–Gordon system, namely, a massive minimally coupled scalar field ϕ propagating over a Lorentzian spacetime (M, g) for which

$$R_{ab} - \frac{1}{2} R g_{ab} = 8\pi T_{ab}, \qquad -\Box\phi + m^2\phi + V'(\phi) = 0, \tag{7}$$

where T_{ab} are the components of the stress tensor of ϕ.

To discuss the linearised perturbation of the theory we consider a field configuration $\Gamma = (g, \phi)$ and expand it around a background solution Γ_0

$$\Gamma = (g, \phi) = \Gamma_0 + \lambda(\gamma, \varphi) + O(\lambda^2),$$

equations for (γ, φ) can now be obtained from (7).

In the case of perturbations in inflationary cosmological models, the background theory corresponds to an FLRW spacetime plus an inflaton ϕ which is constant in space.

The linearised perturbations (γ, φ) can be quantised using standard methods of algebraic quantum field theory on curved background in a manifestly covariant and gauge-invariant manner. Details of this construction are presented in the paper [7]. In particular, a non-local behavior shown by the quantum Bardeen potentials is obtained and it is furthermore shown that a similar effect is present in any local quantum field theory. Finally the known linearised equation for the Mukhanov–Sasaki variable is recovered in that formalism.

4.1 Beyond the linearised approximation

The perturbative construction of quantum gravity in a generally covariant way has been presented in [8]. This construction has been performed in the framework of locally covariant quantum field theory and the gauge problem has been treated by means of the renormalised Batalin–Vilkovisky formalism [32]. The problem of non-renormalisability of the theory persists and, hence, the theory is interpreted as an effective theory at large scales. In spite of this fact, the construction leads to a background-independent theory. Moreover, gauge-invariant observables are considered to be relational observables. This means that they are functionals of four scalar coordinate fields constructed which can be chosen as suitable curvature scalars, see also [33] for related work on these functionals. This idea can be used to construct gauge-invariant observables in cosmology in a simple way.

In the case of the Einstein–Klein–Gordon system the procedure works as follows. One selects 4 scalar fields $X^a_\Gamma, a = 1, \dots 4$, which are local functionals of the field configuration Γ which contains the spacetime metric g, the inflaton field ϕ and possibly other fields. The fields X^a_Γ are supposed to transform under diffeomorphisms χ as

$$X^a_{\chi^*\Gamma} = X^a_\Gamma \circ \chi\,. \tag{8}$$

We choose a background Γ_0 such that the map

$$X_{\Gamma_0} : x \mapsto (X^1_{\Gamma_0}, \dots, X^4_{\Gamma_0}) \tag{9}$$

is injective. We then set for Γ sufficiently near to Γ_0

$$\alpha_\Gamma = X_\Gamma^{-1} \circ X_{\Gamma_0}. \tag{10}$$

We observe that α_Γ transforms under diffeomorphisms as

$$\alpha_{\chi^*\Gamma} = \chi^{-1} \circ \alpha_\Gamma \,. \tag{11}$$

Let now A_Γ be any other scalar field which is a local functional of Γ and transforms under diffeomorphisms as in (8). Then the field

$$\mathcal{A}_\Gamma := A_\Gamma \circ \alpha_\Gamma \tag{12}$$

is invariant under diffeomorphisms and may be considered as a local observable. Note that invariance is obtained by shifting the argument of the field in a way which depends on the configuration.

In [9] this idea is used to show that the standard theory of cosmological perturbations arises as the linear order of a fully quantised perturbative theory of quantum gravity. In particular, in the way explained above, it was possible to obtain gauge-invariant local observables which can be used to generate perturbative invariant expressions at arbitrary order. The standard gauge-invariant observables of cosmological perturbation theory were obtained at first order and explicit expressions at second order were explicitly given. Due to the large degree of symmetry present in the case of cosmological backgrounds, the spatial coordinate fields have been selected to be harmonic coordinates. While this choice works perfectly at the classical level, the gauge invariant observables constructed with them display severe non-localities, which could create problems in the quantisation of the system. Further investigations are needed in order to clarify these points. The ideas of these project have been recently developed further in [34].

5 Perturbative algebraic quantum field theory and equilibrium states

Whenever an interacting theory is treated perturbatively, its elements are usually given as a formal series in the coupling constant. Three major problems arises in these kind of treatments:

- there are ultraviolet problems at each order in perturbation theories;
- there are infrared problems when the interaction Lagrangian is supported in a non compact domain;
- the perturbative series does not converge.

The first problem is nowadays well understood. The second problem can be treated analysing the adiabatic limits of the theory. Regarding the third problem, very little is known. In some integrable cases, usually in lower dimensional theories, it is nevertheless possible to compare perturbatively obtained results with exact ones. As an example the Sine–Gordon model can be treated both exactly and perturbatively. In [35] it is shown that the perturbative methods agrees with the exact treatment. Further developments can be found in [36].

During the development of the present project, methods of algebraic quantum field theory have been developed to treat non-linear theories perturbatively. In particular, the framework of

perturbative algebraic quantum field theory (pAQFT) was developed in [37]. Using this framework, it was possible to clarify the connections between Wilson's concept of the renormalisation group and the original concept of Stückelberg and Petermann. Furthermore, it was recently possible to construct rigorously equilibrium states for interacting theories in the adiabatic limit in [10] and in [11]. Central in this construction was the use of the time slice axiom proved in [17].

5.1 Perturbative algebraic quantum field theory

With the aim of discussing the construction of equilibrium (thermal) states for interacting theories, we briefly recall the main steps of pAQFT in the simple case of an interacting scalar field theory. The starting point is a concrete realisation of the observables as functionals of field configurations

$$\phi \in C^\infty(M;\mathbb{R}).$$

In order to be able to work with them we require that the observables are smooth local functionals, namely, their functional derivatives exist to all orders and at each order they are described by compactly supported distributions. Furthermore, the singular structure of these distributions must be under control. Hence, the observables of the theory are represented by the set of microcausal functionals

$$\mathcal{F}_{\mu c} = \left\{ F : \mathcal{C} \to \mathbb{C} \,\middle|\, \forall n \; F^{(n)} \in \mathcal{E}'(M^n), \mathrm{WF}(F^{(n)}) \cap (\overline{V}_+^n \cup \overline{V}_+^n) = \emptyset \right\}.$$

Among all possible elements of $\mathcal{F}_{\mu c}$ the regular ones are those whose functional derivatives are smooth functions. They correspond to the elements of the algebra generated by linear fields smeared by smooth test functions. The set of regular functionals is denoted by $\mathcal{F}_{reg}$ and it does not contain Wick polynomials. The local functionals are those whose functional derivatives are supported on the diagonals, they are denoted by $\mathcal{F}_{loc}$ and the Wick polynomials are contained in this set. The free algebra of observables can be constructed equipping microcausal functionals with the following product

$$F \star_\omega G = \mathcal{M} \exp\left(\frac{1}{2}\Gamma_\omega\right) F \otimes G$$

where $\mathcal{M}$ denotes the pointwise multiplication $\mathcal{M}(F \otimes G) = FG$ and

$$\Gamma_\omega = \int \omega_2(x,y) \frac{\delta}{\delta\phi(x)} \otimes \frac{\delta}{\delta\phi(y)}$$

where ω_2 is any two-point function of Hadamard form of the chosen free (linear) quantum theory. A two-point function of Hadamard form solves in particular the free equation of motion up to smooth functions, its antisymmetric part is proportional to the causal propagator of the free theory and its wave front set satisfies the microlocal spectrum condition (3).

The product defined above is well-posed among functionals which possess only a finite number of non-vanishing functional derivatives. It can however be used also among more general functionals if a suitable weaker notion of convergence is considered. This is for example the case if observables are formal power series whose coefficients are elements of $\mathcal{F}_{\mu c}$. When equipped with the involution defined by means of the complex conjugation as $F^*(\phi) = \overline{F(\phi)}$ the $(\mathcal{F}_{\mu c}, \star_\omega, *)$ represent the $*-$algebra of the Wick polynomial normal ordered with respect of ω. These are the observables of a free theory.

The canonical commutation relations are encoded in the form of the product $\star_\omega$, in fact, if one considers linear fields

$$F_f(\phi) = \int f\phi \, d\mu_g, \qquad f \in \mathcal{D}(M)$$

it holds that

$$[F_f, F_h]_{\star_\omega} = F_f \star_\omega F_h - F_h \star_\omega F_h = \omega(f,h) - \omega(h,f) = i\Delta(f,h)$$

where Δ is the causal propagator of the free theory, namely, the advanced-minus-retarded fundamental solution. These commutation relations do not depend on the particular form of the chosen Hadamard two-point function ω_2.

Even more, giving two Hadamard functions H, H', the map

$$\alpha_{H-H'} : (\mathcal{F}_{\mu c}, \star_{H'}, *) \to (\mathcal{F}_{\mu c}, \star_H, *)$$

defined by

$$\alpha_w F = \exp \frac{1}{2}\Gamma'_w F, \qquad \Gamma'_w = \int w(x,y) \frac{\delta^2}{\delta\phi(x)\phi(y)} d\mu_g(x) d\mu_g(y)$$

is actually a $*-$isomorphism between the two algebras.

If one restricts attention to the regular functionals, one obtains the well-known Borchers–Uhlmann algebra of fields. We stress that the algebra obtained here is off-shell, this is an essential step in order to be able to treat interactions perturbatively.

The observables associated to interacting field theories can be constructed by means of perturbation theory. To this end one has to consider the time-ordered product. This product satisfies certain requirements, a corresponding list of axioms can be found in [30]. The existence of time-ordered products of local Wick polynomials on curved spacetimes has been established in [38] and a covariant generalisation of this construction can be found in [39]. These constructive methods are generalisations of the inductive construction of Epstein–Glaser [40], according to which, at each inductive step n, the causal factorisation property permits to construct the time-ordered product of $n+1$ local fields up to the total diagonal in terms of the time-ordered products of n local fields. The extension to the total diagonal of the obtained distributions can be done by means of Steinmann-scaling-degree [41] techniques. The obtained time-ordered product is a map from multilocal functionals to microcausal functionals

$$T : \mathcal{F}_{\mathrm{loc}}^{\otimes n} \to \mathcal{F}_{\mu c}$$

and can be used to construct time-ordered exponentials (local S-matrices) of a local functional $V \in \mathcal{F}_{\mathrm{loc}}$

$$S(V) = \exp_T(V).$$

This time-ordered exponential is used to represent the interacting local fields in the free algebra by means of the Bogoliubov-map

$$R_V(F) := \frac{d}{d\lambda} S(V)^{-1} \star S(V + \lambda F)\Big|_{\lambda=0}.$$

The causal factorisation property at the level of S-matrices is such that for every $F, H, G \in \mathcal{F}_{\mathrm{loc}}$ with F later than G

$$S(F+G+H) = S(F+G) \star S(G)^{-1} \star S(G+H),$$

whereby F is said to be later then G if $\mathrm{supp}F \cap J^-(\mathrm{supp}G) = \emptyset$.

The interacting algebra is considered to be the algebra generated by the images of local fields under the Bogoliubov map

$$\mathcal{F}_I \subset \mathcal{F}_{\mu c}.$$

States for the interacting algebra are characterised by their expectation values on $\mathcal{F}_I$. Hence, every state of the free theory can be promoted to a state for the interacting theory by simply composing it with the Bogoliubov-map (or, rather, products of Bogoliubov-maps applied to the generators of the interacting algebra). However, the physical meaning of a given state changes. In particular, in the case of a Minkowski spacetime, the free vacuum and equilibrium states of the theory are not mapped to vacuum and equilibrium states of the interacting theory. However, in the adiabatic limit, the vacuum of the interacting theory can be shown to be equivalent to the free vacuum in this sense, while this is not the case for equilibrium states at finite temperature.

As part of this project, it has been proven that the **time slice axiom** holds both for free and for interacting theories [17]. This result says that if a state is fixed in an $\epsilon-$neighborhood of a Cauchy surface in a globally hyperbolic spacetime, then it is fixed everywhere.

This observation implies that, if we want to define a state for an interacting field theory, it is sufficient to restrict the attention to field observables supported in an $\epsilon-$neighborhood of a Cauchy surface Σ. Denoting by T the time function associated to the Cauchy surface Σ, such that the various Cauchy surfaces are the level sets of T, we have

$$\Sigma_\epsilon := \{p \in M \mid |T(p) - T(p_0)| \leq \epsilon, p_0 \in \Sigma\}.$$

Thanks to the time slice axiom, to fix a state, it is sufficient to prescribe the expectation values of elements of

$$\mathcal{F}_{\mu c}(\Sigma_\epsilon) = \{F \in \mathcal{F}_{\mu c} | \mathrm{supp}F \subset \Sigma_\epsilon\}$$

for free field theories, or of the subalgebra $\mathcal{F}_I(\Sigma_\epsilon) \subset \mathcal{F}_{\mu c}$ generated by $\{R_V(F) | F \in \mathcal{F}_{\mathrm{loc}}(\Sigma_\epsilon)\}$ in the case of interacting theories.

The time slice axiom permits us to restrict the domain of interacting observables. However, although the domain of an interacting field $R_V(F)$ coincides with the domain of F, $\mathrm{supp}R_V(F)$ is larger than $\mathrm{supp}F$. In fact, causality implies that

$$\mathrm{supp}R_V(F) \subset J^-(\mathrm{supp}F) \cap J^+(\mathrm{supp}V).$$

Hence, in order to localize the elements of $\mathcal{F}_I(\Sigma_\epsilon)$, we need to control the support of V. This last step can be done using the causal factorisation property. For every F supported in Σ_ϵ, we have that

$$R_V(F) = R_{V'}(F)$$

if $V - V'$ is supported in the future of Σ_ϵ and that

$$R_V(F) = U^{-1} \star R_{V'}(F) \star U$$

if $V - V'$ is supported in the past of Σ_ϵ, where

$$U = S^{-1}(V') \star S(V).$$

If V and V' are local functionals $S^{-1} = S^*$ and thus both S and U are unitary and the algebras generated by $R_V(\mathcal{F}_{\mathrm{loc}})$ and $R_{V'}(\mathcal{F}_{\mathrm{loc}})$ are $*-$isomorphic with the isomorphism being implemented by the unitary U.

With this in mind, restricting the attention to a Minkowski spacetime and considering the interaction Lagrangian

$$V_\lambda = \int \lambda \mathcal{L}_I d\mu_g$$

with λ a smooth and compactly supported function, it is possible to analyze the adiabatic limit as the inductive limit

$$R_V(F) = \lim_{\lambda \to 1} R_{V_\lambda}(F)\,.$$

This limit is called algebraic adiabatic limit, further details can be found in [38].

In Minkowski spacetime we can use the spacetime symmetries to adapt the form of the cutoff λ to the geometry of the background. Using a standard Minkowskian coordinate system $(t, \mathbf{x})$ where t parametrises the time and $\mathbf{x}$ the space, we choose

$$\lambda(t, \mathbf{x}) = \chi(t)h(\mathbf{x})$$

where χ is a smooth time cutoff which can be chosen to be supported in $J^+(\Sigma_{2\epsilon})$ and equal to 1 in $J^+(\Sigma_\epsilon)$. The spatial cutoff h is a smooth function which is constant in time and compactly supported in space. Using the time slice axiom and the causality of the S matrix, up to suitable unitaries of the above mentioned type, χ can be fixed once and for all and the adiabatic limit amounts to $h \to 1$. For every $F \in \mathcal{F}_I(\mathcal{O})$, the algebraic adiabatic limit $h \to 1$ converges, in fact if h_n is a family of compactly supported smooth functions which are equal to 1 on the sphere $S_n = \{\mathbf{x} \in \mathbb{R}^3 | |x| < n\}$, due to causality, the sequence $R_{V_{\chi h_n}}(F)$ is constant for $n \geq \overline{n}$ depending on the support of F.

In [11] the relation between the free and interacting time evolution has been analysed. The free time evolution corresponds to a translation of the support functions. Indicating by F_f the local field smeared with a test function f, the free time evolution is such that

$$\alpha_s(F_f) = F_{f_s}, \qquad f_s(t, \mathbf{x}) := f(t - s, \mathbf{x}).$$

The interacting time evolution acts on $\mathcal{F}_I$ as

$$\alpha_s^V(R_V(F_f)) = R_V(\alpha_s F_f) = R_V(F_{f_s}).$$

If F is supported in Σ_ϵ, the relation between the interacting and free time evolution is described by a cocycle $U_V(t)$ such that

$$\alpha_t^V(F) = U_V^* \star \alpha_t(F) \star U_V$$

In [11] it has been shown how to construct the cocycle U_V as a Dyson series of products of its generator K_V, see equation (25) in [11] where, for any $V = \int \chi h \mathcal{L}_I$,

$$K_V = R_V(\mathcal{H}), \qquad \mathcal{H} = \int \dot{\chi} h \mathcal{L}_I.$$

Having this cocycle at our disposal it is possible to construct the equilibrium (KMS) state repeating the so-called Araki-construction also for interacting field theories, when h is of compact support. In particular it holds that

$$\omega_\beta^V(A) = \frac{\omega(A \star U_V(i\beta))}{U_V(i\beta)}.$$

The state constructed in this way depends explicitly on h, however, the limit $h \to 1$ taken in the sense of van Hove is well defined, it is independent on χ and it constitutes an equilibrium state for the interacting theory in the adiabatic limit [10, 11] .

The methods developed in this project have opened the path to extending many interesting results of quantum statistical mechanics to quantum field theory. For example, it was possible to prove return to equilibrium and stability for interaction Lagrangians of compact spatial support

$$\lim_{t\to\infty} \omega^\beta \circ \alpha_t^V = \omega^{\beta,V}$$

see [42]. In that paper it is also shown that the return to equilibrium ceases to hold if the adiabatic limit is considered before the large-time limit.

References

[1] C. Dappiaggi, V. Moretti and N. Pinamonti, *Cosmological horizons and reconstruction of quantum field theories*, *Commun. Math. Phys.* **285** (2009) 1129–1163, [0712.1770].

[2] C. Dappiaggi, V. Moretti and N. Pinamonti, *Distinguished quantum states in a class of cosmological spacetimes and their Hadamard property*, *J. Math. Phys.* **50** (2009) 062304, [0812.4033].

[3] C. Dappiaggi, T.-P. Hack and N. Pinamonti, *Approximate KMS states for scalar and spinor fields in Friedmann-Robertson-Walker spacetimes*, *Annales Henri Poincare* **12** (2011) 1449–1489, [1009.5179].

[4] C. Dappiaggi, K. Fredenhagen and N. Pinamonti, *Stable cosmological models driven by a free quantum scalar field*, *Phys. Rev.* **D77** (2008) 104015, [0801.2850].

[5] C. Dappiaggi, T.-P. Hack and N. Pinamonti, *The Extended algebra of observables for Dirac fields and the trace anomaly of their stress-energy tensor*, *Rev. Math. Phys.* **21** (2009) 1241–1312, [0904.0612].

[6] T.-P. Hack, *On the Backreaction of Scalar and Spinor Quantum Fields in Curved Spacetimes*, Ph.D. thesis, Universität Hamburg, 2010. 1008.1776. http://www-library.desy.de/cgi-bin/showprep.pl?thesis10-042.

[7] T.-P. Hack, *Quantization of the linearized Einstein-Klein-Gordon system on arbitrary backgrounds and the special case of perturbations in inflation*, *Class. Quant. Grav.* **31** (2014) 215004, [1403.3957].

[8] R. Brunetti, K. Fredenhagen and K. Rejzner, *Quantum gravity from the point of view of locally covariant quantum field theory*, *Commun. Math. Phys.* **345** (2016) 741–779, [1306.1058].

[9] R. Brunetti, K. Fredenhagen, T.-P. Hack, N. Pinamonti and K. Rejzner, *Cosmological perturbation theory and quantum gravity*, *JHEP* **08** (2016) 032, [1605.02573].

[10] F. Lindner, *Perturbative Algebraic Quantum Field Theory at Finite Temperature*, Ph.D. thesis, Universität Hamburg, 2013. http://www-library.desy.de/cgi-bin/showprep.pl?thesis13-029.

[11] K. Fredenhagen and F. Lindner, *Construction of KMS States in Perturbative QFT and Renormalized Hamiltonian Dynamics*, *Commun. Math. Phys.* **332** (2014) 895–932, [1306.6519]. [Erratum: *Commun. Math. Phys.* **347** (2016) 655].

[12] B. S. Kay and R. M. Wald, *Theorems on the Uniqueness and Thermal Properties of Stationary, Nonsingular, Quasifree States on Space-Times with a Bifurcate Killing Horizon*, *Phys. Rept.* **207** (1991) 49–136.

[13] R. M. Wald, *General Relativity*. Chicago Univ. Pr., Chicago, USA, 1984, 10.7208/chicago/9780226870373.001.0001.

[14] C. Bär, N. Ginoux and F. Pfäffle, *Wave Equations on Lorentzian Manifolds and Quantization*, *EMS Publishing House* (Mar., 2007) , [0806.1036].

[15] M. J. Radzikowski, *Micro-local approach to the Hadamard condition in quantum field theory on curved space-time*, *Commun. Math. Phys.* **179** (1996) 529–553.

[16] R. Brunetti, K. Fredenhagen and M. Kohler, *The Microlocal spectrum condition and Wick polynomials of free fields on curved space-times*, *Commun. Math. Phys.* **180** (1996) 633–652, [gr-qc/9510056].

[17] B. Chilian and K. Fredenhagen, *The Time Slice Axiom in Perturbative Quantum Field Theory on Globally Hyperbolic Spacetimes*, *Commun. Math. Phys.* **287** (Apr., 2009) 513–522, [0802.1642].

[18] C. Dappiaggi, V. Moretti and N. Pinamonti, *Rigorous steps towards holography in asymptotically flat spacetimes*, *Rev. Math. Phys.* **18** (2006) 349–416, [gr-qc/0506069].

[19] N. Pinamonti, *On the initial conditions and solutions of the semiclassical Einstein equations in a cosmological scenario*, *Commun. Math. Phys.* **305** (2011) 563–604, [1001.0864].

[20] C. Dappiaggi, V. Moretti and N. Pinamonti, *Rigorous construction and Hadamard property of the Unruh state in Schwarzschild spacetime*, *Adv. Theor. Math. Phys.* **15** (2011) 355–447, [0907.1034].

[21] C. Lueders and J. E. Roberts, *Local quasiequivalence and adiabatic vacuum states*, *Commun. Math. Phys.* **134** (1990) 29–63.

[22] H. Olbermann, *States of low energy on Robertson-Walker spacetimes*, *Class. Quant. Grav.* **24** (2007) 5011–5030, [0704.2986].

[23] A. Degner and R. Verch, *Cosmological particle creation in states of low energy*, *J. Math. Phys.* **51** (2010) 022302, [0904.1273].

[24] M. Küskü, *A Class of Almost Equilibrium States in Robertson-Walker Spacetimes*, Ph.D. thesis, Universität Hamburg, 2009. 0901.1440. 10.3204/DESY-THESIS-2008-020 https://inspirehep.net/record/1649629/files/arXiv:0901.1440.pdf.

[25] N. Afshordi, S. Aslanbeigi and R. D. Sorkin, *A Distinguished Vacuum State for a Quantum Field in a Curved Spacetime: Formalism, Features, and Cosmology*, *JHEP* **08** (2012) 137, [1205.1296].

[26] M. Brum and K. Fredenhagen, *'Vacuum-like' Hadamard states for quantum fields on curved spacetimes*, *Class. Quant. Grav.* **31** (2014) 025024, [1307.0482].

[27] R. M. Wald, *Trace anomaly of a conformally invariant quantum field in curved spacetime*, *Phys. Rev. D* **17** (Mar, 1978) 1477–1484.

[28] V. Moretti, *Comments on the stress energy tensor operator in curved space-time*, *Commun. Math. Phys.* **232** (2003) 189–221, [gr-qc/0109048].

[29] S. Hollands and R. M. Wald, *Conservation of the stress tensor in interacting quantum field theory in curved spacetimes*, *Rev. Math. Phys.* **17** (2005) 227–312, [gr-qc/0404074].

[30] S. Hollands and R. M. Wald, *Local Wick polynomials and time ordered products of quantum fields in curved space-time*, *Commun. Math. Phys.* **223** (2001) 289–326, [gr-qc/0103074].

[31] N. Pinamonti and D. Siemssen, *Global Existence of Solutions of the Semiclassical Einstein Equation for Cosmological Spacetimes*, *Commun. Math. Phys.* **334** (2015) 171–191, [1309.6303].

[32] K. A. Rejzner, *Batalin-Vilkovisky formalism in locally covariant field theory*, Ph.D. thesis, Universität Hamburg, 2011. 1111.5130. DESY-THESIS-2011-041.

[33] I. Khavkine, *Local and gauge invariant observables in gravity*, *Class. Quant. Grav.* **32** (2015) 185019, [1503.03754].

[34] M. B. Fröb, *Gauge-invariant quantum gravitational corrections to correlation functions*, *Class. Quant. Grav.* **35** (2018) 055006, [1710.00839].

[35] D. Bahns and K. Rejzner, *The Quantum Sine Gordon model in perturbative AQFT*, *Commun. Math. Phys.* **357** (2018) 421–446, [1609.08530].

[36] D. Bahns, K. Fredenhagen and K. Rejzner, *Local nets of von Neumann algebras in the Sine-Gordon model*, 1712.02844.

[37] R. Brunetti, M. Duetsch and K. Fredenhagen, *Perturbative Algebraic Quantum Field Theory and the Renormalization Groups*, *Adv. Theor. Math. Phys.* **13** (2009) 1541–1599, [0901.2038].

[38] R. Brunetti and K. Fredenhagen, *Microlocal analysis and interacting quantum field theories: Renormalization on physical backgrounds*, *Commun. Math. Phys.* **208** (2000) 623–661, [math-ph/9903028].

[39] S. Hollands and R. M. Wald, *Existence of local covariant time ordered products of quantum fields in curved space-time*, *Commun. Math. Phys.* **231** (2002) 309–345, [gr-qc/0111108].

[40] H. Epstein and V. Glaser, *The role of locality in perturbation theory*, *Annales de l'I.H.P. Physique théorique* **19** (1973) 211–295.

[41] O. Steinmann, *Perturbation Expansions in Axiomatic Field Theory*. Lecture Notes in Physics. Springer Berlin Heidelberg, 2014.

[42] N. Drago, F. Faldino and N. Pinamonti, *On the stability of KMS states in perturbative algebraic quantum field theories*, *Commun. Math. Phys.* **357** (2018) 267–293, [1609.01124].

Propagation of Very High Energy Radiation in the Universe

Günter Sigl

II. Institut für Theoretische Physik, Universität Hamburg, Germany

DOI: http://dx.doi.org/10.3204/PUBDB-2018-00782/C8

The sources of cosmic rays, in particular ultra-high energy cosmic rays with macroscopic energies above $\sim 10^{18}$ eV, have still not been identified. This is partly caused by the fact that the sky observed in these cosmic rays is surprisingly isotropic and that deflection in galactic and extragalactic magnetic fields may still be substantial. The main goal of project C8 of the SFB 676 was to further develop a general software tool, known as CRPropa, which allows to propagate ultra-high energy cosmic rays from the sources to the observer and make predictions for spectrum, mass composition and sky distribution with a given astrophysical scenario for distribution and injection spectra and composition of the sources and the structure of cosmic magnetic fields.

1 Introduction

Recent years have seen interesting results on spectrum [1,2], composition [3,4], and anisotropy [5, 6] of ultra-high energy cosmic rays above 10^{17} eV, both from the Pierre Auger Observatory and other experiments such as the Telescope Array and the High Resolution Fly's Eye (HiRes). This continued after the end of project C8. As an example we highlight the recent first unambiguous detection of an anisotropy of ultra-high energy cosmic ray (UHECR) arrival directions around 8×10^{18} eV [7]. In order to interpret these data in the context of concrete astrophysical scenarios for the distribution of the sources, their injection characteristics such as spectrum, maximal energy and mass composition, as well as for the distribution of large scale cosmic magnetic fields requires a comprehensive numerical tool that can simulate the deflection of UHECRs over several orders of magnitude in energy and length scales, ranging from hundreds of megaparsecs down to galactic scales of the order of kiloparsecs, including their interactions such as photo-disintegration, pion production and pair production.

In particular, the distribution of structured cosmic magnetic field plays a central role in the interpretation of sky distribution, spectrum and mass composition of ultra-high energy cosmic rays (UHECR) above 10^{18} eV, as has been shown in Ref. [9]. Motivated by this, the main goal of the project C8 was the development of a general software tool that allows simulating the propagation of extragalactic cosmic ray nuclei and protons, including secondary electromagnetic cascades and neutrinos, within a magnetic field model that can be specified in a general way, taking into account all relevant interactions such as pion-production, photo-disintegration and pair production. This goal was achieved with the public release of the code CRPropa 2.0 [8] which can be accessed at `https://crpropa.desy.de/Main_Page`. This code was developed in close collaboration with Nils Nierstenhöfer from the University of Wuppertal who visited

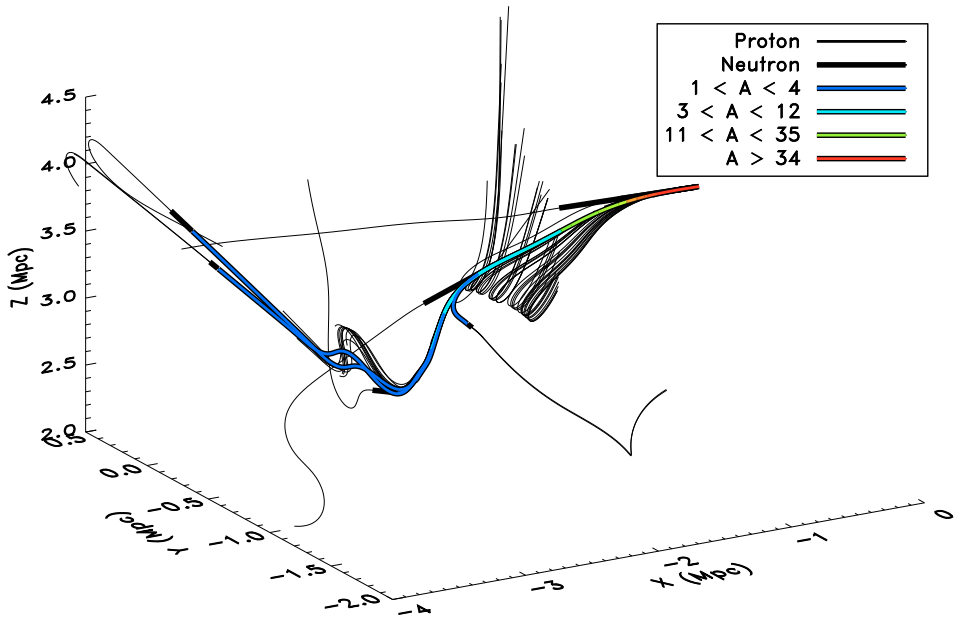


Figure 1: 3D trajectory of an iron nucleus and its hadronic secondaries in the minimum of the photodisintegration mean free path (at energy $E \sim 1.2 \times 10^{21}$ eV) in a high magnetic field region of a structured magnetic field ($10^{-9}\,\mathrm{G} < B < 10^{-7}\,\mathrm{G}$). Color coded is the mass number of the secondary particles. Notice that after photo-disintegration the heavy nucleus and its secondary particles have the same Lorentz factor $\Gamma \sim E/A$ and therefore secondary protons are stronger deflected than heavier nuclei due to their higher charge-to-mass ratio. Reprinted from Ref. [8], with permission from Elsevier.

Hamburg for several months and was partly funded by the SFB fellowship program. As an illustration, Figure 1 shows the simulated development of a nuclear cascade in a structured magnetic field. The code CRPropa has been extensively applied to various astrophysical scenarios for the origin of ultra-high energy cosmic rays above 10^{18} eV within the Pierre Auger Observatory. It is currently being applied systematically to fitting the spectrum and mass composition of the UHECR flux measured by the Pierre Auger experiment in order to extract the properties of the sources such as maximal energy and injected mass composition. In fact, from March 2012 to spring 2014 the PI G. Sigl acted as one of the leaders of a newly created task within the Pierre Auger experiment whose goal is to perform detailed Monte Carlo simulations of all relevant astrophysical scenarios whose predictions are to be compared with the data. The code CRPropa 2.0 developed within project C8 played a central role in this task.

During the more systematic application of CRPropa 2.0 to various astrophysical scenarios it became obvious that such a general simulation tool should be highly modular, since constraining the origin of UHECRs requires simulations predicting spectra, compositions and anisotropies for a large number of astrophysical scenarios, and comparison with experimental data. To

this end, CRPropa was upgraded to version 3.0 in close collaboration with the Universities of Aachen and Wuppertal. All relevant interactions, the solver for trajectory integration and the production of secondary $\gamma-$rays and neutrinos have been inherited from CRPropa 2.0 [8]. In addition, two new features have been implemented:

2 Cosmology in 3D

Cosmological effects such as the redshift evolution of the photon backgrounds and the adiabatic expansion of the universe are important when simulating the propagation of UHECRs. These effects can notably modify the UHECR spectra which is important in particular when comparing predictions with measured spectra at energies below a few 10^{18} eV where experimental statistics is large. Spectral changes can easily be taken into account in 1D simulations. However, in 3D, when deflections due to the pervasive cosmic magnetic fields are considered, it is not possible to know *a priori* the effective propagation length, and therefore the redshift, of the simulated particles. To approximately correct for these effects, one can re-simulate each 3D trajectory in 1D for a propagation time equal to the one of the 3D trajectory. One can then correct the final state of the 3D trajectory by randomly choosing from the final state products and energies of the 1D simulation [10].

3 Galactic propagation

The Galactic magnetic field (GMF) is expected to significantly contribute to the total deflections of charged extragalactic UHECRs. Therefore, the functionality of CRPropa 3.0 was extended to allow forward- and backtracking of UHECRs through different models of the GMF available in the software. Arbitrary field models can be defined using one of the grid techniques, described in the next section. Additionally, several models in analytical form are available, including the JF12 model with both regular and random component [11, 12].
A different, highly efficient, way to model galactic propagation is the lensing technique described and implemented in the PARSEC software [13]. In this approach UHECR interactions with photons and interstellar matter are neglected due to the short distance inside the Galaxy compared to extragalactic distances. The lensing technique uses a set of transformation matrices for different energies to map the directions of UHECRs at the border of the galaxy to directions observed at Earth. CRPropa 3.0 provides an interface to PARSEC to apply the lensing technique on UHECRs that were propagated from an extragalactic source to the border of the Galaxy. This combination allows to simulate the propagation of UHECRs through both the extragalactic and galactic magnetic field, which would be computationally unfeasible with pure forward tracking.

4 Applications

CRPropa 2.0 and 3.0 are now extensively being used to simulate predictions for observable spectra, mass composition and anisotropies in so-called *benchmark scenarios* for the distribution of the UHECR sources, the injected mass composition and maximal energies, as well as for the distribution of cosmic magnetic fields. Figure 2 shows an example where simulated spectra and their mass composition in a scenario in which sources inject a mixed mass composition are

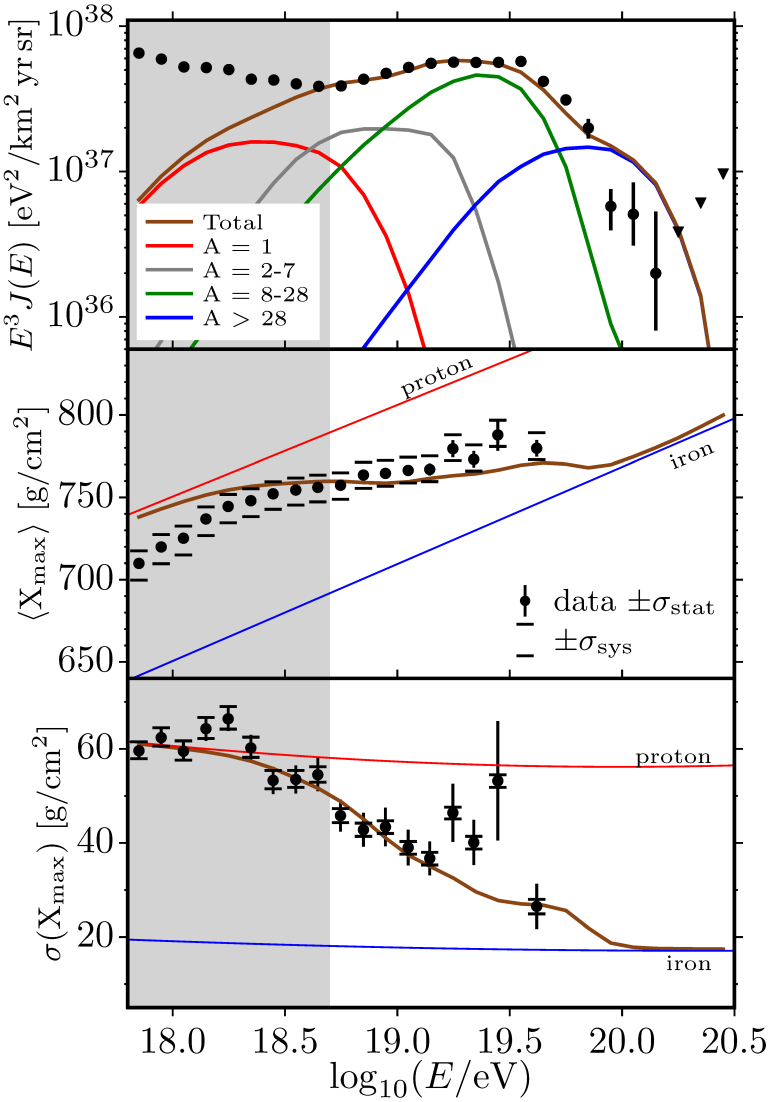


Figure 2: Comparison of simulated predictions and measurements by the Pierre Auger experiment of various observables in a scenario where uniformly distributed sources inject a mixed composition of elements. Upper panel: All-particle spectrum and spectra of the mass groups indicated compared to the measured spectrum. Middle panel: The average depth of shower maximum $X_{\rm max}$ is sensitive to the average mass composition. Lower panel: The variance of $X_{\rm max}$ is sensitive to the width of the arriving mass distribution. The best fit values here correspond to an injection spectrum $\propto E^{-0.62}$ up to a maximum energy per charge $E/Z \leq 3.6 \times 10^{18}$ eV, dominated by nitrogen. Figure adopted from Ref. [14].

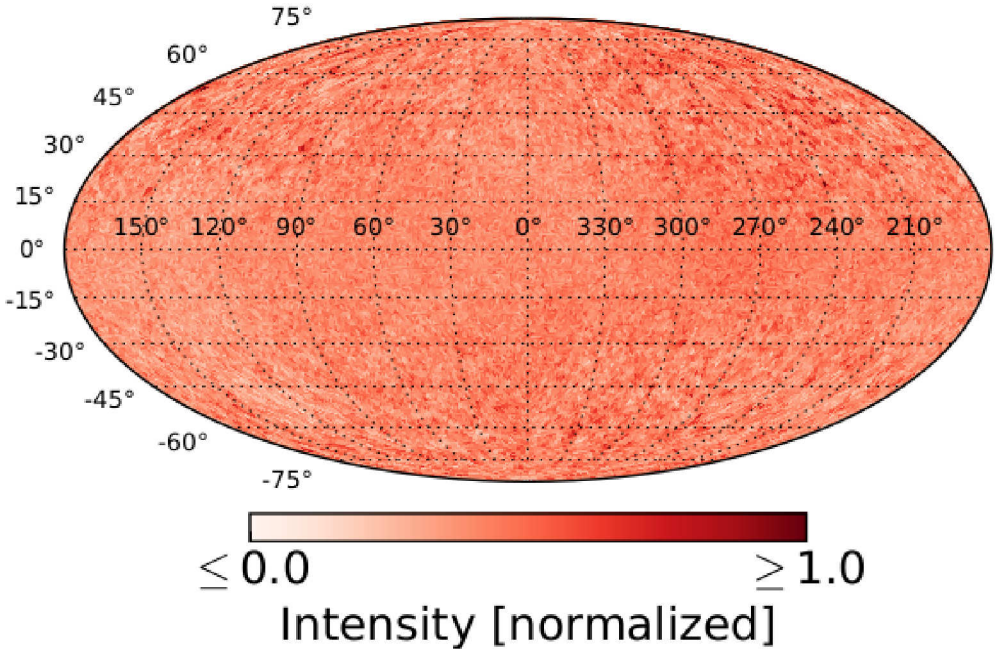


Figure 3: Simulated distribution of arrival directions of UHECRs above 10^{18} eV injected from a discrete set of sources of average density $10^{-3}\,\mathrm{Mpc}^{-3}$, randomly selected with a probability proportional to the baryon density following the local large scale structure. The UHECRs are deflected in an extragalactic magnetic field whose distribution was taken from a model following Ref. [9] and a galactic magnetic field modelled as in Refs. [11,12]. Figure adopted from Ref. [14].

compared to the data. Figure 3 shows an example for the simulated arrival direction distribution at the border of our Galaxy of protons injected in discrete sources. Such kind of simulations have also been used to develop the science case for the continuation of the Pierre Auger project beyond 2015. Furthermore, CRPropa has been extensively used within the first full Pierre Auger collaboration paper on global fits of the data to astrophysical scenarios parametrised by the injected mass distribution and spectra [15]. As an interesting and somewhat unexpected result it was found that very hard injection spectra with relatively low maximal energy were favoured by the fits. This also led to the important conclusion that the suppression of the UHECR flux observed above a few 10^{19} eV may have more to do with the maximal energy to which particles are accelerated within the sources than with energy loss processes, mostly pion production, known as the Greisen–Zatsepin–Kuzmin (GZK) effect, during propagation. In addition, the fits also favour injection of predominantly Helium and Nitrogen.

Our code CRPropa has also been applied to simulate secondary $\gamma-$ray and neutrino fluxes: Recently the IceCube experiments reported the detection of two neutrinos at PeV energies whose origin is likely extragalactic [16]. In Ref. [17] we investigated whether so-called *cosmogenic neutrinos*, i.e. neutrinos that are produced by the interactions of primary UHECRs with the cosmic microwave and infrared backgrounds, could explain the observed events. We found that the predicted neutrino fluxes fall short by a factor of about ten unless extreme, unlikely assumptions are made about the evolution of the UHECR sources and/or the maximal energy

to which protons are accelerated within their sources. It is thus much more likely that the IceCube events are produced within discrete sources such as active galaxies or γ-ray bursts.

The particular role of the Galactic magnetic field, for example, in UHECR lensing and for UHECR anisotropies has been investigated in some details in Refs. [18,19] in collaboration with Gwenael Giacinti who was partially funded by the SFB fellowship program as a visitor. For example, in Ref. [19] through UHECR trajectory simulations in the Galactic magnetic field we found that if the mass composition is light at energies $\sim 10^{18}$ eV around the ankle, the sources very likely have to be extragalactic, otherwise the predicted flux would be too anisotropic, inconsistent with the Pierre Auger observations. This finding also led to a full author paper of the whole Pierre Auger collaboration [20].

Finally, physics beyond the Standard Model in the form of Lorentz symmetry violations have been extensively constrained by applying UHECR observations. In particular, the non-observation of ultra-high energy photons by the Pierre Auger Observatory [21] implies that such photons have to undergo pair production on the cosmic microwave background. This strongly constrains tiny deviations of photon and electron dispersion relations from their Lorentz invariant form which otherwise would strongly modify the kinematics of the pair production reaction [22].

Our results on UHECR propagation have been presented in various conference proceedings, see Refs. [10, 23–26], as well as on summer schools, e.g. Ref. [27]. The also resulted in two PhD theses [28, 29].

5 Summary and Outlook

The development of a general tool for the propagation of UHECRs and their secondary products including $\gamma-$rays and neutrinos has been essentially achieved during project C8 and the focus is now shifting towards applications to various scenarios for the UHECR origin including the sources and their magnetic environment. For this reason, the initial project C8 was not continued. Instead, the numerical tools developed within C8 have been and still are applied to scenarios for the distribution of cosmic magnetic fields developed, in part, within project C9.

At the same time, project C8 set the stage to further develop and generalize CRPropa. For example, at low energies charged particles essentially diffuse, in particular in the Galactic Magnetic field and the simulation of a large number of trajectories becomes computationally inefficient. In this situation it is more efficient to solve a diffusion equation or a stochastic differential equation. To this end, in version 3.1 CRPropa has been extended by a module that allows to simulate Galactic cosmic rays by solving the relevant transport equation using stochastic differential equations which also takes into account anisotropic diffusion with different rates along and perpendicular to the coherent magnetic field component [30]. Furthermore, CRPropa is currently adapted and applied to model high energy cosmic ray sources by groups at DESY/Zeuthen and Bochum.

References

[1] PIERRE AUGER Collaborations, J. Abraham et al., *Measurement of the energy spectrum of cosmic rays above 10^{18} eV using the Pierre Auger Observatory*, *Phys. Lett.* **B685** (2010) 239–246, [1002.1975].

[2] TELESCOPE ARRAY Collaborations, T. Abu-Zayyad et al., *The Cosmic Ray Energy Spectrum Observed with the Surface Detector of the Telescope Array Experiment*, *Astrophys. J.* **768** (2013) L1, [1205.5067].

[3] PIERRE AUGER Collaborations, J. Abraham et al., *Measurement of the Depth of Maximum of Extensive Air Showers above* 10^{18} *eV*, *Phys. Rev. Lett.* **104** (2010) 091101, [1002.0699].

[4] HIRES Collaboration, R. U. Abbasi et al., *Indications of Proton-Dominated Cosmic Ray Composition above 1.6 EeV*, *Phys. Rev. Lett.* **104** (2010) 161101, [0910.4184].

[5] PIERRE AUGER Collaborations, P. Abreu et al., *Update on the correlation of the highest energy cosmic rays with nearby extragalactic matter*, *Astropart. Phys.* **34** (2010) 314–326, [1009.1855].

[6] TELESCOPE ARRAY Collaborations, T. Abu-Zayyad et al., *Search for Anisotropy of Ultra-High Energy Cosmic Rays with the Telescope Array Experiment*, *Astrophys. J.* **757** (2012) 26, [1205.5984].

[7] PIERRE AUGER Collaborations, A. Aab et al., *Observation of a Large-scale Anisotropy in the Arrival Directions of Cosmic Rays above* 8×10^{18} *eV*, *Science* **357** (2017) 1266–1270, [1709.07321].

[8] K.-H. Kampert, J. Kulbartz, L. Maccione, N. Nierstenhoefer, P. Schiffer, G. Sigl et al., *CRPropa 2.0 – a Public Framework for Propagating High Energy Nuclei, Secondary Gamma Rays and Neutrinos*, *Astropart. Phys.* **42** (2013) 41–51, [1206.3132].

[9] G. Sigl, F. Miniati and T. A. Ensslin, *Ultrahigh energy cosmic ray probes of large scale structure and magnetic fields*, *Phys. Rev.* **D70** (2004) 043007, [astro-ph/0401084].

[10] R. Alves Batista, P. Schiffer and G. Sigl, *Propagation of UHECRs in the Universe*, *Nucl. Instrum. Meth.* **A742** (2014) 245–249, [1308.1530].

[11] R. Jansson and G. R. Farrar, *A New Model of the Galactic Magnetic Field*, *Astrophys. J.* **757** (2012) 14, [1204.3662].

[12] R. Jansson and G. R. Farrar, *The Galactic Magnetic Field*, *Astrophys. J.* **761** (2012) L11, [1210.7820].

[13] H.-P. Bretz, M. Erdmann, P. Schiffer, D. Walz and T. Winchen, *PARSEC: A Parametrized Simulation Engine for Ultra-High Energy Cosmic Ray Protons*, *Astropart. Phys.* **54** (2014) 110–117, [1302.3761].

[14] G. Sigl, *Astroparticle Physics: Theory and Phenomenology*, vol. 1 of *Atlantis Studies in Astroparticle Physics and Cosmology*. Atlantis Press, 2017, 10.2991/978-94-6239-243-4.

[15] PIERRE AUGER Collaborations, A. Aab et al., *Combined fit of spectrum and composition data as measured by the Pierre Auger Observatory*, *JCAP* **1704** (2017) 038, [1612.07155]. [Erratum: *JCAP* **1803** (2018) E02].

[16] ICECUBE Collaborations, M. G. Aartsen et al., *First observation of PeV-energy neutrinos with IceCube*, *Phys. Rev. Lett.* **111** (2013) 021103, [1304.5356].

[17] E. Roulet, G. Sigl, A. van Vliet and S. Mollerach, *PeV neutrinos from the propagation of ultra-high energy cosmic rays*, *JCAP* **1301** (2013) 028, [1209.4033].

[18] G. Giacinti, M. Kachelriess, D. V. Semikoz and G. Sigl, *Ultrahigh Energy Nuclei in the Turbulent Galactic Magnetic Field*, *Astropart. Phys.* **35** (2011) 192–200, [1104.1141].

[19] G. Giacinti, M. Kachelriess, D. V. Semikoz and G. Sigl, *Cosmic Ray Anisotropy as Signature for the Transition from Galactic to Extragalactic Cosmic Rays*, *JCAP* **1207** (2012) 031, [1112.5599].

[20] PIERRE AUGER Collaborations, P. Abreu et al., *Constraints on the origin of cosmic rays above* 10^{18} *eV from large scale anisotropy searches in data of the Pierre Auger Observatory*, *Astrophys. J.* **762** (2012) L13, [1212.3083].

[21] PIERRE AUGER Collaborations, J. Abraham et al., *Upper limit on the cosmic-ray photon flux above* 10^{19} *eV using the surface detector of the Pierre Auger Observatory*, *Astropart. Phys.* **29** (2008) 243–256, [0712.1147].

[22] L. Maccione, S. Liberati and G. Sigl, *Ultra high energy photons as probes of Lorentz symmetry violations in stringy space-time foam models*, *Phys. Rev. Lett.* **105** (2010) 021101, [1003.5468].

[23] R. Alves Batista et al., *CRPropa 3.0 – a Public Framework for Propagating UHE Cosmic Rays through Galactic and Extragalactic Space*, in *Proceedings, 33rd International Cosmic Ray Conference (ICRC2013): Rio de Janeiro, Brazil, July 2-9, 2013*, p. 1226, 2013, 1307.2643.

[24] H. P. Bretz, K. Dolag, M. Erdmann, D. Kuempel, G. Mueller, P. Schiffer et al., *A hybrid Monte Carlo generator for ultra-high energy cosmic rays from their sources to the observer*, *J. Phys. Conf. Ser.* **396** (2012) 022036.

[25] G. Sigl, *Interpretation of ultra-high energy multi-messenger data*, *EPJ Web Conf.* **53** (2013) 01013.

[26] A. van Vliet, K.-H. Kampert, J. Kulbartz, L. Maccione, N. Nierstenhoefer, P. Schiffer et al., *CRPropa 2.0*, *EPJ Web Conf.* **52** (2013) 06006.

[27] G. Sigl, *High Energy Neutrinos and Cosmic Rays*, *Proc. Int. Sch. Phys. Fermi* **182** (2012) 145–184, [1202.0466].

[28] R. Alves Batista, *On the cosmological propagation of high energy particles in magnetic fields*, Ph.D. thesis, Universität Hamburg, 2015. http://bib-pubdb1.desy.de/search?of=hd&p=id:10.3204/DESY-THESIS-2015-013.

[29] A. R. van Vliet, *Propagation of ultra-high-energy cosmic rays and their secondaries with CRPropa*, Ph.D. thesis, Universität Hamburg, 2014. http://bib-pubdb1.desy.de/search?of=hd&p=id:10.3204/DESY-THESIS-2015-014.

[30] L. Merten, J. Becker Tjus, H. Fichtner, B. Eichmann and G. Sigl, *CRPropa 3.1—a low energy extension based on stochastic differential equations*, *JCAP* **1706** (2017) 046, [1704.07484].

Cosmic Magnetic Fields and their Role in High Energy Astrophysics

Robi Banerjee[1], *Günter Sigl*[2]

[1]Hamburger Sternwarte, Universität Hamburg, Germany
[2]II. Institut für Theoretische Physik, Universität Hamburg, Germany

DOI: http://dx.doi.org/10.3204/PUBDB-2018-00782/C9

Magnetic fields play an important role in many astrophysical and cosmological situations. The evolution of primordial seed fields crucially depends on the amount of helicity and the properties of the velocity field. On the other hand, magnetic fields can serve as an agent for possible signatures of dark matter in the form of annihilating weakly interacting massive particles, through induced synchrotron radiation of charged annihilation products, and for a possible mixing of axion-like particles and other light states with photons in scenarios beyond the Standard Model. In the context of project C9 of the SFB 676 we investigated both the seeding and evolution of magnetic fields and their effects on other processes.

1 Chiral magnetic effect

One possible effect that was increasingly considered in recent years as a possible contribution to seed magnetic fields is the so-called chiral magnetic effect. This effect can transform an initially present chiral asymmetry between left-chiral and right-chiral electrons and positrons into a helical magnetic field the sign of whose helicity is opposite to the sign of the difference of left-chiral and right-chiral lepton number. The helical fields initially grow exponentially on length scales larger than a critical scale indirectly proportional to the absolute value of the chiral asymmetry which is why it is also known as chiral magnetic instability. It is actually very similar to the classical dynamo, where the role of the chiral asymmetry is played by the helicity of the turbulent eddies. At the same time the chiral asymmetry is reduced until some approximate equipartition between the magnetic field energy and the energy associated with the chiral asymmetry is reached, at which point the magnetic field strength saturates and, at later times is damped by resistivity. The chiral asymmetry necessary for chiral magnetic effect can be produced, for example, by the electroweak interaction which breaks the chiral symmetry. This can play a role both in the early Universe, in particular around the electroweak phase transition, and in hot dense nuclear matter where left-chiral electrons and positrons through charged current interactions can turn into neutrinos which leave the star due to their weak interactions, whereas right-chiral electrons and positrons are only subject to neutral current induced scattering. The chiral magnetic effect will be discussed more quantitatively in the report to project C10 where we will also briefly cover its possible role in the electroweak phase transition. Here we restrict ourselves to a brief summary of the possible role of the chiral magnetic effect in hot neutron stars, based on our publication Ref. [1].

When discussing the chiral magnetic effect one usually assumes approximate equilibrium and

characterises the left- and right-chiral leptons by a chemical potential μ_L and μ_R, respectively. In strict thermal equilibrium and if the lepton mass is non-zero, one would have $\mu_L = mu_R$. However, in the presence of a non-vanishing production rate R_w of a chiral asymmetry one can treat the left- and right-chiral as approximately decoupled and at temperature T one gets

$$\frac{|\mu_5|}{T} \simeq \frac{R_w}{R_f}\,, \tag{1}$$

where $\mu_5 = (\mu_L - \mu_R)/2$ and R_f is the spin-flip rate which is of order $(m_e/T)^2$ times the scattering rate. In hot nuclear matter R_w is governed by URCA interactions and scales roughly as T^4, whereas R_f is only logarithmically dependent on temperature. As a result, $|\mu_5|/T$ is strongly temperature dependent and reaches values of order 10^{-3} for $T \simeq 50\,\mathrm{MeV}$, which are temperatures typical for the formation stage of hot neutron stars following a core collapse supernova. The magnetic fields that could be induced by the chiral magnetic instability reaches about 10^{15} Gauss for such temperatures.

2 Cosmic-ray propagation

The public CRPropa simulation tool for propagation of high energy cosmic rays, $\gamma-$rays and neutrinos in a structured Universe including magnetic fields that was developed partly within project C8 and is described in more detail in the corresponding section, was further extended within project C9 [2]. In this context it was applied to simulate the impact of cosmic large scale magnetic fields on high energy cosmic radiation. To extend the applicability to lower energies, where cosmic rays tend to diffuse and a direct simulation of trajectories becomes inefficient, CRPropa was extended to solve transport equations with stochastic differential equations [3]. The coupling to new models of the extragalactic magnetic field based on large scale structure simulations including magnetic fields was the subject of Ref. [4, 5]. The diffusive mode of extragalactic cosmic ray propagation was investigated in Ref. [6]. It was found that below an energy $E \simeq Z\,\mathrm{EeV}$ the fluxes from cosmological sources tend to be suppressed due to a "magnetic horizon". Finally, the recent dipolar anisotropy of ultra-high energy extragalactic cosmic rays above $8 \times 10^{18}\,\mathrm{eV}$ [7] was interpreted in the context of one dominating nearby source [8]. It was found that a discrete source with a flux corresponding to about 3% of the total flux and a deflection angle $\sim 50^\circ$ at $8 \times 10^{18}\,\mathrm{eV}$ can reproduce the observed dipole as well as limits on the dipole and higher multipoles at higher and lower energies. Interestingly, for a coherence length of $\simeq 100\,\mathrm{kpc}$ this would require an extragalactic magnetic field strength of several nanoGauss. The CRPropa package was also used to clarify the role of the Liouville theorem in the influence of propagation in magnetic fields on ultra-high energy cosmic rays [9].

Cosmic rays at much smaller energies, of the order of 10 MeV kinetic energy, could be accelerated already shortly after the first objects, in particular the first supernovae, formed in the early Universe, starting at redshift $z \simeq 20$. It is not very well known how efficient this process may have been, but in principle it can contribute to heating the neutral intergalactic medium, in addition to contributions from X-rays and possible dark matter (DM) annihilation, before it was significantly re-ionized. We showed in Ref. [10] that such cosmic rays contribute negligibly to re-ionization, but may rise the temperature of the intergalactic medium by between 10 and 200 Kelvin by redshift $z = 10$. Whether this early heating is rather uniform or tends to cluster around the first cosmic ray sources strongly depends on the structure of the magnetic fields present between $z \simeq 20$ and $z \simeq 10$ in which these cosmic rays diffuse. They could, for example,

efficiently confined around their sources if magnetic fields are significantly enhanced by plasma streaming instabilities. These effects can considerably influence the properties of predicted HI 21 cm emission characteristics which is expected to be probed in much detail by future radio surveys with instruments such as LOFAR and the SKA. Heating of the intergalactic medium by energy deposition by early cosmic rays may also influence constraints on DM annihilation and decay based on observations of 21 cm emission. It is also interesting to note in this context that very recently, observations by the Experiment to Detect the Global Epoch of Reionization Signature (EDGES) indicate an absorption profile around 78 MHz, corresponding to the 21 cm line redshifted by $z \simeq 17$, that is about a factor 2 stronger than expected [11]. This suggests that either background radiation temperature was hotter than expected or the temperature of the intergalactic gas around redshift $z \sim 17$ that is much lower than expected. Such and other observations anticipated in the future may thus also constrain the effect of cosmic rays on the intergalactic medium, in particular the cosmic ray production efficiency and the structure of the magnetic fields in which they diffuse.

3 WIMP DM constraints from synchrotron annihilation

WIMP DM annihilation into charged leptons can be constrained through their synchrotron radiation. This signal is also influenced by the diffusion of these charged leptons in the magnetic fields present in the objects where DM annihilation is occurring. Interesting targets are objects that are radio-quiet but at the same time are expected to be dominated by DM. One type of objects are high velocity clouds in the Milky Way, in particular the so-called Smith cloud. There are indications that the Smith cloud has crossed the Galactic plane several times and, in order to not have been disintegrated by tidal forces, should be dominated by DM. In Ref. [12] we analytically modelled the synchrotron emission by first computing the Syrovatskii solution for electrons and positrons produced with a rate given by a radially symmetric DM annihilation profile and an assumed annihilation cross section and branching ratio into electrons and positrons and subsequently diffusing in magnetic fields characterised by an energy dependent spatially constant diffusion coefficient and appropriate continuous energy losses. Based on the resulting radial electron/positron distribution the synchrotron spectrum was computed in a given magnetic field of a few microGauss assumed to be constant. Comparison with sensitivities of radio instruments such as LOFAR, expressed in terms of flux densities or brightness temperature, the lead to constraints on the annihilation cross sections into electrons/positrons as a function of DM mass. Interestingly, for radio frequencies at a few tens of MHz, these constraints can reach below the standard relic thermal cross section $\langle \sigma_{\rm th} \rangle \simeq 3 \times 10^{-26}\,{\rm cm}^3/{\rm s}$ by factors up to ~ 100 for DM masses $> 100\,{\rm GeV}$ and down to $\simeq 1\,{\rm GeV}$. These studies were subsequently extended to dwarf spheroidal galaxies and galaxy clusters in the context of a masters thesis [13]. Figure 1 shows an example for the sensitivities that can be reached for the dwarf spheroidal Triangulum II.

4 Signatures of ALP conversion into photons

In extensions of the Standard Model involving axion-like particles (ALPs) often a coupling between two photons, represented by the field strength tensor $F_{\mu\nu}$ and its dual $\tilde{F}_{\mu\nu}$, and the

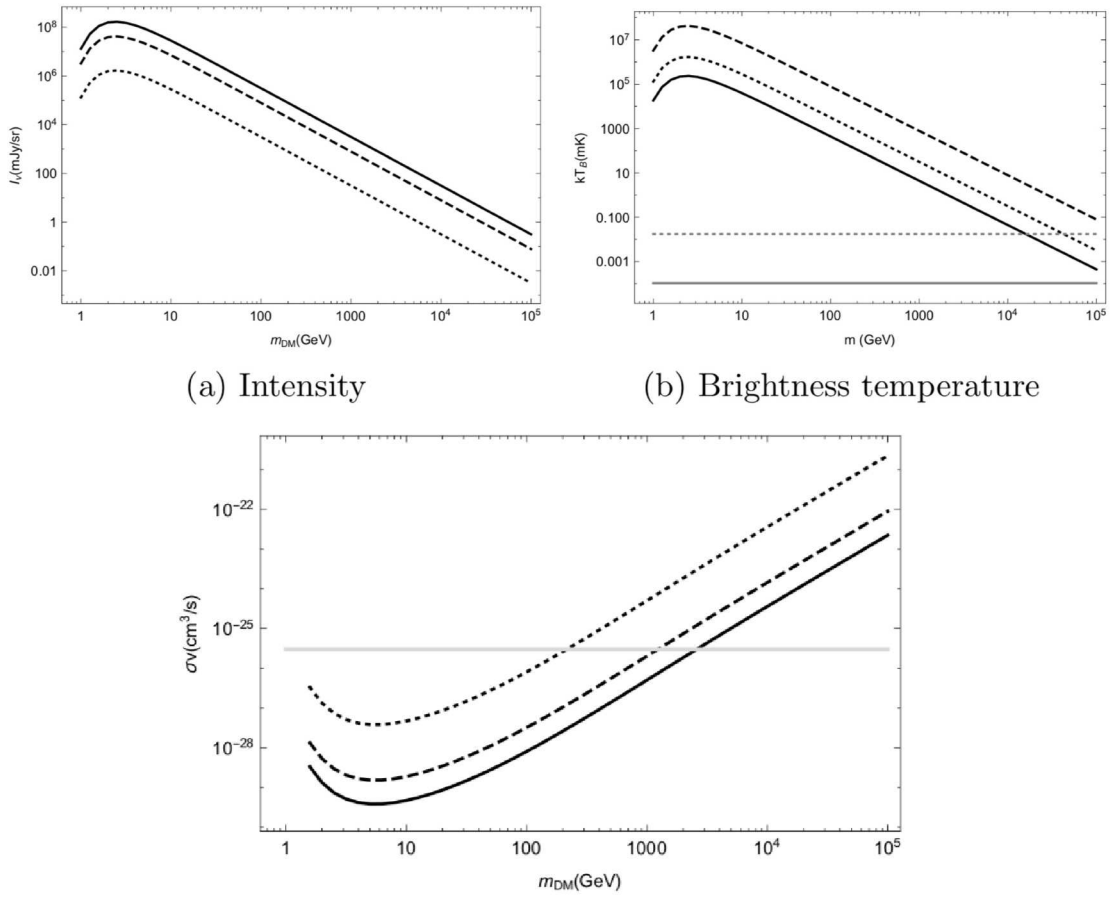


Figure 1: Upper panels: Expected intensity in milliJansky per beam and brightness temperature in milliKelvin for DM self-annihilation into e^+e^- as function of DM mass for the dwarf spheroidal Triangulum II. The different lines indicate uncertainties related to the size of the diffusive halo. Horizontal gray solid line indicates the LOFAR sensitivity for a beamsize of 20×20, the gray dotted line indicates the sensitivity for SKA. Lower panel: Resulting constraints on the annihilation cross section into electrons and positrons as function of DM mass. Horizontal gray line marks the annihilation cross section required for thermal relic cold DM to reproduce the observationally inferred DM abundance. Figure adopted from Ref. [13].

ALP field a of the form

$$\frac{\alpha_{\rm em}}{8\pi}\frac{C_{a\gamma}}{f_a}\, a\, F_{\mu\nu}\tilde{F}^{\mu\nu} = \frac{g_{a\gamma}}{4}\, a\, F_{\mu\nu}\tilde{F}^{\mu\nu} \tag{2}$$

occurs, where $\alpha_{\rm em} = e^2/(4\pi\epsilon_0)$ is the fine structure constant, f_a is a Peccei-Quinn type energy scale, $C_{a\gamma}$ is a model-dependent dimensionless number and $g_{a\gamma} \equiv \alpha_{\rm em} C_{a\gamma}/(2\pi f_a)$ is the effective ALP-photon coupling which is an inverse energy. In the presence of an external electromagnetic field, in particular a magnetic field, this can lead to photon-ALP conversion, also known as Primakoff effect, and can be used to probe the existence of ALPs in contexts rang-

ing from experimental setups, such as light shining through a wall experiments where photons are converted to ALPs which travel through a wall opaque to photons, and are reconverted to photons, or haloscopes where ALPs constitute (part of) DM and are converted to photons, to distortions of the spectra of natural photon sources such as astrophysical $\gamma-$ray sources or the cosmic microwave background (CMB). The conversion efficiency generally depends on the spatial structure, and possibly the time-dependence, of the magnetic field. We will here focus on so-called astrophysical haloscopes where cold DM ALPs are converted to radio lines in magnetised astrophysical objects [14] and distortions of the CMB spectrum through mixing with ALPs in the magnetic fields within galaxy clusters [15].

One can show that in a static magnetic field with isotropic power spectrum per logarithmic wavenumber interval $\rho_m(k, \mathbf{r})$ ALPs convert non-resonantly to a photon line at frequency $\omega_\gamma = m_a$ centered on the ALP mass m_a with fractional width $\Delta = \Delta\omega_\gamma/\omega_\gamma \lesssim 10^{-3}$ and the total flux density of a source at distance d can be written as

$$S \simeq \frac{\pi}{4d^2}\frac{g_{a\gamma}^2}{m_a^2}\frac{1}{\Delta}\int d^3\mathbf{r}\rho_a(\mathbf{r})\rho_m(m_a,\mathbf{r}) \simeq \frac{\pi}{4d^2}\frac{g_{a\gamma}^2}{m_a^2}\frac{1}{\Delta}M_a\rho_m(m_a)\,, \tag{3}$$

where $\rho_a(\mathbf{r})$ is the local ALP mass density and in the last step we have assumed the ALP and magnetic field densities to be roughly constant with M_a the total ALP mass within the object. Inserting characteristic numbers this gives [14]

$$S \simeq 2.8\times 10^{-11}\,\left(g_{a\gamma}10^{14}\,\mathrm{GeV}\right)^2\left(\frac{m_a}{\mu\mathrm{eV}}\right)^{-2}\left(\frac{10^{-3}}{\Delta}\right)\left(\frac{M_a}{10^{-10}\,M_\odot}\right)\left(\frac{d}{\mathrm{kpc}}\right)^{-2}\left(\frac{B}{\mathrm{G}}\right)^2 f(m_a)\,\mathrm{Jy}\,, \tag{4}$$

where $f(k)$ is the fraction of the total magnetic field energy density in a logarithmic wavenumber interval centered at k. However, the total flux density cannot exceed

$$S_{\max} \simeq \frac{\rho_a}{m_a}\frac{v_a}{\Delta}\left(\frac{r_s}{d}\right)^2 \simeq 10^{-10}\,\left(\frac{m_a}{\mu\mathrm{eV}}\right)^{-1}\left(\frac{r_s}{10^6\,\mathrm{cm}}\right)^2\left(\frac{d}{\mathrm{kpc}}\right)^{-2}\mathrm{Jy}\,, \tag{5}$$

which would correspond to complete conversion of all ALPs impinging on the object of radius r_s with velocity v_a. Resonant ALP DM to photon conversion, which is also limited by Eq. (5), was recently considered for neutron stars in Refs. [16, 17].

The conversion of CMB photons to ALPs and the resulting distortion of the CMB is strongly constrained by the very precisely measured CMB spectrum. Viewing the CMB through galaxy clusters is in particular interesting in this case, for one because the magnetic field strength in galaxy clusters is known to be a few micro Gauss, and also because the distortion of the CMB by the hot plasma in these clusters, known as the thermal Sunyaev–Zeldovich (tSZ) effect, is well measured in terms of the distortion parameter y. The idea is then that photon-ALP conversion and the tSZ effect lead to very different distortion spectra, as shown in Fig. 2. Since no deviations from the expected tSZ distortions have been observed, this allows to put constraints on the coupling $g_{a\gamma}$. In particular, for the mass range 2×10^{-14} eV $\lesssim m_a \lesssim 3\times 10^{-12}$ eV we found that a future PRISM-like experiment would allow limits up to $g_{a\gamma} \lesssim \mathcal{O}(10^{-13}\ \mathrm{GeV}^{-1})$, 1.5 orders of magnitude stronger than the currently strongest limits in this mass range.

A thesis on the role of magnetic fields in various astrophysical and cosmological contexts has been published in Ref. [18]. Furthermore, magnetic fields also constitute energy-momentum and thus can source gravitational waves. The strength of the resulting gravitational fields was investigated in the context of a master thesis [19].

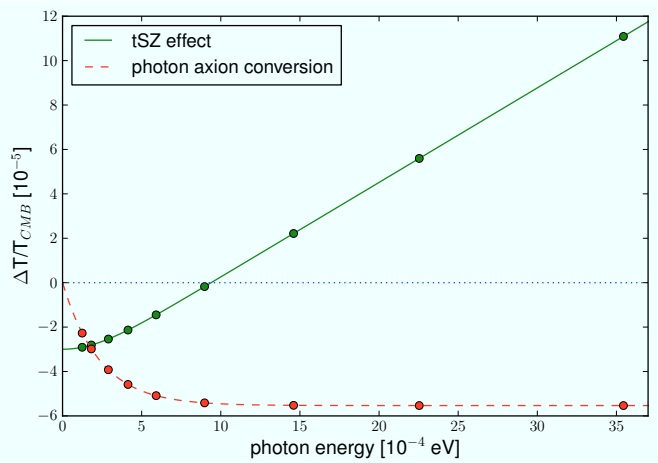


Figure 2: Comparison of the spectral profile of the tSZ effect (with y = 10^{-5}) and the photon-axion conversion. The horizontal axis shows the photon energy, the vertical axis shows the relative distortion of the effective CMB temperature, $\Delta T/T_{\rm CMB}$ in units of 10^{-5}. For this plot, the parameters $g_{a\gamma} = 5 \times 10^{-13}$ GeV^{-1} for the ALP-photon coupling, galaxy cluster magnetic field strength $B = 2$ μG, galaxy cluster size $R = 0.5$ Mpc, ALP mass $m_a = 10^{-13}$ eV were used. Different values for these parameters change the normalization of the effect but not its dependence on the photon frequency. The filled circles refer to the centers of the frequency bands of the *Planck*-mission. Figure taken from Ref. [15].

5 Magnetic field amplification by the small-scale dynamo in the early Universe

In [20] we showed that the Universe is already strongly magnetized at very early epochs during cosmic evolution. Our calculations are based on the efficient amplification of weak magnetic seed fields, which are unavoidably present in the early Universe, by the turbulent small-scale dynamo. We identify two mechanisms for the generation of turbulence in the radiation dominated epoch where velocity fluctuations are produced by the primordial density perturbation and by possible first-order phase transitions at the electroweak or QCD scales. We show that all the necessities for the small-scale dynamo to work are fulfilled. Hence, this mechanism, operating due to primordial density perturbations, guarantees fields with comoving field strength $B_0 \sim 10^{-6}\varepsilon^{1/2}$ nG on scales up to $\lambda_c \sim 0.1$ pc, where ε is the saturation efficiency. The amplification of magnetic seed fields could be even larger if there are first-order phase transitions in the early Universe. Where, on scales up to $\lambda_c \sim 100$ pc, the comoving field strength due to this mechanism will be $B_0 \sim 10^{-3}\varepsilon^{1/2}$ nG at the present time. Such fields, albeit on small scales, can play an important role in structure formation and could provide an explanation to the apparently observed magnetic fields in the voids of the large-scale structure

The discrepancy between theoretically generated and observed magnetic fields in the Universe needs explaining. The galactic dynamo can be a very effective mechanism at producing the μG fields observed in spiral galaxies [21]. However, strong fields in young galaxies, clusters and superclusters of galaxies and in the intergalactic medium require further explanation [22–26].

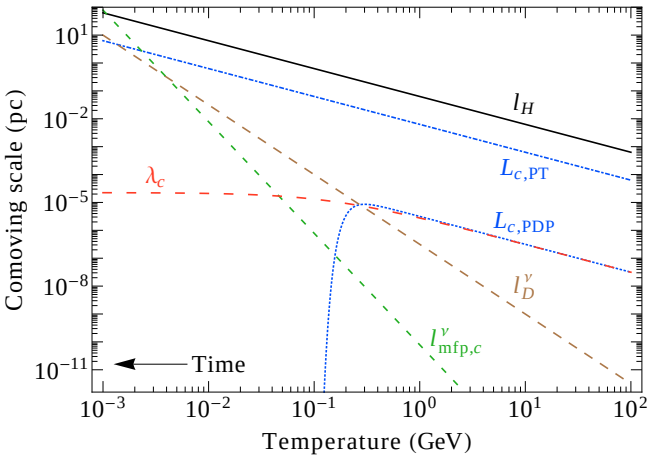


Figure 3: This figure shows the evolution of relevant comoving scales from the EW scale $T_{\mathrm{EW}} \sim 100$ GeV to the time of neutrino decoupling at $T_{\mathrm{dec}} \simeq 2.6$ MeV. In this early epoch the neutrinos generate the plasma viscosity. The QCD phase transition occurs at around $T_{\mathrm{QCD}} \simeq 200$ MeV. Here, $l_H = 1/aH$ is the Hubble scale (solid, black), $l^\nu_{\mathrm{mfp},c}$ is the neutrino mean-free-path (dashed, green) and l^ν_D is the damping scale due to neutrino diffusion (dashed, brown). For turbulence generated by the primordial density perturbation (PDP) and first-order phase transitions (PT), the largest stirring scales $L_c = v_L^{\mathrm{rms}}/aH$. Although the turbulent motions from PDP become completely damped below $T \simeq 0.2$ GeV, the magnetic field gets *frozen-in* with integral scale λ_c (dashed, red). Reprinted figure with permission from Ref. [20]. Copyright (2014) by the American Physical Society.

As noted in a number of numerical and analytical works, the rapid amplification of magnetic seed fields can occur due to the turbulent motions of the conducting plasma. This small-scale dynamo (SSD) mechanism is believed to play a crucial role in the formation of large magnetic fields in a number of astronomical settings, from stars to galaxies and the intergalactic medium [27–31]. For these settings, the turbulent motions arise from gravitational collapse, accretion and supernovae explosions. Hence, the SSD mechanism can be highly effective at magnetizing structures in the early Universe. However, the large field strengths apparently observed in the voids of the large-scale structure [26] still require an explanation.

Magnetic seed fields will almost certainly be generated at some level in the early Universe through a variety of mechanisms. Such mechanisms include inflation [32], phase transitions [33] and the Harrison mechanism through the generation of vorticity [34]. The SSD mechanism for the amplification of such seed fields could play an important role for the explanation of the observed large magnetic fields throughout the Universe. In this paper we have demonstrated that the conditions necessary for such turbulent amplification arise in the radiation dominated Universe before the onset of structure formation. We have shown that significant turbulence is generated in this early epoch by at least two mechanisms; velocity perturbations generated by the primordial density perturbation and bubble collisions in first-order phase transitions.

Turbulent plasma motions arise inevitably from perturbations of the gravitational potential. The continuous production of velocity perturbations upon horizon entry of primordial density modes, act as a continuous forcing of the fluid on the largest scales. Therefore, in regimes of

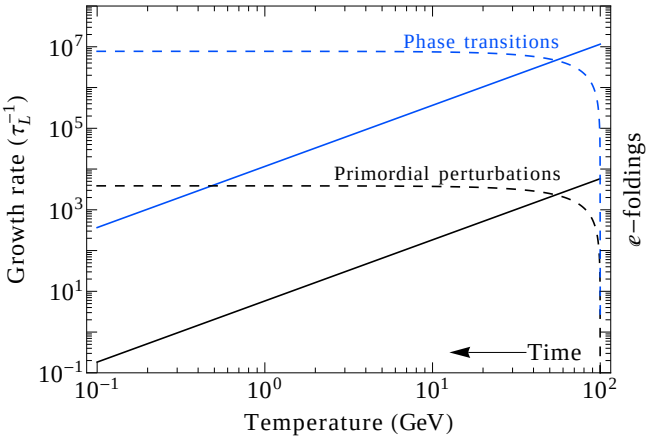


Figure 4: This figure shows the SSD growth rate Γ (solid) and number of e-foldings $N = \int \Gamma(t)dt$ (dashed) from the time of the EW scale $T_{\rm EW} \sim 100$ GeV to the QCD scale $T_{\rm QCD} \simeq 200$ MeV. Recall that the magnetic seed field is amplified as $B_{\rm rms} \propto \exp(\Gamma t)$. The growth rate in units of the eddy-turnover-time where Kolmogorov turbulence $\vartheta = 1/3$ is assumed. The growth rate and the number of e-foldings for turbulence generated by the primordial density perturbation and first-order phase transitions are shown in (black) and (blue) respectively. Reprinted figure with permission from Ref. [20]. Copyright (2014) by the American Physical Society.

large Reynolds numbers, a state of stationary fully developed turbulence is expected. Turbulent flow can be triggered, for example, by thermal fluctuations on very small scales [35]. Turbulence can also be injected into the plasma by bubble collisions during first-order phase transitions. Although the kinetic energy injection occurs only for the duration of the phase transition, we argue, following Refs. [36, 37], that a state of fully developed turbulence is also expected from this mechanism.

Let us first consider the turbulence generated by the primordial density perturbations (PDP). From Fig. 3 we can see that for $T \gtrsim 0.2$ GeV the stirring scale $L_{c,\rm PDP}$ (the lower blue dotted line in the figure) is larger than the damping scale l_D^{ν}. Hence, the velocity perturbations are not damped and one can use density fluctuation-induced rms velocities.

Once fully developed turbulence is established, the Kazantsev model of the SSD mechanism can be used to estimate the magnetic field growth rate. We have demonstrated that the Prandtl numbers are very large in the regime considered. Thus, the results from the Kazantsev theory for $P_m \gg 1$ are applicable. The analytical work shows that the magnetic field growth rate depends on the kinetic Reynolds numbers [38,39], which are very large in our case. We have shown that, for both models of turbulence, the amplification is strong enough for small magnetic seed fields to reach a saturated state. The saturated state is given by the approximate equipartition between magnetic and kinetic energy $E_{\rm M}/E_{\rm kin} \approx \varepsilon$, where the parameter ε characterizes the efficiency of the mechanism. In Fig. 4 we show the magnetic field growth rate Γ, where $B_{\rm rms} \propto \exp(\Gamma t)$, which is determined from the Kazantsev model of the SSD mechanism. The growth rate depends on the type of turbulence, applicable on the inertial range $l_{\rm diss} < l < L$, for Kolmogorov and Burgers type turbulence respectively. Here, we assume that the turbulence is of Kolmogorov type, which is relevant for the subsonic velocity fluctuations determined in this paper. Now, since Γ varies in time, it will be useful to consider the number of e-foldings

given by $N \equiv \int \Gamma(t) \mathrm{d}t$.

We note that numerical studies at Prandtl numbers $P_m \approx 2$ indicate that the SSD mechanism is more efficient for rotational modes, where the saturation efficiency ε is close to unity [40]. Whereas the saturation level is lower for compressive modes $\varepsilon \sim 10^{-3}$–10^{-4} [40]. However, further numerical work is required to establish the saturation level for larger Prandtl numbers and smaller Mach numbers relevant to our settings. We also note that, although only longitudinal velocity modes are generated by first-order primordial density perturbations, rotational modes are generated at second order in cosmological perturbations [41–45]. Also, there is no reason not to expect rotational modes generated by first-order phase transitions. In any case, since the Reynolds numbers are so large, nonlinear interactions can play a role leading to a state of fully developed turbulence with both rotational and longitudinal modes. In particular, we expect that, below the integral scale, Kolmogorov type turbulence is established. But we stress that the SSD mechanism works independently of the type of turbulence [38, 39, 46]. Indeed, even purely irrotational turbulence can still drive a small-scale dynamo [38–40] . Hence, the efficient amplification of magnetic fields seems unavoidable, leading to a strongly magnetized early Universe prior to structure formation.

For the two mechanisms of turbulence investigated in this paper, we calculated the saturated field strengths and their subsequent evolution up to the present day. We note that although turbulence is completely erased in viscous and free-streaming regimes, magnetic fields are overdamped and can survive to the present day. Therefore, the most important epochs of evolution are due to free turbulent decay. This turbulent MHD effect decreases the field strength and increases the coherence length in nonhelical fields [47, 48]. From the turbulence generated by the primordial density perturbation we found $B_0^{\rm rms} \sim 10^{-6}\varepsilon^{1/2}$ nG on scales $\lambda_c \sim 10^{-1}$ pc. Unfortunately, even for a high efficiency factor $\varepsilon \sim 1$, these fields are too weak on too short scales to explain the Fermi observations of TeV Blazars [26]. From the turbulence generated by first-order phase transitions, we found $B_0^{\rm rms} \sim (10^{-6}$–$10^{-3})\varepsilon^{1/2}$ nG on scales $\lambda_c \sim (10^{-1}$–$10^{2})$ pc. Such fields are strong enough to explain the apparent observations of intergalactic magnetic fields suggested by the Fermi results [26]. Thus, in this paper we have demonstrated that the conditions are right for the efficient amplification of magnetic fields via the small-scale dynamo. The mechanism generates large field strengths, albeit on very small scales, which could explain observations of magnetic fields in the voids of the large-scale structure and have an impact on early structure formation.

6 CMB spectral distortions from the decay of causally generated magnetic fields

In [49] we improved previous calculations of the CMB spectral distortions due to the decay of primordial magnetic fields. Our studies are focused on causally generated magnetic fields at the electroweak and QCD phase transitions. We also consider the decay of helical magnetic fields. We show that the decay of non-helical magnetic fields generated at either the electroweak or QCD scale produce μ and y-type distortions below 10^{-8} which are probably not detectable by a future PIXIE-like experiment. We show that magnetic fields generated at the electroweak scale must have a helicity fraction $f_* > 10^{-4}$ in order to produce detectable μ-type distortions. Hence a positive detection coming from the decay of magnetic fields would rule out non-helical primordial magnetic fields and provide a lower bound on the magnetic helicity.

Magnetic fields generated in the very early Universe decay in the radiation dominated epoch

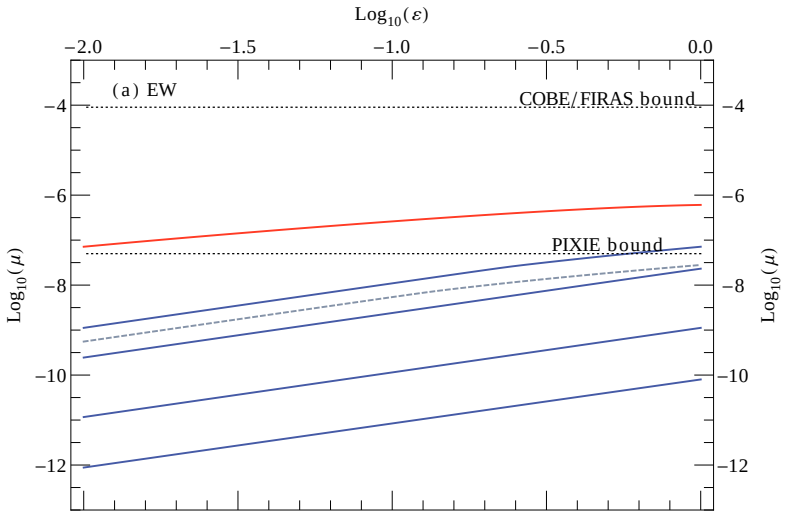


Figure 5: Here we show the μ-type distortion generated due to the decay of magnetic energy initially generated at the EW scale. We plot the spectral distortion μ vs ε, where $\varepsilon \equiv \tilde{\rho}_{B,*}/\rho_{\gamma,0} \approx 1$ corresponds to an initial field strength $\tilde{B}_{\lambda,*} \simeq 3 \times 10^{-6}$ G. The (solid, blue) lines from top to bottom correspond to initial helicity fractions $f_* = \{10^{-3}, 10^{-4}, 10^{-6}, < 10^{-14}\}$. The maximally helical case $f_* = 1$ (solid, red) is also shown. Reprinted figure with permission from Ref. [49]. Copyright (2015) by the American Physical Society.

due to turbulent MHD effects. The decaying magnetic fields inject energy into the primordial plasma which can lead to μ-type and y-type distortions to the CMB black body spectrum. The current COBE/FIRAS limits on these spectral distortions are very tight $|\mu| < 9 \times 10^{-5}$ and $y \lesssim 1.5 \times 10^{-5}$ [50]. However there is the exciting possibility of a new PIXIE-like experiment which could place much stronger upper limits of $|\mu| < 5 \times 10^{-8}$ and $y \lesssim 10^{-8}$ if no detection is made [51]. Any prediction for spectral distortions above the PIXIE limits is what we call detectable.

In this work we consider the evolution of helical and non-helical magnetic fields generated by some causal process in the early Universe. We calculate the spectral distortions using the decays laws of Refs. [47, 52, 53]. We find that causally generated non-helical magnetic fields, with an initial helicity fraction less than $\sim 10^{-14}$, generated at the EW phase transition will not produce any detectable CMB μ-type (see Fig. 5) or y-type (see Fig. 6) spectral distortions. This remains true even if the inverse transfer effect for non-helical fields seen in Refs. [54, 55] is considered. Hence, to produce observable spectral distortions from the decay of magnetic fields generated at the EW phase transition, a non-negligible helical component is required.

Here we note that, if the inverse transfer effect for non-helical fields is applicable [54, 55], it looks possible to generate small amounts of detectable distortions from magnetic fields generated at the QCD phase transition. We also note that magnetogenesis at the QCD phase transition is disfavoured compared to magnetogenesis at the EW phase transition. Under early Universe conditions with very small chemical potentials the QCD phase transition is a smooth transition [56] whereas the EW phase transition could be first-order in certain Standard Model extensions [57].

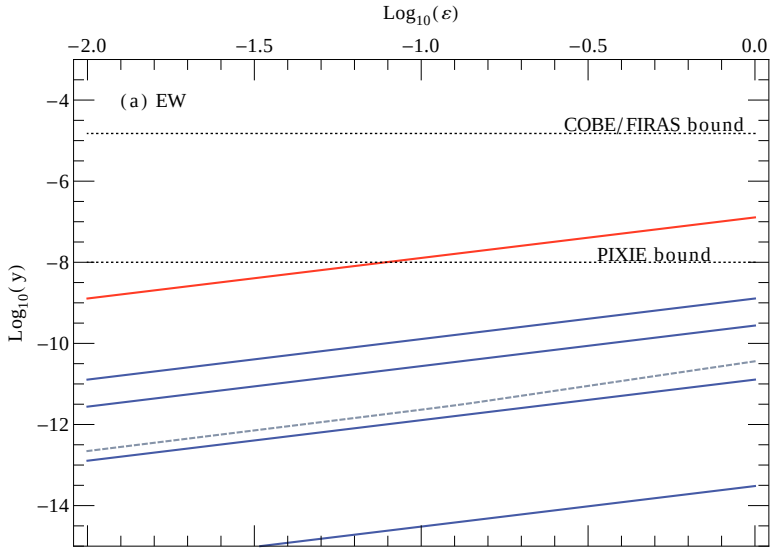


Figure 6: Here we show the y-type distortion produced due to the decay of magnetic energy initially generated at the EW scale. We plot the spectral distortion y vs ε, where $\varepsilon \equiv \tilde{\rho}_{B,*}/\rho_{\gamma,0} \approx 1$ corresponds to an initial field strength of $\tilde{B}_{\lambda,*} \simeq 3 \times 10^{-6}$ G. The (solid, blue) lines from top to bottom correspond to initial helicity fractions $f_* = \left\{10^{-3}, 10^{-4}, 10^{-6}, < 10^{-14}\right\}$ and $f_* = \left\{10^{-1}, 10^{-4}, 10^{-6}, < 10^{-14}\right\}$ respectively. The maximally helical case $f_* = 1$ (solid, red) is also shown. The final field strength B_0 and coherence length λ_B that would be observed today, i.e. after MHD turbulent decay. We also show (dashed, gray lines) the results from non-helical magnetic fields with an inverse transfer of energy. Reprinted figure with permission from Ref. [49]. Copyright (2015) by the American Physical Society.

The conservation of magnetic helicity in the early Universe leads to an inverse cascade of energy and the slowing down of magnetic decay for fully helical fields. This means that, at the time when CMB spectral distortions can be generated, the magnetic field amplitude is relatively large compared to the non-helical case. This can lead to the generation of larger spectral distortions. If CMB spectral distortions are observed by some new PIXIE-like experiment, then it is likely that magnetic helicity plays an important role. However, there is a degeneracy in the parameter space, since different parameter sets can give the same spectral distortions signal. For example, fields generated at the QCD phase transition with smaller $\varepsilon \equiv \tilde{\rho}_{B,*}/\rho_{\gamma,0}$ and/or helicity can produce the same μ-type distortions as fields generated at the EW phase transition but with larger ε and/or helicity. However, if a μ-type distortion is detected by a PIXIE-like experiment, it would rule out non-helical magnetic fields produced at either the EW or QCD phase transition. A positive detection would give us a lower bound on the primordial magnetic helicity. The lower bound would be somewhere of the order $f_* \gtrsim (10^{-4}$–$10^{-3})$. This is much greater than the primordial magnetic helicity generated in the simplest models of EW baryogenesis [58] where $f_* \sim 10^{-24}$ assuming $B_{\lambda,*} = B^{\rm max}_{\lambda,*}$ and $\lambda_{B,*} = \lambda_{\rm EW}$ [59].

The effect of helical and non-helical magnetic fields in the voids on the propagation of electromagnetic cascades from high energy TeV $\gamma-$ray sources has been investigated in Ref. [60].

In this context it is also interesting to mention the recent tentative observations of large scale helical magnetic fields from γ-ray observations [61]. Such studies have seen some evidence, albeit rather weak, of fully helical fields of strength 10^{-14} G on scales of 10 Mpc. If such fields originated from a time before the μ-era, then it is possible that such observations would be accompanied by a detectable signal for a PIXIE-like experiment. The combination of such two observations would be compelling evidence for large scale helical magnetic fields. We also note that the CMB distortions anisotropies (see e.g. Refs. [62, 63]), albeit potentially very hard to detect, could give interesting signals due to the large helicity of the magnetic fields. Unique signatures in the spatial correlations are expected due to the helical nature of the magnetic fields.

7 Extragalactic magnetic fields unlikely generated at the electroweak phase transition

In the letter [64] we show that magnetic fields generated at the electroweak phase transition are most likely too weak to explain the void magnetic fields apparently observed today unless they have considerable helicity. We show that, in the simplest estimates, the helicity naturally produced in conjunction with the baryon asymmetry is too small to explain observations, which require a helicity fraction at least of order 10^{-14}–10^{-10} depending on the void fields constraint used. Therefore new mechanisms to generate primordial helicity are required if magnetic fields generated during the electroweak phase transition should explain the extragalactic fields.

First-order phase transitions can generate magnetic fields in the early Universe. Under early Universe conditions with very small chemical potentials the QCDPT is a smooth transition [56] whereas the EWPT could be first-order in certain Standard Model (SM) extensions [57]. Inflationary magnetogenesis [32], which is also beyond the SM, is another popular mechanism to explain void magnetic fields. Hence, the apparent observations of void fields from γ-ray observations seem to be a signature of physics beyond the SM or of new mechanisms which excite magnetic helicity (see Sec. 1 and Refs. [65, 66]). If the constraints on void fields prove to be conclusive, then it is likely that magnetic helicity must play an important role. Here we show that magnetic fields generated at the EWPT must have significantly more helicity than that produced by electroweak baryogenesis in order to explain the extragalactic magnetic fields. To reach this conclusion we have assumed the magnetic decay laws of [47, 52, 53] and considered the simplest magnetic helicity estimates of [58] (see Fig. 7). Our assumptions on the decay rates could be challenged due to new results of [54, 55].

8 Nonhelical turbulence and the inverse transfer of energy: A parameter study

In [67] we explore the phenomenon of an *inverse transfer* of energy from large to small scales in decaying magnetohydrodynamical turbulence. For this investigation we mainly employ the *Pencil-Code* performing a parameter study, where we vary the Prandtl number, the kinetic viscosity and the initial spectrum. We find that in order to get a decay which exhibits this *inverse transfer*, large Reynolds numbers ($\mathcal{O} \sim 10^3$) are needed and low Prandtl numbers of the order unity $Pr = 1$ are preferred. Compared to *helical* MHD turbulence, though, the *inverse*

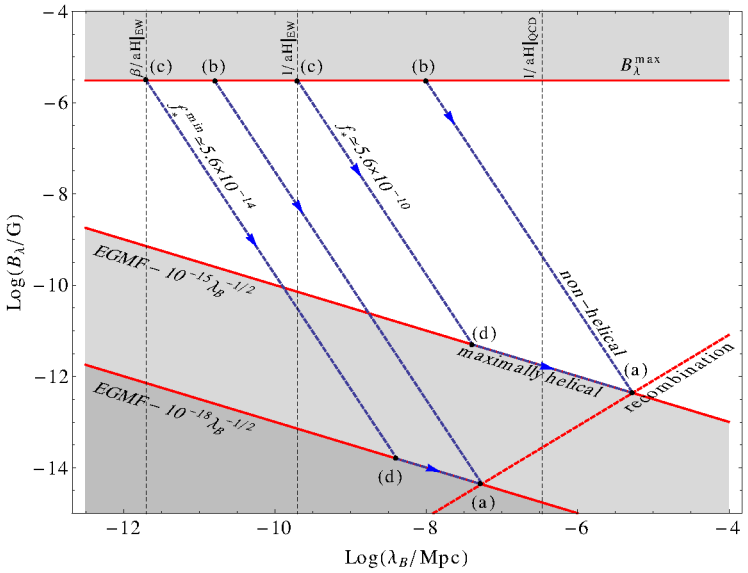


Figure 7: In the greyed out regions, constraints on present day magnetic fields are shown from Fermi observations of γ-ray sources and an upper bound set from energy considerations. Fields generated in the radiation era evolve to the line labelled "recombination". The evolutionary tracks from magnetogenesis until recombination are marked by dashed lines and depend on the helicity fraction f_*. The minimum field configuration at recombination to explain the void fields is marked by point (a). If there is zero helicity, the field configuration at megnetogenesis is marked by point (b). With non-zero helicity the initial field configuration can be reduced e.g point (c), where the field becomes maximally helical at point (d). Figure reprinted from Ref. [64]. © 2016 IOP Publishing Ltd and Sissa Medialab srl.

transfer is much less efficient in transferring magnetic energy to larger scales than the well-known effect of the *inverse cascade*. Hence, applying the *inverse transfer* to the magnetic field evolution in the Early Universe, we question whether the *nonhelical* inverse transfer is effective enough to explain the observed void magnetic fields if a magneto-genesis scenario during the electroweak phase transition is assumed.

Our presented parameter study is based on high-resolution numerical simulations of decaying MHD turbulence. We explored a wide range of numerical parameters and initial conditions in order to find a pattern at which the *inverse transfer* of magnetic energy from small scales to large scales takes place for nonhelical magnetic fields.

Our most prominent finding is the surprising dependency on the Prandtl number: Larger Prandtl numbers lead to a less efficient *inverse transfer* of magnetic energy and might be fully suppressed at Prandtl numbers larger than 10^3. This raises the question whether one can apply the effect of the *inverse transfer* of energy to the evolution of magnetic fields in the early Universe. There, one expects large Prandtl numbers of $\mathrm{Pr} \sim 10^8 (T/\mathrm{keV})^{-3/2}$ [68]. For instance, considering a causally generated field, it will decay according to $E \sim t^{-10/7}$ in the case of suppressed inverse transfer. It will decay as $E \sim t^{-1}$, however, if the inverse transfer is efficient. This results in a many orders of magnitudes weaker field in the former case.

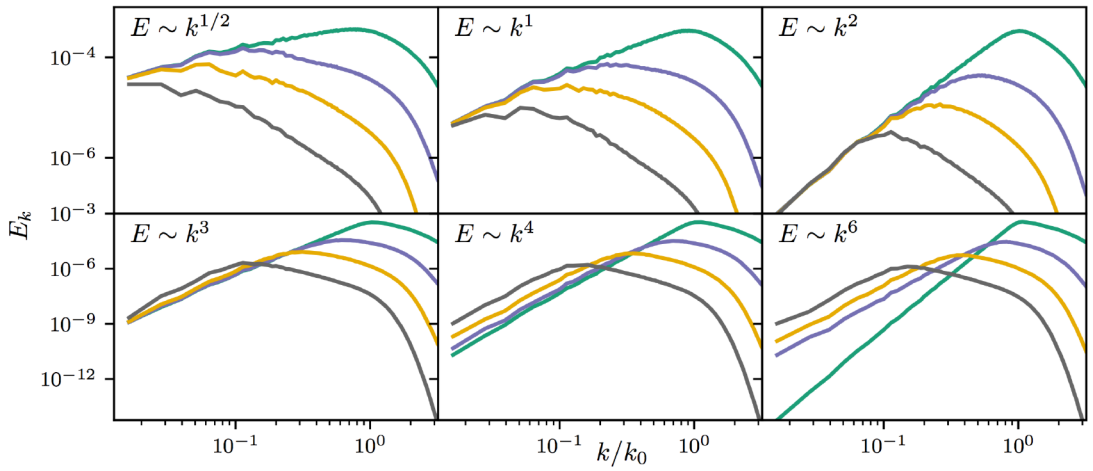


Figure 8: Magnetic power spectra of runs with different spectral indices n. The inverse transfer of energy can only be observed if there is a steep initial spectrum with $n \geq 3$. If an initial spectrum steeper than k^4 is given it will flatten to a *causal* spectrum. Reprinted figure with permission from Ref. [67]. Copyright (2017) by the American Physical Society.

Therefore, it is questionable whether EW phase transition generated fields could be significant enough today to account for the assumed fields in the voids of galaxies (see [64] and [54]).

Furthermore, the efficiency of the *inverse transfer* depends on the Reynolds number. Here, the Reynolds number has to be sufficiently large to observe the effect. With our Pencil-Code simulations we find a critical Reynolds number of $\mathrm{Re} = 500$ for a Prandtl number of $\mathrm{Pr} = 1$.

Another very interesting result of our study is that for shallow and moderately steep slopes of the magnetic power spectrum $n \leq 2$ the effect of the *inverse transfer* is not present. Again, this dependence on n is qualitatively different than the *inverse cascade* of helical fields, which is independent of the spectral index n (see Fig. 8). An $n = 2$ case could be expected from an average over a stochastic distribution of magnetic dipoles [69], and a field with $n = 3/2$ will be generated by the small scale dynamo [70].

Although we find numerical evidence for the effect of non-helical *inverse transfer*, the physics behind this mechanism is yet to be determined. One option could be the enhancement of the magnetic field on large scales by back reactions of velocity fluctuations where the kinetic power spectrum can exceed the magnetic one on scales above the correlation length. Nevertheless, our simulations do not indicate that this mechanism could persist throughout the entire decay phase. See also [55]. Additionally, Brandenburg et al [55] suspect an effect of two-dimensional structure of the turbulence. In two dimensions the square of the vector potential $\langle \mathbf{A}^2 \rangle$ is conserved [71] and could serve as an explanation to the non-helical *inverse transfer*, similar to the conserved helicity in three dimensions. But, $\langle \mathbf{A}^2 \rangle$ varies by at least 80% throughout the simulation time. This is not a lot compared to the magnetic energy which changes by three orders of magnitude during its decay. On the other hand, the helicity in the maximally helical run changes only by a few percent. Nevertheless, the conservation of $\langle \mathbf{A}^2 \rangle$ is not expected in three dimensions and it is not clear why a two-dimensional turbulent structure should develop (depending on the Prandtl number and initial spectral index).

Another way of explaining the inverse transfer is the assumption of a self-similar evolution of the decaying MHD turbulence. Using rescaled MHD variables, Olesen [72] and [73] constructed such a self-similar scenario of decaying MHD turbulence. Although the rescaling of the MHD variables is generally not restricted to a specific choice of the rescaling function, an *inverse transfer* can only be explained by a very specific one where the viscosity is not rescaled, i.e. $\nu \to l^0\nu$ and l is the scale function. First of all, there is no physical reasoning for this (unmotivated) choice and furthermore the rescaling of variables should not impact the physical result. The specific self-similar solution resulting in the *inverse transfer* does not give further insight to this problem. We thus conclude that while there is numerical evidence from our simulations that the non-helical *inverse transfer* of energy can be present, a satisfying physical explanation is still missing.

9 Improved treatment of magnetic heating across the cosmological recombination era

The origin of magnetic fields in the Universe poses many open questions. In [74] we study the evolution of primordial magnetic fields PMF, generated by some early-universe mechanism, across the cosmological recombination epoch, one of the clearly anticipated stages in their evolution. The main goal is to obtain an understanding of the relevant dissipation processes with particular focus on the transition between photon drag-dominated evolution in the pre-recombination era ($z \gtrsim 10^3$) to turbulent decay at later times ($z \lesssim 10^3$). We carry out a suite of numerical MHD simulations studying the dependence of the effective heating rates on the magnetic field strength and spectral index. Our analysis shows that in the drag-dominated phase no real heating of the matter is produced but that the dissipated energy sources small-scale anisotropies and spectral distortions of the cosmic microwave background (CMB). This stage is followed by a new intermediate phase during which magnetic field energy is mainly converted into kinetic energy of the baryons, building up a turbulent velocity field and producing increasing heating that declines later under turbulent decay. Depending on the PMF strength and spectral index, the onset of turbulent decay can be delayed until $z \simeq 600$, diminishing the expected effects on the CMB anisotropies. We provide several analytic approximations and present numerical results that can be used to study CMB constraints on PMF.

For our investigation, we performed 3D numerical simulations of PMFs along with baryon velocity fluctuations across the cosmological recombination era. Photon drag was included using the standard recombination history obtained with `CosmoRec` and the MHD equations were solved in an expanding medium. Our simulations allow us to trace the flow of energy from the magnetic field, through the baryon velocity field to heating via turbulent decay and dissipation. We are able to describe the net heating rates smoothly across the epoch of recombination enabling a clean separation of real heating, which will lead to an increase of the matter temperature, from drag-dominated energy losses to the CMB photon field, which only leads to secondary temperature perturbations and CMB spectral distortions.

We supported our computations with analytic estimates and provide several useful expressions to represent our numerical results. We find that at redshifts below $z \lesssim 500$, in the regime of well-developed turbulent decay, our new analytic approximation with an additional delay-factor taking the spectral slope into account, gives a slightly better fit.

We observed three main evolutionary stages for magnetic heating: i) an initial phase that is dominated by photon drag ($z \gtrsim 1200$), ii) an intermediate transition period around cosmological

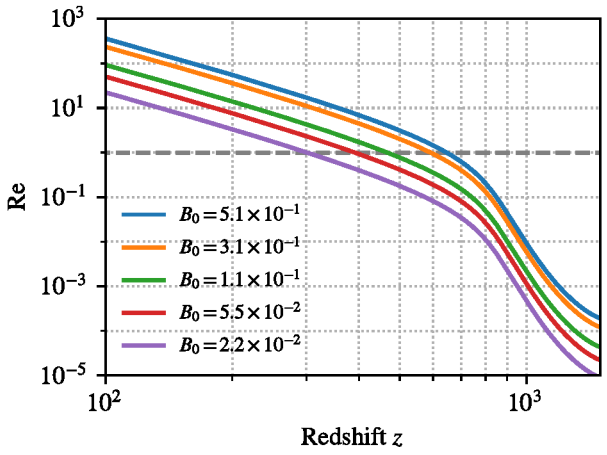


Figure 9: Magnetic Reynolds numbers as a function of redshift for simulation runs where B_0 is varied. The critical magnetic Reynolds number Re = 1 is indicated with a grey dashed line. For different initial amplitudes the Re = 1 redshift varies from $z_{\rm td} \simeq 650$ (fiducial $B_0 = 0.51$) to $z_{\rm td} \simeq 300$. Figure taken from Ref. [74].

recombination, when the photon drag force drops rapidly, and iii) the final fully turbulent MHD phase ($z \lesssim 600$). Only in the latter part of the transition and the turbulent phase do we find significant heating of the medium, a result that is important when deriving and interpreting constraints on PMFs from CMB measurements.

Our computations show that the baryon velocity fluctuations are initially strongly suppressed because of photon drag, but build up during the intermediate transition phase. After recombination, a state approaching equipartition between magnetic and kinetic energy is reached, after which the plasma dissipates energy in a turbulent cascade. In previous treatments, the build-up of the velocity field and its turbulent decay were assumed to proceed instantaneously at recombination ($z \simeq 1100$). Our simulations reveal a substantial delay for the onset of turbulence until redshift $z \simeq 600$–900 (this depends on the amplitude and shape of the initial magnetic power spectrum). In the transition phase, the Lorentz force continuously sources the baryon velocity field until a well developed turbulent state is reached, a process that causes this delay of up to 0.5 Myr.

We also find that the shapes of the net heating rates obtained are broader than previously estimated semi-analytically. Further, for the weaker magnetic fields, their peak broadens to significantly lower redshifts ($z \lesssim 400$). For low magnetic field strengths, the flow reaches turbulence more gradually with the magnetic Reynolds number exceeding unity only in the late stages (see Fig. 9). Steep (blue) spectra produce an earlier peak in the net heating rates at $z_{\rm peak} \simeq 900$. The shape, peak width and epoch of the net heating rate furthermore depends directly on the initial amplitude of the magnetic fields and the spectral index. Our simulations furthermore indicate that the peak magnetic dissipation rate actually occurs once the drag coefficient has already begun to drop sharply and the fluid begins to approach equipartition between magnetic and kinetic dissipation. This again is in contrast to previous interpretations.

Also, while nearly the whole PMF power spectrum is reshaped to a turbulent power-law for the near scale-invariant case, only the intermediate scale wavemodes $k > 10^4$ Mpc^{-1} are

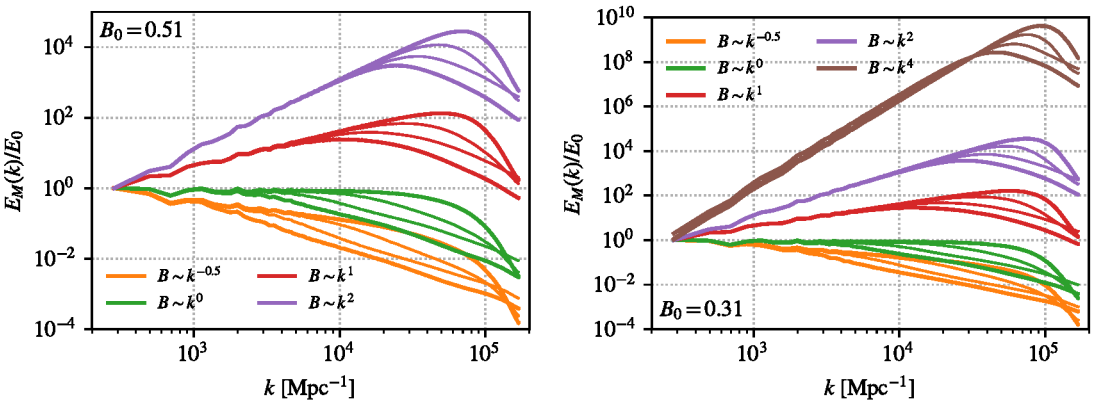


Figure 10: Evolution of the magnetic power spectra of runs with different spectral index n, at four redshifts $z = 2800, 1200, 900$ & 400, decreasing from top to bottom in each panel. The left panel is for $B_{z=3000} = 0.51$ while the right panel shows the curves for $B_{z=3000} = 0.31$. For $B_0 = 0.31$, the case of a causal initial spectrum, $E_M \propto k^4$, is also presented. Figures taken from Ref. [74].

reprocessed for the runs with $E \propto k^1$ and only the smallest scale modes $k > 5.0 \times 10^4$ Mpc^{-1} for the steepest spectrum $E \propto k^4$ (see Fig. 10). The direct observation of the spectral transformation from the initial power-law with cut-off shape to a spectrum in its transitional phase up to the final stage with a turbulent slope is a novel feature of our computations and a benefit of the full 3D treatment of the MHD equations. We can see that for our fiducial case with a near scale-invariant initial power-law with a cutoff at small scales, a turbulent spectrum is developed (with a slope $E \propto k^{-1.4}$ that is slightly shallower than Kolmogorov-type turbulence) as turbulent cascade removes and redistributes power.

To be able to achieve a more complete treatment, more physics at late times need to be included: below a redshift of $z \lesssim 200$ effects like ambipolar diffusion come into play and can contribute substantially to the late time evolution of the magnetic heating history. Stronger magnetic fields along with compressible phenomena would extend the scope of these simulations. A simultaneous treatment of density perturbations induced by PMFs would complement the evolution of heating and its cosmological effects.

References

[1] G. Sigl and N. Leite, *Chiral Magnetic Effect in Protoneutron Stars and Magnetic Field Spectral Evolution*, *JCAP* **1601** (2016) 025, [1507.04983].

[2] R. Alves Batista, A. Dundovic, M. Erdmann, K.-H. Kampert, D. Kuempel, G. Müller et al., *CRPropa 3 - a Public Astrophysical Simulation Framework for Propagating Extraterrestrial Ultra-High Energy Particles*, *JCAP* **1605** (2016) 038, [1603.07142].

[3] L. Merten, J. Becker Tjus, H. Fichtner, B. Eichmann and G. Sigl, *CRPropa 3.1—a low energy extension based on stochastic differential equations*, *JCAP* **1706** (2017) 046, [1704.07484].

[4] S. Hackstein, F. Vazza, M. Brüggen, G. Sigl and A. Dundovic, *Propagation of ultrahigh energy cosmic rays in extragalactic magnetic fields: a view from cosmological simulations*, *Mon. Not. Roy. Astron. Soc.* **462** (2016) 3660–3671, [1607.08872].

[5] R. Alves Batista, M.-S. Shin, J. Devriendt, D. Semikoz and G. Sigl, *Implications of strong intergalactic magnetic fields for ultrahigh-energy cosmic-ray astronomy*, *Phys. Rev.* **D96** (2017) 023010, [1704.05869].

[6] R. Alves Batista and G. Sigl, *Diffusion of cosmic rays at EeV energies in inhomogeneous extragalactic magnetic fields*, *JCAP* **1411** (2014) 031, [1407.6150].

[7] PIERRE AUGER Collaborations, A. Aab et al., *Observation of a Large-scale Anisotropy in the Arrival Directions of Cosmic Rays above* 8×10^{18} *eV*, *Science* **357** (2017) 1266–1270, [1709.07321].

[8] A. Dundović and G. Sigl, *Anisotropies of Ultra-high Energy Cosmic Rays Dominated by a Single Source in the Presence of Deflections*, 1710.05517.

[9] P. Avola, *On the Role of Liouville Theorem in High Energy Cosmic Ray Anisotropy Studies*, Master's thesis, Universität Hamburg, 2017.

[10] N. Leite, C. Evoli, M. D'Angelo, B. Ciardi, G. Sigl and A. Ferrara, *Do Cosmic Rays Heat the Early Intergalactic Medium?*, *Mon. Not. Roy. Astron. Soc.* **469** (2017) 416–424, [1703.09337].

[11] J. D. Bowman, A. E. E. Rogers, R. A. Monsalve, T. J. Mozdzen and N. Mahesh, *An absorption profile centred at 78 megahertz in the sky-averaged spectrum*, *Nature* **555** (2018) 67–70.

[12] N. Leite, R. Reuben, G. Sigl, M. H. G. Tytgat and M. Vollmann, *Synchrotron Emission from Dark Matter in Galactic Subhalos. A Look into the Smith Cloud*, *JCAP* **1611** (2016) 021, [1606.03515].

[13] J.-E. Schönberg, *Sensitivity of radio emission from galaxy clusters and dwarf spheroidal galaxies to dark matter annihilation*, Master's thesis, Universität Hamburg, 2017.

[14] G. Sigl, *Astrophysical Haloscopes*, *Phys. Rev.* **D96** (2017) 103014, [1708.08908].

[15] M. Schlederer and G. Sigl, *Constraining ALP-photon coupling using galaxy clusters*, *JCAP* **1601** (2016) 038, [1507.02855].

[16] F. P. Huang, K. Kadota, T. Sekiguchi and H. Tashiro, *Radio telescope search for the resonant conversion of cold dark matter axions from the magnetized astrophysical sources*, *Phys. Rev.* **D97** (2018) 123001, [1803.08230].

[17] A. Hook, Y. Kahn, B. R. Safdi and Z. Sun, *Radio Signals from Axion Dark Matter Conversion in Neutron Star Magnetospheres*, 1804.03145.

[18] N. Violante Gomes Leite, *On the Connection Between Particle Physics and Properties of Cosmic Magnetic Fields*, Ph.D. thesis, U. Hamburg, Dept. Phys., 2017. http://ediss.sub.uni-hamburg.de/volltexte/2017/8556/.

[19] M. Schlederer, *Generation of gravitational waves by primordial magnetic fields*, Master's thesis, Universität Hamburg, 2017.

[20] J. M. Wagstaff, R. Banerjee, D. Schleicher and G. Sigl, *Magnetic field amplification by the small-scale dynamo in the early Universe*, *Phys. Rev. D* **89** (May, 2014) 103001, [1304.4723].

[21] R. Beck, *Magnetic Fields in Galaxies*, *Space Science Reviews* **166** (2012) 215–230.

[22] M. L. Bernet, F. Miniati, S. J. Lilly, P. P. Kronberg and M. Dessauges-Zavadsky, *Strong magnetic fields in normal galaxies at high redshift*, *Nature* **454** (2008) 302–304, [0807.3347].

[23] L. Feretti, G. Giovannini, F. Govoni and M. Murgia, *Clusters of galaxies: observational properties of the diffuse radio emission*, *A&AR* **20** (2012) 54, [1205.1919].

[24] Y. Xu, P. P. Kronberg, S. Habib and Q. W. Dufton, *A Faraday Rotation Search for Magnetic Fields in Large-scale Structure*, *AstrophysJ* **637** (2006) 19–26, [arXiv:astro-ph/0509826].

[25] S. Chakraborti, N. Yadav, C. Cardamone and A. Ray, *Radio Detection of Green Peas: Implications for Magnetic Fields in Young Galaxies*, *ApJ* **746** (Feb., 2012) L6, [1110.3312].

[26] A. Neronov and I. Vovk, *Evidence for strong extragalactic magnetic fields from Fermi observations of TeV blazars*, *Science* **328** (2010) 73–75, [1006.3504].

[27] R. Beck, A. Brandenburg, D. Moss, A. Shukurov and D. Sokoloff, *Galactic Magnetism: Recent Developments and Perspectives*, *ARA&A* **34** (1996) 155–206.

[28] D. R. G. Schleicher, R. Banerjee, S. Sur, T. G. Arshakian, R. S. Klessen, R. Beck et al., *Small-scale dynamo action during the formation of the first stars and galaxies. I. The ideal MHD limit*, *Astron. Astrophys.* **522** (2010) A115, [1003.1135].

[29] M. A. Latif, D. R. G. Schleicher, W. Schmidt and J. Niemeyer, *The small scale dynamo and the amplification of magnetic fields in massive primordial haloes*, *Mon. Not. Roy. Astron. Soc.* **432** (2013) 668, [1212.1619].

[30] R. Banerjee, S. Sur, C. Federrath, D. R. Schleicher and R. S. Klessen, *Generation of strong magnetic fields via the small-scale dynamo during the formation of the first stars*, 1202.4536.

[31] J. Schober, D. R. G. Schleicher and R. S. Klessen, *Magnetic field amplification in young galaxies*, *A&A* **560** (Dec., 2013) A87, [1310.0853].

[32] M. S. Turner and L. M. Widrow, *Inflation Produced, Large Scale Magnetic Fields*, *Phys.Rev.* **D37** (1988) 2743.

[33] G. Sigl, A. V. Olinto and K. Jedamzik, *Primordial magnetic fields from cosmological first order phase transitions*, *Phys.Rev.* **D55** (1997) 4582–4590, [astro-ph/9610201].

[34] E. Harrison, *Generation of Magnetic Fields in the Radiation ERA*, *Mon. Not. Roy. Astron. Soc.* **147** (1970) 279.

[35] S. Tsugé, *Approach to the origin of turbulence on the basis of two-point kinetic theory*, *Physics of Fluids* **17** (Jan., 1974) 22–33.

[36] A. Kosowsky, A. Mack and T. Kahniashvili, *Gravitational radiation from cosmological turbulence*, *Phys. Rev. D* **66** (July, 2002) 024030, [astro-ph/0111483].

[37] C. Caprini and R. Durrer, *Gravitational waves from stochastic relativistic sources: Primordial turbulence and magnetic fields*, *Phys. Rev. D* **74** (Sept., 2006) 063521, [astro-ph/0603476].

[38] J. Schober, D. Schleicher, C. Federrath, R. Klessen and R. Banerjee, *Magnetic Field Amplification by Small-Scale Dynamo Action: Dependence on Turbulence Models and Reynolds and Prandtl Numbers*, 1109.4571.

[39] A. A. Schekochihin, S. A. Boldyrev and R. M. Kulsrud, *Spectra and Growth Rates of Fluctuating Magnetic Fields in the Kinematic Dynamo Theory with Large Magnetic Prandtl Numbers*, *ApJ* **567** (Mar., 2002) 828–852, [astro-ph/0103333].

[40] C. Federrath, G. Chabrier, J. Schober, R. Banerjee, R. S. Klessen et al., *Mach Number Dependence of Turbulent Magnetic Field Amplification: Solenoidal versus Compressive Flows*, *Phys.Rev.Lett.* **107** (2011) 114504, [1109.1760].

[41] A. Lewis, *Observable primordial vector modes*, *Phys.Rev.* **D70** (2004) 043518, [astro-ph/0403583].

[42] T. H.-C. Lu, K. Ananda and C. Clarkson, *Vector modes generated by primordial density fluctuations*, *Phys.Rev.* **D77** (2008) 043523, [0709.1619].

[43] T. H.-C. Lu, K. Ananda, C. Clarkson and R. Maartens, *The cosmological background of vector modes*, *JCAP* **0902** (2009) 023, [0812.1349].

[44] A. J. Christopherson, K. A. Malik, D. R. Matravers and K. Nakamura, *Comparing two different formulations of metric cosmological perturbation theory*, *Classical and Quantum Gravity* **28** (Nov., 2011) 225024, [1101.3525].

[45] K. Ichiki, K. Takahashi and N. Sugiyama, *Constraint on the primordial vector mode and its magnetic field generation from seven-year Wilkinson Microwave Anisotropy Probe Observations*, *Phys.Rev.* **D85** (2012) 043009, [1112.4705].

[46] A. Gruzinov, S. C. Cowley and R. Sudan, *Small scale field dynamo*, *Phys.Rev.Lett.* **77** (1996) 4342–4345, [astro-ph/9611194].

[47] R. Banerjee and K. Jedamzik, *The Evolution of cosmic magnetic fields: From the very early universe, to recombination, to the present*, *Phys.Rev.* **D70** (2004) 123003, [astro-ph/0410032].

[48] R. Durrer and A. Neronov, *Cosmological magnetic fields: their generation, evolution and observation*, *A&A Rev.* **21** (June, 2013) 62, [1303.7121].

[49] J. M. Wagstaff and R. Banerjee, *CMB spectral distortions from the decay of causally generated magnetic fields*, *Phys. Rev. D* **92** (Dec., 2015) 123004, [1508.01683].

[50] D. J. Fixsen, E. S. Cheng, J. M. Gales, J. C. Mather, R. A. Shafer and E. L. Wright, *The Cosmic Microwave Background Spectrum from the Full COBE FIRAS Data Set*, *ApJ* **473** (Dec., 1996) 576, [astro-ph/9605054].

[51] A. Kogut, D. J. Fixsen, D. T. Chuss, J. Dotson, E. Dwek, M. Halpern et al., *The Primordial Inflation Explorer (PIXIE): a nulling polarimeter for cosmic microwave background observations*, *JCAP* **7** (July, 2011) 025, [1105.2044].

[52] L. Campanelli, *Evolution of magnetic fields in freely decaying magnetohydrodynamic turbulence*, *Phys. Rev. Lett.* **98** (Jun, 2007) 251302.

[53] L. Campanelli, *Evolution of primordial magnetic fields in mean-field approximation*, *Eur. Phys. J.* **C74** (2014) 2690, [1304.4044].

[54] T. Kahniashvili, A. G. Tevzadze, A. Brandenburg and A. Neronov, *Evolution of primordial magnetic fields from phase transitions*, *Phys. Rev. D* **87** (Apr, 2013) 083007.

[55] A. Brandenburg, T. Kahniashvili and A. G. Tevzadze, *Nonhelical Inverse Transfer of a Decaying Turbulent Magnetic Field*, *Physical Review Letters* **114** (Feb., 2015) 075001, [1404.2238].

[56] Y. Aoki, G. Endrődi, Z. Fodor, S. D. Katz and K. K. Szabó, *The order of the quantum chromodynamics transition predicted by the standard model of particle physics*, *Nature* **443** (Oct., 2006) 675–678, [hep-lat/0611014].

[57] M. Laine and K. Rummukainen, *The MSSM electroweak phase transition on the lattice*, *Nuclear Physics B* **535** (Dec., 1998) 423–457, [hep-lat/9804019].

[58] T. Vachaspati, *Estimate of the Primordial Magnetic Field Helicity*, *Physical Review Letters* **87** (Dec., 2001) 251302, [astro-ph/0101261].

[59] J. M. Wagstaff and R. Banerjee, *Extragalactic magnetic fields unlikely generated at the electroweak phase transition*, *JCAP* **1601** (2016) 002, [1409.4223].

[60] R. Alves Batista, A. Saveliev, G. Sigl and T. Vachaspati, *Probing Intergalactic Magnetic Fields with Simulations of Electromagnetic Cascades*, *Phys. Rev.* **D94** (2016) 083005, [1607.00320].

[61] H. Tashiro, W. Chen, F. Ferrer and T. Vachaspati, *Search for CP violating signature of intergalactic magnetic helicity in the gamma-ray sky*, *MNRAS* **445** (Nov., 2014) L41–L45, [1310.4826].

[62] K. Miyamoto, T. Sekiguchi, H. Tashiro and S. Yokoyama, *CMB distortion anisotropies due to the decay of primordial magnetic fields*, *Phys. Rev. D* **89** (Mar., 2014) 063508, [1310.3886].

[63] J. Ganc and M. S. Sloth, *Probing correlations of early magnetic fields using μ-distortion*, *JCAP* **8** (Aug., 2014) 018, [1404.5957].

[64] J. M. Wagstaff and R. Banerjee, *Extragalactic magnetic fields unlikely generated at the electroweak phase transition*, *JCAP* **1** (Jan., 2016) 002, [1409.4223].

[65] A. Boyarsky, J. Fröhlich and O. Ruchayskiy, *Self-Consistent Evolution of Magnetic Fields and Chiral Asymmetry in the Early Universe*, *Physical Review Letters* **108** (Jan., 2012) 031301, [1109.3350].

[66] A. Boyarsky, J. Fröhlich and O. Ruchayskiy, *Magnetohydrodynamics of chiral relativistic fluids*, *Phys. Rev. D* **92** (Aug., 2015) 043004, [1504.04854].

[67] J. Reppin and R. Banerjee, *Nonhelical turbulence and the inverse transfer of energy: A parameter study*, *Phys. Rev.* **E96** (2017) 053105, [1708.07717].

[68] R. Banerjee and K. Jedamzik, *Evolution of cosmic magnetic fields: From the very early Universe, to recombination, to the present*, *Phys. Rev. D* **70** (Dec., 2004) 123003–+.

[69] C. J. Hogan, *Magnetohydrodynamic effects of a first-order cosmological phase transition*, *Physical Review Letters* **51** (Oct., 1983) 1488–1491.

[70] A. P. Kazantsev, *Enhancement of a Magnetic Field by a Conducting Fluid*, *Soviet Journal of Experimental and Theoretical Physics* **26** (1968) 1031.

[71] D. Biskamp, *Magnetohydrodynamic Turbulence*. Cambridge Univserity Press, 2008, Feb., 2008.

[72] P. Olesen, *Inverse cascades and primordial magnetic fields*, *Physics Letters B* **398** (Feb., 1997) 321–325, [astro-ph/9610154].

[73] L. Campanelli, *On the self-similarity of nonhelical magnetohydrodynamic turbulence*, *Eur. Phys. J.* **C76** (2016) 504, [1511.06797].

[74] P. Trivedi, J. Reppin, J. Chluba and R. Banerjee, *Magnetic heating across the cosmological recombination era: Results from 3D MHD simulations*, *MNRAS* (July, 2018) , [1805.05315].

Cosmological Implications of First-Order Phase Transitions

Thomas Konstandin[1], *Günter Sigl*[2]

[1]DESY, Hamburg, Germany
[2]II. Institut für Theoretische Physik, Universität Hamburg, Germany

DOI: http://dx.doi.org/10.3204/PUBDB-2018-00782/C10

Phase transitions in the early Universe can lead to many potentially observable effects such as the generation of primordial magnetic seed fields, gravitational waves and baryon- and lepton number. They depend on yet not well known properties, such as the order of the phase transitions, that can be influenced by physics beyond the Standard Model.

1 Introduction

Project C10 of the SFB 676 is concerned with cosmological implications of first-order phase transitions. The appeal of cosmological phase transitions is that they provide a link between cosmological observations and the energy frontier of particle physics. As an analogy consider the cosmic microwave background (CMB). The observations of the CMB are very predictive because we understand atomic physics well from the laboratory experiments. Image we would have observed the CMB without the detailed knowledge on atomic physics. Ultimately, we could use the CMB data to learn something about the physics of the hydrogen atom. This is basically the situation with the electroweak phase transition. In case it is first order – which depends on the scalar sector of the particle physics theory – many interesting phenomena result that can teach us about particle physics on electroweak energy scales.

The project C10 deals with a variety of aspects of cosmological phase transition. This includes understanding the nature of the phase transition and its properties in various extensions of the Standard Model (SM). The trademark of first-order phase transitions (1st-order PTs) is that they proceed by bubble nucleation. The prime example for this kind of phase transition is boiling water – where bubbles of gas expand into the liquid phase – or chemical combustion where a fireball rapidly consumes all its surroundings. Important characteristics are the latent heat that is released by the phase transition into the plasma or the velocity with which the phase boundary is moving. Part of C10 is concerned with developing tools to assess these characteristics in an efficient way.

Another aspect of C10 is model building. Particle physics models are currently tested by the LHC experiments at CERN which allows to cross-correlate the knowledge from colliders that is relevant for the electroweak phase transition with cosmological observations. For example, additional bosonic degrees of freedom (that might be strongly coupled to the Higgs particle) have a strong impact on the electroweak phase transition. The discovery of an extended scalar sector would hence have far-reaching implications also in cosmology.

Various subfields of physics meet at the theory of cosmological phase transitions, in particular particle physics, thermodynamics and magnetohydrodynamics. A particular example that played a role in C10 is that fact that a chiral asymmetry in the lepton sector can be transformed into helical magnetic fields under certain circumstances. Since electroweak interactions in particular in the broken phase do violate chiral symmetry, this effect, which is known as the chiral magnetic effect, may contribute to or influence magnetogenesis around the electroweak phase transition.

With the observation of the first gravitational waves from binary mergers by LIGO and VIRGO (see, e.g. Ref. [1] for a binary black hole merger and Ref. [2] for a binary neutron star merger), the era of gravitational wave astronomy began. Also 1st-order phase transitions are a potential source of gravitational waves. The nucleated bubbles collide at the end of the phase transition what leads to gravitational wave production. However, the main source of gravitational waves in this context are actually secondary effects. This includes sound waves in the plasma or hydromagnetic turbulence, which both are a consequence of the phase transition. We performed studies quantifying these phenomena within project C10.

Finally, cosmological 1st-order phase transitions can also explain the observed asymmetry between matter and anti-matter via electroweak baryogenesis. The main advantage of electroweak baryogenesis is that all ingredients required for baryogenesis (mostly CP violation and a departure from equilibrium) result from physics that is testable in the laboratory in the near future. Since baryogenesis requires a potent source of CP violation, an additional strong link to particle physics is present in this context.

In the following sections, we discuss these topics in a little bit more detail and in particular the new results achieved within the project C10.

2 The electroweak phase transition

The main tool to study phase transitions and spontaneous symmetry breaking is the effective action [4]. On a technical level, the effective action is so powerful because it resums so-called tadpole diagrams that show up in conventional perturbative expansions.

Still, the evaluation of the effective action is typically performed in a perturbative way (albeit expanding around the broken vacuum). In many cases, the effective action obtained this way suffers from several shortcomings and often these issues are related to the gauge chosen. One common gauge is the Landau gauge. This gauge has the advantage that the ghost degrees of freedom (mostly) decouple. At the same time, the Goldstone bosons are massless in the broken phase in this gauge. This leads to the fact that infrared (IR) enhanced contributions to the effective action can spoil the convergence of the perturbative expansion. In Refs. [5] and [6], members of C10 analyze the impact of these IR issues in the SM potential and propose a general method to resum the offending terms into an IR safe effective potential.

Since this IR issue seems to be a peculiarity of the Landau gauge, the gauge-dependence of the effective action and observables derived from it is the next obvious question. In a series of papers [3, 7, 8], the gauge dependence of the effective action and the resulting phase transition characteristics were studied. The gauge-dependence is in this context a tricky issue, since the effective action depends on the gauge while observables generally don't. For example, Figure 1 shows the Higgs configuration that leads to vacuum decay, calculated in two different gauges (R_ξ-gauge with $\xi = 0$ and $\xi = 200$). The configurations obey different boundary conditions and carry different kinetic and potential energies. In the end, all these effects conspire to yield

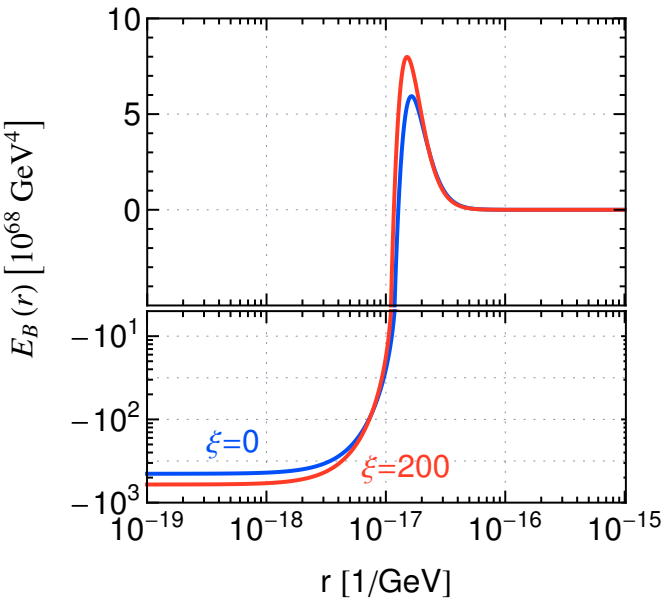


Figure 1: Higgs field configurations that lead to vacuum decay, calculated in two different gauges (R_ξ-gauge with $\xi = 0$ and $\xi = 200$). Figure taken from Ref. [3].

the same (measurable) decay rate.

Another item that is relevant for gravitational wave detection (see sec. 5) and baryogenesis (see sec. 6) are the characteristics of the phase transition. While many properties of the phase transition – as the latent heat or the phase transition temperature – can be readily inferred from the effective potential, some properties require additional work. This is the case for the expansion velocity of the nucleated bubbles during a 1st-order phase transition. The expansion velocity depends on friction which is an out-of-equilibrium phenomenon. Accordingly, one has to grasp the out-of-equilibrium nature of the plasma during the phase transition, which can be tracked using Boltzmann equations. Based on the seminal work by Moore and Prokopec in the SM [9], members of C10 extended the friction calculation to a large variety of models [10].

Another aspect of the electroweak phase transition constitutes model building. Many models beyond the Standard Model that display a strong 1st-order PT, but not all are equally interesting. One guiding principle for model building is minimality. Adding solely a scalar boson or a second Higgs doublet extends the SM particle content marginally while allowing for the rich phenomenology of a 1st-order phase transition [11, 12]. A novel avenue is hereby to connect the phase transition to the flavor puzzle in the Standard Model. The Yukawa couplings of the SM that generate the fermion masses via spontaneous symmetry breaking, span many orders of magnitude in the quark and lepton sector. One way to explain these greatly different coupling constants is to resort to an additional quantum number, a Froggatt–Nielsen charge. Light particles carry larger amounts of this charge leading to smaller couplings. If every additional charge suppresses the coupling by a factor of order one (let's say 10), relatively small quantum numbers can explain the vast hierarchy between the fermion masses. This idea is realized in

the Froggatt–Nielsen mechanism. The novel approach of Ref. [13] connects the mechanism by Froggatt and Nielsen to electroweak symmetry breaking. This greatly enhances the strength of the phase transition and leads to new sources of CP violation as required by baryogenesis. We will come back to this question in sec. 6.

3 The chiral magnetic effect: generalities

In project C10 we also have investigated the chiral magnetic effect in particular in the context of the early Universe [14, 15]. This effect connects the subjects of magnetohydrodynamics with particle physics, in particular the so-called chiral anomaly, i.e. the non-conservation of chiral lepton currents. Here we discuss general aspects and their relevance in the cosmological context. In the report for project C9 we discuss the chiral magnetic effect in a qualitative way and briefly discuss its role in the context of hot neutron stars.

For the electron chiral asymmetry $N_5 \equiv N_L - N_R$ and the magnetic helicity $\mathcal{H} \equiv \int d^3\mathbf{r}\, \mathbf{B}\cdot\mathbf{A}$ the electromagnetic chiral anomaly gives

$$\frac{d}{dt}\left(N_5 - \frac{e^2}{4\pi^2}\mathcal{H}\right) = 0\,, \tag{1}$$

and $e^2\mathcal{H}/(4\pi^2)$ is just the Chern–Simons number of the electromagnetic field. The generalized Maxwell–Ampère law

$$\boldsymbol{\nabla}\times\mathbf{B} = \frac{\partial\mathbf{E}}{\partial t} + \mu_0\left(\mathbf{j}_{\rm em} + \mathbf{j}_{cB}\right)\,, \quad \text{with} \quad \mathbf{j}_{cB} = -\frac{e^2}{2\pi^2}\mu_5\mathbf{B}\,, \tag{2}$$

and in the absence of external currents Ohm's law $\mathbf{j}_{\rm em} = \sigma\mathbf{E}$ gives

$$\mathbf{E} \simeq -\mathbf{v}\times\mathbf{B} + \eta\left(\boldsymbol{\nabla}\times\mathbf{B} + \frac{2e^2}{\pi}\mu_5\mathbf{B}\right)\,, \tag{3}$$

where $\eta = 1/(\mu_0\sigma)$ is the resistivity and the effective chemical potential is given by

$$\mu_5 = \frac{\mu_L - \mu_R}{2} - V_5 = \frac{\mu_L - V_L - \mu_R + V_R}{2}\,, \tag{4}$$

where V_5 is a possible effective potential due to a different forward scattering amplitude for left- and right-chiral electrons. Inserting this into the induction equation the MHD is modified to

$$\partial_t\mathbf{B} = \boldsymbol{\nabla}\times(\mathbf{v}\times\mathbf{B}) + \eta\Delta\mathbf{B} - \frac{2e^2}{\pi}\eta\mu_5\boldsymbol{\nabla}\times\mathbf{B}\,. \tag{5}$$

This equation is similar to the mean field dynamo equation which also has growing solutions. Neglecting the velocity term the evolution equations for the power spectra M_k and H_k [note $U_B = \int d\ln k M_k$ and $\mathcal{H} = \int d\ln k H_k$] now become

$$\begin{aligned}\partial_t M_k &= -\eta k^2\left(2M_k + \frac{e^2}{2\pi^2}\mu_5 H_k\right)\,,\\ \partial_t H_k &= -\eta\left(2k^2 H_k + 32e^2\mu_5 M_k\right)\,.\end{aligned} \tag{6}$$

Integrating over $\ln k$ gives

$$\partial_t \mathcal{H} = -\eta \int d\ln k \left(2k^2 H_k + 32e^2 \mu_5 M_k\right) . \tag{7}$$

In an FLRW metric these are comoving quantities and conformal time.

Now express N_5 in terms of μ_5,

$$N_5 = c(T,\mu_e) V \mu_5 , \quad \text{with} \quad c(T,\mu_e) = \frac{\mu_e^2}{\pi^2} + \frac{T^2}{3} \quad \text{for } \mu_e^2 + T^2 \gg m_e^2 , \tag{8}$$

where the second expression holds for relativistic electrons. Applying this to Eq. (1) we get

$$d\mathcal{H} = \frac{4\pi^2}{e^2} dN_5 = \frac{4\pi^2 V c(T,\mu_e)}{e^2} d\mu_5 . \tag{9}$$

We now take into account damping of μ_5 from *chirality flips*. In the cosmological context after electroweak breaking at $T = T_{\rm ew} \simeq 160\,\text{GeV}$ the rate is

$$R_f \simeq \left(\frac{m_e}{6T}\right)^2 R \sim \left(\frac{m_e}{6T}\right)^2 400 \left(\frac{\alpha_{\rm em}}{6T}\right)^2 10\,T^3 \sim 10^{-4} \frac{m_e^2}{T} , \quad T \lesssim T_{\rm ew} , \tag{10}$$

which is larger than the Hubble rate. Before electroweak breaking

$$R_f \simeq \frac{T_5}{T} H(T_5) , \quad T \gtrsim T_{\rm ew} , \quad T_5 \simeq 10\,\text{TeV} . \tag{11}$$

Inserting Eq. (7) into Eq. (9) then yields

$$\partial_t \mu_5 = -\frac{e^2 \eta}{2\pi^2 V c(T,\mu_e)} \int d\ln k \left(k^2 H_k + 16e^2 \mu_5 M_k\right) - 2R_f \left(\mu_5 - \mu_{5,b}\right) . \tag{12}$$

Here $\mu_{5,b} = -V_5 + \mu_s$ is the equilibrium value of the effective chemical potential μ_5 for $\eta \to 0$. Other processes such as electroweak interactions with other species as for example neutrinos can be taken into account by the term $\mu_{5,b}$ and thus the source term $2R_f\mu_s$.

From Eq. (6) growing solutions exist for wavenumbers

$$k < k_5 \equiv k_5(\mu_5) \equiv \frac{2e^2}{\pi} |\mu_5| . \tag{13}$$

This follows from using helicity modes in Eq. (5) which gives

$$\partial_t b_{\mathbf{k}}^{\pm} = \eta k \left(\mp \frac{2e^2}{\pi} \mu_5 - k\right) b_{\mathbf{k}}^{\pm} , \tag{14}$$

Thus if the condition Eq. (13) is fulfilled, the helicity with the opposite sign as μ_5 will grow whereas the same sign helicity will decay and the absolute value of the helicity will be close to the maximal value given by

$$|H_k| \le \frac{8\pi M_k}{k} . \tag{15}$$

In contrast, for $k \gtrsim k_5$ both helicities will decay with roughly the resistive rate. For the helicity with opposite sign to μ_5 the first term in Eq. (14) corresponds to a growth rate in the cosmological context

$$R_c(k) = \frac{2e^2}{\pi}\eta k|\mu_5| \simeq 2\times 10^{10}\left(\frac{\mathrm{TeV}}{T}\right)\left(\frac{k}{k_5}\right)\left(\frac{\mu_5}{T}\right)^2 H(T)\,, \tag{16}$$

The total rate $R_c - R_r$ reaches its maximum value $R_{\max} = \eta k_5^2/4$ at $k = k_5/2$ which for

$$\frac{\mu_5}{T} \gtrsim 10^{-5}\left(\frac{T}{\mathrm{TeV}}\right)^{1/2} \tag{17}$$

is larger than the Hubble rate. Furthermore, Eq. (12) shows that for growing modes $|\mu_5|$ shrinks for either sign of μ_5. Therefore, the **chiral magnetic instability transforms energy in the electron asymmetry N_5 into magnetic energy**. This is because by definition of the chemical potential μ_5 the energy U_5 associated with the chiral lepton asymmetry is given by

$$dU_5 = \mu_5 dN_5 = Vc(T,\mu_e)\mu_5 d\mu_5\,, \quad U_5 = \frac{Vc(T,\mu_e)\mu_5^2}{2}\,. \tag{18}$$

Now assume that initially $\mu_5 = \mu_{5,i}$ and $U_B = 0$. Since the sign of $d\mu_5$ is opposite to the sign of $\mu_{5,i}$, Eq. (9) implies that the magnetic helicity will have the opposite sign as $\mu_{5,i}$. The growth rate peaks at wavenumber $k = k_5/2$ given by Eq. (13) and for a given mode k growth stops once $|\mu_5|$ has decreased to the point that Eq. (13) is violated. Since the instability produces maximally helical fields saturating Eq. (15), with Eq. (9) we obtain

$$\begin{aligned} dU_B &\simeq dM_{k_5} \simeq k_5|dH_{k_5}|/(8\pi) \simeq k_5|d\mathcal{H}|/(8\pi) = Vc(T,\mu_e)\mu_5 d\mu_5\,,\\ \Delta E_m &\simeq \frac{Vc(T,\mu_e)(\mu_{5,i}^2-\mu_5^2)}{2}\,. \end{aligned} \tag{19}$$

Adding Eqs. (18) and (19) gives a total energy $U_{\mathrm{tot}} = U_5 + U_B \simeq Vc(T,\mu_e)\mu_{5,i}^2/2$ which only depends on $\mu_{5,i}$. The maximal magnetic energy density then becomes

$$\frac{\Delta U_B}{V} \lesssim \frac{c(T,\mu_e)\mu_{5,i}^2}{2} \simeq \frac{\mu_{5,i}^2 T^2}{6}\,, \tag{20}$$

where the last expression follows from Eq. (8). Eq. (12) implies that $\partial_t\mu_5 = 0$ if

$$\tilde{\mu}_5 = \frac{R_f\mu_{5,b} - \frac{2e^2\eta}{\pi c(T,\mu_e)}\int d\ln k\, k\frac{M_k}{V}\left(\frac{H_k}{8\pi M_k/k}\right)}{R_f + \frac{4e^4\eta}{\pi^2 c(T,\mu_e)}\frac{U_B}{V}}\,, \tag{21}$$

where H_k has again be normalized to its maximal value given by Eq. (15). For negligible magnetic fields $\tilde{\mu}_5 \simeq \mu_{5,b}$, as expected and magnetic field modes with $k < k_5(\mu_{5,b})$ are growing exponentially with rate $R_c(k) - R_r$ given by Eq. (16). The magnetic field terms start to dominate for

$$\frac{U_B}{V} \gtrsim \frac{c(T,\mu_e)R_f}{4e^4\eta} \simeq \frac{10\pi}{3e^4}T^2 m_e^2 \simeq 2\times 10^5 T^2 m_e^2\,, \tag{22}$$

In this case Eq. (21) gives

$$\tilde{\mu}_5 \simeq -\frac{\pi}{2e^2 U_B}\int d\ln k\, k M_k\left(\frac{H_k}{8\pi M_k/k}\right)\,. \tag{23}$$

This is what in Ref. [16] was discussed as a so-called *tracking solution*. Note that $\tilde{\mu}_5$ from Eq. (21) varies with rates in general much slower than R_f and R_c. Also, since in general $\tilde{\mu}_5 \neq \mu_{5,b}$, the two terms in Eq. (12) do not vanish separately but only tend to compensate each other and are both roughly constant since μ_5 is approximately constant. Since at saturation, Eq. (23), the first term in Eq. (12) vanishes. Thus μ_5 and due to Eqs. (9) also the magnetic helicity change linearly in time with

$$\partial_t \mathcal{H} \simeq \frac{8\pi^2 V c(T,\mu_e)}{e^2} R_f (\mu_5 - \mu_{5,b})\,. \tag{24}$$

Since helicity is nearly maximal this also implies that the magnetic energy also roughly grows or decreases linearly with time, depending on the sign of $(\mu_5 - \mu_{5,b})/\mathcal{H}$.

Combining Eqs. (6), (12) and (18) the rate of change of the total energy is

$$\begin{aligned} \partial_t U_{\rm tot} &= \partial_t U_B + \partial_t U_5 = \\ &= -2\eta \int d\ln k M_k \left\{ (k-k_5)^2 + 2k_5 k \left[\left(\frac{H_k}{8\pi M_k/k} \right) \mathrm{sign}(\mu_5) + 1 \right] \right\} \\ &\quad -2R_f V c(T,\mu_e)\mu_5 \left(\mu_5 - \mu_{5,b}\right)\,, \end{aligned} \tag{25}$$

where $k_5 = k_5(\mu_5)$ is given by Eq. (13). Since the expression in large braces is non-negative due to Eq. (15), up to the term proportional to $\mu_{5,b}$ which describes a possible energy exchange with external particles, the total energy can only decrease due to the finite resistivity and the chirality-flip rate. The only equilibrium state with $\partial_t U_{\rm tot} = 0$ is given by $\mu_5 = \mu_{5,b}$ and a magnetic energy concentrated in the mode $k = k_0 = k_5(\mu_{5,b})$ with maximal magnetic helicity with the opposite sign as $\mu_{5,b}$, $H_{k_0} = \mathrm{sign}(\mu_{5,b}) 8\pi M_{k_0}/k_0$.

The evolution of $\mu_{5,b}$ due to energy exchange with the background matter can be modeled as follows: In absence of magnetic fields multiplying Eq. (12) with $c(T,\mu_e)$ and using Eq. (8) gives

$$\partial_t n_5 = -2R_f [n_5 - c(T,\mu_e)\mu_{5,b}] = \pm R_w n_b - 2R_f n_5\,, \tag{26}$$

where the gain term was written as a parity breaking electroweak rate R_w times the number density n_b of the background lepton species. This implies

$$n_b = 2c(T,\mu_e)\frac{R_f}{R_w}|\mu_{5,b}|\,, \quad \frac{|\mu_{5,b}|}{T} \simeq 0.1 g_b \frac{R_w}{R_f}\,, \tag{27}$$

where the second expression holds for g_b non-degenerate relativistic fermionic degrees of freedom. The energy U_b associated with these background particles is thus given by

$$\frac{U_b}{V} = \int_0^{\mu_{5,b}} \mu'_{5,b} dn_b = \frac{R_f}{R_w} c(T,\mu_e)\mu_{5,b}^2 \sim 3\times 10^{-3} g_b^2 \frac{R_w}{R_f} T^4\,, \tag{28}$$

where the last expression again holds in the non-degenerate relativistic case. Note that for $\mu_{5,i} \sim \mu_{5,b} \sim (R_w/R_f)T$ Eq. (28) is of order $(R_w/R_f)T^4$ whereas U_5 from Eq. (18) is of order $(R_w/R_f)^2 T^4$. Both energies vanish in the limit of parity conservation, $R_w \to 0$, as it should be. In terms of initial equilibrium chiral potential $\mu_{5,bi}$ and for $R_w \lesssim R_f$ the maximal magnetic energy is then

$$\frac{\Delta U_B}{V} \lesssim \frac{R_f}{R_w} c(T,\mu_e)\mu_{5,bi}^2 \sim 3\times 10^{-3} g_b^2 \frac{R_w}{R_f} T^4\,. \tag{29}$$

Setting $\partial_t U_b = -\partial_t U_5$ to conserve energy and equating $\partial_t U_5$ with the last term in Eq. (25) yields an equation for the evolution of $\mu_{5,b}$,

$$\partial_t \mu_{5,b} = R_w \frac{\mu_5}{\mu_{5,b}} (\mu_5 - \mu_{5,b}) \,. \tag{30}$$

When U_b is included in $U_{\rm tot}$ the second term in Eq. (25) is absent in the time derivative of $U_{\rm tot}$. The total energy is then dissipated exclusively through resistive magnetic field damping. Eq. (30) indicates that $\mu_{5,b}$ typically changes with the rate R_w. A stationary state is reached if $\mu_{5,b} = \mu_5$ and the magnetic field concentrates in $k_5 = k_5(\mu_{5,b})$ with maximal helicity of sign opposite to $\mu_{5,b}$. This requires magnetic field growth rates larger than the Hubble rate, see Eq. (17).

The chemical potential μ_5 is continuously recreated with a rate $R_f \mu_{5,b} \sim 0.1 g_b R_w T$, see Eq. (27), and a time-independent or slowly varying μ_5 can be established which is given by Eq. (21). This can be the case, for example, in a supernova or a neutron star due to URCA processes which absorb left-chiral electrons with a rate R_w and turn them into neutrinos that subsequently escape the star.

Due to Eq. (6) amplification stops and resistive damping sets in when $2\eta k_5^2 t \sim 1$, thus

$$k_5 \sim k_5^0 \left(\frac{t_0}{t}\right)^{1/2} , \quad \mu_5 \sim \mu_5^0 \left(\frac{t_0}{t}\right)^{1/2} . \tag{31}$$

4 The chiral magnetic effect in the presence of turbulent velocity fields

In the drag time approximation the Lorentz force induces a velocity

$$\mathbf{v} \sim \tau_d \frac{\mathbf{j} \times \mathbf{B}}{p + \rho} = \tau_d \frac{(\boldsymbol{\nabla} \times \mathbf{B}) \times \mathbf{B}}{p + \rho} \,, \tag{32}$$

where τ_d is the response or drag time. Assuming Gaussian closure and performing the relevant Wick contractions following Campanelli this generalizes Eq. (6) to

$$\begin{aligned} \partial_t M_k &= -2\eta_{\rm eff} k^2 M_k + \frac{\alpha_+}{4\pi} k^2 H_k \,, \\ \partial_t H_k &= -2\eta_{\rm eff} k^2 H_k + 16\pi \alpha_- M_k \,, \end{aligned} \tag{33}$$

where

$$\begin{aligned} \eta_{\rm eff} &= \eta + \frac{4}{3} \tau_d \frac{U_B/V}{p + \rho} \\ \alpha_\pm &= \frac{2\eta e^2 \mu_5}{\pi} \mp \frac{1}{6} \frac{\tau_d}{p + \rho} \int d \ln k k^2 \frac{H_k}{V} \,, \end{aligned} \tag{34}$$

with V the volume of the system, see also Ref. [17].

However, Eq. (34) only holds for unpolarized magnetic fields, whereas in the limit of maximally helical fields Eq. (32) vanishes ! Thus Eqs. (33) are only applicable if the chiral effect is sub-dominant.

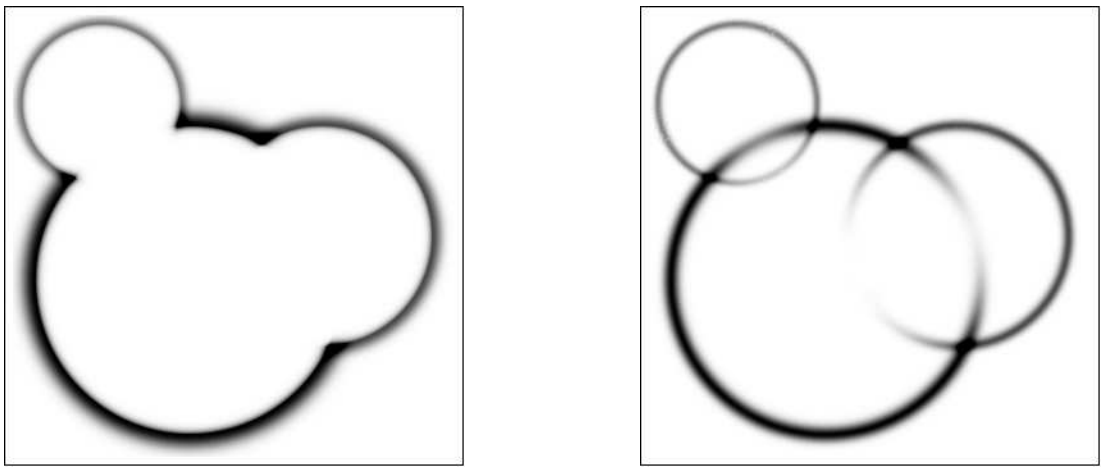


Figure 2: The plots show two sketches of the energy distribution in the envelope (left) and bulk flow (right) approximations. Figures reprinted from Ref. [18]. © 2018 IOP Publishing Ltd and Sissa Medialab.

5 Gravitational waves from hydrodynamics at cosmological phase transitions

One of the most intriguing links between cosmological phase transitions and particle physics are gravitational waves. In case a cosmological phase transition is 1st order, the nucleated bubbles expand and collide towards the end of the phase transition. The latent heat is thereby transformed into kinetic motion of the Higgs field and the plasma. In case the latent heat makes a sizeable fraction of the total energy of the plasma, this can lead to gravitational wave production that is potentially observable with space-based laser interferometers. To assess this effect in the context of the LISA mission is part of the cosmology working group. Several members of C10 are actively involved in this programme [19].

Several effects contribute hereby to the final gravitational wave spectrum. This includes the kinetic energy in the Higgs field itself and the kinetic energy in the plasma. The latter has contributions from sound waves as well as from turbulent motion. The dynamics of the plasma is very rich and in state-of-the-art calculations, the plasma is simulated on a lattice and evolved numerically using a computer cluster. However, also these simulations have technical limitations. Simplified models can overcome these limitations and eventually allow a better understanding of the gravitational wave production. In Ref. [18] the gravitational wave production was quantified in two simplified models. The first is the so-called envelope approximation that dates back to the first papers on the topic [20]. The second is a bulk flow model that takes into account the motion of the plasma after the phase transition is completed. Figure2 shows a sketch of the energy distribution in the two approximations. Due to the simplicity of the model, the resulting GW spectrum can be easily expressed as a function of the characteristics of the phase transition. Figure 3 shows the resulting GW spectrum in the bulk flow model.

Also for the production of GW radiation, model building is an important activity. In particular, it is interesting to assess to what extent models that are appealing due to other

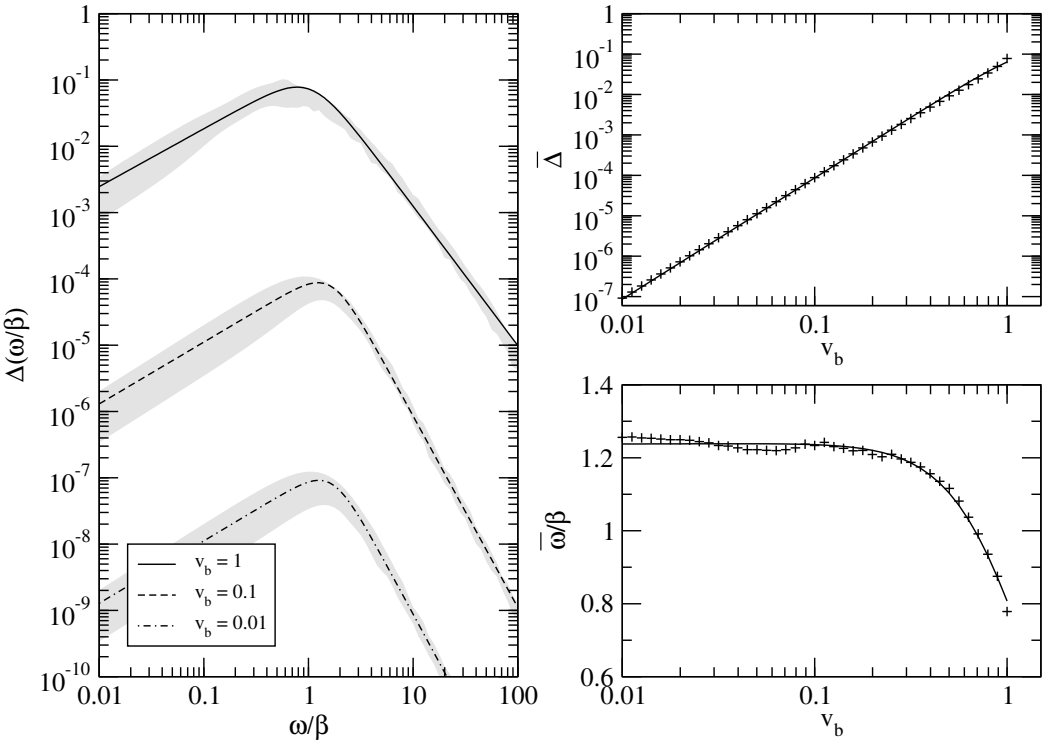


Figure 3: The spectrum of GW as produced by the fluid model. The dependence on the characteristics of the phase transition is almost trivial and can be obtained by rescaling. Figures reprinted from Ref. [18]. © 2018 IOP Publishing Ltd and Sissa Medialab.

model building aspects (e.g. dark matter, baryogenesis, ...) can lead to observable GW signals. One such study was presented in [12] in a singlet extension of the minimal supersymmetric Standard Model that is known to facilitate a good dark matter candidate and electroweak baryogenesis.

In Ref. [21] we calculated the spectrum of gravitational waves originating from a 1st-order phase transition in the primordial cosmological plasma due to magnetohydrodynamic fluctuations. There, we included for the first time the "sweeping effect", which dominates the decorrelation of hydrodynamic fluctuations in turbulent flows. This effect leads to a significant reduction of the gravitational wave spectrum in comparison to previous studies. Moreover, we find that the shape of the spectrum itself depends on the maximal amplitude of the turbulent spectrum and at frequencies larger than the peak frequency the spectrum generally follows a broken power law. This is in contrast to previous studies which considered simple power laws for the limiting case of very small or very large energy scales. We also studied the impact of magnetic helicity on the spectrum and find, in qualitative agreements with previous studies, that magnetic helicity leads to an increase of the gravitational wave spectral energy density at smaller frequencies. Furthermore, we investigated the gravitational wave spectrum caused by compressible turbulence. For the first time, we studied the resulting spectrum in the unified picture of purely compressible (sound waves) and incompressible modes. Until now, these two

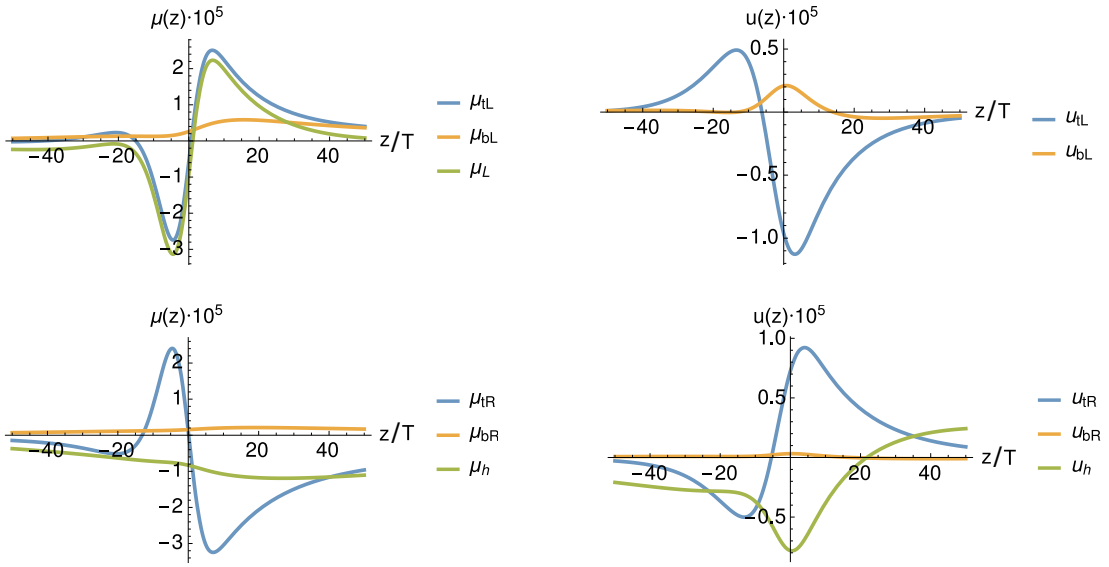


Figure 4: Chemical potentials μ (left) and velocity fields u (right) induced by a varying complex Top quark Yukawa coupling. The upper graphs show the left-handed particle species (and the total left-handed chemical potential) while the lower graphs show the right-handed species and the Higgs. Figures reprinted from Ref. [22]. © 2017 IOP Publishing Ltd and Sissa Medialab.

source terms have been treated independently. Ultimately, we find that the "sweeping effect" due to incompressible modes affects the spectrum driven by purely compressible modes, even if compressible modes are dominant. This leads to a flatter high frequency spectrum and an overall reduced peak amplitude of the gravitational wave spectrum.

6 Electroweak baryogenesis

Any baryogenesis mechanism aims at explaining the apparent disparity between matter and anti-matter. The required ingredients for such a mechanism are a violation of charge and charge-parity conjugation as well as a non-equilibrium situation. The latter ingredients makes a 1st-order cosmological phase transition an interesting target. The resulting baryogenesis mechanism is called electroweak baryogenesis [23].

Since electroweak baryogenesis is based on the non-equilibrium nature of the plasma during the phase transition, it has to be assessed in a framework that can handle genuine quantum effects (CP violation) away from equilibrium. Nowadays, this is achieved using the Schwinger–Keldysh formalism which is an out-of-equilibrium formulation of quantum field theory. In the context of electroweak baryogenesis, the resulting equations are often called quantum (or semi-classical) transport equations (for a review on the topic see [24]).

These quantum transport equations are specific to the model at hand. For example, in the case of Froggatt–Nielsen models mentioned earlier, the Yukawa couplings vary during the phase transition what leads to a very rich phenomenology and new effects in baryogenesis [22].

Figure 4 shows the chemical potentials and the bulk velocity close to the expanding bubbles walls. A mismatch between left- and right- handed chemical potentials is induced by CP-violating interactions in the wall and finally drives the production of the baryon asymmetry.

7 Summary

Cosmological phase transitions of first order have a rich phenomenology and provide many interesting links between cosmology and particle physics. Even though the theoretical foundations are well understood, the field is still in its infancy when it comes to observations. Hopefully, this will change in the near future, with input from particle collider experiments, gravitational wave observatories or a better understanding of magnetic fields in the early Universe.

References

[1] VIRGO, LIGO SCIENTIFIC Collaborations, B. P. Abbott et al., *Observation of Gravitational Waves from a Binary Black Hole Merger*, *Phys. Rev. Lett.* **116** (2016) 061102, [1602.03837].

[2] GROND, SALT GROUP, OzGrav, DFN, INTEGRAL, VIRGO, INSIGHT-HXMT, MAXI TEAM, FERMI-LAT, J-GEM, RATIR, ICECUBE, CAASTRO, LWA, ePESSTO, GRAWITA, RIMAS, SKA SOUTH AFRICA/MEERKAT, H.E.S.S., 1M2H TEAM, IKI-GW FOLLOW-UP, FERMI GBM, PI OF SKY, DWF (DEEPER WIDER FASTER PROGRAM), DARK ENERGY SURVEY, MASTER, ASTROSAT CADMIUM ZINC TELLURIDE IMAGER TEAM, SWIFT, PIERRE AUGER, ASKAP, VINROUGE, JAGWAR, CHANDRA TEAM AT MCGILL UNIVERSITY, TTU-NRAO, GROWTH, AGILE TEAM, MWA, ATCA, AST3, TOROS, PAN-STARRS, NUSTAR, ATLAS TELESCOPES, BOOTES, CALTECHNRAO, LIGO SCIENTIFIC, HIGH TIME RESOLUTION UNIVERSE SURVEY, NORDIC OPTICAL TELESCOPE, LAS CUMBRES OBSERVATORY GROUP, TZAC CONSORTIUM, LOFAR, IPN, DLT40, TEXAS TECH UNIVERSITY, HAWC, ANTARES, KU, DARK ENERGY CAMERA GW-EM, CALET, EURO VLBI TEAM, ALMA, B. P. Abbott et al., *Multi-messenger Observations of a Binary Neutron Star Merger*, *Astrophys. J.* **848** (2017) L12, [1710.05833].

[3] J. R. Espinosa, M. Garny, T. Konstandin and A. Riotto, *Gauge-Independent Scales Related to the Standard Model Vacuum Instability*, *Phys. Rev.* **D95** (2017) 056004, [1608.06765].

[4] R. Jackiw, *Functional evaluation of the effective potential*, *Phys. Rev.* **D9** (1974) 1686.

[5] J. Elias-Miro, J. R. Espinosa and T. Konstandin, *Taming Infrared Divergences in the Effective Potential*, *JHEP* **08** (2014) 034, [1406.2652].

[6] J. R. Espinosa and T. Konstandin, *Resummation of Goldstone Infrared Divergences: A Proof to All Orders*, 1712.08068.

[7] M. Garny and T. Konstandin, *On the gauge dependence of vacuum transitions at finite temperature*, *JHEP* **07** (2012) 189, [1205.3392].

[8] J. R. Espinosa, M. Garny and T. Konstandin, *Interplay of Infrared Divergences and Gauge-Dependence of the Effective Potential*, *Phys. Rev.* **D94** (2016) 055026, [1607.08432].

[9] G. D. Moore and T. Prokopec, *How fast can the wall move? A Study of the electroweak phase transition dynamics*, *Phys. Rev.* **D52** (1995) 7182–7204, [hep-ph/9506475].

[10] T. Konstandin, G. Nardini and I. Rues, *From Boltzmann equations to steady wall velocities*, *JCAP* **1409** (2014) 028, [1407.3132].

[11] G. C. Dorsch, S. J. Huber, T. Konstandin and J. M. No, *A Second Higgs Doublet in the Early Universe: Baryogenesis and Gravitational Waves*, *JCAP* **1705** (2017) 052, [1611.05874].

[12] S. J. Huber, T. Konstandin, G. Nardini and I. Rues, *Detectable Gravitational Waves from Very Strong Phase Transitions in the General NMSSM*, *JCAP* **1603** (2016) 036, [1512.06357].

[13] I. Baldes, T. Konstandin and G. Servant, *A First-Order Electroweak Phase Transition in the Standard Model from Varying Yukawas*, 1604.04526.

[14] P. Pavlović, N. Leite and G. Sigl, *Modified Magnetohydrodynamics Around the Electroweak Transition*, *JCAP* **1606** (2016) 044, [1602.08419].

[15] P. Pavlović, N. Leite and G. Sigl, *Chiral Magnetohydrodynamic Turbulence*, *Phys. Rev.* **D96** (2017) 023504, [1612.07382].

[16] A. Boyarsky, J. Frohlich and O. Ruchayskiy, *Self-consistent evolution of magnetic fields and chiral asymmetry in the early Universe*, *Phys. Rev. Lett.* **108** (2012) 031301, [1109.3350].

[17] M. Dvornikov and V. B. Semikoz, *Influence of the turbulent motion on the chiral magnetic effect in the early Universe*, *Phys. Rev.* **D95** (2017) 043538, [1612.05897].

[18] T. Konstandin, *Gravitational radiation from a bulk flow model*, *JCAP* **1803** (2018) 047, [1712.06869].

[19] C. Caprini et al., *Science with the space-based interferometer eLISA. II: Gravitational waves from cosmological phase transitions*, *JCAP* **1604** (2016) 001, [1512.06239].

[20] A. Kosowsky and M. S. Turner, *Gravitational radiation from colliding vacuum bubbles: envelope approximation to many bubble collisions*, *Phys. Rev.* **D47** (1993) 4372–4391, [astro-ph/9211004].

[21] P. Niksa, M. Schlederer and G. Sigl, *Gravitational Waves produced by Compressible MHD Turbulence from Cosmological Phase Transitions*, *Class. Quant. Grav.* **35** (2018) 144001, [1803.02271].

[22] S. Bruggisser, T. Konstandin and G. Servant, *CP-violation for Electroweak Baryogenesis from Dynamical CKM Matrix*, *JCAP* **1711** (2017) 034, [1706.08534].

[23] V. A. Kuzmin, V. A. Rubakov and M. E. Shaposhnikov, *On the Anomalous Electroweak Baryon Number Nonconservation in the Early Universe*, *Phys. Lett.* **155B** (1985) 36.

[24] T. Konstandin, *Quantum Transport and Electroweak Baryogenesis*, *Phys.Usp.* **56** (2013) 747–771, [1302.6713].

List of Authors

Arutyunov, Gleb, 103

Bagnaschi, Emanuele, 203
Banerjee, Robi, 387
Bartels, Jochen, 19
Bechtle, Philip, 203
Bein, Sam, 169
Boels, Rutger H., 69
Brüggen, Marcus, 301
Buchmüller, Wilfried, 3, 317

Cortés, Vicente, 57

Fredenhagen, Klaus, 363

Hack, Thomas-Paul, 363
Haller, Johannes, 155, 203
Hauschildt, Peter, 333
Horns, Dieter, 285, 301

Kersten, Jörn, 271
Kniehl, Bernd A., 69, 189
Kogler, Roman, 155, 203
Konstandin, Thomas, 407
Kummer, Jannis, 301

List, Jenny, 125
Lobanov, Andrei, 285
Louis, Jan, 3, 57, 341

Mirizzi, Alessandro, 179
Moch, Sven-Olaf, 19, 255
Moortgat-Pick, Gudrid, 125

Nguyen, Le Hoang, 285

Peiffer, Thomas, 203
Pinamonti, Nicola, 363

Reuter, Jürgen, 125, 255
Ringwald, Andreas, 285

Runkel, Ingo, 103

Sander, Christian, 169
Schleper, Peter, 169, 231
Schomerus, Volker, 19
Schweigert, Christoph, 39, 89
Sigl, Günter, 379, 387, 407
Spiering, Christian, 301
Stefaniak, Tim, 203

Tackmann, Frank J., 155
Tackmann, Kerstin, 231
Teschner, Jörg, 89, 103

Waldorf, Konrad, 39
Weiglein, Georg, 203, 231
Westphal, Alexander, 341

Zhang, Chao, 301